ORGANELLE TARGETING: FOCUS ON DRUG DISCOVERY AND THERANOSTICS

EDITED BY: Qixin Chen, Fengshan Wang, Peixue Ling and Jiajie Diao
PUBLISHED IN: Frontiers in Pharmacology

frontiers Research Topics

Frontiers eBook Copyright Statement

The copyright in the text of individual articles in this eBook is the property of their respective authors or their respective institutions or funders. The copyright in graphics and images within each article may be subject to copyright of other parties. In both cases this is subject to a license granted to Frontiers.

The compilation of articles constituting this eBook is the property of Frontiers.

Each article within this eBook, and the eBook itself, are published under the most recent version of the Creative Commons CC-BY licence. The version current at the date of publication of this eBook is CC-BY 4.0. If the CC-BY licence is updated, the licence granted by Frontiers is automatically updated to the new version.

When exercising any right under the CC-BY licence, Frontiers must be attributed as the original publisher of the article or eBook, as applicable.

Authors have the responsibility of ensuring that any graphics or other materials which are the property of others may be included in the CC-BY licence, but this should be checked before relying on the CC-BY licence to reproduce those materials. Any copyright notices relating to those materials must be complied with.

Copyright and source acknowledgement notices may not be removed and must be displayed in any copy, derivative work or partial copy which includes the elements in question.

All copyright, and all rights therein, are protected by national and international copyright laws. The above represents a summary only. For further information please read Frontiers' Conditions for Website Use and Copyright Statement, and the applicable CC-BY licence.

ISSN 1664-8714
ISBN 978-2-83250-488-8
DOI 10.3389/978-2-83250-488-8

About Frontiers

Frontiers is more than just an open-access publisher of scholarly articles: it is a pioneering approach to the world of academia, radically improving the way scholarly research is managed. The grand vision of Frontiers is a world where all people have an equal opportunity to seek, share and generate knowledge. Frontiers provides immediate and permanent online open access to all its publications, but this alone is not enough to realize our grand goals.

Frontiers Journal Series

The Frontiers Journal Series is a multi-tier and interdisciplinary set of open-access, online journals, promising a paradigm shift from the current review, selection and dissemination processes in academic publishing. All Frontiers journals are driven by researchers for researchers; therefore, they constitute a service to the scholarly community. At the same time, the Frontiers Journal Series operates on a revolutionary invention, the tiered publishing system, initially addressing specific communities of scholars, and gradually climbing up to broader public understanding, thus serving the interests of the lay society, too.

Dedication to Quality

Each Frontiers article is a landmark of the highest quality, thanks to genuinely collaborative interactions between authors and review editors, who include some of the world's best academicians. Research must be certified by peers before entering a stream of knowledge that may eventually reach the public - and shape society; therefore, Frontiers only applies the most rigorous and unbiased reviews.
Frontiers revolutionizes research publishing by freely delivering the most outstanding research, evaluated with no bias from both the academic and social point of view. By applying the most advanced information technologies, Frontiers is catapulting scholarly publishing into a new generation.

What are Frontiers Research Topics?

Frontiers Research Topics are very popular trademarks of the Frontiers Journals Series: they are collections of at least ten articles, all centered on a particular subject. With their unique mix of varied contributions from Original Research to Review Articles, Frontiers Research Topics unify the most influential researchers, the latest key findings and historical advances in a hot research area! Find out more on how to host your own Frontiers Research Topic or contribute to one as an author by contacting the Frontiers Editorial Office: frontiersin.org/about/contact

ORGANELLE TARGETING: FOCUS ON DRUG DISCOVERY AND THERANOSTICS

Topic Editors:
Qixin Chen, Shandong First Medical University, China
Fengshan Wang, Shandong University, China
Peixue Ling, Shandong University (Qingdao), China
Jiajie Diao, University of Cincinnati, United States

Citation: Chen, Q., Wang, F., Ling, P., Diao, J., eds. (2022). Organelle Targeting: Focus on Drug Discovery and Theranostics. Lausanne: Frontiers Media SA. doi: 10.3389/978-2-83250-488-8

Table of Contents

05 ***An NIR-Triggered Au Nanocage Used for Photo-Thermo Therapy of Chronic Wound in Diabetic Rats Through Bacterial Membrane Destruction and Skin Cell Mitochondrial Protection***
Jiaxin Ding, Binbin Gao, Zhenhua Chen and Xifan Mei

17 ***Opioids Regulate the Immune System: Focusing on Macrophages and Their Organelles***
Shaohua Wen, Yuan Jiang, Shuang Liang, Zhigang Cheng, Xiaoyan Zhu and Qulian Guo

33 ***Polyadenylated Telomeric Noncoding RNA Functions as a Pivotal Therapeutic Target of Anti-Ageing to Stabilize Telomere Length of Chromosomes* Via *Collaborating With Zscan4c***
Xiaojuan Xu, Zhengju Chen, Wei Wu and Xiaohe Tian

43 ***Efficient Synthesis of 2,3′-Spirobi (Indolin)-2′-Ones and Preliminary Evaluation of Their Damage to Mitochondria in HeLa Cells***
Huajie Li, Zhenjie Yu, Haoyi Sun, Bo Liu, Xin Wang, Zhe Shao, Meiling Wang, Weilin Xie, Xingang Yao, Qingqiang Yao and Ying Zhi

53 ***Lysosome-Targeted Biosensor for the Super-Resolution Imaging of Lysosome–Mitochondrion Interaction***
Han Wang, Guiqian Fang, Huimin Chen, Maomao Hu, Yajuan Cui, Boyang Wang, Yudong Su, Yu Liu, Bo Dong and Xintian Shao

63 ***Restoration of Sarco/Endoplasmic Reticulum Ca^{2+}-ATPase Activity Functions as a Pivotal Therapeutic Target of Anti-Glutamate-Induced Excitotoxicity to Attenuate Endoplasmic Reticulum Ca^{2+} Depletion***
Wen Zhang, Fanghua Ye, Nan Pang, Miriam Kessi, Juan Xiong, Shimeng Chen, Jing Peng, Li Yang and Fei Yin

78 ***A Dual-Labeling Probe for Super-Resolution Imaging to Detect Mitochondrial Reactive Sulfur Species in Live Cells***
Maomao Hu, Boyang Wang, Hongdan Zhang, Han Wang, Huixin Li, Xinyu Zhang, Jinjin Zhang, Qianrun Lu, Guiqian Fang, Juan Wang and Bo Dong

86 ***An Endoplasmic Reticulum-Targeted Ratiometric Fluorescent Molecule Reveals Zn^{2+} Micro-Dynamics During Drug-Induced Organelle Ionic Disorder***
Hongbao Fang, Yaheng Li, Shankun Yao, Shanshan Geng, Yuncong Chen, Zijian Guo and Weijiang He

94 ***Organelle Interaction and Drug Discovery: Towards Correlative Nanoscopy and Molecular Dynamics Simulation***
Zhiwei Yang, Zichen Zhang, Yizhen Zhao, Qiushi Ye, Xuhua Li, Lingjie Meng, Jiangang Long, Shengli Zhang and Lei Zhang

107 ***Super-Resolution Quantification of T2DM-Induced Mitochondrial Morphology Changes and Their Implications in Pharmacodynamics of Metformin and Sorafenib***
Yang Du, Ya-Juan Zhu, Bo Zeng, Xiao-Li Mu and Ji-Yan Liu

114 ***Optical Visualization of Red-GQDs' Organelles Distribution and Localization in Living Cells***
Haifeng Hu, Peng Li, Jie Qiu, Meiji Zhao, Mingjie Kuang, Zhaoyan Zhang and Dachuan Wang

125 ***Fluorescent Probes Design Strategies for Imaging Mitochondria and Lysosomes***
Huimin Chen, Zhenjie Yu, Shiwei Ren and Yuyu Qiu

140 ***Nodosin Exerts an Anti-Colorectal Cancer Effect by Inhibiting Proliferation and Triggering Complex Cell Death* in Vitro *and* in Vivo**
Huixia Fan, Xiaopeng Hao, Yuan Gao, Jian Yang, Aojun Liu, Yarui Su and Yong Xia

155 ***Exosome Derived From Stem Cell: A Promising Therapeutics for Wound Healing***
Hui Lv, Hanxiao Liu, Ting Sun, Han Wang, Xiao Zhang and Wei Xu

167 ***Raman and Fluorescence Micro-Spectroscopy Applied for the Monitoring of Sunitinib-Loaded Porous Silicon Nanocontainers in Cardiac Cells***
E. Tolstik, M. B. Gongalsky, J. Dierks, T. Brand, M. Pernecker, N. V. Pervushin, D. E. Maksutova, K. A. Gonchar, J. V. Samsonova, G. Kopeina, V. Sivakov, L. A. Osminkina and K. Lorenz

frontiers in Pharmacology

ORIGINAL RESEARCH
published: 30 November 2021
doi: 10.3389/fphar.2021.779944

An NIR-Triggered Au Nanocage Used for Photo-Thermo Therapy of Chronic Wound in Diabetic Rats Through Bacterial Membrane Destruction and Skin Cell Mitochondrial Protection

Jiaxin Ding[1], *Binbin Gao*[2], *Zhenhua Chen*[1]* *and Xifan Mei*[1]*

[1]Jinzhou Medical University, Jinzhou, China, [2]Jinzhou Central Hospital, Jinzhou, China

OPEN ACCESS

Edited by:
Qixin Chen,
Shandong First Medical University, China

Reviewed by:
Huaiying Zhang,
University Medical Center Groningen, Netherlands
Zhiyong Wang,
Sun Yat-sen University, China
Xuelian Huang,
University of Washington, United States

***Correspondence:**
Zhenhua Chen
zhchen561@yahoo.com
Xifan Mei
meixifan1971@163.com

Specialty section:
This article was submitted to Pharmacology of Anti-Cancer Drugs, a section of the journal Frontiers in Pharmacology

Received: 20 September 2021
Accepted: 28 October 2021
Published: 30 November 2021

Citation:
Ding J, Gao B, Chen Z and Mei X (2021) An NIR-Triggered Au Nanocage Used for Photo-Thermo Therapy of Chronic Wound in Diabetic Rats Through Bacterial Membrane Destruction and Skin Cell Mitochondrial Protection. Front. Pharmacol. 12:779944. doi: 10.3389/fphar.2021.779944

Bacterial infection and its severe oxidative stress reaction will cause damage to skin cell mitochondria, resulting in long-lasting wound healing and great pain to patients. Thus, delayed wound healing in diabetic patients with *Staphylococcus aureus* infection is a principal challenge worldwide. Therefore, novel biomaterials with multifunction of bacterial membrane destruction and skin cell mitochondrial protection are urgently needed to be developed to address this challenge. In this work, novel gold cage (AuNCs) modified with epigallocatechin gallate (EGCG) were prepared to treat delayed diabetic wounds. The results showed that Au-EGCG had a high and stable photothermal conversion efficiency under near-infrared irradiation, and the scavenging rate of Au-EGCG for *S. aureus* could reach 95%. The production of large amounts of reactive oxygen species (ROS) leads to the disruption of bacterial membranes, inducing bacterial lysis and apoptosis. Meanwhile, Au-EGCG fused into hydrogel (Au-EGCG@H) promoted the migration and proliferation of human umbilical cord endothelial cells, reduced cellular mitochondrial damage and oxidative stress in the presence of infection, and significantly increased the basic fibroblast growth factor expression and vascular endothelial growth factor. In addition, animal studies showed that wound closure was 97.2% after 12 days of treatment, and the healing of chronic diabetic wounds was significantly accelerated. Au-EGCG nanoplatforms were successfully prepared to promote cell migration and angiogenesis in diabetic rats while removing *S. aureus*, reducing oxidative stress in cells, and restoring impaired mitochondrial function. Au-EGCG provides an effective, biocompatible, and multifunctional therapeutic strategy for chronic diabetic wounds.

Keywords: gold nanocages, epigallocatechin gallate (EGCG), hydrogel, antibacterial, photo-thermotherapy, diabetic wound healing

INTRODUCTION

Long-lasting bacterial infection leads to severe oxidative stress and causes damage to skin cell mitochondria. Thus, antibacterial and mitochondrial protection of skin cells are the key factors for skin wound healing (Li et al., 2007; Wlaschek et al., 2019; Liang et al., 2021). Diabetes can cause damage to the microvascular endothelium and result in tissue hypoxia and ischemia, thus delaying

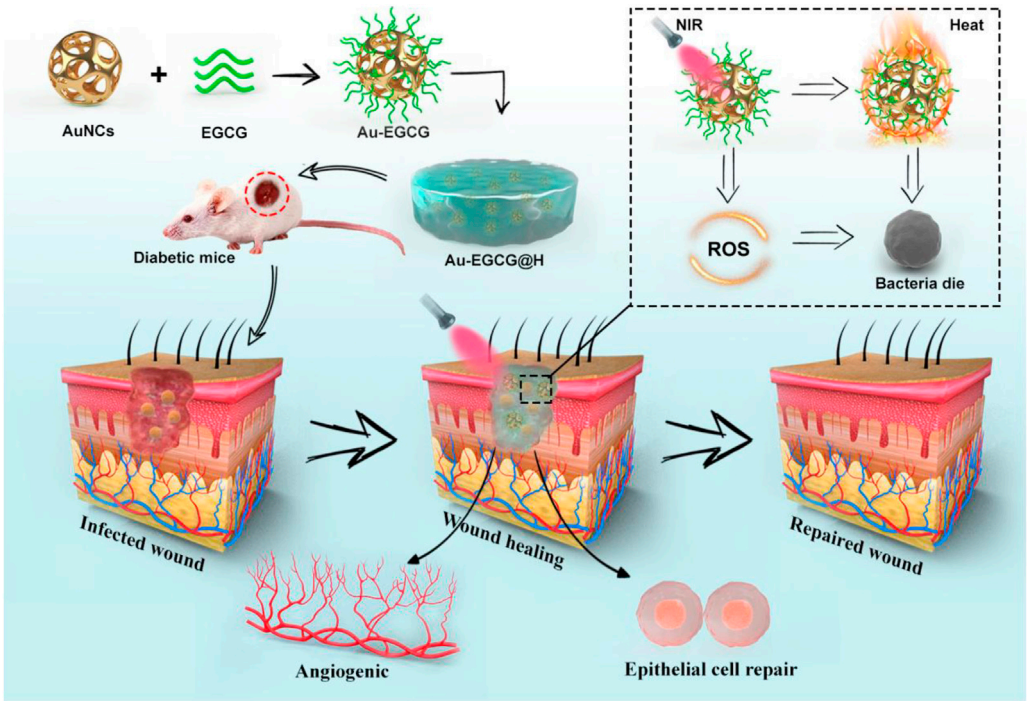

SCHEME 1 | The schematic illustration of the synthesis of Au-EGCG@H nanocomposite and the process of sterilization and stimulation of cell behaviors under NIR irradiation that can facilitate the regeneration of skin cells, involve in the regeneration of skin actively to promote the healing of chronic wounds of infected bacteria.

the wound healing and leading to chronic non-healing (YoonYoona et al., 2016; Zhao et al., 2017; Vanaeia et al., 2021). The management of chronic non-healing wounds in diabetes remains a major challenge for doctors, especially since chronic diabetic foot ulcers (DFU) have resulted in more than 73,000 non-traumatic lower-limb amputations, reducing quality of life with huge cost burden (Randeria et al., 2015; Kalan and Brennan, 2018; Arifuzzaman et al., 2019; Chin et al., 2019). Healthy skin is an effective barrier for the protection of the internal organs from pathogens. However, chronic non-healing wounds that are open, moist, and oozing provide the perfect environment for *Staphylococcus aureus* to settle. For the treatment of bacterial infection, the main clinical choice is to use antibiotics, but the excessive use of antibiotics will inevitably lead to drug resistance. Because of the complex healing environment of diabetic skin wounds, it is very promising to develop a multifunctional nanoplatform that can effectively promote wound healing without causing drug resistance.

Photo-thermotherapy (PTT), a new therapeutic strategy, has little effect on the whole body, owing to its penetration ability to the deep tissue and micro-invasiveness, along with a high spatial resolution of the near-infrared laser (NIR). Therefore, PTT can achieve effective local treatment (Qing et al., 2019; Sun et al., 2019; Wang et al., 2019). So far, metal nanostructures (such as nanoparticles, nanorods, and nanolayers) and two-dimensional (2D) nanomaterials (such as black phosphorus, Prussian blue, and copper sulfide) have been used as photothermic agents for near-infrared absorption. These excellent pioneer works disclosed the brilliant prospect of multifunctional nanoplatforms based on PTT strategy (Gupta et al., 2019; Chen et al., 2020a; Tong et al., 2020; Chang et al., 2021). It is well known that gold nanocages are the basic elements used by people for a long time, which is also a kind of photothermic agent. Gold nanocages have unique physicochemical properties (large surface volume ratio, high surface activity, and ultra-small size), are used in combination with two-dimensional nanomaterials to enhance their antibacterial and anti-inflammatory properties, and have been extensively employed in medical and food industries (Hu et al., 2021). In addition, the good biosafety and biocompatibility of gold nanocages have been proven (Wang et al., 2021). Epigallocatechin gallate (EGCG) is a polyphenol bioactive compound that has an inhibitory effect on the growth of Gram-negative bacteria and Gram-positive bacteria. EGCG also has the biological functions of anti-oxidation, enhancing immunity, and effectively promoting wound healing. However, the application of green tea polyphenols (GTP) is limited by its weak lipo-solubility, easy oxidation, and low activity in an alkaline solution (Krook and Hagerman, 2012; Li et al., 2012; Barbalho et al., 2019). Hydrogels are macromolecular biomaterials that absorb large amounts of water or other water-soluble substances; have excellent biocompatibility and biodegradability; and can deliver functional drugs, molecules, and cells in a variety of therapies. Hydrogel has been widely applied in the field of tissue engineering and medicine as the carrier of the sustained-release drug to protect the injured part from harmful stimulation, to keep the injured part moist, and to improve the drug utilization rate (Zhao et al., 2019a; Wu et al., 2019; Zhang et al., 2019; Chen et al., 2020b).

A NIR-triggered Au nanocage with functions of bacterial membrane destruction and skin cell mitochondrial protection was developed to solve these problems, as shown in **Scheme 1**. A stable drug dispersion system was prepared by loading EGCG onto hollow porous gold cage (AuNCs) and coating it uniformly in a novel hydrogel with excellent biocompatibility. We use Au-EGCG fused into hydrogel (Au-EGCG@H) in diabetic wounds with *Staphylococcus aureus* infection. The results showed that Au-EGCG@H possessed a high and stable photothermal conversion efficiency under NIR irradiation, and the generation of a large amount of reactive oxygen species (ROS) led to the destruction of the bacterial membranes, thereby inducing bacterial lysis and apoptosis. Meanwhile, Au-EGCG@H promoted the migration and proliferation of human umbilical cord endothelial cells, reduced oxidative stress in cells under infection, restored cellular mitochondrial function, and significantly increased the expression of basic fibroblast growth factor and vascular endothelial growth factor. The ability to promote epithelial repair will then be further tested in a combination of cell and animal studies. We hope that this composite nanomaterial system can protect the chronic non-healing wounds of diabetes from the interference of the external environment and at the same time it can promote the proliferation of endothelial cells and the repair of epithelia by eliminating bacteria through photothermal therapy, accelerating the repair of chronic non-healing wounds. More importantly, we also hope to develop a new, economical, safe, and multifunctional combination as an effective nanodrug platform treatment strategy.

MATERIALS AND METHODS

Materials

The fetal bovine serum (FBS), 3-(4,5-dimethylthiazol-2-yl)-2,5-diphenyl tetrazolium bromide (MTT), and Dulbecco's modified Eagle's medium (DMEM) were provided by Gibco (United States). From Beyotime, we obtained 2,7-dichlorodihydrofluorescein diacetate (DCFH-DA). The primary antibodies for glyceraldehyde 3-phosphate dehydrogenase (GAPDH), vascular endothelial growth factor (VEGF), and basic fibroblast growth factor (bFGF) were offered by Cell Signaling Technology (United States). From the American Type Culture Collection (ATCC), the human umbilical vein endothelial cells (HUVECs) and human skin keratinocyte cells (HACT) can be acquired. The ultrapure water was utilized in the whole experiment, which was acquired from the system of Milli-Q. The expression of relevant proteins in the cells was observed by confocal laser scanning microscopy (CLSM; Leica TSC SP5 confocal unit).

Preparation of Au-EGCG@H

We prepared the AuNCs and then combined them with EGCG to form Au-EGCG fused into the hydrogel. In short, we put 10 ml PVP (4 mg/ml) into a three-port flask and added 4 ml of silver nanoparticles. Then, the solution was heated in an oil bath (100°C, 500 r/min). After 15 min, $HAuCl_4$ (0.0543 mg/ml) was subsequently slowly added at 3 ml/min until the color of the reaction was stable. Washing the samples with saturated NaCl solution and deionized water, respectively, was done after cooling to room temperature. Subsequently, EGCG (2 ml, 50 μg/ml) was added to the prepared Au solution and then mixed for 2 h at room temperature (500 r/min) to form Au-EGCG. The samples were collected by centrifugation (12,000 rmp, 20 min). The hydrogel was prepared by adding 0.1 g to 10 ml PVA solution (8%), and then, the solution was stirred for 1 h (50°C, 350 r/min). Finally, Au-EGCG were fused into the hydrogel to obtain Au-EGCG@H.

Characterization

Dynamic laser scattering (DLS, Malvern, NanoZS90, Worcestershire, United Kingdom) and transmission electron microscopy (TEM, JEM-1200EX, Tokyo, Japan) were respectively employed to characterize the size and morphology of AuNCs. The crystallographic structure of AuNCs was demonstrated using a PXRD analysis (Shimadzu, Kyoto, Japan) applying Cu K radiation. Fourier transform infrared spectroscopy (FTIR, Shimadzu, Kyoto, Japan) was employed to explore the component of Au-EGCG@H utilizing the KBr disk approach. The fluorescence photometer (F97PRO, Shanghai, China) and UV-vis spectrophotometer (PerkinElmer Lambda 605S UV-vis spectrometer) were exploited to acquire fluorescence data and ultraviolet-visible data.

Photothermal Performance and Photothermal Stability of Au-EGCG@H

Thermo photographic research was used to assess the photothermal properties of Au-EGCG@H. We added Au-EGCG@H at various concentrations (50, 100, or 200 μg/ml), AuNCs, and water into centrifuge tubes. Then, we irradiated them with NIR laser (1 W/cm^2, 808 nm) for 10 min while recording the thermal images and temperature with an NIR thermal imager (ABFRX500) every 30 s. To evaluate the photothermal stability of Au-EGCG@H, AuNCs and Au-EGCG@H were warmed and cooled for three cycles. Each cycle irradiated them for 10 min while recording the temperature at intervals of 30 s.

Scratch Assay

The migration capability of HUVECs was measured *via* scratch detection. HUVECs were inoculated into 24-well plates (1×10^6 cells/well) and starved with FBS-free medium at 37°C (5% CO_2, 95% humidity). The tip of a sterile pipette was used, and the cells were scratched with a line at the bottom of the plate. Phosphate-buffered saline (PBS) was used to wash the floating debris and cells. Subsequently, HUVECs were treated with Au-EGCG@H, Au@H, or PBS, and then, they were incubated under a temperature of 37°C. Afterward, 4% paraformaldehyde (PFA) was utilized to fix HUVECs, and then, HUVECs were treated with 0.1% Triton X-100 (Sigma-Aldrich, United States) and stained by DAPI. An inverted Leica fluorescence microscope was exploited to take the migration images. After determining the distance of scratch healing, the migration images were quantified.

Immunofluorescence Staining

In each group, after the incubation, the HUVECs were cleaned three times by utilizing PBS. Afterward, the HUVECs were fixed for half an hour in 4% PFA. Next, the cells were cleaned in PBS for three times and incubated using Triton X-100 for 20 min. The cells were subsequently incubated utilizing goat serum for 2 h. After that, the treatment of the cells was conducted *via* the bFGF antibodies and primary anti-VEGF antibodies at 4°C overnight. Next, the incubation of cells was performed through Alexa Fluor 488 goat anti-rabbit IgG or Alexa Fluor 594 goat anti-mouse IgG at RT for 2 h. In the end, DAPI (Invitrogen, United States) was utilized to stain the nuclei for 20 min.

Au-EGCG@H *In Vitro* Antibacterial Efficiency

The antibacterial ability of near-infrared laser irradiation combined with nanomaterials was evaluated with *S. aureus*. In brief, 200 μl of Au-EGCG@H was mixed with 800 μl bacterial solution and incubated for 30 min. Afterward, we irradiated the solution by applying the NIR laser (808 nm, 2.5 W/cm^2, 5 min). Next, the treated bacterial suspension was diluted and then diffused onto the nutrient agars. After incubation for 1 day at 37°C, we can count the number of cloned bacteria.

Detection of ROS

The fluorescent probe DCFH-DA was provided by Beyotime to detect the intracellular levels of ROS of treated bacteria. In brief, *S. aureus* cells were treated with PBS, Au-EGCG@H, or Au-EGCG@H by the irradiation of NIR (5 min, 2.5 W/cm^2) at 37°C for 30 min. Then, in various treatments, *S. aureus* cells were incubated in darkness for 20 min through the probe of DCFH-DA. The samples were ultimately visualized *via* an inverted Leica fluorescence microscope to obtain bacterial images.

In Vivo Treatment of Diabetic Rat *S. aureus*-Infected Wounds

We acquired the female SD rats from Jinzhou Medical University Animal Center. All the studies were conducted using female SD rats with weight between 200 and 220 g. The diabetes animal model was constructed with streptozocin (80 mg/kg, STZ; Sigma, Louis, MO, United States). After anesthesia and disinfection, the dorsal area was fully shaved, and then, a 1.5-cm full-thickness excision wound was formed on the back. *S. aureus* was selected as a bacterial strain for infection. Afterward, *S. aureus* suspension (400 μl) was added to the circular wound to infect all of the rats. All of the animal researches were performed adhering to the Guidelines for Care and Use of Laboratory Animals of Jinzhou Medical University, and the researches were authorized through the Animal Ethics Committee of Jinzhou Medical University.

Western Blot Analysis

The skin tissues around the wound were harvested on the 8th day after the injury and then dissolved by using the RIPA buffer (Beyotime, China). The supernatant was subsequently harvested through centrifugation at 12,000 rpm, at 4°C for 15 min, and the concentration of protein was determined *via* the BCA Protein Assay Kit (Solarbio, China). Each channel is loaded with an equal amount of protein lysate isolated on an acrylamide gel (10%) and subsequently transferred to the membrane of PVDF. After blocking, corresponding primary antibodies, including VEGF, bFGF, and GAPDH, were incubated at 4°C for 12 h. The GAPDH expression was exploited as a control. Images were captured by Alpha Innotech Photo-documentation System.

Tissue Histology

The sections of skin tissue were taken on the 12th day after injury. The skin tissue was soaked in PFA (4%) for 2 days, dehydrated in graded alcohol, and finally degreased in xylene. After embedding the samples in paraffin, the samples were cut into sections (4 μm), and they were subsequently stained by hematoxylin and eosin (H&E). All images were captured using a light microscope.

Statistical Analysis

All of the studies were implemented in triplicate. The Origin 9.0 software was utilized to plot all of the graphs. Multiple comparisons were conducted with one-way ANOVA. A P value less than 0.05 was regarded statistically significant.

RESULT AND DISCUSSION

Preparation and Characterization of Au-EGCG@H

DLS and TEM were respectively employed to characterize the size distribution and morphology of the created AuNCs. The TEM image (**Figure 1A**) showed that AuNCs possess excellent uniformity, regular morphology, and a hollow and porous (8 nm) structure. DLS (**Figure 1B**) proved that the AuNCs' diameter was about 40 nm, and their polydispersity index (PDI) was <0.1, further demonstrating that these AuNCs are uniform. Of the AuNCs, the particle size range of 40 ± 10.5 nm accounts for about 80%. The FTIR spectrum confirmed the successful formation of Au-EGCG@H. As reported in **Figure 1C**, compared with the FTIR of AuNCs, the strong and wide absorption peaks of Au-EGCG@H at 3,755 cm^{-1} was owing to the O–H stretching vibration on aromatic ring, and the wide absorption band between 1,600 and 1,450 cm^{-1} was associated with the stretching vibration C=C in EGCG benzene ring; the absorption peaks at 1,327 cm^{-1} were also the basic characteristics of EGCG, that is, C–O stretching vibration, and the role of hydrogen bond, indicating that Au-EGCG has been successfully prepared and fused into the hydrogel. The successful preparation of gold nanocages means that the hydrogel system is photo-responsive.

The XRD patterns (**Figure 1D**) of AuNCs had sharp diffraction peaks at 38.2°, 44.97°, 64.67°, and 77.64°, which correspond to (111), (200), (220), and (311) crystal surfaces (JCPDS 4–0784), suggesting the crystalline nature of the AuNCs. The UV-vis spectroscopy demonstrated the formation of Au-EGCG. As presented in **Figure 1E**, the surface plasmon resonance absorption of AuNCs at 523 nm

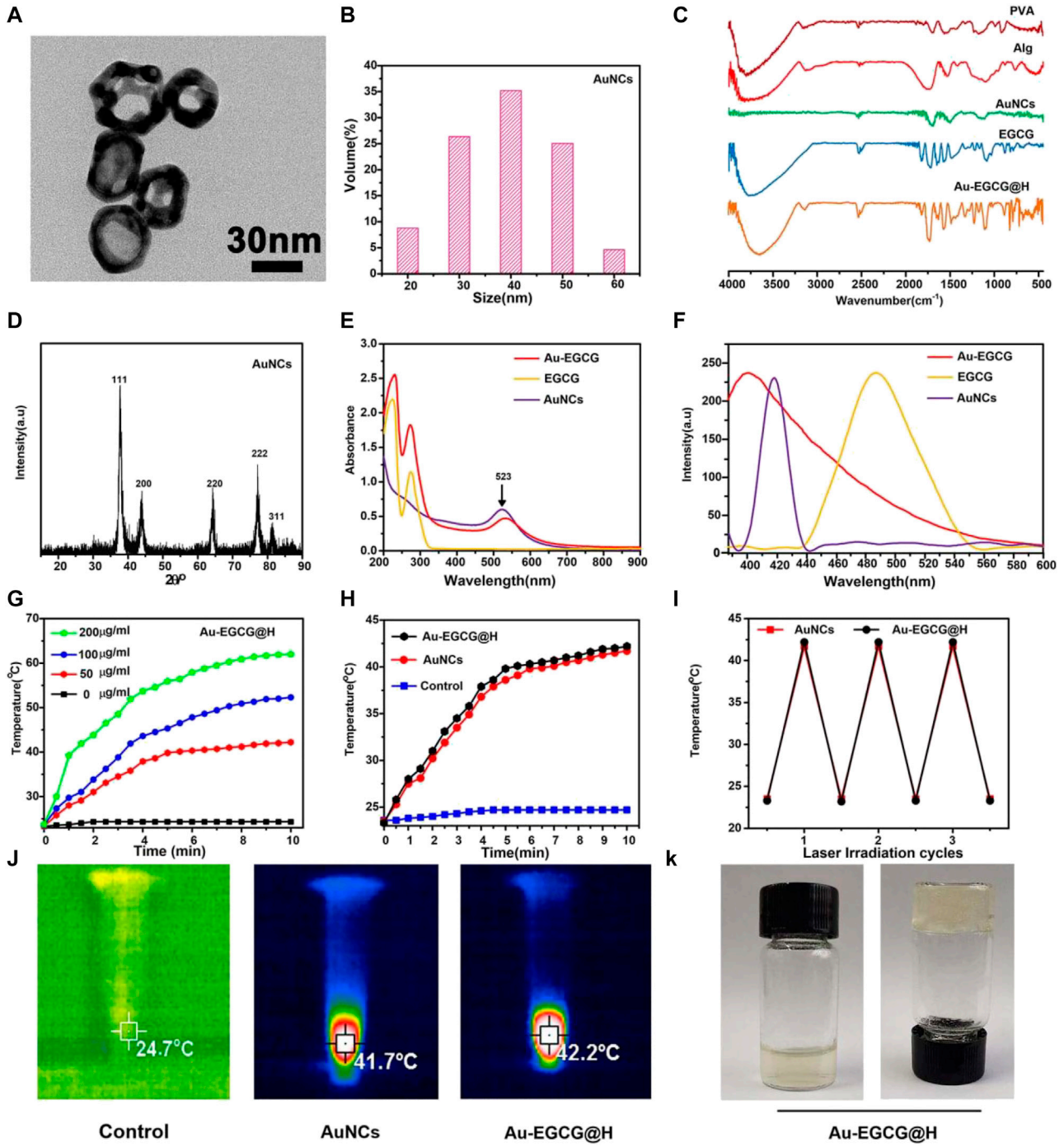

FIGURE 1 | TEM images **(A)**; DLS size distribution of AuNCs **(B)**; Fourier Transform Infra-Red spectra **(C)**; the patterns of XRD **(D)**; Ultraviolet-visible **(E)**; Steady-state fluorescence spectra of the samples **(F)**; Heating curves of Au-EGCG@H at various concentrations **(G)**; Heating curves of Au-EGCG@H, AuNCs, and water **(H)**; Photostability of Au-EGCG@H and AuNCs **(I)**; Thermal images of Au-EGCG@H, AuNCs, and water exposed to laser (1 W/cm^2, 808 nm) for 10 min **(J)**; Digital photos of Au-EGCG@H **(K)**.

and the characteristic absorption peak of EGCG at 273 nm were found in the Au-EGCG ultraviolet-visible spectrum, indicating successfully prepared Au-EGCG. Fluorescence spectra further indicated that EGCG and AuNCs synthesized Au-EGCG (**Figure 1F**). The fluorescence spectrum of AuNCs appeared at a peak at 418 nm, and the fluorescence spectrum of EGCG displayed a peak at 486 nm. The emission peak of Au-EGCG (400 nm) revealed a diverse

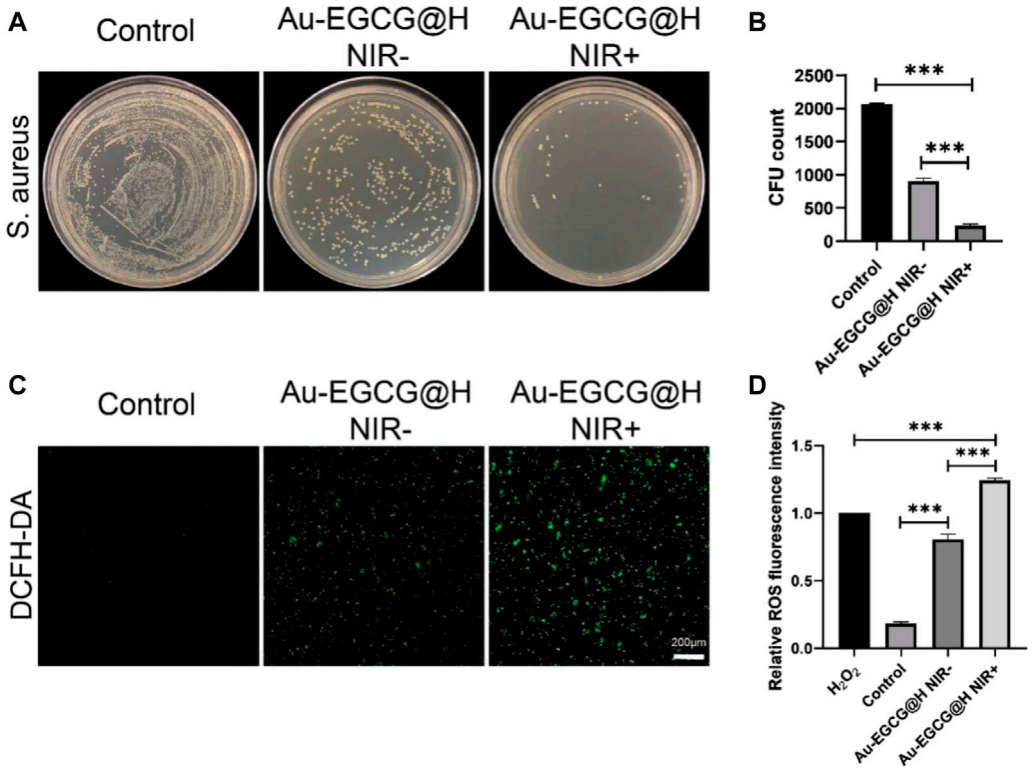

FIGURE 2 | effectiveness of Au-EGCG@H laser irradiation for sterilization. **(A)** *S. aureus* agar plate photos of distinct treatments. **(B)** The corresponding colony-forming unit (CFU) amount of *S. aureus* with different treatments. **(C)** *In vitro* reactive oxygen species (ROS) effects with various treatments. Stained by 2,7-dichlorodihydrofluorescein diacetate (DCFH-DA), bar = 20 μm. **(D)** The relevant statistical histogram revealing the relative ROS fluorescence intensity. *$p < 0.05$, **$p < 0.01$, ***$p < 0.001$.

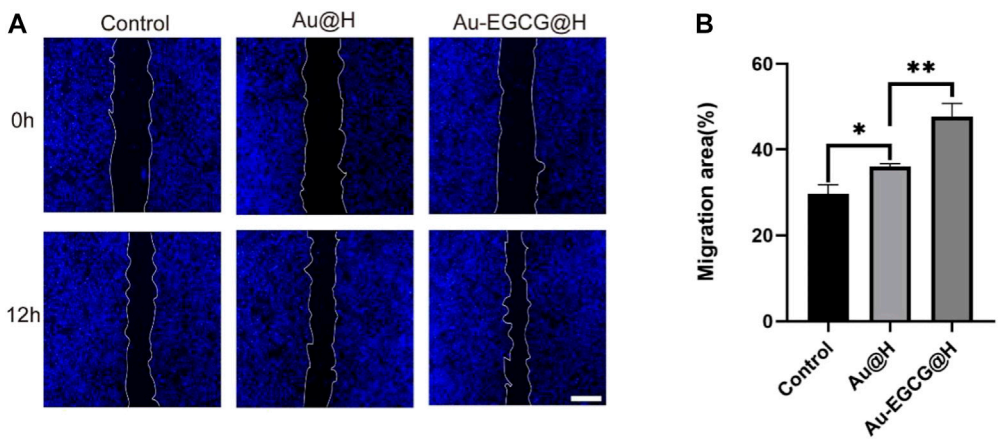

FIGURE 3 | The human umbilical vein endothelial cell (HUVEC) migration treated by Au-EGCG@H and Au@H, respectively. **(A)** The scratch-wound assay in different treatments, bar = 200 μm. **(B)** Migration area analysis. *$p < 0.05$, **$p < 0.01$, ***$p < 0.001$.

blue shift. These outcomes demonstrated the successful preparation of Au-EGCG. To estimate the photothermal performance of Au-EGCG@H, we measured the photothermal heating curves of Au-EGCG@H during 808-nm laser irradiation (1 W/cm^2). As can be seen in **Figure 1G**, Au-EGCG@H showed a concentration-

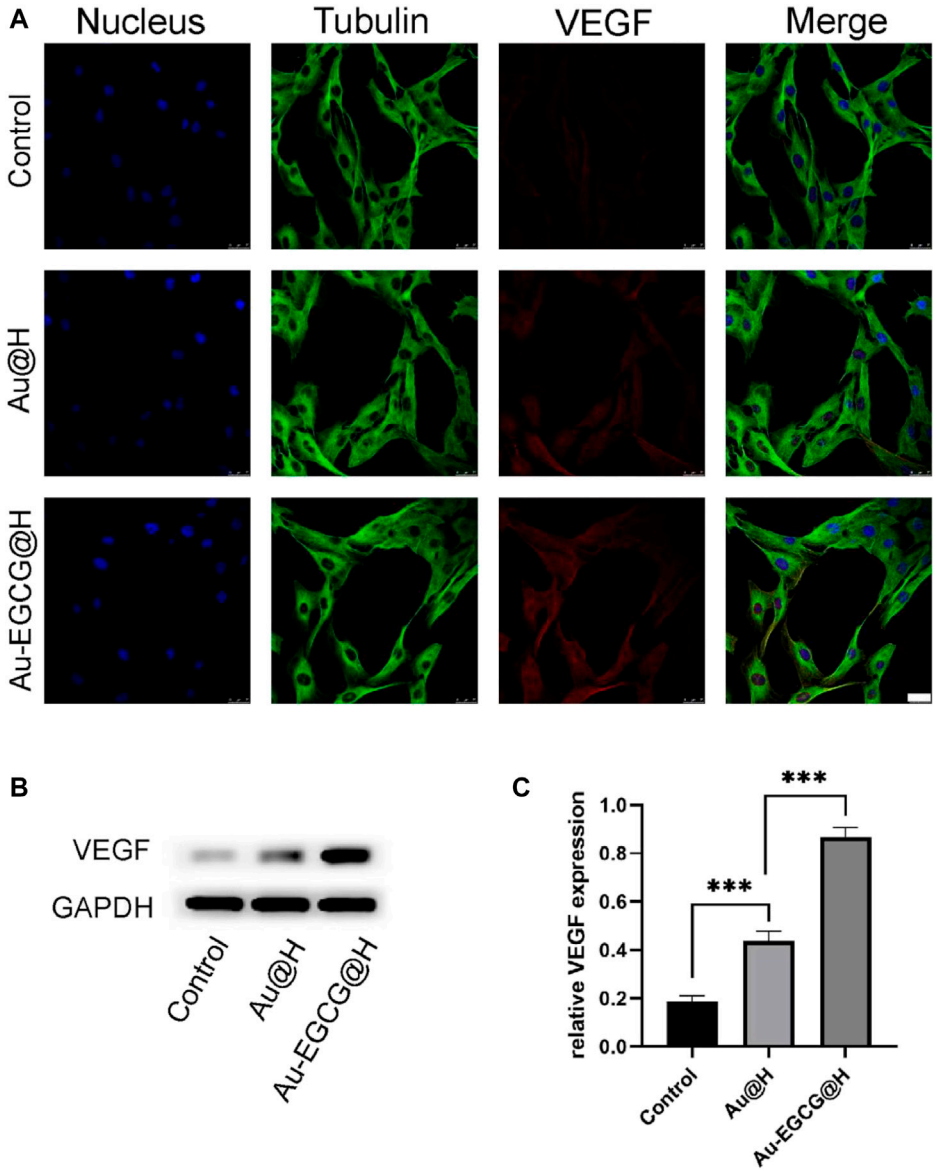

FIGURE 4 | The expression analysis of vascular endothelial growth factor (VEGF) under different treatments. **(A)** The images of confocal laser scanning microscopy (CLSM) for the VEGF expression analysis, bar = 25 μm. **(B)** The VEGF protein expression level was explored through western blot. **(C)** Quantification analysis of the VEGF protein. $^{*}p < 0.05$, $^{**}p < 0.01$, $^{***}p < 0.001$.

dependent photothermal effect. The highest temperature increased significantly as the concentration of Au-EGCG@H increased at the same irradiation condition. As indicated in **Figure 1H**, in contrast to the control group, the maximum temperature of AuNCs and Au-EGCG@H upregulated evidently, as the increasing time of irradiation and the maximum temperature of Au-EGCG@H are slightly higher than those of AuNCs at an identical irradiation condition. These outcomes suggested that Au-EGCG fused into the hydrogel does not influence the AuNC photothermal property. To estimate the photothermal conversion stability of Au-EGCG@H, the heat production efficiency of AuNCs and Au-EGCG@H was assessed after three cycles of heating and cooling processes. As detected (**Figure 1I**), after three cycles, the temperature increase of AuNCs and Au-EGCG@H did not change significantly, reflecting the excellent photothermal stability of Au-EGCG@H. In **Figure 1J**, the highest temperature of AuNCs and Au-EGCG@H could reach 41.7°C and 42.2°C, respectively. These results demonstrated that Au-EGCG@H had excellent photothermal performance, which is beneficial for the photothermal elimination of bacteria. According to **Figure 1K**, gelation was successfully obtained after adding Au-EGCG to the hydrogel, which indicates that the prepared Au-EGCG@H has good gelation

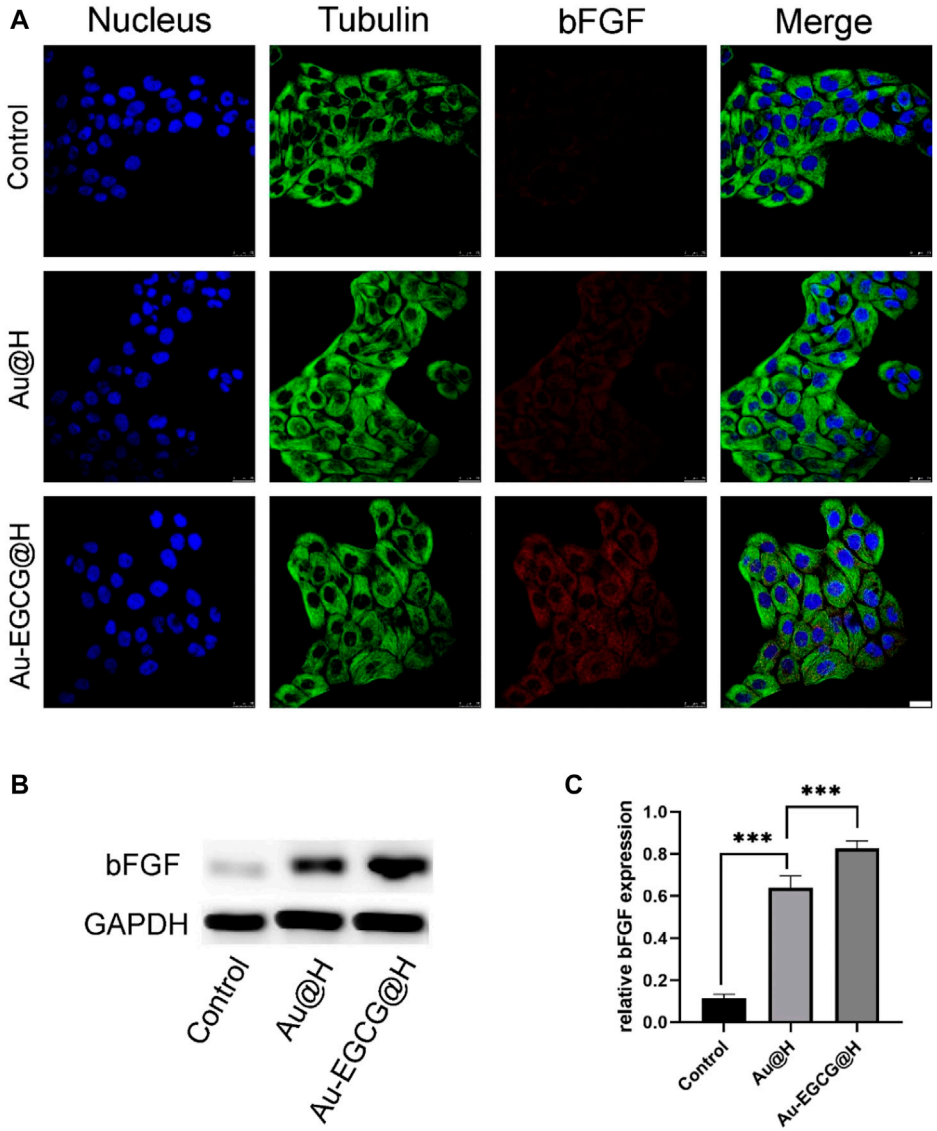

FIGURE 5 | The expression analysis of basic fibroblast growth factor (bFGF) under different treatments. **(A)** The images of confocal laser scanning microscopy (CLSM) for the bFGF expression analysis, bar = 25 μm. **(B)** The expression level of bFGF protein was analyzed by western blot. **(C)** Quantification analysis of the bFGF protein. $^{*}p < 0.05$, $^{**}p < 0.01$, $^{***}p < 0.001$.

properties. This indicates that we have successfully prepared a solid hydrogel, which facilitates fixation to the wound after application to the skin surface.

In Vitro Antibacterial Properties of Au-EGCG@H

The antibacterial activity of Au-EGCG@H was investigated through the spread plate method. As we expected, treatment with PBS had no distinct effect on the bacterial viability (**Figure 2A**). The viability of bacteria showed an obvious decrease upon being treated with Au-EGCG@H, while it was more significant when NIR was exerted (**Figure 2B**). This means that Au-EGCG@H with NIR could more effectively inhibit bacterial survival and suppress the growth of *S. aureus*. ROS can oxidize and modify nucleic acid, protein, lipid, and other cell components, leading to genomic damage, enzyme dysfunction, membrane fluidity changes, and ultimately bacterial death (Panda et al., 2018; Wang et al., 2017; Lee et al., 2014). To investigate the level of ROS after irradiation, we can quantify the level of ROS *via* the measurement of the 2,7-dichlorofluorescein (DCF) fluorescence intensity. We found that after treatment with PBS, almost no green fluorescent spots were observed in the bacteria, indicating no induction of ROS. ROS generation was present in the Au-EGCG@H group, while NIR irradiation

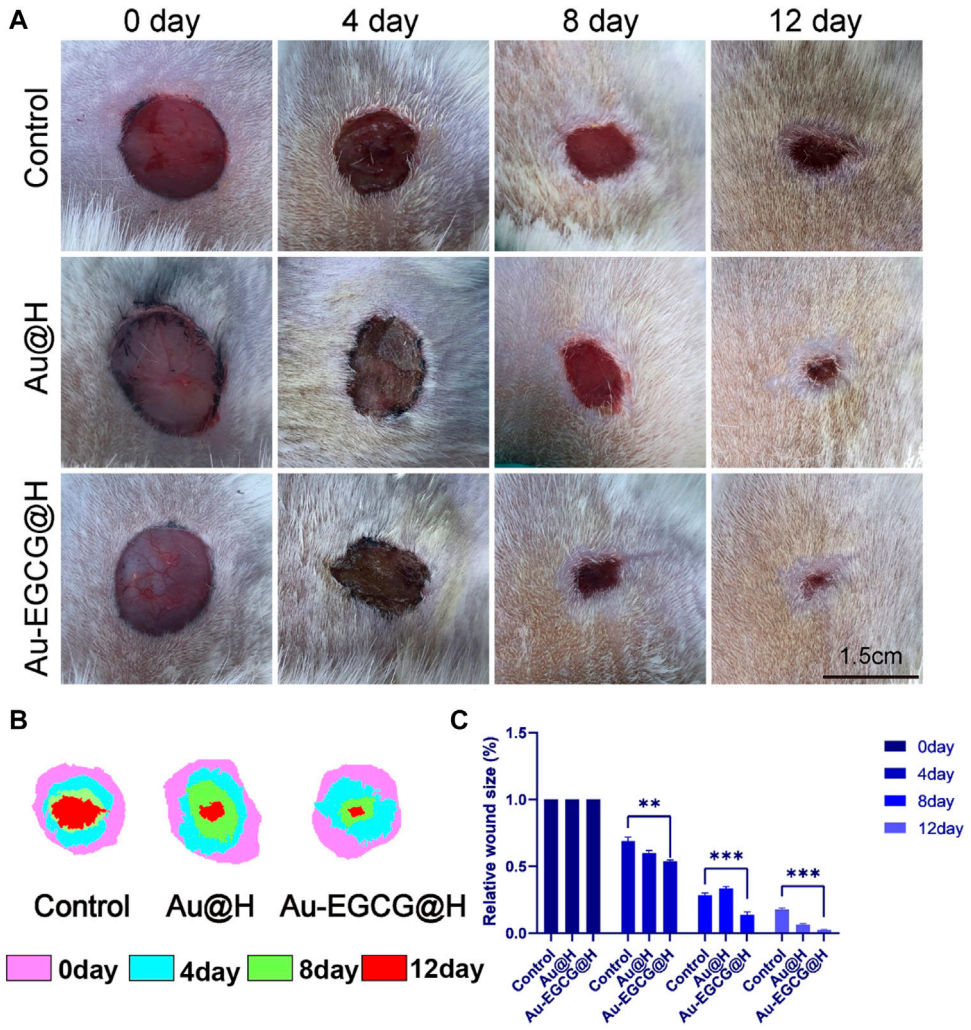

FIGURE 6 | Gross changes of the wound site. **(A)** The image of the diabetic skin wound after operation, bar = 1.5 cm. **(B)** The wound-bed closure traces within 12 days of each treatment. **(C)** Wound closure rate analysis. *$p < 0.05$, **$p < 0.01$, ***$p < 0.001$.

significantly enhanced the production of ROS level after treatment (**Figure 2C, D**). Various theories have been put forward about how AuNCs work against bacteria. We believe that AuNCs can interact with bacterial cell walls and penetrate them, resulting in structural damage, cellular destruction, and bacterial death (Burdușel et al., 2018). ROS induction is thought to be another mechanism by which AuNCs induce bacterial death. At the same time, the phenolic hydroxyl group of EGCG can bind to the bacterial lipid bilayer and the amino and carboxyl groups in the bacterial membrane protein, thus destroying the integrity of the bacterial membrane (Steinmann et al., 2013; Xiong et al., 2017). We believe this combined effect contributes to effective antimicrobial therapy. In addition to this, we stimulated HUVEC with LPS to simulate bacterial infections *in vivo*. The intracellular ROS was detected by a fluorescence microplate reader, and the results showed that the intracellular ROS content was significantly reduced in the Au-EGCG-treated group (**Supplementary Figure S1**).

The Effect of Au-EGCG@H on Cell Migration and Proliferation *In Vitro*

Subsequently, we assayed the toxicity of AuNCs as well as Au-EGCG on HUVECs by MTT assay. As shown in **Supplementary Figure S1**, cell viability decreased slightly with increasing concentrations, while at the highest concentration of AuNCs (50 μm), it decreased to 88%, indicating lower toxicity. Notably, the cytotoxicity of Au-EGCG was lower than that of AuNCs when the concentrations were the same (**Supplementary Figure S2**). Next, to demonstrate the role of Au-EGCG@H in accelerating skin tissue repair, we selected HUVEC for scratch test *in vitro*. The degree of migration showed

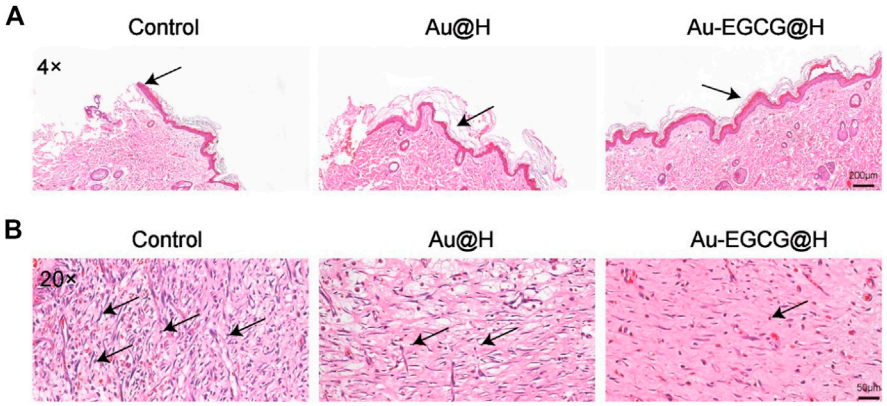

FIGURE 7 | Histological changes at the wound site. **(A)** The staining of hematoxylin and eosin (H&E) in wound sites after 12 days of distinct treatments, bar = 200 μm. **(B)** Local enlargement of H&E stain, bar = 50 μm.

significant differences after different treatments of cell scratch (**Figure 3A**). The cells exhibited the strongest migration after treatment with Au-EGCG@H. The results of the quantitative analysis were also consistent with the migration observations, with the Au-EGCG@H group showing the highest migration rate (**Figure 3B**).

In addition, CLSM was employed to observe the expression of the relevant proteins in the cells. Our result showed that Au-EGCG further enhanced the expression of VEGF in HUVECs (**Figure 4A**). To further confirm our speculation, we next examined protein levels of VEGF in the wound region by utilizing western blot (**Figure 4B**). By the CLSM observations, the VEGF protein expression in the two groups treated with Au-EGCG@H and Au@H, respectively, was higher than the expression of the control group, and the VEGF expression in the Au-EGCG@H-treated group was higher than the expression in the Au@H-treated group (**Figure 4C**).

Considering that epithelial cells are an integral part of repairing skin defects, we used CLSM to examine bFGF expression in HACAT cells. The growth factor of bFGF stimulates cell proliferation and migration, thereby promoting wound healing and tissue repair. According to the fluorescence results (**Figure 5A**), bFGF in the AU-EGCG@H group showed a trend towards increased relative protein expression in comparison with the control group. Thereafter, we examined and quantified the expression of the relevant proteins by western blot (**Figure 5B**). After different biological treatments, the amount of bFGF protein increased to different degrees in Au@H- and Au-EGCG@H-treated tissues (**Figure 5C**). The highest expression levels were found in the Au-EGCG@H group (**Figure 5C**). This demonstrates that the Au-EGCG@H has a higher growth-promoting ability than Au@H alone.

In the process of wound healing, angiogenesis, the proliferation of keratinocyte, and the migration of endothelial cells are critical for the generation (re-epithelialization) of the novel epidermal layers and the restoration of tissue integrity (Chen et al., 2018). EGCG has also been shown to be an excellent mediator of cell proliferation in accelerating wound healing. Simultaneously, EGCG has beneficial pharmacological effects as anti-bacterial, anti-inflammatory, and angiogenesis promoter. Our functional tests *in vitro* suggested that AU-EGCG@H enhanced the migration and proliferation of HUVECS. Meanwhile, we determined an increase in a related vasculogenic protein expression, an early marker of angiogenesis.

Evaluation of Materials for Promoting Wound Healing in Diabetic Rats Infected With *S. aureus*

In order to investigate the diabetic wound-healing process, a full-length wound is formed on the back of the rat as described in the *Materials and Methods*. Different groups were treated with Au-EGCG@H, Au@H, and vehicle (control), and wound closure sizes were photographed on postoperative days 0, 4, 8, and 12 (**Figure 6A**). TPN@H revealed significant influence against wound healing in rats with diabetes (**Figure 6B**). It is worth mentioning that Au-EGCG@H significantly promoted wound healing in diabetic rats (**Figure 6C**). Images of the wound area exhibited a remarkable reduction in the size of wound closure over time in all groups, particularly on postoperative days 8 and 12. Also, the wound size was down-regulated in the group of Au-EGCG@H, in contrast to the control group, indicating that Au-EGCG@H accelerates wound healing.

Inflammatory response possesses a significant effect in the repair together with the regeneration of chronic healing wounds in diabetic patients with bacterial infection. Inflammatory reaction also operates repair mechanisms that promote epithelial cell proliferation. However, excessive inflammation could mitigate wound healing and disrupt the normal wound-healing sequence (Zhao et al., 2019b). To evaluate the histological changes in the wounds, we utilized H&E staining to observe the healing skin microstructure. In comparison with the group of Au-EGCG@H, the control group did not generate complete epithelial tissue. The group of Au@H already had re-epithelialization, but the epithelium in the group of Au-EGCG@H was more regular and smoother than that in the Au@H group (**Figure 7A**, the arrow points to the repaired epithelium). In addition, we examined wound healing in rats by Masson's staining (**Supplementary Figure S3**). The results

showed that Au-EGCG@H had an excellent promotion effect on wound healing in rats. Subsequent H&E staining inflammatory analysis indicates there are many inflammatory cells in the control group, while the inflammatory cell number in wounds of Au-EGCG@H and consolidation treatment Au@H decreased significantly (**Figure 7B**, the arrow points to infiltrating inflammatory cells). The most significant reduction in inflammatory cells was seen in the group treated with Au-EGCG@H. All of these outcomes confirmed the effectiveness of Au-EGCG@H photothermal treatment mediated by NIR irradiation to enhance epidermis regeneration and anti-inflammatory properties by reducing the burden of bacterial infection.

CONCLUSION

In conclusion, a NIR-triggered Au nanocage with functions of bacterial membrane destruction and skin cell mitochondrial protection was developed in this work. The designed nanohydrogel effectively slowed down the oxidation of EGCG and prolonged its action time. Under the irradiation of 808-nm laser, Au-EGCG@H has good photo-thermal stability, and the photo-thermal properties are improved obviously. EGCG and AuNCs synergistically promoted wound angiogenesis, reduced oxidative stress generated within vascular endothelial cells, and preserved impaired mitochondria. After 12 days of treatment, the diabetic rats in the Au-EGCG@H group had excellent wound-healing results. This photo-responsive, spreadable antimicrobial hydrogel system has a certain degree of adhesion to the wound, which is more prominent than ordinary hydrogels. In addition to this, the composite material with antimicrobial ability has a better repair effect compared to regular dressings. Thus, the AU-EGCG@H nanocomposite offers a promising strategy for efficient wound healing in diabetes.

DATA AVAILABILITY STATEMENT

The original contributions presented in the study are included in the article/**Supplementary Material**, further inquiries can be directed to the corresponding authors.

ETHICS STATEMENT

The animal study was reviewed and approved by the Animal Ethics Committee of Jinzhou Medical University.

AUTHOR CONTRIBUTIONS

JD, XM, and ZC contributed in the conception and design of the experiment, as well as manuscript writing. JD and BG contributed in the collection and assembly of data and data interpretation. ZC and XM edited the manuscript and provided support and discussions. JD and BG performed the experiment. XM and ZC provided technical and financial support. All authors contributed to the article and approved the submitted version.

FUNDING

This present study was supported through the National Natural Science Foundation of China (nos. 82072076 and 82072165).

SUPPLEMENTARY MATERIAL

The Supplementary Material for this article can be found online at: https://www.frontiersin.org/articles/10.3389/fphar.2021.779944/full#supplementary-material

REFERENCES

Arifuzzaman, M., Mobley, Y. R., Choi, H. W., Bist, P., Salinas, C. A., Brown, Z. D., et al. (2019). MRGPR-mediated Activation of Local Mast Cells Clears Cutaneous Bacterial Infection and Protects against Reinfection. *Sci. Adv.* 5 (1), eaav0216. doi:10.1126/sciadv.aav0216

Barbalho, S. M., Bosso, H., Salzedas-Pescinini, L. M., and de Alvares Goulart, R. (2019). Green tea: A Possibility in the Therapeutic Approach of Inflammatory Bowel Diseases?: Green tea and Inflammatory Bowel Diseases. *Complement. Ther. Med.* 43, 148–153. doi:10.1016/j.ctim.2019.01.015

Burduşel, A-C., Gherasim, O., Grumezescu, A. M., Mogoantă, L., Ficai, A., and Andronescu, E. (2018). Biomedical Applications of Silver Nanoparticles: An Up-To-Date Overview. *Nanomaterials* 8 (9), 681. doi:10.3390/nano8090681

Chang, L., Huang, S., Zhao, X., Hu, Y., Ren, X., Mei, X., et al. (2021). Preparation of ROS Active and Photothermal Responsive Hydroxyapatite Nanoplatforms for Anticancer Therapy. *Mater. Sci. Eng. C* 125 (125), 112098. doi:10.1016/j.msec.2021.112098

Chen, C. Y., Rao, S. S., Ren, L., Hu, X. K., Tan, Y. J., Hu, Y., et al. (2018). Exosomal DMBT1 from Human Urine-Derived Stem Cells Facilitates Diabetic Wound Repair by Promoting Angiogenesis. *Theranostics* 8 (6), 1607–1623. doi:10.7150/thno.22958

Chen, C. Y., Yin, H., Chen, X., Chen, T. H., Liu, H. M., Rao, S. S., et al. (2020). Ångstrom-scale Silver Particle-Embedded Carbomer Gel Promotes Wound Healing by Inhibiting Bacterial Colonization and Inflammation. *Sci. Adv.* 6 (43), eaba0942. doi:10.1126/sciadv.aba0942

Chen, G., He, L., Zhang, P., Zhang, J., Mei, X., Wang, D., et al. (2020). Encapsulation of green tea Polyphenol Nanospheres in PVA/alginate Hydrogel for Promoting Wound Healing of Diabetic Rats by Regulating PI3K/AKT Pathway. *Mater. Sci. Eng. C Mater. Biol. Appl.* 110, 110686. doi:10.1016/j.msec.2020.110686

Chin, J. S., Madden, L., Chew, S. Y., and Becker, D. L. (2019). Drug Therapies and Delivery Mechanisms to Treat Perturbed Skin Wound Healing. *Adv. Drug Deliv. Rev.* 149-150, 2–18. doi:10.1016/j.addr.2019.03.006

Gupta, A., Mumtaz, S., Li, C. H., Hussain, I., and Rotello, V. M. (2019). Combatting Antibiotic-Resistant Bacteria Using Nanomaterials. *Chem. Soc. Rev.* 48 (2), 415–427. doi:10.1039/c7cs00748e

Hu, Y., Huang, S., Zhao, X., Chang, L., Ren, X., Mei, X., et al. (2021). Preparation of Photothermal Responsive and ROS Generative Gold Nanocages for Cancer Therapy. *Chem. Eng. J.* 421, 129744. doi:10.1016/j.cej.2021.129744

Kalan, L. R., and Brennan, M. B. (2018). The Role of the Microbiome in Nonhealing Diabetic Wounds. *Ann. N. Y Acad. Sci.* 1435, 79–92. doi:10.1111/nyas.13926

Krook, M. A., and Hagerman, A. E. (2012). Stability of Polyphenols Epigallocatechin Gallate and Pentagalloyl Glucose in a Simulated

Digestive System. *Food Res. Int.* 49 (1), 112–116. doi:10.1016/j.foodres.2012.08.004

Lee, W., Kim, K. J., and Lee, D. G. (2014). A Novel Mechanism for the Antibacterial Effect of Silver Nanoparticles on *Escherichia coli*. *Biometals* 27 (6), 1191–1201. doi:10.1007/s10534-014-9782-z

Li, J., Chen, J., and Kirsner, R. (2007). Pathophysiology of Acute Wound Healing. *Clin. Dermatol.* 25 (1), 9–18. doi:10.1016/j.clindermatol.2006.09.007

Li, N., Taylor, L. S., Ferruzzi, M. G., and Mauer, L. J. (2012). Kinetic Study of Catechin Stability: Effects of pH, Concentration, and Temperature. *J. Agric. Food Chem.* 60 (51), 12531–12539. doi:10.1021/jf304116s

Liang, Y., He, J., and Guo, B. (2021). Functional Hydrogels as Wound Dressing to Enhance Wound Healing. *ACS nano* 15 (8), 12687–12722. doi:10.1021/acsnano.1c04206

Panda, S., Rout, T. K., Prusty, A. D., Ajayan, P. M., and Nayak, S. (2018). Electron Transfer Directed Antibacterial Properties of Graphene Oxide on Metals. *Adv. Mater.* 30 (7), 1702149. doi:10.1002/adma.201702149

Qing, G., Zhao, X., Gong, N., Chen, J., Li, X., Gan, Y., et al. (2019). Thermo-responsive Triple-Function Nanotransporter for Efficient Chemo-Photothermal Therapy of Multidrug-Resistant Bacterial Infection. *Nat. Commun.* 10, 4336. doi:10.1038/s41467-019-12313-3

Randeria, P. S., Seeger, M. A., Wang, X. Q., Wilson, H., Shipp, D., Mirkin, C. A., et al. (2015). siRNA-Based Spherical Nucleic Acids Reverse Impaired Wound Healing in Diabetic Mice by Ganglioside GM3 Synthase Knockdown. *Proc. Natl. Acad. Sci. U S A.* 112 (18), 5573–5578. doi:10.1073/pnas.1505951112

Steinmann, J., Buer, J., Pietschmann, T., and Steinmann, E. (2013). Anti-infective Properties of Epigallocatechin-3-Gallate (EGCG), a Component of green tea. *Br. J. Pharmacol.* 168 (5), 1059–1073. doi:10.1111/bph.12009

Sun, J., Song, L., Fan, Y., Tian, L., Luan, S., Niu, S., et al. (2019). Synergistic Photodynamic and Photothermal Antibacterial Nanocomposite Membrane Triggered by Single NIR Light Source. *ACS Appl. Mater. Inter.* 11, 26581–26589. doi:10.1021/acsami.9b07037

Tong, C., Zhong, X., Yang, Y., Liu, X., Zhong, G., Xiao, C., et al. (2020). PB@PDA@Ag Nanosystem for Synergistically Eradicating MRSA and Accelerating Diabetic Wound Healing Assisted with Laser Irradiation. *Biomaterials* 243, 119936. doi:10.1016/j.biomaterials.2020.119936

Vanaeia, S., Parizib, M. S., Vanaei, S., Salemizadehparizi, F., and Vanaei, H. R. (2021). An Overview on Materials and Techniques in 3D Bioprinting toward Biomedical Application. *Engineered Regen.* 2, 1–18. doi:10.1016/j.engreg.2020.12.001

Wang, G., Jin, W., Qasim, A. M., Gao, A., Peng, X., Li, W., et al. (2017). Antibacterial Effects of Titanium Embedded with Silver Nanoparticles Based on Electron-Transfer-Induced Reactive Oxygen Species. *Biomaterials* 124, 25–34. doi:10.1016/j.biomaterials.2017.01.028

Wang, H., Song, Z., Li, S., Wu, Y., and Han, H. (2019). One Stone with Two Birds: Functional Gold Nanostar for Targeted Combination Therapy of Drug-Resistant *Staphylococcus aureus* Infection. *ACS Appl. Mater. Inter.* 11, 32659–32669. doi:10.1021/acsami.9b09824

Wang, L., Yang, J., Li, S., Li, Q., Liu, S., Zheng, W., et al. (2021). Oral Administration of Starting Materials for *In Vivo* Synthesis of Antibacterial Gold Nanoparticles for Curing Remote Infections. *Nano Lett.* 21 (2), 1124–1131. doi:10.1021/acs.nanolett.0c04578

Wlaschek, M., Singh, K., Sindrilaru, A., Crisan, D., and Scharffetter-Kochanek, K. (2019). Iron and Iron-dependent Reactive Oxygen Species in the Regulation of Macrophages and Fibroblasts in Non-healing Chronic Wounds. *Free Radic. Biol. Med.* 133, 262–275. doi:10.1016/j.freeradbiomed.2018.09.036

Wu, J., Zheng, K., Huang, X., Liu, J., Liu, H., Boccaccini, A. R., et al. (2019). Thermally Triggered Injectable Chitosan/silk Fibroin/bioactive Glass Nanoparticle Hydrogels for *In-Situ* Bone Formation in Rat Calvarial Bone Defects. *Acta Biomater.* 91, 60–71. doi:10.1016/j.actbio.2019.04.023

Xiong, L. G., Chen, Y. J., Tong, J. W., Huang, J. A., Li, J., Gong, Y. S., et al. (2017). Tea Polyphenol Epigallocatechin Gallate Inhibits *Escherichia coli* by Increasing Endogenous Oxidative Stress. *Food Chem.* 217, 196–204. doi:10.1016/j.foodchem.2016.08.098

YoonYoona, D. S., Lee, Y., Ryu, H. A., Jang, Y., Lee, K. M., Choi, Y., et al. (2016). Cell Recruiting Chemokine-Loaded Sprayable Gelatin Hydrogel Dressings for Diabetic Wound Healing. *Acta Biomater.* 38, 59–68. doi:10.1016/j.actbio.2016.04.030

Zhang, P., He, L., Zhang, J., Mei, X., Zhang, Y., Tian, H., et al. (2019). Preparation of Novel Berberine Nano-Colloids for Improving Wound Healing of Diabetic Rats by Acting Sirt1/NF-Kb Pathway. *Colloids Surf. B Biointerfaces* 187, 110647. doi:10.1016/j.colsurfb.2019.110647

Zhao, L., Niu, L., Liang, H., Tan, H., Liu, C., and Zhu, F. (2017). pH and Glucose Dual-Responsive Injectable Hydrogels with Insulin and Fibroblasts as Bioactive Dressings for Diabetic Wound Healing. *ACS Appl. Mater. Inter.* 9 (43), 37563–37574. doi:10.1021/acsami.7b09395

Zhao, Q., Zhao, Y., Lu, Z., and Tang, Y. (2019). Amino Acid-Modified Conjugated Oligomer Self-Assembly Hydrogel for Efficient Capture and Specific Killing of Antibiotic-Resistant Bacteria. *ACS Appl. Mater. Inter.* 11 (18), 16320–16327. doi:10.1021/acsami.9b02643

Zhao, Y., Li, Z., Song, S., Yang, K., Liu, H., Yang, Z., et al. (2019). Skin-Inspired Antibacterial Conductive Hydrogels for Epidermal Sensors and Diabetic Foot Wound Dressings. *Adv. Funct. Mater.* 29 (31), 1901474. doi:10.1002/adfm.201901474

Conflict of Interest: The authors declare that the research was conducted in the absence of any commercial or financial relationships that could be construed as a potential conflict of interest.

Publisher's Note: All claims expressed in this article are solely those of the authors and do not necessarily represent those of their affiliated organizations, or those of the publisher, the editors and the reviewers. Any product that may be evaluated in this article, or claim that may be made by its manufacturer, is not guaranteed or endorsed by the publisher.

Copyright © 2021 Ding, Gao, Chen and Mei. This is an open-access article distributed under the terms of the Creative Commons Attribution License (CC BY). The use, distribution or reproduction in other forums is permitted, provided the original author(s) and the copyright owner(s) are credited and that the original publication in this journal is cited, in accordance with accepted academic practice. No use, distribution or reproduction is permitted which does not comply with these terms.

frontiers in Pharmacology

REVIEW
published: 12 January 2022
doi: 10.3389/fphar.2021.814241

Opioids Regulate the Immune System: Focusing on Macrophages and Their Organelles

Shaohua Wen[1,2], *Yuan Jiang*[1,2], *Shuang Liang*[1,2], *Zhigang Cheng*[1,2], *Xiaoyan Zhu*[1,2]* and *Qulian Guo*[1,2]

[1]Department of Anesthesiology, Xiangya Hospital, Central South University, Changsha, Hunan, China, [2]National Clinical Research Center for Geriatric Disorders, Xiangya Hospital, Central South University, Changsha, China

Opioids are the most widely used analgesics and therefore have often been the focus of pharmacological research. Macrophages are the most plastic cells in the hematopoietic system. They show great functional diversity in various organism tissues and are an important consideration for the study of phagocytosis, cellular immunity, and molecular immunology. The expression of opioid receptors in macrophages indicates that opioid drugs act on macrophages and regulate their functions. This article reviewed the collection of research on effects of opioids on macrophage function. Studies show that opioids, both endogenous and exogenous, can affect the function of macrophages, effecting their proliferation, chemotaxis, transport, phagocytosis, expression of cytokines and chemokine receptors, synthesis and secretion of cytokines, polarization, and apoptosis. Many of these effects are closely associated with mitochondrial function and functions of other organelles in macrophages. Therefore, in depth research into effects of opioids on macrophage organelles may lead to some interesting new discoveries. In view of the important role of macrophages in HIV infection and tumor progression, this review also discusses effects of opioids on macrophages in these two pathological conditions.

Keywords: opioids, macrophages, tumor progression, human immunodeficiency virus, organelles

OPEN ACCESS

Edited by:
Qixin Chen,
Shandong First Medical University, China

Reviewed by:
Sang Hoon Lee,
University of Cincinnati, United States
Jinchao Hou,
Washington University in St. Louis, United States

***Correspondence:**
Xiaoyan Zhu
xiaoyanzhu@csu.edu.cn

Specialty section:
This article was submitted to Pharmacology of Anti-Cancer Drugs, a section of the journal Frontiers in Pharmacology

Received: *13 November 2021*
Accepted: *20 December 2021*
Published: *12 January 2022*

Citation:
Wen S, Jiang Y, Liang S, Cheng Z, Zhu X and Guo Q (2022) Opioids Regulate the Immune System: Focusing on Macrophages and Their Organelles. Front. Pharmacol. 12:814241. doi: 10.3389/fphar.2021.814241

INTRODUCTION

Opioids, such as morphine, are widely used in clinical pain treatment worldwide and are most commonly used to treat pain from cancer and various forms of acute intraoperative pain. However, opioids pose a risk to patients and society, as their misuse or abuse can lead to addiction and overdose (Webster, 2017). In recent years, the number of people who have died from opioid overdose has increased worldwide, exposing a potential opioid drug crisis (Volkow and Blanco, 2021).

Abbreviations: AIDS, Acquired Immune Deficiency Syndrome; cAMP, Cyclic adenosine monophosphate; DOP, δ-opioid; ER, endoplasmic reticulum; GPCRs, G protein-coupled receptors; HDM, high dose of morphine; HIF1α, hypoxia-inducible factor 1α; HIV, human immunodeficiency virus; h-MDMs, human monocyte-derived macrophages; IRF5, Interferon regulatory factor 5; KOP, κ-opioid; LDN, Low-dose naltrexone.; MAPK, mitogen-activated protein kinase; MCP, monocyte chemoattractant protein; MMP-9, matrix metallopeptidase 9; MOP, μ-opioid; NC-IUPHAR, the Committee on Receptor Nomenclature and Drug Classification; NO, nitric oxide; NOP, nociceptin receptor; NOS2, nitric oxide synthase 2; oxLDL, oxidized low-density lipoprote; ROS, reactive oxygen species; RT-PCR, Reverse Transcription-Polymerase Chain Reaction; TAMs, Tumor-associated macrophages; TCA, tricarboxylic acid

Macrophages are immune cells that are studied for their role in cellular phagocytosis, cellular immunity, and molecular immunology. They play a central role in regulating humoral and cellular immunity against infectious diseases and cancer. Macrophages can eradicate bacteria invading the body; phagocytize foreign particles, aging or damaged cells and the degenerating intercellular matrix; kill tumor cells; and activate lymphocytes or other immune cells.

The immunomodulatory effects of opioids in the context of immunosuppression and infection have been widely reviewed (Liang et al., 2016; Boland and Pockley, 2018; Plein and Rittner, 2018). The review published by Eisenstein in 1998 elaborated on the influence of opioids on macrophage function and the regulation of immune response (Eisenstein and Hilburger, 1998). Many studies have shown that human and rodent macrophages can express opioid receptors. Opioid drugs, such as morphine, interacting with opioid receptors can inhibit phagocytosis and chemotaxis of macrophages. *In vitro* experiments have also shown that opioids or opioid peptides have direct effects on macrophages.

This review paper summarized the latest evidence regarding effects of opioids on macrophage function in the last 20 years. Morphine is the most well studied opioid with regards to macrophage function and significantly less research has been done on other opioids, such as fentanyl, methadone, tramadol, oxycodone, hydromorphone, and buprenorphine. Opioids, both endogenous and exogenous, can have an effect on the function of macrophages, including macrophage proliferation, chemotaxis, transport, phagocytosis, expression of cytokines and chemokine receptors, synthesis and secretion of cytokines, polarization, and apoptosis. These effects have been mainly evaluated *in vitro*, and the results are often contradictory, depending on different experimental conditions, for example cultured cell type, cell line or clone, culture duration, culture medium composition, dose, and opioid exposure time. In the following sections we introduce the opioids, opioid receptors, and macrophages, and discuss their relationship. We also discuss the relationship between opioids and organelles in macrophages, a promising topic for future studies. Additionally, in view of the critical role of macrophages in HIV infection and tumor progression, we discuss the influence of opioids on macrophages under these two pathological conditions.

CLASSIFICATION AND BASIC PHARMACOLOGY OF OPIOIDS

Opioids can be divided into natural opioid alkaloids, semi-synthetic opioids, and synthetic opioids, depending on the source of the compound and the processing involved. Four natural alkaloids—morphine, codeine, papaverine, and thebaine—are all extracted from *Papaver somniferum*, among which, morphine is the most widely used in the clinic. Semi-synthetic opioids, such as diamorphine and oxycodone, are produced by simple chemical treatment of natural opioid alkaloids. Synthetic opioids, widely used in clinics in the past half-century, can be further subdivided into four groups: morphinan derivatives, diphenyl heptane derivatives, benzomorphan derivatives, and phenylpiperidine derivatives. Opioids can also be classified as agonists, partial agonists, antagonists, and agonist-antagonists, depending on their effect on opioid receptors.

Since the last century, the classification of opioid receptors has changed with time. At present, the commonly used NC-IUPHAR divides opioid receptors into four categories: DOP or δ, KOP or κ, MOP or μ, and nociceptin receptor (NOP) (James and Williams, 2020). The first three are classical opioid receptors, all of which are G protein-coupled receptors (GPCRs). The NOP receptor is also a GPCR system, which has obvious similarity with the known amino acid sequence of classical opioid receptors. NC-IUPHAR states that the NOP receptor is a non-opioid branch of the opioid receptor family because when the NOP receptor is activated by an agonist at the cellular level, it produces similar effects to the classic opioid receptors mentioned above. Classical opioid receptors have been divided into subtypes, μ_1, μ_2, and μ_3 for MOP, δ_1 and δ_2 for DOP, and κ_{1a}, κ_{1b}, κ_{2a}, κ_{2b} and κ_3 for KOP.

Previous studies have confirmed that the primary mechanism of opioid-induced analgesia is through activation of the midbrain MOP receptor in the central nervous system. MOP agonists have an analgesic effect by indirectly increasing neuronal flow in the nucleus reticularis paragigantocellularis and periaqueductal gray descending pathway, or by directly inhibiting peripheral nociceptive afferent sensitivity. In addition, MOP agonists can indirectly inhibit the transmission of spinal cord pain and reduce the sensation of spinal cord injury. Although analgesic properties of opioids may be attributed to the activation of the MOP receptor, this may also be the reason for many of the side effects associated with opioids. Opioids may lead to euphoria and decreased awareness, making them prone to abuse. They also affect the respiratory system, reducing the respiratory rate and airway reflex, which is considered to be beneficial during anesthesia. Although opioids are generally considered to maintain the stability of the heart, the release of histamine and the decrease of systemic vascular resistance and blood pressure are evident in the case of morphine. They can also cause constipation, nausea, vomiting, urinary retention, itching, muscle stiffness, mydriasis, and irritability in some individuals. Many side effects may limit their use.

OVERVIEW OF MACROPHAGES

In adult mammals, macrophages are not only present in the blood, but also in various tissues throughout the body. They demonstrate huge anatomical and functional diversity in these tissues. Depending on the location, the names and shapes of macrophages may also be different. For example, they are referred to as pulmonary macrophages in the lungs, microglia in the nervous system, Kupffer cells in the liver, and osteoclasts in the bone.

In the past, various systems were used to classify phagocytic mononuclear cells and their precursors, but the most successful is the mononuclear phagocytic system, which is defined as progenitor cells in the bone marrow, monocytes in the blood,

and macrophages in tissues as phagocytic mononuclear cells or precursors. Another classification method reflects two extreme conditions of macrophages, including activated and alternative activated macrophages, otherwise known as M1 and M2, respectively. Under the influence of the local microenvironment cytokines, macrophage populations usually differentiate into two phenotypes, in a process known as macrophage polarization (Wang et al., 2014; de Gaetano et al., 2016; Yunna et al., 2020). M1 macrophages participate in the positive immune response by secreting pro-inflammatory cytokines and chemokines and presenting antigens, thereby monitoring the immune system. M2 macrophages only have a weak antigen-presenting ability and play an important role in immune regulation by secreting inhibitory cytokines, such as IL-10 or TGF-β (Wynn et al., 2013). However, it is worth noting that the idea of dichotomy is largely oversimplified and is mainly based on the *in vitro* response to polarization stimulation. In fact, many macrophage subtypes have overlapping functions and phenotypes since they are exposed to hundreds of different stimuli. These functions are integrated by complex signal pathways and finally produce specific effects.

Macrophages are the most plastic cells in the hematopoietic system and show great functional diversity in various tissues of organisms. Changes in macrophage phenotype and function lead to dramatic changes in cell metabolism. These metabolic adaptations, in turn, support the activity of macrophages and maintain their polarization in specific environments (Viola et al., 2019). For example, M1 macrophage metabolism mainly depends on glycolysis. Interestingly, in M1 macrophages, two points of interruption in the tricarboxylic acid (TCA) cycle results in the accumulation of itaconate (a microbicidal compound) and succinate. The accumulation of succinate leads to the stabilization of hypoxia-inducible factor 1α (HIF1α), which in turn activates the transcription of glycolytic genes, thus maintaining the glycolytic metabolism of M1 macrophages.

Macrophages not only regulate the normal metabolic balance and immune response *in vivo*, but also play an important role in the pathophysiological process of various system diseases. Studies have confirmed that macrophages play an important role in the development of inflammatory bowel disease, atherosclerosis, diabetic nephropathy, AIDS, and tumors. The plasticity of macrophages in the process of intestinal inflammation indicates that these cells not only play an extensive role in the occurrence of inflammation, but also in termination, healing, and repair of inflammation (Moreira Lopes et al., 2020). During the development and progression of atherosclerosis, macrophages respond to various environmental signals, such as lipids and their derivatives, pro-inflammatory and anti-inflammatory cytokines, and heme in aging red blood cells, thus regulating different phenotypes of macrophages (Jinnouchi et al., 2020). In the experimental model of diabetes mellitus, it has been found that macrophage infiltration (mainly M1) occurs in the early stage of the disease, which is one of the reasons renal matrix hyperplasia and irreversible pathological changes of the glomerulus (Calle and Hotter, 2020). Tumor-associated macrophages (TAMs) are the key driving factors of tumor progression, metastasis, and resistance therapy (Wu et al., 2020).

MACROPHAGE-ASSOCIATED OPIOID RECEPTORS

Opioids are agonists of MOP, DOP, and KOP receptors, while nociception/orphanin FQ peptide is an agonist of NOP receptors. In animal models, all four opioid receptors on neurons can induce analgesia, but the most relevant ones are MOP receptors and their agonists, such as morphine and fentanyl. Opioids can affect the function of immune cells and their role in immunosuppression and infection has been widely discussed. Here, we analyze the expression of opioid receptors in macrophages.

Four opioid receptors have been found in the human, rhesus monkey, rat, and mouse macrophages at mRNA and protein levels (Eisenstein, 2019; Machelska and Celik, 2020) (**Table 1**). Sedqi et al. (1995) confirmed expression of MOP receptor-related transcripts in rat peritoneal macrophages by reverse transcription-polymerase chain reaction (RT-PCR). Ignatowski et al. analyzed the differential expression of the KOP receptor on mouse lymphocytes and mouse macrophages at different maturation stages after selective induction and found that resident peritoneal macrophages showed more specific receptor markers and about 50% of resting macrophages expressed KOP receptors (Ignatowski and Bidlack, 1999).

OPIOIDS AFFECT THE CHEMOTAXIS, RECRUITMENT, MIGRATION, AND PHAGOCYTOSIS OF MACROPHAGES

Previous studies mostly focused on the effects of morphine, at different doses and with different administration methods, on macrophage function. Limited studies have systematically analyzed the effects of morphine on macrophage recruitment and migration. These studies have shown that morphine treatment results in a significant delay and decrease in macrophage recruitment at the wound site, which was attributed to the inhibition of effective macrophage chemokine monocyte chemoattractant protein-1 (MCP-1). The immunosuppressive effect of morphine on the recruitment of early innate immune cells makes neutrophils unable to fully migrate to the injury site within 24 hours after injury. This leads to less production and secretion of MCP-1 and reduced chemotaxis gradient, which is crucial for subsequent macrophage recruitment. Macrophage infiltration decreases, resulting in decreased neutrophil clearance and increased pro-inflammatory response. Morphine regulates inflammation induced CCR2 expression, which may be a potential mechanism by which morphine affects the continuous recruitment of macrophages (Martin et al., 2010). There may also be other mechanisms by which morphine affects macrophage recruitment and migration, therefore further studies are warranted.

Phagocytosis by macrophages is extremely important. Macrophages swallow and process large foreign bodies, old waste excreted by cells and red blood cells at the end of their life. Macrophages can locate and infiltrate a site of inflammation to deal with foreign bodies. Some studies have explored the effects

TABLE 1 | The distributions of opioid receptors in macrophages among different models.

Opioid receptor	mRNA, protein	Cell types	References
MOR	mRNA	Rat peritoneal macrophages	Sedqi et al. (1995), Gomez-Flores et al. (2001), Stanojević et al. (2008), Machelska and Celik (2020)
	—	Rat splenic macrophages	Gomez-Flores et al. (2001)
	—	Mice peritoneal macrophages	Balog et al. (2010)
	mRNA	Human macrophages	Machelska and Celik, (2020)
KOP	protein	Mouse peritoneal macrophages	Ignatowski and Bidlack (1999)
	protein	Rat alveolar macrophage cell line (NR8383)	Zeng et al. (2020)
DOP	—	Rat peritoneal macrophages	Gomez-Flores et al. (2001), Stanojević et al. (2008)
	—	Rat splenic macrophages	Gomez-Flores et al. (2001)
	protein	Murine macrophage cell line (RAW 264.7)	Husted et al. (2005)
	—	Rat peritoneal macrophages	Stanojević et al. (2008), Tang et al. (2011)

of opioids, such as morphine, on macrophage phagocytosis. Bhaskaran et al. found that a high dose of morphine (HDM), equal to 40 mg/kg body weight every 12 h, impaired the ability of macrophages to inhibit and kill bacteria by phagocytosis (Bhaskaran et al., 2007). In the HDM group, peritoneal bacterial leakage and the number of macrophages migrating into the peritoneal cavity decreased significantly. HDM promoted the phosphorylation of p38MAPK in macrophages, while morphine pretreatment attenuated this effect. Tomassini et al. showed that MOP and DOP receptors mediate morphine's effect on the phagocytosis of mouse peritoneal macrophages (Tomassini et al., 2003). Ninković et al. found that long-term morphine treatment increased cAMP and activated protein kinase A in macrophages, resulting in inhibition of Rac1 GTPase and p38MAPK, weakening actin polymerization and FCGR-mediated phagocytosis, and reducing bacterial clearance (Ninković and Roy, 2012). Ninković et al. (2016) confirmed that opioid therapy can reduce the phagocytosis by macrophages of gram-positive bacteria compared to gram-negative bacteria. Lipopolysaccharide (LPS)-stimulated chronic morphine-treated macrophages could enhance phagocytosis and killing of gram-positive and gram-negative bacteria through the p38MAPK-dependent signaling pathway. These studies explored the effects of morphine on macrophage phagocytosis from different aspects (including different doses of morphine, receptors of morphine on macrophages, and types of bacteria phagocytized). However, the relevant downstream mechanism is not clear and need further exploration.

Several other studies have compared the effects of different opioids on macrophage phagocytosis. Shirzad et al. (2009) compared the effects of morphine and tramadol on the phagocytic activity of mouse peritoneal phagocytes and found that after 10 days of treatment, the number of phagocytes and the phagocytic index in the morphine-treated group decreased, while the number of phagocytes in the tramadol group increased. Acute exposure to morphine and methadone inhibited phagocytosis in human monocyte-derived macrophages (h-MDMs) in a dose-dependent manner. In contrast, long-term exposure leads to the eventual normalization of phagocytosis, indicating that a hypothetical state of tolerance to opioids has been formed. When opioids are withdrawn from long-exposed h-MDMs with tolerance to opioids and reintroduced, phagocytosis is inhibited again (Delgado-Vélez et al., 2008). Comparing the effects of different opioids on macrophage phagocytosis and exploring the mechanism of effects are helpful to regulate the immune state of the body and the clinical application of opioids.

OPIOIDS AFFECT THE PRODUCTION OF VARIOUS CYTOKINES AND THE POLARIZATION OF MACROPHAGES

In addition to affecting the phagocytosis of macrophages, opioids can also act on opioid receptors on macrophages, thereby affecting intracellular molecular targets and the production of various cytokines (**Table 2**). The change of the production ratio of various cytokines can provide a basis for judging the polarization of macrophages in different directions (M1 or M2). Therefore, in this section, we talk about the effects of opioids on the production of various cytokines and the polarization of macrophages.

When macrophages are stimulated by zymosan or LPS, opioids can promote the production of reactive oxygen species (ROS) intermediate and cytokines and reduce the expression of surface antigen presentation markers in peritoneal macrophages. Opioids promote the production of pro-inflammatory cytokines, including IL-6 and TNF-α, in the early stage. Secretion of IL-10 is then activated 1 day after the release of pro-inflammatory cytokines. All the antigen-presenting molecules (CD14, CD80, CD86, and MHC II) on the surface of macrophages are shown to be significantly inhibited by different opioids (morphine, fentanyl, or methadone) (Filipczak-Bryniarska et al., 2012). Limiroli et al. (2002) also found that morphine treatment can impair the production of cytokines by macrophages in mice, and the changes in cytokines IL-10 and IL-12 are altered by acute or chronic morphine treatment. Furthermore, Pacifici et al. (1995) found that NO_2^- production by L1210-activated macrophages increased significantly immediately after injection of morphine, whereas NO_2^- production was significantly inhibited by

TABLE 2 | Opioids affect the molecular targets of macrophages and the production of various cytokines.

Opioids	*Vivo./vitro.*	Cell type or mouse model	Molecular	Cytokines	References
Morphine, fentanyl, methadone	*Vivo.*	Murine peritoneal macrophages	CD14, CD80, CD86, MHCII	IL-6, TNF-α, IL-10, ROIs	Filipczak-Bryniarska et al. (2012)
Morphine	*Vivo.*	Murine peritoneal macrophages	Not mentioned	IL-10, IL-12	Limiroli et al. (2002)
Morphine	*Vivo.*	Murine peritoneal macrophages	Not mentioned	NO_2^-	Pacifici et al. (1995)
Morphine	*Vivo. and vitro.*	Murine splenic macrophages	Not mentioned	NO	Alexander et al. (2005)
Morphine	*Vivo. and vitro.*	WT and RelB−/− mice, peritoneal macrophages	NF-κB, RelB	IL-1, TNF-β, IL-12, IL-10	Martucci et al. (2007)
Oxycodone, buprenorphine	*Vivo. and vitro.*	CBA/J mice, oil-induced peritoneal Mf	Not mentioned	ROS, NO	Kozlowski et al. (2017)
Heroin	*Vivo. and vitro.*	Murine peritoneal macrophages	Not mentioned	↑IL-1 β, INF- γ, IL-12, NO ↓IL-4, IL-10	Holán et al. (2003)
Morphine	*Vivo. and vitr.o*	BV-2, HEK 293T, PM, BMMs; C57BL/6 mice	P65, TRAF6, miR-124		Qiu et al. (2015)
M3G	*Vivo. and vitro.*	Sprague-Dawley rats, murine microglial cell line, BV-2	TLR4/MD2, CD11b	IL-1β	Lewis et al. (2010); Khabbazi et al. (2016)

morphine after 24 h. Naloxone pretreatment completely antagonized the regulatory effects of morphine on NO_2^- release. Alexander et al. demonstrated the effect of exogenous morphine on immune dysfunction in a mouse model of burns (Alexander et al., 2005). It was found that the combination of burn injury and morphine did not change the ability of macrophages to produce cytokines, but there was increased LPS-induced NO_2^- production of spleen macrophages in morphine-treated mice.

The RelB factor plays an important role in the morphine regulation of macrophage cytokine production (Martucci et al., 2007). Morphine inhibits the expression of iNOS mediated by NF-κB in mice, which leads to the overactivation of cNOS and an increase in NO production. Morphine significantly decreased the production of pro-inflammatory cytokines IL-1, TNF-β, and IL-12 by animal macrophages, but had little effect on the anti-inflammatory cytokine IL-10. It has been suggested that RelB is an important target for morphine to regulate pro-inflammatory factors, but not anti-inflammatory factors. It should be noted that lack of RelB may alter the expression of cellular components downstream of the opioid receptor activation pathway and this factor may not be the direct target of opioid action.

In addition to morphine, some laboratories have explored and compared the effects of different opioids on macrophage cytokine production. Kozlowski et al. (2017) studied the effects of oxycodone and buprenorphine on the production of ROS intermediates and NO in peritoneal macrophages of mice *in vivo* and *in vitro*, and compared the effects of morphine, fentanyl, and methadone on macrophage immune function previously studied by Filipczak-Bryniarska et al. (2012). It was found that buprenorphine and oxycodone showed weaker immunomodulatory properties than morphine, which could prevent redundant inhibition of physiological immune defense. Some studies have found that the effect of heroin on macrophages is complex (Holán et al., 2003), for example, a study showed that within 2 h of heroin administration, the proliferation response to alloantigens and the production of IL-1β, IFN-γ, IL-12, and NO were significantly enhanced, while the production of anti-inflammatory cytokines IL-4 and IL-10 decreased.

There are several studies that specifically report the effects of opioids on macrophage polarization. Morphine may induce local macrophage phenotypic changes in the early stage of pain through the COX2/PGE2-dependent pathway (Godai et al., 2014). At the site of local morphine injection, pro-inflammatory F4/80 + iNOS + M1 macrophages decreased during pain formation, while F4/80 + CD206 + M2 macrophages increased in the early stage of wound healing. Buprenorphine, a synthetic opioid analgesic with MOP receptor activation and antagonism, has been found to have different regulatory effects on M1 and M2 macrophages (Sun et al., 2017). Buprenorphine inhibited the expression of many kinds of cytokine mRNAs and proteins in M1 macrophages and enhanced the expression of Ym1 and Fizz1 in M2 macrophages. In addition, buprenorphine did not affect the regulation of LPS on the cascade of NF-κB and MAPK in M1 macrophages but inhibited the expression of IRF5 and reduced the binding of DNA to IRF5. This suggests that buprenorphine can downregulate the IRF5 pathway and restrict the phenotype of M1 macrophages. Tramadol also has different regulatory effects on M1 and M2 macrophages. Tramadol regulates inflammation by inhibiting M1 macrophages, thereby inhibiting the killing process, and promoting M2 macrophage function, thereby promoting the healing process (Zhang et al., 2017). Tramadol significantly upregulated the expression of Arg1, Mrc1, Ym1, and Fizz1 in M2 macrophages. The STAT6 pathway may be the basis of tramadol's effects because tramadol promotes the phosphorylation of STAT6, the Arg1 expression of STAT6, and the DNA binding of STAT6 in a dose-dependent manner.

In recent years, the polarization of macrophages has been a hot topic in research. The above research shows that opioids can

TABLE 3 | Opioids affect the apoptosis of macrophages.

Opioids	Cell type/animal model	Mechanism or approach	Organelles involved	References
Morphine	J 774.16 cells	Induces oxidative stress; caspase-3 activation	Mitochondria, endoplasmic reticulum	Bhat et al. (2004)
Morphine	J774 cells	Through opiate receptors *via* P38 MAPK phosphorylation TGF-β and iNOS activate proteins involved in exogenous (Fas and FasL) and endogenous (p53 and Bax) cell death pathways	Mitochondria, endoplasmic reticulum	Singhal et al. (2002)
Morphine	J774 cells Murine peritoneal Mf	The generation of TGF-β	Mitochondria	Singhal et al. (2000)
Morphine	Sprague Dawley rats	Accumulation of p53 (the induction phase of apoptosis); accumulation of Bax and activation of ICE-1 (the effector phase)	Mitochondria	Singhal et al. (1998)
Morphine	FVB/N mice	Heme oxygenase-1 (HO-1)	Mitochondria	Patel et al. (2003)

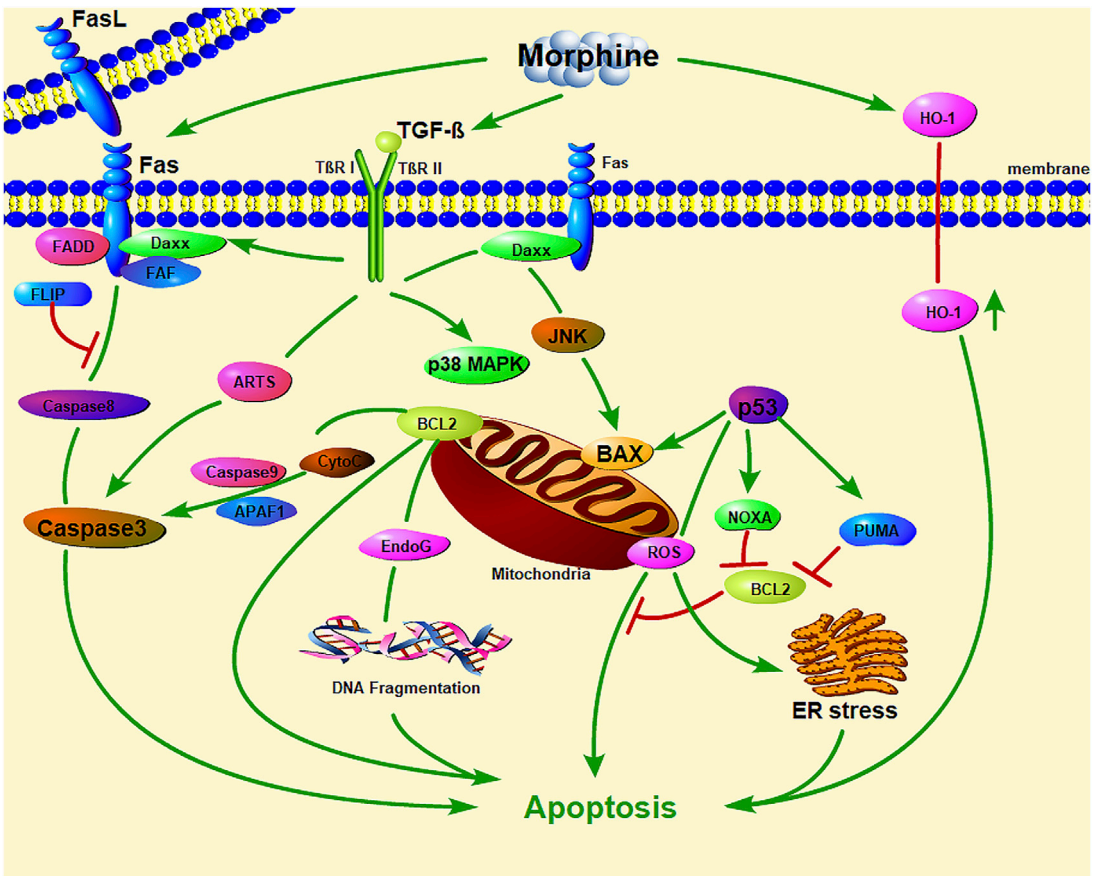

FIGURE 1 | The important role of mitochondrial and endoplasmic reticulum stress in morphine-induced macrophage apoptosis. (Daxx: death domain-associated protein; FADD: Fas-associated with death domain protein; JNK: c-Jun N-terminal kinase; CytC: Cytochrome C; EndoG: Endonuclease G; PUMA: p53 upregulated modulator of apoptosis; ER stress: endoplasmic reticulum stress; HO-1: Heme oxygenase-1).

affect the polarization of macrophages. The factors that affect the polarization direction of macrophages (M1 or M2) include the types of opioids and how they are used, the local environment of macrophages and physiological or pathological conditions. However, more basic and clinical research on the mechanism of opioids influencing macrophage polarization is needed in the future.

OPIOIDS AFFECT THE APOPTOSIS OF MACROPHAGES

Studies showed that, morphine induced macrophage apoptosis in a dose-dependent manner (**Table 3**). Morphine-induced macrophage apoptosis is caused by morphine acting on opioid receptors through the p38 MAPK phosphorylation pathway.

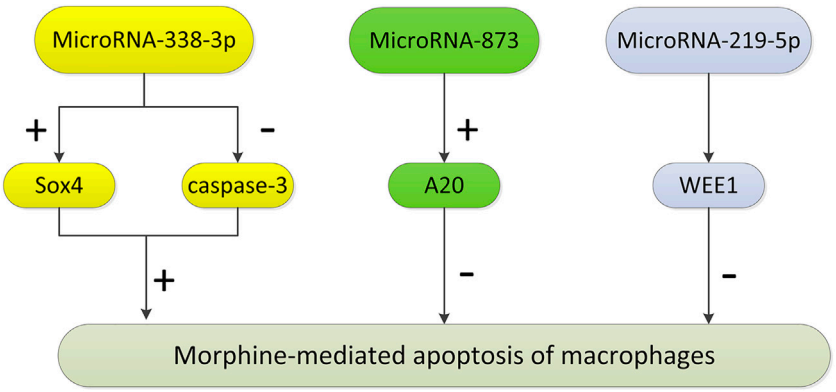

FIGURE 2 | The pathways regulated by microRNAs in morphine-mediated apoptosis of macrophages. After morphine treatment, the expression level of miR-338-3p in peritoneal macrophages increased significantly, which decreased the expression level of Sox4, leading to the increase of caspase-3 expression level, and then promoting cell apoptosis. MicroRNA-873 inhibits morphine-induced macrophage apoptosis by increasing the expression of A20. MicroRNA-219-5p inhibits morphine-induced apoptosis by targeting WEE1, the key cell cycle regulator. ("+" represents promotion, and "–" represents inhibition.)

TGF-β and iNOS play important roles in morphine-induced downstream signal transduction (Singhal et al., 1998; Singhal et al., 2000; Singhal et al., 2002; Bhat et al., 2004), which seems to activate proteins involved in exogenous (Fas and FasL) and endogenous (p53 and Bax) cell death pathways (**Figure 1**). Morphine enhances iNOS mRNA expression in macrophages and induces macrophage apoptosis, which could be inhibited by iNOS inhibitors (L-NAME and L-NMMA), suggesting that morphine-induced macrophage apoptosis may be mediated by NO production. Morphine induces macrophage apoptosis through the accumulation of p53, while the period of morphine-induced apoptosis seems to be mediated by the accumulation of Bax and the activation of ICE-1 (Singhal et al., 1998). More interestingly, morphine-induced J774 cell apoptosis and Bax expression were inhibited by an anti-TGF-β antibody; therefore, morphine-induced J774 cell apoptosis may be mediated by the production of TGF-β (Singhal et al., 2000).

Morphine also induces macrophage apoptosis in other ways. The apoptosis of macrophages is related to organelles such as mitochondria (Chen et al., 2020; Wang K. et al., 2020; Chen et al., 2021; Liu et al., 2021a; Liu et al., 2021b) (**Figure 1**). Mitochondria are not only the main sites for intracellular oxidative phosphorylation and the formation of ATP (Wei et al., 2022), but also the sites for the production of ROS (Forte et al., 2021; Wang et al., 2021). Oxidation and endoplasmic reticulum (ER) stress can accelerate the apoptosis of macrophages (Cominacini et al., 2015). It is worth noting that ROS inhibit the apoptosis of macrophages while mediating the apoptosis of other cells, especially tumor cells. This may be the basis for macrophages exerting tumor immunity. Bhat et al. found that this process involves the oxidative activation of NADPH with phospholipase D and calcium ions, leading to the production of superoxide (Bhat et al., 2004). Antioxidants have a protective effect on morphine-induced macrophage injury, which further confirms the role of mitochondrial oxidative stress in morphine-induced macrophage apoptosis. *in vivo* and *in vitro* experiments by Patel *et al.* showed that heme oxygenase-1 plays a role in morphine-induced macrophage migration and apoptosis (Patel et al., 2003).

A variety of miRNAs control the molecular pathways involved in the regulation of the immune system and regulate many aspects of the immune response, including proliferation, differentiation, immune cell function, and intracellular signaling pathways. Some studies have found that these miRNAs play an important role in morphine-induced macrophage apoptosis (**Figure 2**). MiR-338-3p promotes cancer cell death by regulating specific signaling pathways or related genes (such as p38, mitogen-activated protein kinase, and AKT) during cancer treatment. Morphine may promote apoptosis by regulating the expression of miR-338-3p (Weng and Wang, 2016). After morphine treatment, the expression level of miR-338-3p in mouse peritoneal macrophages increased significantly, which decreased the expression level of Sox4, increased caspase-3 expression, and promoted cell apoptosis. MicroRNA-873 inhibits morphine-induced macrophage apoptosis by increasing A20 (Li et al., 2015). MicroRNA-219-5p inhibits morphine-induced apoptosis by targeting WEE1, a key cell cycle regulator (Lou et al., 2016).

EFFECT OF EXOGENOUS SYNTHETIC OPIOIDS ON MACROPHAGES

In recent years, an increasing number of studies have explored the effects of synthetic opioids on immune function. For opioid receptor agonists, their activities on opioid receptors and their effects on immune cells can all differ. Selective MOP agonists are generally associated with immunosuppression, whereas DOP receptor-selective agonists are usually associated with immune enhancement (Gomez-Flores et al., 2001). KOP receptor agonists may play an important role in

TABLE 4 | The effects of exogenous synthetic opioids on macrophage's function.

Exogenous synthetic opioids	Animal models/cell types	Effects on macrophages	References
CGPM-9	Rat peritoneal macrophages	Inhibits the production of NO and TNF-α	Hicks et al. (2001)
SNC80	Rat peritoneal macrophages Rat splenic macrophages	Stimulates the production of NO and TNF-α	Gomez-Flores et al. (2001)
DPDPE	Murine macrophage cell line (RAW 264.7)	Changes the dimer composition of NF-κB; slightly inhibit the production of MIP-2	Husted et al. (2005)
DADLE	Rat peritoneal macrophages; septic models	Inhibits the release of HMGB1, TNF-α, and IFN-γ	Tang et al. (2011)
U50488	Rat alveolar macrophage cell line (NR8383)	Anti-inflammatory effect on pulmonary macrophages	Zeng et al. (2020)
Salvinorin A	Mouse peritoneal macrophages	Moderate anti-inflammatory effects	Aviello et al. (2011); Zeng et al. (2020)
Ohmefentanyl	Rat peritoneal macrophages	Reduces the concentration of TNF-α and IL-1β; reduce phagocytic and bactericidal activity	Li et al. (2008)
Nalbuphine	Mouse contact allergic dermatitis model	Increases the production of M1 and IL-10	Inan et al. (2019)
MENK	Rat peritoneal macrophages	Regulates H_2O_2 release	Stanojević et al. (2008)
	Tumor-associated macrophages	Promotes the transformation from M1 to M2	Wang et al. (2018)

CGPM-9: 4-tyrosylamido-6-benzyl-1,2,3,4 tetrahydroquinoline; SNC80: 4-[alpha-(4-allyl-2,5-dimethyl-1-piperazinyl)-3-methoxybenzyl]-N,N-diethylbenzamide; DPDPE: (D2,5Pen)-enkephalin; DADLE: (D-Ala2, D-Leu5)-enkephalin; HMGB1: high-mobility group box 1 protein; U50488: trans-(±)3,4-dichloro-N-methyl-N-[2-(1-pyrrolidinyl)-cyclohexyl]-benzeneacetamide; MENK: methionine-enkephalin.

pulmonary inflammation by activating macrophages (Zeng et al., 2020). In this section, we will discuss the effect of exogenous synthetic opioids on macrophage function (**Table 4**).

The non-peptide opioid, CGPM-9, activates the proliferation of thymocytes and inhibits the function of macrophages, including the production of NO and TNF-α, by acting on MOP receptors (Hicks et al., 2001). Intracerebroventricular injection of the non-peptide DOP receptor agonist, SNC80, did not alter some parameters of immune activity. However, at concentrations of 10^{-7} M and 10^{-6} M, SNC80 could significantly stimulate resident and LPS-stimulated peritoneal macrophages to produce TNF-α and NO (Gomez-Flores et al., 2001). The stimulation of the δ_2-opioid receptor inhibits the activation of the p38MAPK pathway in macrophages, which is related to the decrease in TNF-α and MIP-2 production by macrophages. DPDPE, a specific δ_1-opioid receptor agonist, can change the dimer composition of the transcription factor NF-κB and slightly inhibit the production of MIP-2 (Husted et al., 2005). In addition, DADLE can inhibit the release of HMGB1 from macrophages induced by LPS, TNF-α, and IFN-γ. DADLE may protect rats with sepsis by reducing serum HMGB1 levels (Tang et al., 2011). U50488, a selective KOP agonist, had a strong anti-inflammatory effect on pulmonary macrophages within one to 2 hours after LPS-stimulated inflammatory response *in vitro* (Zeng et al., 2020). Salvinorin A (SA) is an effective KOP agonist, which can exert an intense effect on macrophages through KOP and cannabinoid CB1 receptors and shows moderate anti-inflammatory effects *in vivo* (Aviello et al., 2011; Zeng et al., 2020).

In vitro, ohmefentanyl inhibited the immunosuppressive function of rat peritoneal macrophages, including reducing the concentration of TNF-α and IL-1β, as well as inhibiting phagocytic and bactericidal activity (Li et al., 2008). Nalbuphine is a KOP receptor agonist and a MOP receptor antagonist, which can reduce pruritus and increase the production of M1 macrophages and IL-10 in a mouse model of contact dermatitis (Inan et al., 2019). The regulation of methionine-enkephalin (MENK) on the release of H_2O_2 from rat peritoneal macrophages involves different types of opioid receptors. The enhancement of H_2O_2 release induced by MENK is mediated by the functional interaction of δ_1 or δ_2 opioid receptor subtypes or MOP-KOP receptors, while the inhibition of MENK induced release involves the functional interaction between δ_1 and MOP, δ_2 and MOP or δ_1 and KOP receptors (Stanojević et al., 2008). MENK may cause macrophages in tumors to change from the M1 phenotype to the M2 phenotype and induce apoptosis by blocking the OGFr/PI3K/AKT/mTOR signalling pathway (Wang et al., 2018). Recently, Tian et al. (2020) found that MENK can inhibit influenza A virus infection and this antiviral effect is related to the promotion of opioid receptors (MOP) and the activation of NF-κB p65 to induce an antiviral state.

THE REGULATION OF ENDOGENOUS OPIOID PEPTIDES ON MACROPHAGES' FUNCTION

In addition to exogenous synthetic opioids, many immune cells also secrete endogenous opioid peptides, including enkephalins,

TABLE 5 | The effects of endogenous opioid peptides on macrophage's function.

Endogenous opioid peptides	Animal models/cell types	Effects on macrophages	References
Endomorphin	Rat peritoneal macrophages	Enhances the adhesion of macrophages and the expression of the adhesion molecule Mac-1; inhibits the chemotaxis and superoxide anion production of macrophages; inhibits the production of TNF-α, IL-10, and IL-12	Inui et al. (2002)
	Murine macrophage cell line, J774; mice peritoneal macrophages	Activates NOS2 activity, downregulate NOS2 gene expression, and inhibit the release of NO	Sarić et al. (2007); Balog et al. (2010)
	Human lipid-laden macrophages	Regulates the release of cytokines by human lipid macrophages by downregulating CD36	Chiurchiù et al. (2011)
β-endorphin	THP-1 monocyte-derived macrophages	Increases oxLDL uptake by macrophages and promote oxLDL-induced macrophages to form foam cells; transforms the macrophage phenotype into pro-inflammatory M1 through NF-κB phosphorylation; increases macrophage migration and apoptosis	Okano et al. (2020)
Dynorphin A	Murine IC-21 macrophages	Enhances Mac-1-mediated phagocytosis of macrophages	Podolnikova et al. (2015)

NOS2: Nitric oxide synthase 2; oxLDL: oxidized low-density lipoprote.

endorphins, dynorphins, FQ nociceptin/orphanin peptide, and endomorphins 1 and 2 (Gein and Baeva, 2011). They also work through opioid receptors and can bind to opioid receptors on immune cells to regulate immune function. In this section, we review the role of endogenous opioid peptides in regulating the key functions of macrophages (**Table 5**).

Endomorphin is a newly discovered MOP receptor-selective immunoreactive opioid peptide. Endomorphin-1 is mainly distributed in the brain, whereas endomorphin-2 is widely distributed in the spinal cord. Endomorphin-1 can enhance the adhesion of macrophages and the expression of the adhesion molecule Mac-1 but does not affect the phagocytosis by macrophages of *Escherichia coli*. In addition, endomorphin-1 not only inhibits the chemotaxis and superoxide anion production of macrophages, but also inhibits the production of TNF-α, IL-10, and IL-12 by macrophages stimulated by LPS (Inui et al., 2002). Endomorphin-1 can activate NOS2 activity, downregulate NOS2 gene expression, and inhibit the release of NO, which seems to be mediated by the MOP-opioid receptor (Sarić et al., 2007; Balog et al., 2010). It is worth noting that endomorphin-1 can inhibit lipid accumulation and regulate the release of cytokines by human lipid macrophages by downregulating CD36, suggesting the potential for new treatments of anti-atherosclerosis based on endomorphin (Chiurchiù et al., 2011).

β-endorphin is an endogenous opioid peptide that can play various roles in the whole body. β-endorphin, as the main agonist of MOP receptors, can be found in the brain and immune system cells. β-endorphin can increase oxidized LDL (oxLDL) uptake by macrophages and promote oxLDL-induced macrophages to form foam cells. This effect confirms that there is a close relationship between endogenous opioids and the ER metabolism of macrophages. In the process of mononuclear macrophage differentiation, β-endorphin also significantly transformed the macrophage phenotype into pro-inflammatory M1, rather than anti-inflammatory M2, through NF-κB phosphorylation. Furthermore, β-endorphin was also associated with c-Jun-N terminal kinase, p38, and NF-κB phosphorylation, which increases macrophage migration and apoptosis (Okano et al., 2020).

Integrin Mac-1 is a multi-ligand receptor that mediates a variety of monocyte/macrophage responses in the immune-inflammatory response. Dynorphin A can induce strong migration of leukocytes expressing Mac-1 and enhance Mac-1-mediated phagocytosis of latex beads by mouse IC-21 macrophages (Podolnikova et al., 2015).

OPIOIDS, MACROPHAGES, AND HIV INFECTION

Macrophages play an important role in all stages of HIV infection. They are not only the main target cells and repositories of HIV, but also the transmitters of HIV to CD4+T cells. CC chemokine receptor 5 (CCR5) is necessary for entry of macrophages by R5 HIV. Morphine may promote the entry of HIV into cells by increasing the expression of CCR5, thus promoting HIV infection and virus replication in monocytes/macrophages (Guo et al., 2002; Li et al., 2003) (**Figure 3**). The MOP receptor agonist, methadone, can also increase HIV infection in adult macrophages, which is also related to the upregulated expression of CCR5 (Li et al., 2002). In contrast, morphine can downregulate the production or expression of the CCR5 β chemokine ligand (MIP-1 α, MIP-1 β, or RANTES) in human macrophages. Since CCR5 receptor interaction promotes HIV infection and replication, morphine may increase HIV entry into macrophages by downregulating the expression of competitive CCR5 receptor ligands. It is worth noting that there is an interaction between the opioid receptor and chemokine receptor CCR5 on macrophages, and the oligomerization of the two receptors on the cell membrane may regulate receptor function (Suzuki et al., 2002). The selective KOP ligand, U50488, can inhibit HIV-1 expression in acutely infected h-MDMS, indicating that the KOP ligand may have therapeutic potential in the treatment of AIDS (Chao et al., 2001).

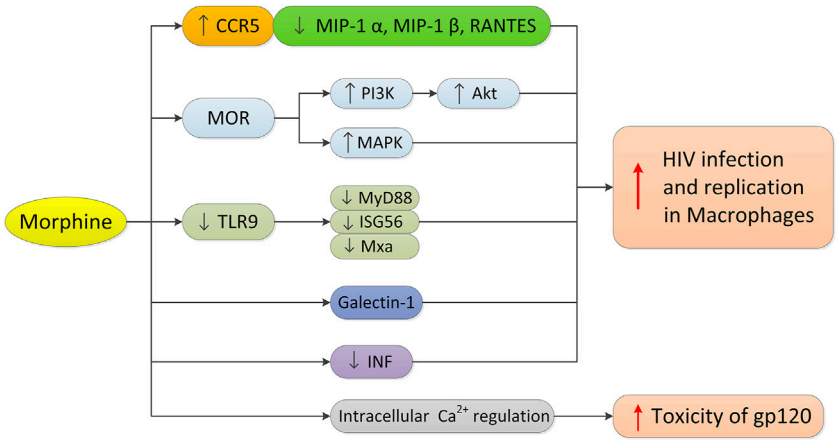

FIGURE 3 | Morphine's mechanism in regulating HIV infection in macrophages. Morphine promotes the infection and replication of HIV in macrophages as follows: 1) upregulating the expression of CCR5 and downregulating the expression of CCR5 competitive ligand in macrophages; 2) activating MOR, PI3K/Akt and MAPK signaling pathways; 3) inhibiting the TLR9 pathway and down-regulating the expression of MyD88, ISG56 and Mxa; 4) increasing the expression of Galectin-1; and 5) significantly inhibiting the interferon signaling pathway and interferon-induced gene expression, and destroying the inherent antiviral mechanism of macrophages. In addition, morphine can enhance the cytotoxicity of HIV-1 virus protein gp120 through intracellular calcium regulation.

HIV affects microglia and astrocytes, resulting in neurodegenerative changes. In HIV-infected opioid abusers, central nervous system inflammation may increase even when HIV infection is under control (Murphy et al., 2019). Opioids can enhance the cytotoxicity of the HIV-1 virus protein gp120 through an intracellular calcium regulation mechanism, making it an important cellular target for HIV-opioid interaction (Mahajan et al., 2005). Opioids not only directly affect astrocytes and macrophages or microglia that express MOP (Hauser et al., 2005; Bruce-Keller et al., 2008), but also regulate inflammation and disrupt the interaction between normal immune cells, including macrophages and lymphocytes. The neural pathways involved in opioid enhancement of HIV-induced inflammation and cell death appear to involve the activation of MOP and downstream effects through PI3K/Akt and/or MAPK signal transduction (Hauser et al., 2005). Recent studies by Liao et al. (2017) have shown that combined with HIV-1 infection, morphine reduces the expression of MyD88, ISG56, and Mxa in macrophages by inhibiting the TLR9 pathway, which in turn promotes the replication of HIV-1 in macrophages.

Many studies have shown that opioids can promote HIV infection by regulating the expression of various factors in human macrophages. Morphine can enhance the effect of HIV gp160 protein on macrophage apoptosis, iNOS expression, and NO production (Kapasi et al., 2004). Chronic morphine exposure to HIV-infected h-MDMs can lead to significant changes in the secretion of IL-6 and monocyte chemoattractant protein-2 (MCP-2) (Dave, 2012). Morphine promotes the secretion of h-MDMs infected with HIV and inactivates the secretion of MCP-2 by IL-6, which has a potential additive effect. In addition, the increased expression of Galectin-1 induced by morphine may also regulate HIV-1 infection and increase the infection of HIV-1 (Reynolds et al., 2012). H-MDMs treated with morphine and methadone can significantly inhibit the interferon signaling pathway and interferon-induced gene expression (Wang et al., 2012; Wang MR. et al., 2020), thus damaging the inherent antiviral mechanism in macrophages and increasing the susceptibility of cells to HIV infection.

Differentially expressed miRNAs (hsa-miR-15b and 181Mub) may play a potential role in regulating morphine-induced inflammation and oxidative stress in h-MDMS, leading to the expansion of the central nervous system reservoir of HIV-1 and the progression of AIDS (Dave and Khalili, 2010). Heroin and methadone can inhibit microRNA restriction (miRNA-28, -125b, -150, and -382) and enhance HIV infection and replication in macrophages (Wang et al., 2015; Wang MR. et al., 2020). Sudden or slow withdrawal of morphine can inhibit the expression of many HIV inhibitors in macrophages, including APOBE3G/F, SAMHD1, MX2, and HIV-restricted microRNA (miR-28, miR-125b, and miR-150), and further enhance the sensitivity of macrophages to HIV infection (Wang et al., 2019).

OPIOIDS, MACROPHAGES, AND TUMORS

Some studies have shown that TAMs play an important role in tumor invasion and metastasis, and the role of TAMs in tumors is almost the same as that of M2 macrophages (Rolny et al., 2011). This view has been confirmed by TAM and M2 macrophage expression profiles (Porta et al., 2009). The conversion of M1 macrophages to M2 in tumors has also become one of the main directions of current research. Many studies have shown that opioids can combine with opioid receptors to regulate immunity or other pathways that affect the occurrence, development, and prognosis of tumors (Fujioka et al., 2011; Kuzumaki et al., 2012; Long et al., 2016).

Morphine can regulate tumor invasiveness by regulating the production of macrophage proteases and M2 polarization in the tumor microenvironment (Khabbazi et al., 2015). IL-4 leads to

the production of MMP-9 and increased expression of the M2 markers Arg-1 and MRC-1. Morphine inhibits IL-4-induced increase of MMP-9 and selective activation of macrophages in a reversible manner with naloxone and methylnaltrexone. When macrophage cell line RAW264.7 was subjected to paracrine activation by 4T1 breast cancer cells, the expression of MMP-9 and Arg-1 increased, and this effect was blocked by morphine through an opioid receptor-mediated mechanism. Morphine further reduced the invasion of 4T1 breast cancer cells co-cultured with RAW264.7.

There is also evidence that opioid receptor agonists or antagonists affect tumor growth by regulating macrophage function. The opioid receptor agonist leu-enkephalin has an anti-survival effect in renal clear cell carcinoma, mainly through Th2 immunity and the NRF2-dependent macrophage network (Scarpa et al., 2020). Low-dose naltrexone (LDN) reduces tumor size by increasing the level of M1-like macrophages and activating the Bax/Bcl-2/caspase-3/PARP signaling pathway to induce apoptosis (Ma et al., 2020). In addition, LDN indirectly reduced the number of TAMs (mainly M2) and decreased the expression of anti-inflammatory factor IL-10 in the serum of nude mice, indicating that LDN may be a potential treatment for cervical cancer (Liu et al., 2020).

In short, the effects of opioids on macrophage subtypes may further affect the occurrence and development of tumors. Research in this direction may provide a new strategy for the use of opioids, such as morphine, and the prognosis and treatment of tumors.

OPIOIDS AND ORGANELLES IN MACROPHAGES: A VALUABLE RESEARCH DIRECTION

Organelles are generally regarded as micro-structures or micro-organs with certain morphology and functions dispersed throughout the cytoplasm of cells. Key organelles in macrophages include mitochondria, endoplasmic reticulum, Golgi apparatus, ribosomes, lysosomes, and centrosomes. They constitute the basic structure of macrophages, which enable cells to work and operate normally and enable macrophages to play a role in human physiological and pathological conditions. In view of the important role of mitochondria and endoplasmic reticulum in the metabolism and function of macrophages, we mainly discuss these two organelles here.

There is growing evidence that mitochondria are central regulators of metabolic reprogramming and control the activation and function of immune cells (El Kasmi and Stenmark, 2015; Corrêa-da-Silva et al., 2018; Liu and Ho, 2018; Ramond et al., 2019). Macrophages that differentiate into M1 can increase glucose uptake and glycolysis (Rodríguez-Prados et al., 2010). This is associated with the production of HIF1α. HIF1 induces the production of the pro-inflammatory factor IL-1β and the upregulation of several enzymes associated with glycolysis (Tannahill et al., 2013). The expression of carbohydrate kinase-like protein, which inhibits the pentose phosphate pathway, is down-regulated in M1 macrophages, leads to an increased pentose phosphate pathway (Haschemi et al., 2012). The pentose phosphate pathway produces nucleotides and NADPH, the latter of which is important for mitochondrial ROS production (Haschemi et al., 2012). M1 macrophages also increase glutamine metabolism, and glutamine is used as α-ketoglutaric acid in the TCA cycle after its decomposition (Tannahill et al., 2013). This stimulates the accumulation of succinic acid (Tannahill et al., 2013). As mentioned earlier, the TCA cycle of M1 macrophages is impaired with two defective steps (Tannahill et al., 2013; Jha et al., 2015). The first defective step results in the accumulation of citric acid in the cytoplasm of cells (Newsholme et al., 1986). Citric acid can then be used to synthesize lipids (prostaglandins), NO, or ROS (Infantino et al., 2011), which are important for the function of M1 macrophages. Another defective step in the TCA cycle results in the accumulation of succinic acid (Tannahill et al., 2013), which stabilizes HIF1α. With the increase of glycolysis, the coordinated rearrangement of the TCA cycle, and the decrease of mitochondrial oxidative phosphorylation, the production of intermediates (such as succinic acid, citric acid) and ROS/NO is promoted. The accumulation of these substances plays a specific role in enhancing the ability of macrophages to initiate an inflammatory response and participate in paracrine signals (El Kasmi and Stenmark, 2015). In addition, like the role of mitochondrial nucleotides in inducing inflammation (Kuck et al., 2015), the regulation of macrophage plasticity, by the reprogramming of mitochondrial metabolism, has become another important feature of mitochondria. More interestingly, the increase of aerobic glycolysis is a key prerequisite for maintaining mitochondrial membrane potential, thus preventing macrophage apoptosis. Compared with M1, M2 macrophages do not increase glycolysis (Rodríguez-Prados et al., 2010). The metabolism of M2 macrophages depends on the TCA cycle and oxidative phosphorylation (mainly β-oxidation) (Vats et al., 2006; Huang et al., 2014). Enhanced β-oxidation was associated with increased TCA, increased respiratory capacity, and thus with an increased ability to produce ATP through oxidative phosphorylation. This may be important for the physiological function of M2 macrophages.

The dysfunction of organelles caused by various factors often leads to metabolic disorders and functional disorders of macrophages. The endoplasmic reticulum (ER) is a complex cytoplasmic membrane structure involved in protein synthesis, folding and modification, lipid synthesis and transport, and intracellular calcium balance regulation (Sukhorukov et al., 2020). ER stress severely interferes with ER function, Ca^{2+} signaling, and protein synthesis, and is associated with a variety of pathophysiologies, such as macrophage apoptosis (Scull and Tabas, 2011; Cominacini et al., 2015), efferocytosis (Linton et al., 2016), foam cell formation (Han and Kaufman, 2016), and inflammation. ER stress can activate or accelerate apoptosis of macrophages through a variety of pathways, such as excessive accumulation of lipids (free cholesterol, sterols, and oxLDL), inflammatory pathways (acceleration of INF-γ), oxHDL binding to TLR4, and increased Ca^{2+} concentration in the ER

leading to mitochondrial uptake of calcium ions. ER stress regulates lipid metabolism in macrophages by stimulating cholesterol uptake, inhibiting cholesterol outflow, and regulating the expression of cholesterol membrane transporters, resulting in lipid accumulation and subsequent differentiation into foam cells in macrophages (Sukhorukov et al., 2020). Addressing how to mitigate metabolic disorders by controlling ER stress-mediated macrophage plasticity is crucial for the progression of atherosclerosis. In addition, ER stress may be involved in cellular inflammation through NF-κB, activated protein-1 and JNK signaling pathways, and ROS production (Sukhorukov et al., 2020). A link between cholesterol accumulation, ER stress, and the pro-inflammatory response has been established, but the complex relationships between the processes involved still need to be described in detail. Some studies have also emphasized the key role of mitochondria in the response of macrophages to bacterial pathogens (Ramond et al., 2019). Mitochondria can meet the energy needs of cells and maintain the phagocytosis of macrophages in the lytic stage. Mitochondrial disorders may be a cause of susceptibility to bacterial infection.

Mitochondria and other organelles play an irreplaceable role in the cellular metabolism and immune response of macrophages. It has already been mentioned that mitochondrial and ER stress is extremely important in morphine-induced macrophage apoptosis (**Figure 1**). However, there are limited studies on the effects of other opioid drugs on the functions of various organelles of macrophages. Exploring how opioids control the flexibility of macrophage metabolic programs and influence the connections between macrophage metabolism and transcriptional networks during inflammatory activation and anti-inflammatory processes is crucial to better understand the effects of opioids on macrophage plasticity and macrophage biology. Whether opioids can change macrophages from a pro-inflammatory phenotype to a less inflammatory phenotype or even repair macrophage phenotype, remains to be further studied.

CONCLUSION

Opioids are one of the most effective painkillers that can be used to treat pain in the clinic. It has been confirmed that opioids have potential effects on the functioning of the immune system. Many studies have explored the relationship between macrophages and different opioids *in vitro*, *in vivo*, and in epidemiological and clinical studies in different patient groups. Opioids mediate the effects on macrophages through direct and indirect mechanisms. The binding with various opioid receptors on the surface of macrophages is a direct actional pathway, affecting the migration and phagocytic activity of macrophages. Indirect effects include the production of opioid receptors and endogenous opioid peptides in the central nervous system. Because macrophages provide antigens for lymphocytes, the effects of opioids on macrophage function may change host immune defense and changes in macrophage function may also affect the immune response. Different types of opioids, different doses, and administration methods have different regulatory effects on macrophages and their subtypes. The single and combined effects of opioids may impair the functioning of macrophages in the host defense system. Morphine induced macrophage apoptosis in a dose-dependent manner, indicating that the impairment of macrophage function induced by morphine may be indirectly caused by morphine-induced macrophage apoptosis. A number of studies have shown that opioids can regulate macrophages to promote HIV infection and the progression of AIDS in a variety of ways. Exploring suitable opioid receptor ligands may be one of the strategies for the treatment of AIDS. Opioids can combine with opioid receptors to regulate immunity or other pathways that affect the occurrence, development, and prognosis of tumors. Therefore, how opioids affect tumor progression through macrophage subtypes is worth exploring.

Although there have been some studies on the effects of opioids on macrophages, the mechanism is still not clear, and more prospective studies are needed. In addition, the study on the effects of commonly used opioids, such as fentanyl and sufentanil, on macrophages during the perioperative period can provide suggestions for the guidance of perioperative drug use, but some studies are limited due to the particularity of narcotic drugs. The study of the possible correlation between the use of opioids and macrophage effects will help to provide a theoretical basis for the better application of opioids in clinical pain treatment and tumor outcome and treatment.

AUTHOR CONTRIBUTIONS

SW and XZ designed the structure of this article. SW and XZ wrote the manuscript. ZC and QG reviewed the manuscript. YJ, SL, XZ, and ZC made substantial and intellectual contributions to the work. All authors approved the article for publication.

FUNDING

This work was supported by the National Natural Science Foundation of China (81400916 to XZ), Natural Science Foundation of Hunan Province (2021JJ41060 to XZ), Changsha Municipal Natural Science Foundation (kq2014280 to XZ).

ACKNOWLEDGMENTS

We would like to thank Editage (www.editage.com) for English language editing. We would also like to thank the library of Central South University for its academic support.

REFERENCES

Alexander, M., Daniel, T., Chaudry, I. H., and Schwacha, M. G. (2005). Opiate Analgesics Contribute to the Development of Post-Injury Immunosuppression. *J. Surg. Res.* 129 (1), 161–168. doi:10.1016/j.jss.2005.04.028

Aviello, G., Borrelli, F., Guida, F., Romano, B., Lewellyn, K., De Chiaro, M., et al. (2011). Ultrapotent Effects of Salvinorin A, a Hallucinogenic Compound from Salvia Divinorum, on LPS-Stimulated Murine Macrophages and its Anti-inflammatory Action *In Vivo*. *J. Mol. Med. (Berl)* 89 (9), 891–902. doi:10.1007/s00109-011-0752-4

Balog, T., Sarić, A., Sobocanec, S., Kusić, B., and Marotti, T. (2010). Endomorphin-Suppressed Nitric Oxide Release from Mice Peritoneal Macrophages. *Neuropeptides* 44 (1), 25–29. doi:10.1016/j.npep.2009.11.004

Bhaskaran, M., Kapasi, A. A., Reddy, K., and Singhal, P. C. (2007). Morphine Priming Rescues High-Dose Morphine-Induced Biological Perturbations. *J. Infect. Dis.* 195 (12), 1860–1869. doi:10.1086/518039

Bhat, R. S., Bhaskaran, M., Mongia, A., Hitosugi, N., and Singhal, P. C. (2004). Morphine-induced Macrophage Apoptosis: Oxidative Stress and Strategies for Modulation. *J. Leukoc. Biol.* 75 (6), 1131–1138. doi:10.1189/jlb.1203639

Boland, J. W., and Pockley, A. G. (2018). Influence of Opioids on Immune Function in Patients with Cancer Pain: from Bench to Bedside. *Br. J. Pharmacol.* 175 (14), 2726–2736. doi:10.1111/bph.13903

Bruce-Keller, A. J., Turchan-Cholewo, J., Smart, E. J., Geurin, T., Chauhan, A., Reid, R., et al. (2008). Morphine Causes Rapid Increases in Glial Activation and Neuronal Injury in the Striatum of Inducible HIV-1 Tat Transgenic Mice. *Glia* 56 (13), 1414–1427. doi:10.1002/glia.20708

Calle, P., and Hotter, G. (2020). Macrophage Phenotype and Fibrosis in Diabetic Nephropathy. *Int. J. Mol. Sci.* 21 (8), 2806. doi:10.3390/ijms21082806

Chao, C. C., Gekker, G., Sheng, W. S., Hu, S., and Peterson, P. K. (2001). U50488 Inhibits HIV-1 Expression in Acutely Infected Monocyte-Derived Macrophages. *Drug Alcohol Depend* 62 (2), 149–154. doi:10.1016/s0376-8716(00)00185-x

Chen, H., Wang, H., Wei, Y., Hu, M., Dong, B., Fang, H., et al. (2021). Super-Resolution Imaging Reveals the Subcellular Distribution of Dextran at the Nanoscale in Living Cells. *Chin. Chem. Lett.*. doi:10.1016/j.cclet.2021.10.025

Chen, Q., Shao, X., Hao, M., Fang, H., Guan, R., Tian, Z., et al. (2020). Quantitative Analysis of Interactive Behavior of Mitochondria and Lysosomes Using Structured Illumination Microscopy. *Biomaterials* 250, 120059. doi:10.1016/j.biomaterials.2020.120059

Chiurchiù, V., Izzi, V., D'Aquilio, F., Vismara, D., Carotenuto, F., Catanzaro, G., et al. (2011). Endomorphin-1 Prevents Lipid Accumulation via CD36 Down-Regulation and Modulates Cytokines Release from Human Lipid-Laden Macrophages. *Peptides* 32 (1), 80–85. doi:10.1016/j.peptides.2010.09.024

Cominacini, L., Garbin, U., Mozzini, C., Stranieri, C., Pasini, A., Solani, E., et al. (2015). The Atherosclerotic Plaque Vulnerability: Focus on the Oxidative and Endoplasmic Reticulum Stress in Orchestrating the Macrophage Apoptosis in the Formation of the Necrotic Core. *Curr. Med. Chem.* 22 (13), 1565–1572. doi:10.2174/0929867322666150311150829

Corrêa-da-Silva, F., Pereira, J. A. S., de Aguiar, C. F., and de Moraes-Vieira, P. M. M. (2018). Mitoimmunity-when Mitochondria Dictates Macrophage Function. *Cell Biol Int* 42 (6), 651–655. doi:10.1002/cbin.10921

Dave, R. S., and Khalili, K. (2010). Morphine Treatment of Human Monocyte-Derived Macrophages Induces Differential miRNA and Protein Expression: Impact on Inflammation and Oxidative Stress in the central Nervous System. *J. Cel Biochem* 110 (4), 834–845. doi:10.1002/jcb.22592

Dave, R. S. (2012). Morphine Affects HIV-Induced Inflammatory Response without Influencing Viral Replication in Human Monocyte-Derived Macrophages. *FEMS Immunol. Med. Microbiol.* 64 (2), 228–236. doi:10.1111/j.1574-695X.2011.00894.x

de Gaetano, M., Crean, D., Barry, M., and Belton, O. (2016). M1- and M2-Type Macrophage Responses Are Predictive of Adverse Outcomes in Human Atherosclerosis. *Front. Immunol.* 7, 275. doi:10.3389/fimmu.2016.00275

Delgado-Vélez, M., Lugo-Chinchilla, A., Lizardo, L., Morales, I., Robles, Y., Bruno, N., et al. (2008). Chronic Exposure of Human Macrophages *In Vitro* to Morphine and Methadone Induces a Putative Tolerant/Dependent State. *J. Neuroimmunol* 196 (1-2), 94–100. doi:10.1016/j.jneuroim.2008.03.004

Eisenstein, T. K., and Hilburger, M. E. (1998). Opioid Modulation of Immune Responses: Effects on Phagocyte and Lymphoid Cell Populations. *J. Neuroimmunol* 83 (1-2), 36–44. doi:10.1016/s0165-5728(97)00219-1

Eisenstein, T. K. (2019). The Role of Opioid Receptors in Immune System Function. *Front. Immunol.* 10, 2904. doi:10.3389/fimmu.2019.02904

El Kasmi, K. C., and Stenmark, K. R. (2015). Contribution of Metabolic Reprogramming to Macrophage Plasticity and Function. *Semin. Immunol.* 27 (4), 267–275. doi:10.1016/j.smim.2015.09.001

Filipczak-Bryniarska, I., Nowak, B., Sikora, E., Nazimek, K., Woroń, J., Wordliczek, J., et al. (2012). The Influence of Opioids on the Humoral and Cell-Mediated Immune Responses in Mice. The Role of Macrophages. *Pharmacol. Rep.* 64 (5), 1200–1215. doi:10.1016/s1734-1140(12)70916-7

Forte, M., Bianchi, F., Cotugno, M., Marchitti, S., Stanzione, R., Maglione, V., et al. (2021). An Interplay between UCP2 and ROS Protects Cells from High-Salt-Induced Injury through Autophagy Stimulation. *Cell Death Dis* 12 (10), 919. doi:10.1038/s41419-021-04188-4

Fujioka, N., Nguyen, J., Chen, C., Li, Y., Pasrija, T., Niehans, G., et al. (2011). Morphine-Induced Epidermal Growth Factor Pathway Activation in Non-Small Cell Lung Cancer. *Anesth. Analg* 113 (6), 1353–1364. doi:10.1213/ANE.0b013e318232b35a

Gein, S. V., and Baeva, T. A. (2011). Endogenous Opioid Peptides in Regulation of Innate Immunity Cell Functions. *Biochemistry (Mosc)* 76 (3), 309–319. doi:10.1134/s0006297911030035

Godai, K., Hasegawa-Moriyama, M., Kurimoto, T., Saito, T., Yamada, T., Sato, T., et al. (2014). Peripheral Administration of Morphine Attenuates Postincisional Pain by Regulating Macrophage Polarization through COX-2-Dependent Pathway. *Mol. Pain* 10, 36. doi:10.1186/1744-8069-10-36

Gomez-Flores, R., Rice, K. C., Zhang, X., and Weber, R. J. (2001). Increased Tumor Necrosis Factor-Alpha and Nitric Oxide Production by Rat Macrophages Following *In Vitro* Stimulation and Intravenous Administration of the delta-opioid Agonist SNC 80. *Life Sci.* 68 (24), 2675–2684. doi:10.1016/s0024-3205(01)01082-7

Guo, C. J., Li, Y., Tian, S., Wang, X., Douglas, S. D., and Ho, W. Z. (2002). Morphine Enhances HIV Infection of Human Blood Mononuclear Phagocytes through Modulation of Beta-Chemokines and CCR5 Receptor. *J. Investig. Med.* 50 (6), 435–442. doi:10.1136/jim-50-06-03

Han, J., and Kaufman, R. J. (2016). The Role of ER Stress in Lipid Metabolism and Lipotoxicity. *J. Lipid Res.* 57 (8), 1329–1338. doi:10.1194/jlr.R067595

Haschemi, A., Kosma, P., Gille, L., Evans, C. R., Burant, C. F., Starkl, P., et al. (2012). The Sedoheptulose Kinase CARKL Directs Macrophage Polarization through Control of Glucose Metabolism. *Cell Metab* 15 (6), 813–826. doi:10.1016/j.cmet.2012.04.023

Hauser, K. F., El-Hage, N., Buch, S., Berger, J. R., Tyor, W. R., Nath, A., et al. (2005). Molecular Targets of Opiate Drug Abuse in neuroAIDS. *Neurotox Res.* 8 (1-2), 63–80. doi:10.1007/bf03033820

Hicks, M. E., Gomez-Flores, R., Wang, C., Mosberg, H. I., and Weber, R. J. (2001). Differential Effects of the Novel Non-Peptidic Opioid 4-Tyrosylamido-6-Benzyl-1,2,3,4 Tetrahydroquinoline (CGPM-9) on *In Vitro* Rat T Lymphocyte and Macrophage Functions. *Life Sci.* 68 (24), 2685–2694. doi:10.1016/s0024-3205(01)01083-9

Holáň, V., Zajícová, A., Krulová, M., Blahoutová, V., and Wilczek, H. (2003). Augmented Production of Proinflammatory Cytokines and Accelerated Allotransplantation Reactions in Heroin-Treated Mice. *Clin. Exp. Immunol.* 132 (1), 40–45. doi:10.1046/j.1365-2249.2003.02103.x

Huang, S. C., Everts, B., Ivanova, Y., O'Sullivan, D., Nascimento, M., Smith, A. M., et al. (2014). Cell-Intrinsic Lysosomal Lipolysis Is Essential for Alternative Activation of Macrophages. *Nat. Immunol.* 15 (9), 846–855. doi:10.1038/ni.2956

Husted, T. L., Govindaswami, M., Oeltgen, P. R., Rudich, S. M., and Lentsch, A. B. (2005). A delta2-Opioid Agonist Inhibits P38 MAPK and Suppresses Activation of Murine Macrophages. *J. Surg. Res.* 128 (1), 45–49. doi:10.1016/j.jss.2005.04.003

Ignatowski, T. A., and Bidlack, J. M. (1999). Differential Kappa-Opioid Receptor Expression on Mouse Lymphocytes at Varying Stages of Maturation and on Mouse Macrophages after Selective Elicitation. *J. Pharmacol. Exp. Ther.* 290 (2), 863–870.

Inan, S., Torres-Huerta, A., Jensen, L. E., Dun, N. J., and Cowan, A. (2019). Nalbuphine, a Kappa Opioid Receptor Agonist and Mu Opioid Receptor Antagonist Attenuates Pruritus, Decreases IL-31, and Increases IL-10 in Mice with Contact Dermatitis. *Eur. J. Pharmacol.* 864, 172702. doi:10.1016/j.ejphar.2019.172702

Infantino, V., Convertini, P., Cucci, L., Panaro, M. A., Di Noia, M. A., Calvello, R., et al. (2011). The Mitochondrial Citrate Carrier: A New Player in Inflammation. *Biochem. J.* 438 (3), 433–436. doi:10.1042/bj20111275

Inui, Y., Azuma, Y., and Ohura, K. (2002). Differential Alteration of Functions of Rat Peritoneal Macrophages Responsive to Endogenous Opioid Peptide Endomorphin-1. *Int. Immunopharmacol* 2 (8), 1133–1142. doi:10.1016/s1567-5769(02)00065-6

James, A., and Williams, J. (2020). Basic Opioid Pharmacology - an Update. *Br. J. Pain* 14 (2), 115–121. doi:10.1177/2049463720911986

Jha, A. K., Huang, S. C., Sergushichev, A., Lampropoulou, V., Ivanova, Y., Loginicheva, E., et al. (2015). Network Integration of Parallel Metabolic and Transcriptional Data Reveals Metabolic Modules that Regulate Macrophage Polarization. *Immunity* 42 (3), 419–430. doi:10.1016/j.immuni.2015.02.005

Jinnouchi, H., Guo, L., Sakamoto, A., Torii, S., Sato, Y., Cornelissen, A., et al. (2020). Diversity of Macrophage Phenotypes and Responses in Atherosclerosis. *Cell Mol Life Sci* 77 (10), 1919–1932. doi:10.1007/s00018-019-03371-3

Kapasi, A. A., Coscia, S. A., Pandya, M. P., and Singhal, P. C. (2004). Morphine Modulates HIV-1 Gp160-Induced Murine Macrophage and Human Monocyte Apoptosis by Disparate Ways. *J. Neuroimmunol* 148 (1-2), 86–96. doi:10.1016/j.jneuroim.2003.11.015

Khabbazi, S., Goumon, Y., and Parat, M. O. (2015). Morphine Modulates Interleukin-4- or Breast Cancer Cell-Induced Pro-Metastatic Activation of Macrophages. *Sci. Rep.* 5, 11389. doi:10.1038/srep11389

Khabbazi, S., Xie, N., Pu, W., Goumon, Y., and Parat, M. O. (2016). The TLR4-Active Morphine Metabolite Morphine-3-Glucuronide Does Not Elicit Macrophage Classical Activation *In Vitro*. *Front. Pharmacol.* 7, 441. doi:10.3389/fphar.2016.00441

Kozlowski, M., Nazimek, K., Wąsik, M., Filipczak-Bryniarska, I., and Bryniarski, K. (2017). The Impact of Advanced Opioid Drugs and Analgesic Adjuvants on Murine Macrophage Oxygen Burst. *Folia Med. Cracov* 57 (2), 15–30.

Kuck, J. L., Obiako, B. O., Gorodnya, O. M., Pastukh, V. M., Kua, J., Simmons, J. D., et al. (2015). Mitochondrial DNA Damage-Associated Molecular Patterns Mediate a Feed-Forward Cycle of Bacteria-Induced Vascular Injury in Perfused Rat Lungs. *Am. J. Physiol. Lung Cel Mol Physiol* 308 (10), L1078–L1085. doi:10.1152/ajplung.00015.2015

Kuzumaki, N., Suzuki, A., Narita, M., Hosoya, T., Nagasawa, A., Imai, S., et al. (2012). Effect of κ-Opioid Receptor Agonist on the Growth of Non-Small Cell Lung Cancer (NSCLC) Cells. *Br. J. Cancer* 106 (6), 1148–1152. doi:10.1038/bjc.2011.574

Lewis, S. S., Hutchinson, M. R., Rezvani, N., Loram, L. C., Zhang, Y., Maier, S. F., et al. (2010). Evidence that Intrathecal Morphine-3-Glucuronide May Cause Pain Enhancement via Toll-like Receptor 4/MD-2 and Interleukin-1beta. *Neuroscience* 165 (2), 569–583. doi:10.1016/j.neuroscience.2009.10.011

Li, M. C., Yu, J. H., Yu, S. S., Chi, Y. Y., and Xiang, Y. B. (2015). MicroRNA-873 Inhibits Morphine-Induced Macrophage Apoptosis by Elevating A20 Expression. *Pain Med.* 16 (10), 1993–1999. doi:10.1111/pme.12784

Li, W. Y., Yang, J. J., Zhu, S. H., Liu, H. J., and Xu, J. G. (2008). Endomorphins and Ohmefentanyl in the Inhibition of Immunosuppressant Function in Rat Peritoneal Macrophages: An Experimental *In Vitro* Study. *Curr. Ther. Res. Clin. Exp.* 69 (1), 56–64. doi:10.1016/j.curtheres.2008.02.004

Li, Y., Merrill, J. D., Mooney, K., Song, L., Wang, X., Guo, C. J., et al. (2003). Morphine Enhances HIV Infection of Neonatal Macrophages. *Pediatr. Res.* 54 (2), 282–288. doi:10.1203/01.Pdr.0000074973.83826.4c

Li, Y., Wang, X., Tian, S., Guo, C. J., Douglas, S. D., and Ho, W. Z. (2002). Methadone Enhances Human Immunodeficiency Virus Infection of Human Immune Cells. *J. Infect. Dis.* 185 (1), 118–122. doi:10.1086/338011

Liang, X., Liu, R., Chen, C., Ji, F., and Li, T. (2016). Opioid System Modulates the Immune Function: A Review. *Transl Perioper. Pain Med.* 1 (1), 5–13.

Liao, Y., Jiang, J., Liang, B., Wei, F., Huang, J., Pan, P., et al. (2017). Opiate Use Inhibits TLR9 Signaling Pathway *In Vivo*: Possible Role in Pathogenesis of HIV-1 Infection. *Sci. Rep.* 7 (1), 13071. doi:10.1038/s41598-017-12066-3

Limiroli, E., Gaspani, L., Panerai, A. E., and Sacerdote, P. (2002). Differential Morphine Tolerance Development in the Modulation of Macrophage Cytokine Production in Mice. *J. Leukoc. Biol.* 72 (1), 43–48.

Linton, M. F., Babaev, V. R., Huang, J., Linton, E. F., Tao, H., and Yancey, P. G. (2016). Macrophage Apoptosis and Efferocytosis in the Pathogenesis of Atherosclerosis. *Circ. J.* 80 (11), 2259–2268. doi:10.1253/circj.CJ-16-0924

Liu, N., Ma, M., Qu, N., Wang, R., Chen, H., Hu, F., et al. (2020). Low-Dose Naltrexone Inhibits the Epithelial-Mesenchymal Transition of Cervical Cancer Cells *In Vitro* and Effects Indirectly on Tumor-Associated Macrophages *In Vivo*. *Int. Immunopharmacol* 86, 106718. doi:10.1016/j.intimp.2020.106718

Liu, P. S., and Ho, P. C. (2018). Mitochondria: A Master Regulator in Macrophage and T Cell Immunity. *Mitochondrion* 41, 45–50. doi:10.1016/j.mito.2017.11.002

Liu, Z., Wang, H., Hu, C., Wu, C., Wang, J., Hu, F., et al. (2021a). Targeting Autophagy Enhances Atezolizumab-Induced Mitochondria-Related Apoptosis in Osteosarcoma. *Cel Death Dis* 12 (2), 164. doi:10.1038/s41419-021-03449-6

Liu, Z., Zheng, Y., Xie, T., Chen, Z., Huang, Z., Ye, Z., et al. (2021b). Clickable Rhodamine Spirolactam Based Spontaneously Blinking Probe for Super-resolution Imaging. *Chin. Chem. Lett.*. doi:10.1016/j.cclet.2021.04.038

Long, X., Li, Y., Qiu, S., Liu, J., He, L., and Peng, Y. (2016). MiR-582-5p/miR-590-5p Targeted CREB1/CREB5-NF-Kb Signaling and Caused Opioid-Induced Immunosuppression in Human Monocytes. *Transl Psychiatry* 6, e757. doi:10.1038/tp.2016.4

Lou, W., Zhang, X., Hu, X. Y., and Hu, A. R. (2016). MicroRNA-219-5p Inhibits Morphine-Induced Apoptosis by Targeting Key Cell Cycle Regulator WEE1. *Med. Sci. Monit.* 22, 1872–1879. doi:10.12659/msm.895439

Ma, M., Wang, X., Liu, N., Shan, F., and Feng, Y. (2020). Low-Dose Naltrexone Inhibits Colorectal Cancer Progression and Promotes Apoptosis by Increasing M1-Type Macrophages and Activating the Bax/Bcl-2/Caspase-3/PARP Pathway. *Int. Immunopharmacol* 83, 106388. doi:10.1016/j.intimp.2020.106388

Machelska, H., and Celik, M. Ö. (2020). Opioid Receptors in Immune and Glial Cells-Implications for Pain Control. *Front. Immunol.* 11, 300. doi:10.3389/fimmu.2020.00300

Mahajan, S. D., Aalinkeel, R., Reynolds, J. L., Nair, B. B., Fernandez, S. F., Schwartz, S. A., et al. (2005). Morphine Exacerbates HIV-1 Viral Protein Gp120 Induced Modulation of Chemokine Gene Expression in U373 Astrocytoma Cells. *Curr. HIV Res.* 3 (3), 277–288. doi:10.2174/1570162054368048

Martin, J. L., Koodie, L., Krishnan, A. G., Charboneau, R., Barke, R. A., and Roy, S. (2010). Chronic Morphine Administration Delays Wound Healing by Inhibiting Immune Cell Recruitment to the Wound Site. *Am. J. Pathol.* 176 (2), 786–799. doi:10.2353/ajpath.2010.090457

Martucci, C., Franchi, S., Lattuada, D., Panerai, A. E., and Sacerdote, P. (2007). Differential Involvement of RelB in Morphine-Induced Modulation of Chemotaxis, NO, and Cytokine Production in Murine Macrophages and Lymphocytes. *J. Leukoc. Biol.* 81 (1), 344–354. doi:10.1189/jlb.0406237

Moreira Lopes, T. C., Mosser, D. M., and Gonçalves, R. (2020). Macrophage Polarization in Intestinal Inflammation and Gut Homeostasis. *Inflamm. Res.* 69 (12), 1163–1172. doi:10.1007/s00011-020-01398-y

Murphy, A., Barbaro, J., Martínez-Aguado, P., Chilunda, V., Jaureguiberry-Bravo, M., and Berman, J. W. (2019). The Effects of Opioids on HIV Neuropathogenesis. *Front. Immunol.* 10, 2445. doi:10.3389/fimmu.2019.02445

Newsholme, P., Curi, R., Gordon, S., and Newsholme, E. A. (1986). Metabolism of Glucose, Glutamine, Long-Chain Fatty Acids and Ketone Bodies by Murine Macrophages. *Biochem. J.* 239 (1), 121–125. doi:10.1042/bj2390121

Ninkovic, J., Jana, N., Anand, V., Vidhu, A., Dutta, R., Raini, D., et al. (2016). Differential Effects of Gram-Positive and Gram-Negative Bacterial Products on Morphine Induced Inhibition of Phagocytosis. *Sci. Rep.* 6, 21094. doi:10.1038/srep21094

Ninković, J., and Roy, S. (2012). Morphine Decreases Bacterial Phagocytosis by Inhibiting Actin Polymerization through cAMP-, Rac-1-, and P38 MAPK-dependent Mechanisms. *Am. J. Pathol.* 180 (3), 1068–1079. doi:10.1016/j.ajpath.2011.11.034

Okano, T., Sato, K., Shirai, R., Seki, T., Shibata, K., Yamashita, T., et al. (2020). β-Endorphin Mediates the Development and Instability of Atherosclerotic Plaques. *Int. J. Endocrinol.* 2020, 4139093. doi:10.1155/2020/4139093

Pacifici, R., Minetti, M., Zuccaro, P., and Pietraforte, D. (1995). Morphine Affects Cytostatic Activity of Macrophages by the Modulation of Nitric Oxide Release. *Int. J. Immunopharmacol* 17 (9), 771–777. doi:10.1016/0192-0561(95)00046-5

Patel, K., Bhaskaran, M., Dani, D., Reddy, K., and Singhal, P. C. (2003). Role of Heme Oxygenase-1 in Morphine-Modulated Apoptosis and Migration of Macrophages. *J. Infect. Dis.* 187 (1), 47–54. doi:10.1086/346042

Plein, L. M., and Rittner, H. L. (2018). Opioids and the Immune System - Friend or Foe. *Br. J. Pharmacol.* 175 (14), 2717–2725. doi:10.1111/bph.13750

Podolnikova, N. P., Brothwell, J. A., and Ugarova, T. P. (2015). The Opioid Peptide Dynorphin A Induces Leukocyte Responses via Integrin Mac-1 (αMβ2, CD11b/CD18). *Mol. Pain* 11, 33. doi:10.1186/s12990-015-0027-0

Porta, C., Rimoldi, M., Raes, G., Brys, L., Ghezzi, P., Di Liberto, D., et al. (2009). Tolerance and M2 (Alternative) Macrophage Polarization Are Related Processes Orchestrated by P50 Nuclear Factor kappaB. *Proc. Natl. Acad. Sci. U S A.* 106 (35), 14978–14983. doi:10.1073/pnas.0809784106

Qiu, S., Feng, Y., LeSage, G., Zhang, Y., Stuart, C., He, L., et al. (2015). Chronic Morphine-Induced microRNA-124 Promotes Microglial Immunosuppression by Modulating P65 and TRAF6. *J. Immunol.* 194 (3), 1021–1030. doi:10.4049/jimmunol.1400106

Ramond, E., Jamet, A., Coureuil, M., and Charbit, A. (2019). Pivotal Role of Mitochondria in Macrophage Response to Bacterial Pathogens. *Front. Immunol.* 10, 2461. doi:10.3389/fimmu.2019.02461

Reynolds, J. L., Law, W. C., Mahajan, S. D., Aalinkeel, R., Nair, B., Sykes, D. E., et al. (2012). Morphine and Galectin-1 Modulate HIV-1 Infection of Human Monocyte-Derived Macrophages. *J. Immunol.* 188 (8), 3757–3765. doi:10.4049/jimmunol.1102276

Rodríguez-Prados, J.-C., Través, P. G., Cuenca, J., Rico, D., Aragonés, J., Martín-Sanz, P., et al. (2010). Substrate Fate in Activated Macrophages: A Comparison between Innate, Classic, and Alternative Activation. *J. Immunol.* 185 (1), 605–614. doi:10.4049/jimmunol.0901698

Rolny, C., Mazzone, M., Tugues, S., Laoui, D., Johansson, I., Coulon, C., et al. (2011). HRG Inhibits Tumor Growth and Metastasis by Inducing Macrophage Polarization and Vessel Normalization through Downregulation of PlGF. *Cancer Cell* 19 (1), 31–44. doi:10.1016/j.ccr.2010.11.009

Sarić, A., Balog, T., Sobocanec, S., and Marotti, T. (2007). Endomorphin 1 Activates Nitric Oxide Synthase 2 Activity and Downregulates Nitric Oxide Synthase 2 mRNA Expression. *Neuroscience* 144 (4), 1454–1461. doi:10.1016/j.neuroscience.2006.11.020

Scarpa, J. R., DiNatale, R. G., Mano, R., Silagy, A. W., Kuo, F., Irie, T., et al. (2020). Identifying Clear Cell Renal Cell Carcinoma Coexpression Networks Associated with Opioid Signaling and Survival. *Cancer Res.* 81, 1101–1110. doi:10.1158/0008-5472.Can-20-1852

Scull, C. M., and Tabas, I. (2011). Mechanisms of ER Stress-Induced Apoptosis in Atherosclerosis. *Arterioscler Thromb. Vasc. Biol.* 31 (12), 2792–2797. doi:10.1161/atvbaha.111.224881

Sedqi, M., Roy, S., Ramakrishnan, S., Elde, R., and Loh, H. H. (1995). Complementary DNA Cloning of a Mu-Opioid Receptor from Rat Peritoneal Macrophages. *Biochem. Biophys. Res. Commun.* 209 (2), 563–574. doi:10.1006/bbrc.1995.1538

Shirzad, H., Shahrani, M., and Rafieian-Kopaei, M. (2009). Comparison of Morphine and Tramadol Effects on Phagocytic Activity of Mice Peritoneal Phagocytes *In Vivo*. *Int. Immunopharmacol* 9 (7-8), 968–970. doi:10.1016/j.intimp.2009.04.002

Singhal, P. C., Bhaskaran, M., Patel, J., Patel, K., Kasinath, B. S., Duraisamy, S., et al. (2002). Role of P38 Mitogen-Activated Protein Kinase Phosphorylation and Fas-Fas Ligand Interaction in Morphine-Induced Macrophage Apoptosis. *J. Immunol.* 168 (8), 4025–4033. doi:10.4049/jimmunol.168.8.4025

Singhal, P. C., Kapasi, A. A., Franki, N., and Reddy, K. (2000). Morphine-Induced Macrophage Apoptosis: The Role of Transforming Growth Factor-Beta. *Immunology* 100 (1), 57–62. doi:10.1046/j.1365-2567.2000.00007.x

Singhal, P. C., Sharma, P., Kapasi, A. A., Reddy, K., Franki, N., and Gibbons, N. (1998). Morphine Enhances Macrophage Apoptosis. *J. Immunol.* 160 (4), 1886–1893.

Stanojević, S., Vujić, V., Mitić, K., Kustrimović, N., Kovacević-Jovanović, V., Miletić, T., et al. (2008). Methionine-Enkephalin Modulation of Hydrogen Peroxide (H2O2) Release by Rat Peritoneal Macrophages Involves Different Types of Opioid Receptors. *Neuropeptides* 42 (2), 147–158. doi:10.1016/j.npep.2007.12.004

Sukhorukov, V. N., Khotina, V. A., Bagheri Ekta, M., Ivanova, E. A., Sobenin, I. A., and Orekhov, A. N. (2020). Endoplasmic Reticulum Stress in Macrophages: The Vicious Circle of Lipid Accumulation and Pro-Inflammatory Response. *Biomedicines* 8 (7), 210. doi:10.3390/biomedicines8070210

Sun, J., Guo, W., and Du, X. (2017). Buprenorphine Differentially Affects M1- and M2-Polarized Macrophages from Human Umbilical Cord Blood. *Eur. Cytokine Netw.* 28 (2), 85–92. doi:10.1684/ecn.2017.0392

Suzuki, S., Chuang, L. F., Yau, P., Doi, R. H., and Chuang, R. Y. (2002). Interactions of Opioid and Chemokine Receptors: Oligomerization of Mu, Kappa, and delta with CCR5 on Immune Cells. *Exp. Cel Res* 280 (2), 192–200. doi:10.1006/excr.2002.5638

Tang, C. W., Feng, W. M., Du, H. M., Bao, Y., and Zhu, M. (2011). Delayed Administration of D-Ala2-D-Leu5-Enkephalin, a Delta-Opioid Receptor Agonist, Improves Survival in a Rat Model of Sepsis. *Tohoku J. Exp. Med.* 224 (1), 69–76. doi:10.1620/tjem.224.69

Tannahill, G. M., Curtis, A. M., Adamik, J., Palsson-McDermott, E. M., McGettrick, A. F., Goel, G., et al. (2013). Succinate Is an Inflammatory Signal that Induces IL-1β through HIF-1α. *Nature* 496 (7444), 238–242. doi:10.1038/nature11986

Tian, J., Qu, N., Jiao, X., Wang, X., Geng, J., Griffin, N., et al. (2020). Methionine Enkephalin Inhibits Influenza A Virus Infection through Upregulating Antiviral State in RAW264.7 Cells. *Int. Immunopharmacol* 78, 106032. doi:10.1016/j.intimp.2019.106032

Tomassini, N., Renaud, F. L., Roy, S., and Loh, H. H. (2003). Mu and delta Receptors Mediate Morphine Effects on Phagocytosis by Murine Peritoneal Macrophages. *J. Neuroimmunol* 136 (1-2), 9–16. doi:10.1016/s0165-5728(02)00463-0

Vats, D., Mukundan, L., Odegaard, J. I., Zhang, L., Smith, K. L., Morel, C. R., et al. (2006). Oxidative Metabolism and PGC-1beta Attenuate Macrophage-Mediated Inflammation. *Cel Metab* 4 (1), 13–24. doi:10.1016/j.cmet.2006.05.011

Viola, A., Munari, F., Sánchez-Rodríguez, R., Scolaro, T., and Castegna, A. (2019). The Metabolic Signature of Macrophage Responses. *Front. Immunol.* 10, 1462. doi:10.3389/fimmu.2019.01462

Volkow, N. D., and Blanco, C. (2021). The Changing Opioid Crisis: Development, Challenges and Opportunities. *Mol. Psychiatry* 26 (1), 218–233. doi:10.1038/s41380-020-0661-4

Wang, K., Ma, W., Xu, Y., Liu, X., Chen, G., Yu, M., et al. (2020a). Design of a Novel Mitochondria Targetable Turn-On Fluorescence Probe for Hydrogen Peroxide and its Two-Photon Bioimaging Applications. *Chin. Chem. Lett.* 31 (12), 3149–3152. doi:10.1016/j.cclet.2020.08.039

Wang, K. N., Shao, X., Tian, Z., Liu, L. Y., Zhang, C., Tan, C. P., et al. (2021). A Continuous Add-On Probe Reveals the Nonlinear Enlargement of Mitochondria in Light-Activated Oncosis. *Adv. Sci. (Weinh)* 8 (17), e2004566. doi:10.1002/advs.202004566

Wang, M. R., Wu, D. D., Luo, F., Zhong, C. J., Wang, X., Zhu, N., et al. (2020b). Methadone Inhibits Viral Restriction Factors and Facilitates HIV Infection in Macrophages. *Front. Immunol.* 11, 1253. doi:10.3389/fimmu.2020.01253

Wang, N., Liang, H., and Zen, K. (2014). Molecular Mechanisms that Influence the Macrophage M1-M2 Polarization Balance. *Front. Immunol.* 5, 614. doi:10.3389/fimmu.2014.00614

Wang, X., Jiao, X., Meng, Y., Chen, H., Griffin, N., Gao, X., et al. (2018). Methionine Enkephalin (MENK) Inhibits Human Gastric Cancer through Regulating Tumor Associated Macrophages (TAMs) and PI3K/AKT/mTOR Signaling Pathway inside Cancer Cells. *Int. Immunopharmacol* 65, 312–322. doi:10.1016/j.intimp.2018.10.023

Wang, X., Liu, J., Zhou, L., and Ho, W. Z. (2019). Morphine Withdrawal Enhances HIV Infection of Macrophages. *Front. Immunol.* 10, 2601. doi:10.3389/fimmu.2019.02601

Wang, X., Ma, T. C., Li, J. L., Zhou, Y., Geller, E. B., Adler, M. W., et al. (2015). Heroin Inhibits HIV-Restriction miRNAs and Enhances HIV Infection of Macrophages. *Front. Microbiol.* 6, 1230. doi:10.3389/fmicb.2015.01230

Wang, Y., Wang, X., Ye, L., Li, J., Song, L., Fulambarkar, N., et al. (2012). Morphine Suppresses IFN Signaling Pathway and Enhances AIDS Virus Infection. *PLoS One* 7 (2), e31167. doi:10.1371/journal.pone.0031167

Webster, L. R. (2017). Risk Factors for Opioid-Use Disorder and Overdose. *Anesth. Analg* 125 (5), 1741–1748. doi:10.1213/ane.0000000000002496

Wei, Y., Kong, L., Chen, H., Liu, Y., Xu, Y., Wang, H., et al. (2022). Super-Resolution Image-Based Tracking of Drug Distribution in Mitochondria of a Label-Free Naturally Derived Drug Molecules. *Chem. Eng. J.* 429, 132134. doi:10.1016/j.cej.2021.132134

Weng, H. L., and Wang, M. J. (2016). Effects of microRNA-338-3p on Morphine-Induced Apoptosis and its Underlying Mechanisms. *Mol. Med. Rep.* 14 (3), 2085–2092. doi:10.3892/mmr.2016.5506

Wu, K., Lin, K., Li, X., Yuan, X., Xu, P., Ni, P., et al. (2020). Redefining Tumor-Associated Macrophage Subpopulations and Functions in the Tumor Microenvironment. *Front. Immunol.* 11, 1731. doi:10.3389/fimmu.2020.01731

Wynn, T. A., Chawla, A., and Pollard, J. W. (2013). Macrophage Biology in Development, Homeostasis and Disease. *Nature* 496 (7446), 445–455. doi:10.1038/nature12034

Yunna, C., Mengru, H., Lei, W., and Weidong, C. (2020). Macrophage M1/M2 Polarization. *Eur. J. Pharmacol.* 877, 173090. doi:10.1016/j.ejphar.2020.173090

Zeng, S., Zhong, Y., Xiao, J., Ji, J., Xi, J., Wei, X., et al. (2020). Kappa Opioid Receptor on Pulmonary Macrophages and Immune Function. *Transl Perioper. Pain Med.* 7 (3), 225–233. doi:10.31480/2330-4871/117

Zhang, J., Chen, L., Sun, Y., and Li, Y. (2017). Tramadol Differentially Regulates M1 and M2 Macrophages from Human Umbilical Cord Blood. *Inflammopharmacol* 25, 533–541. doi:10.1007/s10787-017-0338-z

Conflict of Interest: The authors declare that the research was conducted in the absence of any commercial or financial relationships that could be construed as a potential conflict of interest.

Publisher's Note: All claims expressed in this article are solely those of the authors and do not necessarily represent those of their affiliated organizations, or those of the publisher, the editors and the reviewers. Any product that may be evaluated in this article, or claim that may be made by its manufacturer, is not guaranteed or endorsed by the publisher.

Copyright © 2022 Wen, Jiang, Liang, Cheng, Zhu and Guo. This is an open-access article distributed under the terms of the Creative Commons Attribution License (CC BY). The use, distribution or reproduction in other forums is permitted, provided the original author(s) and the copyright owner(s) are credited and that the original publication in this journal is cited, in accordance with accepted academic practice. No use, distribution or reproduction is permitted which does not comply with these terms.

frontiers in Pharmacology

ORIGINAL RESEARCH
published: 09 February 2022
doi: 10.3389/fphar.2021.822779

Polyadenylated Telomeric Noncoding RNA Functions as a Pivotal Therapeutic Target of Anti-Ageing to Stabilize Telomere Length of Chromosomes *Via* Collaborating With Zscan4c

Xiaojuan Xu[1,2†], *Zhengju Chen*[2†], *Wei Wu*[3] *and Xiaohe Tian*[2*]

[1]Huaxi MR Research Centre (HMRRC), Functional and Molecular Imaging Key Laboratory of Sichuan Province, Department of Radiology and National Clinical Research Center for Geriatrics, West China Hospital of Sichuan University, Chengdu, China, [2]School of Life Sciences, Hefei Normal University, Hefei, China, [3]School of Life Sciences, Anhui University, Hefei, China

OPEN ACCESS

Edited by:
Qixin Chen,
Shandong First Medical University, China

Reviewed by:
Xuanjun Zhang,
University of Macau, China
Senio Campos De Souza,
University of Macau, China

***Correspondence:**
Xiaohe Tian
xiaohe.t@wchscu.cn

[†]These authors have contributed equally to this work

Specialty section:
This article was submitted to Pharmacology of Anti-Cancer Drugs, a section of the journal Frontiers in Pharmacology

Received: 26 November 2021
Accepted: 27 December 2021
Published: 09 February 2022

Citation:
Xu X, Chen Z, Wu W and Tian X (2022) Polyadenylated Telomeric Noncoding RNA Functions as a Pivotal Therapeutic Target of Anti-Ageing to Stabilize Telomere Length of Chromosomes Via Collaborating With Zscan4c. Front. Pharmacol. 12:822779. doi: 10.3389/fphar.2021.822779

Telomeres are closely associated with the development of cell aging. Shortening or erosion of telomeres will cause cell mortality, suggesting that the maintenance of telomere integrity facilitates cell anti-senescence. However, the mechanism of how to keep the telomere length remains fragmentary. Here, we found that polyadenylated telomeric noncoding RNA (TERRA) can promote the self-renewal when overexpressed in mouse embryonic stem cells (mESCs), implying that TERRA with polyadenylation is critical for mESC maintenance. Further studies revealed that TERRA with a polyadenylated tail plays an important role in the sustenance of telomere length. High-throughput sequencing and quantitative real-time PCR show that zinc finger and SCAN domain containing 4C (Zscan4c) may be a potential target of TERRA. Zscan4c is negatively regulated by TERRA and collaborates with TERRA to stabilize the telomere length of chromosomes in mESCs. Our study not only identifies TERRA as a potential novel factor of telomere length regulation and uncovers the new molecular mechanism of cell anti-aging, but also indicates that Zscan4c could be a key therapeutic target candidate for therapy in dysfunctional chromosome diseases. These data will expand our understanding of the cell fate regulatory network and will be beneficial to drug discovery and theragnostics for antiaging and anticancer therapy in the future.

Keywords: telomeric noncoding RNA, polyadenylation, telomere length, Zscan4c, anti-aging

INTRODUCTION

Aging, a progressive physiological degeneration, is a risk factor for many age-related diseases, even cancer (Lopez-Otin et al., 2013). Slowing the underlying process of aging and leading to an increase in a healthy lifespan is a paramount issue of biology. Studies on anti-aging therapies are usually performed at the molecular, cellular, and organismal level.

Accumulating evidence indicates that preventing cellular senescence strongly contributes to organismal anti-aging and anti-cancer (Chen et al., 2020; Khosla et al., 2020). It should be noted that

TABLE 1 | List of shRNA specific sequences used for target gene knockdown.

Transcript	shRNA Sequence (5'–3')
TERRA-sh#1	AGGGTTAGGGTTAGGGTTAGG
TERRA-sh#2	GGGTTAGGGTTAGGGTTAGGG
shZscan4c	CAGAAGCCTGGCATTCCCT

a prominent phenomenon underlying the senescence process at the molecular level is the shortening of telomeres inside the cell nucleus (Chakravarti et al., 2021). Telomeres are specialized structures containing tandem short G-rich repeats at the ends of linear chromosomes that ensure chromosomes stabilization. They have an inherent ability to prevent end-to-end fusions and inappropriate DNA damage response. However, due to the end replication problem, telomere length decreases gradually in dividing cells, until it becomes too short for the cell to divide, resulting in cellular senescence (Blackburn, 2000). Current studies report that telomere length may be associated with several chronic conditions, such as dyslipidemia, atherosclerosis, and hypertension (Bhupatiraju et al., 2012; Dei Cas et al., 2013; Kark et al., 2013). Shortening of telomere length also appears in many different cancer cells, including colorectal, ovarian, and breast (Martinez-Delgado et al., 2011; Martinez-Delgado et al., 2012; Riegert-Johnson et al., 2012). All diseases are considered related to cell senescence. It is implied that telomere length is a critical cellular hallmark of biological aging. Telomere length is likely altered by a variety of factors; however, the mechanism by which telomere length is regulated remains fragmentary.

Telomeres of mammals are considered to be transcribed, giving rise to a special long noncoding RNA (lncRNA) that contains UUAGGG-repeats, known as telomeric repeat-containing RNA (TERRA) (Azzalin et al., 2007). TERRA molecules are noticeably located at the chromosome ends in nuclear fractions, which indicates that TERRA may play an important role in telomere maintenance and genome stability (Bettin et al., 2019). Further studies demonstrate that TERRA interacts with shelterin components and that downregulation of TERRA expression results in the activation of DNA damage responses at telomeres that make chromosome abnormalities in cancer cells (Silanes et al., 2010; Arora et al., 2012; Porro et al., 2014). Similar phenomena are observed in mouse embryonic fibroblasts (MEF) when TERRA is partially depleted (Silanes et al., 2014). Worthy of note, TERRA transcripts are highly expressed in mouse embryonic stem cells (mESCs) which contain much longer telomere length than human cells (Marion et al., 2009; Xu et al., 2018). Further, a decrease in TERRA also brings about dysregulation of several genes in mESCs (Chu et al., 2017). These data imply that TERRA may be involved in the regulation of telomere length in mESCs.

Notably, TERRA transcripts resolve as highly heterogeneous, while parts of TERRA molecules are polyadenylated at their 3′-ends (Azzalin et al., 2007; Schoeftner and Blasco, 2009). Polyadenylated TERRA exhibits a much longer half-life than nonpolyadenylated TERRA (Schoeftner and Blasco, 2008; Porro et al., 2010). However, the specific function of TERRA in telomere length regulation in mESCs and whether it is related to TERRA polyadenylation have not yet been addressed. Here, we reveal that polyadenylated TERRA positively regulates telomere length to maintain mESC stemness. Moreover, the expression of zinc finger and SCAN domain containing 4c (Zcan4c) is suppressed by TERRA and may mediate the telomere length regulation effect of TERRA.

MATERIALS AND METHODS

Cell Culture

46C mESCs, kindly provided by Shoudong Ye (Anhui University, China), were maintained under 5% CO_2 at 37°C on 0.1% gelatin-coated plates. LIF/serum medium was used as basal medium for mESC maintenance. LIF/serum medium consisted of DMEM (HyClone) combined with 10% FBS (HyClone), 1 × nonessential amino acids (Gibco), 1 × sodium pyruvate (Gibco), 2 mM Glutamax (Gibco), 0.1 mM β-mercaptoethanol (Gibco), and 100 U/ml LIF (Millipore). N2B27 medium supplemented with 1 μM PD0325901 (PD03, Sigma) and 3 μM CHIR99021 (CHIR, Sigma) was used as a serum-free culture condition. N2B27 medium: one volume DMEM/F12 (HyClone) and one volume Neurobasal medium mixed (Life Technology), supplemented with 0.5 × N_2 (Life Technology), 1 × B27 (Life Technology), 1 × nonessential amino acids (Gibco), 2 mM Glutamax (Gibco), and 0.1 mM β-mercaptoethanol (GIBCO).

Construction of Recombinant Plasmid

For stable recombinant expression of nonpolyadenylated and polyadenylated TERRA, we cloned telomeric DNA fragments containing 50 repeats into pLKO.1 or PiggyBac (PB) plasmids and introduced them into 46C mESCs. For knockdown of the

TABLE 2 | List of primers used for qRT-PCR.

Transcript	Forward sequence (5'–3')	Reverse sequence(5'3')
Zscan4	GAGATTCATGGAGAGTCTGACTGATGAGTG	GCTGTTGTTTCAAAAGCTTGATGACTTC
Zscan4c	CCGGAGAAAGCAGTGAGGTGGA	CGAAAATGCTAACAGTTGAT
Zscan4d	GTCCTGACAGAGGCCTGCC	GAGATGTCTGAAGAGGCAAT
Total	-	-
TERRA	CGGTTTGTTTGGGTTTGGGTTTGGGTTTGGGTTTGGGTT	GGCTTGCCTTACCCTTACCCTTACCCTTACCCTTACCC
TL	CGGTTTGTTTGGGTTTGGGTTTGGGTTTGGGTTTGGGTT	GGCTTGCCTTACCCTTACCCTTACCCTTACCCTTACCCT
36B4	ACTGGTCTAGGACCCGAGAAG	TCAATGGTGCCTCTGGAGATT
Rpl19	TGAAATCGCCAATGCCAACT	TCCCTATGCCCATATGCCTG

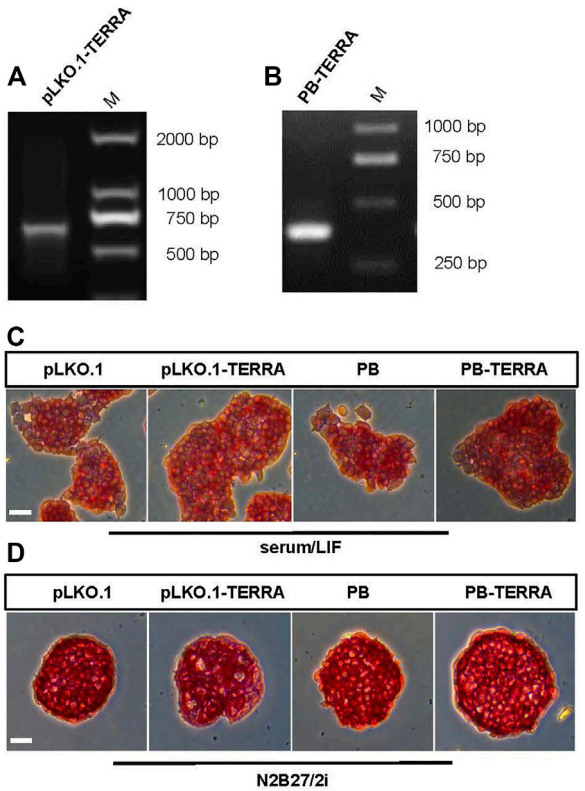

FIGURE 1 | Exogenous TERRA expression in mouse embryonic stem cells (mESCs). **(A,B)** PCR identification of recombinant TERRA expression with and without polyadenylation in 46C mESCs, using primers specific for PB-TERRA and pLKO.1-TERRA plasmids. **(A)**: the fragment at 708-bp contains the 300-bp recombinant TERRA and the 408 bp plasmid fragment. **(B)**: the fragment at 466-bp contains the 300-bp recombinant TERRA and the 166 bp plasmid fragment. M, molecular marker. **(C,D)** Alkaline phosphatase (AP) staining images of mESCs overexpressing TERRA with and without polyadenylation cultured in serum with LIF or N2B27 with 2i (CHIR and PD03) media. Scale bar, 100 μm.

target gene in mESCs, the short hairpin RNA (shRNA) plasmids were generated to target specific regions of TERRA and Zscan4c. The specific sequences for TERRA and Zscan4c used in this study are listed in **Table 1**.

Alkaline Phosphatase Activity Assay

46C mESCs cultured on 0.1% gelatin-coated plates were washed with PBS 2–3 times and fixed in 4% paraformaldehyde. Then the Alkaline Phosphatase Kit (Sigma) was used to detect alkaline phosphatase (AP) activity.

Quantitative Real-Time PCR

Total RNA isolated from cells by the TransZol Up Plus RNA Kit (Transgene Biotech, China) was reverse transcribed using a specific primer $(CCCTAA)_6$ to obtain total TERRA cDNA by the Reverse Transcription Kit (Transgene Biotech) according to the manufacturer's instructions. The detection of total TERRA levels and the average telomere length ratio was performed as previously described (Sampl et al., 2012). qPCR analysis was performed using the TransStart Top SYBR Green qPCR SuperMix (Transgene Biotech) in a Pikoreal Real-Time PCR machine (Thermo Fisher). The expression level of the target gene was normalized to internal control Rpl19 expression. The primers used are listed in **Table 2**.

Quantification of Telomerase Activity

Quantification of telomerase activity (TA) in 46C mESCs was performed with a mouse telomerase ELISA kit (Shanghai Jining, China) according to the instructions. A standard curve was made by measuring the optical density of known concentrations of standard telomerase samples from 0 to 35 IU/L. Then, the telomerase activity of mESCs was analyzed against the standard curve.

Accession Number

Data and details for the RNA-seq in this study are available in the Gene Expression Omnibus under accession number GSE103933.

Statistical Analysis

All data are reported as means ± SD. Student's t-test was used to determine the significance of differences in comparisons. Values of $p < 0.05$ were considered as statistically significant.

RESULTS

Establishment of Exogenous Telomeric Noncoding RNA Expressing Mouse Embryonic Stem Cells

To understand the possible function of TERRA in mESC, we overexpressed TERRA with and without polyadenylation in 46C mESCs, respectively. After infection of cells with recombinant TERRA constructs, specific primers for pLKO.1-TERRA and PB-TERRA vectors were used to identify exogenous TERRA expression in 46C mESCs, which indicated that recombinant TERRA was expressed (**Figures 1A,B**). For mESC stemness can be maintained under serum/LIF medium or serum-free medium N2B27/2i conditions [2i contains the two small molecule inhibitors CHIR99021 (CHIR) and PD0325901 (PD03)], the pLKO.1-TERRA and PB-TERRA cells were cultured under these conditions. As shown in **Figures 1C,D**, enforced TERRA cells grew robustly in N2B27/2i or serum/LIF media which implied that maintenance of 46C mESCs may not be negatively impacted by enhanced TERRA.

Enhanced Polyadenylated Telomeric Noncoding RNA Promotes Mouse Embryonic Stem Cells Self-Renewal Without CHIR

To examine whether polyadenylated and nonpolyadenylated TERRA have the capability to reproduce the pluripotent effect of the individual factor, we withdrew LIF, PD03, or CHIR in serum/LIF and N2B27/2i media. As shown in **Figures 2A–C**,

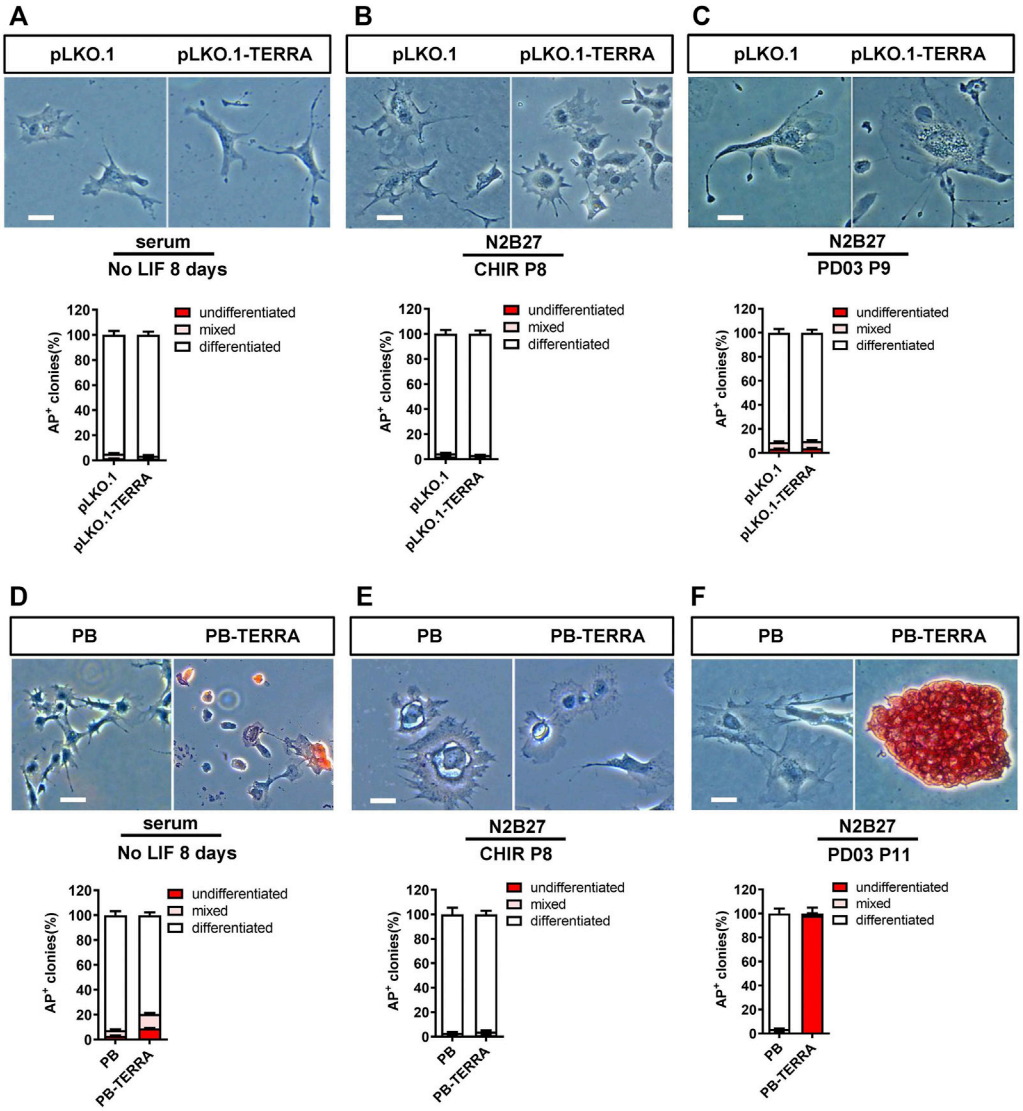

FIGURE 2 | Polyadenylated TERRA maintains mESC self-renewal in the absence of CHIR. **(A–C)** AP staining images and AP-positive colonies quantification of pLKO.1 and pLKO.1-TERRA mESCs cultured in different conditions. **(A)**: mESCs cultured in serum without LIF for 8 days. **(B)**: mESCs cultured in N2B27/CHIR (without PD03) medium for 8 passages. **(C)**: mESCs cultured in N2B27/PD03 (without CHIR) medium for 9 passages. Scale bar, 100 μm. **(D–F)** AP staining images and AP-positive colonies quantification of PiggyBac (PB) and PB-TERRA mESCs cultured in different conditions. **(D)**: mESCs cultured in serum without LIF condition for 8 days. **(E)**: mESCs cultured in N2B27/CHIR (without PD03) medium for 8 passages. **(F)**: mESCs cultured in N2B27/PD03 (without CHIR) medium for 11 passages. Scale bar, 100 μm.

nearly all mESCs introduced with empty vector pLKO.1 or pLKO.1-TERRA acquired an enlarged and flattened morphology for the indicated times. TERRA without polyadenylation therefore is not sufficient to be a substitute for other factors to maintain mESCs.

Similarly, most PB or PB-TERRA transgenic mESCs died or differentiated in the absence of LIF or N2B27/CHIR (without PD03) (**Figures 2D,E**). Nevertheless, compared with PB mESCs differentiated, PB-TERRA cells retained a typical mESC-like morphology, a robust colony formation without CHIR (N2B27/PD03) until 11 passages (**Figure 2F**). Accordingly, they showed high alkaline phosphatase activity, and statistical analysis suggested that more than 90% of the cells were undifferentiated. Together, these data imply that polyadenylation is necessary for TERRA to mimic CHIR to facilitate mESC self-renewal.

Polyadenylated Telomeric Noncoding RNA Regulates Telomere Length and Telomerase Activity in Mouse Embryonic Stem Cells

Telomere length (TL) and telomerase activity (TA) are determinants of cell fate. To investigate more about the role of

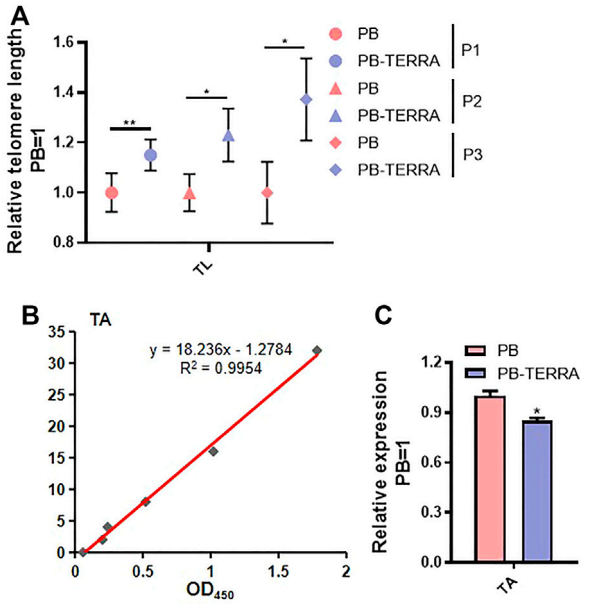

FIGURE 3 | TERRA with polyadenylation increases telomere length while inhibits telomerase activity in mESCs. **(A)** Relative telomere length (TL) of PB and PB-TERRA mESCs at different passages was measured by quantitative real-time PCR (qRT-PCR). P1: mESCs cultured for 1 passage. P2: mESCs cultured for 2 passages. P3: mESCs cultured for 3 passages. Relative TL were normalized against PB control. **(B, C)** Telomerase activity (TA) was detectable in PB and PB-TERRA mESCs by ELISA. **(B)**: Linear relationship between optical density (OD) at 450 nm and standard telomerase activity using a mouse telomerase ELISA kit. **(C)**: Relative telomerase activities compared in PB and PB-TERRA mESCs. Data were normalized to PB cells. **(A, C)** Data represent means ± SD of three biological replicates. $*p < 0.05$, $**p < 0.01$ vs. PB.

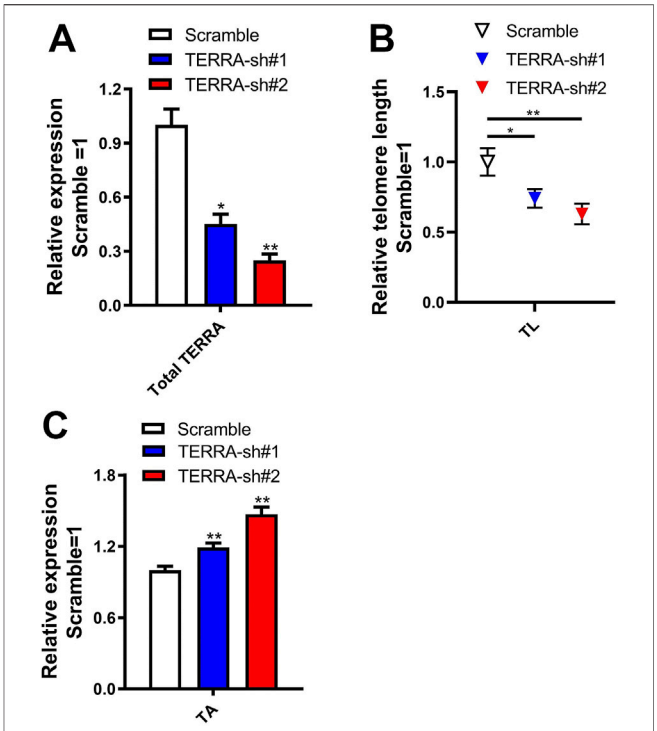

FIGURE 4 | Knockdown of TERRA shortens telomere length and enhances telomerase activity in mESCs. **(A)** qRT-PCR analysis of total TERRA expression levels using the method published for measuring the relative telomeric repeat DNA content. Transcript levels were normalized against Scramble shRNA control. $*p < .05$, $**p < .01$ vs. Scramble control. **(B)** Relative telomere length (TL) of TERRA knockdown mESCs was measured by qPCR. Relative TL were normalized against Scramble control. $*p < 0.05$, $**p < 0.01$ vs. Scramble control. **(C)** Telomerase activity (TA) was detectable in PB and TERRA shRNA mESCs by ELISA. Data were normalized to PB cells. $**p < 0.01$ vs. PB. **(A–C)** Data represent means ± SD of three biological replicates.

TERRA input is integrated in the cell fate regulatory network, telomere length and telomerase activity were determined in PB and PB-TERRA 46C mESCs. First, telomere length was analyzed by quantitative real-time PCR (qRT-PCR). As shown in **Figure 3A**, overexpression of TERRA with polyadenylation resulted in an approximately 15% increase in relative telomere length compared to empty vector PB mESCs in the first passage, while a similar tendency was also found in succession and TERRA had a positive effect from 20 to 30% on TL. Thus, expression of ectopic polyadenylated TERRA resulted in a general increasing trend in telomeric content. Additionally, using the ELISA standard curve (**Figure 3B**), relative telomerase activity was calibrated by enzyme-linked immunosorbent assay. The results show that recombinant TERRA with polyadenylation results in strong inhibition of telomerase activity (**Figure 3C**). Taken together, these studies demonstrate that ectopic polyadenylated TERRA promotes the clonal growth capacity of mESCs in a telomere length dependent manner.

To ascertain whether knockdown of TERRA impacts telomere length and telomerase activity in mESCs, lentiviruses encoding two shRNAs specific for TERRA (TERRA-sh#1 and TERRA-sh#2) were infected into 46C mESCs. TERRA transcripts dropped 55–75% following puromycin selection, as confirmed by qRT-PCR (**Figure 4A**). Telomere length became shorter while telomerase activity was enhanced in TERRA shRNA mESCs (**Figures 4B,C**), implying that TERRA downregulation impaired the telomere elongation and telomerase activity in 46C mESCs.

Zscan4 Genes are the Targets for Polyadenylated Telomeric Noncoding RNA in Mouse Embryonic Stem Cells

As mentioned above, telomere length was upregulated by polyadenylated TERRA in mESCs. To determine the functional targets of TERRA in telomere regulation, RNA-sequence analysis (GEO ID Number: GSE103933) was performed in PB and PB-TERRA 46C mESCs. The results showed that a number of genes were differentially expressed in PB-TERRA mESCs compared with PB cells by PossionDis analysis (**Figures 5A,B**). To screen the possible targets from the differentially expressed genes, we then performed gene ontology (GO) analyses and filtered out these involved in pluripotency. Compared with PB mESCs, PB-TERRA mESCs displayed an upregulation of the most definitive self-renewal

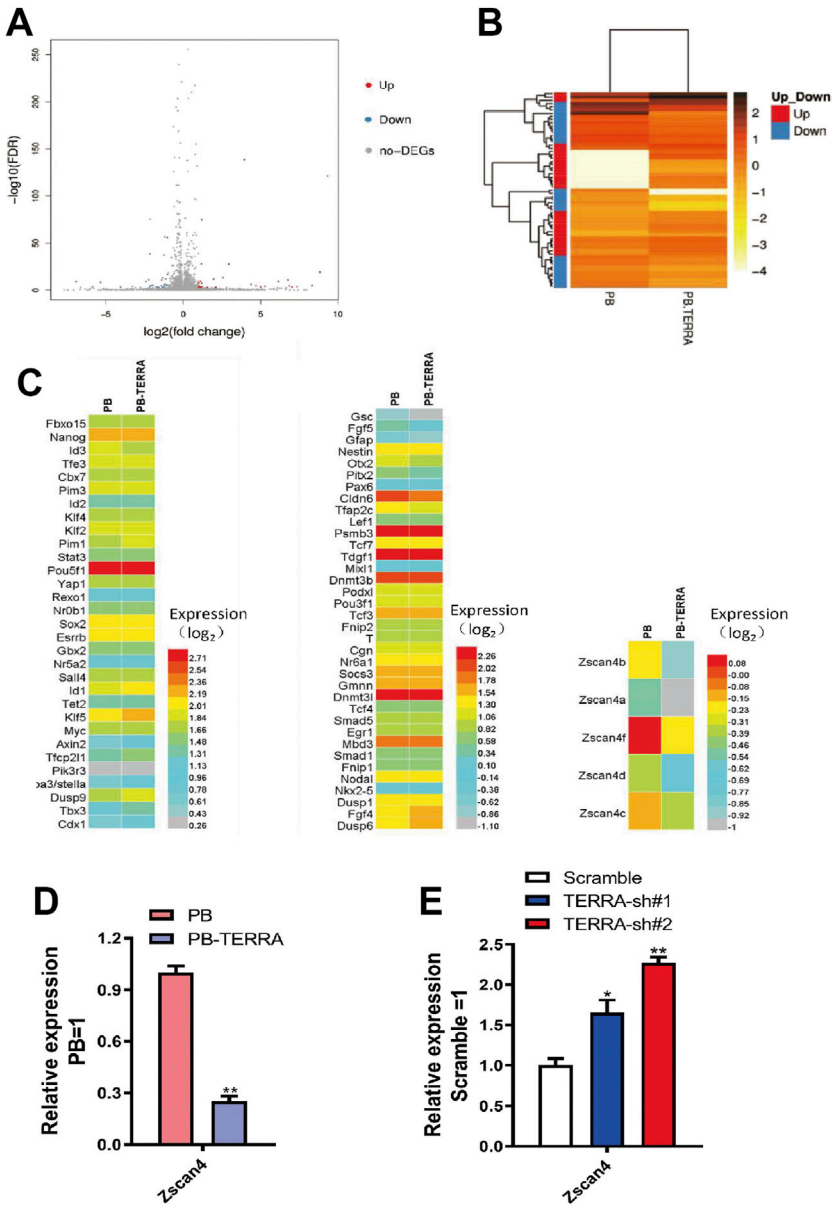

FIGURE 5 | TERRA with polyadenylation upregulates pluripotency genes and downregulates Zscan4 gene cluster. **(A)** Volcano-plot showed differently expressed genes in PB and PB-TERRA mESCs. **(B)** Heatmap showed differently expressed genes in PB and PB-TERRA mESCs. **(C)** Heatmap showed the transcriptome-resequencing data of the indicated gene expression pattern in PB and PB-TERRA mESCs. Left: pluripotent markers expression in PB and PB-TERRA mESCs. Middle: the expression of gene markers associated with differentiation in PB and PB-TERRA mESCs. Right: gene expression analysis of Zscan4b, Zscan4a, Zscan4f, Zscan4d, and Zscan4c in PB and PB-TERRA mESCs. **(D)** qRT-PCR analysis of Zscan4 expression levels in PB and PB-TERRA mESCs. Data were normalized to PB cells. Data represent means ± SD of three biological replicates. $^{**}p < 0.01$ vs. PB. **(E)** Zscan4 expression levels in TERRA knockdown cells were analyzed by qRT-PCR. Data represent means ± SD of three biological replicates. $^{*}p < 0.05$, $^{**}p < 0.01$ vs. Scramble control.

markers while expressed lower levels of the most differentiated markers (**Figure 5C**), confirming the function of polyadenylated TERRA in cell fate of mESCs. Of note, the expression levels of Zscan4a-Zscan4d and Zscan4f were significantly decreased in PB-TERRA mESCs (**Figure 5C**). Previous reports revealed that these targets are members of the zinc finger and SCAN domain containing 4 (Zscan4) gene clusters which correlates with genomic stability (Falco et al., 2007). qRT-PCR analysis was used to validate the effect of TERRA on Zscan4 (**Figure 5D**). Further, we examined whether TERRA knockdown has an effect on Zscan4 expression. As expected, the transcripts of Zscan4 increased in TERRA shRNA mESCs whereas the Scramble control shRNA did not affect equivalent cells at the transcription level (**Figure 5E**). These results support the idea that the Zscan4 expression level is negatively regulated

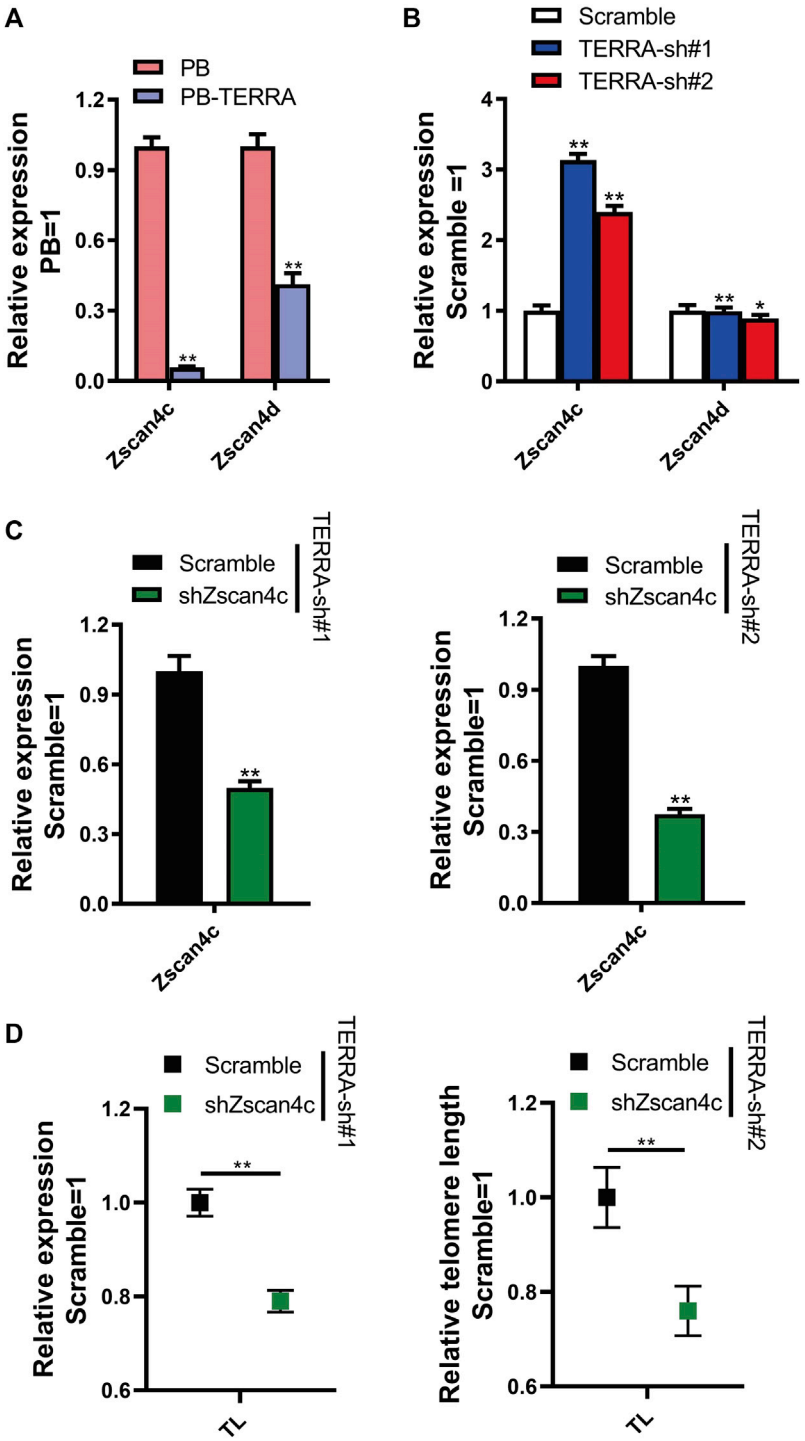

FIGURE 6 | Zscan4c is a primary target of polyadenylated TERRA and impairs telomere length. **(A)** Zscan4c and Zscan4d expression levels in PB and PB-TERRA 46C mESCs were analyzed by qRT-PCR. Data were normalized to PB cells. $^{**}p < .01$ vs. PB. **(B)** Gene expression analysis of Zscan4c and Zscan4d in TERRA shRNA 46C mESCs. Data were normalized to Scramble control cells. $^{*}p < 0.05$, $^{**}p < 0.01$ vs. Scramble control. **(C)** qRT-PCR analysis of Zscan4c expression levels in TERRA shRNA mESCs with Zscan4c knockdown. Transcript levels were normalized against Scramble shRNA control. $^{**}p < 0.01$ vs. Scramble control. **(D)** qRT-PCR analysis of relative telomere length (TL) in TERRA knockdown mESCs carrying Zscan4c shRNA. $^{**}p < 0.01$ vs. Scramble control. **(A–D)** Data represent means ± SD of three biological replicates.

by polyadenylated TERRA and that it is a potential target for TERRA.

Polyadenylated Telomeric Noncoding RNA Collaborates With Zscan4c to Regulate Telomere Length in Mouse Embryonic Stem Cells

To survey the primary target of TERRA in the Zscan4 gene cluster, we detected the mRNA levels of Zscan4c and Zscan4d, which are reported not only to be related to genomic stability but also to be predominantly associated with embryo development and self-renewal in embryonic stem cells (ESCs). We observed that although both Zscan4c and Zscan4d were downregulated by polyadenylated TERRA at the transcriptional level, the Zscan4c transcripts dropped more than 90% whereas 40% Zscan4d molecules still expressed (**Figure 6A**). To verify that the effect of TERRA on Zscan4c is truly different from that on Zscan4d, we examined their expression levels in TERRA depleted cells. qRT-PCR analysis displayed that TERRA knockdown induced a 2.4- to 3.1-fold increase in Zscan4c levels but did not show any influence on Zscan4d expression (**Figure 6B**). These data collectively demonstrate that Zscan4c is a potential key target of TERRA.

As mentioned above, TERRA negatively regulated Zscan4c while having positive effects on telomere length. We then utilized an RNA interference approach to further test whether Zscan4c mediates the effect of TERRA in telomere length. Initially, a shRNA targeting the Zscan4c transcripts (shZscan4c) was placed into the lentiviral vector. Additionally, a construct containing a Scramble shRNA was used as a control. Then Scramble and Zscan4c shRNA lentiviral particles were used to infect TERRA-sh#1 and TERRA-sh#2 mESCs, respectively. Expression of Zscan4c was reduced by 60–70% at the transcriptional level compared to that in the Scramble control cells (**Figure 6C**). Surprisingly, the relative telomere length in TERRA shRNA mESCs transfected with Zscan4c shRNA became shorter than that in TERRA-knockdown cells (**Figure 6D**). Overall, these findings indicate that the inhibition of endogenous Zscan4c increases the instability of telomeres and that Zscan4c might mediate the regulation of telomere length by TERRA in mESCs.

DISCUSSION

TERRA is a special lncRNA that has been recently identified at telomeres. The role of TERRA has yet to be clearly established, especially the distinct functions between polyadenylated TERRA and nonpolyadenylated TERRA. Here, we revealed that only polyadenylated TERRA can reproduce the individual factor to promote mESC self-renewal, indicating that TERRA may have a positive impact on proliferation in mESCs and that polyadenylation is critical for TERRA to gain this ability. In fact, the potency of TERRA that facilitates the proliferative capacity has been found in different kinds of cells, including some tumor tissues, pluripotent stem cells, and progenitor cells. For example, stomach and lung cancer, human and mouse induced pluripotent stem cells, and progenitor cells in the developing mouse brain (Marion et al., 2009; Deng et al., 2012). Therefore, TERRA with poly-A tail can be used as a pluripotency marker.

To investigate more about how polyadenylated TERRA affects pluripotent capacity of mESCs, we detected telomere length and telomerase activity that are closely related to cell fate. Polyadenylated TERRA increased the telomere length, and it is likely that TERRA makes a distinctive contribution to the sustenance of chromosome in mESCs, as the knockdown of TERRA shortens the telomere length. The observation is consistent with the notion that TERRA may play an important role in maintaining genomic stability (Silanes et al., 2010; Porro et al., 2014). In contrast, telomerase activity was suppressed by polyadenylated TERRA. This comes as no surprise, as TERRA contains 5′-UUAGGG-3′ repeats which are complementary to the template sequence of telomerase RNA and thus considered as a natural ligand and direct inhibitor of human telomerase (Redon et al., 2010). However, telomerase can also be involved in telomere lengthening through a catalytic unit termed protein reverse transcriptase (Marion et al., 2009). It is possible that TERRA-mediated telomere extension does not require telomerase, due to mESC employing both telomerase and alternative lengthening of telomeres identically to maintain their telomeres (Niida et al., 2000; Conomos et al., 2013).

Moreover, to gain insight into the molecular mechanism by which polyadenylated TERRA acts to regulate telomere length, we performed RNA-sequencing to screen the targets of TERRA and identified Zscan4. Enforced polyadenylated TERRA markedly reduced Zscan4 expression while decreased TERRA triggered upregulation of Zscan4 levels. Similar to TERRA, Zscan4 can also positively regulate telomere independent of telomerase in mESCs (Zalzman et al., 2010). In addition, telomere shortening activated Zscan4 in mESCs (Nakai-Futatsugi and Niwa, 2016). Therefore, Zscan4 may behave as a significant factor in linking TERRA to regulate the telomere length of mESCs. Notably, as a member of Zscan4, Zscan4c, which correlates with embryonic stem cell self-renewal is likely to be the pivotal target of TERRA, as TERRA induced changes in Zscan4c expression were more dramatic than those in the Zscan4 gene cluster. Additionally, we found that telomere length became much shorter after downregulation of Zscan4c in TERRA knockdown cells in support of this report that overexpression of Zscan4c rescued telomere length (Amano et al., 2013), implying that Zscan4c might be a novel regulatory factor for telomere length. Interestingly, pioneering studies identified that hyperactive Zscan4 triggers a higher incidence of cell death (Nakai-Futatsugi and Niwa, 2016), which suggests that the expression levels of Zscan4 must be tightly regulated. Therefore, we speculate that Zscan4c may act as a bridge for TERRA to negatively regulate Zscan4, while TERRA might cooperate with Zscan4c in telomere length dynamic balance controlling in mESCs. However, how Zscan4c and TERRA coregulate telomere is still elusive. It will be of great interest to investigate whether Zscan4c is a direct target of TERRA and how

Zscan4c and TERRA input are integrated in the telomere length controlling network in the future.

In summary, our study uncovers a novel role of polyadenylated TERRA in maintaining the telomere length of mESCs. TERRA may exert this function by modulating the expression of Zcan4c, a factor for genomic stability and telomere elongation. If TERRA or Zscan4c expression can be induced and controlled, it may provide means to increase genomic stability in various cell types to anti-aging and anti-cancer. Therefore, polyadenylated TERRA and Zscan4c may provide novel and sensitive biomarkers for telomere dysfunction. An understanding of the functions of TERRA in telomere stability in mESCs will expand our understanding of the molecular mechanisms underlying the regulatory network of cellular senescence and facilitate drug development for therapy in clinical applications in the future.

DATA AVAILABILITY STATEMENT

The datasets presented in this study can be found in online repositories. The names of the repository/repositories and accession number(s) can be found below: https://www.ncbi.nlm.nih.gov/geo/, GSE103933.

AUTHOR CONTRIBUTIONS

XX and XT conceived and designed experiments. XX, ZC. and WW performed the experiments. XX and ZC analyzed the data. XX and XT wrote the article.

FUNDING

The study was funded by the National Natural Science Foundation of China (32171448 and 32171361), the Natural Science Foundation of Universities of Anhui Province (No. KJ2021A0923), Scientific Research Foundation for Advanced Talents of Hefei Normal University (No. 2020rcjj51), International Collaborative Research Center for Huangshan Biodiversity and Tibetan Macaque Behavioral Ecology, Anhui University, Hefei, China (No. KF 200015).

ACKNOWLEDGMENTS

The authors would like to thank the technical support from Shoudong Ye of the Center for Stem Cell and Translational Medicine, School of Life Sciences, Anhui University.

REFERENCES

Amano, T., Hirata, T., Falco, G., Monti, M., Sharova, L. V., Amano, M., et al. (2013). Zscan4 Restores the Developmental Potency of Embryonic Stem Cells. *Nat. Commun.* 4, 1966. doi:10.1038/ncomms2966

Arora, R., Brun, C. M., and Azzalin, C. M. (2012). Transcription Regulates Telomere Dynamics in Human Cancer Cells. *RNA* 18 (4), 684–693. doi:10.1261/rna.029587.111

Azzalin, C. M., Reichenbach, P., Khoriauli, L., Giulotto, E., and Lingner, J. (2007). Telomeric Repeat Containing RNA and RNA Surveillance Factors at Mammalian Chromosome Ends. *Science* 318 (5851), 798–801. doi:10.1126/science.1147182

Bettin, N., Oss Pegorar, C., and Cusanelli, E. (2019). The Emerging Roles of TERRA in Telomere Maintenance and Genome Stability. *Cells* 8 (3), 246. doi:10.3390/cells8030246

Bhupatiraju, C., Saini, D., Patkar, S., Deepak, P., Das, B., and Padma, T. (2012). Association of Shorter Telomere Length with Essential Hypertension in Indian Population. *Am. J. Hum. Biol.* 24 (4), 573–578. doi:10.1002/ajhb.22264

Blackburn, E. H. (2000). Telomere States and Cell Fates. *Nature* 408 (6808), 53–56. doi:10.1038/35040500

Chakravarti, D., LaBella, K. A., and DePinho, R. A. (2021). Telomeres: History, Health, and Hallmarks of Aging. *Cell* 184 (2), 306–322. doi:10.1016/j.cell.2020.12.028

Chen, Q., Shao, X., Hao, M., Fang, H., Guan, R., Tian, Z., et al. (2020). Quantitative Analysis of Interactive Behavior of Mitochondria and Lysosomes Using Structured Illumination Microscopy. *Biomaterials* 250, 120059. doi:10.1016/j.biomaterials.2020.120059

Chu, H. P., Cifuentes-Rojas, C., Kesner, B., Aeby, E., Lee, H. G., Wei, C., et al. (2017). TERRA RNA Antagonizes ATRX and Protects Telomeres. *Cell* 170 (1), 86–e16. doi:10.1016/j.cell.2017.06.017

Conomos, D., Pickett, H. A., and Reddel, R. R. (2013). Alternative Lengthening of Telomeres: Remodeling the Telomere Architecture. *Front. Oncol.* 3, 27. doi:10.3389/fonc.2013.00027

Dei Cas, A., Spigoni, V., Franzini, L., Preti, M., Ardigò, D., Derlindati, E., et al. (2013). Lower Endothelial Progenitor Cell Number, Family History of Cardiovascular Disease and Reduced HDL-Cholesterol Levels Are Associated with Shorter Leukocyte Telomere Length in Healthy Young Adults. *Nutr. Metab. Cardiovasc. Dis.* 23 (3), 272–278. doi:10.1016/j.numecd.2011.04.005

Deng, Z., Wang, Z., Xiang, C., Molczan, A., Baubet, V., Conejo-Garcia, J., et al. (2012). Formation of Telomeric Repeat-Containing RNA (TERRA) Foci in Highly Proliferating Mouse Cerebellar Neuronal Progenitors and Medulloblastoma. *J. Cel. Sci.* 125 (Pt 18), 4383–4394. doi:10.1242/jcs.108118

Falco, G., Lee, S. L., Stanghellini, I., Bassey, U. C., Hamatani, T., and Ko, M. S. (2007). Zscan4: a Novel Gene Expressed Exclusively in Late 2-cell Embryos and Embryonic Stem Cells. *Dev. Biol.* 307 (2), 539–550. doi:10.1016/j.ydbio.2007.05.003

Kark, J. D., Nassar, H., Shaham, D., Sinnreich, R., Goldberger, N., Aboudi, V., et al. (2013). Leukocyte Telomere Length and Coronary Artery Calcification in Palestinians. *Atherosclerosis* 229 (2), 363–368. doi:10.1016/j.atherosclerosis.2013.05.030

Khosla, S., Farr, J. N., Tchkonia, T., and Kirkland, J. L. (2020). The Role of Cellular Senescence in Ageing and Endocrine Disease. *Nat. Rev. Endocrinol.* 16 (5), 263–275. doi:10.1038/s41574-020-0335-y

López de Silanes, I., Graña, O., De Bonis, M. L., Dominguez, O., Pisano, D. G., and Blasco, M. A. (2014). Identification of TERRA Locus Unveils a Telomere protection Role through Association to Nearly All Chromosomes. *Nat. Commun.* 5 (5), 4723. doi:10.1038/ncomms5723

López de Silanes, I., Stagno d'Alcontres, M., and Blasco, M. A. (2010). TERRA Transcripts Are Bound by a Complex Array of RNA-Binding Proteins. *Nat. Commun.* 1 (3), 33. doi:10.1038/ncomms1032

López-Otín, C., Blasco, M. A., Partridge, L., Serrano, M., and Kroemer, G. (2013). The Hallmarks of Aging. *Cell* 153 (6), 1194–1217. doi:10.1016/j.cell.2013.05.039

Marion, R. M., Strati, K., Li, H., Tejera, A., Schoeftner, S., Ortega, S., et al. (2009). Telomeres Acquire Embryonic Stem Cell Characteristics in Induced Pluripotent Stem Cells. *Cel. Stem Cel.* 4 (2), 141–154. doi:10.1016/j.stem.2008.12.010

Martinez-Delgado, B., Yanowsky, K., Inglada-Perez, L., de la Hoya, M., Caldes, T., Vega, A., et al. (2012). Shorter Telomere Length Is Associated with Increased Ovarian Cancer Risk in Both Familial and Sporadic Cases. *J. Med. Genet.* 49 (5), 341–344. doi:10.1136/jmedgenet-2012-100807

Martinez-Delgado, B., Yanowsky, K., Inglada-Perez, L., Domingo, S., Urioste, M., Osorio, A., et al. (2011). Genetic Anticipation Is Associated with Telomere Shortening in Hereditary Breast Cancer. *Plos. Genet.* 7 (7), e1002182. doi:10.1371/journal.pgen.1002182

Nakai-Futatsugi, Y., and Niwa, H. (2016). Zscan4 Is Activated after Telomere Shortening in Mouse Embryonic Stem Cells. *Stem Cel Rep.* 6 (4), 483–495. doi:10.1016/j.stemcr.2016.02.010

Niida, H., Shinkai, Y., Hande, M. P., Matsumoto, T., Takehara, S., Tachibana, M., et al. (2000). Telomere Maintenance in Telomerase-Deficient Mouse Embryonic Stem Cells: Characterization of an Amplified Telomeric DNA. *Mol. Cel. Biol.* 20 (11), 4115–4127. doi:10.1128/MCB.20.11.4115-4127.2000

Porro, A., Feuerhahn, S., Delafontaine, J., Riethman, H., Rougemont, J., and Lingner, J. (2014). Functional Characterization of the TERRA Transcriptome at Damaged Telomeres. *Nat. Commun.* 5, 5379. doi:10.1038/ncomms6379

Porro, A., Feuerhahn, S., Reichenbach, P., and Lingner, J. (2010). Molecular Dissection of Telomeric Repeat-Containing RNA Biogenesis Unveils the Presence of Distinct and Multiple Regulatory Pathways. *Mol. Cel. Biol.* 30 (20), 4808–4817. doi:10.1128/MCB.00460-10

Redon, S., Reichenbach, P., and Lingner, J. (2010). The Non-coding RNA TERRA Is a Natural Ligand and Direct Inhibitor of Human Telomerase. *Nucleic Acids Res.* 38 (17), 5797–5806. doi:10.1093/nar/gkq296

Riegert-Johnson, D. L., Boardman, L. A., Crook, J. E., Thomas, C. S., Johnson, R. A., and Roberts, M. E. (2012). Shorter Peripheral Blood Telomeres Are a Potential Biomarker for Patients with Advanced Colorectal Adenomas. *Int. J. Biol. Markers* 27 (4), e375–80. doi:10.5301/JBM.2012.9347

Sampl, S., Pramhas, S., Stern, C., Preusser, M., Marosi, C., and Holzmann, K. (2012). Expression of Telomeres in Astrocytoma WHO Grade 2 to 4: TERRA Level Correlates with Telomere Length, Telomerase Activity, and Advanced Clinical Grade. *Transl. Oncol.* 5 (1), 56–65. doi:10.1593/tlo.11202

Schoeftner, S., and Blasco, M. A. (2009). Chromatin Regulation and Non-coding RNAs at Mammalian Telomeres. *Semin. Cel. Dev. Biol.* 21 (2), 186–193. doi:10.1016/j.semcdb.2009.09.015

Schoeftner, S., and Blasco, M. A. (2008). Developmentally Regulated Transcription of Mammalian Telomeres by DNA-dependent RNA Polymerase II. *Nat. Cel. Biol.* 10 (2), 228–236. doi:10.1038/ncb1685

Xu, X., Guo, M., Zhang, N., and Ye, S. (2018). Telomeric Noncoding RNA Promotes Mouse Embryonic Stem Cell Self-Renewal through Inhibition of TCF3 Activity. *Am. J. Physiol. Cel Physiol* 314 (6), C712–C720. doi:10.1152/ajpcell.00292.2017

Zalzman, M., Falco, G., Sharova, L. V., Nishiyama, A., Thomas, M., Lee, S. L., et al. (2010). Zscan4 Regulates Telomere Elongation and Genomic Stability in ES Cells. *Nature* 464 (7290), 858–863. doi:10.1038/nature08882

Conflict of Interest: The authors declare that the research was conducted in the absence of any commercial or financial relationships that could be construed as a potential conflict of interest.

Publisher's Note: All claims expressed in this article are solely those of the authors and do not necessarily represent those of their affiliated organizations, or those of the publisher, the editors, and the reviewers. Any product that may be evaluated in this article, or claim that may be made by its manufacturer, is not guaranteed or endorsed by the publisher.

Copyright © 2022 Xu, Chen, Wu and Tian. This is an open-access article distributed under the terms of the Creative Commons Attribution License (CC BY). The use, distribution or reproduction in other forums is permitted, provided the original author(s) and the copyright owner(s) are credited and that the original publication in this journal is cited, in accordance with accepted academic practice. No use, distribution or reproduction is permitted which does not comply with these terms.

frontiers in Pharmacology

ORIGINAL RESEARCH
published: 23 February 2022
doi: 10.3389/fphar.2021.821518

Efficient Synthesis of 2,3′-Spirobi (Indolin)-2′-Ones and Preliminary Evaluation of Their Damage to Mitochondria in HeLa Cells

Huajie Li[1,2†], Zhenjie Yu[1,2†], Haoyi Sun[1,2†], Bo Liu[1,2], Xin Wang[1,2], Zhe Shao[1,2], Meiling Wang[1,2], Weilin Xie[1,2], Xingang Yao[3], Qingqiang Yao[1,2] and Ying Zhi[1,2*]*

[1]School of Pharmacy and Pharmaceutical Sciences, Shandong First Medical University, Jinan, China, [2]Institute of Materia Medica, Shandong Academy of Medical Sciences, Jinan, China, [3]School of Pharmaceutical Sciences, Southern Medical University, Guangzhou, China

A novel formal (4 + 1) annulation between *N*-(*o*-chloromethyl)aryl amides and 3-chlorooxindoles through *in situ* generated aza-*ortho*-QMs with 3-chlorooxindoles is reported for the synthesis of a series of 2,3′-spirobi (indolin)-2′-ones in high yields. Under structured illumination microscopy, compound **3a** is found to change the mitochondrial morphology and induce mitophagy pathway, which might then trigger mitophagy in cancer cells.

Keywords: spirooxindole, aza-ortho-quinone methides, mitochondria, morphology, annulation

OPEN ACCESS

Edited by:
Peixue Ling,
Shandong University (Qingdao), China

Reviewed by:
Yinan Zhang,
Nanjing University of Chinese Medicine, China
Fabrizio Vetica,
Sapienza University of Rome, Italy

****Correspondence:***
Ying Zhi
zhiying@sdfmu.edu.cn
Qingqiang Yao
qqyao@sdfmu.edu.cn

†These authors have contributed equally to this work and share first authorship

Specialty section:
This article was submitted to Pharmacology of Anti-Cancer Drugs, a section of the journal Frontiers in Pharmacology

Received: *24 November 2021*
Accepted: *31 December 2021*
Published: *23 February 2022*

Citation:
Li H, Yu Z, Sun H, Liu B, Wang X, Shao Z, Wang M, Xie W, Yao X, Yao Q and Zhi Y (2022) Efficient Synthesis of 2,3′-Spirobi (Indolin)-2′-Ones and Preliminary Evaluation of Their Damage to Mitochondria in HeLa Cells. Front. Pharmacol. 12:821518. doi: 10.3389/fphar.2021.821518

1 INTRODUCTION

The high prevalence and fatal incidence of cancer in the population worldwide has fueled an intensified search for new therapeutic treatment options. Chemotherapy is one of the most common strategies. The major challenging factors in developing cancer chemotherapeutics is to increase selectivity and to reduce side effects toward normal cells and tissues. (Wheeler et al., 2013) Since the efficacy and toxicity of a drug is closely associated with its subcellular distribution, interest in subcellular organelle-targeting theranostics is substantially increasing. (Kang, 2018).

Among organelles, mitochondria which is a regulatory center for cellular energy metabolism, substance synthesis and death, function as dynamic networks that often come in varied morphologies and subcellular distribution to fulfill their multiple tasks and thus have received substantial attention. (Li et al., 2020; Chen H. et al., 2021; Zou et al., 2021) Amount of researches disclosed that many human diseases have been closely related with functional mitochondria, such as neurodegenerative disorders, cardiovascular disorders, metabolic disorders, and cancers. (Cho et al., 2020) Recent studies demonstrated dramatic alterations in mitochondrial form during the early stages of cell apoptosis that is a fragmentation of the network and the remodeling of the cristae, indicating mitochondria are closely associated with apoptotic pathways. (Karbowski and Youle, 2003) Moreover, accumulating evidence indicates that the occurrence, development and metastasis of tumors has been linked to mitochondrial dysfunction and malfunctions, whose morphology is sensitive to their effects, featuring mitochondria a striking target in the design of anti-cancer drugs. (Mo et al., 2012; Hao et al., 2019) So far, some interesting and innovative examples have been reported, such as the increased anti-tumor effect of photodynamic therapy through the regulation of mitochondrial form by paclitaxel. (Zhao et al., 2017) However, these therapies are not yet in the preclinical phase. Therefore, the search for new natural or synthetic compounds that can target mitochondria as anticancer treatment is imperative.

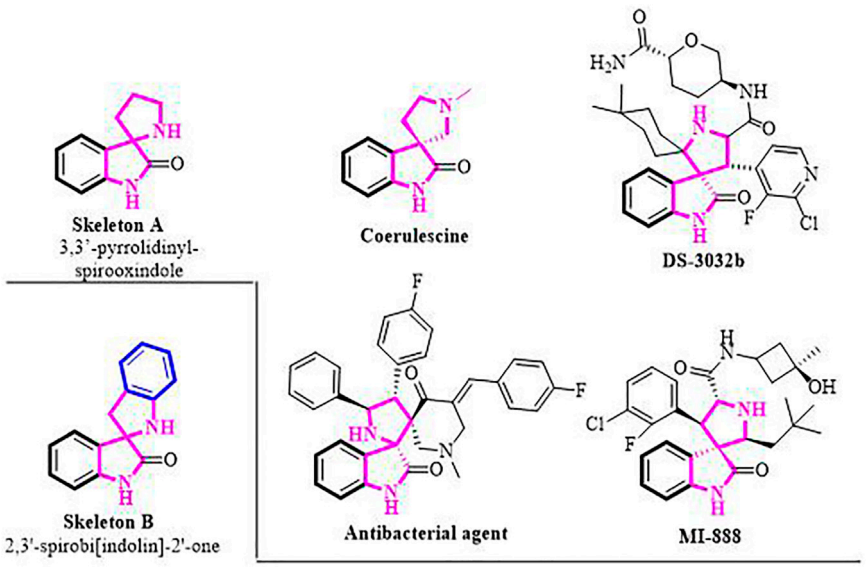

FIGURE 1 | Representative biologically active 3,3′-pyrrolidinyl-spirooxindoles.

The 3,3′-pyrrolidinyl-spirooxindole skeleton is a privileged class of heterocyclic motifs, which form the core of a large family of bioactive oxindole alkaloids and medicinally important compounds. (Kumar et al., 2008; Girgis, 2009; Zhao et al., 2013a; Zhao et al., 2013b; Arumugam et al., 2021; Liu et al., 2021) For instance, coerulescine, the simplest prototype member, was isolated from *Horsfieldia superba*, extracts of which have found use in indigenous medicine. (Neil et al., 1997) Spirooxindole derivative DS-3032b exhibits MDM2 inhibitory activity employed in the treatment of patients with advanced solid tumors and lymphomas (**Figure 1**). (Gounder et al., 2016) Their notable biological activities prompted the development of numerous strategies toward the syntheses of 3,3′-pyrrolidinyl-spirooxindole moiety. (Cao and Zhou, 2015; He et al., 2020; Liu X. et al., 2020; Nakamura et al., 2020; Reddy et al., 2020; Bortolami et al., 2021; Nasri et al., 2021; Saranya et al., 2021) Nevertheless, the construction of the structurally similar spirobi (indolin) frameworks (Skeleton B, **Figure 1** bottom left) has been less studied, and until now, only two synthetic methods have been reported for the synthesis of 2,3′-spirobi (indolin)-2′-ones. (Gui et al., 2019; Wang et al., 2019) In 2019, Shi and co-workers pioneered the (4 + 1) annulation of 3-isothiocyanato oxindoles and aza-*o*-quinone methides, affording the corresponding condensed products in two steps. Meanwhile, Zhong's group reported an ioide salts catalyzed functionalization of carbonyl compounds with sulfonamides.

Although these were elegant and creative strategies, it is still highly desirable to develop a concise protocol to construct the 2,3′-spirobi (indolin)-2′-ones framework from readily available starting materials, especially under mild conditions. Based on our research expertise in the field of domino-cycloaddition, (Enders et al., 2015; Zhao et al., 2016a; Zhao et al., 2016b; Zhi et al., 2016; Zhi et al., 2018) we envisioned that the assembly of 2,3′-spirobi (indolin)-2′-ones 3 could be realized through a formal (4 + 1) reaction between *in situ* generated aza-*ortho*-QM 2′ from *N*-(*o*-chloromethyl) aryl amide 2 and 3-chloroindolin-2-one 1 in the presence of an appropriate base (**Scheme 1**). We hope this annulation reaction could provide a general and straightforward method to access 2,3′-spirobi (indolin)-2′-ones 3 that will serve as the basis for evaluation of bioavailabilty especially their effect on mitochondria which is understudied.

2 RESULTS AND DISCUSSIONS

2.1 Chemistry

To test the feasibility of our hypothesis, we chose 3-chloroindolin-2-one **1a** and N-[2-(chloromethyl) phenyl]-4-methylbenzenesulfonamide **2a** as the model substrates to optimize the reaction conditions (**Table 1**). First, an initial experiment was conducted in ethyl ester at room temperature in the presence of Cs_2CO_3. To our delight, the expected product **3a** was obtained in a yield of 15% (**Table 1**, entry 1). To improve the reaction yield, the commonly used organic base Et_3N was tested while there was no compound **3a** obtained. We found that the use of the suitable base is very crucial for the success of this reaction and thus an extensive screening of base was performed (**Table 1**, entries 3–6). Fortunately, inorganic bases K_2CO_3 and NH_4HCO_3 delivered the desired product **3a** in 80 and 82% yield respectively. Striving for higher efficiency, kinds of solvents and different temperature were screened and the best result was obtained by raising the reaction temperature to 40°C and using MTBE as the solvent, leading to the desired product **3a** in a yield of 88% (**Table 1**, entry 17).

Having identified the optimal reaction conditions, the substrate scope of the new protocol was explored and the results are shown in **Table 2**. Initially, we examined the

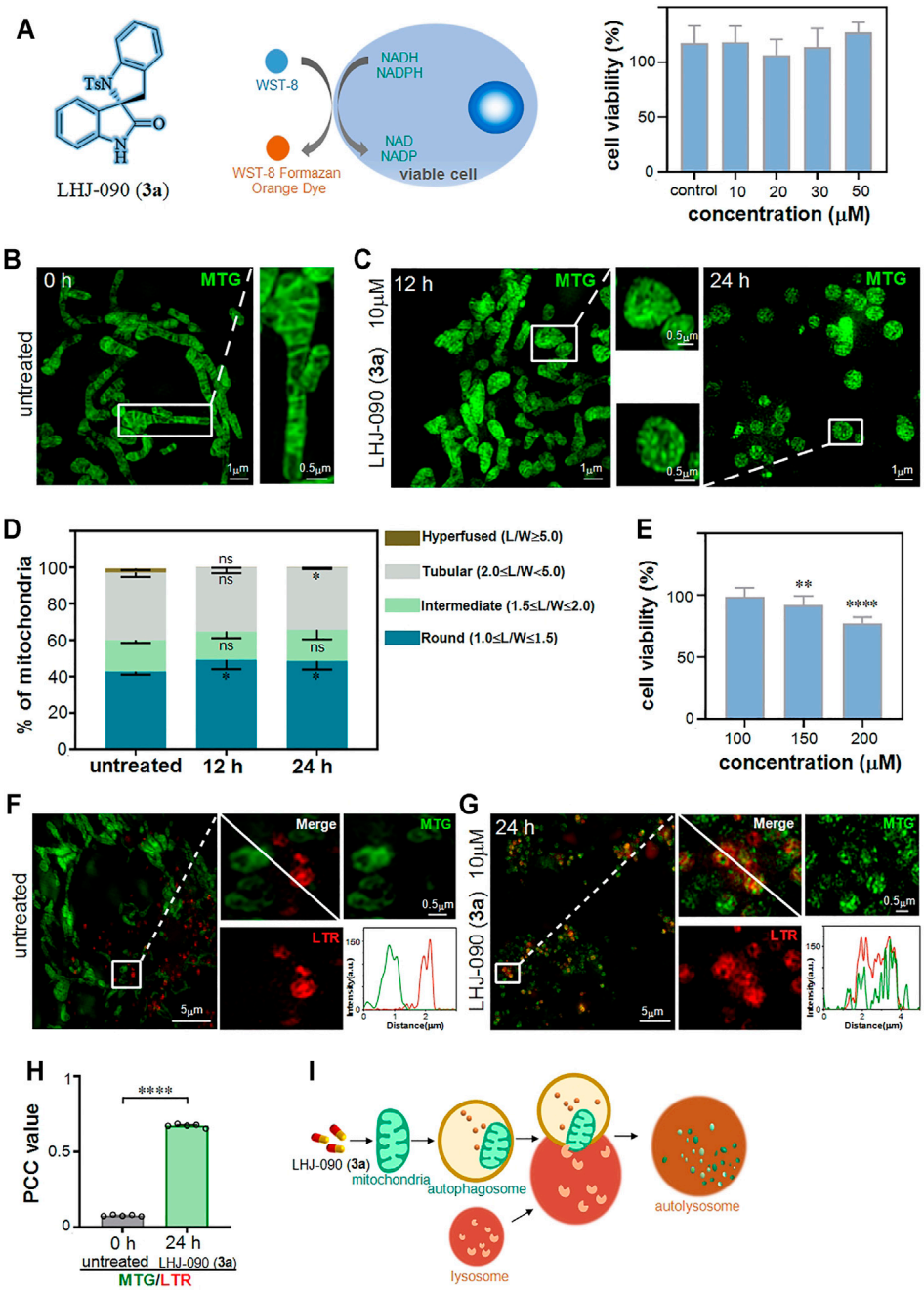

FIGURE 2 | LHJ-090 (**3a**) damage mitochondria and stimulate the process of mitophagy. **(A)** The cell viability (%) obtained with cck8 assay. Percentage of viable HeLa cells after treated with different concentrations of **3a** (0 10, 20, 30 and 50 μM) for 24 h **(B,C)** SIM imaging of mitochondria in HeLa cells were treated with **3a** (10 μM) for 0, 12, and 24 h and then stained with the mitochondrial tracker probe (mito-tracker-green, MTG) (λex = 488 nm) for 0.5 h. **(D)** Quantitative analyze of mitochondrial morphology in HeLa cells after treated with **3a** for 0, 12, and 24 h. Data was appeared as Mean ± SEM ($n = 5$). *$p < 0.05$, all compared with untreated cells. **(E)** The cell viability (%) obtained with CCK-8 assay at high concentration **3a** stimulation, more than 150 μM shows toxicity to cells. **(F,G)** SIM colocalization images of MTG-stained mitochondria and LTR-stained lysosome with **(G)** or without **(F)** **3a** treatment, the white solid square indicates fluorescence intensity. **(H)** The *PCC* values for MTG and LTR in HeLa cells from **(F)** and **(G)**. **(I)** A schematic diagram of the role of **3a** in mitochondrial damage.

generality of 3-chloro isatin component. A variety of isatins **1** underwent the formal (4 + 1) aunulation reaction to furnish **3b-3g** in 70–90% yield. Notably, substrates bearing electron-donating (R = Me, OCF_3) or electron-withdrawing groups (R = Cl, Br) at the C5 position of the phenyl ring of **1** underwent this annulation process to furnish the corresponding products in good to excellent efficiencies **(3b-3e)**. Moreover, the C7 position substituted compounds were suitable substrates, and the target

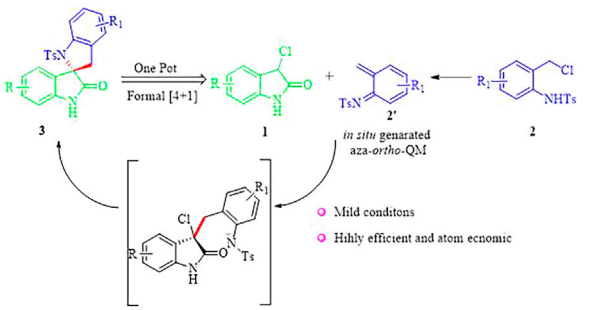

SCHEME 1 | Strategy for the synthesis of 2,3′-spirobi (indolin)-2′-ones.

products **3f-3g** were synthesized with good results under the optimal condition. However, if fluoro group was introduced at the C7 position of isatin **1**, the yield of the reaction under the optimal condition was very low. Next, the substrate scope of this reaction was examined further by varying the reaction partner **2**. We found that all the substrates **2h**-**2n** reacted efficiently with 1a, furnishing the desired products (**Table 2**, **3h–3n**) in 70–92% yield. The substitution groups on the tosyl benzene ring were well tolerated and delivered the desired compounds with high efficiency (**Table 2**, **3h–3j**). Especially, substrates bearing electron-with-drawing groups (R_1 = Cl, Br) on the phenyl ring of **2** readily ccould be easily processed to give the products in good to excellent yields (**3j–3n**).

In order to test the robustness and general utility of this 1,4-addition reaction, a gram-scale reaction was carried out under the optimal conditions and the expected product **3a** could be isolated in 80% yield without erosion of the efficiency of this process

TABLE 1 | Reaction condition optimization studies.[a]

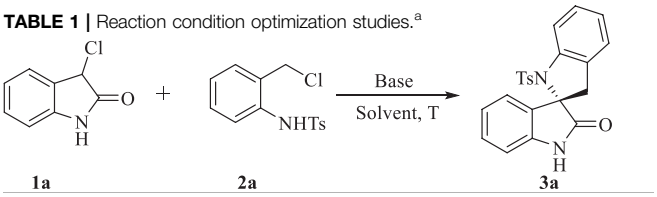

1a 2a 3a

Entry	Base	Solvent	Yield[b] (%)
1	Cs_2CO_3	EA	15
2	Et_3N	EA	—
3	$NaHCO_3$	EA	38
4	Na_2CO_3	EA	66
5	NaOH	EA	11
6	K_2CO_3	EA	80
7	NH_4HCO_3	EA	82
8	NH_4HCO_3	DCM	65
9	NH_4HCO_3	$CHCl_3$	52
10	NH_4HCO_3	Et_2O	61
11	NH_4HCO_3	Toluene	73
12	NH_4HCO_3	DCE	70
13	NH_4HCO_3	MTBE	85
14	NH_4HCO_3	CCl_4	54
15[c]	NH_4HCO_3	MTBE	88
16[d]	NH_4HCO_3	MTBE	80

[a]*All reactions were conducted with 0.4 mmol of* ***1a*** *(1.0 equiv.), 0.44 mmol of* ***2a*** *(1.1 equiv.), and 1.2 mmol of base in 4.0 ml of solvent at rt.*
[b]*Yield of isolated compound* ***3a*** *after chromatography.*
[c]*The reaction was conducted at 40°C.*
[d]*The reaction was conducted at 50°C.*
All the reactions were conducted with 0.4 mmol of 1 (1.0 equiv.), 0.44 mmol of 2 (1.1 equiv.) and 1.2 mmol of base in MTBE (4.0 mL) at 40°C. Yields are those of the isolated products ***3a–3n*** *after column chromatography.*

(**Scheme 1A**). In addition, as shown in **Scheme 1B**, the relative configuration of compound **3n** was determined unambiguously by X-ray crystallography.

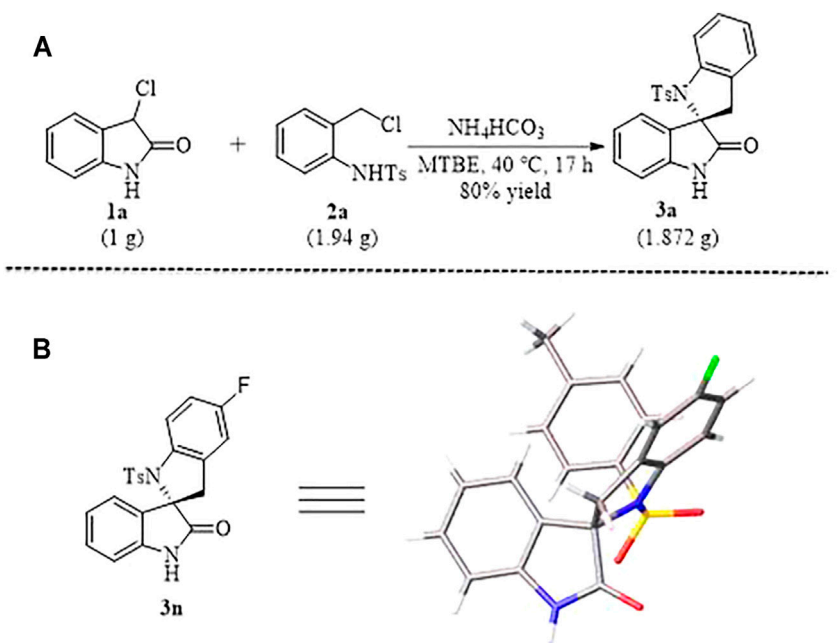

SCHEME 2 | Gram-Scale synthesis **(A)** of N-tosylated spirobi (indolin) **3a** and X-ray Structure **(B)** of **3n**.

TABLE 2 | Substrate scope.

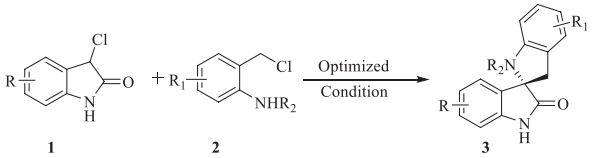

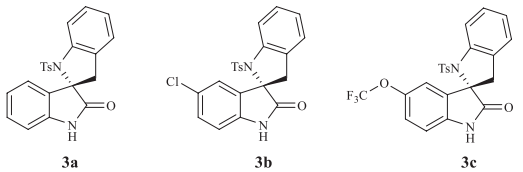

Yield: 88% Yield: 82% Yield: 75%

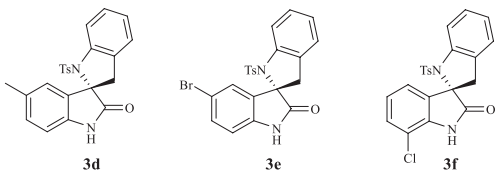

Yield: 82% Yield: 90% Yield: 70%

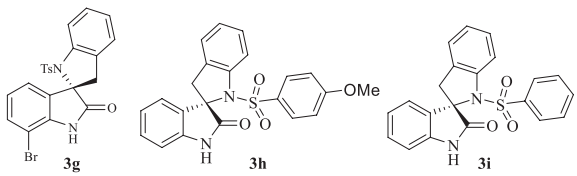

Yield: 72% Yield: 70% Yield: 88%

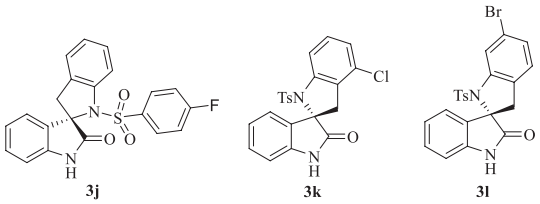

Yield: 90% Yield: 78% Yield: 73%

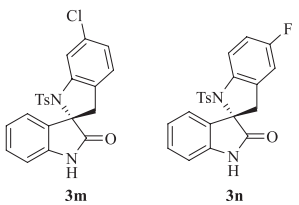

Yield: 85% Yield: 92%

All the reactions were conducted with 0.4 mmol of 1 (1.0 equiv.), 0.44 mmol of 2 (1.1 equiv.) and 1.2 mmol of base in MTBE (4.0 mL) at 40°C. Yields are those of the isolated products 3a–3n after column chromatography.

2.2 Super-resolution Imaging Reveals 3a (LHJ-090) Changes Mitochondrial Morphology and Distribution

After the series of 2,3′-spirobi (indolin)-2′-ones were synthesized, **3a** was selected to evaluate its damage effect on mitochondria. To verify the cytotoxicity of **3a**, we chose a colorimetric measurement tool commonly used in laboratories, CCK-8, (Lou et al., 2010) which relies on WST-8 that can be reduced by mitochondrial dehydrogenase (such as succinate dehydrogenase, SDH) to produce a highly water-soluble orange-yellow formazan product for counting the number of live cells (**Figure 2A**). (Liu L. Y. et al., 2020) We found that the cells did not respond to the detection threshold for the CCK-8 assay after treatment with **3a** at the concentration ranging from 10 to 50 μM. As it is generally accepted that the activity of SDH was applied as an indicator to evaluate the tricarboxylic acid cycle for reflecting cell activity rather than mitochondria behavior, (Farshbaf and Kiani-Esfahani, 2018) colorimetric tools based on a large number of cells are inaccurately for clarifying the regulation of drugs on a single mitochondria.

To more accurately reflect the damage of **3a** to the mitochondria, we applied recently developed structured illumination microscopy (SIM), a new tool for investing the effect of drugs at the single mitochondria level in living cells. (Wei et al., 2022) SIM based on a known spatially structured pattern of light to excite a sample whose fringe position and direction can be changed multiple times and to record the emission fluorescence signal at each position, thereby providing up to 100 nm spatial resolution. (Chen et al., 2018) Therefore, this tool can help us accurately and quantitatively study the behavior of **3a** at the nanoscale in living cells system.

Next, we checked the **3a** at the concentration of 10 μM in HeLa cells, and then observed it under SIM. We used a commercial mitochondrial probe (Mito-Tracker Green, MTG) to label mitochondria in HeLa cells after **3a** stimulation. (Chen et al., 2020a; Zhang et al., 2021) Compared to the SIM images captured at 0 h (**Figure 2B**), we observed that mitochondrial morphology has changed from fibrous-like to round-like after the **3a** treatment for 12 and 24 h (**Figure 2C**), showing the mitochondria were destroyed. To evaluate the mitochondrial morphology, the length-to-width ratio (L/W), was introduced as previously reported. (Shao et al., 2020) This system propose four standards to measure the morphology of mitochondria, namely round or nearly round ($1.0 \leq L/W < 1.5$), intermediate ($1.5 \leq L/W < 2.0$), tubular ($2.0 \leq L/W < 5.0$), and hyperfused ($L/W \geq 5.0$). We then quantify the distribution of individual mitochondria in HeLa cells, and found that the distribution of mitochondrial morphology was changed with the **3a** treatment for 12 and 24 h (**Figure 2D**), indicating that **3a** at 10 μM could damage mitochondrial morphology's distribution.

Finally, we increased the concentration of **3a** to check the detection threshold of CCK-8, and found that it could not be responded until 150 μM (**Figure 2E**), which shows that SIM is more accurate in exploring the sensitivity of drugs to subcellular behavior.

2.3 3a Damages Mitochondria Which Then Involved in the Process of Mitophagy

Mitophagy is a process by which cells remove and degrade damaged mitochondria, and its typical feature is the overlap of lysosomes and mitochondria. (Chen et al., 2020b; Chen Q. et al., 2021) After clarifying that **3a** can damage mitochondria, we further studied whether drug-induced mitochondrial damage is involved in the mitophagy pathway.

We then use MTG and commercial lysosomal probe (Lyso-Tracker Red, LTR) to simultaneously label drug-treated HeLa cells. (Wang et al., 2020; Zhang C. et al., 2021) Results revealed that the mitochondria was damaged to be granular after 24 h of the drug treatment as the green mitochondria stained by MTG and the red lysosome stained by LTR overlapped into yellow (**Figure 2F**). Compared with that in untreated cells, the overlap of mitochondria and lysosome in cells treated with **3a** for 24 h was increased significantly (**Figure 2G**). Together, these results suggested that **3a** induced the change of mitochondrial morphology, and then triggered the mitophagy pathway.

3 CONCLUSION

Taken together, we reported a novel (4 + 1) annulation reaction between 3-chlorooxindoles and *N*-(*o*-chloromethyl) aryl amides through *in situ* generated aza-*ortho*-QM with 3-chlorooxindoles for the efficient synthesis of various 2,3′-spirobi (indolin)-2′-ones in good to excellent yield under mild conditions. By using the highly accurate tool structured illumination microscopy, we found that compound 3a could damage the distribution of mitochondrial form and induce mitophagy pathway, which finally might promote the mitophagy in cancer cells. Further efforts are in progress to evaluate the antiproliferative activity of these spiropyrrolidine analogs against tumor cell lines.

4 EXPERIMENTAL SECTIONS

4.1 Chemistry

4.1.1 General Information

The chemical reagents are commercially available and were used without further purification. Reactions were monitored by Thin Layer Chromatography (TLC) (Silica gel HF254 or GF254 from Qingdao Haiyang Chemical Co., Ltd., Qingdao, China), and the spots were visualized with ultraviolet irradiation (254 nm). Compounds were purified by solvent beating or silica gel column chromatography (200–300 mesh). ^{1}H NMR and ^{13}C NMR spectra were recorded on a Bruker AVANCE AV III 600 spectrometer using $CDCl_3$ or d-DMSO as solvent. Data for ^{1}H NMR are reported as follows: chemical shift (ppm), multiplicity (s = singlet, d = doublet, t = triplet, q = quartet, dd = doublet of doublet, td = triplet of doublet, m = multiplet, br = broad), integration, and coupling constant (Hz). Data for ^{13}C NMR are reported in terms of chemical shift and multiplicity where appropriate. High resolution mass spectra (HRMS) were obtained from Thermo Scientific Q Exactive Plus. The melting

points were determined by Büchi 510 apparatus without corrected.

4.1.2 General Procedure for the Synthesis of Products 3a-3n

To an oven-dried flask were added **1** (0.4 mmol, 66.8 mg, 1.0 equiv), **2** (0.44 mmol, 130 mg, 1.1 equiv) and NH_4HCO_3 (1.2 mmol, 94.9 mg, 3.0 equiv) followed by the addition of MTBE (4.0 ml). The reaction mixture was allowed to stir at 40°C for 17 h and then directly poured into water. The solution was extracted with dichloromethane (3 × 15 ml). The organic phases were combined, washed with brine and dried over Na_2SO_4. Then the solvent was evaporated to give a crude product which was purified by silica gel chromatography (hexane/ethyl acetate = 10/1 to 4/1) to provide the desired products **3a**-**3n**. The scale-up synthesis of **3a** was the same as the above steps.

(S)-1-Tosyl-2,3′-spirobi (indolin)-2′-one (3a)

According to general procedure, the crude product was purified by silica gel chromatography (hexane/ethyl acetate = 10/1 to 4/1) to provide **3a** as a white solid (132.6 mg, 88% yield). mp: 267–269°C.^{1}H NMR (400 MHz, DMSO-d_6) δ 10.76 (s, 1H), 7.70 (d, J = 8.4 Hz, 2H), 7.33 (d, J = 8.4 Hz, 2H), 7.28–7.17 (m, 4H), 7.04–7.00 (m, 1H), 6.94 (d, J = 8.4 Hz, 1H), 6.83 (d, J = 7.6 Hz, 1H), 6.76 (d, J = 7.6 Hz, 1H), 3.54 (d, J = 16.0 Hz, 1H), 3.23 (d, J = 16.4 Hz, 1H), 2.36 (s, 3H) ppm; ^{13}C NMR (150 MHz, $CDCl_3$) δ 177.5, 144.1, 141.6, 139.5, 136.4, 130.9, 129.8, 129.5 (2C), 128.1, 128.0 (2C), 127.2, 125.2, 123.0, 123.0, 122.9, 112.5, 110.6, 71.7, 42.2, 21.6 ppm. HRMS (ESI): m/z (M + H)$^+$ calcd for $C_{22}H_{19}N_2O_3S^+$ 391.1116; found 391.1112.

(S)-5′-Chloro-1-Tosyl-2,3′-Spirobi (indolin)-2′-One (3b)

According to general procedure, the crude product was purified by silica gel chromatography (hexane/ethyl acetate = 10/1 to 4/1) to provide **3b** as a white solid (140 mg, 82% yield). mp: 253–255°C. ^{1}H NMR (400 MHz, DMSO-d_6) δ 10.91 (s, 1H), 7.59 (d, J = 8.0 Hz, 2H), 7.36–7.23 (m, 6H), 7.05 (t, J = 7.2 Hz, 1H), 6.95 (d, J = 8.4 Hz, 1H), 6.50 (s, 1H), 3.51 (d, J = 16.4 Hz, 1H), 3.30 (d, J = 16.4 Hz, 1H), 2.36 (s, 3H) ppm; ^{13}C NMR (100 MHz, DMSO-d6) δ 176.8, 145.0, 141.5, 140.6, 136.3, 131.7, 130.1 (2C), 130.0, 128.6, 127.8, 127.6, 126.3, 126.0, 123.6 (2C), 123.3, 112.5, 112.4, 71.4, 41.7, 21.5 ppm; HRMS (ESI): m/z (M + H)$^+$ calcd for $C_{22}H_{18}ClN_2O_3S^+$ 425.0727; found 425.0718.

(S)-1-Tosyl-5'-(trifluoromethoxy)-2,3′-spirobi (indolin)-2′-one (3c)

According to general procedure, the crude product was purified by silica gel chromatography (hexane/ethyl acetate = 10/1 to 4/1) to provide **3c** as a white solid (142 mg, 75% yield). mp: 98–102°C. ^{1}H NMR (600 MHz, DMSO-d_6) δ 10.96 (s, 1H), 7.69 (d, J = 8.4 Hz, 2H), 7.34 (d, J = 8.4 Hz, 2H), 7.30 (d, J = 8.4 Hz, 1H), 7.27 (d, J = 7.8 Hz, 1H), 7.24–7.20 (m, 2H), 7.05–7.02 (m, 2H), 6.74 (s, 1H), 3.54 (d, J = 16.2 Hz, 1H), 3.33 (d, J = 15.6 Hz, 1H), 2.36 (s, 3H) ppm; ^{13}C NMR (150 MHz, DMSO-d_6) δ 177.1, 145.0, 143.6, 143.5 141.5, 140.9, 136.4, 132.1, 130.2 (2C),128.5, 127.7 (2C), 125.9, 123.6, 116.8, 112.4, 111.8, 71.7, 41.8, 21.4 ppm; HRMS (ESI): m/z (M + H)$^+$ calcd for $C_{23}H_{18}F_3N_2O_4S^+$ 475.0939; found 475.0935.

(S)-5′-Methyl-1-Tosyl-2,3′-Spirobi (indolin)-2′-One (3d)

According to general procedure, the crude product was purified by silica gel chromatography (hexane/ethyl acetate = 10/1 to 4/1) to provide **3d** as a white solid (132 mg, 82% yield). mp: 282–284°C. ^{1}H NMR (400 MHz, DMSO-d_6) δ 10.64 (s, 1H), 7.55 (d, J = 8.0 Hz, 2H), 7.34–7.25 (m, 5H), 7.07–7.02 (m, 2H), 6.83 (d, J = 8.0 Hz, 1H), 6.34 (s, 1H), 3.51 (d, J = 16.4 Hz, 1H), 3.20 (d, J = 18.8 Hz, 1H), 2.36 (s, 3H), 2.01 (s, 3H) ppm; ^{13}C NMR (150 MHz, $CDCl_3$) δ 177.5, 143.9, 141.8, 137.1, 136.6, 132.5,130.4, 130.1, 129.3 (2C), 128.1, 127.9 (2C), 127.3, 125.2, 123.7, 123.0, 112.6, 110.3, 71.6, 42.2, 21.5, 20.8 ppm; HRMS (ESI): m/z (M + H)$^+$ calcd for $C_{23}H_{21}N_2O_3S^+$ 405.1273; found 405.1261.

(S)-5′-Bromo-1-Tosyl-2,3′-Spirobi (indolin)-2′-One (3e)

According to general procedure, the crude product was purified by silica gel chromatography (hexane/ethyl acetate = 10/1 to 4/1) to provide **3e** as a white solid (169 mg, 90% yield). mp: 269–273°C.^{1}H NMR (400 MHz, DMSO-d_6) δ 10.91 (s, 1H), 7.56 (d, J = 8.0 Hz, 2H), 7.44 (d, J = 8.0 Hz, 1H), 7.37 (d, J = 8.0 Hz, 1H), 7.31–7.25 (m, 4H), 7.06 (t, J = 7.6 Hz, 1H), 6.91 (d, J = 8.0 Hz, 1H), 6.57 (s, 1H), 3.51 (d, J = 16.0 Hz, 1H), 3.30 (d, J = 16.4 Hz, 1H), 2.37 (s, 3H) ppm; ^{13}C NMR (100 MHz, DMSO-d_6) δ 176.6, 145.0, 141.5, 141.0, 136.3, 132.9, 132.0, 130.2 (2C), 128.6, 127.8, 127.5 (2C), 126.0, 125.9, 123.7, 114.0, 112.9, 112.5, 71.3, 41.7, 21.6 ppm; HRMS (ESI): m/z (M + H)$^+$ calcd for $C_{22}H_{18}BrN_2O_3S^+$ 469.0222; found 469.0196.

(S)-7′-Chloro-1-Tosyl-2,3′-Spirobi (indolin)-2′-One (3f)

According to general procedure, the crude product was purified by silica gel chromatography (hexane/ethyl acetate = 10/1 to 4/1) to provide **3f** as a yellow solid (119 mg, 70% yield). mp: 250–255°C.^{1}H NMR (600 MHz, DMSO-d_6) δ 11.24 (s, 1H), 7.74 (d, J = 8.4 Hz, 2H), 7.37 (d, J = 7.8 Hz, 3H), 7.26 (d, J = 7.2 Hz, 1H), 7.22 (t, J = 7.8 Hz, 1H), 7.16 (d, J = 8.4 Hz, 1H), 7.03 (t, J = 7.2 Hz, 1H), 6.88 (t, J = 7.8 Hz, 1H), 6.78 (d, J = 7.8 Hz, 1H), 3.55 (d, J = 16.2 Hz, 1H), 3.30 (d, J = 16.2 Hz, 1H), 2.37 (s, 3H) ppm; ^{13}C NMR (150 MHz, DMSO-d_6) δ 176.7, 144.5, 140.9, 138.8, 135.8, 132.3, 129.8 (2C),128.0, 127.5 (2C),127.3, 125.5, 123.5, 123.1, 121.1, 114.5, 111.8, 71.8, 41.6, 21.0 ppm; HRMS (ESI): m/z (M + H)$^+$ calcd for $C_{22}H_{18}ClN_2O_3S^+$ 425.0727; found 425.0725.

(S)-7′-bromo-1-tosyl-2,3′-spirobi (indolin)-2′-one (3g).

According to general procedure, the crude product was purified by silica gel chromatography (hexane/ethyl acetate = 10/1 to 4/1) to provide **3g** as a yellow solid (135 mg, 72% yield). mp: 270–274°C.^{1}H NMR (400 MHz, $CDCl_3$) δ 7.88 (d, J = 8.4 Hz, 2H), 7.74 (s, 1H), 7.40 (d, J = 8.0 Hz, 1H), 7.25 (d, J = 9.6 Hz, 2H), 7.21–7.15 (m, 3H), 7.01–6.93 (m, 2H), 6.80 (t, J = 7.6 Hz, 1H), 3.73 (d, J = 15.6 Hz, 1H), 3.21 (d, J = 15.6 Hz, 1H), 2.39 (s, 3H) ppm; ^{13}C NMR (150 MHz, $CDCl_3$) δ 176.2, 144.4, 141.4, 138.7, 136. 2, 132.5, 132.4, 129.6 (2C), 128.2, 128.1 (2C), 126.8, 125.2, 124.4, 123.1, 121.5, 112.4, 103.6, 72.9, 42.3, 21.6 ppm; HRMS (ESI): m/z (M + H)$^+$ calcd for $C_{22}H_{18}BrN_2O_3S^+$ 469.0222; found 469.0222.

(S)-1-[(4-methoxyphenyl)sulfonyl]-2,3′-spirobi (indolin)-2′-one (3h)

According to general procedure, the crude product was purified by silica gel chromatography (hexane/ethyl acetate = 10/1 to 4/1) to provide **3h** as a white solid (113.7 mg, 70% yield).

mp: 245–248°C.^{1}H NMR (600 MHz, $CDCl_3$) δ 7.87 (d, J = 9.0 Hz, 2H), 7.71 (s, 1H), 7.25–7.23 (m, 2H), 7.19–7.15 (m, 2H), 6.99 (t, J = 7.2 Hz, 1H), 6.95 (d, J = 7.2 Hz, 1H), 6.92 (d, J = 7.8 Hz, 1H), 6.89- 6.86 (m, 3H), 3.83 (s, 3H), 3.74 (d, J = 15.6 Hz, 1H), 3.22 (d, J = 16.2 Hz, 1H) ppm; ^{13}C NMR (150 MHz, $CDCl_3$) δ 177.4, 163.3, 141.7, 139.4, 131.0, 130.9, 130.3 (2C), 129.7, 128.1, 127.2, 125.2, 123.1, 122.9, 122.9, 114.1 (2C), 112.4, 110.5, 71.7, 55.6, 42.2 ppm; HRMS (ESI): m/z $(M + H)^+$ calcd for $C_{22}H_{19}N_2O_4S^+$ 407.1065; found 407.1062.

(S)-1-(phenylsulfonyl)-2,3′-spirobi (indolin)-2′-one (3i)

According to general procedure, the crude product was purified by silica gel chromatography (hexane/ethyl acetate = 10/1 to 4/1) to provide **3i** as a red solid (132.5 mg, 88% yield). mp: 138–140°C.^{1}H NMR (400 MHz, DMSO-d_6) δ 10.77 (s, 1H), 7.81 (d, J = 7.6 Hz, 2H), 7.67 (t, J = 7.2 Hz, 1H), 7.53 (t, J = 7.6 Hz, 2H), 7.29–7.23 (m, 4H), 7.06–7.02 (m, 1H), 6.95 (d, J = 8.0 Hz, 1H), 6.80 (t, J = 7.2 Hz, 1H), 6.73 (t, J = 7.2 Hz, 1H), 3.55 (d, J = 16.2.4 Hz, 1H), 3.25 (d, J = 16.4 Hz, 1H) ppm; ^{13}C NMR (100 MHz, DMSO-d_6) δ 177.1, 141.6, 141.5, 139.34, 134.2, 130.8, 130.2, 129.7 (2C), 128.4, 128.0, 127.8 (2C), 125.9, 123.5, 123.0, 122.5, 112.3, 110.8, 71.8, 42.1 ppm; HRMS (ESI): m/z $(M + H)^+$ calcd for $C_{21}H_{17}N_2O_3S^+$ 377.0960; found 377.0955.

(S) -1-[(4-fluorophenyl)sulfonyl]-2,3′-spirobi (indolin)-2′-one (3j)

According to general procedure, the crude product was purified by silica gel chromatography (hexane/ethyl acetate = 10/1 to 4/1) to provide **3j** as a red solid (141 mg, 90% yield). mp: 207–210°C. ^{1}H NMR (400 MHz, DMSO-d_6) δ 10.80 (s, 1H), 7.88–7.85 (m, 2H), 7.38 (t, J = 13.2 Hz, 2H) 7.29–7.25 (m, 4H), 7.07–7.03 (m, 1H), 6.95 (d, J = 7.6 Hz, 1H), 6.81 (t, J = 7.6 Hz, 1H), 6.73 (d, J = 7.2 Hz, 1H) 3.55 (d, J = 16.4 Hz, 1H), 3.25 (d, J = 16.4 Hz, 1H) ppm; ^{13}C NMR (125 MHz, $CDCl_3$) δ 177.7, 141.4, 139.7, 136.4, 130.8, 130.8, 130.5, 130.0, 128.2, 127.3, 125.4, 123.3, 123.0, 122.8, 116.2, 116.1, 112.5, 110.9, 71.8, 42.2, 29.7 ppm; HRMS (ESI): m/z $(M + H)^+$ calcd for $C_{21}H_{16}FN_2O_3S^+$ 395.0866; found 395.0863.

(S)-4-Chloro-1-tosyl-2,3′-spirobi (indolin)-2′-one (3k)

According to general procedure, the crude product was purified by silica gel chromatography (hexane/ethyl acetate = 10/1 to 4/1) to provide **3k** as a red solid (132.6 mg, 78% yield). mp: 222–226°C.^{1}H NMR (600 MHz, $CDCl_3$) δ 8.07 (s, 1H), 7.76 (d, J = 7.6 Hz, 2H), 7.26 (t, J = 9.6 Hz, 1H), 7.22–7.18 (m, 3H), 7.14 (t, J = 8.4 Hz, 1H), 6.98 (d, J = 7.8 Hz, 1H), 6.94 (t, J = 7.8 Hz, 2H),6.88 (t, J = 7.8 Hz, 1H) 3.72 (d, J = 16.8 Hz, 1H), 3.30 (d, J = 16.2 Hz, 1H), 2.38 (s, 3H) ppm; ^{13}C NMR (150 MHz, $CDCl_3$) δ 177.1, 144.5, 142.9, 139.6, 136.2, 131.0, 130.6, 123.0, 129.7, 129.6 (2C),128.0 (2C),125.7, 123.1, 123.2, 123.0, 110.7, 110.6, 71.4, 41.5, 21.6 ppm; HRMS (ESI): m/z $(M + H)^+$ calcd for $C_{22}H_{18}ClN_2O_3S^+$ 425.0727; found 425.0718.

(S)-6-Bromo-1-tosyl-2,3′-spirobi (indolin)-2′-one (3l)

According to general procedure, the crude product was purified by silica gel chromatography (hexane/ethyl acetate = 10/1 to 4/1) to provide **3l** as a white solid (137 mg, 73% yield). mp: 89–93°C.^{1}H NMR (600 MHz, $CDCl_3$) δ 7.76 (d, J = 8.4 Hz, 2H), 7.72 (s, 1H), 7.44 (s, 1H), 7.28-7.27 (m, 1H), 7.23 (d, J = 8.4 Hz, 2H), 7.13–7.12 (m, 1H), 7.01 (d, J = 7.8 Hz, 1H), 6.93–6.90 (M, 2H), 6.87 (d, J = 8.4 Hz, 1H), 3.65 (d, J = 16.2 Hz, 1H), 3.15 (d, J = 15.6 Hz, 1H), 2.39 (s, 3H) ppm; ^{13}C NMR (150 MHz, $CDCl_3$) δ 176.8, 144.5, 143.0, 139.4, 136.0, 130.4, 130.0, 129.7 (2C), 128.0 (2C),126.3, 126.2, 125.9, 123.2, 123.0, 121.7, 115.7, 110.6, 72.1, 41.7, 21.6 ppm; HRMS (ESI): m/z $(M + H)^+$ calcd for $C_{22}H_{18}BrN_2O_3S^+$ 469.0222; found 469.0108.

(S)-6-Chloro-1-tosyl-2,3′-spirobi (indolin)-2′-one (3m)

According to general procedure A, the crude product was purified by silica gel chromatography (hexane/ethyl acetate = 10/1 to 4/1) to provide **3m** as a white solid (144.5 mg, 85% yield). mp: 174–177°C. ^{1}H NMR (400 MHz, DMSO-d_6) δ 10.79 (s, 1H), 7.69 (d, J = 8.0 Hz, 2H), 7.37 (d, J = 8.0 Hz, 2H), 7.28 (d, J = 7.6 Hz, 2H), 7.10 (d, J = 10.4 Hz, 2H), 6.94 (d, J = 8.0 Hz, 1H), 6.86–6.82 (m, 2H), 3.51 (d, J = 16.4 Hz, 1H), 3.25 (d, J = 16.4 Hz, 1H), 2.38 (s, 3H) ppm; ^{13}C NMR (100 MHz, DMSO-d_6) δ 176.7, 145.2, 143.0, 141.6, 136.1, 132.6, 130.4, 130.3 (2C), 127.9 (2C), 127.3, 127.2 123.2, 122.6, 112.0, 110.9, 72.6, 67.5, 41.4, 25.6, 21.5 ppm; HRMS (ESI): m/z $(M + H)^+$ calcd for $C_{22}H_{18}ClN_2O_3S^+$ 425.0727; found 425.0725.

(S)-5-Fluoro-1-tosyl-2,3′-spirobi (indolin)-2′-one (3n)

According to general procedure, the crude product was purified by silica gel chromatography (hexane/ethyl acetate = 10/1 to 4/1) to provide **3n** as a white solid (150 mg, 92% yield). mp: 195–198°C.^{1}H NMR (400 MHz, DMSO-d_6) δ 10.77 (s, 1H), 7.67 (d, J = 8.0 Hz, 2H), 7.33 (d, J = 8.4 Hz, 2H), 7.28 (t, J = 7.6 Hz, 1H), 7.19–7.16 (m, 2H), 7.05 (d, J = 9.2 Hz, 1H), 6.94 (d, J = 8.0 Hz, 1H), 6.85-6.77 (m, 2H), 3.53 (d, J = 15.2 Hz, 1H), 3.24 (d, J = 16.4 Hz, 1H), 2.37 (s, 3H) ppm; ^{13}C NMR (100 MHz, DMSO-d_6) δ 176.8, 144.9, 141.5, 138.0, 136.3, 130.6, 130.1 (2C), 127.9 (2C), 123.1, 122.5, 114.8, 114.5, 113.6, 113.3, 113.0, 112.9, 110.8, 41.8, 25.6, 21.5 ppm; HRMS (ESI): m/z $(M + H)^+$ calcd for $C_{22}H_{18}FN_2O_3S^+$ 409.1022; found 409.1010.

4.2 Biological Part

4.2.1 Cell Culture

HeLa cells were cultured in Dulbecco's modified Eagle's medium (#11965118, DMEM, Thermo Fisher Scientific) supplemented with 10% Certified fetal bovine serum (#C04001-500, FBS, VivaCell, Shanghai, China) penicillin (100 units/ml), and streptomycin (100 μg/ml; #15140163, 10,000 units/ml, Thermo Fisher Scientific) in a 5% CO_2 humidified incubator at 37°C.

4.2.2 OMX-SIM Super Resolution Imaging

HeLa cells were incubated with MTG and LTR at 37°C for 30 min in fresh DMEM and then washed three times with fresh DMEM. Super-resolution images were acquired on a commercial OMX-3D-SIM Microscope. Images were obtained at 512 × 512 using Z-stacks with a step size of 0.125 μm. The laser model was set to fast 272 MHz, the gain was set to 1, the output powers at the fiber end: 65 mW. All fluorescence images were analyzed, and their backgrounds were subtracted with Image J software.

4.2.3 Data Analysis

Statistical analysis was performed with Prism 8 (GraphPad). Normality and lognormality test to check the normal distribution. In the case of normal distribution, the statistical comparison of results was test with a Student's t test. In the case of non-normal distribution, the statistical comparison of results was test with a Mann-Whitney test, with levels of significance set at n. s. (no significant difference), $*p < 0.05$, $**p < 0.01$, $***p < 0.001$, and $****p < 0.0001$. Data are presented as mean ± SEM. Analyzed cells were obtained from three replicates. Statistical significances and sample sizes in all graphs are indicated in the corresponding figure legends.

DATA AVAILABILITY STATEMENT

The original contributions presented in the study are included in the article/**Supplementary Material**, further inquiries can be directed to the corresponding authors.

AUTHOR CONTRIBUTIONS

All authors listed have made a substantial, direct, and intellectual contribution to the work and approved it for publication.

FUNDING

This work was supported by Academic Promotion Programme of Shandong First Medical University (No. 2019LJ003) and grants from National Natural Science Foundation of China (Grant No. 81903473).

SUPPLEMENTARY MATERIAL

The Supplementary Material for this article can be found online at: https://www.frontiersin.org/articles/10.3389/fphar.2021.821518/full#supplementary-material

REFERENCES

Arumugam, N., Almansour, A. I., Kumar, R. S., Siva Krishna, V., Sriram, D., and Dege, N. (2021). Stereoselective Synthesis and Discovery of Novel Spirooxindolopyrrolidine Engrafted Indandione Heterocyclic Hybrids as Antimycobacterial Agents. *Bioorg. Chem.* 110, 104798. doi:10.1016/j.bioorg.2021.104798

Bortolami, M., Leonelli, F., Feroci, M., and Vetica, F. (2021). Step Economy in the Stereoselective Synthesis of Functionalized Oxindoles via Organocatalytic Domino/One-Pot Reactions. *Coc* 25, 1321–1344. doi:10.2174/1385272825666210518124845

Cao, Z.-Y., and Zhou, J. (2015). Catalytic Asymmetric Synthesis of Polysubstituted Spirocyclopropyl Oxindoles: Organocatalysis versus Transition Metal Catalysis. *Org. Chem. Front.* 2, 849–858. doi:10.1039/c5qo00092k

Chen, Q., Fang, H., Shao, X., Tian, Z., Geng, S., Zhang, Y., et al. (2020a). A Dual-Labeling Probe to Track Functional Mitochondria-Lysosome Interactions in Live Cells. *Nat. Commun.* 11 (1), 6290–6300. doi:10.1038/s41467-020-20067-6

Chen, Q., Shao, X., Hao, M., Fang, H., Guan, R., Tian, Z., et al. (2020b). Quantitative Analysis of Interactive Behavior of Mitochondria and Lysosomes Using Structured Illumination Microscopy. *Biomaterials* 250, 120059. doi:10.1016/j.biomaterials.2020.120059

Chen, H., Wang, H., Wei, Y., Hu, M., Dong, B., Fang, H., et al. (2021). Super-resolution Imaging Reveals the Subcellular Distribution of Dextran at the Nanoscale in Living Cells. *Chin. Chem. Lett.* doi:10.1016/j.cclet.2021.10.025

Chen, Q., Hao, M., Wang, L., Li, L., Chen, Y., Shao, X., et al. (2021). Prefused Lysosomes Cluster on Autophagosomes Regulated by VAMP8. *Cell Death Dis* 12 (10), 939. doi:10.1038/s41419-021-04243-0

Chen, Q., Jin, C., Shao, X., Guan, R., Tian, Z., Wang, C., et al. (2018). Super-Resolution Tracking of Mitochondrial Dynamics with an Iridium(III) Luminophore. *Small* 14 (41), 1802166. doi:10.1002/smll.201802166

Cho, H., Cho, Y. Y., Shim, M. S., Lee, J. Y., Lee, H. S., and Kang, H. C. (2020). Mitochondria-targeted Drug Delivery in Cancers. *Biochim. Biophys. Acta Mol. Basis. Dis.* 1866 (8), 165808. doi:10.1016/j.bbadis.2020.165808

Enders, D., Zhi, Y., Zhao, K., and Shu, T. (2015). Synthesis of Benzotriazepine Derivatives via [4+3] Cycloaddition of Aza-O-Quinone Methide Intermediates and Azomethine Imines. *Synthesis* 48 (02), 238–244. doi:10.1055/s-0035-1560809

Farshbaf, M. J., and Kiani-Esfahani, A. (2018). Succinate Dehydrogenase: Prospect for Neurodegenerative Diseases. *Mitochondrion* 42, 77–83. doi:10.1016/j.mito.2017.12.002

Girgis, A. S. (2009). Regioselective Synthesis of dispiro[1H-indene-2,3'-pyrrolidine-2',3''-[3H]indole]-1,2''(1''H)-diones of Potential Anti-tumor Properties. *Eur. J. Med. Chem.* 44 (1), 91–100. doi:10.1016/j.ejmech.2008.03.013

Gounder, M. M., Bauer, T. M., Schwartz, G. K., Masters, T., Carvajal, R. D., Song, S., et al. (2016). A Phase 1 Study of the MDM2 Inhibitor DS-3032b in Patients (Pts) with Advanced Solid Tumors and Lymphomas. *J. Clin. Oncol.* 34 (15), 2581. doi:10.1200/jco.2016.34.15_suppl.2581

Gui, H. Z., Wu, X. Y., Wei, Y., and Shi, M. (2019). A Formal Condensation and [4+1] Annulation Reaction of 3-Isothiocyanato Oxindoles with Aza- *O*-Quinone Methides. *Adv. Synth. Catal.* 361 (23), 5466–5471. doi:10.1002/adsc.201901124

Hao, L., Li, Z. W., Zhang, D. Y., He, L., Liu, W., Yang, J., et al. (2019). Monitoring Mitochondrial Viscosity with Anticancer Phosphorescent Ir(iii) Complexes via Two-Photon Lifetime Imaging. *Chem. Sci.* 10 (5), 1285–1293. doi:10.1039/c8sc04242j

He, Y., Liu, Y., Liu, Y., Kou, X. X., Li, Q. Z., Li, J. H., et al. (2020). Diastereodivergent Formal 1,3-Dipolar Cycloaddition of 5-alkenyl Thiazolones to Access Stereochemically Diverse Pyrrolidinyl Spirooxindoles. *Adv. Synth. Catal.* 362 (10), 2052–2058. doi:10.1002/adsc.201901541

Kang, H. C. (2018). Mitochondria-targeting Theranostics. *Biomater. Res.* 22, 34. doi:10.1186/s40824-018-0145-7

Karbowski, M., and Youle, R. J. (2003). Dynamics of Mitochondrial Morphology in Healthy Cells and during Apoptosis. *Cell Death Differ* 10 (8), 870–880. doi:10.1038/sj.cdd.4401260

Kumar, R. R., Perumal, S., Senthilkumar, P., Yogeeswari, P., and Sriram, D. (2008). Discovery of Antimycobacterial spiro-piperidin-4-ones: an Atom Economic, Stereoselective Synthesis, and Biological Intervention. *J. Med. Chem.* 51 (18), 5731–5735. doi:10.1021/jm800545k

Li, X., Zheng, J., Liu, W., Qiao, Q., Chen, J., Zhou, W., et al. (2020). Long-term Super-resolution Imaging of Mitochondrial Dynamics. *Chin. Chem. Lett.* 31 (11), 2937–2940. doi:10.1016/j.cclet.2020.05.043

Liu, S. J., Zhao, Q., Peng, C., Mao, Q., Wu, F., Zhang, F. H., et al. (2021). Design, Synthesis, and Biological Evaluation of Nitroisoxazole-Containing spiro[pyrrolidin-oxindole] Derivatives as Novel Glutathione Peroxidase 4/mouse Double Minute 2 Dual Inhibitors that Inhibit Breast Adenocarcinoma Cell Proliferation. *Eur. J. Med. Chem.* 217, 113359. doi:10.1016/j.ejmech.2021.113359

Liu, X., Lu, D., Wu, J. H., Tan, J. P., Jiang, C., Gao, G., et al. (2020). Stereoselective Synthesis of CF 3 -Containing Spirooxindoles via 1,3-Dipolar Cycloaddition by Dipeptide-Based Phosphonium Salt Catalysis. *Adv. Synth. Catal.* 362 (7), 1490–1495. doi:10.1002/adsc.202000001

Liu, L. Y., Fang, H., Chen, Q., Chan, M. H., Ng, M., and Wang, K. N. (2020). Multiple-Color Platinum Complex with Super-large Stokes Shift for Super-

resolution Imaging of Autolysosome Escape. *Angew. Chem. Int. Ed.* 59 (43), 19229–19236. doi:10.1002/anie.202007878

Lou, J., Chu, G., Zhou, G., Jiang, J., Huang, F., Xu, J., et al. (2010). Comparison between Two Kinds of Cigarette Smoke Condensates (CSCs) of the Cytogenotoxicity and Protein Expression in a Human B-Cell Lymphoblastoid Cell Line Using CCK-8 Assay, Comet Assay and Protein Microarray. *Mutat. Res.* 697 (1-2), 55–59. doi:10.1016/j.mrgentox.2010.01.014

Mo, R., Sun, Q., Xue, J., Li, N., Li, W., Zhang, C., et al. (2012). Multistage pH-Responsive Liposomes for Mitochondrial-Targeted Anticancer Drug Delivery. *Adv. Mater.* 24 (27), 3659–3665. doi:10.1002/adma.201201498

Nakamura, A., Kuwano, S., Sun, J., Araseki, K., Ogino, E., and Arai, T. (2020). Chiral Dinuclear Benzyliminobinaphthoxy-Palladium Catalyst for Asymmetric Mannich Reaction of Aldimines and Isatin-Derived Ketimines with Alkylmalononitriles. *Adv. Synth. Catal.* 362 (15), 3105–3109. doi:10.1002/adsc.202000447

Nasri, S., Bayat, M., and Mirzaei, F. (2021). Recent Strategies in the Synthesis of Spiroindole and Spirooxindole Scaffolds. *Top. Curr. Chem. (Cham)* 379 (4), 25. doi:10.1007/s41061-021-00337-7

Neil, A., Peter, A., Steven, M., and John, A. (1997). Oxindoles from Phalaris Coerulescens. *Photochem* 48 (3), 437–439.

Reddy, A. C. S., Reddy, P. M., and Anbarasan, P. (2020). Diastereoselective Palladium Catalyzed Carbenylative Amination of Ortho -Vinylanilines with 3-Diazoindolin-2-ones. *Adv. Synth. Catal.* 362 (4), 801–806. doi:10.1002/adsc.201901286

Saranya, P. V., Neetha, M., Aneeja, T., and Anilkumar, G. (2021). Transition Metal-Catalyzed Synthesis of Spirooxindoles. *RSC Adv.* 11 (13), 7146–7179. doi:10.1039/d1ra00139f

Shao, X., Chen, Q., Hu, L., Tian, Z., Liu, L., Liu, F., et al. (2020). Super-resolution Quantification of Nanoscale Damage to Mitochondria in Live Cells. *Nano Res.* 13, 2149–2155. doi:10.1007/s12274-020-2822-9

Wang, D., Lu, X., Sun, S., Yu, H., Su, H., Wu, Y., et al. (2019). Unified and Benign Synthesis of Spirooxindoles via Bifunctional and Recyclable Iodide-Salt-Catalyzed Oxidative Coupling in Water. *Eur. J. Org. Chem.* 2019 (35), 6028–6033. doi:10.1002/ejoc.201900751

Wang, Y., Duan, H., Shi, H., Zhang, S., Xu, Y., Zhu, W., et al. (2020). A Highly Sensitive Fluorescent Probe for Tracking Intracellular Zinc Ions and Direct Imaging of Prostatic Tissue in Mice. *Chin. Chem. Lett.* 31 (11), 2933–2936. doi:10.1016/j.cclet.2020.05.028

Wei, Y., Kong, L., Chen, H., Liu, Y., Xu, Y., Wng, H., et al. (2022). Super-resolution Image-Based Tracking of Drug Distribution in Mitochondria of a Label-free Naturally Derived Drug Molecules. *Chem. Eng. J.* 429, 132134. doi:10.1016/j.cej.2021.132134

Wheeler, H. E., Maitland, M. L., Dolan, M. E., Cox, N. J., and Ratain, M. J. (2013). Cancer Pharmacogenomics: Strategies and Challenges. *Nat. Rev. Genet.* 14 (1), 23–34. doi:10.1038/nrg3352

Zhang, X., Ren, T., Yang, F., and Yuan, L. (2021). Rational Design of Far Red to Near-Infrared Rhodamine Analogues with Huge Stokes Shifts for Single-Laser Excitation Multicolor Imaging. *Chin. Chem. Lett.* doi:10.1016/j.cclet.2021.06.038

Zhang, C., Shao, H., Zhang, J., Guo, X., Liu, Y., Song, Z., et al. (2021). Long-term Live-Cell Lipid Droplet-Targeted Biosensor Development for Nanoscopic Tracking of Lipid Droplet-Mitochondria Contact Sites. *Theranostics* 11 (16), 7767–7778. doi:10.7150/thno.59848

Zhao, H., Yin, R., Wang, Y., Lee, Y. H., Luo, T., Zhang, J., et al. (2017). Modulating Mitochondrial Morphology Enhances Antitumor Effect of 5-ALA-Mediated Photodynamic Therapy Both *In Vitro* and *In Vivo*. *J. Photochem. Photobiol. B* 176, 81–91. doi:10.1016/j.jphotobiol.2017.09.017

Zhao, K., Zhi, Y., Li, X., Puttreddy, R., Rissanen, K., and Enders, D. (2016a). Asymmetric Synthesis of 3,3'-Pyrrolidinyl-Dispirooxindoles via a One-Pot Organocatalytic Mannich/deprotection/aza-Michael Sequence. *Chem. Commun. (Camb)* 52 (11), 2249–2252. doi:10.1039/c5cc10057g

Zhao, K., Zhi, Y., Shu, T., Valkonen, A., Rissanen, K., and Enders, D. (2016b). Organocatalytic Domino Oxa-Michael/1,6-Addition Reactions: Asymmetric Synthesis of Chromans Bearing Oxindole Scaffolds. *Angew. Chem. Int. Ed. Engl.* 55 (39), 12104–12108. doi:10.1002/anie.201606947

Zhao, Y., Liu, L., Sun, W., Lu, J., McEachern, D., Li, X., et al. (2013a). Diastereomeric Spirooxindoles as Highly Potent and Efficacious MDM2 Inhibitors. *J. Am. Chem. Soc.* 135 (19), 7223–7234. doi:10.1021/ja3125417

Zhao, Y., Yu, S., Sun, W., Liu, L., Lu, J., McEachern, D., et al. (2013b). A Potent Small-Molecule Inhibitor of the MDM2-P53 Interaction (MI-888) Achieved Complete and Durable Tumor Regression in Mice. *J. Med. Chem.* 56 (13), 5553–5561. doi:10.1021/jm8400570810.1021/jm4005708

Zhi, Y., Zhao, K., Liu, Q., Wang, A., and Enders, D. (2016). Asymmetric Synthesis of Functionalized Trifluoromethyl-Substituted Pyrrolidines via an Organocatalytic Domino Michael/Mannich [3+2] Cycloaddition. *Chem. Commun. (Camb)* 52 (97), 14011–14014. doi:10.1039/c6cc08352h

Zhi, Y., Zhao, K., von Essen, C., Rissanen, K., and Enders, D. (2018). Synthesis of Trans-disubstituted-2,3-dihydrobenzofurans by a Formal [4 + 1] Annulation between Para-Quinone Methides and Sulfonium Salts. *Org. Chem. Front.* 5 (8), 1348–1351. doi:10.1039/c8qo00008e

Zou, W., Chen, Q., Slone, J., Yang, L., Lou, X., Diao, J., et al. (2021). Nanoscopic Quantification of Sub-mitochondrial Morphology, Mitophagy and Mitochondrial Dynamics in Living Cells Derived from Patients with Mitochondrial Diseases. *J. Nanobiotechnol* 19 (1), 136–146. doi:10.1186/s12951-021-00882-9

Conflict of Interest: The authors declare that the research was conducted in the absence of any commercial or financial relationships that could be construed as a potential conflict of interest.

Publisher's Note: All claims expressed in this article are solely those of the authors and do not necessarily represent those of their affiliated organizations, or those of the publisher, the editors and the reviewers. Any product that may be evaluated in this article, or claim that may be made by its manufacturer, is not guaranteed or endorsed by the publisher.

Copyright © 2022 Li, Yu, Sun, Liu, Wang, Shao, Wang, Xie, Yao, Yao and Zhi. This is an open-access article distributed under the terms of the Creative Commons Attribution License (CC BY). The use, distribution or reproduction in other forums is permitted, provided the original author(s) and the copyright owner(s) are credited and that the original publication in this journal is cited, in accordance with accepted academic practice. No use, distribution or reproduction is permitted which does not comply with these terms.

frontiers in Pharmacology

ORIGINAL RESEARCH
published: 15 March 2022
doi: 10.3389/fphar.2022.865173

Lysosome-Targeted Biosensor for the Super-Resolution Imaging of Lysosome–Mitochondrion Interaction

Han Wang[1,2], Guiqian Fang[2], Huimin Chen[2], Maomao Hu[1], Yajuan Cui[1,2], Boyang Wang[1], Yudong Su[3], Yu Liu[1], Bo Dong[1,3] and Xintian Shao[2]**

[1]Department of Cardiology, Shandong Provincial Hospital Affiliated to Shandong First Medical University, Jinan, China, [2]School of Life Sciences, Shandong First Medical University & Shandong Academy of Medical Sciences, Jinan, China, [3]Department of Cardiology, Shandong Traditional Chinese Medicine University, Jinan, China

Background: The interaction between lysosomes and mitochondria includes not only mitophagy but also mitochondrion–lysosome contact (MLC) that enables the two organelles to exchange materials and information. In our study, we synthesised a biosensor with fluorescence characteristics that can image lysosomes for structured illumination microscopy and, in turn, examined morphological changes in mitochondria and the phenomenon of MLC under pathological conditions.

Methods: After designing and synthesising the biosensor, dubbed CNN, we performed an assay with a Cell Counting Kit-8 to detect CNN's toxicity in relation to H9C2 cardiomyocytes. We next analysed the co-localisation of CNN and the commercial lysosomal probe LTG in cells, qualitatively analysed the imaging characteristics of CNN in different cells (i.e. H9C2, HeLa and HepG2 cells) *via* structured illumination microscopy and observed how CNN entered cells at different temperatures and levels of endocytosis. Last, we treated the H9C2 cells with mannitol or glucose to observe the morphological changes of mitochondria and their positions relative to lysosomes.

Results: After we endocytosed CNN, a lysosome-targeted biosensor with a wide, stable pH response range, into cells in an energy-dependent manner. SIM also revealed that conditions in high glucose induced stress in lysosomes and changed the morphology of mitochondria from elongated strips to round spheres.

Conclusion: CNN is a new tool for tracking lysosomes in living cells, both physiologically and pathologically, and showcases new options for the design of similar biosensors.

Keywords: organelle, lysosome, mitochondria, super-resolution imaging, nanoscopic, mitochondria-lysosome contact

OPEN ACCESS

Edited by:
Peixue Ling,
Shandong University (Qingdao), China

Reviewed by:
Kangqiang Qiu,
University of Cincinnati, United States
Chaomin Gao,
University of Jinan, China
Xinfu Zhang,
Dalian University of Technology, China

****Correspondence:***
Bo Dong
bodong@sdu.edu.cn
Xintian Shao
shaoxintian@sdfmu.edu.cn

Specialty section:
This article was submitted to Pharmacology of Anti-Cancer Drugs, a section of the journal Frontiers in Pharmacology

Received: *29 January 2022*
Accepted: *24 February 2022*
Published: *15 March 2022*

Citation:
Wang H, Fang G, Chen H, Hu M, Cui Y, Wang B, Su Y, Liu Y, Dong B and Shao X (2022) Lysosome-Targeted Biosensor for the Super-Resolution Imaging of Lysosome–Mitochondrion Interaction. Front. Pharmacol. 13:865173. doi: 10.3389/fphar.2022.865173

INTRODUCTION

Lysosomes, as the main sites of degradation in cells, play an important role in intracellular signal transduction, energy metabolism and homeostasis (Settembre et al., 2013; Chen Q. et al., 2021). Their most representative feature is the series of hydrolases that form the acidic environment within them, which provides a favourable environment for the degradation of various foreign substances, damaged proteins and even other organelles. Under normal physiological conditions, the pH of lysosomes is

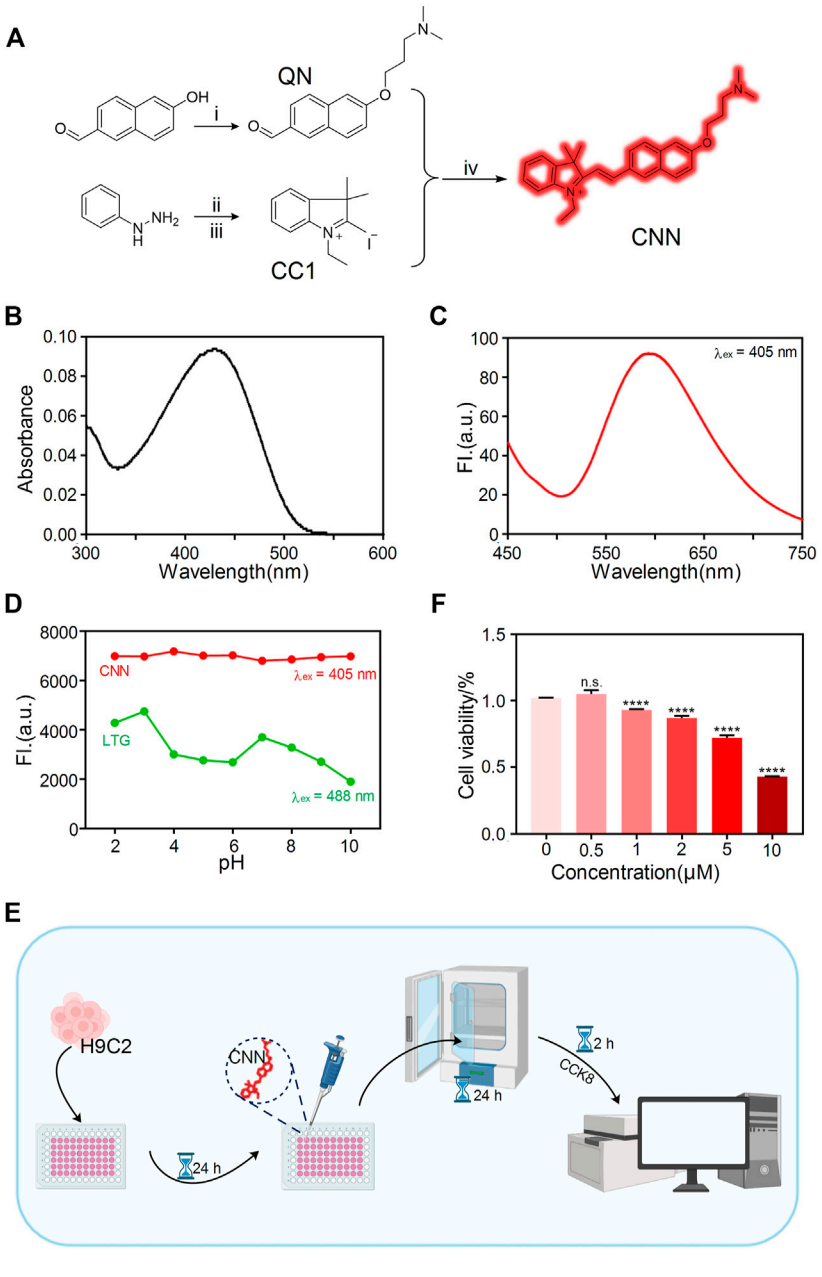

FIGURE 1 | Design and characterization of the biosensor CNN. **(A)** Synthetic route of probe CNN. 1) 3-Chloro-N, N-dimethylpropan-1-amine, 6-hydroxynaphthalene-2-carbaldehyde, K_2CO_3, acetone, reflux. 2) AcOH, NaOAc, 3-methylbutan-2-one, reflux. 3) Iodoethane, acetonitrile, reflux. 4) EtOH, reflux. **(B)** UV-vis absorption spectrum of CNN (10 μM) in solution (1% DMSO, 99% PBS, pH = 7.4). **(C)** Fluorescence spectra changes of CNN (10 μM) in solution (1% DMSO, 99% PBS, pH = 7.4), λ_{ex} = 405 nm. Slit: 5.0 nm; 5.0 nm. **(D)** Fluorescence emission spectra of CNN (0.5 μM, λ_{ex} = 405 nm. Slit: 5.0 nm; 10.0 nm) and LTG (100 nM, λ_{ex} = 488 nm. Slit: 5.0 nm; 5.0 nm) in different pH solution (HCl, NaOH, PBS). **(E)** Cell counting kit (CCK-8) experiment operation flow chart. **(F)** Cytotoxicity of the CNN on H9C2 cells at various concentrations (0, 0.5, 1, 2, 5, 10 μmol/L). Data are presented as mean ± SEM. (*n.s.* represents no statistical significance, ****$p < 0.0001$, all compared with 0 μmol/L).

not fixed but fluctuates within the range of 4.5–6.5. However, in pathological conditions, including cell apoptosis, the pH of lysosomes increases (Li et al., 2019), which results in abnormal functioning that accelerates the occurrence and development of disease.

As organelles involved in intracellular metabolism, lysosomes cannot function without interacting with other organelles, including for autophagy, for mitophagy and in mitochondrion–lysosome contact (MLC) (Wong et al., 2019). In particular, mitochondria and lysosomes were recently found to form

dynamic contact sites in order to mediate the inter-membrane interchange of metabolites. However, defective MLC is closely related to cancer (Audano et al., 2020), cardiovascular disease (Yu et al., 2020) and neurodegenerative disease (Kim et al., 2021). Therefore, research focused on MLC is of great significance.

To date, lysosomes and mitochondria have often been studied at the cellular level by conventional methods such as western blotting, immunofluorescence and confocal fluorescence microscopy. However, due to limitations in resolution, those methods make observing MLC difficult. Against that trend, the emergence of stimulated emission depletion (STED) (Hanne et al., 2015), photo-activated localisation microscopy (PALM) (Quirin et al., 2012), stochastic optical reconstruction microscopy (STORM) (Huang et al., 2008) and structured illumination microscopy (SIM) (Huang et al., 2018) has made it possible to image crosstalk in different organelles at the nanoscale (Chen H. et al., 2021; Liu Y. et al., 2021; Zhang et al., 2021; Wei et al., 2022) as well as MLC. Beyond that, research conducted to quantitatively analyse MLC produced a new method involving the *M-value* (Chen et al., 2020b) in order to distinguish the fusion of mitochondria and lysosomes. In that method, an *M-value* less than 0.4 indicates MLC, whereas *M-values* in the range of 0.5–1.0 indicate mitophagy. Using those innovations, it is crucial to further introduce the concept of MLC into subsequent clinical research on disease. In addition, a variety of lysosome-targeted probes reported in the past few years shows that the synthetic biosensor need possess a certain properties, such as self-fluorescence or the fluorophores, to image in cells under SIM.

In our study, we designed a lysosome-targeted biosensor, CNN, to observe changes in lysosomal morphology and fluorescence signals in different cells under SIM. Afterwards, CNN was used to track the interaction of lysosomes and mitochondria in a diabetic cardiomyopathy model under conditions in high glucose at the nano-scale. Owing to its wide pH response range, low background and exceptional cell permeability, CNN can be used to detect morphological changes in mitochondria and lysosome–mitochondrion interaction under different conditions *via* SIM. Because CNN can be used to track lysosomes under SIM, it stands as a powerful new tool for studying lysosome-related diseases.

RESULTS

Biosensor Design and Characterisation

After being designed and synthesised (**Figure 1A**), the biosensor, CNN, was characterised by ^{1}H NMR, ^{13}C NMR and HRMS (**Supplementary Figures S7–S9**), the results of which suggest its correct structure and high purity. Its large conjugate structure allows CNN to achieve bright red fluorescence and an ultraviolet absorbance peak at 428 nm and fluorescence peak at 596 nm (**Figures 1B,C**). Another key design element is that CNN is protonated in the presence of a weakly basic triamino and selectively accumulates in an acidic environment. Therefore, we measured changes of CNN's fluorescence intensity in solutions with different pH values (**Figure 1D**). When the pH ranged from 2 to 10, CNN showed approximately consistent emission peaks at 567 nm. Compared with LTG, a commercial lysosomal probe, CNN thus has the advantage of stable fluorescence characteristics independent of changes in pH. To further investigate the characteristics of CNN on the cellular scale, we determined safe concentrations of CNN for cells *via* an assay with a Cell Counting Kit-8 (**Figure 1E**). The results showed that when the concentration of CNN was 1, 2, 5 and 10 μM, cell proliferation was inhibited (**Figure 1F**), and when the concentration reached 10 μM, cell viability was significantly reduced (<50% vs control group). Therefore, we chose 0.5 μM as a safe working concentration for living cells.

Subcellular Distribution of CNN in Living H9C2 Cells Under SIM

To verify whether CNN can be imaged in cells using SIM, H9C2 cells were incubated with CNN for 1 h, and the results revealed that the biosensor could be clearly imaged under red channel excitation at 405 nm (**Figure 2A**). That finding was consistent with the spectral results measured earlier and with the characteristics of CNN's multi-conjugate structure. In addition, we could clearly observe CNN's randomly distribution within cells in the shape of circular dots ranging in diameter from 0.4 to 2.3 μm (**Figure 2B**), with an average of 0.9 μm. The average area of the dots was thus 0.3 μm^2 (**Figure 2C**). Based on a set of imaging characteristics found in cells, we speculate that CNN targets lysosomes. To verify that conjecture, a commercial lysosomal probe, LTG, was used to co-stain with CNN (**Figure 2D**). The results, shown in **Figure 2E**, indicated that the green fluorescence of LTG overlapped well with the red fluorescence of CNN, and the Pearson correlation coefficient was 0.8 according to co-location analysis conducted in ImageJ software (**Figure 2F**). Meanwhile, to ascertain the specificity of CNN's localisation in lysosomes, commercial lipid droplets or nuclear probes were used to co-stain with CNN. As a result, we observed that those probes were independent of each other (**Supplementary Figures S10**). Altogether, CNN can indeed be imaged in cells using SIM and specifically targets lysosomes in living cells.

SIM Images of CNN in H9C2 Cells Under Different Conditions

Extracellular substances enter cells in a variety of ways that can be classified into two types: energy-dependent and non-energy-dependent. We thus speculated that CNN's entry into cells could be hindered by low temperatures and endocytosis inhibitors (**Figure 3A**). Therefore, to determine how CNN enters cells, H9C2 cells with CNN were treated under different incubation conditions in the dark (**Figures 3B–D**). Compared with the control group (i.e. cultivated at 37°C), the fluorescence intensity of CNN in the inhibitor group [i.e. pretreated with the endocytosis inhibitor chlorpromazine (Gambhire et al., 2019)] decreased, whereas the low temperature group (cultivated at 4°C) exhibited diffuse but uniform red signals both within or outside cells. Moreover, clustered red dots were not observed in the H9C2 cells. Those results all suggest that CNN enters cells primarily *via* endocytosis in an energy-dependent manner (**Figures 3E,F**).

Imaging of Quantitative Molecule CNN in Different Cell Lines

To evaluate whether CNN shows differences in cell lines other than H9C2 cells under SIM, we stained HeLa cells and HepG2

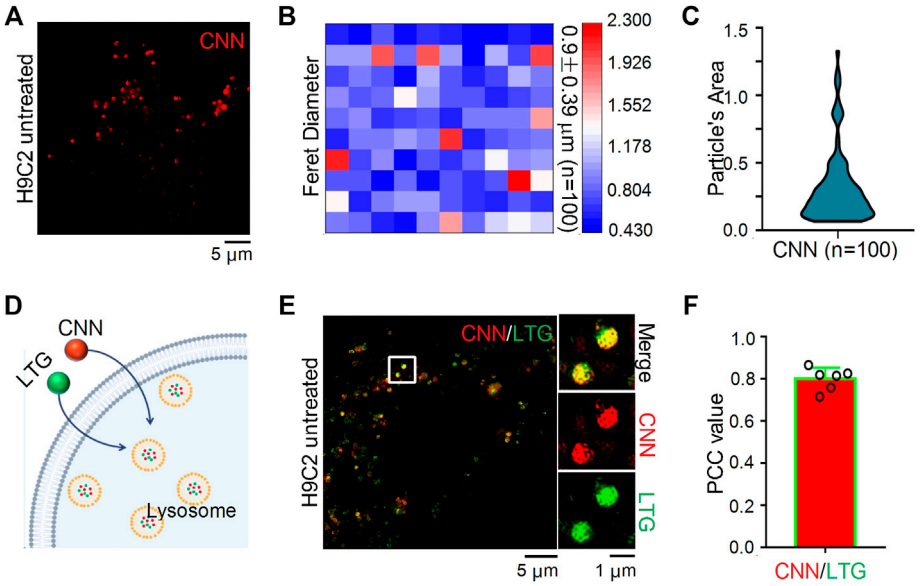

FIGURE 2 | SIM images and Co-localization of CNN in H9C2 cells. **(A)** SIM image of H9C2 cells stained with CNN (0.5 μM, λ_{ex} = 405 nm) for 1 h. **(B)** Particle's diameter of the CNN puncta. *n* = 100. **(C)** Particle's area of the CNN in living cell. *n* = 100. **(D)** Schematic diagram of LTG (100 nM, λ_{ex} = 488 nm) and CNN jointly labeling lysosomes. **(E)** Merged SIM images of H9C2 cells stained with CNN and LTG. White circle notes the enlarged part. **(F)** Quantitative analysis of the colocalization between CNN and LTG.

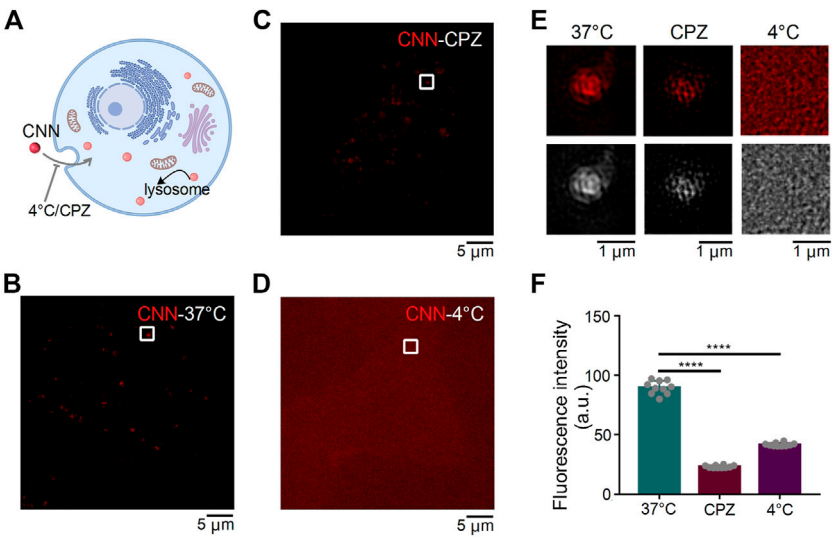

FIGURE 3 | SIM images of CNN under different conditions in H9C2 cells. **(A)** Effect of different treatment conditions on CNN entry into cells. **(B)** H9C2 cells were incubated with CNN (0.5 μM, λ_{ex} = 405 nm) for 1 h at 37°C. **(C)** H9C2 cells were incubated with the Chlorpromazine (CPZ, 20 μM) at 37°C for 2 h and incubated with CNN at 37°C for 1 h **(D)** H9C2 cells were incubated with CNN for 1 h at 4°C. **(E)** Fluorescence and grayscale images of the enlarged region indicated by white rectangles in **(B,C,D)**. **(F)** Fluorescence intensity of CNN with 37°C, 4°C and CPZ. Data are presented as mean ± SEM (*n* = 10, ****$p < 0.0001$). All compared with 37°C.

cells with CNN for 1 h and subsequently performed SIM imaging (**Figure 4A**). As shown in **Figure 4B**, CNN not only located in normal cells but also targeted lysosomes in tumour cells. Our statistical analysis of those three kinds of cells compared with the control group (i.e. H9C2 cells) revealed that the experimental group (i.e. HeLa and HepG2 cells) remained unchanged in fluorescence intensity, particle diameter and particle area (**Figures 4C–E**). Combined with the shape, size and distribution of dots, it further indicated that CNN, as a fluorescent biosensor, can track lysosomes precisely within cells. That characteristic stands to provide an experimental basis for the future application and extension of probes.

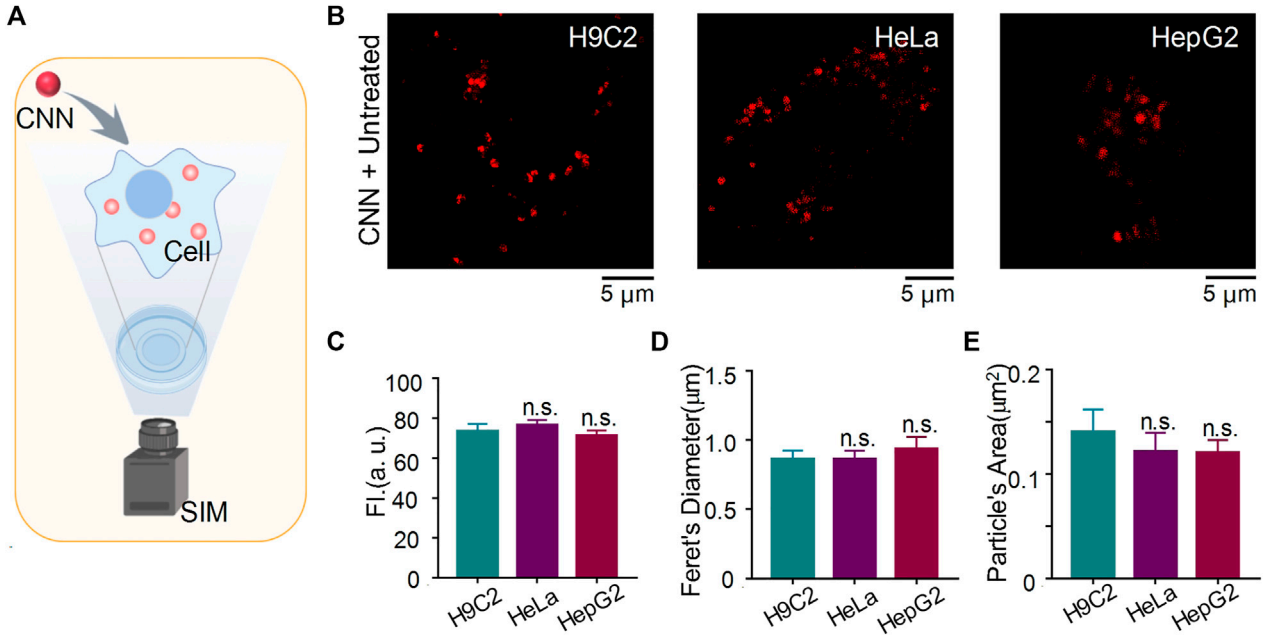

FIGURE 4 | CNN tracking lysosome in H9C2 cells, HeLa cells and HepG2 cells under SIM. **(A)** Imaging schematic of CNN in living cells. **(B)** SIM images of CNN (0.5 μM, λ_{ex} = 405 nm) in H9C2 cells, HeLa cells and HepG2 cells. **(C–E)** Fluorescence intensity, feret's diameter and particle's area of CNN in different cells. Data are shown as mean ± SEM (*n* = 8; *n.s.* represents no statistical significance). All compared with untreated cells.

Application of CNN to Disease Models *in vitro*

The common interactions of mitochondria and lysosomes include mitophagy, which plays an essential role in eliminating damaged mitochondria, as well as the more recently discovered contact of mitochondria and lysosomes in normal cells. To characterise MLC, we used CNN together with the commercial probe PKMTDR to track lysosomes and mitochondria. The images showed mitochondria and lysosomes next to each other and engaging in MLC in normal untreated cells, as consistent with previous findings (Chen et al., 2018) (**Figures 5A,B**). We also observed MLC events in other conditions, including ones with high glucose and in a hypertonic environment (**Figures 5C–F**). Even so, compared with the untreated group, we observed that when H9C2 cells were treated with 35 mM of glucose, the morphology of mitochondria showed severe damage and changed in shape from fibrous rods to round spheres, whereas ones treated with mannitol showed a typical morphology of mitochondria (**Figure 5G**). Those findings align with the results of a previous quantitative analysis (Chen et al., 2019). Other findings reveals that after treatment with glucose, the proportion of round mitochondria increased compared with untreated cells, whereas the distribution of hyperfused mitochondria decreased (**Figure 5H**). Afterwards, we also found that compared with the untreated and hypertonic groups, lysosomes became larger and more numerous in the excess glucose environment (**Supplementary Figures S11, S12**). Those results confirm that conditions in high glucose induced intracellular stress responses, including mitochondrial swelling and lysosomal enlargement (**Supplementary Figure S13**).

DISCUSSION

As vital intracellular structures, lysosomes are responsible for recovery and digestion in eukaryotic cells, which participate widely in the regulation of autophagy (Cheng et al., 2018), apoptosis (Brunk et al., 2001), antigen processing (Cabukusta and Neefjes, 2018) and other biological processes. Impaired lysosomal functioning affects normal degradation and, in turn, leads to various diseases, including Alzheimer's disease (Colacurcio and Nixon, 2016), lysosomal storage disease (Colacurcio and Nixon, 2016; Platt et al., 2018) and Parkinson's disease (Colacurcio and Nixon, 2016; Burbulla et al., 2017; Kim et al., 2021). However, most traditional techniques used to indirectly determine lysosomal dysfunction have kept organelle-level examinations in their infancy. Against that trend are recent innovations in instruments for observing organelles and the development of fluorescent probes for labelling various organelles in living cells.

Research has shown that numerous diseases are accompanied by pH changes within lysosomes. In diabetic cardiomyopathy, conditions in high glucose can increase levels of the prorenin receptor (PRR) (Yu et al., 2019), a subunit of the vacuolar ATPase (V-ATPase) complex, which is critical for maintaining the pH of intracellular vesicles, especially in lysosomes. In addition, researchers have verified that PRR deletion leads to

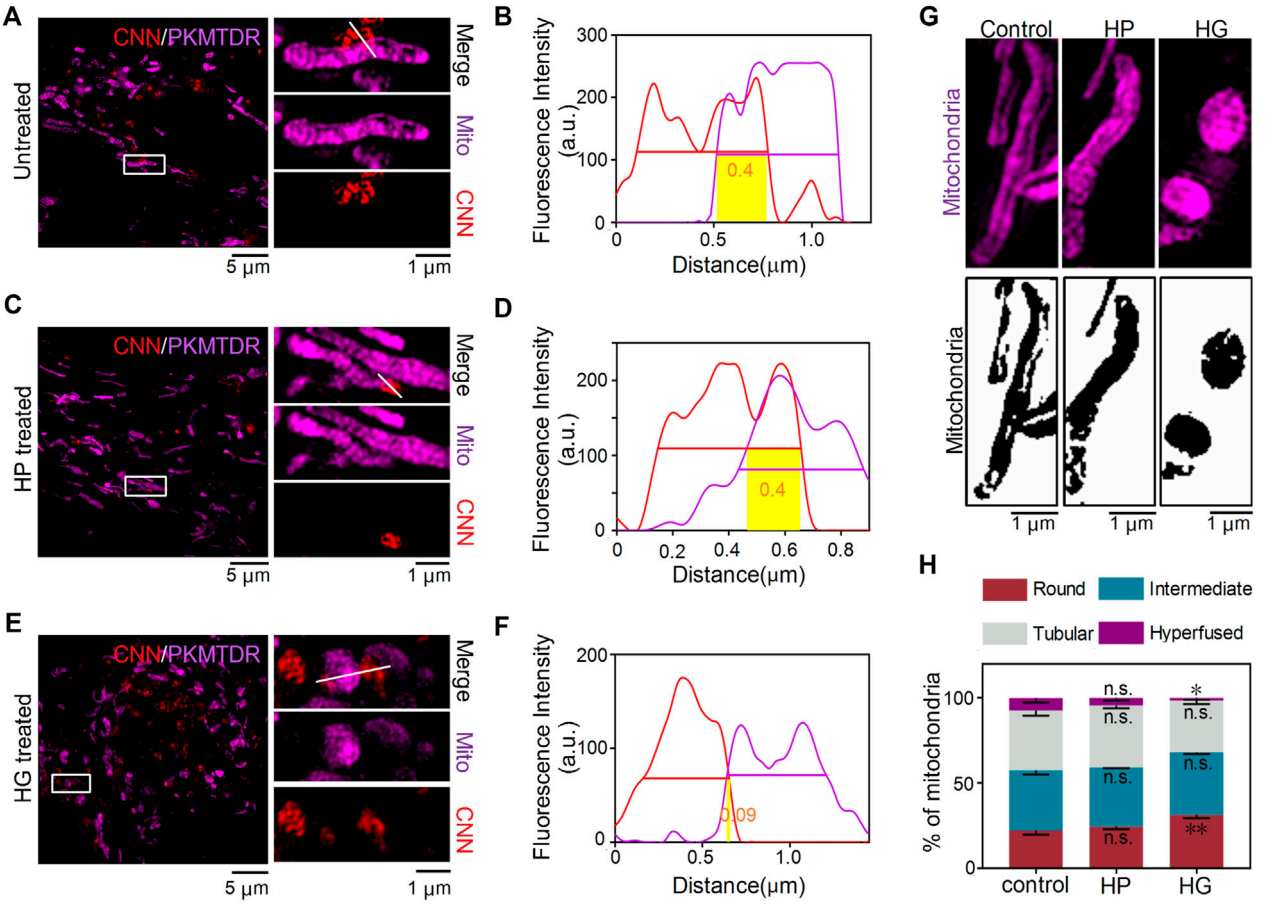

FIGURE 5 | CNN tracking of mitochondria–lysosomes contact sites in living H9C2 cells. **(A,B)** SIM images of MLC in untreated cells. The white line refers to a contact site between CNN (0.5 μM, λ_{ex} = 405 nm) and PKMTDR (0.5 μM, λ_{ex} = 640 nm). **(C,D)** MLC under mannitol treatment. The white line refers to a contact site between CNN and PKMTDR. **(E,F)** MLC under glucose treatment. The white line refers to a contact site between CNN and PKMTDR. **(B,D,F)** The yellow rectangle represents *M-value*. **(G)** Mitochondrial morphology of the control group, HP group, and HG group. **(H)** The quantitative analysis of mitochondrial morphology in H9C2 cells treated with mannitol (HP) or glucose (HG). Round means $1.0 \leq L/W < 1.5$. Intermediate means $1.5 \leq L/W < 2.0$. Tubular means $2.0 \leq L/W < 5.0$. Hyperfused means $L/W \geq 5.0$. Data are presented as mean ± SEM (n = 3, *n.s.* represents no statistical significance; $^{*}p < 0.05$, $^{**}p < 0.01$.). All compared with control group.

damage in podocytes due to lysosomal acidification, indicated by the weakened fluorescence intensity of the lysotracker. Thus, it is crucial to invent a lysosomal biosensor with stable expression in different pH environments for tracking morphological and quantitative changes in lysosomes under disease conditions. To date, lysosomal probes have emerged one after the other, including ratio probes (Li et al., 2018; Yan et al., 2020), viscosity probes (Wang et al., 2013) and double-labelled probes (Chen et al., 2020a; Liu Z. et al., 2021). Taking into account the changes in pH within lysosomes under different processing conditions, we developed a lysosomal probe with a wide pH response range to track lysosomal changes within cells. Owing to their unique fluorescent properties, probes are often used to label biological tissues or cells for convenient imaging under various microscopes. Moreover, with the development of super-resolution microscopy, the interaction between lysosomes and other organelles, including MLC (Wong et al., 2019), lipid droplet–lysosome interaction (Drizyte-Miller et al., 2020) and peroxisome–lysosome contact (Chu et al., 2015), can be visualised at the nanometre scale (<200 nm). After synthesising the probe, we co-stained the cells with CNN and commercial PKMTDR (Yang et al., 2020) to observe the interaction between mitochondria and lysosomes under different treatment conditions with SIM. Research has shown that under healthy conditions, approximately 15% of lysosomes are in long-term contact with mitochondria, with a contact duration that can reach 1 min (Han et al., 2017), which suggests that MLC occurs under normal physiological conditions. In addition, other research has shown that after knocking out genes related to autophagy, contact-related phenomena continued (Chen et al., 2018). And the expression of autophagy related proteins, such as LC3, ATG5 and ATG12 (Wong et al., 2018), could not be activated in the occurrence of MLC. Thereby demonstrating that MLC is independent of mitophagy. Since then, other researchers investigated MLC amid certain diseases and found that TBC1D15 played a vital role in the occurrence

of MLC (Wong et al., 2018; Peng et al., 2020; Yu et al., 2020; Kim et al., 2021). Under physiological conditions, TBC1D15 is recruited by Fis1 on mitochondria to promote the hydrolysis of RAB7GTP, a site of MLC, and the immediate separation of mitochondria and lysosomes (Wong et al., 2018). Under conditions of ischemia and hypoxia, lacking the TBC1D15 prolonged MLC to the point that lysosomal dysfunction occurred and osmotic pressure increased (Yu et al., 2020). Other research has also revealed that under normal circumstances, MLC can cause Ca^{2+} to enter the mitochondria *via* the transient receptor potential mucolipin 1 (TRPML1, located in lysosomes), the voltage-dependent anion channel 1 (VDAC1, located in mitochondrial outer membrane) and the mitochondrial calcium uniporter (MCU, located in mitochondrial inner membrane) (Peng et al., 2020). When TRPML1 on the lysosomes is dysfunctional, the calcium dynamics of the mitochondria are unregulated, which demonstrates the important role of MLC in the exchange of materials and information between organelles. Using SIM imaging, we found that conditions in high glucose caused morphological changes of mitochondria, some of which were still in contact with lysosomes. As indicated in our study, conditions in high glucose induced the overproduction of reactive oxygen species, which disrupted the antioxidant defence mechanism and mitochondrial function (Pal et al., 2020). However, the specific mechanism of the influence of excessive glucose on MLC remains unclear, which should motivate future investigations into the crosstalk of mitochondria and lysosomes.

CONCLUSION

We developed a lysosome tracker, CNN, that can be used to observe the crosstalk of lysosomes and mitochondria in living cells under SIM. Using CNN, we found that MLC can not only be captured under normal conditions but also induced by glucose and mannitol. Therefore, CNN stands as a new tool for tracking lysosomes in living cells under both physiological and pathological conditions and showcases new options for the design of similar biosensors.

EXPERIMENTAL SECTIONS

Materials

Dulbecco's modified Eagle's medium (#11965118, DMEM), phenol-free medium (#1894117), fetal bovine serum (#26140079, FBS) and Penicillin-streptomycin (#15140163, 10,000 units/ml), Trypsin-EDTA (#25200-072) and other reagents for cell culture were obtained from Gibco BRL (Grand Island, NY, United States). Lyso-Tracker Green (#C1047S, LTG) and Hoechst (#C1022) were obtained from Beyotime (Wuhan, China). Lipi-Blue (LD01) were from DOJINDO Laboratories (Kumamoto, Japan). PK Mito-Tracker Deep Red (PKMTDR) were obtained from Peking University. The Cell Counting Kit-8 (#HY-K0301, CCK-8) Assay Kit,Chlorpromazine (#HY-12708, CPZ)was obtained from MedChemExpress (Monmouth Junction, NJ, United States).

Synthesis of Probes

Synthesis of Compound QN

A mixture of 3-chloro-N, N-dimethylpropan-1-amine (3.63 g, 30 mmol), 6-hydroxynaphthalene-2-carbaldehyde (1.72 g, 10 mmol) and K_2CO_3 (1.37 g, 10 mmol) were stirred in acetone (60 ml) and then refluxed overnight. After removal of the solvent in vacuo, the crude compound was obtained and then purified by column chromatography (3:50, MeOH/DCM), and then yellow liquid (**QN**) was obtained after dried (1.62 g, 6.3 mmol, 63%). ^{1}H NMR (600 MHz, DMSO-d_6) δ (ppm) (**Supplementary Figure S1**): 10.09 (s, 1H), 8.45 (s, 1H), 8.05 (d, J = 9.0 Hz, 1H), 7.93 (d, J = 8.5 Hz, 1H), 7.86 (dd, J = 8.5, 1.2 Hz, 1H), 7.42 (d, J = 2.3 Hz, 1H), 7.29 (dd, J = 8.9, 2.4 Hz, 1H), 4.16 (t, J = 6.5 Hz, 2H), 2.41 (t, J = 7.1 Hz, 2H), 2.18 (s, 6H), 1.96–1.90 (m, 2H). ^{13}C NMR (151 MHz, DMSO-d_6) δ (ppm) (**Supplementary Figure S2**): 192.76, 159.73, 138.34, 134.54, 132.48, 131.65, 128.12, 127.96, 123.50, 120.31, 107.68, 66.71, 56.06, 45.53, 27.24. HRMS *m/z* (**Supplementary Figure S3**): calculated for $C_{16}H_{20}NO_2^+$ $(M + H)^+$: 258.1489, found 258.1259.

Synthesis of Compound CC1

A mixture of 4-hydrazinobenzoic acid (0.5 g, 4.6 mmol), 3-methylbutan-2-one (1.7 g, 19.4 mmol) and sodium acetate (0.76 g, 9.2 mmol) were stirred in glacial acetic acid (3 ml) and then refluxed overnight. After removal of the solvent in vacuo, the crude compound was obtained and then purified by column chromatography (1:9, MeOH/DCM), and then brown liquid was obtained after dried (0.43 g, 2.7 mmol, 59%). Subsequently, a mixture of the previous product (0.16 g, 1 mmol) and iodoethane (0.78 g, 5 mmol) refluxed in acetonitrile (5 ml). A large amount of white powder solids precipitated after reacted 24 h. Then the crude product was obtained by filtered, following washed by cold ethanol and ethyl ester. A white compound **CC1** (0.13 g, 0.7 mmol, 70%) was obtained after dried. ^{1}H NMR (600 MHz, DMSO-d_6) δ (ppm) (**Supplementary Figure S4**): 8.03–7.94 (m, 1H), 7.90–7.81 (m, 1H), 7.64 (dd, J = 6.2, 2.7 Hz, 2H), 4.52 (q, J = 7.3 Hz, 2H), 2.86 (s, 3H), 1.55 (s, 6H), 1.46 (t, J = 7.4 Hz, 3H). ^{13}C NMR ^{13}C NMR (151 MHz, DMSO-d_6) δ (ppm) (**Supplementary Figure S5**): 196.61, 142.49, 141.21, 129.90, 129.45, 124.02, 115.82, 54.65, 43.64, 22.45, 14.45, 13.17. HRMS *m/z* (**Supplementary Figure S6**): calculated for $C_{29}H_{35}N_2O^+$ $(M)^+$: 188.1434, found 188.1494.

Synthesis of Compound CNN

A mixture of the previous product **QN** (0.13 g, 0.5 mmol) and **CC1** (0.09 g, 0.5 mmol) were refluxed in ethanol (6 ml). A large amount of yellow powder solids precipitated after reacted overnight. Then the crude product was obtained by filtered, following washed by cold ethanol and ethyl ester. A yellow compound **CNN** (0.13 g, 0.3 mmol, 60%) was obtained after dried. ^{1}H NMR (600 MHz, DMSO-d_6) δ (ppm) (**Supplementary Figure S7**): 8.76 (s, 1H), 8.62 (d, J = 16.2 Hz, 1H), 8.39 (d, J = 8.8 Hz, 1H), 8.02 (dd, J = 8.6, 6.1 Hz, 2H), 7.96 (d, J = 7.4 Hz, 1H), 7.92 (d, J = 6.7 Hz, 1H), 7.76 (d, J = 16.2 Hz, 1H),

7.68–7.63 (m, 2H), 7.32 (dd, J = 8.9, 1.8 Hz, 1H), 4.78 (d, J = 7.2 Hz, 2H), 4.27 (t, J = 6.0 Hz, 2H), 3.29–3.25 (m, 3H), 2.84 (s, 6H), 2.25–2.18 (m, 2H), 1.86 (s, 6H), 1.51 (t, J = 7.2 Hz, 3H). ^{13}C NMR (151 MHz, DMSO-d_6) δ (ppm) (**Supplementary Figure S8**): 181.80 159.43, 154.74, 144.39, 140.94, 137.58, 135.00, 131.69, 130.64, 129.82, 129.62, 128.61, 128.25, 125.64, 123.60 120.36, 115.54, 111.89, 108.19, 65.79, 54.92, 52.75, 43.20, 42.69, 26.21, 24.59, 14.25. HRMS *m/z* (**Supplementary Figure S9**): calculated for $C_{29}H_{35}N_2O^+$ [M^+: 427.2744, found 427.2394.

Cell Culture

The frozen H9C2 cells were taken out of the liquid nitrogen tank and put into the preheated water bath for rapid melting. All the solution in the frozen storage tube was transferred to the centrifuge tube for 1,000 r/min, 5 min. The supernatant was discarded, and the bottom cells were precipitated by mixing with the complete medium (DMEM containing 10% FBS, 1% penicillin and streptomycin). All of them were transferred to culture flask and cultured at 37°C in 5% CO_2. Then it was transferred to the second generation for subsequent experiments.

Cell Treatment

H9C2 cells with a density of 2.5×10^5 were inoculated into a 35 mm SIM-specific petri dish containing 2 ml complete medium. After 24 h culture, the cells were washed twice with preheated PBS. The cells were treated with CNN at 500 nM for 1 h and then incubated with or without commercial lysosomal probe LTG at 100 nM for 30 min. Then the cells were washed with phenol-free red DMEM medium for 5 times. Finally, the cells were cultured in complete medium without phenol red and observed under super resolution confocal microscope.

Membrane making and grouping of diabetic cardiomyopathy model *in vitro*: the blank control group was treated with 5.5 mM low-glucose medium. The hypertonic group (HP group) was treated with 5.5 mM low-sugar medium and 29.5 mM mannitol for 24 h H9C2 cardiomyocytes were stimulated with 35 mM high glucose solution for 24 h in the high glucose group (HG group). After film-making, H9C2 cells were treated with CNN and PKMTDR for 1 h and 20 min, respectively. Finally, images were captured and processed by super-resolution confocal microscope.

Cytotoxicity Assay

Cell Counting Kit-8 (CCK-8) was used to detect the cytotoxicity of probe CNN. H9C2 cells diluted with complete medium were inoculated into 96-well plates at a density of 8×10^3 cells/well, and cultured for 24 h in an incubator containing 5% CO_2 at 37°C. Then CNN and DMEM containing 0, 0.5, 1, 2, 5, 10 μM were used to replace the original media in 96-well plates. After 24 h, each well was added 10 μL CCK8 solution and incubated in an incubator for 2 h. Finally, the absorbance at 450 nm was determined by enzyme-linked immunosorbent assay.

OMX 3D-SIM Imaging

A total of 2.5×10^5 H9C2 cells were seeded on a 35 mm glass-bottom microwell dish and incubated with 2 ml of DMEM medium supplemented with 10% FBS for 24 h. After treatment, the cells were washed twice with preheated PBS. The cells were treated with CNN at 500 nM for 1 h. Then the cells were washed with PBS for 3 times and phenol-free red DMEM medium for 4 times. H9C2 cells cultured in a phenol-free DMEM were observed under an OMX 3D-SIM (Delta Vision, Inc., Issaquah, WA, United States) equipped with a 60×/1.42 numerical aperture oil-immersion objective lens and solid-state lasers. Obtained SIM images were analyzed using ImageJ software.

Data Analysis

The calculation method of *M-value* is referred to the previous article (Chen et al., 2020b). Statistical analysis was performed with GraphPad Prism and Origin 2019. Normality test is used to check the normal distribution. In the case of non-normal distribution, the statistical comparison of results was presented with a Student's t test. Data are presented as mean ± SEM. * was defined as $p < 0.05$, ** as $p < 0.01$, *** as $p < 0.001$, *** as $p < 0.0001$, and *n.s.* as no significant difference. Sample sizes in all graphs are indicated in the corresponding figure legends.

DATA AVAILABILITY STATEMENT

The original contributions presented in the study are included in the article/**Supplementary Material**, further inquiries can be directed to the corresponding author.

AUTHOR CONTRIBUTIONS

HW, GF, HC, and XS contributed to conception and design of the study. HW wrote the first draft of the manuscript. GF and HC wrote sections of the manuscript. XS, HC, and GF has critically revised the manuscript. All authors contributed to manuscript revision, read, and approved the submitted version.

FUNDING

This work was supported by National Natural Science Foundation of China (Nos. 81870283, 82070382), Program of Taishan Scholars Programme (No. 20190979).

ACKNOWLEDGMENTS

We thank Translational Medicine Core Facility of Shandong University for consultation and instrument support.

SUPPLEMENTARY MATERIAL

The Supplementary Material for this article can be found online at: https://www.frontiersin.org/articles/10.3389/fphar.2022.865173/full#supplementary-material

REFERENCES

Audano, M., Pedretti, S., Ligorio, S., Crestani, M., Caruso, D., De Fabiani, E., et al. (2020). "The Loss of Golden Touch": Mitochondria-Organelle Interactions, Metabolism, and Cancer. *Cells* 9 (11). doi:10.3390/cells9112519

Brunk, U. T., Neuzil, J., and Eaton, J. W. (2001). Lysosomal Involvement in Apoptosis. *Redox Rep.* 6 (2), 91–97. doi:10.1179/135100001101536094

Burbulla, L. F., Song, P., Mazzulli, J. R., Zampese, E., Wong, Y. C., Jeon, S., et al. (2017). Dopamine Oxidation Mediates Mitochondrial and Lysosomal Dysfunction in Parkinson's Disease. *Science* 357 (6357), 1255–1261. doi:10.1126/science.aam9080

Cabukusta, B., and Neefjes, J. (2018). Mechanisms of Lysosomal Positioning and Movement. *Traffic* 19 (10), 761–769. doi:10.1111/tra.12587

Chen, H., Wang, H., Wei, Y., Hu, M., Dong, B., Fang, H., et al. (2021a). Super-resolution Imaging Reveals the Subcellular Distribution of Dextran at the Nanoscale in Living Cells. *Chin. Chem. Lett.* doi:10.1016/j.cclet.2021.10.025

Chen, Q., Fang, H., Shao, X., Tian, Z., Geng, S., Zhang, Y., et al. (2020a). A Dual-Labeling Probe to Track Functional Mitochondria-Lysosome Interactions in Live Cells. *Nat. Commun.* 11 (1), 6290. doi:10.1038/s41467-020-20067-6

Chen, Q., Jin, C., Shao, X., Guan, R., Tian, Z., Wang, C., et al. (2018). Super-Resolution Tracking of Mitochondrial Dynamics with an Iridium(III) Luminophore. *Small* 14 (41), e1802166. doi:10.1002/smll.201802166

Chen, Q., Shao, X., Hao, M., Fang, H., Guan, R., Tian, Z., et al. (2020b). Quantitative Analysis of Interactive Behavior of Mitochondria and Lysosomes Using Structured Illumination Microscopy. *Biomaterials* 250, 120059. doi:10.1016/j.biomaterials.2020.120059

Chen, Q., Hao, M., Wang, L., Li, L., Chen, Y., Shao, X., et al. (2021b). Prefused Lysosomes Cluster on Autophagosomes Regulated by VAMP8. *Cell Death Dis* 12 (10), 939. doi:10.1038/s41419-021-04243-0

Chen, Q., Shao, X., Tian, Z., Chen, Y., Mondal, P., Liu, F., et al. (2019). Nanoscale Monitoring of Mitochondria and Lysosome Interactions for Drug Screening and Discovery. *Nano Res.* 12 (5), 1009–1015. doi:10.1007/s12274-019-2331-x

Cheng, X. T., Xie, Y. X., Zhou, B., Huang, N., Farfel-Becker, T., and Sheng, Z. H. (2018). Revisiting LAMP1 as a Marker for Degradative Autophagy-Lysosomal Organelles in the Nervous System. *Autophagy* 14 (8), 1472–1474. doi:10.1080/15548627.2018.1482147

Chu, B. B., Liao, Y. C., Qi, W., Xie, C., Du, X., Wang, J., et al. (2015). Cholesterol Transport through Lysosome-Peroxisome Membrane Contacts. *Cell* 161 (2), 291–306. doi:10.1016/j.cell.2015.02.019

Colacurcio, D. J., and Nixon, R. A. (2016). Disorders of Lysosomal Acidification-The Emerging Role of V-ATPase in Aging and Neurodegenerative Disease. *Ageing Res. Rev.* 32, 75–88. doi:10.1016/j.arr.2016.05.004

Drizyte-Miller, K., Schott, M. B., and McNiven, M. A. (2020). Lipid Droplet Contacts with Autophagosomes, Lysosomes, and Other Degradative Vesicles. *Contact* 3, 251525642091089. doi:10.1177/2515256420910892

Gambhire, V. M., Gambhire, M. S., and Ranpise, N. S. (2019). Solid Lipid Nanoparticles of Dronedarone Hydrochloride for Oral Delivery: Optimization, *In Vivo* Pharmacokinetics and Uptake Studies. *Pharm. Nanotechnol* 7 (5), 375–388. doi:10.2174/2211738507666190802140607

Han, Y., Li, M., Qiu, F., Zhang, M., and Zhang, Y. H. (2017). Cell-permeable Organic Fluorescent Probes for Live-Cell Long-Term Super-resolution Imaging Reveal Lysosome-Mitochondrion Interactions. *Nat. Commun.* 8 (1), 1307. doi:10.1038/s41467-017-01503-6

Hanne, J., Falk, H. J., Görlitz, F., Hoyer, P., Engelhardt, J., Sahl, S. J., et al. (2015). STED Nanoscopy with Fluorescent Quantum Dots. *Nat. Commun.* 6, 7127. doi:10.1038/ncomms8127

Huang, B., Wang, W., Bates, M., and Zhuang, X. (2008). Three-Dimensional Super-resolution Imaging by Stochastic Optical Reconstruction Microscopy. *Science* 319(5864), 810–813. doi: doi:doi:10.1126/science.1153529

Huang, X.-h., Yang, J., Liu, Q.-f., Zhu, J., Bai, L., Wang, F.-l., et al. (2018). A Simplified Flange-Lip Model for Distortional Buckling of Cold-Formed Steel Channel-Sections with Stiffened Web. *Int. J. Mech. Sci.* 136, 451–459. doi:10.1016/j.ijmecsci.2017.12.034

Kim, S., Wong, Y. C., Gao, F., and Krainc, D. (2021). Dysregulation of Mitochondria-Lysosome Contacts by GBA1 Dysfunction in Dopaminergic Neuronal Models of Parkinson's Disease. *Nat. Commun.* 12 (1), 1807. doi:10.1038/s41467-021-22113-3

Li, M., Fan, J., Li, H., Du, J., Long, S., and Peng, X. (2018). A Ratiometric Fluorescence Probe for Lysosomal Polarity. *Biomaterials* 164, 98–105. doi:10.1016/j.biomaterials.2018.02.044

Li, S. S., Zhang, M., Wang, J. H., Yang, F., Kang, B., Xu, J. J., et al. (2019). Monitoring the Changes of pH in Lysosomes during Autophagy and Apoptosis by Plasmon Enhanced Raman Imaging. *Anal. Chem.* 91 (13), 8398–8405. doi:10.1021/acs.analchem.9b01250

Liu, Y., Zhang, C., Wei, Y., Chen, H., Kong, L., Chen, Q., et al. (2021a). De Novo-Designed Landmine Warfare Strategy Luminophore for Super-resolution Imaging Reveal ONOO- Evolution in Living Cells. *Chem. Eng. J.* 422, 130151. doi:10.1016/j.cej.2021.130151

Liu, Z., Zheng, Y., Xie, T., Chen, Z., Huang, Z., Ye, Z., et al. (2021b). Clickable Rhodamine Spirolactam Based Spontaneously Blinking Probe for Super-resolution Imaging. *Chin. Chem. Lett.* 32, 3862–3864. doi:10.1016/j.cclet.2021.04.038

Pal, S., Rao, G. N., and Pal, A. (2020). High Glucose-Induced ROS Accumulation Is a Critical Regulator of ERK1/2-Akt-Tuberin-mTOR Signalling in RGC-5 Cells. *Life Sci.* 256, 117914. doi:10.1016/j.lfs.2020.117914

Peng, W., Wong, Y. C., and Krainc, D. (2020). Mitochondria-lysosome Contacts Regulate Mitochondrial Ca2+ Dynamics via Lysosomal TRPML1. *Proc. Natl. Acad. Sci. U S A.* 117 (32), 19266–19275. doi:10.1073/pnas.2003236117

Platt, F. M., d'Azzo, A., Davidson, B. L., Neufeld, E. F., and Tifft, C. J. (2018). Lysosomal Storage Diseases. *Nat. Rev. Dis. Primers* 4 (1), 27. doi:10.1038/s41572-018-0025-4

Quirin, S., Pavani, S. R., and Piestun, R. (2012). Optimal 3D Single-Molecule Localization for Superresolution Microscopy with Aberrations and Engineered point Spread Functions. *Proc. Natl. Acad. Sci. U S A.* 109 (3), 675–679. doi:10.1073/pnas.1109011108

Settembre, C., Fraldi, A., Medina, D. L., and Ballabio, A. (2013). Signals from the Lysosome: a Control centre for Cellular Clearance and Energy Metabolism. *Nat. Rev. Mol. Cel Biol* 14 (5), 283–296. doi:10.1038/nrm3565

Wang, L., Xiao, Y., Tian, W., and Deng, L. (2013). Activatable Rotor for Quantifying Lysosomal Viscosity in Living Cells. *J. Am. Chem. Soc.* 135 (8), 2903–2906. doi:10.1021/ja311688g

Wei, Y., Kong, L., Chen, H., Liu, Y., Xu, Y., Wang, H., et al. (2022). Super-resolution Image-Based Tracking of Drug Distribution in Mitochondria of a Label-free Naturally Derived Drug Molecules. *Chem. Eng. J.* 429, 132134. doi:10.1016/j.cej.2021.132134

Wong, Y. C., Kim, S., Peng, W., and Krainc, D. (2019). Regulation and Function of Mitochondria-Lysosome Membrane Contact Sites in Cellular Homeostasis. *Trends Cel Biol* 29 (6), 500–513. doi:10.1016/j.tcb.2019.02.004

Wong, Y. C., Ysselstein, D., and Krainc, D. (2018). Mitochondria-lysosome Contacts Regulate Mitochondrial Fission via RAB7 GTP Hydrolysis. *Nature* 554 (7692), 382–386. doi:10.1038/nature25486

Yan, Y., Zhang, X., Zhang, X., Li, N., Man, H., Chen, L., et al. (2020). Ratiometric Sensing Lysosomal pH in Inflammatory Macrophages by a BODIPY-Rhodamine Dyad with Restrained FRET. *Chin. Chem. Lett.* 31 (5), 1091–1094. doi:10.1016/j.cclet.2019.10.025

Yang, Z., Li, L., Ling, J., Liu, T., Huang, X., Ying, Y., et al. (2020). Cyclooctatetraene-conjugated Cyanine Mitochondrial Probes Minimize Phototoxicity in Fluorescence and Nanoscopic Imaging. *Chem. Sci.* 11 (32), 8506–8516. doi:10.1039/d0sc02837a

Yu, S., Yuan, H., Yang, M., Cao, X., Chen, J., Zhou, X., et al. (2019). (Pro)renin Receptor RNA Interference Silencing Attenuates Diabetic Cardiomyopathy Pathological Process in Rats. *Hum. Gene Ther.* 30 (6), 727–739. doi:10.1089/hum.2018.155

Yu, W., Sun, S., Xu, H., Li, C., Ren, J., and Zhang, Y. (2020). TBC1D15/RAB7-regulated Mitochondria-Lysosome Interaction Confers Cardioprotection

against Acute Myocardial Infarction-Induced Cardiac Injury. *Theranostics* 10 (24), 11244–11263. doi:10.7150/thno.46883

Zhang, C., Shao, H., Zhang, J., Guo, X., Liu, Y., Song, Z., et al. (2021). Long-term Live-Cell Lipid Droplet-Targeted Biosensor Development for Nanoscopic Tracking of Lipid Droplet-Mitochondria Contact Sites. *Theranostics* 11 (16), 7767–7778. doi:10.7150/thno.59848

Conflict of Interest: The authors declare that the research was conducted in the absence of any commercial or financial relationships that could be construed as a potential conflict of interest.

The handling editor PL declared a past co-authorship with the author XS.

Publisher's Note: All claims expressed in this article are solely those of the authors and do not necessarily represent those of their affiliated organizations, or those of the publisher, the editors and the reviewers. Any product that may be evaluated in this article, or claim that may be made by its manufacturer, is not guaranteed or endorsed by the publisher.

Copyright © 2022 Wang, Fang, Chen, Hu, Cui, Wang, Su, Liu, Dong and Shao. This is an open-access article distributed under the terms of the Creative Commons Attribution License (CC BY). The use, distribution or reproduction in other forums is permitted, provided the original author(s) and the copyright owner(s) are credited and that the original publication in this journal is cited, in accordance with accepted academic practice. No use, distribution or reproduction is permitted which does not comply with these terms.

frontiers | Frontiers in Pharmacology

ORIGINAL RESEARCH
published: 20 April 2022
doi: 10.3389/fphar.2022.877175

Restoration of Sarco/Endoplasmic Reticulum Ca^{2+}-ATPase Activity Functions as a Pivotal Therapeutic Target of Anti-Glutamate-Induced Excitotoxicity to Attenuate Endoplasmic Reticulum Ca^{2+} Depletion

Wen Zhang[1,2,3], *Fanghua Ye*[1], *Nan Pang*[1,2,3], *Miriam Kessi*[1,2,3,4], *Juan Xiong*[1,2,3], *Shimeng Chen*[1,2,3], *Jing Peng*[1,2,3], *Li Yang*[1,2,3]* and *Fei Yin*[1,2,3]*

[1]Department of Pediatrics, Xiangya Hospital, Central South University, Changsha, China, [2]Hunan Intellectual and Developmental Disabilities Research Center, Pediatrics, Changsha, China, [3]Clinical Research Center for Children Neurodevelopmental Disabilities of Hunan Province, Xiangya Hospital, Central South University, Changsha, China, [4]Kilimanjaro Christian Medical University College, Moshi, Tanzania

OPEN ACCESS

Edited by:
Peixue Ling,
Shandong University (Qingdao), China

Reviewed by:
Yang Chen,
Dalian Institute of Chemical Physics, (CAS), China
Cecilia Hidalgo,
University of Chile, Chile

***Correspondence:**
Li Yang
yangli525@csu.edu.cn
Fei Yin
yf2323@hotmail.com

Specialty section:
This article was submitted to Pharmacology of Anti-Cancer Drugs, a section of the journal Frontiers in Pharmacology

Received: 16 February 2022
Accepted: 05 April 2022
Published: 20 April 2022

Citation:
Zhang W, Ye F, Pang N, Kessi M, Xiong J, Chen S, Peng J, Yang L and Yin F (2022) Restoration of Sarco/Endoplasmic Reticulum Ca^{2+}-ATPase Activity Functions as a Pivotal Therapeutic Target of Anti-Glutamate-Induced Excitotoxicity to Attenuate Endoplasmic Reticulum Ca^{2+} Depletion. Front. Pharmacol. 13:877175. doi: 10.3389/fphar.2022.877175

Glutamate-induced excitotoxicity is a pathological basis of many acute/chronic neurodegenerative diseases. Sarco/endoplasmic reticulum Ca^{2+}-ATPase (SERCA2b) is a membrane-embedded P-type ATPase pump that manages the translocation of calcium ions (Ca^{2+}) from cytosol into the lumen of the endoplasmic reticulum (ER) calcium stores. It participates in a wide range of biological functions in the central nervous system (CNS). However, the role of SERCA2b in glutamate-induced excitotoxicity and its mechanism must be elucidated. Herein, we demonstrate that SERCA2b mutants exacerbate the excitotoxicity of hypo-glutamate stimulation on HT22 cells. In this study, SERCA2b mutants accelerated Ca^{2+} depletion through loss-of-function (reduced pumping capacity) or gain-of-function (acquired leakage), resulting in ER stress. In addition, the occurrence of ER Ca^{2+} depletion increased mitochondria-associated membrane formation, which led to mitochondrial Ca^{2+} overload and dysfunction. Moreover, the enhancement of SERCA2b pumping capacity or inhibition of Ca^{2+} leakage attenuated Ca^{2+} depletion and impeded excitotoxicity in response to hypo-glutamate stimulation. In conclusion, SERCA2b mutants exacerbate ER Ca^{2+}-depletion-mediated excitotoxicity in glutamate-sensitive HT22 cells. The mechanism of disruption is mainly related to the heterogeneity of SERCA2b mutation sites. Stabilization of SRECA2b function is a critical therapeutic approach against glutamate-induced excitotoxicity. These data will expand understanding of organelle regulatory networks and facilitate the discovery and creation of drugs against excitatory/inhibitory imbalance in the CNS.

Keywords: SERCA2b, excitotoxicity, calcium depletion, endoplasmic reticulum stress, mitochondria, CDN1163

INTRODUCTION

Glutamate is the primary excitatory neurotransmitter in the mammalian central nervous system (CNS). Glutamatergic neurotransmission controls many cognitive, motor, sensory, and autonomic activities. In addition, glutamate is critical in maintaining the balance between excitation and inhibition in the CNS (Meldrum, 2000). Glutamate is released from glutamatergic neurons into the synaptic gap and transmits excitatory output by binding to ionotropic or metabotropic receptors. High-affinity transport proteins expressed in neurons and glial cells are responsible for rapidly removing the glutamate from the synaptic gap to the astrocytes. Astrocytes then convert glutamate to inert glutamine by intracellular glutamine synthetase (GS) and release it into the synaptic gap for re-uptake by neurons in what is known as the "glutamate–glutamine" cycle (Hayashi, 2018). Glutamate accumulation at the synapse exceeding the physiological range is detrimental. Too much glutamate released at the synapse results in intracellular calcium-ion (Ca^{2+}) overload, which leads to neuronal excitotoxicity and subsequent neuronal dysfunction and apoptosis (Angelova et al., 2019).

Impaired glutamate homeostasis has severe neuropathological consequences and is associated with a variety of CNS disorders, such as epilepsy, Alzheimer's disease (AD), Huntington's disease, and Parkinson's disease (Hynd et al., 2004; Andre et al., 2010; Eid et al., 2016; Zhang et al., 2019; Rezaeian et al., 2022). Neuroprotective strategies for glutamate receptors and transporters include targeting ion-channel pores, glutamate binding sites, and glycine binding sites. For example, non-competitive N-methyl-D-aspartic acid receptor (NMDAR) antagonists, such as aptiganel hydrochloride, dizocilpine, memantine, and dextromethorphan, have shown neuroprotective effects in cultured neurons and animal models (Kroppenstedt et al., 1998; Pu et al., 2015; de Miranda et al., 2017; Liu et al., 2020). However, only memantine has shown neuroprotective effects in clinical trials (Brown et al., 2013). The competitive NMDAR antagonist (selfotel) increases the mortality rate in acute ischemic stroke patients (Davis et al., 2000), and SDZ EAA 494 has been reported to cause memory impairment and to have no clinical benefit in traumatic brain injury patients (Slieker et al., 2008). Targeting excitatory amino acid transporter 2 (EAAT2), the major glutamate transporter in the CNS, is a novel approach for developing epilepsy therapy (Ngomba and van Luijtelaar, 2018; Green et al., 2021). However, the functional characteristics of the glutamate transporter and its implications for epileptic neuropathology and behavior require further study (Zaitsev et al., 2020). Excitotoxicity can lead to neuronal death through multiple death pathways and targets. Therefore, it is essential to explore the potential excitotoxic mechanisms for developing neuroprotective drugs.

Ca^{2+} is an essential cellular signaling regulator that acts as a crucial second messenger in many cellular processes and "enforcers" of glutamate excitotoxicity. The activation of the glutamate receptors leads to an inward flow of extracellular Ca^{2+} and an increase in intracellular Ca^{2+} levels ($[Ca^{2+}]_{cyto}$). The elevated amount of $[Ca^{2+}]_{cyto}$ further triggers the opening of Ca^{2+}-releasing channels in the endoplasmic reticulum (ER), activating inositol 1,4,5-trisphosphate receptors (IP3Rs) and ryanodine receptors (RYRs). This process is known as calcium-induced calcium release (CICR), which is a primary mechanism of calcium signal generation and amplification in the cells (Verkhratsky and Shmigol, 1996). Inefficient removal of $[Ca^{2+}]_{cyto}$ may affect numerous Ca^{2+}-dependent biological functions, ultimately leading to cellular dysfunction and neuronal death. There are several hypotheses for this phenomenon. The downstream effects of increased levels of the $[Ca^{2+}]_{cyto}$ are mitochondrial Ca^{2+} overload via mitochondrial Ca^{2+} uniporter protein (MCU). Mitochondrial Ca^{2+} overload results in increased mitochondrial membrane permeability, imbalance of redox reaction, release of reactive oxygen species (ROS), and release and activation of apoptosis-related factors, all of which are associated with glutamate-induced neuronal death (Nicholls and Budd, 1998; Plotegher et al., 2021). Another possible explanation is that impaired levels of $[Ca^{2+}]_{cyto}$ clearance lead to ER Ca^{2+} depletion. Since chaperones require high concentrations of Ca^{2+} and ATP in the process of protein folding, excessive unfolded proteins or misfolded proteins accumulate in the ER lumen, causing endoplasmic reticulum stress (ERS) (Hetz and Saxena, 2017; Ghemrawi and Khair, 2020). ERS can cause cells to produce adaptive responses, including reducing protein translation, enhancing degradation of unfolded proteins, and folding chaperone proteins, a process known as unfolded protein response (UPR) (Ghemrawi and Khair, 2020). ER Ca^{2+} depletion pushes UPR out of balance, leading to forms of cell death such as apoptosis and autophagy. In glutamate-induced neuronal toxicity, the interactions between $[Ca^{2+}]_{cyto}$, ER Ca^{2+}, mitochondrial Ca^{2+}, UPR, and mitochondrial dysfunction require further investigation.

Sarco/endoplasmic reticulum Ca^{2+}-ATPases (SERCA2b) pumps are membrane-embedded P-type ATPases pumps that mediate the translocation of $[Ca^{2+}]_{cyto}$ to the ER lumen by hydrolyzing ATP against a concentration gradient (Chen J. et al., 2020). *ATP2A2* encodes SERCA2a–c and is widely distributed in various cells. SERCA2b is the most widely expressed pump in brain tissue (Baba-Aissa et al., 1998; Mata and Sepúl`veda, 2005), including in the soma, dendrites, and axon terminals (Hartter et al., 1987; Lysakowski et al., 1999; Bouchard et al., 2003). There is growing evidence that *ATP2A2* mutations are associated with neuropsychological disorders such as epilepsy, mild intellectual disability, bipolar disorder, and schizophrenia (Cederlöf et al., 2015; Britzolaki et al., 2018; Gordon-Smith et al., 2018), but the *in vivo* significance of SERCA2b in neurons and the brain has not been extensively studied (Nakajima et al., 2021). It is understood that excessive glutamate leads to cell toxicity, but it remains unknown whether low amounts of glutamate can also impair cell functions via ER Ca^{2+} depletion, an increase in levels of $[Ca^{2+}]_{cyto}$, and induction of mitochondrial toxicity. Since SERCA2b has a vital role in regulating neuronal Ca^{2+} homeostasis, we speculate that SERCA2b is involved in glutamate-induced excitotoxicity processes by regulating ER Ca^{2+} storage. We also hypothesize that the loss-of-function (LOF) mechanism of *ATP2A2* mutations demonstrated in Darier's disease (Ahn et al., 2003)

can explain the relationship between ER Ca^{2+} storage and glutamate-induced excitotoxicity.

We built glutamate excitotoxicity models of HT22 cells transfected with four SERCA2b mutants (G23R, D567Y, G860S, and I1014V). The G806S mutant has been published previously (Peng et al., 2018), whereas the other three mutants were from our in-house database of genetic epilepsy, a typical excitotoxic pathogenic disease. We found that the SERCA2b mutants exacerbated ER Ca^{2+} depletion, led to mitochondrial Ca^{2+} overload, and increased ERS and mitochondria-mediated apoptosis induced by low glutamate concentration. The mechanism of ER Ca^{2+} depletion depended on the effect of different mutation sites on calcium channels, including pumping capacity and passive leakage. Rescue of ER Ca^{2+} depletion facilitated the suppression of excitotoxicity. These results expand the knowledge of glutamate-induced excitotoxicity.

MATERIALS AND METHODS

Cell Culture and Transfection

HT22 cells were obtained from Kunming Cell Bank of the Chinese Academy of Sciences (Kunming, China), and they were cultured in DMEM medium (Hyclone, USA) supplemented with 10% FBS (Gibco, USA), 100 U/ml penicillin, and 100 μg/ml streptomycin (Gibco, USA). Cell culture was performed at 37°C in an incubator filled with 5% CO_2 and 95% air. Glutamate (0.5, 1, 2, 5, 10, 20 mM) (Sigma, USA) was applied to HT22 cells 24 h for subsequent analysis. According to the DNA transfection protocol, the SERCA plasmids were transfected into HT22 cells by jetOPTIMUS (Polyplus transfection, France). The control group (CON) mentioned in this article refers to the cells transfected with the empty plasmid (pcDNA3.1) only. The cells were analyzed for the glutamate response 24 after transfection.

Mutant SERCA2 Plasmid Construct

The pcDNA3.1-SERCA2b-3xFLAG plasmid containing human SERCA2b was purchased from GenScript. Site-directed mutagenesis was performed using the QuickMutation™. After sequencing confirmation of the wildtype SERCA2b, all mutants (G23R, D567Y, G860S, I1014V) studied were induced by site-directed mutagenesis using Serca2b as a template and confirmed by sequencing again. Primers used for site-directed mutagenesis PCR are listed in **Supplementary Table S1**.

Cell Viability Assay

Cell Counting Kit-8 assay (CCK-8): Cells were seeded into 96-well plates at a density of 5×10^3 cells per well. After 12 h, cells in each well were incubated with 10 μl CCK-8 solution (Beyotime, China) for 2 h at 37°C. The incubation plates were then placed in a microplate reader (Biotek Synergy H1, USA) to determine the optical density (OD) values at 450 nm. The curves were plotted according to the OD values. Thiazolyl Blue Tetrazolium Bromide assay (MTT): Cells were seeded into 96-well plates at a density of 5×10^3 cells per well. After 12 h, cells in each well were incubated with 10 μl MTT solution (Beyotime, China) for 4 h at 37°C. After that, 100 μl of Formazan solution (Beyotime, China) was added to each well, mixed properly, followed by incubation for another 4 h. Then the OD of each well was measured at 570 nm. Lactate dehydrogenase (LDH) release assay was performed using the LDH Cytotoxicity Assay Kit (Beyoutime, China). Briefly, cells were plated in a 96-well plate, and 60 μl of LDH assay working solution was added to each well according to the operation manual, mixed well, and incubated at room temperature (about 25°C) in a dark place for 30 min. Then the OD value of each well was measured at 490 nm. The absorbance after Triton X-100 treatment was regarded as A_{max}. Cell activity (%) = $[1 - (A_{samples} - A_{con})/(A_{max} - A_{con})] \times 100$.

Detection of Cytoplasmic and Mitochondrial Ca^{2+}

Cells were incubated with 5 μM Fluo-4 AM (Invitrogen, USA) or Rhod-2 AM (Abcam, USA) for 20 min. After washing with PBS twice, the buffer was replaced with HBSS without Ca^{2+} and Mg^{2+}. Cells were scanned and imaged at 5 s intervals under a microplate reader (Biotek Synergy H1, USA) by successive addition to a final concentration of 1 mM glutamate, 10 mM caffeine, and 5 mM EGTA. For the rescue of $[Ca^{2+}]_{ER}$ experiment, CDN1163 (10 μM, Selleck) or thapsigargin (2 μM, Sigma) was added and incubated for 10 min, followed by glutamate stimulation. Fluo-2 AM Ex/Em = 549/578 nm, Fluo-4 AM Ex/Em = 494/506 nm.

Transmission Electron Microscope

Cells were fixed with 1% osmic acid for 2 h at 4°C and centrifuged at 200 rpm for 10 min; then, cell pellets were collected. The cell pellets were fixed again by 1% osmic acid and 0.1 M PBS (PH7.4) for 2 h at 20°C, followed by dehydration, infiltration, embedding, sectioning, and staining (2% Uranyl acetate and lead citrate). Finally, they were observed under an electron microscope (Hitachi, Japan).

Mitochondrial Membrane Potential Detection

Cells were incubated with 10 nM tetramethylrhodamine, ethyl ester (TMRE) (Beyotime, China) for 30 min at 37°C at 24 h after glutamate stimulation. Then, cells were washed twice with a pre-warmed cell culture medium and observed in a confocal laser microscope (LEICA TCS SP8, Germany). Cells treated with 10 μM carbonyl cyanide-m-chlorophenyl hydrazone (Beyotime, China) were used as a positive control. Image J software was used for analyzing fluorescence intensity. Ex/Em = 550/575 nm.

ROS Detection

Cells were incubated with 10 nM 2′,7′-Dichlorodihydrofluorescein diacetate (DCFH-DA) (Nanjing Jiancheng Bioengineering Institute, China) for 1 h at 37°C, and then centrifuged at 1,000 rpm for 5 min. The cell pellets were observed under a confocal laser microscope (LEICA TCS SP8, Germany). ImageJ software was used for analyzing fluorescence intensity. Ex/Em = 500/525 nm.

Western Blotting

The cells were rinsed with ice-cold PBS two times before the total protein was extracted. The extraction process took place on ice. After adding RIPA buffer (50 mM Tris-HCl pH 7.5, 150 mM NaCl 1% sodium deoxycholate, 0.1% SDS, 2 mM EDTA) the homogenate was centrifuged at 12,000 rpm for 10 min at 4°C. For SERCA2 solubility analysis experiments, the addition of 1% Triton X-100 and repeated ultrasonic fragmentation helped lysis, and the supernatant was subjected to denaturation (98°C, 10 min) to enhance lysis. The bicinchoninic acid protein assay kit determined the protein concentration. Equal amounts of protein (20–40 μg) were separated by a 10%–15% SDS-PAGE gel and transferred onto a PVDF membrane. PVDF membrane was blocked with 5% skim milk at room temperature in TBST for 1 h. Membranes were incubated with primary antibodies (details in **Supplementary Table S2**) and horseradish peroxidase-conjugated secondary antibodies (Jackson ImmunoResearch). The membranes were then treated using an enhanced chemiluminescence kit (Millipore). Image J software (National Institutes of Health, USA) was used to analyze protein expression levels quantitatively.

TdT-Mediated dUTP Nick-End Labeling Assay

TUNEL kit (C1088, Beyotime) was used to detect apoptotic cells according to the manufacturer's instructions. In brief, samples were fixed with 4% PFA, permeabilized with 0.1% Triton X-100 in PBS for 10 min at room temperature, incubated with working solution (terminal deoxynucleotidyl transferase, TdT) for 1 h, and shielded from light at 37°C. The nuclei were then stained with the DAPI for 10 min. The specimens were analyzed using a confocal laser microscope (LEICA TCS SP8, Germany.

Quantitative RT-PCR

Total RNA was isolated using TRIzol Lysis Reagent (Invitrogen), and cDNA was synthesized by All-in-OneTMFirst-Strand cDNA Synthesis Kit (GeneCopoeia, USA). For qPCR, amplification reactions were performed using All-in-One™qPCR Mix (GeneCopoeia, USA), run on the ABI-VII Real-Time PCR detection system. The primers were synthesized by Tsingke Company (China); the details of sequences are listed in **Supplementary Table S3**. All experimental steps were performed following the manufacturers' instructions. Data analysis was performed using the $2^{-(\Delta\Delta CT)}$ method to determine the relative quantitative level and was expressed as a fold-difference to the relevant control (recognized as 1 ± 0.00).

Isolation of Microsomes

According to the modified Parsons's protocol, microsomes (crude ER) were isolated by serial centrifugation (Parsons et al., 2000; Wang et al., 2011). Briefly, cells cultured in 6-well plates were transiently transfected and then collected and suspended with 350 ul of low-tonic buffer per well (10 mM Tris-HCl, pH 7.5, 0.5 mM MgCl, and 1 mM phenylmethanesulfonyl fluoride). The cells were homogenized for 45 strokes with a glass homogenizer and then made isotonic by adding 350 ul buffer (0.5 M sucrose, 0.3 M KCl, 6 mM β-mercaptoethanol, 40 uM CaCl2, 10 mM Tris-HCl, pH 7.5). The homogenate was centrifuged at 5,000 g for 10 min to yield a supernatant (S1) and a crude nuclear pellet. S1 was then centrifuged for 20 min at 18,000 g to yield a supernatant (S2) and a crude mitochondrial pellet (P2). S2 was then centrifuged for 3 h at 20,000 g to yield a cytosolic fraction (S3) and the crude microsomal pellet (P3). The P3 pellets (microsomes) were suspended in 65 μl buffer containing 10 mM Tris-HCl, pH 7.5, 0.15 M KCl, 0.25 M sucrose, 20 mM $CaCl_2$and 3 mM β-mercaptoethanol. The concentration of microsomes was determined by the Lowry method.

SERCA2 Activity

SERCA2 activity was measured by the inorganic phosphorus method (A070-4-2, Nanjing Jiancheng Bioengineering Institute). Briefly, ATP was decomposed into ADP and inorganic phosphorus by ATPase. The reagents were added separately, then mixed according to the protocol, and the reaction was carried out at 37°C for 10 min. After that, 100 ul of the sample was added and mixed for the enzymatic reaction. After centrifugation at 3,500 rpm for 10 min, 150 μl of the supernatant was collected to determine phosphorus. The absorbance was measured at A636 wavelength with 0.02 μmol/ml standard phosphorus solution as a reference. The amount of ATPase to produce 1umol of inorganic phosphorus per mg of microsomes per hour was defined as 1 ATPase activity unit (μmolPi/mg protein/hour).

Statistical Analysis

The student's t-test was used to determine significant differences between the two groups. One-way analysis of variance was utilized to determine significant differences among multiple groups. A p-value of less than 0.05 was considered statistically significant. Results were expressed as means ± SEM.

RESULTS

SERCA2b Mutants Exacerbate Hypo-Glutamate-Induced ER Stress and Cell Death in HT22 Cells

Excitotoxicity plays an essential role in CNS injury. Intracellular calcium overload and mitochondrial dysfunction are the leading causes of high glutamate-induced neuronal death (Meldrum, 1993; Olloquequi et al., 2018). We tested the impacts of different concentrations of glutamate stimulation on HT22 cell viability using both CCk-8 and MTT assays and found that cell viability was reduced in a dose-dependent manner (**Figure 1A**). High concentrations of glutamate (5 mM) stimulation for 24 h resulted in reduced cell activity approaching 60%–70%. LDH release assays further confirmed the excitatory neurotoxic effect of excess glutamate (**Figure 1B**). Low glutamate stimulation concentration (1 mM) did not directly affect cell viability. However, in transfected SERCA2b mutants (G23R, D567Y, G860S, and I1014V), cell viability was significantly decreased after 24 h of stimulation with a low concentration of glutamate (**Figure 1C**). Furthermore, LDH release assays also confirmed the sensitivity of mutant cells to excitotoxicity of low glutamate (**Figure 1D**). TUNEL analysis revealed frequent apoptotic cells in all mutant groups, but few

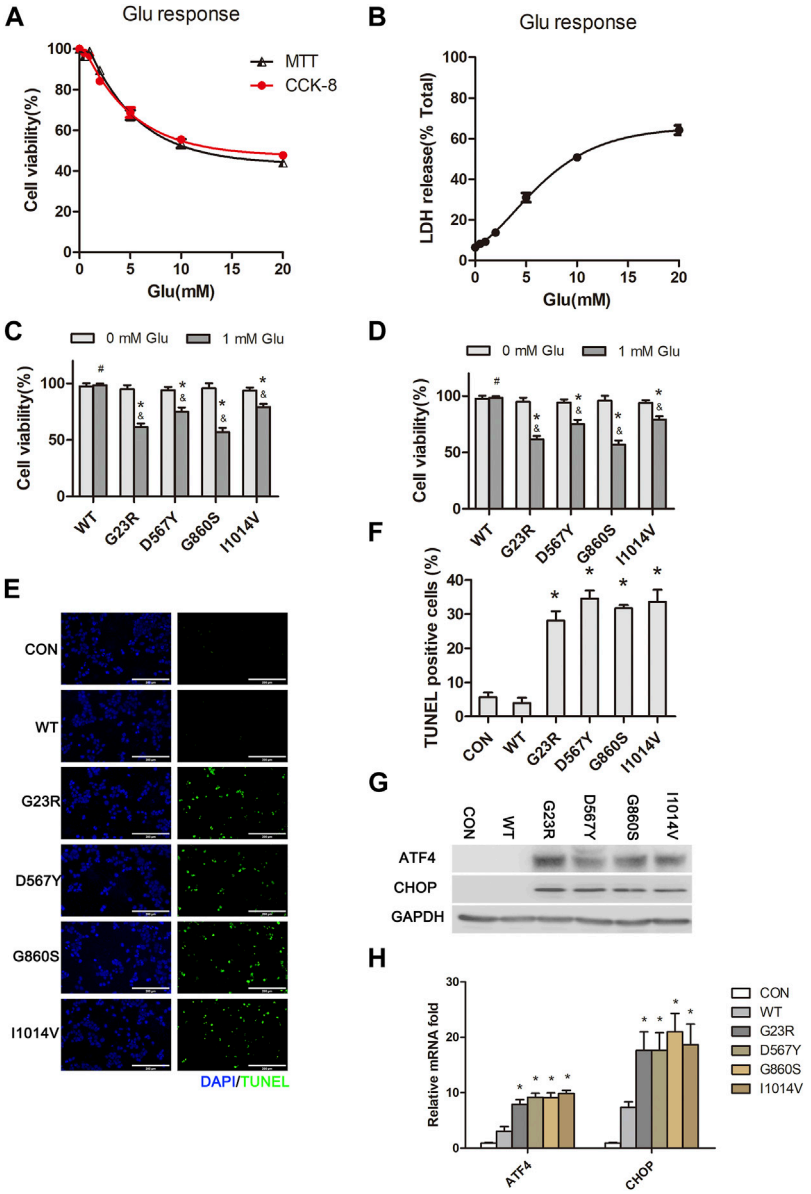

FIGURE 1 | SERCA2 mutants exacerbate hypo-glutamate-induced ERS and cell death in HT22 cells. **(A,B)**: MTT assay, CCK-8 assay **(A)**, and LDH release assay **(B)** show decreased cellular activity in a glutamate concentration-dependent manner in native HT22 cells. **(C,D)**: CCK-8 assay **(C)** and LDH assay **(D)** show SERCA2 mutants exacerbated hypo-glutamate-induced cell death. $^{*}p < 0.05$ compared with respective 0 mM glutamate stimulation. $^{\#}p > 0.05$ compared with respective 0 mM glutamate stimulation. $^{\&}p < 0.05$ compared with WT in 1 mM glutamate stimulation, respectively. **(E,F)**: Representative images **(E)** and summary data **(F)** show increased cell apoptosis of *SRCA2* mutants under hypo-glutamate stimulation by TUNEL staining. $^{*}p < 0.05$ compared with WT group, respectively. Scale bar, 200 μm. **(G,H)**: Increased expression of ERS marker of indicated proteins **(G)** and mRNAs **(H)** under hypo-glutamate stimulation by Western blotting, real-time qPCR, respectively. $^{*}p < 0.05$ compared with WT group.

apoptotic cells were observed in the wildtype (WT) or CON group after 24 h of glutamate stimulation (**Figures 1E,F**). To explore the cause of apoptosis in HT222 cells, we evaluated the severity of ERS after 1-mM glutamate stimulation. It was found that low glutamate-induced apoptosis and protein kinase R-like ER kinase- C/EBP homologous protein (PERK-CHOP) signaling pathways were activated in mutant cells, which was confirmed by increased protein and mRNA levels of ERS markers (**Figures 1G,H**). In summary, these results suggest that the four SERCA2b mutants exacerbate the excitotoxicity induced by low concentrations of glutamate by affecting ERS.

Reduced Pump Activity and Cytoplasmic Ca^{2+} Clearance Efficiency in SERCA2b Mutants

Severe ERS is often caused by the depletion of ER Ca^{2+}, as the process of proteins folding by the molecular chaperones requires

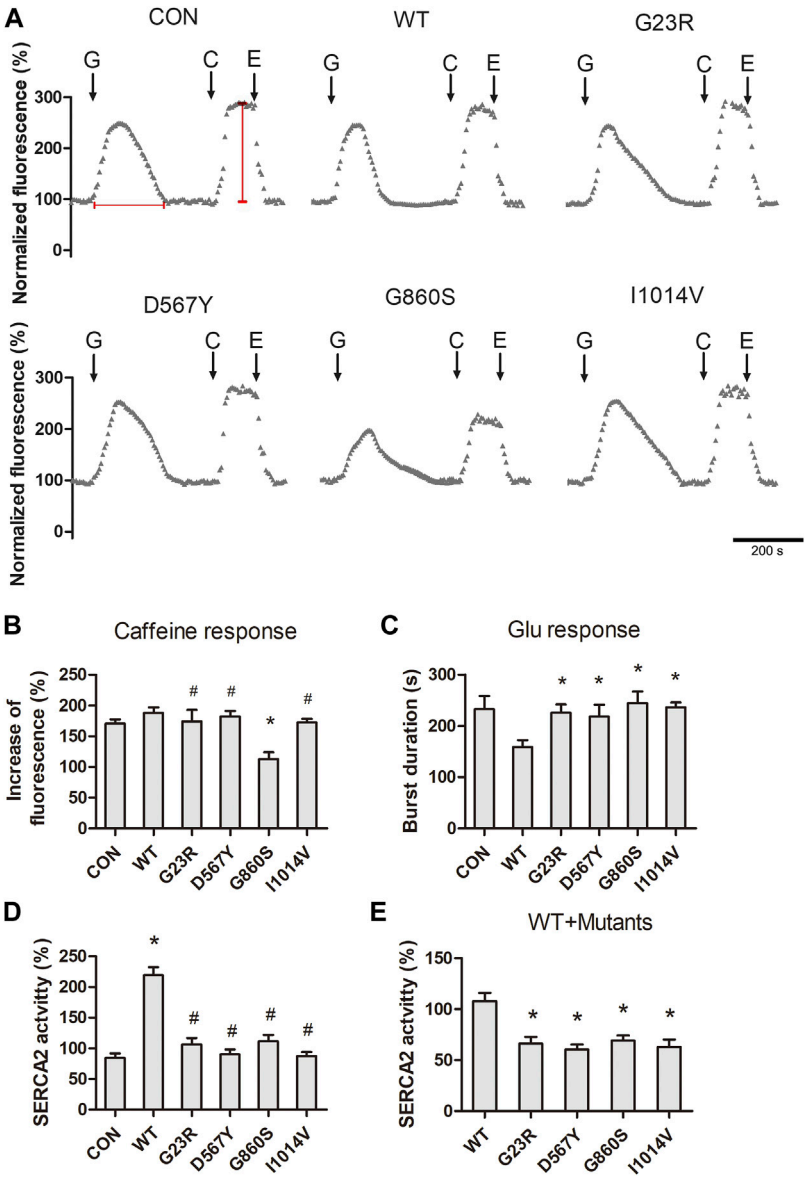

FIGURE 2 | Declined pump activity and cytoplasmic Ca^{2+} clearance efficiency in SERCA2 mutants. **(A)** Representative $[Ca^{2+}]_{cyto}$ response of SERCA2 mutants. The addition of glutamate (G), caffeine (C), EGTA (E) is indicated with black arrows. Scale bar, 200 s. Horizontal and vertical red lines represent the level of the $[Ca^{2+}]_{cyto}$ clearance efficiency and $[Ca^{2+}]_{ER}$ storage, respectively. **(B)** Quantification of $[Ca^{2+}]_{ER}$ storage in response to caffeine. $^{*}p < 0.05$ compared with WT group, $^{\#}p > 0.05$ compared with WT group, respectively. **(C)** Quantification of $[Ca^{2+}]_{cyto}$ clearance efficiency in response to glutamate. $^{*}p < 0.05$ compared with WT group, respectively. **(D,E)**: Quantification of SERCA2 activity of mutants when transfected alone **(D)** or co-transfected **(E)**, SERCA2 mutants were inactive and even inhibited endogenous SERCA2 activity. **(D)**: $^{*}p < 0.05$ compared with CON group, $^{\#}p > 0.05$ compared with CON groups respectively. **(E)**: $^{*}p < 0.05$ compared with WT group.

high levels of Ca^{2+}. We next measured the levels of $[Ca^{2+}]_{cyto}$ concentration in response to glutamate stimulation and ER Ca^{2+} storage levels. After 10 min of loading with Fluo-4 AM, cells stimulated with 1-mM glutamate showed a transient increase in calcium fluorescence signal and gradually returned to the resting levels. The magnitude of the glutamate response was significantly lower in the G860S mutant than in the WT group (**Figures 2A–C**). The $[Ca^{2+}]_{cyto}$ clearance efficiency was significantly lower in all groups than the WT group (**Figures 2A–C**), suggesting SERCA2b-mediated Ca^{2+} uptake dysfunction in mutants. Rapid addition of 10-mM caffeine was used to release ER Ca^{2+}, and the results showed Ca^{2+} storage in G23R/D567Y/I1014V groups was similar to the WT group, which was significantly decreased in the G860S group (**Figures 2A,B**). We next assayed SERCA2b activity of isolated microsomes (including both the intrinsic activity of SERCA2b and exogenously transferred mutant activity). SERCA2b activity was significantly increased in the WT group compared with the CON group, while the activity was not significantly altered in the G23R/D567Y/G860S/I1014V groups (**Figure 2D**). However, when the WT and mutant plasmids were

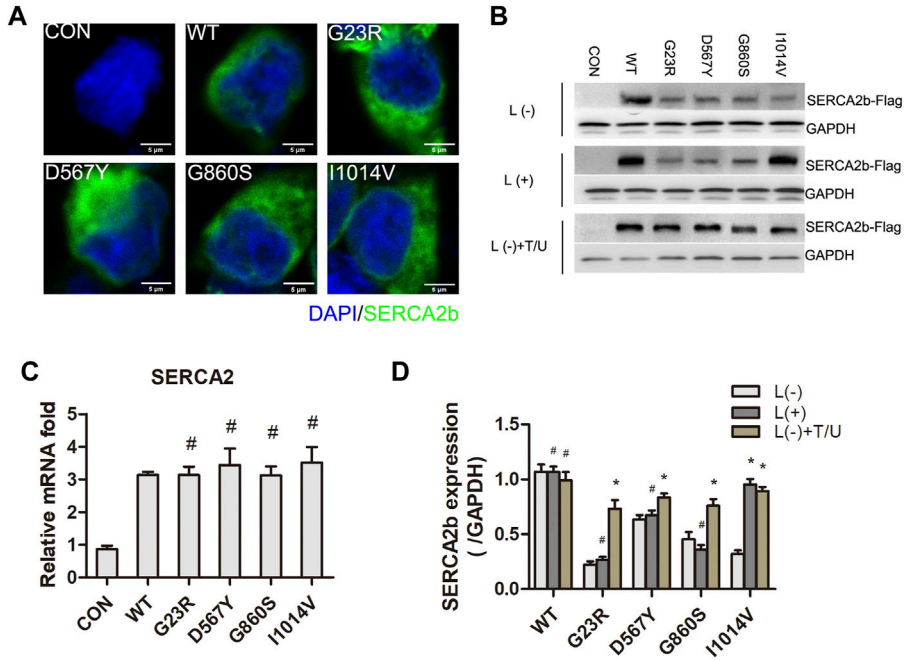

FIGURE 3 | LOF of SERCA2 is caused by insoluble and low-expression of mutants protein. A- B: Intracellular distribution and expression of SERCA2 in mutant cells. Anti-Flag antibody was used to detect the expression of WT and mutant proteins by immunostaining **(A)** and Western Blotting **(B)**. L: lactacystin, T/U: Cells were treated with an additional 1% Triton-X100 and ultrasonic fragmentation. Scale bar, 5 μm. **(C)**: Expression level of SERCA2 mRNA by qPCR. $^{\#}p > 0.05$ compared with WT group, respectively. **(D)**: Quantification of SERCA2 protein level with or without lactacystin and T/U treatment. $^{*}p < 0.05$ compared with L (-) treatment cells in each groups, $^{\#}p > 0.05$ compared with L (-) treatment cells in each groups, respectively.

co-transfected (WT:mutants = 1:1), the SERCA2 activity of each mutant group decreased when compared with WT groups alone (**Figure 2E**). These results suggested that the SERCA2b mutants were inactive and might have affected the endogenous pump activity, which is consistent with the decreased $[Ca^{2+}]_{cyto}$ scavenging efficiency in the glutamate response. In summary, SERCA2b mutants lost the ability to pump Ca^{2+} against concentration, resulting in a slow $[Ca^{2+}]_{cyto}$ clearance responding to glutamate stimulation.

Insoluble, Low-Expression Mutant Protein Causes Loss-of-Function of SERCA2b

We examined the expression and intracellular distribution of exogenously expressed SERCA2 protein by Flag tags. Immunofluorescence results showed that SERCA2 was widely distributed in the cytoplasm (**Figure 3A**). Compared with the WT group, the exogenous SERCA2 protein expression was significantly reduced in the mutant groups (**Figures 3B,D**), and this reduction was not significantly associated with the regulation of mRNA transcript levels because qPCR results confirmed that the transcript levels were unaffected (**Figure 3C**). Further reasons for the decrease in SERCA2 expression could be proteasome-mediated degradation or the formation of aggregates. The aggregates are insoluble in conventional protein lysis buffers, resulting in reduced soluble proteins separated by SDS-PAGE gel. To confirm these two possibilities, we first examined SERCA2 expression after treating cells with the proteasome inhibitor lactacystin (L). As shown in **Figures 3B,D**, lactacystin treatment did not increase SERCA2 protein expression levels in the WT/G23R/D567Y/G860S groups, indicating that these mutant proteins were not degraded by the proteasome, while partial degradation of the I1014V group was apparent. We then improved the protein lysis treatment process (e.g., adding 1% TritonX-100 to enhance lysis, repeated ultrasonic fragmentation, and denaturation at 98°C extended to 10 min). These results showed that the soluble fraction of the protein was significantly increased compared to that treated by conventional lysis methods (**Figures 3B,D**), suggesting that some missense mutations may be expressed at levels similar to WT proteins but form insoluble aggregates, which may be related to misfolding of the mutants.

SERCA2b Mutants Increase Mitochondrial-ER Contacts Leading to Mitochondrial Ca^{2+} Overload and Dysfunction Under Hypo-Glutamate Stimulation

Mitochondria are closely associated with the ER through a physical structure, the mitochondria-associated membrane (MAM), which provides energy for the assembly, folding, and modification of ER and the uptake of Ca^{2+} and lipids transferred from the ER. These contact sites are enriched with specific proteins, such as IP3R, Mitofusin 2 (Mfn2), and voltage-dependent anion channel 1 (VDAC1). After confirming that

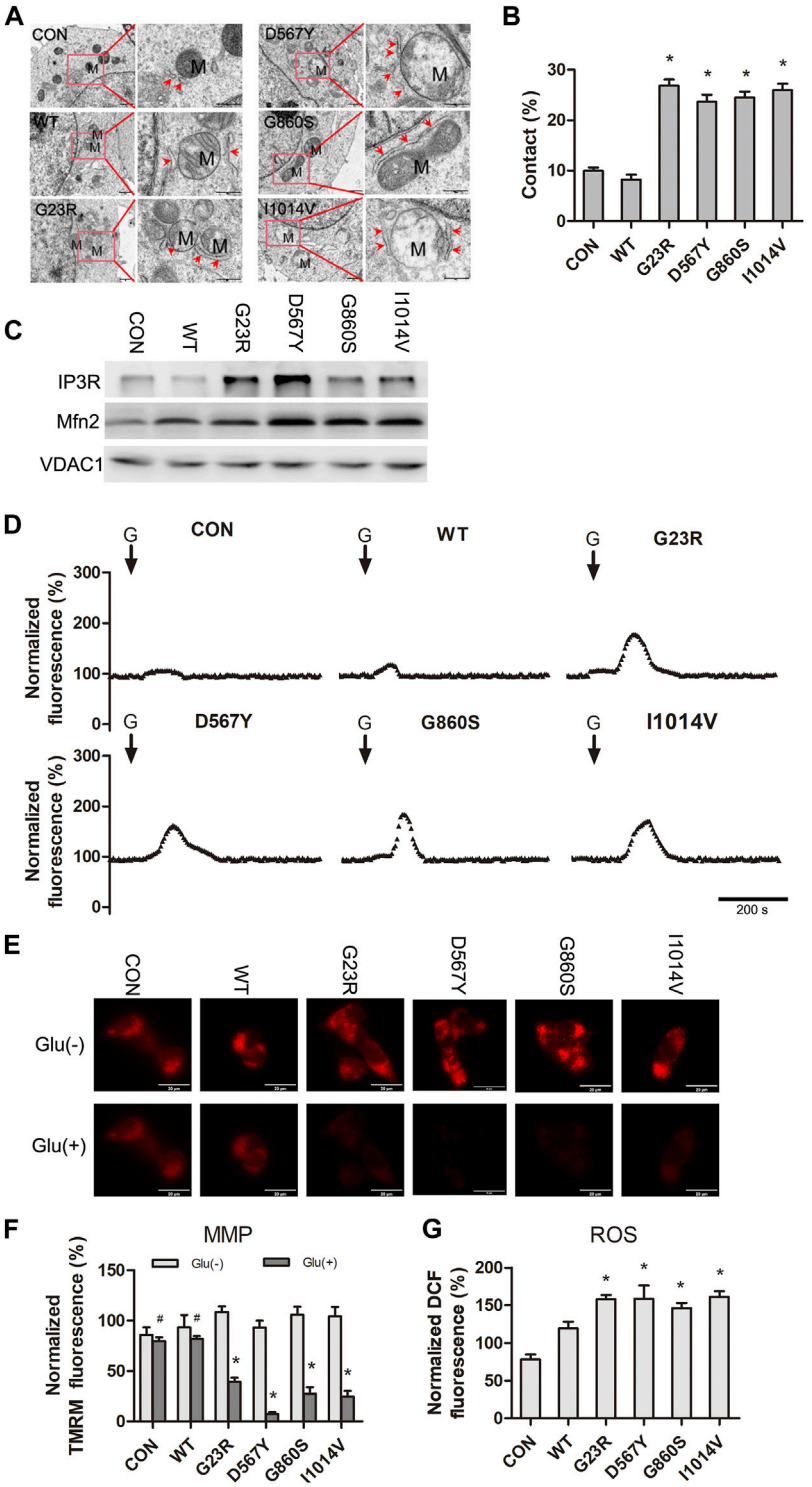

FIGURE 4 | SERCA2 mutants increase mitochondrial-ER contacts leading to mitochondrial Ca^{2+} overload and dysfunction under hypo-glutamate stimulation. **(A)**: Representative electron micrographs of mitochondria-ER contact *SERCA2* mutants. M: mitochondria; red arrows indicate ER. The scale bar is 1 μm (left line), 500 nm (right line). **(B)** Quantification of the mitochondrial surface percentage in close apposition to the ER. $^{*}p < 0.05$ compared with WT group. **(C)**: Increasing of the calcium channel protein (IP3R and Mfn2) from specifically isolated MAM fractions in *SERCA2* mutants by Western Blotting. **(D)**: Representative normalized fluorescence of mitochondria Ca^{2+} by Rhod-2AM. Scale bar, 200 s. **(G)**: glutamate. **(E,F)**: Decreased mitochondrial membrane potential in *SERCA2* mutants. Representative immunostaining **(E)** and quantification **(F)** of TMRM fluorescence. $^{*}p < 0.05$ compared with no-glutamate treatment. $^{\#}p > 0.05$ compared with no-glutamate treatment. **(G)**: Increased level of ROS in *SRECA2* mutants by DCFH immunostaining. $^{*}p < 0.05$ compared with WT group.

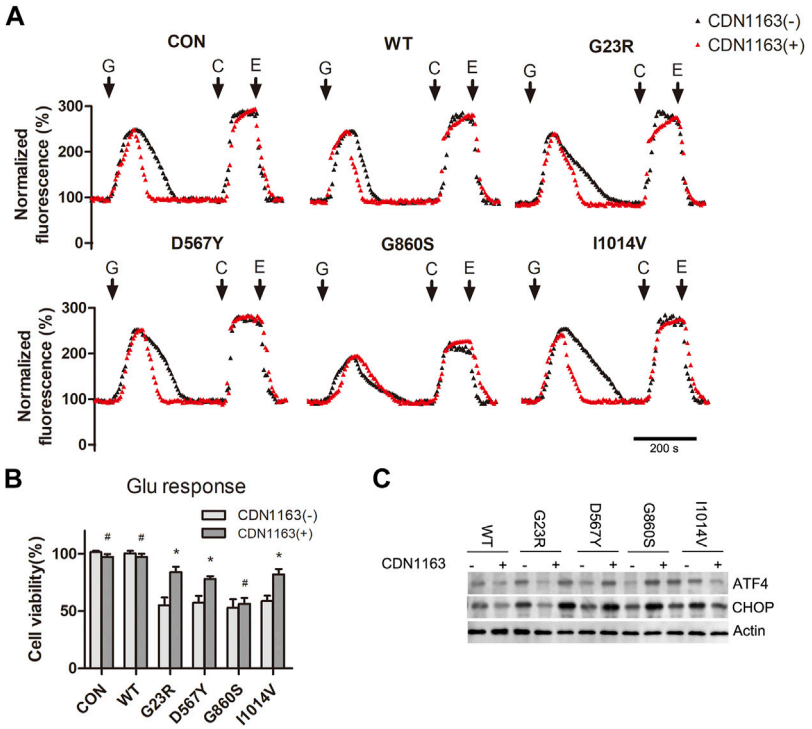

FIGURE 5 | CDN1163 inhibits hypo-glutamate-induced excitotoxicity by reducing SERCA2 mutant-mediated ER Ca^{2+} depletion and stress. **(A)**: Representative normalized fluorescence of cytoplasmic Ca^{2+} by Furo-4 AM. CDN1163 enhanced cytoplasmic Ca^{2+} clearance of SERCA2 mutants. The addition of glutamate (G), caffeine (C), EGTA (E) is indicated with black arrows. Scale bar, 200 s. **(B)**: CDN1163 rescues the cell viability of SERCA2 mutants under hypo-glutamate loading. $^{*}p < 0.05$ compared with no-CDN1163 treatment, $^{\#}p > 0.05$ compared with no-CDN1163 treatment. **(C)**: Low protein level of ERS marker in SERCA2 mutants with CDN1163 treatment by Western blotting.

ER Ca^{2+} uptake is impaired in SERCA2b mutants, we wondered whether the mitochondrial function is altered and involved in hypo-glutamate-induced excitotoxicity. Following experiments, we discovered an increased proportion of mitochondrial-ER contacts in the mutants compared to WT group cells by transmission electron microscopy (**Figures 4A,B**). WB results of isolated MAM fractions showed that the expression of IP3R and Mfn2 was significantly higher in the mutant groups than in the WT group (**Figure 4C**), suggesting that these proteins may be redistributed from the ER or mitochondrial membrane to the MAM. These results demonstrated that mitochondrial-ER contact sites were increased in SERCA2 mutant cells.

The increased mitochondrial-ER contact and calcium channel proteins of the MAM were the most likely causes of the increased Ca^{2+} flux to mitochondria, resulting in mitochondrial Ca^{2+} overload. We then assessed the kinetics of mitochondrial Ca^{2+} by specifically labeling mitochondrial Ca^{2+} with Rhod-2 AM. Subsequently, mitochondrial Ca^{2+} fluorescence showed a strong response to hypo-glutamate stimulation in the four mutants, followed by a return to the resting levels (**Figure 4D**). These results suggested that SERCA2b mutants are more prone to mitochondrial Ca^{2+} overload in response to excitatory events. The mutants' mitochondrial membrane potential (MMP) was significantly decreased after glutamate stimulation (**Figures 4E,F**), and no significant changes were observed in the WT group. In addition, ROS levels were increased in the mutants compared to the WT group (**Figure 4G**). These results further confirmed that SERCA2b inactivation causes an increased MAM Ca^{2+} flux associated with mitochondrial dysfunction.

CDN1163 Inhibits Hypo-Glutamate-Induced Excitotoxicity by Reducing SERCA2 Mutant-Mediated ER Ca^{2+} Depletion and Stress

Glutamate-induced CICR causes a rapid increase in the levels of $[Ca^{2+}]_{cyto,}$ and SERCA2 mutants fails to remove Ca^{2+} effectively, resulting in sustained $[Ca^{2+}]_{cyto}$ overload and ER Ca^{2+} depletion. CDN1163 is a small-molecule trans-activator of SERCA that improves intracellular Ca^{2+} homeostasis. We aimed to attenuate glutamate-induced excitotoxicity by increasing the Ca^{2+} capacity of SERCA2. The G23R/D567Y/I140V groups (CDN1163 intervention groups) showed shortened recovery time from the $[Ca^{2+}]_{cyto}$ oscillations compared to the group without CDN1163 intervention (**Figures 5A,B**), suggesting enhanced Ca^{2+} uptake capacity of ER. The efficiency of $[Ca^{2+}]_{cyto}$ clearance was unaffected in the G860S group. CCK-8 assay results showed that cell activity in the G23R/D567Y/I140V groups was significantly increased after CDN1163 intervention (**Figure 5B**), accompanied by a decrease in ERS

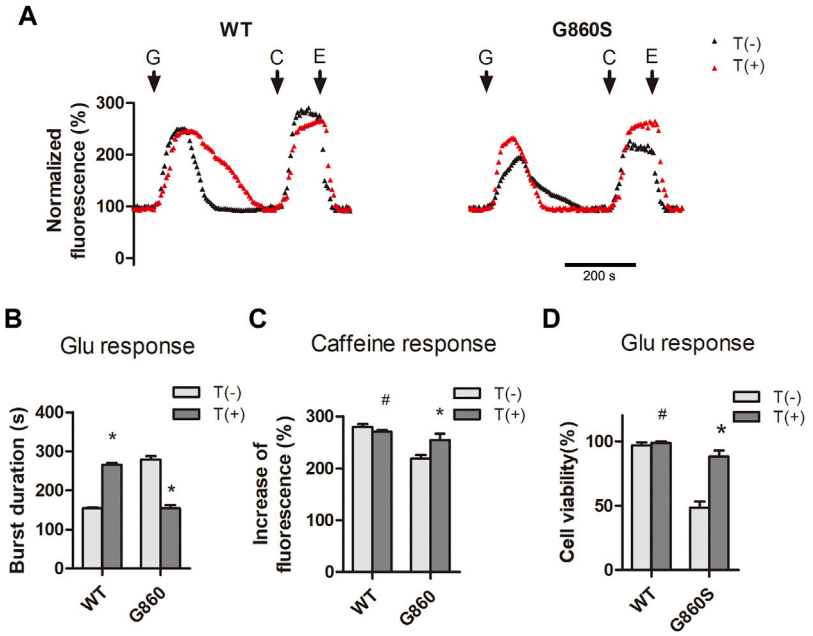

FIGURE 6 | Inhibition of GOF-type pump leakage reduces ER Ca^{2+} depletion and attenuates glutamate-induced excitotoxicity. **(A–C)**: Thapsigargin inhibits pump leakage of G860S mutant. Representative normalized fluorescence of cytoplasmic Ca^{2+} by Furo-4 AM **(A)**. The addition of glutamate (G), caffeine (C), and EGTA (E) is indicated with black arrows. **(B)**: Quantification of the $[Ca^{2+}]_{cyto}$ clearance efficiency in response to glutamate. T: Thapsigargin. **(C)**: Quantification of the $[Ca^{2+}]_{ER}$ storage in response to caffeine. **(D)**: Thapsigargin rescues the cell viability of the G860S mutant under glutamate loading. **(B–D)**$^{*}p < 0.05$ compared with no-thapsigargin treatment, $^{\#}p > 0.05$ compared with no-thapsigargin treatment.

markers (**Figure 5C**), while the G860S group did not show significant changes (**Figures 5B,C**). Taken together, CDN1163 inhibited hypo-glutamate-induced excitotoxicity by reducing mutant-mediated ER Ca^{2+} depletion and stress.

Inhibition of Pump Leakage Reduces ER Ca^{2+} Depletion and Attenuates Hypo-Glutamate-Induced Excitotoxicity

Interestingly, in the above experiments, CDN1163 neither enhanced the $[Ca^{2+}]_{cyto}$ clearance efficiency of G860S nor restored the ER Ca^{2+} storage. We speculate that the G860S mutation may lead to the coupling mistake of the SERCA2 gated-channel structure and the acquisition of cis-concentration "leakage capacity." When the cis-concentration leakage capacity is greater than the inverse "pumping capacity," the total ER Ca^{2+} flux is toward the cytoplasmic side, leading to the depletion of Ca^{2+} storage, which may be one of the mechanisms of the gain-of-function (GOF) pathogenesis. To confirm this hypothesis, WT and G860S cells were treated with thapsigargin before glutamate stimulation. Thapsigargin is a non-competitive inhibitor of SERCA and does not affect the activity of other ATPases. Calcium signal imaging results showed that thapsigargin reduced the glutamate response time of G860S and partially restored ER Ca^{2+} storage (**Figures 6A–C**). In contrast, thapsigargin prolonged the $[Ca^{2+}]_{cyto}$ clearance of glutamate response in WT-group cells, which is consistent with our previous hypothesis. CCK-8 assay suggested that cell viability in the G860S group significantly increased after thapsigargin intervention (**Figure 6D**). Taken together, the inhibited leakage of SERCA2 mutants could attenuate ER Ca^{2+} depletion and reduce glutamate-induced excitotoxicity.

DISCUSSION

Excitotoxicity refers to neuronal damage and death due to chronic or excessive exposure to excitatory amino acids, particularly glutamate, the primary neurotransmitter in mammals. The concept of excitotoxicity was introduced following Olney's observation of neuropathic damage in rodent and primate brains after systemic injection of glutamate and its analogs (Olney, 1969). Excitotoxicity is widely recognized as a critical player in the occurrence of numerous acute/chronic neurodegenerative pathologies (Ikonomidou and Turski, 1995; Binvignat and Olloquequi, 2020). Although the activation of glutamate receptors leads to the inward flow of different ions, there is a consensus that Ca^{2+} plays a crucial role in excitotoxicity (Choi, 1987), and mitochondrial dysfunction is a critical deleterious effect of excitotoxicity (Mira and Cerpa, 2021). Several clinical trials and animal studies have aimed to address the mechanisms involved in excitotoxicity (Olloquequi et al., 2018; Zaitsev et al., 2020), focusing on the functional effects of glutamate receptors/transporters on cell membranes. These studies brought new questions, such as the memory impairment,

hallucinogenic, schizophrenic, and potentially addictive effects of NMDAR antagonists (Allen and Ivester, 2017); the enhancement of the neuronal apoptotic effects (Monti and Contestabile, 2000; Parsons and Raymond, 2014); and the actual relevance of EAAT as a target of pharmacological intervention, which remains to be fully understood and validated (Zaitsev et al., 2020). Given the complex mechanisms of excitotoxicity and the brain's susceptibility to progressive and long-term damage, there is a need to delve into the underlying mechanisms and facilitate the development of new and effective treatments. The current study investigated the impact of four SERCA2b mutants carried by epileptic patients who suffered from a typical excitotoxic pathogenic disease.

The SERCA2b mutants (G23R, D567Y, G860S, and I1014V) exacerbated Ca^{2+} depletion in the ER under excitatory loading, as evidenced by delayed $[Ca^{2+}]_{cyto}$ removal or reduced Ca^{2+} storage. A severe ER Ca^{2+} depletion is an upstream event in the pathophysiology of many neurological diseases. Conversely, impaired ER Ca^{2+} release may no longer maintain essential cellular functions. However, depletion of $[Ca^{2+}]_{ER}$ causes ERS and activates UPR, which depends on the duration and severity of the ERS. The mechanism of ER Ca^{2+} depletion is inextricably linked to the functional state of the Ca^{2+} channels of the ER membrane (SERCA, RYR, and IP3R). In the GM1 gangliosidosis model, GM1 accumulates in the microstructure domain of the MAM, which increases ER Ca^{2+} depletion and Ca^{2+} flux to the mitochondria by interacting with phosphorylated IP3R, ultimately leading to mitochondrial Ca^{2+} overload-mediated apoptosis (Sano et al., 2009). In glucocerebroside disease, overactivation of RyR indirectly mediates ER Ca^{2+} depletion, and the redox sensor of RyR may be involved (Lloyd-Evans et al., 2003). In neuropathic pain models, the reduction in SERCA2 leads to decreased ER Ca^{2+} storage, and the resulting disruption of CICR and protein synthesis may contribute to the development of neuropathic pain (Gemes et al., 2009). Unlike the pathogenic mechanism of ER Ca^{2+} depletion in this study, some researchers have suggested that the increased ER Ca^{2+} storage by amyloid oligomers results in the remodeling of Ca^{2+} signaling, which would lead to early learning and memory deficits in the onset of AD (Berridge, 2010).

Intracellular Ca^{2+} regulatory mechanisms can buffer excitatory stimuli from low glutamate concentrations and maintain intracellular homeostasis. However, for SERCA2 mutant cells, this excitatory stimulus is a devastating signal, mainly attributed to the LOF effect due to abnormal SERCA2 expression or activity. Many studies have confirmed that different SERCA2 mutations lead to LOF effects in pump defects or reduced protein levels that underlie dominant diseases. Gordon-Smith et al. found a significantly higher rate of disrupting *ATP2A2* mutations in cases with Darier's disease accompanied with neuropsychiatric disorders (Gordon-Smith et al., 2018). Ahn's study confirmed proteasome degradation in the SERCA2 protein (K542X, Q790X, and E917X) (Ahn et al., 2003). However, increased proteasome degradation was also observed in missense mutants (S920Y and I1014V). In addition, a heterozygous splicing mutation in *ATP2A2* also resulted in a shift code and an early termination codon (Nakamura et al., 2016). In addition, Wang et al. discovered that the SERCA2 mutant underwent protein aggregation and formed insoluble aggregates. We performed enhanced treatments on cell lysates in our experiments and confirmed the decreased solubility of SERCA2 mutants. Notably, interactions between SERCA2b monomers were found to dimerize in Ahn's study (Ahn et al., 2003), affecting the activity of each other, which explains why the pump function of WT is inhibited when WT and mutants coexist. The complicated regulation mechanism of SERCA2 fundamentally affects the differences in local and global Ca^{2+} release kinetics of the mutants.

Only the ER Ca^{2+} storage of G860S was decreased in this experiment. Moreover, the activation of the SERCA2 by CDN1163 failed to rescue ER Ca^{2+} storage. Moreover, the addition of thapsigargin, which is an irreversible SERCA pump inhibitor, did not prevent calcium removal in the G860S mutant. These results indicate that other pathways are implicated in the observed decrease of $[Ca^{2+}]_{cyto}$ and uptake by the ER, such as the calcium leakage in G860S mutant or insufficient concentration of thapsigargin. Ion pumps can be thought of as two gated-controlled ion-selective channels, with the gates facing different sides of the membrane. The ATPase enzyme cycle controls the gates and ensures the unidirectional transport of ions. The ability of both gates to open simultaneously is critical to prevent the passive transport of ions through the trans-membrane region. When a minor defect disrupts the coupling between the enzymatic cycle and gating properties, this uncoupling may lead to passive leakage of ions to form GOF channels (Gadsby, 2009). Indeed, SERCA2 can form leaks for Ca^{2+} under certain conditions. For example, the A617T mutation of mSERCA causes ion leakage under heating conditions, and M494L and R131Q also cause ion leakage even without heating, while heating exacerbates the degree of leakage (Kaneko et al., 2014). The marine toxin palytoxin disrupts the coordination of the two gates in the Na^+/K^+ ATPase, leading to ion leakage (Artigas and Gadsby, 2003). Ultimately, ER Ca^{2+} storage depends on the balance between the cis-concentration leakage capacity and inverse pumping capacity. In the present study, thapsigargin may have increased ER Ca^{2+} storage primarily through attenuating calcium leakage from G860S. In addition, the concentration window of thapsigargin in inhibiting SERCA pumping or leakage requires further research.

The link between the ER and mitochondria is considered to be highly dynamic, as local Ca^{2+} ions can regulate the ER-mitochondria linkage in different ways (García-Pérez et al., 2008). The increased Ca^{2+} blocks the motility of both organelles and enhances their interactions (Yi et al., 2004), leading to an increase in the contact sites between the MAM and ER, which may be the main reason that SERCA2b mutants lead to mitochondrial disorders under glutamate excitatory loading. MAM is a crucial determinant of cell function and survival, achieved by regulating intracellular Ca^{2+} signaling. MAM dominates the efficient transferring of Ca^{2+} from the ER to the mitochondria, and mitochondrial Ca^{2+} oscillations play a significant role in energy production by regulating calcium-dependent enzymic reactions that generate ATP (Hajnóczky et al., 1995; Rizzuto et al., 2004). Thus, they control the

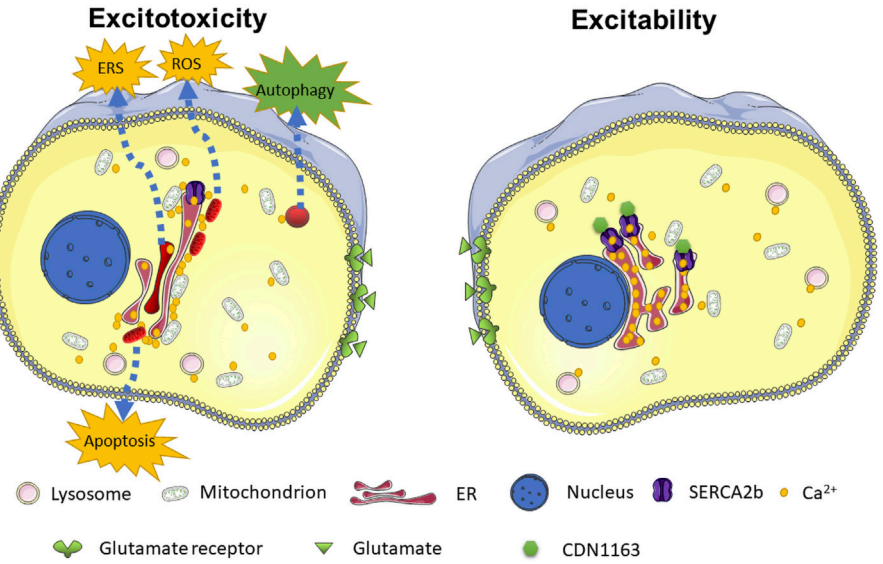

FIGURE 7 | Schematic model depicting the ER Ca^{2+} depletion in response to glutamate-induced excitotoxicity. SERCA2b mutants increase susceptibility to glutamate-induced excitotoxicity by exacerbating ER Ca^{2+} depletion. ER Ca^{2+} depletion leads to increased levels of the $[Ca^{2+}]_{cyto}$ and ER-mitochondria contact, which in turn leads to abnormal activation of many Ca^{2+}-dependent pathways, such as ERS, oxidative stress, apoptosis, autophagy, and ultimately promotes cell death. CDN1163 enhances SERCA2b activity and inhibits ER Ca^{2+} depletion, maintaining intracellular Ca^{2+} homeostasis. The affected dysfunctional mitochondria, lysosomes, and ER are highlighted in red.

fundamental processes of energy production and determine the cell's fate by triggering or preventing apoptosis (Green and Kroemer, 2004; Walter and Hajnóczky, 2005). However, MAM is enriched with different functional enzymes involved in lipid metabolism, glucose metabolism, redox reactions, and chaperone molecule folding (Lebiedzinska et al., 2009; Hayashi et al., 2009). Moreover, MAM contains critical Ca^{2+} handling proteins of two organelles (Giorgi et al., 2009; Decuypere et al., 2011). SERCA2 mutants exacerbate mitochondrial dysfunction under excitatory loading by affecting the function of the MAM (**Figure 4**). Oxidative stress dysregulation is another important factor in mitochondrial dysfunction under excitatory loading. Increased $[Ca^{2+}]_{cyto}$ or impaired clearance leads to nitric oxide synthase activation for nitric oxide synthesis, which inhibits mitochondrial electron transport, results in increased production of ROS, and causes a wide range of toxic oxidative responses (Moncada and Erusalimsky, 2002). In excitotoxicity, protein dysfunction, lipid peroxidation, DNA breakage, inhibition of mitochondrial respiratory chain enzymes, and disruption of energy synthesis may occur at any time once the intracellular accumulation of reactive nitrogen species and ROS exceeds the maximum load of the neuronal antioxidant system (Martínez-Ruiz et al., 2011). Therefore, new technologies targeting subcellular delivery of drugs have great potential to rescue mitochondrial dysfunction (Sun et al., 2019).

Different SERCA2b mutants lead to ER Ca^{2+} depletion and mitochondrial dysfunction in response to excitatory events. It is noteworthy that part of the reason is the decrease in pumping capacity (LOF type) and the other factor is the increase in leakage (GOF type), which determines the difference in the scheme of restoring ER Ca^{2+} homeostasis. It is also true that CDN1163 enhances the activity of LOF-type pumps (G23R, D567, and I1014V) to inhibit glutamate-induced excitotoxicity, but not the GOF-type mutant (G860S) (**Figure 5**). Genetic and phenotypic heterogeneity leads to differences in regimens to treat gene-related disorders. For example, in *SCN2A*, patients with GOF mutations (increased sodium channel activity) respond well to sodium channel blockers (SCBs), whereas patients with LOF (decreased channel availability and membrane excitability) mutations experience exacerbated seizures due to SCB use (Wolff et al., 2017). Notably, the severity of the *ATP2A2* mutant phenotypes parallels the preserved SERCA2 pump activity (Ahn et al., 2003), suggesting that enhancing SERCA2 pump activity and stabilizing ER Ca^{2+} storage are vital to the treatment of excitotoxicity-related disorders. For example, in a neuropathic pain model, enhanced SERCA2 expression or activity in dorsal root ganglia neurons alleviated mechanical and thermal abnormalities in pain, and the reduction of ERS was accompanied by morphological and functional recovery (Li et al., 2022). CDN1163 increased ER Ca^{2+} content, rescued ERS-induced neuronal death *in vitro*, and showed significant efficacy in a 6-hydroxydopamine-induced Parkinson's disease rat model (Dahl, 2017). The dystrophic phenotype of dystrophin-null transgenic mice was ameliorated by CDN1163, which effectively prevented exercise-induced muscle damage and restored mitochondrial function (Nogami et al., 2021).

Organelles are in a delicate and dynamic homeostasis conducted by Ca^{2+}. As depicted in **Figure 7**, ER Ca^{2+} depletion caused by SERCA2b mutations disrupts this balance, leading to the activation of a series of cell-death signaling pathways. Targeted treatments against organelles may be a potential approach to synergistically enhance the

neuroprotective function of glutamate receptor inhibitors or glutamate transporters (Wang K. et al., 2022; Wei et al., 2022). For example, recovery of the mitochondrial function shows potential therapeutic strategies for traumatic brain injury (Cheng et al., 2012) and neurodegenerative diseases (Cunnane et al., 2020). The suppression of ERS also mitigates epileptic behaviors of the seizure model (Yokoi et al., 2015; Zhu et al., 2017) and AMPA-induced cognitive impairment in rats (Bhardwaj et al., 2021). In recent years, another essential Ca^{2+} storage-related organelle, the lysosome, has gradually been emphasized with excitotoxicity (Vucicevic et al., 2020; Davis et al., 2021). Furthermore, enhanced cytoprotective autophagy can mitigate glutamate-induced excitotoxicity. We may have long overlooked that other cations, such as zinc ions, may play an essential role in AMPK-mediated excitotoxicity (Granzotto et al., 2020; Kim et al., 2020). New ion-tracing techniques, such as ultrahigh-resolution optical microscopy, are promising approaches that can be used to unravel these mysteries (Chen Q. et al., 2020; Fang et al., 2021; Wang L. et al., 2022).

CONCLUSION

The current study demonstrates that SERCA2 mutants exacerbate the excitotoxicity of hypo-glutamate stimulation on HT22. SERCA2 mutants accelerate ER Ca^{2+} depletion by either LOF (reduced pumping capacity) or GOF (acquired ion leakage), leading to ERS. The occurrence of ER Ca^{2+} depletion increases MAM formation, contributing to mitochondrial Ca^{2+} overload and dysfunction. Rescuing the SERCA2 pumping capacity or inhibition of Ca^{2+} leak attenuates Ca^{2+} depletion and inhibits excitotoxicity in response to hypo-glutamate stimulation. The stabilization of SRECA2b function is a critical therapeutic target against glutamate-induced excitotoxicity. These data will expand understanding of organelle regulatory networks and facilitate the discovery and creation of drugs against excitatory/inhibitory imbalance in the CNS.

DATA AVAILABILITY STATEMENT

The original contributions presented in the study are included in the article/**Supplementary Materials**, further inquiries can be directed to the corresponding authors.

AUTHOR CONTRIBUTIONS

FY, JP, WZ, and NP designed research; WZ, FHY, JX, LY performed research; WZ, FHY, JX; MK, FY, JP and NP performed data analysis; WZ, LY, MK and FY wrote the manuscript. All others read, edited, and approved the manuscript.

FUNDING

This work was supported by the National Key R&D Program of China (2021YFC2700903), National Natural Science Foundation of China (81771408, 82001449), the Hunan Key Research and Development Program (No. 2019SK2081), the Fundamental Research Funds for the Central Universities of Central South University (2019zzts347).

ACKNOWLEDGMENTS

We thank the Center for Medical Genetics and Clinical Research Center for Children Neurodevelopmental disabilities of Hunan Province for providing the platform and the personnel who work there for giving support and guidance.

SUPPLEMENTARY MATERIAL

The Supplementary Material for this article can be found online at: https://www.frontiersin.org/articles/10.3389/fphar.2022.877175/full#supplementary-material

REFERENCES

Ahn, W., Lee, M. G., Kim, K. H., and Muallem, S. (2003). Multiple Effects of SERCA2b Mutations Associated with Darier's Disease. *J. Biol. Chem.* 278 (23), 20795–20801. doi:10.1074/jbc.M301638200

Allen, C. A., and Ivester, J. R. (2017). Ketamine for Pain Management-Side Effects & Potential Adverse Events. *Pain Manag. Nurs.* 18 (6), 372–377. doi:10.1016/j.pmn.2017.05.006

Andre, V. M., Cepeda, C., and Levine, M. S. (2010). Dopamine and Glutamate in Huntington's Disease: A Balancing Act. *CNS Neurosci. Ther.* 16 (3), 163–178. doi:10.1111/j.1755-5949.2010.00134.x

Angelova, P. R., Vinogradova, D., Neganova, M. E., Serkova, T. P., Sokolov, V. V., Bachurin, S. O., et al. (2019). Pharmacological Sequestration of Mitochondrial Calcium Uptake Protects Neurons against Glutamate Excitotoxicity. *Mol. Neurobiol.* 56 (3), 2244–2255. doi:10.1007/s12035-018-1204-8

Artigas, P., and Gadsby, D. C. (2003). Na^+/K^+-pump Ligands Modulate Gating of Palytoxin-Induced Ion Channels. *Proc. Natl. Acad. Sci. U S A.* 100 (2), 501–505. doi:10.1073/pnas.0135849100

Baba-Aissa, F., Raeymaekers, L., Wuytack, F., Dode, L., and Casteels, R. (1998). Distribution and Isoform Diversity of the Organellar Ca^{2+} Pumps in the Brain. *Mol. Chem. Neuropathol.* 33 (3), 199–208. doi:10.1007/BF02815182

Berridge, M. J. (2010). Calcium Hypothesis of Alzheimer's Disease. *Pflugers Arch. Eur. J. Physiol.* 459 (3), 441–449. doi:10.1007/s00424-009-0736-1

Bhardwaj, A., Bhardwaj, R., Sharma, S., Sharma, S. K., Dhawan, D. K., and Kaur, T. (2021). AMPA Induced Cognitive Impairment in Rats: Establishing the Role of Endoplasmic Reticulum Stress Inhibitor, 4-PBA. *J. Neurosci. Res.* 99 (10), 2573–2591. doi:10.1002/jnr.24859

Binvignat, O., and Olloquequi, J. (2020). Excitotoxicity as a Target against Neurodegenerative Processes. *Curr. Pharm. Des.* 26 (12), 1251–1262. doi:10.2174/1381612826666200113162641

Bouchard, R., Pattarini, R., and Geiger, J. D. (2003). Presence and Functional Significance of Presynaptic Ryanodine Receptors. *Prog. Neurobiol.* 69 (6), 391–418. doi:10.1016/s0301-0082(03)00053-4

Britzolaki, A., Saurine, J., Flaherty, E., Thelen, C., and Pitychoutis, P. M. (2018). The SERCA2: A Gatekeeper of Neuronal Calcium Homeostasis in the Brain. *Cell. Mol. Neurobiol.* 38 (5), 981–994. doi:10.1007/s10571-018-0583-8

Brown, P. D., Pugh, S., Laack, N. N., Wefel, J. S., Khuntia, D., Meyers, C., et al. (2013). Memantine for the Prevention of Cognitive Dysfunction in Patients

Receiving Whole-Brain Radiotherapy: A Randomized, Double-Blind, Placebo-Controlled Trial. *Neuro Oncol.* 15 (10), 1429–1437. doi:10.1093/neuonc/not114

Cederlöf, M., Bergen, S. E., Långström, N., Larsson, H., Boman, M., Craddock, N., et al. (2015). The Association between Darier Disease, Bipolar Disorder, and Schizophrenia Revisited: a Population-Based Family Study. *Bipolar Disord.* 17 (3), 340–344. doi:10.1111/bdi.12257

Chen J, J., Sitsel, A., Benoy, V., Sepúlveda, M. R., and Vangheluwe, P. (2020). Primary Active Ca^{2+} Transport Systems in Health and Disease. *Cold Spring Harb. Perspect. Biol.* 12 (2), a035113. doi:10.1101/cshperspect.a035113

Chen Q, Q., Shao, X., Hao, M., Fang, H., Guan, R., Tian, Z., et al. (2020). Quantitative Analysis of Interactive Behavior of Mitochondria and Lysosomes Using Structured Illumination Microscopy. *Biomaterials* 250, 120059. doi:10.1016/j.biomaterials.2020.120059

Cheng, G., Kong, R.-h., Zhang, L.-m., and Zhang, J.-n. (2012). Mitochondria in Traumatic Brain Injury and Mitochondrial-Targeted Multipotential Therapeutic Strategies. *Br. J. Pharmacol.* 167 (4), 699–719. doi:10.1111/j.1476-5381.2012.02025.x

Choi, D. W. (1987). Ionic Dependence of Glutamate Neurotoxicity. *J. Neurosci.* 7 (2), 369–379. doi:10.1523/jneurosci.07-02-00369.1987

Cunnane, S. C., Trushina, E., Morland, C., Prigione, A., Casadesus, G., Andrews, Z. B., et al. (2020). Brain Energy rescue: an Emerging Therapeutic Concept for Neurodegenerative Disorders of Ageing. *Nat. Rev. Drug Discov.* 19 (9), 609–633. doi:10.1038/s41573-020-0072-x

Dahl, R. (2017). A New Target for Parkinson's Disease: Small Molecule SERCA Activator CDN1163 Ameliorates Dyskinesia in 6-OHDA-Lesioned Rats. *Bioorg. Med. Chem.* 25 (1), 53–57. doi:10.1016/j.bmc.2016.10.008

Davis, S. M., Lees, K. R., Albers, G. W., Diener, H. C., Markabi, S., Karlsson, G., et al. (2000). Selfotel in Acute Ischemic Stroke : Possible Neurotoxic Effects of an NMDA Antagonist. *Stroke* 31 (2), 347–354. doi:10.1161/01.str.31.2.347

Davis, S. E., Roth, J. R., Aljabi, Q., Hakim, A. R., Savell, K. E., Day, J. J., et al. (2021). Delivering Progranulin to Neuronal Lysosomes Protects against Excitotoxicity. *J. Biol. Chem.* 297 (3), 100993. doi:10.1016/j.jbc.2021.100993

de Miranda, A. S., Brant, F., Vieira, L. B., Rocha, N. P., Vieira, É. L. M., Rezende, G. H. S., et al. (2017). A Neuroprotective Effect of the Glutamate Receptor Antagonist MK801 on Long-Term Cognitive and Behavioral Outcomes Secondary to Experimental Cerebral Malaria. *Mol. Neurobiol.* 54 (9), 7063–7082. doi:10.1007/s12035-016-0226-3

Decuypere, J. P., Monaco, G., Bultynck, G., Missiaen, L., De Smedt, H., and Parys, J. B. (2011). The IP(3) Receptor-Mitochondria Connection in Apoptosis and Autophagy. *Biochim. Biophys. Acta* 1813 (5), 1003–1013. doi:10.1016/j.bbamcr.2010.11.023

Eid, T., Gruenbaum, S. E., Dhaher, R., Lee, T. W., Zhou, Y., and Danbolt, N. C. (2016). The Glutamate-Glutamine Cycle in Epilepsy. *Adv. Neurobiol.* 13, 351–400. doi:10.1007/978-3-319-45096-4_14

Fang, H., Geng, S., Hao, M., Chen, Q., Liu, M., Liu, C., et al. (2021). Simultaneous Zn^{2+} Tracking in Multiple Organelles Using Super-resolution Morphology-Correlated Organelle Identification in Living Cells. *Nat. Commun.* 12 (1), 109. doi:10.1038/s41467-020-20309-7

Gadsby, D. C. (2009). Ion Channels versus Ion Pumps: the Principal Difference, in Principle. *Nat. Rev. Mol. Cel Biol.* 10 (5), 344–352. doi:10.1038/nrm2668

García-Pérez, C., Hajnóczky, G., and Csordás, G. (2008). Physical Coupling Supports the Local Ca^{2+} Transfer between Sarcoplasmic Reticulum Subdomains and the Mitochondria in Heart Muscle. *J. Biol. Chem.* 283 (47), 32771–32780. doi:10.1074/jbc.M803385200

Gemes, G., Rigaud, M., Weyker, P. D., Abram, S. E., Weihrauch, D., Poroli, M., et al. (2009). Depletion of Calcium Stores in Injured Sensory Neurons: Anatomic and Functional Correlates. *Anesthesiology* 111 (2), 393–405. doi:10.1097/ALN.0b013e3181ae63b0

Ghemrawi, R., and Khair, M. (2020). Endoplasmic Reticulum Stress and Unfolded Protein Response in Neurodegenerative Diseases. *Int. J. Mol. Sci.* 21 (17), 6127. doi:10.3390/ijms21176127

Giorgi, C., De Stefani, D., Bononi, A., Rizzuto, R., and Pinton, P. (2009). Structural and Functional Link between the Mitochondrial Network and the Endoplasmic Reticulum. *Int. J. Biochem. Cel Biol.* 41 (10), 1817–1827. doi:10.1016/j.biocel.2009.04.010

Gordon-Smith, K., Green, E., Grozeva, D., Tavadia, S., Craddock, N., and Jones, L. (2018). Genotype-phenotype Correlations in Darier Disease: A Focus on the Neuropsychiatric Phenotype. *Am. J. Med. Genet. B Neuropsychiatr. Genet.* 177 (8), 717–726. doi:10.1002/ajmg.b.32679

Granzotto, A., Canzoniero, L. M. T., and Sensi, S. L. (2020). A Neurotoxic Ménage-À-Trois: Glutamate, Calcium, and Zinc in the Excitotoxic Cascade. *Front. Mol. Neurosci.* 13, 600089. doi:10.3389/fnmol.2020.600089

Green, D. R., and Kroemer, G. (2004). The Pathophysiology of Mitochondrial Cell Death. *Science* 305 (5684), 626–629. doi:10.1126/science.1099320

Green, J. L., Dos Santos, W. F., and Fontana, A. C. K. (2021). Role of Glutamate Excitotoxicity and Glutamate Transporter EAAT2 in Epilepsy: Opportunities for Novel Therapeutics Development. *Biochem. Pharmacol.* 193, 114786. doi:10.1016/j.bcp.2021.114786

Hajnóczky, G., Robb-Gaspers, L. D., Seitz, M. B., and Thomas, A. P. (1995). Decoding of Cytosolic Calcium Oscillations in the Mitochondria. *Cell* 82 (3), 415–424. doi:10.1016/0092-8674(95)90430-1

Hartter, D. E., Burton, P. R., and Laveri, L. A. (1987). Distribution and Calcium-Sequestering Ability of Smooth Endoplasmic Reticulum in Olfactory Axon Terminals of Frog Brain. *Neuroscience* 23 (1), 371–386. doi:10.1016/0306-4522(87)90297-1

Hayashi, T., Rizzuto, R., Hajnoczky, G., and Su, T. P. (2009). MAM: More Than Just a Housekeeper. *Trends Cel Biol.* 19 (2), 81–88. doi:10.1016/j.tcb.2008.12.002

Hayashi, M. K. (2018). Structure-Function Relationship of Transporters in the Glutamate-Glutamine Cycle of the Central Nervous System. *Int. J. Mol. Sci.* 19 (4), 1177. doi:10.3390/ijms19041177

Hetz, C., and Saxena, S. (2017). ER Stress and the Unfolded Protein Response in Neurodegeneration. *Nat. Rev. Neurol.* 13 (8), 477–491. doi:10.1038/nrneurol.2017.99

Hynd, M., Scott, H. L., and Dodd, P. R. (2004). Glutamate-mediated Excitotoxicity and Neurodegeneration in Alzheimer's Disease. *Neurochem. Int.* 45, 583–595. doi:10.1016/j.neuint.2004.03.007

Ikonomidou, C., and Turski, L. (1995). Excitotoxicity and Neurodegenerative Diseases. *Curr. Opin. Neurol.* 8 (6), 487–497. doi:10.1097/00019052-199512000-00017

Kaneko, M., Desai, B. S., and Cook, B. (2014). Ionic Leakage Underlies a Gain-Of-Function Effect of Dominant Disease Mutations Affecting Diverse P-type ATPases. *Nat. Genet.* 46 (2), 144–151. doi:10.1038/ng.2850

Kim, Y. H., Eom, J. W., and Koh, J. Y. (2020). Mechanism of Zinc Excitotoxicity: A Focus on AMPK. *Front. Neurosci.* 14, 577958. doi:10.3389/fnins.2020.577958

Kroppenstedt, S. N., Schneider, G. H., Thomale, U. W., and Unterberg, A. W. (1998). Neuroprotective Properties of Aptiganel HCL (Cerestat) Following Controlled Cortical Impact Injury. *Acta Neurochir Suppl.* 71, 114–116. doi:10.1007/978-3-7091-6475-4_34

Lebiedzinska, M., Szabadkai, G., Jones, A. W., Duszynski, J., and Wieckowski, M. R. (2009). Interactions between the Endoplasmic Reticulum, Mitochondria, Plasma Membrane and Other Subcellular Organelles. *Int. J. Biochem. Cel Biol.* 41 (10), 1805–1816. doi:10.1016/j.biocel.2009.02.017

Li, S., Zhao, F., Tang, Q., Xi, C., He, J., Wang, Y., et al. (2022). Sarco/endoplasmic Reticulum Ca^{2+}-ATPase (SERCA2b) Mediates Oxidation-induced Endoplasmic Reticulum Stress to Regulate Neuropathic Pain. *Br. J. Pharmacol.* 179, 2016–2036. doi:10.1111/bph.15744

Liu, Z., Qiu, X., Mak, S., Guo, B., Hu, S., Wang, J., et al. (2020). Multifunctional Memantine Nitrate Significantly Protects against Glutamate-Induced Excitotoxicity via Inhibiting Calcium Influx and Attenuating PI3K/Akt/GSK3beta Pathway. *Chem. Biol. Interact* 325, 109020. doi:10.1016/j.cbi.2020.109020

Lloyd-Evans, E., Pelled, D., Riebeling, C., Bodennec, J., De-Morgan, A., Waller, H., et al. (2003). Glucosylceramide and Glucosylsphingosine Modulate Calcium Mobilization from Brain Microsomes via Different Mechanisms. *J. Biol. Chem.* 278 (26), 23594–23599. doi:10.1074/jbc.M300212200

Lysakowski, A., Figueras, H., Price, S. D., and Peng, Y. Y. (1999). Dense-cored Vesicles, Smooth Endoplasmic Reticulum, and Mitochondria Are Closely Associated with Non-specialized Parts of Plasma Membrane of Nerve Terminals: Implications for Exocytosis and Calcium Buffering by Intraterminal Organelles. *J. Comp. Neurol.* 403 (3), 378–390. doi:10.1002/(sici)1096-9861(19990118)403:3<378::aid-cne7>3.0.co;2-x

Martínez-Ruiz, A., Cadenas, S., and Lamas, S. (2011). Nitric Oxide Signaling: Classical, Less Classical, and Nonclassical Mechanisms. *Free Radic. Biol. Med.* 51 (1), 17–29. doi:10.1016/j.freeradbiomed.2011.04.010

Mata, A. M., and Sepúlveda, M. R. (2005). Calcium Pumps in the central Nervous System. *Brain Res. Brain Res. Rev.* 49 (2), 398–405. doi:10.1016/j.brainresrev.2004.11.004

Meldrum, B. S. (1993). Excitotoxicity and Selective Neuronal Loss in Epilepsy. *Brain Pathol.* 3 (4), 405–412. doi:10.1111/j.1750-3639.1993.tb00768.x

Meldrum, B. S. (2000). Glutamate as a Neurotransmitter in the Brain: Review of Physiology and Pathology. *J. Nutr.* 130 (4), 1007S–15S. doi:10.1093/jn/130.4.1007S

Mira, R. G., and Cerpa, W. (2021). Building a Bridge between NMDAR-Mediated Excitotoxicity and Mitochondrial Dysfunction in Chronic and Acute Diseases. *Cel. Mol. Neurobiol.* 41 (7), 1413–1430. doi:10.1007/s10571-020-00924-0

Moncada, S., and Erusalimsky, J. D. (2002). Does Nitric Oxide Modulate Mitochondrial Energy Generation and Apoptosis? *Nat. Rev. Mol. Cel Biol.* 3 (3), 214–220. doi:10.1038/nrm762

Monti, B., and Contestabile, A. (2000). Blockade of the NMDA Receptor Increases Developmental Apoptotic Elimination of Granule Neurons and Activates Caspases in the Rat Cerebellum. *Eur. J. Neurosci.* 12 (9), 3117–3123. doi:10.1046/j.1460-9568.2000.00189.x

Nakajima, K., Ishiwata, M., Weitemier, A. Z., Shoji, H., Monai, H., Miyamoto, H., et al. (2021). Brain-specific Heterozygous Loss-Of-Function of ATP2A2, Endoplasmic Reticulum Ca^{2+} Pump Responsible for Darier's Disease, Causes Behavioral Abnormalities and a Hyper-Dopaminergic State. *Hum. Mol. Genet.* 30 (18), 1762–1772. doi:10.1093/hmg/ddab137

Nakamura, T., Kazuno, A. a., Nakajima, K., Kusumi, I., Tsuboi, T., and Kato, T. (2016). Loss of Function Mutations in ATP2A2 and Psychoses: A Case Report and Literature Survey. *Psychiatry Clin. Neurosci.* 70, 342–350. doi:10.1111/pcn.12395

Ngomba, R. T., and van Luijtelaar, G. (2018). Metabotropic Glutamate Receptors as Drug Targets for the Treatment of Absence Epilepsy. *Curr. Opin. Pharmacol.* 38, 43–50. doi:10.1016/j.coph.2018.01.012

Nicholls, D. G., and Budd, S. L. (1998). Neuronal Excitotoxicity: the Role of Mitochondria. *Biofactors* 8 (3-4), 287–299. doi:10.1002/biof.5520080317

Nogami, K., Maruyama, Y., Sakai-Takemura, F., Motohashi, N., Elhussieny, A., Imamura, M., et al. (2021). Pharmacological Activation of SERCA Ameliorates Dystrophic Phenotypes in Dystrophin-Deficient Mdx Mice. *Hum. Mol. Genet.* 30 (11), 1006–1019. doi:10.1093/hmg/ddab100

Olloquequi, J., Cornejo-Córdova, E., Verdaguer, E., Soriano, F. X., Binvignat, O., Auladell, C., et al. (2018). Excitotoxicity in the Pathogenesis of Neurological and Psychiatric Disorders: Therapeutic Implications. *J. Psychopharmacol.* 32 (3), 265–275. doi:10.1177/0269881118754680

Olney, J. W. (1969). Brain Lesions, Obesity, and Other Disturbances in Mice Treated with Monosodium Glutamate. *Science* 164 (3880), 719–721. doi:10.1126/science.164.3880.719

Parsons, M. P., and Raymond, L. A. (2014). Extrasynaptic NMDA Receptor Involvement in central Nervous System Disorders. *Neuron* 82 (2), 279–293. doi:10.1016/j.neuron.2014.03.030

Parsons, J. T., Churn, S. B., Kochan, L. D., and Delorenzo, R. J. (2000). Pilocarpine-induced Status Epilepticus Causes N-Methyl-D-Aspartate Receptor-dependent Inhibition of Microsomal Mg(2+)/Ca(2+) ATPase-Mediated Ca(2+) Uptake. *J. Neurochem.* 75 (3), 1209–1218. doi:10.1046/j.1471-4159.2000.0751209.x

Peng, J., Wang, Y., He, F., Chen, C., Wu, L. W., Yang, L. F., et al. (2018). Novel West Syndrome Candidate Genes in a Chinese Cohort. *CNS Neurosci. Ther.* 24 (12), 1196–1206. doi:10.1111/cns.12860

Plotegher, N., Filadi, R., Pizzo, P., and Duchen, M. R. (2021). Excitotoxicity Revisited: Mitochondria on the Verge of a Nervous Breakdown. *Trends Neurosci.* 44 (5), 342–351. doi:10.1016/j.tins.2021.01.001

Pu, B., Xue, Y., Wang, Q., Hua, C., and Li, X. (2015). Dextromethorphan Provides Neuroprotection via Anti-inflammatory and Anti-excitotoxicity Effects in the Cortex Following Traumatic Brain Injury. *Mol. Med. Rep.* 12 (3), 3704–3710. doi:10.3892/mmr.2015.3830

Rezaeian, A. H., Wei, W., and Inuzuka, H. (2022). The Regulation of Neuronal Autophagy and Cell Survival by MCL1 in Alzheimer's Disease. *Acta Mater. Med.* 1, 42–55. doi:10.15212/amm-2021-0002

Rizzuto, R., Duchen, M. R., and Pozzan, T. (2004). Flirting in Little Space: the ER/mitochondria Ca2+ Liaison. *Sci. STKE* 2004 (215), re1. doi:10.1126/stke.2152004re1

Sano, R., Annunziata, I., Patterson, A., Moshiach, S., Gomero, E., Opferman, J., et al. (2009). GM1-ganglioside Accumulation at the Mitochondria-Associated ER Membranes Links ER Stress to Ca(2+)-dependent Mitochondrial Apoptosis. *Mol. Cel.* 36 (3), 500–511. doi:10.1016/j.molcel.2009.10.021

Slieker, F. J., Kompanje, E. J., Murray, G. D., Ohman, J., Stocchetti, N., Teasdale, S. G., et al. (2008). Importance of Screening Logs in Clinical Trials for Severe Traumatic Brain Injury. *Neurosurgery* 62 (6). doi:10.1227/01.neu.0000333304.79931.4d

Sun, Y., Zhan, A., Zhou, S., Kuang, X., Shen, H., Liu, H., et al. (2019). A Novel Mitochondria-Targeting Tetrapeptide for Subcellular Delivery of Nanoparticles. *Chin. Chem. Lett.* 30, 1435–1439. doi:10.1016/j.cclet.2019.05.001

Verkhratsky, A., and Shmigol, A. (1996). Calcium-induced Calcium Release in Neurones. *Cell Calcium* 19 (1), 1–14. doi:10.1016/S0143-4160(96)90009-3

Vucicevic, L., Misirkic, M., Ciric, D., Martinovic, T., Jovanovic, M., Isakovic, A., et al. (2020). Transcriptional Block of AMPK-Induced Autophagy Promotes Glutamate Excitotoxicity in Nutrient-Deprived SH-SY5Y Neuroblastoma Cells. *Cell. Mol. Life Sci.* 77 (17), 3383–3399. doi:10.1007/s00018-019-03356-2

Walter, L., and Hajnóczky, G. (2005). Mitochondria and Endoplasmic Reticulum: The Lethal Interorganelle Cross-Talk. *J. Bioenerg. Biomembr.* 37 (3), 191–206. doi:10.1007/s10863-005-6600-x

Wang, Y., Bruce, A. T., Tu, C., Ma, K., Zeng, L., Zheng, P., et al. (2011). Protein Aggregation of SERCA2 Mutants Associated with Darier Disease Elicits ER Stress and Apoptosis in Keratinocytes. *J. Cel Sci.* 124 (21), 3568–3580. doi:10.1242/jcs.084053

Wang K, K., Xiang, Y., Pan, W., Wang, H., Li, N., and Tang, B. (2022). An Endoplasmic Reticulum-Targeted Organic Photothermal Agent for Enhanced Cancer Therapy. *Chin. Chem. Lett.* 33 (2), 793–797. doi:10.1016/j.cclet.2021.08.087

Wang L, L., Chen, R., Han, G., Liu, X., Huang, T., Diao, J., et al. (2022). Super-resolution Analyzing Spatial Organization of Lysosomes with an Organic Fluorescent Probe. *Exploration*, 0210215. doi:10.1002/EXP.20210215

Wei, Y., Kong, L., Chen, H., Liu, Y., Xu, Y., Wang, H., et al. (2022). Super-resolution Image-Based Tracking of Drug Distribution in Mitochondria of a Label-free Naturally Derived Drug Molecules. *Chem. Eng. J.* 429, 132134. doi:10.1016/j.cej.2021.132134

Wolff, M., Johannesen, K. M., Hedrich, U. B. S., Masnada, S., Rubboli, G., Gardella, E., et al. (2017). Genetic and Phenotypic Heterogeneity Suggest Therapeutic Implications in SCN2A-Related Disorders. *Brain* 140 (5), 1316–1336. doi:10.1093/brain/awx054

Yi, M., Weaver, D., and Hajnóczky, G. (2004). Control of Mitochondrial Motility and Distribution by the Calcium Signal: A Homeostatic Circuit. *J. Cel Biol.* 167 (4), 661–672. doi:10.1083/jcb.200406038

Yokoi, N., Fukata, Y., Kase, D., Miyazaki, T., Jaegle, M., Ohkawa, T., et al. (2015). Chemical Corrector Treatment Ameliorates Increased Seizure Susceptibility in a Mouse Model of Familial Epilepsy. *Nat. Med.* 21 (1), 19–26. doi:10.1038/nm.3759

Zaitsev, A. V., Smolensky, I. V., Jorratt, P., and Ovsepian, S. V. (2020). Neurobiology, Functions, and Relevance of Excitatory Amino Acid Transporters (EAATs) to Treatment of Refractory Epilepsy. *CNS Drugs* 34 (11), 1089–1103. doi:10.1007/s40263-020-00764-y

Zhang, Z., Zhang, S., Fu, P., Zhang, Z., Lin, K., Ko, J. K., et al. (2019). Roles of Glutamate Receptors in Parkinson's Disease. *Int. J. Mol. Sci.* 20 (18), 4391. doi:10.3390/ijms20184391

Zhu, X., Dong, J., Xia, Z., Zhang, A., Chao, J., and Yao, H. (2017). Repeated Restraint Stress Increases Seizure Susceptibility by Activation of Hippocampal Endoplasmic Reticulum Stress. *Neurochem. Int.* 110, 25–37. doi:10.1016/j.neuint.2017.09.002

Conflict of Interest: The authors declare that the research was conducted in the absence of any commercial or financial relationships that could be construed as a potential conflict of interest.

Publisher's Note: All claims expressed in this article are solely those of the authors and do not necessarily represent those of their affiliated organizations, or those of the publisher, the editors and the reviewers. Any product that may be evaluated in this article, or claim that may be made by its manufacturer, is not guaranteed or endorsed by the publisher.

Copyright © 2022 Zhang, Ye, Pang, Kessi, Xiong, Chen, Peng, Yang and Yin. This is an open-access article distributed under the terms of the Creative Commons Attribution License (CC BY). The use, distribution or reproduction in other forums is permitted, provided the original author(s) and the copyright owner(s) are credited and that the original publication in this journal is cited, in accordance with accepted academic practice. No use, distribution or reproduction is permitted which does not comply with these terms.

frontiers | Frontiers in Pharmacology

ORIGINAL RESEARCH
published: 01 June 2022
doi: 10.3389/fphar.2022.871059

A Dual-Labeling Probe for Super-Resolution Imaging to Detect Mitochondrial Reactive Sulfur Species in Live Cells

Maomao Hu[1], Boyang Wang[1], Hongdan Zhang[1], Han Wang[2,3], Huixin Li[4], Xinyu Zhang[1], Jinjin Zhang[1], Qianrun Lu[5], Guiqian Fang[3], Juan Wang[6]* and Bo Dong[1,2,4]**

[1]Department of Cardiology, Shandong Provincial Hospital, Shandong University, Jinan, China, [2]Department of Cardiology, Shandong Provincial Hospital Affiliated to Shandong First Medical University, Jinan, China, [3]School of Life Sciences, Shandong First Medical University & Shandong Academy of Medical Sciences, Jinan, China, [4]Department of Cardiology, Shandong Traditional Chinese Medicine University, Jinan, China, [5]Shandong Cancer Hospital and Institute, Jinan, China, [6]Jinan Maternity and Child Care Hospital Affiliated to Shandong First Medical University, Jinan, China

OPEN ACCESS

Edited by:
Qixin Chen,
Shandong First Medical University, China

Reviewed by:
Christopher V. Kelly,
Wayne State University, United States
Chengzhi Jin,
Guangzhou Medical University, China

***Correspondence:**
Bo Dong
bodong@sdu.edu.cn
Juan Wang
smartjww@126.com
Guiqian Fang
fangguiqian@sdfmu.edu.cn

Specialty section:
This article was submitted to Pharmacology of Anti-Cancer Drugs, a section of the journal Frontiers in Pharmacology

Received: 07 February 2022
Accepted: 30 March 2022
Published: 01 June 2022

Citation:
Hu M, Wang B, Zhang H, Wang H, Li H, Zhang X, Zhang J, Lu Q, Fang G, Wang J and Dong B (2022) A Dual-Labeling Probe for Super-Resolution Imaging to Detect Mitochondrial Reactive Sulfur Species in Live Cells. Front. Pharmacol. 13:871059. doi: 10.3389/fphar.2022.871059

Background: Mitochondria are the main sites of reactive sulfur species (RSS) production in living cells. RSS in mitochondria play an important role in physiological and pathological processes of life. In this study, a dual-labeling probe that could simultaneously label the mitochondrial membrane and matrix was designed to quantitatively detect RSS of mitochondria in living cells using nano-level super-resolution imaging.

Methods: A fluorescent probe CPE was designed and synthesized. The cytotoxicity of CPE was determined and co-localization of CPE with a commercial mitochondrial probe was analyzed in HeLa cells. Then, the uptake patterns of CPE in HeLa cells at different temperatures and endocytosis levels were investigated. The staining characteristics of CPE under different conditions were imaged and quantitated under structured illumination microscopy.

Results: A fluorescence probe CPE reacting to RSS was developed, which could simultaneously label the mitochondrial membrane with green fluorescence and the mitochondrial matrix with red fluorescence. CPE was able to demonstrate the mitochondrial morphology and detect the changes of RSS in mitochondria. With the increase of mitochondrial RSS concentration, the light of the red matrix will be quenched.

Conclusion: CPE provides a strategy for the design of probes and an attractive tool for accurate examination to changes of mitochondrial morphology and RSS in mitochondria in living cells at the nanoscale.

Keywords: super-resolution imaging, mitochondria, RSS, small molecules probe, nanoscale

Abbreviations: SIM, structured illumination microscopy; CCK-8, Cell Counting Kit-8; TEM, traditional transmission microscope; H_2S, hydrogen sulfide; SO_2, sulfur dioxide; Cys, cysteine; Hcy, homocysteine; GSH, reduced glutathione; RSS, reactive sulfur species; MMP, mitochondrial membrane potential.

1 INTRODUCTION

Mitochondria serve as very important organelles in eukaryotic cells, which mainly provide energy for cell activities and are known as the "power factory" of cells (Yousif et al., 2009; Rezaeian et al., 2022; Chen et al., 2021). In addition, mitochondria have various functions of other vital life activities including participating in lipid synthesis, buffering intracellular calcium, and modulating immune response. Moreover, mitochondria are the main sites of reactive sulfur species (RSS) production in living organisms (Vinten, 2020). Intracellular RSS have emerged as a general term for active sulfur-containing biomolecules including hydrogen sulfide (H_2S), sulfur dioxide (SO_2), cysteine (Cys), homocysteine (Hcy), and reduced glutathione (GSH) that play an important role in many physiological and pathological processes. For example, sulfur dioxide (SO_2) is not only likely a primary energy generation for important biosynthetic reactions but also involved in a multitude of biological signaling (Lau and Pluth, 2019). Moderate concentrations of RSS can be healthy, but many studies have shown that excessive RSS would be associated with many diseases, including cardiovascular diseases, neurological diseases, and tumors (Cai et al., 2010; Yan et al., 2019; Shi et al., 2022). Therefore, it is of great significance to develop fluorescent probes that can rapidly, real-time, and accurately detect changes of RSS concentrations in living cells for the diagnosis of related diseases.

At present, fluorescent probes have been developed to detect the content of active sulfur in mitochondria, with good selectivity, quick response (3 min), low cytotoxicity, and good cell permeability (Bai et al., 2021). However, they are not able to reflect the morphology of mitochondria, which could be damaged by excess active sulfur in the body. Mitochondrial morphology including the integrity of mitochondrial outer membrane and the presence of cristae is the most direct reflection of mitochondrial functional integrity (Wiemerslage and Lee, 2016; Ke et al., 2018). In addition, morphological changes in mitochondria that were divided into mitochondrial swelling, rupture, integrity of inner or outer membrane destructions, and mitochondrial crest fracture play a crucial role in occurrence and development of mitochondria-related diseases (Alirol and Martinou, 2006; Yu et al., 2006; Shao et al., 2020). Apart from the deficiencies mentioned earlier, due to the limited resolution and sensitivity of conventional electron microscopy, mitochondria cannot be clearly distinguished from other membranous structures, which is sometimes confusing (Chen et al., 2019).

To solve this problem, we developed a small-molecule fluorescent probe containing nitrogen ions with specific organelle-targeting ability of the mitochondrial membrane and matrix, which could not only demonstrate the morphology of mitochondria but also tract the changes of RSS in the matrix of mitochondria. At the same time, recent development of the extended-resolution microscopy technique and structured illumination microscopy (SIM) (Gustafsson, 2000; Huang et al., 2018) have made it possible to investigate delicate structures of mitochondria in living cells at the nanoscale level (Chen et al., 2018), and based on that, we incubated HeLa cells with **CPE** for 1 h, and then imaged under SIM using a dual-channel mode with excitation at 405 and 561 nm. As expected, **CPE** labeled the mitochondria membrane with green fluorescence and the matrix with red fluorescence. With the increase of active sulfur in the mitochondria, the red matrix fluorescence would be quenched. Meanwhile, mitochondrial morphology may also be changed, which make it possible to further clarify the relationship between the content of active sulfur in mitochondria and the functional status of mitochondria at the nanoscale level. According to the aforementioned information, **CPE** may be a new tool for tracking RSS and the function of mitochondria under SIM, providing a powerful method for investigating diagnosis and treatment strategies for mitochondria-related diseases.

2 RESULTS AND DISCUSSION

2.1 Characterization of CPE

Mitochondria are two-membrane-bound sub-organelles surrounded by an outer and an inner smooth membrane, which is folded to form the cristae (Sasaki, 2010). The inner mitochondrial membrane encircles a space identified as the matrix. The membrane potential difference of mitochondria tends to attract positively charged molecules to accumulate in its interior (Leung et al., 2013). Based on this, we modified the coumarin group with pyridine to make it positively charged. Under the attraction of mitochondrial membrane potential difference, **CPE** can accurately target mitochondria (**Figures 1A,B**) (Zhao et al., 2013; Zhao et al., 2014; Zhao et al., 2015; Shi et al., 2016; Gui et al., 2017). In addition, the fluorophores possess two emission peaks (~500 and 660 nm) (**Figure 1H**), which provides them the chance to label the mitochondrial membrane and matrix. To indicate this point, we incubated **CPE** *in vitro* with lecithin for 1 h, and then imaged using SIM with 405 and 561 channels emitted. As expected, lecithin that loaded **CPE** showed green fluorescence at the excitation of 405 nm and red fluorescence at the excitation of 561 nm (**Supplementary Figure S1**), which suggests that **CPE** is a double-labeled probe. In addition, the fluorophores can react with RSS such as H_2S and SO_2 (**Figures 1C,F**). It is shown that the color of **CPE** changed from mauve to light yellow when it reacted with Na_2SO_3 *in vitro* experiments (**Supplementary Figure S2**). To measure the degree of response to RSS, we used Na_2S as an H_2S donor and Na_2SO_3 as an SO_2 donor to simulate the environment rich in RSS of mitochondria. As observed, the fluorescence of **CPE** decreased distinctly with the increase of RSS (**Figures 1D,G**). The 561 excited light was quenched at 10 equivalent Na_2SO_3, while the 405 excited light did not quench and remained at a certain fluorescence intensity still. Moreover, the probe did not respond to other biologically relevant species such as H_2O_2, ClO^-, and F^- (**Figure 1E**). These results suggest that **CPE** can not only respond to active sulfur and detect the active sulfur content but also have the potential to label mitochondria.

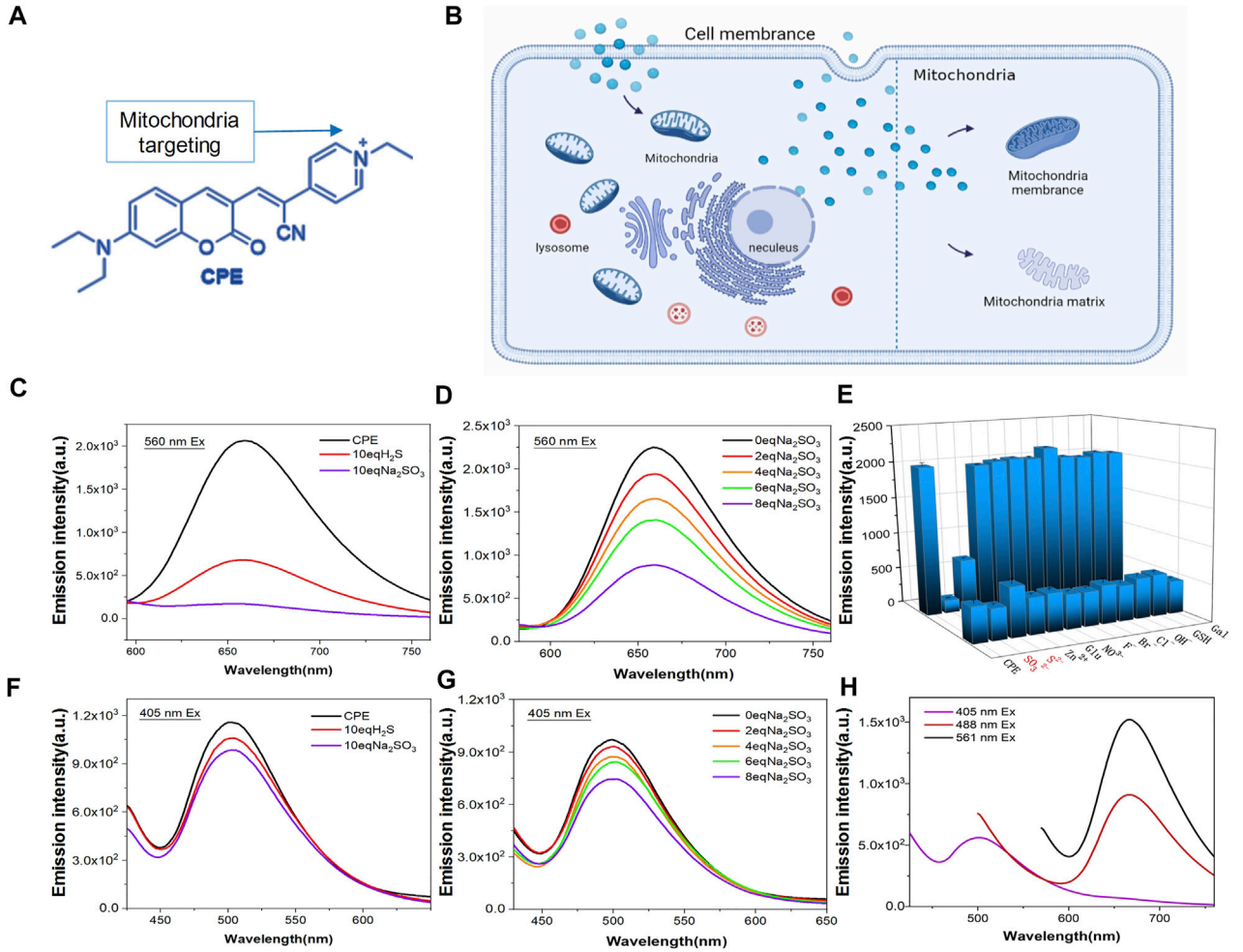

FIGURE 1 | Design and fluorescence characterization of CPE. **(A)** Chemical structure of CPE. **(B)** Staining organelles of CPE. **(E)** Responsive substance of CPE. **(H)** CPE emission spectrogram. **(C,F)** Fluorescence spectra determined with H_2S and Na_2SO_3 treatments. **(D,G)** Fluorescence spectra were determined after response with different concentrations of Na_2SO_3.

2.2 Imaging of CPE in Living Cells

To verify whether **CPE** could target organelles in living cells or not, HeLa cells were incubated with **CPE** and imaged under SIM using a dual-channel mode with excitation at 405 and 561 nm. As shown in SIM images, green fluorescence excited at 405 nm stained the outer membrane of mitochondria, which revealed fibrous, rod-like, and punctate morphology (**Figures 2C,D**), consistent with previous literature reports (Sasaki, 2010). Red particles or fibers with weaker fluorescence excited at 561 were encased in a green membrane, illustrating it targets the mitochondrial matrix (**Figure 2A**). Here is the surprise, **CPE** could show the crest line distribution of mitochondria (**Figure 2B**), which is closely associated with the pathology of cancer, osteoarthritis, and AIDS (Guarani et al., 2015; Blanco et al., 2011). In addition, this scene in live cells could only be captured by SIM compared to other reported methods of imaging (Shao et al., 2020). Therefore, the combination of SIM can take advantage of the probe **CPE**, which suggests its potential for use in the diagnosis of mitochondrial diseases. Next, we used the length-to-width ratio (L/W) to quantitatively analyze the distribution of mitochondria and found that various morphologies could be assigned into four groups as follows: hyperfused ($L/W \geq 5.0$), tubular ($2.0 \leq L/W < 5.0$), intermediate ($1.5 \leq L/W < 2.0$), and round or nearly round ($1.0 \leq L/W < 1.5$) (**Figures 2C–E**) (Cao et al., 2017). The fibrous, rod-shaped, and spotted once mentioned earlier might be classified as hyperfused, tubular, and round (**Figure 2F**), and then, we used CCK-8 assay to evaluate the cytotoxicity of **CPE** to HeLa cells (Qin et al., 2015). No cytotoxicity was shown at the range of 0–20 μM to HeLa cells during 24 h, demonstrating that 10 μM is a relatively safe working concentration for **CPE** with no interference in mitochondrial imaging under SIM in living cells. Finally, different temperatures and endocytosis levels of **CPE** incubated to HeLa cells were observed to define the uptake properties of **CPE**. The cells showed weaker fluorescence when incubated with **CPE** at 4°C (**Supplementary Figure S3**) or with an endocytosis inhibitor (NH_4Cl) (**Supplementary Figure S4**) than that of cells incubated with **CPE** at 37°C (Fang et al., 2019),

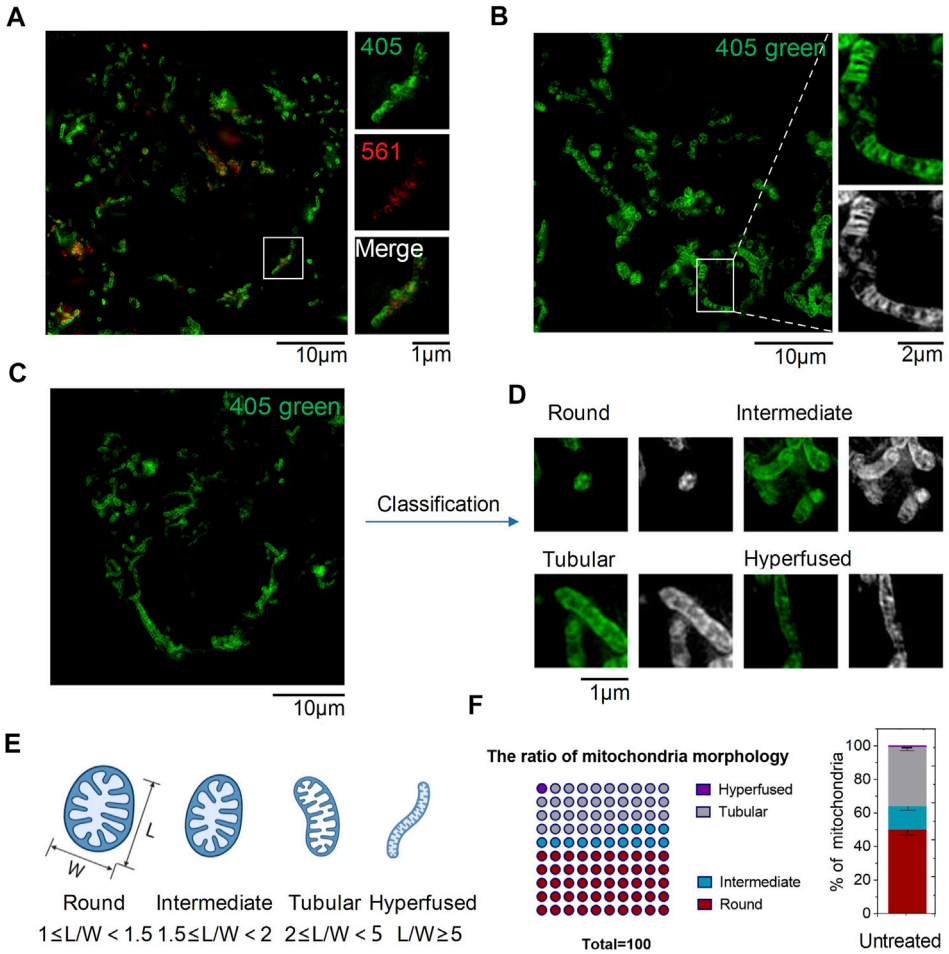

FIGURE 2 | SIM images of CPE puncta in HeLa cells ($\lambda_{ex}1$ = 405 nm and $\lambda_{ex}2$ = 561 nm). **(A)** SIM image of cells labeled with CPE (10 μM) for 1 h. **(B)** Mitochondrial crista. **(C–E)** Mitochondrial morphology of distribution parameters of *L*/*W*. **(F)** Ratio of mitochondrial morphology.

whether it is red or green fluorescence. These results strongly indicate that **CPE** enters cells through energy-dependent endocytosis. Therefore, we conclude that **CPE** stains organelles in living cells with low toxicity and good cell permeability.

2.3 CPE Could Specifically Label Mitochondria

To determine whether **CPE** can specifically label mitochondria, we co-stained the cells with a commercial probe, PKMTDR, for 1 h. The following merged SIM images revealed that the green fluorescence signal of **CPE** colocalized well with the red fluorescence signal of PKMTDR (**Figures 3A,B**), whose Pearson colocalization coefficient (PCC) was as high as 0.72 with PKMTDR (**Figure 3C**). It is clear that **CPE** has high specificity for mitochondrial attachment. Next, we observed whether **CPE**-labeled mitochondria depends on mitochondrial membrane potential (MMP) or not. To damage the membrane potential of mitochondria, HeLa cells were treated with 10 μM carbonyl cyanide m-chlorophenyl hydrazone (CCCP), which was used as a common mitophagy inducer (Chen et al., 2020a). After that, we re-stained the cells with both **CPE** and PKMTDR for co-location imaging (**Figures 3D,E**), while most did not attach to broken mitochondria. This indicates that labeled mitochondria depends on MMP. These results show that **CPE** could not only label mitochondria specifically but also provide references for measuring MMP.

2.4 CPE Can Detect the Active Sulfur Content and Indicate Mitochondrial Status

To confirm whether **CPE** can detect the content of active sulfur in mitochondria, we processed mitochondria with CCCP of 50 μM for 30 min. Mitochondria were broken into round shapes (**Figure 4A**), consistent with previous literature reports (Chen et al., 2020b). Then, *L*/*W* was used to quantitatively analyze the distribution of mitochondrial morphology as before. After that, we used automatic analysis software (ImageJ) to calculate the distribution of individual mitochondria in CCCP-treated HeLa cells and found that the ratio of round structures accounts for

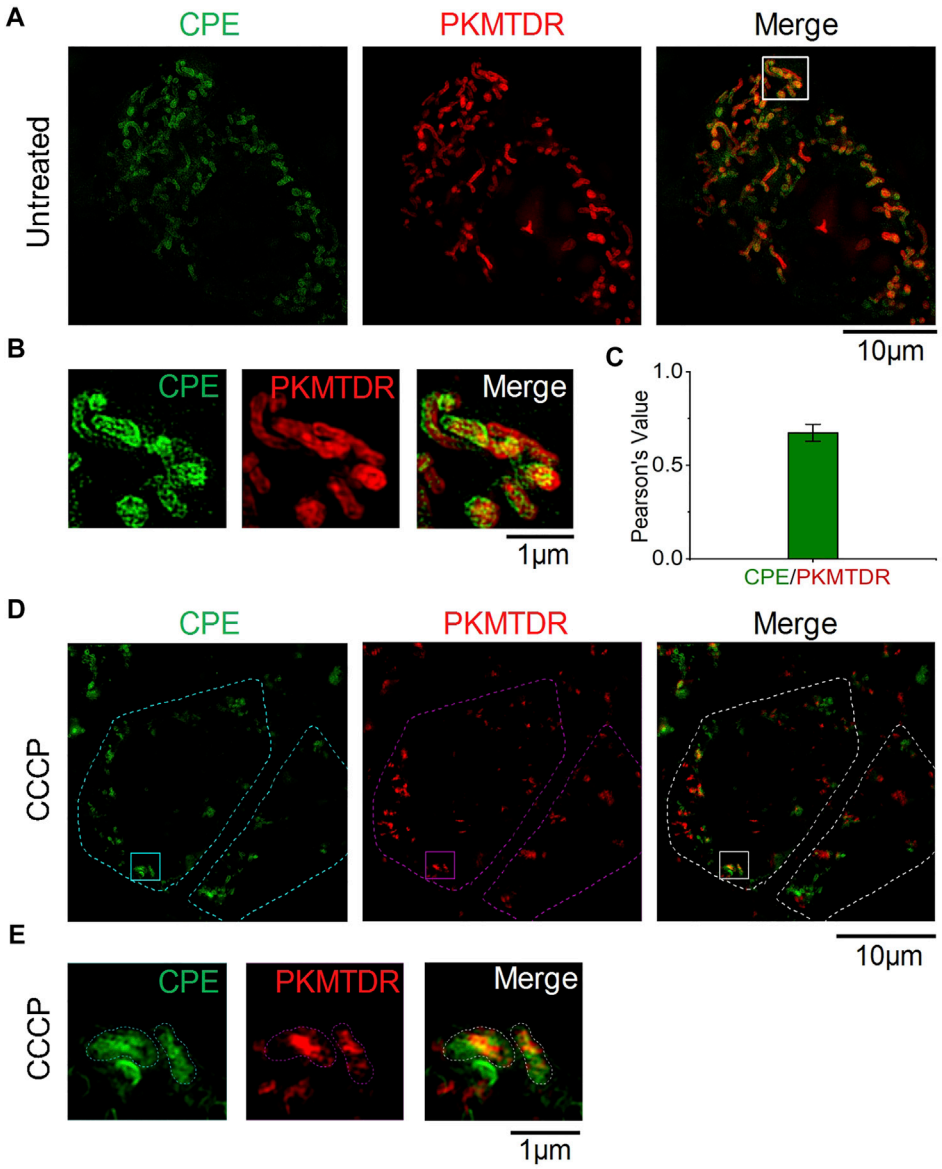

FIGURE 3 | Colocalization of CPE and PKMTDR in HeLa cells under SIM. **(A)** Merged SIM images of cells stained with CPE and PKMTDR. **(B)** Enlarged images of the indicated regions in **(A)**. **(C)** Quantitative analysis of the colocalization between CPE and PKMTDR. **(D)** CCCP-treated HeLa cells. **(E)** Enlarged images of the indicated regions in **(D)**

nearly a half (**Figure 4D**), which indicates the mitochondria were in an unhealthy status. In addition, we found that red fluorescent excited by 561 was quenched in round shape mitochondria (**Figure 4C**), which was due to CCCP treatment increased the concentrations of ROS (Kane et al., 2018), high concentrations of ROS then increased RSS levels (Tabassum and Jeong, 2019). However, there was still some red fluorescent outside mitochondria, thus we hypothesized that it was caused by the destruction of mitochondrial outer membrane and the outflow of mitochondrial matrix (**Figure 4B**). Meanwhile, the content of active sulfur flowing out of the matrix was not enough to quench red fluorescent. All these indicate that **CPE** has the potential of detecting active sulfur in mitochondria and judging the status of mitochondria, which can provide a powerful reference value for the diagnosis of mitochondrial diseases.

3 CONCLUSION

Mitochondria-related diseases are closely associated to mitochondrial damage, which is characterized by morphological distribution changes and crest damage (Schapira, 2006; Senyilmaz et al., 2015). In addition, RSS in mitochondria can regulate mitochondrial morphogenesis and

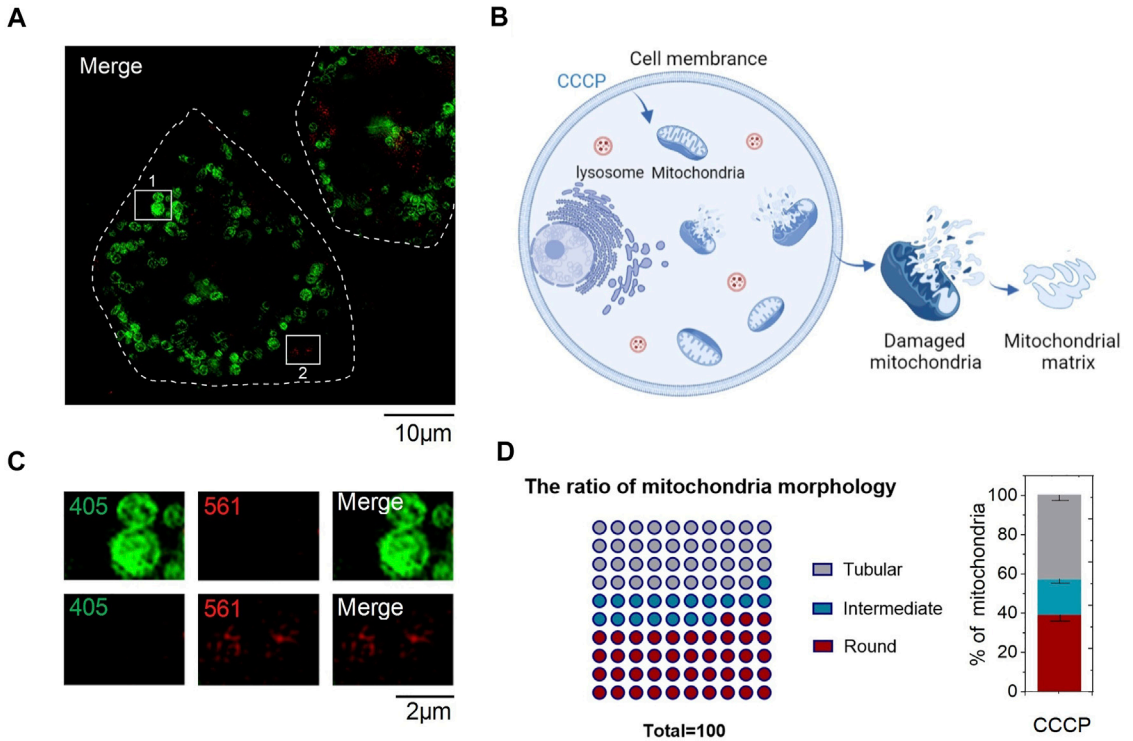

FIGURE 4 | Staining characteristics of CPE in CCCP-treated HeLa cells. **(A)** CCCP-treated HeLa cells. **(B)** Sketch map of staining characteristics of CPE in HeLa cells after CCCP treatment. **(C)** Enlarged images of the indicated regions in **(A)**. **(D)** Quantitative analysis for mitochondrial morphology of HeLa cells treated after CCCP.

play a crucial role in the physiological and pathological processes of living organisms (Kashatus, 2018). However, traditional methods of observing mitochondrial morphology, such as transmission electron microscopy, magnetic resonance imaging, and confocal fluorescence microscopy, are unable to capture the morphology of living cells and simulate the actual *in vivo* state (Chen et al., 2019). To address this problem, here, we developed **CPE**, a dual-labeling probe enabling the evaluation for mitochondrial morphology and the detection of RSS through simultaneous labeling of the mitochondria membrane and matrix in living cells, which make it possible for the diagnosis of early mitochondria-related diseases under SIM. Thus, **CPE** not only provides strategies for the design of accurate positioning probes but may also become a powerful approach for investigating mitochondrial biology.

4 EXPERIMENTAL SECTIONS

4.1 Synthetic Route

A mixture of 7-(diethylaMino)-2-oxo-2H-chromene-3-carbaldehyde (0.26 g, 1 mmol) and 4-pyridineacetonitrile (0.12 g, 1 mmol) refluxed in dry ethanol (15 ml). A large amount of brown powder solids precipitated after reacted overnight. After cooling to room temperature, the crude product was filtered and washed with cool acetonitrile. Subsequently, a mixture of the previous product (0.172 g, 0.5 mmol) and iodoethane (0.47 g, 3 mmol) refluxed in acetonitrile (3 ml). A large amount of purple powder solids precipitated after reacted for 24 h. Then, the crude product was obtained by filtering, followed by washing with cold ethanol and ethyl ester. A purple compound **CPE** (0.11 g, 0.3 mmol, 60%) was obtained after drying. ^{1}H NMR (600 MHz, DMSO-d_6) δ (ppm) (**Supplementary Figure S5**): 9.05 (d, J = 7.1 Hz, 2H), 8.84 (s, 1H), 8.39 (s, 1H), 8.32 (d, J = 7.1 Hz, 2H), 7.66 (d, J = 9.1 Hz, 1H), 6.88 (dd, J = 9.1, 2.4 Hz, 1H), 6.68 (d, J = 2.2 Hz, 1H), 4.62 (q, J = 7.3 Hz, 2H), 3.56 (q, J = 7.0 Hz, 4H), 1.55 (t, J = 7.3 Hz, 3H), and 1.18 (t, J = 7.1 Hz, 6H). ^{13}C NMR (151 MHz, DMSO-d_6) δ (ppm) (**Supplementary Figure S6**): 160.46, 158.10, 154.22, 150.01, 145.28, 144.98, 144.82, 132.97, 123.23 116.91, 111.58, 111.31, 108.85, 102.17, 97.29, 56.04, 45.28, 16.61, and 12.94. HRMS *m/z* (**Supplementary Figure S7**): calculated for $C_{23}H_{24}N_3O_2^+$ $[M]^+$: 374.1863, found 374.1775.

4.2 General Materials

Dulbecco's modified Eagle's medium (#11965118, DMEM), phenol-free medium (#1894117), penicillin–streptomycin (#15140163, 10,000 units/ml), trypsin-EDTA (#25200–072), and other reagents for cell culture were obtained from Gibco BRL (Grand Island, NY, United States). Fetal bovine serum (FBS) was obtained from VivaCell (Shanghai, China). HeLa cells were gifted from the Chunyan Liu's lab (Shandong First Medical University).

4.3 Cell Culture

HeLa cells were cultured in Dulbecco modified Eagle medium supplemented with 10% fetal bovine serum, penicillin (100 μg/ml), and streptomycin (100 μg/ml) in a 5% CO_2 humidified incubator at 37°C.

4.4 Experiments *In Vitro*

CPE (10 μM) was put into a color dish and allowed to react with different concentrations such as 0, 2, 4, 6, and 8 eq., Na_2SO_2 or H_2S in order to complete the reactive sulfur concentration response experiment, and then the fluorescence spectra of **CPE** at different concentrations were detected. Next, we incubated **CPE** with lecithin for 1 h and imaged under SIM to search for the luminescence properties of **CPE**.

4.5 Cell Culture and Imaging Under OMX 3D-SIM

HeLa cells were seeded on 35 mm glass-bottom micro dishes at a density of 1×10^5 and incubated with 2 ml of DMEM medium supplemented with 10% FBS for 24 h. After that, cells were incubated with 10 μM **CPE** for 1 h and washed with fresh DMEM for five times. At last, the cells with no phenol in culture medium were imaged under an OMX 3D-SIM extended-resolution microscope. Images were acquired at 512 × 512, with a step size of 0.125 μm, and **CPE** was excited at 405 and 561 nm.

4.6 Cytotoxicity Assay

The Cell Counting Kit-8 (CCK-8) assay was used to measure the cytotoxicity assay. HeLa cells at a density of 8×10^3 every well were seeded in a 96-well plate in DMEM with 10% FBS at 37°C for 24 h. Then, the original medium was replaced with 100 μL fresh medium, each well containing **CPE** with the concentrations of 0, 1, 5, 10, and 20 μM. After 24 h incubation, 10 μL CCK-8 solution was added to each well, and the plate was incubated in the incubator for 1 h. Finally, the absorbance at 450 nm was determined by enzyme-linked immunosorbent assay.

4.7 Colocalization Experiments

Cells at a density of 1×10^5 were seeded on 35 mm glass-bottom culture dishes and incubated with 2 ml of DMEM medium supplemented with 10% FBS. After 24 h incubation, cells were incubated with 100 nM PKMTDR and 10 μM **CPE** for 1 h. Finally, the cells were cultured in a phenol-free medium and imaged under an OMX 3D-SIM. PKMTDR was excited at 561 nm, and **CPE** was at 405 nm. The images were analyzed using ImageJ.

4.8 Cellular Uptake Assay

HeLa cells were stained with 10 μM **CPE** under different conditions. 37 °C: the cells were stained with **CPE** at 37 °C for 1 h. 4 °C: the cells were stained with **CPE** at 4 °C for 1 h. NH_4Cl: the cells were pre-incubated with NH_4Cl (50 mM) in FBS-free DMEM at 37 °C for 2 h, and then incubated with **CPE** at 37 °C for 1 h.

4.9 Statistical Analysis

Statistical analysis was performed with Prism 9 (GraphPad) and ImageJ. Statistical significances and sample sizes in all graphs are indicated in the corresponding figure legends.

DATA AVAILABILITY STATEMENT

The original contributions presented in the study are included in the article/**Supplementary Material**, further inquiries can be directed to the corresponding authors.

AUTHOR CONTRIBUTIONS

MH has collected all 3D-SIM super-resolution microscopy data. MH and BW analyzed and processed the SIM data. MH and HW cultured cell. GF synthesized and characterized **CPE**. MH, GF, JW, and BD conceived the project, designed the experiments, and wrote the manuscript with the help of all authors.

FUNDING

This work was supported by the National Natural Science Foundation of China (Nos. 81870283 and 82070382), Taishan Scholars Programme (No. 20190979). We thank Translational Medicine Core Facility of Shandong University for consultation and instrument support.

SUPPLEMENTARY MATERIAL

The Supplementary Material for this article can be found online at: https://www.frontiersin.org/articles/10.3389/fphar.2022.871059/full#supplementary-material

REFERENCES

Alirol, E., and Martinou, J. C. (2006). Mitochondria and Cancer: Is There a Morphological Connection? *Oncogene* 25 (34), 4706–4716. doi:10.1038/sj.onc.1209600

Bai, H., Liu, H., Chen, X., Hu, R., Li, M., He, W., et al. (2021). Augmenting Photosynthesis through Facile AIEgen-Chloroplast Conjugation and Efficient Solar Energy Utilization. *Mater. Horiz.* 8 (5), 1433–1438. doi:10.1039/d1mh00012h

Blanco, F. J., Rego, I., and Ruiz-Romero, C. (2011). The Role of Mitochondria in Osteoarthritis. *Nat. Rev. Rheumatol.* 7 (3), 161–169. doi:10.1038/nrrheum.2010.213

Cai, W. J., Wang, M. J., Ju, L. H., Wang, C., and Zhu, Y. C. (2010). Hydrogen Sulfide Induces Human colon Cancer Cell Proliferation: Role of Akt, ERK and P21. *Cell. Biol. Int.* 34 (6), 565–572. doi:10.1042/CBI20090368

Cao, X., Wang, H., Wang, Z., Wang, Q., Zhang, S., Deng, Y., et al. (2017). *In Vivo* imaging Reveals Mitophagy independence in the Maintenance of Axonal Mitochondria during normal Aging. *Aging Cell* 16 (5), 1180–1190. doi:10.1111/acel.12654

Chen, H., Wang, H., Wei, Y., Hu, M., Dong, B., Fang, H., et al. (2021). Super-resolution Imaging Reveals the Subcellular Distribution of Dextran at the Nanoscale in Living Cells. *Chin. Chem. Lett.* doi:10.1016/j.cclet.2021.10.025

Chen, Q., Fang, H., Shao, X., Tian, Z., Geng, S., Zhang, Y., et al. (2020a). A Dual-Labeling Probe to Track Functional Mitochondria-Lysosome Interactions in Live Cells. *Nat. Commun.* 11 (1), 6290. doi:10.1038/s41467-020-20067-6

Chen, Q., Jin, C., Shao, X., Guan, R., Tian, Z., Wang, C., et al. (2018). Super-Resolution Tracking of Mitochondrial Dynamics with an Iridium(III) Luminophore. *Small* 14 (41), e1802166. doi:10.1002/smll.201802166

Chen, Q., Shao, X., Hao, M., Fang, H., Guan, R., Tian, Z., et al. (2020b). Quantitative Analysis of Interactive Behavior of Mitochondria and Lysosomes Using Structured Illumination Microscopy. *Biomaterials* 250, 120059. doi:10.1016/j.biomaterials.2020.120059

Chen, Q., Shao, X., Tian, Z., Chen, Y., Mondal, P., Liu, F., et al. (2019). Nanoscale Monitoring of Mitochondria and Lysosome Interactions for Drug Screening and Discovery. *Nano Res.* 12, 1009–1015. doi:10.1007/s12274-019-2331-x

Fang, H., Yao, S., Chen, Q., Liu, C., Cai, Y., Geng, S., et al. (2019). *De Novo*-Designed Near-Infrared Nanoaggregates for Super-resolution Monitoring of Lysosomes in Cells, in Whole Organoids, and *In Vivo*. *ACS. Nano* 13 (12), 14426–14436. doi:10.1021/acsnano.9b08011

Guarani, V., McNeill, E. M., Paulo, J. A., Huttlin, E. L., Fröhlich, F., Gygi, S. P., et al. (2015). QIL1 Is a Novel Mitochondrial Protein Required for MICOS Complex Stability and Cristae Morphology. *Elife* 4, e06265. doi:10.7554/eLife.06265

Gui, C., Zhao, E., Kwok, R. T. K., Leung, A. C. S., Lam, J. W. Y., Jiang, M., et al. (2017). AIE-active Theranostic System: Selective Staining and Killing of Cancer Cells. *Chem. Sci.* 8 (3), 1822–1830. doi:10.1039/c6sc04947h

Gustafsson, M. G. (2000). Surpassing the Lateral Resolution Limit by a Factor of Two Using Structured Illumination Microscopy. *J. Microsc.* 198 (Pt2), 82–87. doi:10.1046/j.1365-2818.2000.00710.x

Huang, X., Fan, J., Li, L., Liu, H., Wu, R., Wu, Y., et al. (2018). Fast, Long-Term, Super-resolution Imaging with Hessian Structured Illumination Microscopy. *Nat. Biotechnol.* 36 (5), 451–459. doi:10.1038/nbt.4115

Kane, M. S., Paris, A., Codron, P., Cassereau, J., Procaccio, V., Lenaers, G., et al. (2018). Current Mechanistic Insights into the CCCP-Induced Cell Survival Response. *Biochem. Pharmacol.* 148, 100–110. doi:10.1016/j.bcp.2017.12.018

Kashatus, D. F. (2018). The Regulation of Tumor Cell Physiology by Mitochondrial Dynamics. *Biochem. Biophys. Res. Commun.* 500 (1), 9–16. doi:10.1016/j.bbrc.2017.06.192

Ke, H., Dass, S., Morrisey, J. M., Mather, M. W., and Vaidya, A. B. (2018). The Mitochondrial Ribosomal Protein L13 Is Critical for the Structural and Functional Integrity of the Mitochondrion in Plasmodium Falciparum. *J. Biol. Chem.* 293 (21), 8128–8137. doi:10.1074/jbc.RA118.002552

Lau, N., and Pluth, M. D. (2019). Reactive Sulfur Species (RSS): Persulfides, Polysulfides, Potential, and Problems. *Curr. Opin. Chem. Biol.* 49, 1–8. doi:10.1016/j.cbpa.2018.08.012

Leung, C. W., Hong, Y., Chen, S., Zhao, E., Lam, J. W., and Tang, B. Z. (2013). A Photostable AIE Luminogen for Specific Mitochondrial Imaging and Tracking. *J. Am. Chem. Soc.* 135 (1), 62–65. doi:10.1021/ja310324q

Qin, J., Peng, Z., Li, B., Ye, K., Zhang, Y., Yuan, F., et al. (2015). Gold Nanorods as a Theranostic Platform for *In Vitro* and *In Vivo* Imaging and Photothermal Therapy of Inflammatory Macrophages. *Nanoscale* 7 (33), 13991–14001. doi:10.1039/c5nr02521d

Rezaeian, A. H., Wei, W., and Inuzuka, H. (2022). The Regulation of Neuronal Autophagy and Cell Survival by MCL1 in Alzheimer's Disease. *Acta Mater. Med.* 1 (1), 42–55. doi:10.15212/amm-2021-0002

Sasaki, S. (2010). Determination of Altered Mitochondria Ultrastructure by Electron Microscopy. *Methods Mol. Biol.* 648, 279–290. doi:10.1007/978-1-60761-756-3_19

Schapira, A. H. (2006). Mitochondrial Disease. *Lancet* 368, 70–82. doi:10.1016/S0140-6736(06)68970-8

Senyilmaz, D., Virtue, S., Xu, X., Tan, C. Y., Griffin, J. L., Miller, A. K., et al. (2015). Regulation of Mitochondrial Morphology and Function by Stearoylation of TFR1. *Nature* 525 (7567), 124–128. doi:10.1038/nature14601

Shao, X., Chen, Q., Hu, L., Tian, Z., Liu, L., Liu, F., et al. (2020). Super-resolution Quantification of Nanoscale Damage to Mitochondria in Live Cells. *Nano Res.* 13, 2149–2155. doi:10.1007/s12274-020-2822-9

Shi, B., Jie, K., Zhou, Y., Zhou, J., Xia, D., and Huang, F. (2016). Nanoparticles with Near-Infrared Emission Enhanced by Pillararene-Based Molecular Recognition in Water. *J. Am. Chem. Soc.* 138 (1), 80–83. doi:10.1021/jacs.5b11676

Shi, D., Liu, W., Wang, G., Guo, Y., and Li, J. (2022). Small-molecule Fluorescence-Based Probes for Aging Diagnosis. *Acta Materia. Med.* 1 (1), 4–23. doi:10.15212/AMM-2021-0004

Tabassum, R., and Jeong, N. Y. (2019). Potential for Therapeutic Use of Hydrogen Sulfide in Oxidative Stress-Induced Neurodegenerative Diseases. *Int. J. Med. Sci.* 16 (10), 1386–1396. doi:10.7150/ijms.36516

Vinten-Johansen, J. (2020). Commentary: Mitochondria Are More Than Just the Cells' Powerhouse. *J. Thorac. Cardiovasc. Surg.* 160 (2), e33–e34. doi:10.1016/j.jtcvs.2019.07.029

Wiemerslage, L., and Lee, D. (2016). Quantification of Mitochondrial Morphology in Neurites of Dopaminergic Neurons Using Multiple Parameters. *J. Neurosci. Methods* 262, 56–65. doi:10.1016/j.jneumeth.2016.01.008

Yan, Y. H., He, X. Y., Miao, J. Y., and Zhao, B. X. (2019). A Near-Infrared and Mitochondria-Targeted Fluorescence Probe for Ratiometric Monitoring of Sulfur Dioxide Derivatives in Living Cells. *J. Mater. Chem. B.* 7 (42), 6585–6591. doi:10.1039/c9tb01686d

Yousif, L. F., Stewart, K. M., and Kelley, S. O. (2009). Targeting Mitochondria with Organelle-specific Compounds: Strategies and Applications. *Chembiochem* 10, 1939–1950. doi:10.1002/cbic.200900185

Yu, T., Robotham, J. L., and Yoon, Y. (2006). Increased Production of Reactive Oxygen Species in Hyperglycemic Conditions Requires Dynamic Change of Mitochondrial Morphology. *Proc. Natl. Acad. Sci. U S A.* 103 (8), 2653–2658. doi:10.1073/pnas.0511154103

Zhao, E., Deng, H., Chen, S., Hong, Y., Leung, C. W., Lam, J. W., et al. (2014). A Dual Functional AEE Fluorogen as a Mitochondrial-specific Bioprobe and an Effective Photosensitizer for Photodynamic Therapy. *Chem. Commun. (Camb)* 50 (92), 14451–14454. doi:10.1039/c4cc07128j

Zhao, N., Chen, S., Hong, Y., and Tang, B. Z. (2015). A Red Emitting Mitochondria-Targeted AIE Probe as an Indicator for Membrane Potential and Mouse Sperm Activity. *Chem. Commun. (Camb)* 51 (71), 13599–13602. doi:10.1039/c5cc04731e

Zhao, N., Li, M., Yan, Y., Lam, J. W. Y., Zhang, Y. L., Zhao, Y. S., et al. (2013). A Tetraphenylethene-Substituted Pyridinium Salt with Multiple Functionalities: Synthesis, Stimuli-Responsive Emission, Optical Waveguide and Specific Mitochondrion Imaging. *J. Mater. Chem. C* 1, 4640. doi:10.1039/c3tc30759j

Conflict of Interest: The authors declare that the research was conducted in the absence of any commercial or financial relationships that could be construed as a potential conflict of interest.

Publisher's Note: All claims expressed in this article are solely those of the authors and do not necessarily represent those of their affiliated organizations, or those of the publisher, the editors, and the reviewers. Any product that may be evaluated in this article, or claim that may be made by its manufacturer, is not guaranteed or endorsed by the publisher.

Copyright © 2022 Hu, Wang, Zhang, Wang, Li, Zhang, Zhang, Lu, Fang, Wang and Dong. This is an open-access article distributed under the terms of the Creative Commons Attribution License (CC BY). The use, distribution or reproduction in other forums is permitted, provided the original author(s) and the copyright owner(s) are credited and that the original publication in this journal is cited, in accordance with accepted academic practice. No use, distribution or reproduction is permitted which does not comply with these terms.

frontiers | Frontiers in Pharmacology

ORIGINAL RESEARCH
published: 06 June 2022
doi: 10.3389/fphar.2022.927609

An Endoplasmic Reticulum-Targeted Ratiometric Fluorescent Molecule Reveals Zn^{2+} Micro-Dynamics During Drug-Induced Organelle Ionic Disorder

Hongbao Fang[1], Yaheng Li[1], Shankun Yao[1], Shanshan Geng[1], Yuncong Chen[1,2], Zijian Guo[1,2]* and Weijiang He[1,2]**

[1]State Key Laboratory of Coordination Chemistry, School of Chemistry and Chemical Engineering, Chemistry and Biomedicine Innovation Center (ChemBIC), Nanjing University, Nanjing, China, [2]Nanchuang (Jiangsu) Institute of Chemistry and Health, Nanjing, China

OPEN ACCESS

Edited by:
Peixue Ling,
Shandong University (Qingdao), China

Reviewed by:
Lei Wang,
University of Cincinnati, United States
Yang Chen,
Dalian Institute of Chemical Physics (CAS), China
Guangle Niu,
Shandong University (Jinan), China

***Correspondence:**
Yuncong Chen
chenyc@nju.edu.cn
Zijian Guo
zguo@nju.edu.cn
Weijiang He
heweij69@nju.edu.cn

Specialty section:
This article was submitted to Pharmacology of Anti-Cancer Drugs, a section of the journal Frontiers in Pharmacology

Received: 24 April 2022
Accepted: 20 May 2022
Published: 06 June 2022

Citation:
Fang H, Li Y, Yao S, Geng S, Chen Y, Guo Z and He W (2022) An Endoplasmic Reticulum-Targeted Ratiometric Fluorescent Molecule Reveals Zn^{2+} Micro-Dynamics During Drug-Induced Organelle Ionic Disorder. Front. Pharmacol. 13:927609. doi: 10.3389/fphar.2022.927609

The endoplasmic reticulum (ER) is the main storage site of Zn^{2+}, and Zn^{2+} plays an important role in regulating ER homeostasis. Therefore, we designed and synthesized a ratiometric fluorescent Zn^{2+} probe ER-Zn targeting ER stress. The probe displayed a specific Zn^{2+} induced blue shift at the spectral maximum values of excitation (80 nm) and emission (30 nm). The ratio imaging capability of Zn^{2+} under dual excitation mode can be applied not only to quantitative and reversible detection of exogenous Zn^{2+}, but also the observation of the Zn^{2+} level change under ER stress, elucidating the different behaviors of Zn^{2+} release in ER stimulated by tunicamycin and thapsigargin. Additionally, the NIR imaging capability of ER-Zn provides an important basis for further research on animal models and is expected to realize the visualization and treatment of ER stress-related diseases through the regulation of ER stress by Zn^{2+}. We envision that this probe can be applied to screen drugs for diseases related to ER stress regulation.

Keywords: organelle targeting, Zn^{2+} dynamics, ER stress, ionic disorder, drug regulation

1 INTRODUCTION

Zinc (Zn^{2+}) is the second most abundant transition metal ion after iron in the body, involving in a variety of pathological and physiological processes, such as enzyme transport, gene transcription, and immune function (Kambe et al., 2015; Maret, 2019; Bird and Wilson, 2020). Endoplasmic reticulum (ER) homeostasis was found to be closely related to Zn^{2+}. It has been reported that zinc deficiency can cause ER stress and a decrease of metallothionein level, which leads to oxidative stress, cell damage, and acute kidney injury (Inagi, 2009; Hadj Abdallah et al., 2018; Hancock et al., 2020). Therefore, it is necessary to detect Zn^{2+} level changes in ER and even *in vivo* to study the physiological process associated with ER.

Fluorescent probe method has been widely used to detect ionic dynamics in living cells due to its advantages of low toxicity, easy preparation, and *in situ* non-destructive detection (Chen et al., 2015; Li et al., 2020; Chen et al., 2021; Fang et al., 2021a; Liu et al., 2021; Wang and Diao, 2022; Wang et al., 2022). Therefore, the use of fluorescent probes to study Zn^{2+} in ER provides a powerful tool for the detection and treatment of ER stress-related diseases by regulating the Zn^{2+} level (Chabosseau et al., 2018; Huang et al., 2021; Liu et al., 2022). Although many Zn^{2+} fluorescent probes have been

developed, most of them show turn-on response and are difficult to use for *in vivo* detection (Fang et al., 2021b; Qi et al., 2021; Wang et al., 2021).

In this paper, due to the lack of research on near-infrared (NIR) ratiometric Zn^{2+} fluorescent probes targeting ER, such a probe combined with the intramolecular charge transfer (ICT) mechanism was rationally designed by us. For one thing, the styrene group was introduced into the α site of BODIPY fluorophore, which not only increased its excitation wavelength, but also extended the emission wavelength of the fluorophore to the NIR region for reducing the interference of spontaneous fluorescence in organisms and damage to cells during imaging. For another, *N*, *N*, *N′*-tri (pyridin-2-ylmethyl) ethane-1,2-diamine (TPEA) was introduced at the *α* position as the Zn^{2+} chelating group. Finally, p-toluenesulfonamide was introduced at the meso position of the fluorophore as the ER targeting group to construct a highly selective NIR Zn^{2+} fluorescent probe targeting ER, ER-Zn. Cell imaging experiments showed that ER-Zn had good cytocompatibility, which not only realized reversibly ratiometric imaging of exogenous Zn^{2+}, but also quantitatively monitored the fluctuation of Zn^{2+} level in ER under ER stress. ER-Zn provides a new method to study the relationship between ER stress regulation and Zn^{2+} level.

2 MATERIALS AND METHODS

2.1 Materials and Instruments

The commonly used chemicals (e.g., potassium carbonate, piperazine, acid and base, etc.) and general solvents (e.g., dichloromethane, methanol, ethanol, ethyl acetate, petroleum ether, etc.) were all from the domestic reagents purchased by School of Chemistry and Chemical Engineering of Nanjing University, and they were not further purified before use. In the spectral characterization, the solvents such as DMSO and DMF were both spectrally pure reagents purchased from Aldrich. The water used was ultrapure from Millipore. $CuSO_4$, $MgCl_2{\cdot}6H_2O$, $CaCl_2$, $Zn(NO_3)_2{\cdot}7H_2O$, NaCl, KCl, $FeCl_2$, $CoCl_2{\cdot}6H_2O$, and $NiCl_2{\cdot}6H_2O$ were dissolved in ultrapure water to prepare corresponding concentrations of metal ion stock solution. The stock solution of Zn^{2+} was prepared by dissolving $ZnCl_2$ in ultrapure water.

Mass spectrometry was determined by LCQ electrospray ionization mass spectrometry (ESI-MS, Finnigan). High-resolution mass spectrometry (HRMS) was determined by Thermo scientific quadrupole orbit trap tandem high-resolution mass spectrometer. ^1H and ^{13}C NMR were determined by Bruker DRX-500 and Bruker DRX-400 NMR spectrometers using standard pulse sequence with tetramethylsilane (TMS) as internal standard (298 K). The absorption spectra were measured by PerkinElmer Lambda 35 UV-vis spectrometer. Fluorescence emission spectra were recorded by FluoroMax-4 fluorescence spectrometer (HORIBA Jvon Inc.). The pH assay was determined by SevenCompact S210 pH meter (Mettle Toledo). Cell imaging was performed on Olympus FV10-ASW laser confocal fluorescence microscope and Leica SP8 STED 3X confocal microscope. The excitation wavelength was 570 and 650 nm, and the collection wavelength was 660–720 nm.

2.2 Synthesis and Characterization

The synthesis steps of ER-Zn are shown in **Supplementary Figure S1**. 1 and 2 were synthesized according to the literature method (Aydin et al., 2016), and 3 and ER-Zn were synthesized as described in the literature after corresponding improvement.

At 0°C, 3 (3.3 mmol, 1.12 g) and 4-methylbenzenesulfonyl chloride (3.3 mmol, 627 mg) were dissolved in dichloromethane (20 ml), and then several drops of pyridine were added to the solution. After stirring for 2 h, the solvent was removed by rotary evaporation. The target product in orange solid form (1.34 g, 82.3%) was obtained by using dichloromethane/petroleum ether (v:v = 2:1) preparative chromatography on silica gel. ^1H NMR (400 MHz, $CDCl_3$) δ 7.65 (d, J = 7.9 Hz, 2H), 7.25–7.17 (m, 4H), 7.13 (d, J = 8.4 Hz, 2H), 5.96 (s, 2H), 2.53 (s, 6H), 2.38 (s, 3H), 1.25 (s, 6H). ^{13}C NMR (101 MHz, $CDCl_3$) δ 155.71, 144.16, 142.77, 140.52, 137.52, 135.27, 132.08, 131.38, 129.59, 129.12, 127.42, 122.31, 121.32, 21.55, 14.58, and 14.45.

ER-Zn: 3 (0.73 mmol, 360 mg) and TPEA-CHO (0.73 mmol, 317 mg) were weighed and added into a 50 ml three-necked flask. Then the activated molecular sieve was added into the bottle with a water separator. Pumped the pressure of the system to vacuum. Under the protection of nitrogen, 10 ml toluene, a drop of acetic acid and a drop of pyridine were added and refluxed overnight. The reaction process was monitored by TLC until the reaction finished. The reaction was further processed after cooling to room temperature. The saturated NaCl solution was used to extract for three times, and the organic phase was selected to remove water by Na_2SO_4. After the solid was removed by filtration, the crude product in the filtrate was collected by rotary evaporation. The target product in blue-black solid form (532 mg, 80.1%) was obtained by preparative chromatography with dichloromethane/methanol (v:v, 100:1→90:10) system on silica gel. ^1H NMR (400 MHz, $CDCl_3$) δ 8.57 (dd, J = 5.1, 1.6 Hz, 2H), 7.66–7.63 (m, 4H), 7.61 (d, J = 1.8 Hz, 1H), 7.42 (d, J = 7.7 Hz, 4H), 7.38 (d, J = 8.3 Hz, 2H), 7.24–7.20 (m, 3H), 7.20–7.16 (m, 5H), 7.12 (dd, J = 8.7, 2.4 Hz, 3H), 6.55 (d, J = 6 Hz, 2H), 6.52 (s, 1H), 5.93 (s, 1H), 3.93 (s, 4H), 3.20 (t, J = 5.8 Hz, 2H), 2.91 (t, J = 5.5 Hz, 2H), 2.56 (s, 3H), 2.37 (s, 3H), 2.11 (s, 3H), 1.28 (s, 3H), and 1.24 (s, 3H). ^{13}C NMR (101 MHz, $CDCl_3$) δ 174.77, 158.46, 155.07, 152.89, 149.77, 149.26, 148.83, 143.97, 142.53, 140.30, 140.03, 138.28, 137.63, 137.56, 137.25, 136.92, 135.43, 133.06, 132.34, 131.08, 129.52, 129.47, 127.40, 125.20, 123.52, 122.46, 122.20, 120.46, 117.82, 113.97, 112.62, 106.55, 60.04, 52.66, 40.91, 21.54, 21.01, 14.79, 14.58, and 14.33. HRMS (positive mode, m/z): Calcd: 913.39896, found: 913.39630 for $[M + H]^+$ and Calcd: 935.38090, found: 935.37921 for $[M + Na]^+$.

2.3 Spectral Characterization

7.78 mg ER-Zn was accurately weighed and then dissolved with 8.52 ml DMSO to prepare 1 mM ER-Zn storage solution. No special instructions, the test system is 50 mM HEPES solution with 60% DMSO (containing 100 mM KNO_3, pH = 7.2).

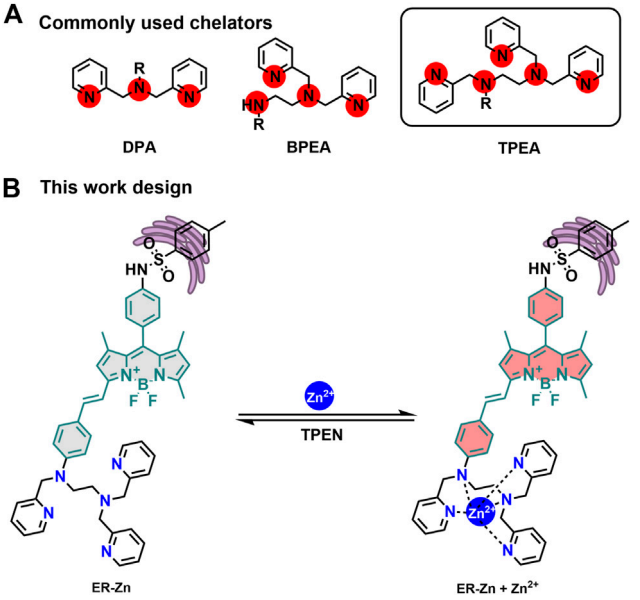

FIGURE 1 | (A) Commonly used Zn^{2+} chelators. **(B)** The Zn^{2+} sensing mechanism of ER-Zn.

2.3.1 Absorption and Excitation Spectra Tests

10 μM ER-Zn solution was prepared with 3 ml buffer solution, and its absorption and fluorescence spectra were collected. Then, 1 μl $ZnCl_2$ (3 mM) was equivalently dropped into the test system to record the absorption titration spectra, fluorescence titration spectra, and excitation titration spectra. The absorption band was collected from 480 to 750 nm, the excitation spectra test parameters are as follows: the emission at 700 nm and excitation collection band from 475 to 685 nm, the slit is 4 * 4 nm.

2.3.2 Selectivity and pH Dependence Assays

Selectivity test: The different metal ions 2 mM Mg^{2+}, K^{+}, Ca^{2+} and Na^{+}, and 10 μM Ni^{2+}, Co^{2+}, Al^{3+}, Cr^{3+}, Cu^{2+}, Fe^{3+}, Mn^{2+}, Pb^{2+} solutions, respectively, were dripped to the probe solution before collecting their excitation spectra. Then, 10 μl $ZnCl_2$ solution (3 mM) was added into the test system containing different ions to determine their excitation spectra.

pH-dependent experiment: Using NaOH and HCl, the buffer solution (50 mM HEPES, containing 60% DMSO, 100 mM KNO_3, pH = 7.2) was adjusted to pH range of 2–10, then 30 μl ER-Zn storage solution (1 mM) was added to the solutions to make the final concentration as 10 μM. Finally, 10 μl $ZnCl_2$ storage solution (3 mM) was dropped into the above solutions, and the fluorescence spectra were performed.

2.4 Cell Imaging

2.4.1 Cell Culture

The HeLa cells used in the experiment were cultured in the air with 5% CO_2 at 37°C. The cells were cultured in Dulbecco's Modified Eagle Medium (DMEM, Invitrogen) containing 10% fetal bovine serum (FBS), penicillin (100 units/ml), and streptomycin (100 mg/ml). There is no special indication that HeLa cells are used for cell imaging.

2.4.2 Cytotoxicity Experiment

MTT (3-(4,5-dimethylthiazol-2)-2,5-diphenyltetrazolium bromide) method was used to determine the number of living cells by using MTT to produce purple precipitate formazan with the mitochondrial succinate dehydrogenase of living cells. HeLa cells in the exponential growth phase were collected and inoculated into 96-well plates. About 5,000 cells and 100 μl medium containing 10% FBS were added to each plate. HeLa cells in 96-well plates were placed in a 37°C, 5% CO_2 incubator. After cell adherent growth for 12 h, the original culture medium was washed away, and 200 μl ER-BDP with different concentrations were added to each well, and then put back into the incubator for 24 h. Then 30 μl MTT solution was added to each well. After incubation in the incubator for 12 h, the supernatant was carefully removed, and 200 μl DMSO was added to each well to fully dissolve the purple precipitate. Finally, the absorbance of each well at 490 nm was measured by a microplate reader. Each group of experiments was measured three times in parallel.

2.4.3 Colocalization Experiment

Two groups of cells were prepared, and the co-localization experiments between the nucleus, ER and ER-Zn were carried out respectively. Two groups of cells were treated with 100 nM ER-Tracker™ Blue-White DPX dye for 30 min and 100 nM DAPI for 10 min, respectively. The cells were taken out and washed three times with PBS buffer, then incubated with 5 μM ER-Zn solution for 30 min and washed three times with PBS buffer.

The excitation wavelength and emission channel of ER-Blue Tracker dye were as follows: the excitation wavelength was 405 nm, and the emission channel was 415–450 nm; the excitation wavelength of the probe ER-Zn was 570 nm, and the emission channel was 660–720 nm. For DAPI, the excitation wavelength was 405 nm, and the emission channel was 430–500 nm; the excitation wavelength of ER-Zn was 633 nm, and the emission channel was 645–700 nm.

2.4.4 Detection of Exogenous Zn^{2+}

The cultured cells were washed three times with metal-free PBS solution and then incubated with 5 μM ER-BDP solution at room temperature for 2 h. Remove the probe solution, wash the cells three times with PBS solution without metal ions, and then observe them with a laser confocal fluorescence microscope. The introduction of exogenous zinc in cells was carried out by incubation in a 1:1 mixture of 5 mM $ZnCl_2$ and 5 mM 2-mercaptopyidine-N-oxide aqueous solution (diluted to a specific concentration by DMEM). After incubation for 20 min, the imaging was performed with a laser confocal fluorescence microscope. After imaging, the cells were washed three times with PBS without metal ions and then treated with 50 μM TPEN (diluted by the TPEN storage solution through DMEM medium) for 20 min, and then washed once with PBS.

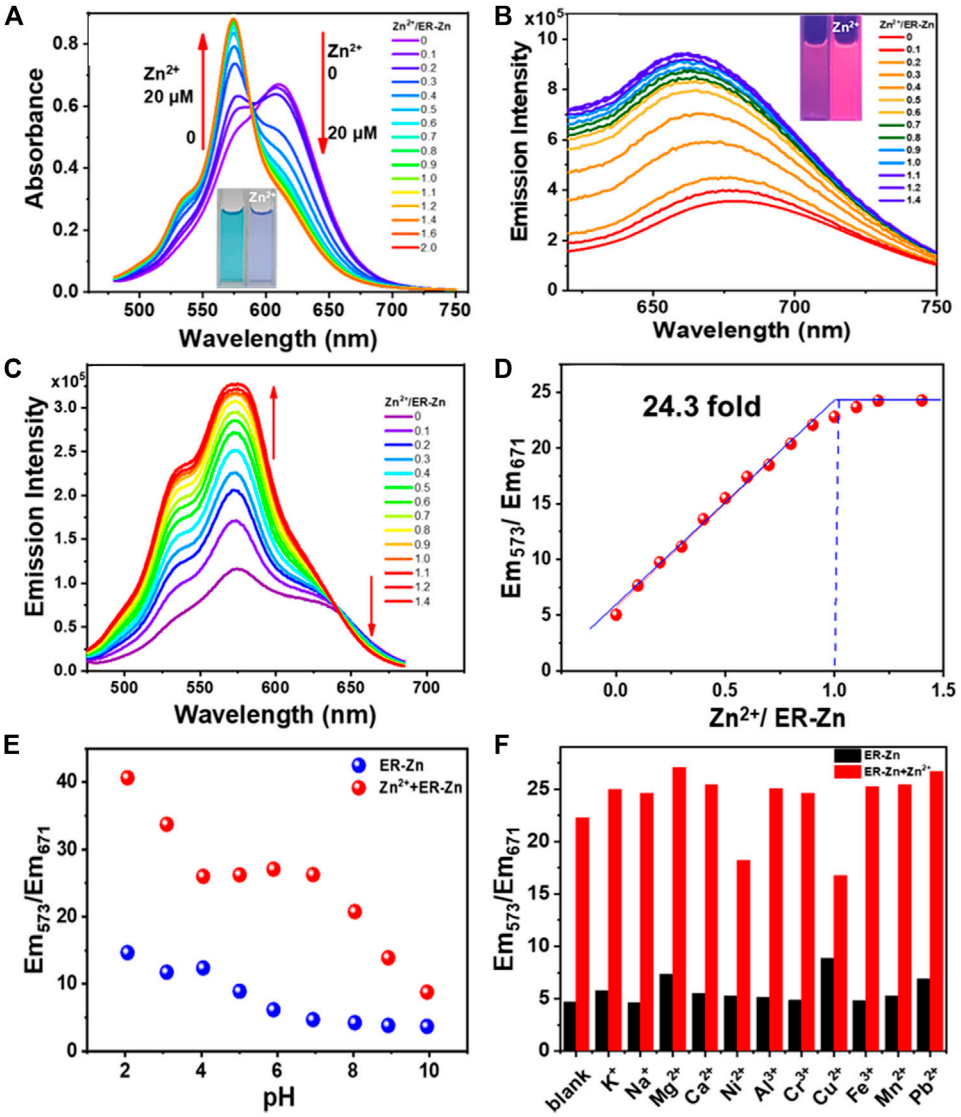

FIGURE 2 | (A) Absorption titration spectra of 10 μM ER-Zn with Zn^{2+}. The inset: photographs of 10 μM ER-Zn with 0 and 1.0 eq. Zn^{2+} under the natural light; **(B)** Zn^{2+} fluorescence titration spectra of 10 μM ER-Zn with Zn^{2+}. The inset: photographs of 10 μM ER-Zn with 0 and 1.0 eq. Zn^{2+} under the 365 nm UV light. λ_{ex} = 600 nm; **(C)** Excitation spectra of 10 μM ER-Zn upon the addition of Zn^{2+}. **(D)** Scatter plot between Em_{573}/Em_{671} with different concentrations of Zn^{2+}. λ_{em} = 700 nm, the excitation collection band is 475–685 nm, the slit is 4 * 4 nm; **(E)** Em_{573}/Em_{671} of ER-Zn and ER-Zn + Zn^{2+} in the pH range from 2 to 10; **(F)** Selectivity of ER-Zn and ER-Zn + Zn^{2+} under different cation conditions.

2.4.5 Detection of Endogenous Zn^{2+} Under Endoplasmic Reticulum Stress

Time-course imaging: The cells were incubated with 5 μM ER-Zn for 2 h and then washed with PBS buffer three times. Then, the cells were incubated with 25 μg/ml thapsigargin (TG) and collected images with time.

Cell imaging under different stimuli: Three groups of cells were stimulated by TM and TG to induce ER stress, respectively. The cells were treated with medium, 25 μg/ml tunicamycin (TM), and 25 μg/ml TG for 12 h, respectively. After incubation with 5 μM ER-Zn solution for 2 h, the cells were washed three times with PBS buffer. The cells were washed with PBS solution three times, and the cells were imaged.

3 RESULT AND DISCUSSION

3.1 Rational Design and Spectral Characterization of ER-Zn

The design of Zn^{2+} fluorescent probes has encountered the following problems so far: 1) Sensitivity and selectivity. Since DPA (Di (2-methylpyridine) amine) was first linked with fluorescein, the chelating group has become the most commonly used recognition group for the construction of Zn^{2+} sensors (Walkup et al., 2000). However, binding ability and stability are still the main problems for high sensitivity monitoring of Zn^{2+} in biological systems. Hence, we improved

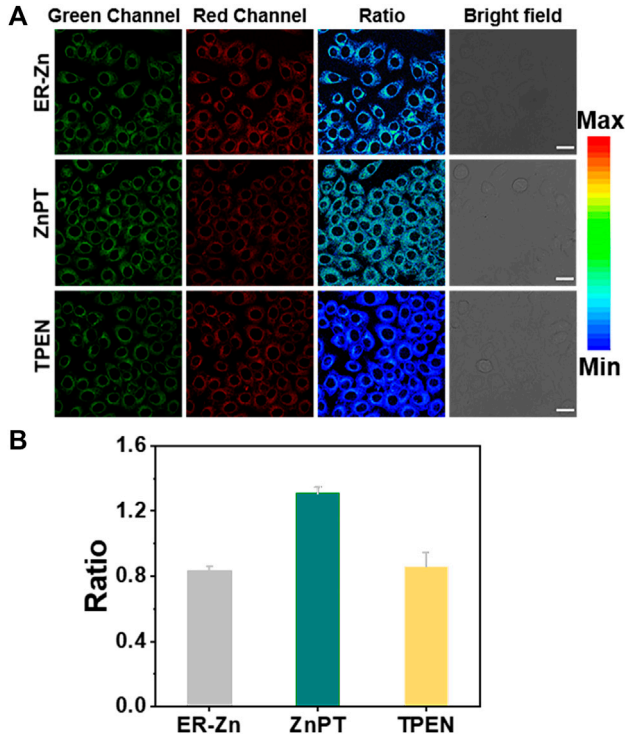

FIGURE 3 | Reversible ratiometric imaging of ER-Zn for exogenous Zn^{2+}. **(A)** Ratiometric imaging of the ER-Zn-stained HeLa cells (5 μM, 2 h, 37°C) upon incubation with 5 μM ZnPT for 20 min and subsequent TPEN (50 μM, 30 min) treatment; **(B)** Fluorescence ratio quantification of **(A)**. The corresponding histograms of the determined average fluorescence intensity in cells from $n = 3$ biologically independent experiments, mean ± SD. The green channel: λ_{ex} = 570 nm, λ_{em} = 660–720 nm, the red channel: λ_{ex} = 650 nm, λ_{em} = 660–720 nm, Ratio = F_G/F_R, scale bar: 25 μm.

the binding ability, coordination rate, and zinc complex stability by increasing coordination sites to form DPA derivatives with five ligands as TPEA (**Figure 1A**). 2) Organelle-targeting capability. To achieve the ER targeting effect, glibenclamide fragment acting on K^+ channel in the ER was selected as the targeting group of the probe (Zünkler et al., 2004). 3) Imaging depth limitation. We expanded the conjugation of the BODIPY fluorophore to achieve depth imaging in biological tissues. In addition, the conjugated structure has an obvious ICT effect and can achieve quantitative imaging. To this end, we constructed a highly selective NIR ER targeting ratiometric Zn^{2+} probe, ER-Zn (**Figure 1B**). Its synthetic route and structural characterization including NMR and MS are shown in **Supplementary Figures S1–S4**.

The probe molecule ER-Zn was prepared as a 10 μM solution in HEPES buffer (50 mM, containing 60% DMSO, 100 mM KNO_3, pH = 7.2). Absorption and fluorescence titration were performed by adding different concentrations of Zn^{2+}. As can be seen from **Figure 2A**, with the increase of Zn^{2+} concentration, the absorbance at 610 nm decreases continuously until it disappears, while a new absorption peak at 575 nm appears and keeps increasing. Therefore, when Zn^{2+} was added, the absorption peak was blue-shifted from 610 to 575 nm with an isosbestic point appearing at 588 nm, and the solution color changed from cyan to blue. The nitrogen atom in the chelating group of the free probe had a strong electron donating ability. However, Zn^{2+} binding TPEA weakened the electron-donating ability of nitrogen atom, which diminished the ICT effect of the structure, inducing a hypochromatic shift of absorption peak.

Subsequently, the Zn^{2+} fluorescence titration spectra of ER-Zn were determined. As can be seen from **Figure 2B**, with the increase of Zn^{2+} concentration, the emission intensity at 660 nm was enhanced. Based on this, we further tested its excitation spectra with a collection band of 475–685 nm at 700 nm emission. The excitation titration spectra of ER-Zn upon Zn^{2+} were shown in **Figure 2C**, with the addition of Zn^{2+}, the fluorescence intensity at 700 nm excited with 573 nm increased, meanwhile, the fluorescence intensity at 700 nm excited with 671 nm decreased. This excitation ratio sensing ability enables ER-Zn to present dual-excitation with single-channel emission ratiometric imaging, which means that during the titration process of Zn^{2+}, the emission at 700 nm under 573 nm excitation enhances, while the emission at 700 nm under 671 nm excitation underwent slightly decrement. The emission ratio (Em_{573}/Em_{671}) reached equilibrium when Zn^{2+} was added to 1 eq. It indicated that ER-Zn binds with Zn^{2+} in the manner of 1:1. In addition, the detection limit (3σ/slope) of this probe was estimated to be 31.8 nM (**Figure 2D**). It was demonstrated that ER-Zn and Zn^{2+} exhibited the characteristic of ratiometric sensing, which can eliminate background fluorescence, providing a basis for the realization of quantitative detection in the cell.

3.2 The Associate Mechanism of ER-Zn to Zn^{2+}

According to the Zn^{2+} fluorescence titration spectra of ER-Zn, when the concentration of ER-Zn and Zn^{2+} was 1:1, the ratio of Em_{573}/Em_{671} reached plague, indicating that ER-Zn associated with Zn^{2+} was 1:1. To further determine the binding ratio of ER-Zn to Zn^{2+}, the work curve was determined as the concentration ratio (ER-Zn/ER-Zn + Zn^{2+}) ranges from 0.1 to 1. As shown in **Supplementary Figure S5**, when the concentration ratio was 0.5, the fluorescence intensity at 660 nm came up to maximum, that is, the binding ratio of ER-Zn and Zn^{2+} is 1:1. Notably, the dissociation constant of the ER-Zn-Zn^{2+} complex was calculated as 3.65 nM (**Supplementary Figure S6**). In addition, HRMS determination of the probe solution in the presence of Zn^{2+} was also carried out (**Supplementary Figure S7**). We can find that the mass peak of $[ER\text{-}Zn + Zn]^{2+}$ is 488.1596, which is consistent with the predicted peak of 488.1599, further proving that the association ratio of ER-Zn to Zn^{2+} is 1:1.

3.3 pH Dependence and Selectivity of ER-Zn

After confirming the ratiometric sensing ability of ER-Zn to Zn^{2+}, we further investigated the pH stability and sensing specificity of ER-Zn. Firstly, we examined whether the response behavior of ER-Zn to Zn^{2+} would be interfered with the physiological pH range. As shown in **Figure 2E**, the Em_{573}/Em_{671} ratio of ER-Zn in the absence and presence of Zn^{2+} did not change significantly in the pH range of 4–8. It can be inferred that ER-Zn can be applied to detecting the dynamic change of Zn^{2+} in the physiological environment.

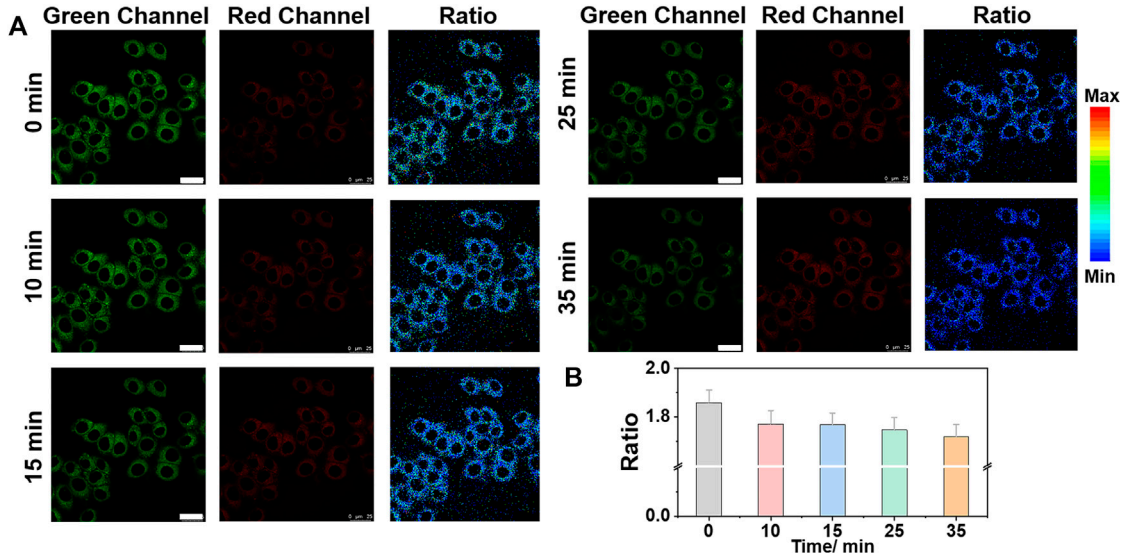

FIGURE 4 | Ratiometric imaging of Zn^{2+} in ER under TG (thapsigargin) stimulation with time. **(A)** Ratiometric images and **(B)** the corresponding fluorescence intensity changes of ER-Zn (5 μM, 2 h) in HeLa cells at ER stress state induced by TG (25 μg/ml) for different time. The green channels: λ_{ex} = 570 nm, λ_{em} = 660–720 nm, the red fluorescence channels: λ_{ex} = 650 nm, λ_{em} = 660–720 nm; Ratio = F_G/F_R, Mean ± SD, scale bar: 25 μm.

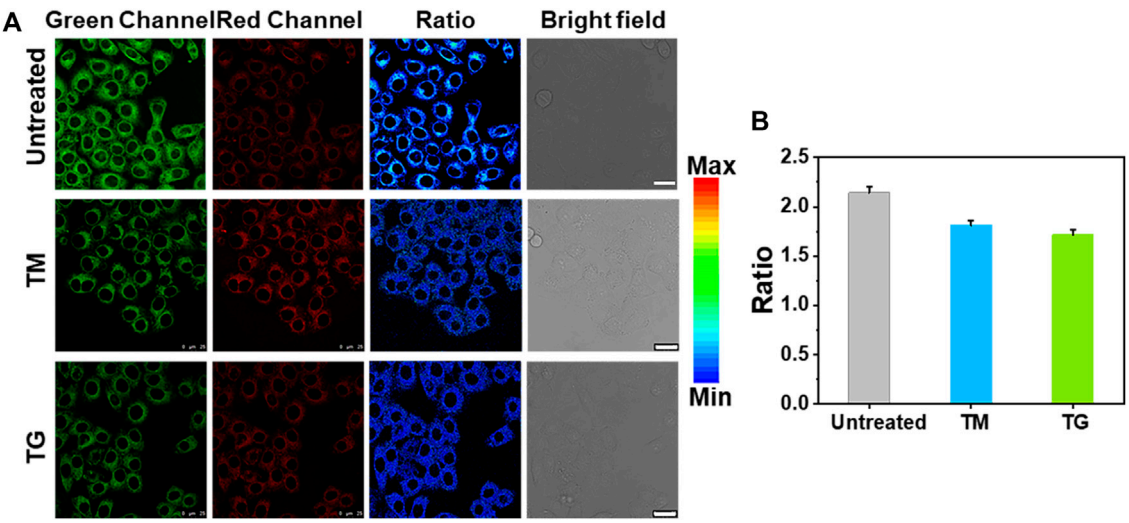

FIGURE 5 | Ratiometric imaging of Zn^{2+} in ER under ER stress regulation by different stimuli. **(A)** Ratiometric images of HeLa cells treated with medium, 25 μg/ml TM and 25 μg/ml TG for 12 h, respectively, then incubatied with ER-Zn (5 μM, 2 h). **(B)** The corresponding mean fluorescence intensity ratio of **(A)**. The green channels: λ_{ex} = 570 nm, λ_{em} = 660–720 nm, the red fluorescence channels: λ_{ex} = 650 nm, λ_{em} = 660–720 nm; Ratio = F_G/F_R, Mean ± SD, scale bar: 25 μm.

Next, we explored the selectivity and anti-interference ability of ER-Zn to Zn^{2+}. It can be seen from **Figure 2F** that Em_{573}/Em_{671} of ER-Zn added with different metal ions was similar to that of the blank sample, indicating ER-Zn's excellent selectivity. Notably, the solution containing different metal ions was then added with equivalent Zn^{2+}, it was found that Em_{573}/Em_{671} exhibited a significant enhancement compared with that of without the addition of Zn^{2+}, only the solution containing Ni^{2+} and Cu^{2+} increased slightly. The content of Ni^{2+} and Cu^{2+} in ER and even cells are much less than that of Zn^{2+}, so their influence on ER-Zn recognition of Zn^{2+} can be ignored. The above result revealed that ER-Zn has a specific response to Zn^{2+} at physiological pH, which is expected to be used to detect the Zn^{2+} level change in living cells.

3.4 Reversibility of ER-Zn

Reversible responses are very important to studying the dynamic changes of Zn^{2+} level in cells. To this end, the reversibility of ER-Zn with between Zn^{2+} and TPEN was studied. **Supplementary Figure**

S8 showed that Em_{573}/Em_{671} ratio increased after the Zn^{2+} addition, and the TPEN addition made Em_{573}/Em_{671} ratio decreased. The reversibility cycle can be repeated at least four times, providing a clue for the study of Zn^{2+} dynamic change in the cell.

3.5 Photostability and Colocalization of ER-Zn in Cells

To study the cytocompatibility of ER-Zn and select the appropriate concentration for subsequent cell experiments, MTT was used to determine the cell survival rate after the HeLa cells were incubated with ER-Zn at the concentrations of 0, 5, 7.5, 10, 12.5, 15, 17.5, 20, 22.5, and 25 μM for 24 h. When the concentration of ER-Zn reached 25 μM, the cell survival rate was even close to 100% (**Supplementary Figure S9**). Therefore, ER-Zn has good biocompatibility and can be used for bioimaging. Considering the good photophysical properties of ER-Zn, 5 μM can be selected as the following cell imaging experiment.

Then we studied the photostability of ER-Zn in cells. The cells were incubated with ER-Zn for 2 h and were imaged every 2 min after continuous illumination. As can be seen from **Supplementary Figure S10**, the fluorescence intensity of the green channel and the red channel did not change significantly within 10 min, and the fluorescence ratio remained almost the same, indicating that ER-Zn had good photostability to be suitable for long time dynamic imaging.

Next, to confirm the distribution of ER-Zn in the cell, we conducted a colocalization experiment using ER commercial dye and ER-Zn, and found that the probe and ER commercial dye has a very high overlap, the calculation of Pearson's colocalization coefficient can reach 0.93 (**Supplementary Figure S11**). However, its colocalization coefficient with the nucleus is only 0.13. It demonstrated that ER-Zn is mainly located in ER, which is consistent with our original design purpose.

3.6 Reversible Cell Imaging of Exogenous Zn^{2+} by ER-Zn

The ER targeting ability of ER-Zn has been confirmed via a colocalization experiment. To further study the sensing ability of ER-Zn on Zn^{2+} in ER, we next conducted cell imaging experiments of endogenous and exogenous Zn^{2+} using ER-Zn. We selected membrane permeable Zn^{2+} carrier (zinc pyrithione, ZnPT) as an exogenous Zn^{2+} supplement and TPEN as an intracellular Zn^{2+} chelator. When the cells were incubated with ER-Zn for 2 h, excitation ratiometric imaging was performed, and the probe showed dual-channel imaging in the cells. Then the cells were incubated with 5 μM ZnPT for 10 min for cell imaging. As shown in **Figure 3**, the fluorescence intensity of the green channel was significantly enhanced compared with the control group, while the fluorescence intensity of the red channel weakened, and the image ratio was significantly enhanced, showing the elevated Zn^{2+} in cells. When the cells were incubated with 50 μM TPEN for 20 min, the image ratio was significantly decreased. It is proved from the result that ER-Zn can be used for quantitative imaging of exogenous Zn^{2+} in cells, which provides a basis for quantitative and dynamic imaging of endogenous Zn^{2+} in ER.

3.7 Zn^{2+} Change Under Endoplasmic Reticulum Stress Regulation

To study the effect of different stimuli (e.g., TG and TM, etc.) on Zn^{2+} in the ER, we set up cell imaging of endogenous Zn^{2+} by ER-Zn under ER stress. TG can affect ER calcium (Ca^{2+}) homeostasis by specific inhibition of ER Ca^{2+}-ATPase and induce ER stress (Zhang et al., 2014; Sehgal et al., 2017). Therefore, we selected TG as the agent to stimulate ER stress. We investigated the Zn^{2+} level change in ER of HeLa cells after TG stimulation for different time periods. **Figure 4** showed that with the extension of stimulation time, the fluorescence intensity of the green channel gradually decreased and that of the red channel increased slightly, showing that the ER stress-induced by TG can lead to a decreased Zn^{2+} level in ER.

In addition, TM is also commonly used to induce ER stress (Jackisch et al., 2020; Suganya et al., 2014). We stimulated the cells with TM and TG to produce ER stress. As can be seen from **Figure 5**, the fluorescence ratio of the cell induced by both TM and TG decreased to varying degrees, further indicating that ER stress regulates the decline of Zn^{2+} level in ER. We speculate that Zn^{2+} homeostasis, like Ca^{2+} homeostasis, is controlled by IP3Rs, which may allow Zn^{2+} to enter the cytoplasm and pump Zn^{2+} from the cytoplasm into ER through TG sensitive ATPase activity (Stork and Li, 2010; Liang et al., 2016). When ER stress occurs, especially after the stimulation of TG and TM, Zn^{2+} will be released from the ER into the cytoplasm, resulting in the decrease of Zn^{2+} in the ER.

4 CONCLUSION

In summary, based on the ICT mechanism, we designed and synthesized a novel NIR ratiometric fluorescent probe targeting ER, ER-Zn, which has a good ratio response to Zn^{2+}, good selectivity, and anti-interference ability. In addition, ER-Zn not only possesses double excitation ratio detection of exogenous Zn^{2+} but made clear the relationship between ER stress regulation by different stimuli and the endogenous Zn^{2+} level in the ER. ER-Zn with the ability of NIR imaging provides a reliable technical basis and design strategy for the further development of quantitative imaging of Zn^{2+} probes *in vivo*. We envision that this probe can be applied to screen drugs for diseases related to ER stress regulation.

DATA AVAILABILITY STATEMENT

The raw data supporting the conclusion of this article will be made available by the authors, without undue reservation.

AUTHOR CONTRIBUTIONS

HF, SG, and WH contributed in the conception and design of the experiment, as well as manuscript writing. HF and SG contributed in the collection and assembly of data and data interpretation. YC and WH edited the manuscript and provided support and discussions.

YL, SG, and SY performed the experiment. HF, YC, ZG, and WH provided technical and financial support. All authors contributed to the article and approved the submitted version.

FUNDING

WH, ZG, and YC were supported by the Natural Science Foundation of China (Nos. 21977044, 21731004, 22122701, and 21907050), the Natural Science Foundation of Jiangsu Province (BK20190282 and BK20202004). HF was fund by the National Postdoctoral Program for Innovative Talents (BX2021123), the China Postdoctoral Science Foundation (2021M691505) and the Jiangsu Postdoctoral Research Funding Program (2021K125B).

SUPPLEMENTARY MATERIAL

The Supplementary Material for this article can be found online at: https://www.frontiersin.org/articles/10.3389/fphar.2022.927609/full#supplementary-material

REFERENCES

Aydın Tekdaş, D., Viswanathan, G., Zehra Topal, S., Looi, C. Y., Wong, W. F., Min Yi Tan, G., et al. (2016). Antimicrobial Activity of a Quaternized BODIPY against Staphylococcus Strains. *Org. Biomol. Chem.* 14 (9), 2665–2670. doi:10.1039/c5ob02477c

Bird, A. J., and Wilson, S. (2020). Zinc Homeostasis in the Secretory Pathway in Yeast. *Curr. Opin. Chem. Biol.* 55, 145–150. doi:10.1016/j.cbpa.2020.01.011

Chabosseau, P., Woodier, J., Cheung, R., and Rutter, G. A. (2018). Sensors for Measuring Subcellular Zinc Pools. *Metallomics* 10 (2), 229–239. doi:10.1039/c7mt00336f

Chen, Q., Hao, M., Wang, L., Li, L., Chen, Y., Shao, X., et al. (2021). Prefused Lysosomes Cluster on Autophagosomes Regulated by VAMP8. *Cell Death Dis.* 12 (10), 939. doi:10.1038/s41419-021-04243-0

Chen, Y., Bai, Y., Han, Z., He, W., and Guo, Z. (2015). Photoluminescence Imaging of Zn^{2+} in Living Systems. *Chem. Soc. Rev.* 44 (14), 4517–4546. doi:10.1039/C5CS00005J

Fang, H., Geng, S., Hao, M., Chen, Q., Liu, M., Liu, C., et al. (2021a). Simultaneous Zn^{2+} Tracking in Multiple Organelles Using Super-resolution Morphology-Correlated Organelle Identification in Living Cells. *Nat. Commun.* 12 (1), 109. doi:10.1038/s41467-020-20309-7

Fang, L., Crespo-Otero, R., Jones, C. R., and Watkinson, M. (2021b). Protect to Detect: A Golgi Apparatus Targeted Probe to Image Mobile Zinc through the Use of a Lipophilic Cell-Labile Protecting Group Strategy. *Sensors Actuators B Chem.* 338, 129850. doi:10.1016/j.snb.2021.129850

Hadj Abdallah, N., Baulies, A., Bouhlel, A., Bejaoui, M., Zaouali, M. A., Ben Mimouna, S., et al. (2018). Zinc Mitigates Renal Ischemia-Reperfusion Injury in Rats by Modulating Oxidative Stress, Endoplasmic Reticulum Stress, and Autophagy. *J. Cell. Physiol.* 233 (11), 8677–8690. doi:10.1002/jcp.26747

Hancock, S. M., Portbury, S. D., Gunn, A. P., Roberts, B. R., Bush, A. I., and Adlard, P. A. (2020). Zinc Transporter-3 Knockout Mice Demonstrate Age-dependent Alterations in the Metalloproteome. *Int. J. Mol. Sci.* 21 (3), 839. doi:10.3390/ijms21030839

Huang, H., Dong, C., Chang, M., Ding, L., Chen, L., Feng, W., et al. (2021). Mitochondria-specific Nanocatalysts for Chemotherapy-augmented Sequential Chemoreactive Tumor Therapy. *Exploration* 1 (1), 50–60. doi:10.1002/EXP.20210149

Inagi, R. (2009). Endoplasmic Reticulum Stress as a Progression Factor for Kidney Injury. *Curr. Opin. Pharmacol.* 10 (2), 156–165. doi:10.1016/j.coph.2009.11.006

Jackisch, L., Murphy, A. M., Kumar, S., Randeva, H., Tripathi, G., and Mcternan, P. G. (2020). Tunicamycin-Induced Endoplasmic Reticulum Stress Mediates Mitochondrial Dysfunction in Human Adipocytes. *J. Clin. Endocrinol. Metab.* 105 (9), 2905–2918. doi:10.1210/clinem/dgaa258

Kambe, T., Tsuji, T., Hashimoto, A., and Itsumura, N. (2015). The Physiological, Biochemical, and Molecular Roles of Zinc Transporters in Zinc Homeostasis and Metabolism. *Physiol. Rev.* 95 (3), 749–784. doi:10.1152/physrev.00035.2014

Li, W., Liu, Z., Fang, B., Jin, M., and Tian, Y. (2020). Two-photon Fluorescent Zn^{2+} Probe for Ratiometric Imaging and Biosensing of Zn^{2+} in Living Cells and Larval Zebrafish. *Biosens. Bioelectron.* 148, 111666. doi:10.1016/j.bios.2019.111666

Liang, X., Dempski, R. E., and Burdette, S. C. (2016). Zn^{2+} at a Cellular Crossroads. *Curr. Opin. Chem. Biol.* 31, 120–125. doi:10.1016/j.cbpa.2016.02.008

Liu, R., Kowada, T., Du, Y., Amagai, Y., Matsui, T., Inaba, K., et al. (2022). Organelle-Level Labile Zn^{2+} Mapping Based on Targetable Fluorescent Sensors. *ACS Sens.* 7 (3), 748–757. doi:10.1021/acssensors.1c02153

Liu, R., Xu, Y., Xu, K., and Dai, Z. (2021). Current Trends and Key Considerations in the Clinical Translation of Targeted Fluorescent Probes for Intraoperative Navigation. *Aggregate* 2 (3). doi:10.1002/agt2.23

Maret, W. (2019). The Redox Biology of Redox-Inert Zinc Ions. *Free Radic. Biol. Med.* 134, 311–326. doi:10.1016/j.freeradbiomed.2019.01.006

Qi, J., Ou, H., Liu, Q., and Ding, D. (2021). Gathering Brings Strength: How Organic Aggregates Boost Disease Phototheranostics. *Aggregate* 2 (1), 95–113. doi:10.1002/agt2.25

Sehgal, P., Szalai, P., Olesen, C., Praetorius, H. A., Nissen, P., Christensen, S. B., et al. (2017). Inhibition of the Sarco/endoplasmic Reticulum (ER) Ca^{2+}-ATPase by Thapsigargin Analogs Induces Cell Death via ER Ca^{2+} Depletion and the Unfolded Protein Response. *J. Biol. Chem.* 292 (48), 19656–19673. doi:10.1074/jbc.M117.796920

Stork, C. J., and Li, Y. V. (2010). Zinc Release from thapsigargin/IP3-Sensitive Stores in Cultured Cortical Neurons. *J. Mol. Signal* 5, 5. doi:10.1186/1750-2187-5-5

Suganya, N., Bhakkiyalakshmi, E., Suriyanarayanan, S., Paulmurugan, R., and Ramkumar, K. M. (2014). Quercetin Ameliorates Tunicamycin-Induced Endoplasmic Reticulum Stress in Endothelial Cells. *Cell Prolif.* 47 (3), 231–240. doi:10.1111/cpr.12102

Walkup, G. K., Burdette, S. C., Lippard, S. J., and Tsien, R. Y. (2000). A New Cell-Permeable Fluorescent Probe for Zn^{2+}. *J. Am. Chem. Soc.* 122 (23), 5644–5645. doi:10.1021/ja000868p

Wang, F., Wang, K., Kong, Q., Wang, J., Xi, D., Gu, B., et al. (2021). Recent Studies Focusing on the Development of Fluorescence Probes for Zinc Ion. *Coord. Chem. Rev.* 429, 213636. doi:10.1016/j.ccr.2020.213636

Wang, L., and Diao, J. (2022). VAMP8 Phosphorylation Regulates Lysosome Dynamics during Autophagy. *Autophagy Rep.* 1 (1), 79–82. doi:10.1080/27694127.2022.2031378

Wang, L., Chen, R., Han, G., Liu, X., Huang, T., Diao, J., et al. (2022). Super-resolution Analyzing Spatial Organization of Lysosomes with an Organic Fluorescent Probe. *Exploration*, 0210215. doi:10.1002/EXP.20210215

Zhang, X., Yuan, Y., Jiang, L., Zhang, J., Gao, J., Shen, Z., et al. (2014). Endoplasmic Reticulum Stress Induced by Tunicamycin and Thapsigargin Protects against Transient Ischemic Brain Injury: Involvement of PARK2-dependent Mitophagy. *Autophagy* 10 (10), 1801–1813. doi:10.4161/auto.32136

Zünkler, B. J., Wos-Maganga, M., and Panten, U. (2004). Fluorescence Microscopy Studies with a Fluorescent Glibenclamide Derivative, a High-Affinity Blocker of Pancreatic β-cell ATP-Sensitive K^+ Currents. *Biochem. Pharmacol.* 67 (8), 1437–1444. doi:10.1016/j.bcp.2003.12.011

Conflict of Interest: The authors declare that the research was conducted in the absence of any commercial or financial relationships that could be construed as a potential conflict of interest.

Publisher's Note: All claims expressed in this article are solely those of the authors and do not necessarily represent those of their affiliated organizations, or those of the publisher, the editors and the reviewers. Any product that may be evaluated in this article, or claim that may be made by its manufacturer, is not guaranteed or endorsed by the publisher.

Copyright © 2022 Fang, Li, Yao, Geng, Chen, Guo and He. This is an open-access article distributed under the terms of the Creative Commons Attribution License (CC BY). The use, distribution or reproduction in other forums is permitted, provided the original author(s) and the copyright owner(s) are credited and that the original publication in this journal is cited, in accordance with accepted academic practice. No use, distribution or reproduction is permitted which does not comply with these terms.

frontiers | Frontiers in Pharmacology

REVIEW
published: 20 June 2022
doi: 10.3389/fphar.2022.935898

Organelle Interaction and Drug Discovery: Towards Correlative Nanoscopy and Molecular Dynamics Simulation

Zhiwei Yang[1,2†], Zichen Zhang[1†], Yizhen Zhao[1], Qiushi Ye[1], Xuhua Li[1], Lingjie Meng[3,4], Jiangang Long[2], Shengli Zhang[1] and Lei Zhang[1*]*

[1]MOE Key Laboratory for Nonequilibrium Synthesis and Modulation of Condensed Matter, School of Physics, Xi'an Jiaotong University, Xi'an, China, [2]School of Life Science and Technology, Xi'an Jiaotong University, Xi'an, China, [3]School of Chemistry, Xi'an Jiaotong University, Xi'an, China, [4]Instrumental Analysis Center, Xi'an Jiaotong University, Xi'an, China

OPEN ACCESS

Edited by:
Qixin Chen,
Shandong First Medical University, China

Reviewed by:
Yang Chen,
Dalian Institute of Chemical Physics (CAS), China
Xing Zhang,
Tsinghua University, China

***Correspondence:**
Zhiwei Yang
yzws-123@xjtu.edu.cn
Lei Zhang
zhangleio@xjtu.edu.cn

[†]These authors have contributed equally to this work and share first authorship

Specialty section:
This article was submitted to Pharmacology of Anti-Cancer Drugs, a section of the journal Frontiers in Pharmacology

Received: 04 May 2022
Accepted: 01 June 2022
Published: 20 June 2022

Citation:
Yang Z, Zhang Z, Zhao Y, Ye Q, Li X, Meng L, Long J, Zhang S and Zhang L (2022) Organelle Interaction and Drug Discovery: Towards Correlative Nanoscopy and Molecular Dynamics Simulation. Front. Pharmacol. 13:935898. doi: 10.3389/fphar.2022.935898

The inter-organelle interactions, including the cytomembrane, endoplasmic reticulum, mitochondrion, lysosome, dictyosome, and nucleus, play the important roles in maintaining the normal function and homeostasis of cells. Organelle dysfunction can lead to a range of diseases (e.g., Alzheimer's disease (AD), Parkinson's disease (PD), and cancer), and provide a new perspective for drug discovery. With the development of imaging techniques and functional fluorescent probes, a variety of algorithms and strategies have been developed for the ever-improving estimation of subcellular structures, organelle interaction, and organelle-related drug discovery with accounting for the dynamic structures of organelles, such as the nanoscopy technology and molecular dynamics (MD) simulations. Accordingly, this work summarizes a series of state-of-the-art examples of the recent progress in this rapidly changing field and uncovering the drug screening based on the structures and interactions of organelles. Finally, we propose the future outlook for exciting applications of organelle-related drug discovery, with the cooperation of nanoscopy and MD simulations.

Keywords: organelle interaction, subcellular structure, drug discovery, nanoscopy, molecular dynamics simulation

INTRODUCTION

Cellular organelles with specific morphology and functions are highly dynamic in maintaining the normal operation of eukaryotic cell life activities (Xu et al., 2016; Passmore et al., 2021), and they interact with each other through coordination to complete a series of important physiological functions (Valm et al., 2017). The fine division of labor, cooperation, and close contact of organelles from the interaction network to realize rapid exchanges of substance and information and carry out various biological processes under different conditions (Schwarz and Blower, 2016). Dysfunctional interactions between organelles are usually accompanied by serious diseases (Sakhrani and Padh, 2013), including Alzheimer's disease (AD) (Santos et al., 2010; Burte et al., 2015; Wong et al., 2018), Parkinson's disease (PD) (Hauser and Hastings, 2013; Jin et al., 2014; Pickrell and Youle, 2015; Burbulla et al., 2017), and cancer (Doria et al., 2013; Nixon, 2013; Huang et al., 2016; Mc Donald and Krainc, 2017; Plotegher and Duchen, 2017). The dysfunction of organelles in various human diseases (**Figure 1**) could be mechanistically resolved by studying their architectures and interactions, as well as closely monitoring the dynamic alterations (Plotegher and Duchen, 2017; Samanta et al., 2019).

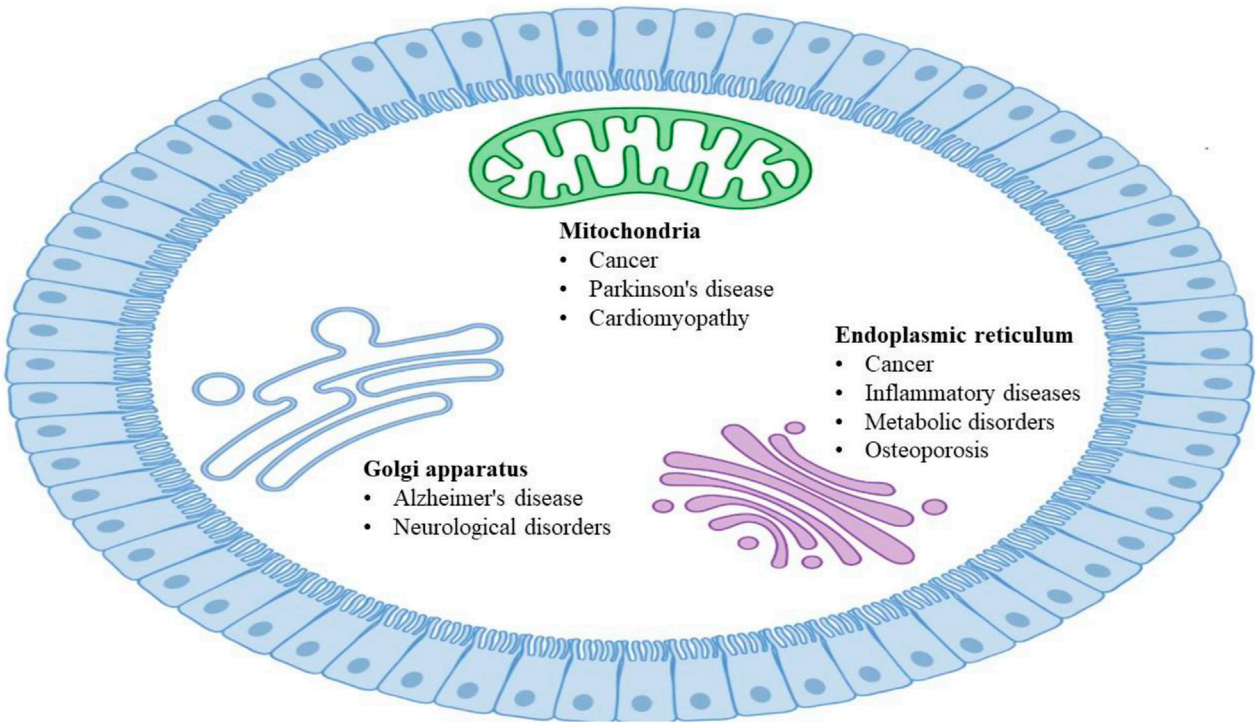

FIGURE 1 | Diseases associated with the specific organelles.

Organelle bioimaging can aid our understanding of the organelle functions and the development of organelle-targeting therapy for various diseases. Conventional fluorescence microscopy (FM) opens the door to fine structural details of cellular architectures and dynamics, while the resolution is limited to approximately 200 nm because of the light diffraction (Cox and Sheppard, 2004). As the dimension of the interaction between organelles is much smaller than the light diffraction limit, such as autophagosome, mitochondria-lysosome contact, and transport vesicles, many methods and techniques surpassing the diffraction limit have been developed (Carrington et al., 1995; Huang et al., 2008; Patterson et al., 2010). Among these technologies, super-resolution microscopy (SRM) (Reiter et al., 2011) and cryo-electron microscopy (cryo-EM) (Bai et al., 2015) have established their roles in overcoming these limits and allowing the study on organelles to enter the nanoage, helping us to elucidate the dynamics structures of organelles and present the intrinsically dynamic behavior of organelle interactions.

With the status of interactions between organelles in the improvements of pathogenesis and therapeutics, related articles are emerging as an endless stream. Recent advances in organelle-targeted fluorescent probes (FPs) provide us with a more suitable selection and high resolution scale under SRM (Ning et al., 2017). Meanwhile, some review articles have deliberated on the pathways to mitochondria-lysosome interactions (Audano et al., 2018) and molecules or ions transports between mitochondria and lysosomes (Raffaello et al., 2016; Todkar et al., 2017). In this review, various strategies will be summarized to the introduction and application of nanoscopy (SRM and cryo-EM) and molecular dynamics (MD) simulations in the dynamic nature of subcellular structures, the subcellular interactions, and the organelle-related drug discovery. In addition, this review presents the future developments working in concert towards the spatial evolution and throughput necessary for nanoscopy and MD simulations to promote the organelle-related drug pipeline.

NANOSCOPY ON ORGANELLE INTERACTIONS AND DRUG DISCOVERY

Super-resolution Microscopy

Precise imaging of intracellular and subcellular structures and their dynamic processes are crucial to fundamental research in biology and medicine (Dean and Palmer, 2014; Specht et al., 2017). Super-resolution microscopy (SRM) techniques (Gustafsson et al., 2016) enable the observation of fluorescence images of subcellular organelles beyond the diffraction limit by precluding fluorescence emission when fluorophores are exposed to the excitation light, have been developed (Hell, 2007; Yang et al., 2016). More recently, SRM has been used to investigate the properties of soft matters (Woell and Flors, 2017) such as polymers (Park et al., 2015), catalysts (Peng and Long, 2011), DNA origami (Iinuma et al., 2014), and lipid-based materials (Sharonov and Hochstrasser, 2006). There are two distinct conceptual approaches to obtaining the super-resolution image. One strategy based on probes for achieving supper

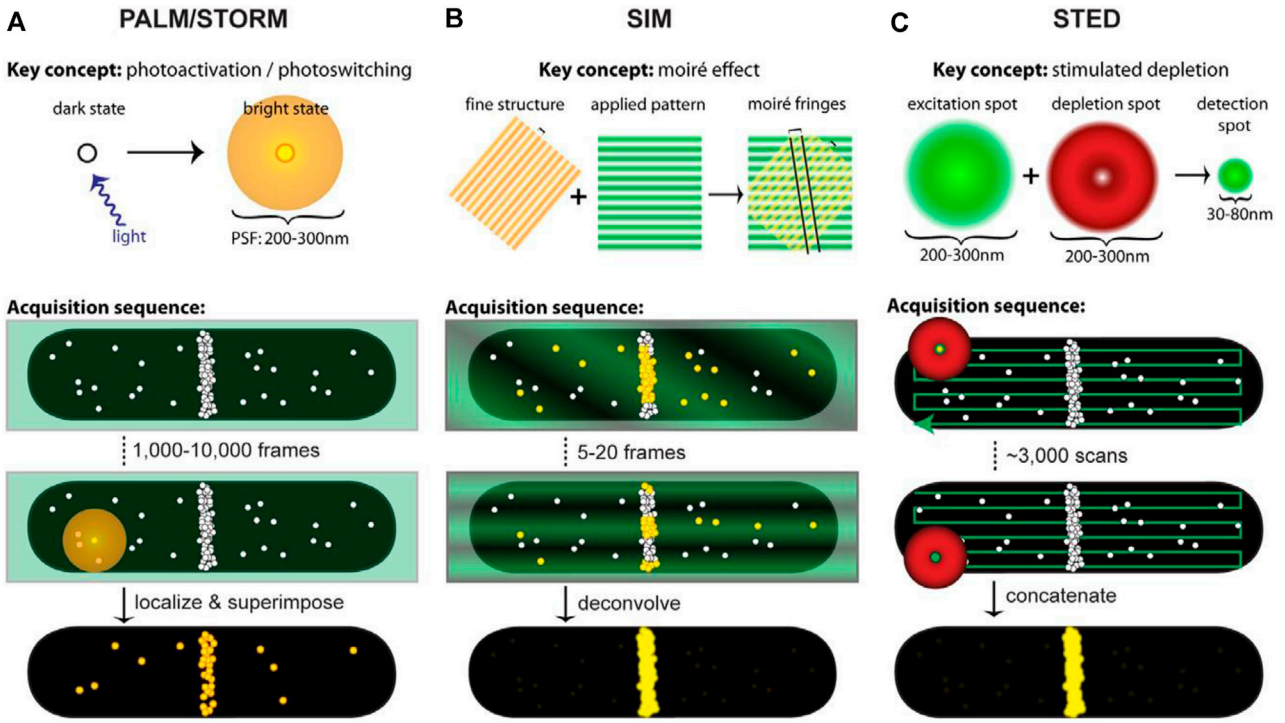

FIGURE 2 | Acquisition schematics for each super-resolution technique. White circles represent molecules, green represents excitation light, red represents depletion light, and yellow highlights fluorescing molecules. In acquisition schematics, molecular positions mimic the cellular distributions of the FtsZ protein (Coltharp and Xiao, 2012). **(A)** ALM and STORM based on single-molecule localization use low levels of activation light (violet arrow) to stochastically activate and localize single molecules. An activated molecule produces a diffraction-limited spot (diffuse yellow circle) to localize the molecule's position. Different spots are superimposed to create a superresolution image. **(B)** SIM utilizes the moiré effect. Interference between the illumination pattern (green stripes) and the sample (yellow stripes) produces moiré fringes (black lines). Although the emission from fluorescing molecules (yellow circles) is diffraction-limited, spatial information extracted from the Fourier transforms of each image with illumination patterns is combined to generate the super-resolution image. **(C)** STED projects concentric excitation (green circle) and depletion beams (red donut) onto a sample. Although the fluorophore can be excited (large green circle), the depletion beam (red donut) stimulates molecules outside the central 30–80 nm region back to the ground state before they fluoresce, generating a super-resolution PSF (small green circle). The super-resolution image is obtained by collecting beams.

resolution employs stochastic activation of fluorescence to switch on individual photoactivatable molecules and then images and bleaches them at different time points, including photoactivated localization microscopy (PALM) (Betzig et al., 2006) (**Figure 2A**), fluorescence photoactivated localization microscopy (FPALM) (Hess et al., 2006), and stochastic optical reconstruction microscopy (STORM) (Rust et al., 2006) (**Figure 2A**). The other category of strategies is based on modulating the spatial pattern of fluorescence emission of molecules, including stimulated emission depletion (STED) (Zhan et al., 2017) (**Figure 2C**) microscopy and its generalization reversible saturable optical transitions (RESOLFT) technique (Klar et al., 2000; Gustafsson, 2005; Hell, 2007) and structured illumination microscopy (SIM) (Gustafsson, 2005; Li et al., 2015) (**Figure 2B**). Commercial (e.g., Volocity, Amira, and Imaris) and open-source [e.g., Fiji (Schindelin et al., 2012), ImageJ (Collins, 2007), CellProfiler (Carpenter et al., 2006), Icy (de Chaumont et al., 2011) and V3D (Peng and Long, 2011)] software packages have been developed to enable the processing and analysis of microscopy images of organelles, further reducing the difficulty of analysis. SRM can obtain the images of dynamic structures during the processes of organelle interactions, and multicolor makes it more accurate in responding to subcellular effects with the conventional fluorescent group and simple operating device. But the resolution is largely affected by the selected fluorescent probe. Besides, the introduction to fluorophore will destroy cell activity and affect the physiological environment. However, current ultra-resolution imaging methods based on light and probe can visualize the structure and dynamic processes of cells at the subcellular organelle level, which provides great possibilities for studying the pathogenesis and therapeutic of organelle-related diseases.

With the technical advancements in SRM, in practice, however, many factors can influence the achievable resolution, including the excitation and detection schemes, the properties of fluorescent probes (FPs), as well as the labeling and sampling density of FPs. SRM technologies have also enhanced the requirements of FPs, which need especially low cytotoxicity, high photostability, photobleaching resistance (Uno et al., 2014), and specific background (Han et al., 2017) to monitor organelle interplay in living cells. In recent studies, FPs (**Table 1**) were mainly divided into organic small-molecule probes and

TABLE 1 | Properties of different fluorescent probes.

Probe	Properties
LTR (Zhitomirsky et al., 2018)	high quantum yield, cheap, and convenient but easily washed out, low photostability, and cytotoxicity
MTG (Chen et al., 2014)	
ERTG (Phaniraj et al., 2016)	
TPE-Ade (Xing et al., 2021)	used Ade acts as an active site of many small molecules and the fluorescence intensity was enhanced by 160 times
DTPA-BTN (Shen et al., 2021)	the FWHM value was decreased by 130 and 281 nm, which increased the signal-to-noise ratios
LC (Shen et al., 2018)	recorded mtDNA distribution at unprecedented resolution
DTPA-BT-F (Xu et al., 2022)	nanoparticle and have a diffusion limit during LMP

LTR: Lysosome Tracker Red, MTG: Mitochondria Tracker Green, ERTG: Endoplasmic Reticulum Tracker Green, TPE-Ade: Tetraphenylethylene- Adenosine, DTPA-BTN: 4,7-ditriphenylamine-[1,2,5]- thiadiazolo [3,4-c]pyridine, LC: a thiophene-based terpyridine Zn(II) complex, DTPA-BT-F: 4,4 '-(5,6-difluorobenzo[c][1,2,5]thiadiazole-4,7-diyl)bis(N,N-bis(4-methoxyphenyl)aniline).

TABLE 2 | Common commercial probes.

Organelle	Probes
Mitochondrion	Mito-Tracker Green FM(Pendergrass et al., 2004)
	Mito-Tracker Red FM(Buravkov et al., 2014)
Nuclear	DAPI (Castanheira et al., 2009)
	Hoechst 33342 (Zhang et al., 1999)
ER	ER-Tracker Green (Zhang et al., 2019b)
	ER-Tracker Red (Wu et al., 2018)
	ER-Tracker Blue-White DPX (Chini et al., 2018)
Lysosome	Lyso-Tracker Green (Sintes and del Giorgio, 2010)
	Lyso-Tracker Red (Freundt et al., 2007)
Golgi apparatus	Golgi-Tracker Red (Li et al., 2017)

ER:Endoplasmic Reticulum.

organelle-targeting phosphor transition metal complex probes (Kim and Cho, 2015; Wu et al., 2017). Commercial dyes (**Table 2**) are representative organic small-molecule probes for studying the interactions between organelles, especially in STED-based imaging. Because diluted dye solutions are used in the imaging process, the photostability of these probes leaves much to be desired. In addition, some commercial dyes alter the permeability of organelles and the inhibition of complexes at very low concentrations (Zielonka et al., 2017). Therefore, the development of new FPs is important to reveal the dynamic process of organelles for the special characters. The concept of "aggregation-induced emission" (AIE) was proposed by Tang et al. (2016) (Luo et al., 2001). Since then a series of AIE luminogens (AIEgens) can emit bright fluorescence in the aggregation state and do nothing in solution state (Zhang et al., 2019; Ni et al., 2019). Organic fluorophores for STED nanoscopy usually suffer from quenched emission in the aggregated state and inferior photostability (Dang et al., 2019). AIEgens have better photostability and photobleaching resistance than commercial dyes, so it has been considered to have great potential in STED applications (Zhang et al., 2018). TPE-Ade, a Golgi-targeting probe, was first used Ade acts as an active site of many small molecules in the Golgi apparatus and TPE with AIE characteristics, and the fluorescence intensity was enhanced by 160 times (Xing et al., 2021). Together with the good characteristics of AIE luminogens, Shen et al. synthesized whole-cell targeting nanoparticles, DTPA-BTN (Shen et al., 2021). Compared to the wide field images, the FWHM value of SIM images with DTPA-BTN was decreased by 130 and 281 nm, which increased the signal-to-noise ratios. AIEgens display good photostability and biocompatibility and can avoid fluorescence from the background. To overcome the limitations of small molecules during lysosomal membrane permeability (LMP), Xu et al. (2022) used DTPA-BT-F, an organic nanocrystal with high brightness for the lysosome imaging, at STED to monitor and long-term address lysosomal movements, including lysosomal contact. Due to the larger size, DTPA-BT-F had a diffusion limit during LMP, which prolongs their retention time with lysosomes for the long-term STED images which is the first case of AIE nanoparticles prepared by nanoprecipitation for STED. Compared with organic small-molecule probes, metal complex probes have stronger photostability, photobleaching resistance, and a large Stokes shift (Fernandez-Moreira et al., 2010). Hence, it is more suitable to observe the dynamic process of organelles for a long time (Chen et al., 2018). This provides the added advantage that lifetimes of phosphorescence are much longer than those of fluorescence, which makes changes in them potentially easier to detect (Shewring et al., 2017). Shen et al. (2018) designed and synthesized a mitochondrial-target probe LC, a Zn(II) complex based on a thiophene unit, binding with mtDNA in living cells. Due to the LC probe, the STED images recorded mtDNA distribution within mitochondrial cristae and inner matrix in living at unprecedented resolution (Shen et al., 2018). Tang et al. (2016) reported a mitochondria-targeting Zn (II) complex dye, Znsalen J-S-Alk, whose fluorescence intensity decayed to 10% of its maximum after 360 s of continuous scanning under STORM (Tang et al., 2016).

The search for new therapies is a tedious process with long cycles and high risks (Bialer and White, 2010). In the last 20 years, technological advances in genomics (Xu et al., 2018), proteomics (Han et al., 2008), and metabolomics (Wishart, 2016) have greatly increased the number of potential therapeutic targets for a wide variety of important clinical diseases (Zhu et al., 2012; Li et al., 2018). However, there still exists a gap in quickly and effectively identifying the target compound with the best efficacy from a large number of candidate compounds with high specificity and sensitivity, which is also a difficulty in current scientific research. Organelles are highly dynamic and equipped to constantly and rapidly change their motility, positioning, morphology, and identity for different functions (Passmore et al., 2021). Highly dynamic organelle interactions at the subcellular level regulate

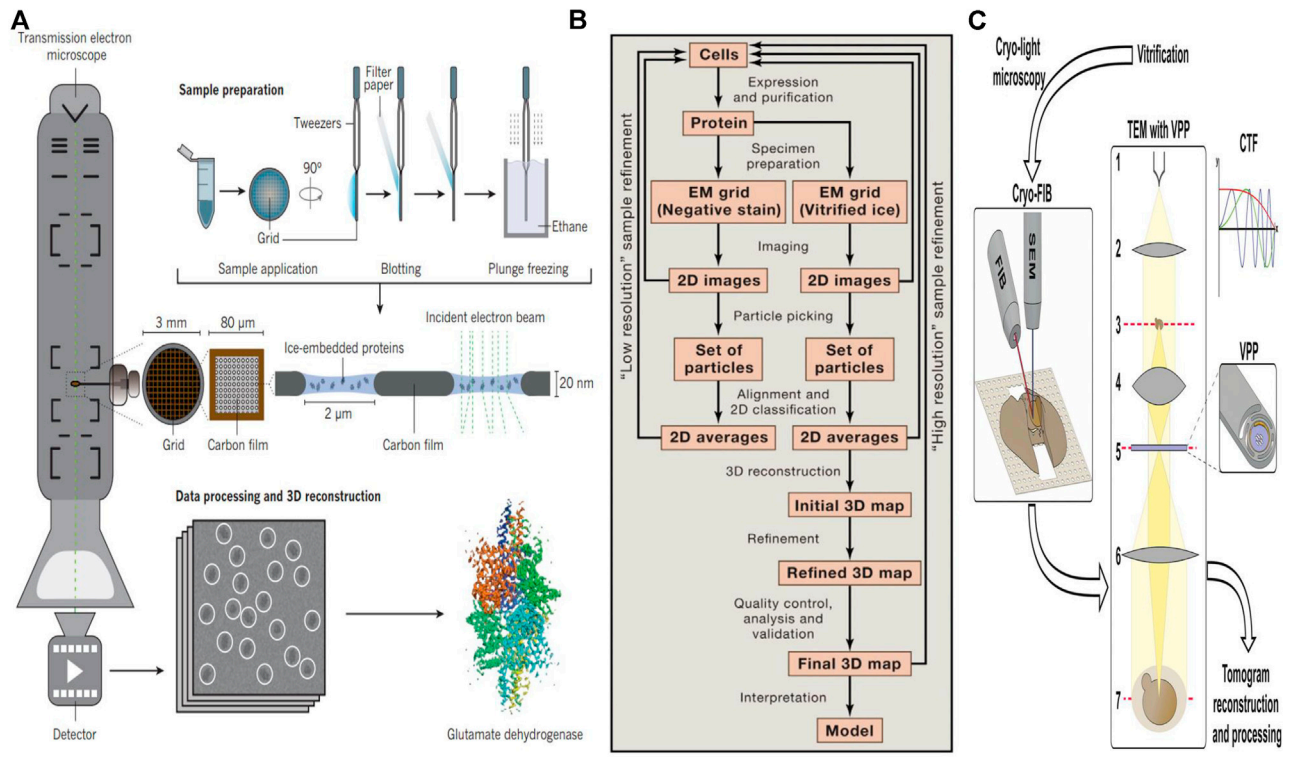

FIGURE 3 | (A) Protein structure determination through cryo-EM involves several stages: sample grid preparation, data collection, and data processing followed by 3D reconstruction (Fernandez-Leiro and Scheres, 2016); **(B)** Steps Involved in Structure Determination by Single Particle Cryo-EM(Cheng et al., 2015); **(C)** Workflow of cellular cryo-ET by cryo-FIB milling and VPP imaging (Wagner et al., 2017).

intracellular equilibrium and homeostasis and have been considered as the important targets for drug discovery. SRM can realize the observation of organelle interactions in living cells, find possible targets for treating diseases, and then observe the influence of drugs on the target. For example, there are thousands of proteins attached to the mitochondria. However, most proteins are encoded by nuclear genes except 13 proteins controlled by mtDNA (Beattie et al., 1966). These proteins are synthesized in the cytosol and imported into mitochondria by highly conserved translocation machinery (Harbauer et al., 2014). Through the analysis of mitochondrial protein composition, over fifty proteins were found to be shared with the endoplasmic reticulum. Cellular proteins include apoptosis inducing factor (AIF) (Chiang et al., 2012), acyl-CoA: diacylglycerol acyl-transferase 2 (DGAT2) (Stone et al., 2009), and retinol dehydrogenase 10 (Rdh10) (Jiang and Napoli, 2013) trafficking from the ER to the mitochondria directly. In addition, pathogen-encoded proteins such as human cytomegalovirus (CMV) (Bozidis et al., 2008) encode viral mitochondrial-localized inhibitor of apoptosis (vMIA), hepatitis c virus (HCV) encodes the N3/4A protease, and human immunodeficiency virus 1 (HIV-1) encodes viral protein R (Vpr), which also traffics from the ER to mitochondria (Huang et al., 2012). The contacts of ER and outer mitochondrial membrane (OMM) may facilitate the transportation of proteins between the ER and mitochondria (Kornmann et al., 2009). Mitochondrial localization inhibitor of human cytomegalovirus (HCMV) vMIA protein, which is transmitted to the mitochondrial associated membrane (MAM) and ER is in contact with OMM. For visualizing vMIA association with MAM, a series of images under STED showed vMIA is distributed in clusters (Bhuvanendran et al., 2014). The distribution established the ability of super-resolution imaging to provide valuable insight into viral protein localization, particularly in the sub-mitochondrial compartments, and into drug discovery and medical treatment of Cytomegalovirus. In contrast to direct transport from the cytosol to the OMM and vMIA traffics sequentially from the ER to mitochondria through mitochondria-associated membrane contacts between the two organelles rather than direct transport from the cytosol to the outer mitochondrial membrane. To investigate the role of host proteins in vMIA trafficking from the ER to mitochondria, Salka et al. (2017) designed a series of experiments, and the results revealed that the Mitofusin (Mfn1/2)- and phosphofurin acidic cluster sorting protein 2 (PACS-2)-mediated ER-mitochondria tethering is not required for the ER-mitochondria trafficking, proven by a fluorescence lifetime comparison of PACS-2- and

Mfn1/2-knockdown human primary fibroblasts and mouse embryos *via* STED method.

Cryo-Electron Microscopy

Although SRM can achieve the imaging of subcellular structures, it is difficult to detect dense material structures by using FPs, which prohibits the understanding of organelle interactions at the nanoscale level. Cryo-electron microscopy (cryo-EM) (Glaeser, 2018) (**Figure 3A**) can observe hyperfine structures of organelles at near atomic resolution under the conditions closest to the physiological environment, without the need for probes to label the samples. Due to the imaging and processing processes of cryo-EM strategy, the time series of dynamic structures are difficult to extract. However, cryo-EM remains firmly established as a central tool in the arsenal of structural biology, enabling the generation of numerous near-atomic resolution structures with the highest resolution of 1.22 Å (the β3 $GABA_A$ receptor) (Nakane et al., 2020). The establishment of cryo-EM benefits from the development of cryofixation through rapid cooling, which compels aqueous samples into a vitreous state, the development of efficient data processing [i.e., RELION (Zivanov et al., 2020)] and detector technology [direct electron detector, DDD (Barak et al., 2020)]. The two most prevalent approaches of cryo-EM are 1) to determine the three-dimensional (3D) structures of biological specimens: single particle analysis (SPA) (**Figure 3B**) (Nakane et al., 2020) and 2) cryo-electron tomography (cryo-ET) (**Figure 3C**) (Ng and Gan, 2020). In cryo-ET, the sample itself is imaged in 3D, and a series of 2D EM images are photographed by the sequentially tilted specimen (Wagner et al., 2017). The cryo-ET reconstruction method uses large micrographs for reconstruction, believing that large images can provide more signals and help to find the center of images at various tilting angles, but this kind of large image limits the resolution. Subtomogram averaging (STA) (Kucukelbir et al., 2014) is a recent successful development in tomography which collects data by tilt stage before tomographic reconstruction. Due to each molecule frozen in a completely random direction, there is no need to rotate the specimen stage for the projection in different directions and the projection range of SPA also exceeds the inclination range of specimen stage. The tilt angle limitation can be regarded as missing part of the sample information (Murata and Wolf, 2018). However, when the background noise is high, such as in the complex cellular environment, it is difficult to find and distinguish individual particles, only the conventional method (e.g., single particle analysis) can be adopted. In addition, the third dimension of STA is another advantage over the 2D image of SPA, because the 2D projection does not contain the absolute handedness of the structure, which increases the possibility of incorrect 3D reconstructions. STA can solve the brand-new structure with unknown symmetry and get the positive deterministic structure. However, the wrong symmetry information will cause the deviation of SPA and get the inaccurate 3D classification results.

Ren and Zhang invented the IPET method and FETR algorithm to perform the three-dimensional reconstruction. *Via* IPET and FETR, the adverse effect caused by the inclination error can be effectively limited, and the macromolecular center can be found more accurately, thus greatly improving the resolution of reconstruction results (Zhang et al., 2013). Interaction or crosstalk between organelles occurs in the blink of an eye at the nanoscale level. The dynamics of microenvironmental processes can be visualized by SRM with fluorescence probe labeling organelles however at the cost of wasting the structural and morphological information around the probes (Song and Murata, 2018). Whereas the dynamic processes of organelles are almost impossible to obtain due to the mechanism of cryo-EM forcing us to get a static picture (Ohta et al., 2021). Combining with fluorescence light microscopy and cryo-EM, correlative light and electron microscopy (CLEM) (Murata and Wolf, 2018; Ohta et al., 2021) can break through such technical limitations to meet the needs of life sciences and pharmacotherapeutics. Fluorescence microscopy captures the dynamics of the cellular process, then cell samples are fixed at a specific time. Subsequently, cryo-EM provides the surrounding ultrastructure at fluorescence localization. Focused ion beam SEM (FIB-SEM) can further improve the resolution of electron microscopy imaging of intracellular structures. Fermie was the first to use CLEM to link the dynamic characteristics and interactions of organelles to the hyperfine integrity of the structure of the labeled region. Combining CLEM and FIB-SEM, live images of the endo-lysosomal system were written down realizing the real-time tracking of late endosome-lysosome interactions (Fermie et al., 2018). In addition, Cryo-FIB provides a reliable technical option for understanding how subcellular organelles work together. Guo et al. (2022) visualized organelles of microalgae in unprecedented detail under cryo-FIB. The organelle volume of nuclear radiation mutant cells was significantly larger than that of wild-type cells.

The ER forms a continuous network of tubules and cisternae that extends throughout all cell compartments, including neuronal dendrites and axons (Griffing et al., 2017). There are two pathways in organelle communication: 1) vesicle transport between organelles and 2) membrane contacts without leading to the bulk transfer of organelle luminal content (Winters et al., 2020). Interorganellar communication at membrane contact sites (MCSs) plays a major role in lipid metabolism, Ca^{2+} homeostasis, and other fundamental cellular processes (Parnis et al., 2013). The ER forms MCSs with virtually all other organelles, such as the Golgi apparatus, mitochondria, lysosomes, or endosomes, as well as the plasma membrane (PM). The DHPR–RyR couplon is an excellent example of the importance of supramolecular architecture for MCS function. Visualization of components of the junction smaller than RyRs or DHPRs has been hindered by technical limitations, but pioneering cryo-ET work approached this issue in fully hydrated, unstained isolated triad junctions (Renken et al., 2009). These studies measured an average separation between sarcoplasmic reticulum and T-tubule membranes of 15.5 nm and hinted at a periodic arrangement of the calsequestrin layer, which is separated from the RyRs by a 5 nm gap bridged by fine filaments that could correspond to proteins such as triadin or junction. There are three protein coats, COPI (Zachaus et al., 2017), COPII (Hurley and Young, 2017), and clathrin (Kaksonen and Roux, 2018) mediating the formation and trafficking of vesicles in transport. The COPI coat mediates

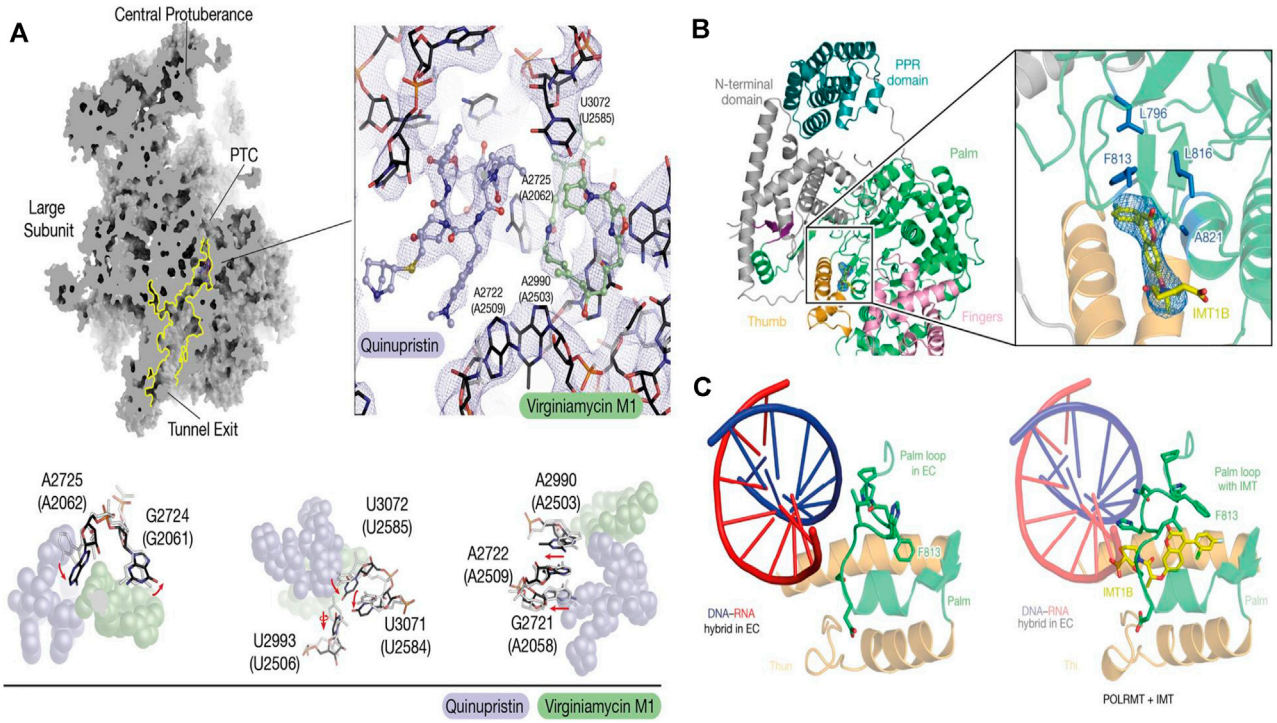

FIGURE 4 | (A) Cryo-EM of the mitoribosome from Q/D-treated cells (Sighel et al., 2021); **(B)** Cartoon representation of the cryo-EM structure of POLRMT bound to IMT1B. The cryo-EM density for IMT1B is shown as blue mesh (Bonekamp et al., 2020); **(C)** Structure of the palm loop in the mitochondrial transcription elongation complex (EC) (PDB code: 5OLA) and the palm loop in the presence of IMT(Bonekamp et al., 2020).

intra-Golgi and retrograde Golgi-ER trafficking and is fundamental to the polarized Golgi structure (Duden, 2003). Bykov et al. (2017) reported the *in situ* cryo-ET studies of Golgi stacks and the native structure of the COPI coat within Chlamydomonas reinhardtii cells, which provided reproducible Golgi architecture. Structural analysis of the Golgi apparatus and vesicle topology (**Figure 4A**) showed that vesicles change their size, membrane thickness, and cargo content as they progress from cis to trans, but the structure of the coat machinery remains constant. During apoptosis, mitochondria permeabilize the outer membranes to release apoptogenic proteins from the intermembrane space (Dingeldein et al., 2018). To further investigate mitochondrial outer membrane permeabilization (MOMP), Kuwana developed simple but faithful vesicle systems—outer membrane vesicles (OMVs) and liposomes—to visualize the pores in the membrane and dynamics by using cryo-EM *in vitro* preserving the native and hydrated membrane structure (Schafer et al., 2009; Gillies et al., 2015; Kuwana et al., 2016; Kuwana, 2019). Studies have indicated that Bax, an effector proapoptotic molecule that permeabilizes lipid membranes (Yang et al., 2006), is localized on the pore edges constituting part of the pore walls, and the pore exclusively formed by Bax oligomers will enlarge while more Bax molecules join.

Drug discovery and targeted drug transport are two links in the whole process of disease treatment. Although SRM can observe the structural changes and interaction dynamics of organelles in living cells, specific binding to organelle membrane proteins or other contact sites is still required for organelle-related drug development. Cryo-EM can image specific targets on organelles at a resolution of atomic level benefiting the understanding of therapeutic targets and drugs. By determining the structural basis for the improved affinity of the peptidic agonist of an aGPCR, peptidic antagonists toward aGPCRs were developed by converting the “finger residues” to acidic residues (Xiao et al., 2022). In search of drugs to treat hypertension and Parkinson’s disease - highly selective DRD1 agonists—Xiao et al. (2021) determined near-atomic-resolution cryo-EM structures of activated DRD1 with a downstream Gs effector revealing a conserved motif for dopaminergic receptor recognition with catecholamine agonists. With cell aging or cytopathic effect, the expression of mitochondrial DNA was changed. Inhibitors of mitochondrial transcription (IMTs) impair mtDNA transcription and inhibit mtDNA expression and the oxidative phosphorylation (OXPHOS) system. The OXPHOS system plays a vital role in the persistence of therapy-resistant cancer cell growth. Through the reconstruction of human mitochondrial RNA polymerase by cryo-EM, Bonekamp et al.(2020) found the allosteric binding site near the active center cleft of POLRMT (**Figures 4B,C**). After the treatment of IMT, the viability of cancer cells strongly decreased, but importantly, treatment with IMT was not cytotoxic to human PBMCs or pooled primary human hepatocytes. Prolonged treatment with an IMT thus

specifically affects the proliferation of cancer cells, which suggests that cancer therapy may be a potential *in vivo* application of IMTs. Glioblastoma (GBM) is the most common malignant primary brain tumor in adults. However, existing treatments, such as surgery and chemotherapy, have little effect on glioblastoma stem cells (GSCs) (Schulze et al., 2018). After high-content screening in a custom-made library of potential mitochondrial translation inhibitors, Sighel et al. (2021) identified the bacterial antibiotic quinupristin/dalfopristin (Q/D) as an effective suppressor of GSC growth that can disrupt the cell cycle, induce cell death and inhibit the replication of GSCs. Cryo-EM results revealed that Q/D binds to the large mitoribosomal subunit, inhibiting the mitochondrial protein synthesis and functionally dysregulating the OXPHOS complexes, suggesting that Q/D could potentially be repurposed for the treatment of tumors.

MOLECULAR DYNAMICS SIMULATIONS APPROACH FOR ORGANELLE INTERACTIONS

Although the dynamic process of organelle interactions can be obtained by nanoscopy, it is still necessary to analyze the evolution behavior at the all-atom level. Molecular dynamics (MD) simulations could obtain structural and dynamical insight into organelle interactions at the all-atom level (Fiorin et al., 2013). MD simulations have been used not only to study the dynamics of short-term organelle interactions in the presence and absence of membrane proteins but also to study the formation of structures and nanodomains around the organelle proteins. During these simulations, the coarsening models (Saunders and Voth, 2013) are usually adopted to save computing resources with the cost of sacrificing spatial resolution by allowing a significant increase in the integration time step in the numerical solution of Newton's equation of motion (Pluhackova and Bockmann, 2015).

With the increase in understanding of organelle composition and the importance of organelle interactions, modeling of organelle interactions has become more complex. An energy-based model has been designed for the molecular reaction-diffusion dynamics involved with the cytomembrane, cytoskeletons, and organelle membranes. The existence of a clustering associated with receptor-cluster rafts and the "fluid mosaic model" in the plasma membrane was confirmed based on this perspective (Azuma et al., 2006). With the development of computer hardware and algorithms, Coarse-Grained MD simulations have been widely extended beyond the cytomembrane, entering the domain of organelles and subcellular structures (Chavent et al., 2016). A model integrating multiple data from structural biology, mass spectroscopy, and biophysics realized the near atomic resolution of synaptic vesicles (Takamori et al., 2006). Based on MD simulations of bovine heart mitochondria, Arnarez et al. (2016) revealed the reason why cardiolipins glue complexes together is cardiolipin binding strength is higher than mitochondrial lipids resulting from non-additive electrostatic and van der Waals forces, suggesting that lipids have the ability to selectively mediate protein-protein interactions. The study of interactions between membraneless organelles has also benefited from MD simulations. For example, membraneless organelles exhibit classic signatures of liquids which allows to concentrate molecular reactants and organelle interactions to take place. Wei et al. (2017) found that the effective mesh size of intracellular droplets is ~ 3–8 nm, which determines the size scale of droplet characteristics affecting molecular diffusion and permeability, and reveals how specific intrinsically disordered proteins (IDPs) phase separate to form permeable, low-density liquid. Liquid-liquid phase separation (LLPS) condensates can simulate membraneless organelles *in vitro*. The rebalancing MD simulation force fields, based on experimental data on LLPS and without limiting specific coarse-particle sizes, not only perfect the interaction between proteins, but also correct the potential energy surface, improving the reliability of modeling interactions between membraneless organelles (Benayad et al., 2021). With the support of a new MD simulation approach equipped with a subtractive assembly technique to eliminate the overlap in space, Vermaas et al. (2022) simulated one protocell model at the organelle scale level and one protocell model at the cell scale level. The MD results revealed how membrane curvature plays a role in diffusion and protein organization at the subcellular scale level.

OUTLOOK

Organelle interactions play the important roles in maintaining cell homeostasis and function, and the fine organelle structures have extraordinary implications for drug discovery. Super-resolution microscopy (SRM) techniques enable the observation of fluorescence images of subcellular organelles beyond the diffraction limit and arouse the discovery of mitochondrial lysosome contact (MLC), providing a new perspective on the drug screening and the treatment of diseases (Chen et al., 2018; Chen et al., 2020). However, the resolution of ultra-resolution microscopy is still lower than that of cryo-EM, and the three-dimensional reconstruction results of organelles obtained by SRM seem to be different from those of cryo-EM approaches (e.g., cryo-ET) (Diebolder et al., 2012; Broeken et al., 2015). With the development of cryo-EM, the resolution of organelle structures has reached the approximate atomic level, especially the dynamic structural changes of the organelle interactions. While, the three-dimensional reconstruction of cryo-EM captures the configuration frozen in various random states, with the less time sequence information of captured structures.

The ideal of organelle interaction research is to capture a series of atomic resolution images in active state in chronological order, construct the dynamic structures during the interaction processes, and deeply understand the details of conformational transitions and "energy motion" transformation mechanism. Due to the limitation of current nanoscopy techniques, SRM and cryo-EM analyses cannot reach the atomic resolution or look at how a particular change over time trends. The two deficiencies could be

partially compensated by molecular dynamics (MD) simulation. Although the computational power of MD simulation is far from being able to replace the experiments, through careful design, especially constrained by the key dynamic spatial and temporal data provided by nanoscopy (SRM and cryo-EM), it can provide sufficient information for the construction of the initial model. Combined with Coarse-Grained MD and all-atom MD simulations, it is expected to not only connect the dynamic evolution process of organelle interaction on a large scale (the application of CG models sacrifices degrees of freedom), but also analyze the evolution behavior of key dynamic nodes at the all-atom level (reintroducing the atomic details by subsequent all-atom models), then summarize the physical characteristics and laws of the structure-activity changes of the system, and establish the correlation between the dynamic structure and function of organelles (Marrink et al., 2019).

With the continued advances in SRM, cryo-EM, and MD simulation, the combination of the three techniques and the cooperation of super-resolution time series and cryo-EM structure information will be an effective solution for the in-depth investigation of large-scale dynamic structural evolution and will provide new insight for the organelle interaction and drug discovery. It is promising to see the breakthroughs with this approach in the field of organelle-related drug discovery.

AUTHOR CONTRIBUTIONS

The manuscript was written through contributions of all authors. All authors have given approval to the final version of the manuscript.

FUNDING

This research was supported by the National Natural Science Foundation of China (Nos. 11774279, 11774280) and the National Science Fund for Outstanding Young Scholars (No. 11922410).

REFERENCES

Arnarez, C., Marrink, S. J., and Periole, X. (2016). Molecular Mechanism of Cardiolipin-Mediated Assembly of Respiratory Chain Supercomplexes. *Chem. Sci.* 7 (7), 4435–4443. doi:10.1039/c5sc04664e

Audano, M., Schneider, A., and Mitro, N. (2018). Mitochondria, Lysosomes, and Dysfunction: Their Meaning in Neurodegeneration. *J. Neurochem.* 147 (3), 291–309. doi:10.1111/jnc.14471

Azuma, R., Kitagawa, T., Kobayashi, H., and Konagaya, A. (2006). "Particle Simulation Approach for Sub-cellular Dynamics and Interactions of Biological Molecules," in FIRST INTERNATIONAL MULTI-SYMPOSIUMS ON COMPUTER AND COMPUTATIONAL SCIENCES (IMSCCS 2006), PROCEEDINGS, Hangzhou, China, 20-24 June 2006. doi:10.1109/imsccs.2006.101

Bai, X. C., McMullan, G., and Scheres, S. H. (2015). How Cryo-EM Is Revolutionizing Structural Biology. *Trends Biochem. Sci.* 40 (1), 49–57. doi:10.1016/j.tibs.2014.10.005

Barak, L., Bloch, I. M., Cababie, M., Cancelo, G., Chaplinsky, L., Chierchie, F., et al. (2020). SENSEI: Direct-Detection Results on Sub-GeV Dark Matter from a New Skipper CCD. *Phys. Rev. Lett.* 125 (17), 171802. doi:10.1103/PhysRevLett.125.171802

Beattie, D. S., Basford, R. E., and Koritz, S. B. (1966). Studies on the Biosynthesis of Mitochondrial Protein Components. *BIOCHEMISTRY* 5 (3), 926–930. doi:10.1021/bi00867a018

Benayad, Z., von Bülow, S., Stelzl, L. S., and Hummer, G. (2021). Simulation of FUS Protein Condensates with an Adapted Coarse-Grained Model. *J. Chem. Theory Comput.* 17 (1), 525–537. doi:10.1021/acs.jctc.0c01064

Betzig, E., Patterson, G. H., Sougrat, R., Lindwasser, O. W., Olenych, S., Bonifacino, J. S., et al. (2006). Imaging Intracellular Fluorescent Proteins at Nanometer Resolution. *SCIENCE* 313 (5793), 1642–1645. doi:10.1126/science.1127344

Bhuvanendran, S., Salka, K., Rainey, K., Sreetama, S. C., Williams, E., Leeker, M., et al. (2014). Superresolution Imaging of Human Cytomegalovirus vMIA Localization in Sub-mitochondrial Compartments. *Viruses* 6 (4), 1612–1636. doi:10.3390/v6041612

Bialer, M., and White, H. S. (2010). Key Factors in the Discovery and Development of New Antiepileptic Drugs. *Nat. Rev. Drug Discov.* 9 (1), 68–82. doi:10.1038/nrd2997

Bonekamp, N. A., Peter, B., Hillen, H. S., Felser, A., Bergbrede, T., Choidas, A., et al. (2020). Small-molecule Inhibitors of Human Mitochondrial DNA Transcription. *NATURE* 588(7839), 712, 716-+. doi: doi:10.1038/s41586-020-03048-z

Bozidis, P., Williamson, C. D., and Colberg-Poley, A. M. (2008). Mitochondrial and Secretory Human Cytomegalovirus UL37 Proteins Traffic into Mitochondrion-Associated Membranes of Human Cells. *J. Virol.* 82 (6), 2715–2726. doi:10.1128/JVI.02456-07

Broeken, J., Johnson, H., Lidke, D. S., Liu, S., Nieuwenhuizen, R. P., Stallinga, S., et al. (2015). Resolution Improvement by 3D Particle Averaging in Localization Microscopy. *Methods Appl. Fluoresc.* 3 (1), 014003. doi:10.1088/2050-6120/3/1/014003

Buravkov, S. V., Pogodina, M. V., and Buravkova, L. B. (2014). Comparison of Mitochondrial Fluorescent Dyes in Stromal Cells. *Bull. Exp. Biol. Med.* 157 (5), 654–658. doi:10.1007/s10517-014-2637-3

Burbulla, L. F., Song, P., Mazzulli, J. R., Zampese, E., Wong, Y. C., Jeon, S., et al. (2017). Dopamine Oxidation Mediates Mitochondrial and Lysosomal Dysfunction in Parkinson's Disease. *SCIENCE* 357 (6357), 1255–1261. doi:10.1126/science.aam9080

Burté, F., Carelli, V., Chinnery, P. F., and Yu-Wai-Man, P. (2015). Disturbed Mitochondrial Dynamics and Neurodegenerative Disorders. *Nat. Rev. Neurol.* 11 (1), 11–24. doi:10.1038/nrneurol.2014.228

Bykov, Y. S., Schaffer, M., Dodonova, S. O., Albert, S., Plitzko, J. M., Baumeister, W., et al. (2017). The Structure of the COPI Coat Determined within the Cell. *ELIFE* 6, e32493. doi:10.7554/eLife.32493

Carpenter, A. E., Jones, T. R., Lamprecht, M. R., Clarke, C., Kang, I. H., Friman, O., et al. (2006). CellProfiler: Image Analysis Software for Identifying and Quantifying Cell Phenotypes. *Genome Biol.* 7 (10), R100. doi:10.1186/gb-2006-7-10-r100

Carrington, W. A., Lynch, R. M., Moore, E. D., Isenberg, G., Fogarty, K. E., and Fay, F. S. (1995). Superresolution Three-Dimensional Images of Fluorescence in Cells with Minimal Light Exposure. *SCIENCE* 268 (5216), 1483–1487. doi:10.1126/science.7770772

Castanheira, P., Torquetti, L. T., Magalhães, D. R., Nehemy, M. B., and Goes, A. M. (2009). DAPI Diffusion after Intravitreal Injection of Mesenchymal Stem Cells in the Injured Retina of Rats. *Cell. Transpl.* 18 (4), 423–431. doi:10.3727/096368909788809811

Chavent, M., Duncan, A. L., and Sansom, M. S. (2016). Molecular Dynamics Simulations of Membrane Proteins and Their Interactions: from Nanoscale to Mesoscale. *Curr. Opin. Struct. Biol.* 40, 8–16. doi:10.1016/j.sbi.2016.06.007

Chen, Q., Jin, C., Shao, X., Guan, R., Tian, Z., Wang, C., et al. (2018a). Super-Resolution Tracking of Mitochondrial Dynamics with an Iridium(III) Luminophore. *SMALL* 14 (41), e1802166. doi:10.1002/smll.201802166

Chen, Q., Shao, X., Hao, M., Fang, H., Guan, R., Tian, Z., et al. (2020). Quantitative Analysis of Interactive Behavior of Mitochondria and Lysosomes Using

Structured Illumination Microscopy. *BIOMATERIALS* 250, 120059. doi:10.1016/j.biomaterials.2020.120059

Chen, Y., Qiao, L., Ji, L., and Chao, H. (2014). Phosphorescent Iridium(III) Complexes as Multicolor Probes for Specific Mitochondrial Imaging and Tracking. *BIOMATERIALS* 35 (1), 2–13. doi:10.1016/j.biomaterials.2013.09.051

Chen, Y., Rees, T. W., Ji, L., and Chao, H. (2018b). Mitochondrial Dynamics Tracking with Iridium(III) Complexes. *Curr. Opin. Chem. Biol.* 43, 51–57. doi:10.1016/j.cbpa.2017.11.006

Cheng, Y., Grigorieff, N., Penczek, P. A., and Walz, T. (2015). A Primer to Single-Particle Cryo-Electron Microscopy. *Cell* 161 (3), 438–449. doi:10.1016/j.cell.2015.03.050

Chiang, S. F., Huang, C. Y., Lin, T. Y., Chiou, S. H., and Chow, K. C. (2012). An Alternative Import Pathway of AIF to the Mitochondria. *Int. J. Mol. Med.* 29 (3), 365–372. doi:10.3892/ijmm.2011.849

Chini, C. E., Fisher, G. L., Johnson, B., Tamkun, M. M., and Kraft, M. L. (2018). Observation of Endoplasmic Reticulum Tubules via TOF-SIMS Tandem Mass Spectrometry Imaging of Transfected Cells. *BIOINTERPHASES* 13 (3), 03B409. doi:10.1116/1.5019736

Collins, T. J. (2007). ImageJ for Microscopy. *BIOTECHNIQUES* 43 (1), 25–30. doi:10.2144/000112517

Coltharp, C., and Xiao, J. (2012). Superresolution Microscopy for Microbiology. *Cell. Microbiol.* 14 (12), 1808–1818. doi:10.1111/cmi.12024

Cox, G., and Sheppard, C. J. (2004). Practical Limits of Resolution in Confocal and Non-linear Microscopy. *Microsc. Res. Tech.* 63 (1), 18–22. doi:10.1002/jemt.10423

Dang, D., Zhang, H., Xu, Y., Xu, R., Wang, Z., Kwok, R. T. K., et al. (2019). Super-Resolution Visualization of Self-Assembling Helical Fibers Using Aggregation-Induced Emission Luminogens in Stimulated Emission Depletion Nanoscopy. *ACS Nano* 13 (10), 11863–11873. doi:10.1021/acsnano.9b05914

de Chaumont, F., Dallongeville, S., and Olivo-Marin, J. C. (2011). "ICY: A NEW OPEN-SOURCE COMMUNITY IMAGE PROCESSING SOFTWARE," in 2011 8TH IEEE INTERNATIONAL SYMPOSIUM ON BIOMEDICAL IMAGING: FROM NANO TO MACRO, Chicago, IL, USA, 30 March 2011-02 April 2011. doi:10.1109/isbi.2011.5872395

Dean, K. M., and Palmer, A. E. (2014). Advances in Fluorescence Labeling Strategies for Dynamic Cellular Imaging. *Nat. Chem. Biol.* 10 (7), 512–523. doi:10.1038/NCHEMBIO.1556

Diebolder, C. A., Koster, A. J., and Koning, R. I. (2012). Pushing the Resolution Limits in Cryo Electron Tomography of Biological Structures. *J. Microsc.* 248 (1), 1–5. doi:10.1111/j.1365-2818.2012.03627.x

Dingeldein, A. P. G., Sparrman, T., and Gröbner, G. (2018). Oxidatively Stressed Mitochondria-Mimicking Membranes: A Molecular Insight into Their Organization during Apoptosis. *Biochim. Biophys. Acta Biomembr.* 1860 (12), 2644–2654. doi:10.1016/j.bbamem.2018.10.007

Doria, A., Gatto, M., and Punzi, L. (2013). Autophagy in Human Health and Disease. *N. Engl. J. Med.* 368 (19), 1845. doi:10.1056/NEJMc1303158

Duden, R. (2003). ER-to-Golgi Transport: COP I and COP II Function (Review). *Mol. Membr. Biol.* 20 (3), 197–207. doi:10.1080/0968768031000122548

Fermie, J., Liv, N., ten Brink, C., van Donselaar, E. G., Müller, W. H., Schieber, N. L., et al. (2018). Single Organelle Dynamics Linked to 3D Structure by Correlative Live-Cell Imaging and 3D Electron Microscopy. *TRAFFIC* 19 (5), 354–369. doi:10.1111/tra.12557

Fernandez-Leiro, R., and Scheres, S. H. (2016). Unravelling Biological Macromolecules with Cryo-Electron Microscopy. *NATURE* 537 (7620), 339–346. doi:10.1038/nature19948

Fernández-Moreira, V., Thorp-Greenwood, F. L., and Coogan, M. P. (2010). Application of D6 Transition Metal Complexes in Fluorescence Cell Imaging. *Chem. Commun. (Camb)* 46 (2), 186–202. doi:10.1039/b917757d

Fiorin, G., Klein, M. L., and Hénin, J. (2013). Using Collective Variables to Drive Molecular Dynamics Simulations. *Mol. Phys.* 111 (22-23), 3345–3362. doi:10.1080/00268976.2013.813594

Freundt, E. C., Czapiga, M., and Lenardo, M. J. (2007). Photoconversion of Lysotracker Red to a Green Fluorescent Molecule. *Cell. Res.* 17 (11), 956–958. doi:10.1038/cr.2007.80

Gillies, L. A., Du, H., Peters, B., Knudson, C. M., Newmeyer, D. D., and Kuwana, T. (2015). Visual and Functional Demonstration of Growing Bax-Induced Pores in Mitochondrial Outer Membranes. *Mol. Biol. Cell.* 26 (2), 339–349. doi:10.1091/mbc.E13-11-0638

Glaeser, R. M. (2018). Proteins, Interfaces, and Cryo-EM Grids. *Curr. Opin. COLLOID & INTERFACE Sci.* 34, 1–8. doi:10.1016/j.cocis.2017.12.009

Griffing, L. R., Lin, C., Perico, C., White, R. R., and Sparkes, I. (2017). Plant ER Geometry and Dynamics: Biophysical and Cytoskeletal Control during Growth and Biotic Response. *PROTOPLASMA* 254 (1), 43–56. doi:10.1007/s00709-016-0945-3

Guo, W., Feng, L., Wang, Z., Guo, J., Park, D., Carroll, B. L., et al. (2022). In-situ High-Resolution 3D Imaging Combined with Proteomics and Metabolomics Reveals Enlargement of Subcellular Architecture and Enhancement of Photosynthesis Pathways in Nuclear-Irradiated Chlorella Pyrenoidosa. *Chem. Eng. J.* 430, 133037. doi:10.1016/j.cej.2021.133037

Gustafsson, M. G. (2005). Nonlinear Structured-Illumination Microscopy: Wide-Field Fluorescence Imaging with Theoretically Unlimited Resolution. *Proc. Natl. Acad. Sci. U. S. A.* 102 (37), 13081–13086. doi:10.1073/pnas.0406877102

Gustafsson, N., Culley, S., Ashdown, G., Owen, D. M., Pereira, P. M., and Henriques, R. (2016). Fast Live-Cell Conventional Fluorophore Nanoscopy with ImageJ through Super-resolution Radial Fluctuations. *Nat. Commun.* 7, 12471. doi:10.1038/ncomms12471

Han, M. H., Hwang, S. I., Roy, D. B., Lundgren, D. H., Price, J. V., Ousman, S. S., et al. (2008). Proteomic Analysis of Active Multiple Sclerosis Lesions Reveals Therapeutic Targets. *NATURE* 451 (7182), 1076–1081. doi:10.1038/nature06559

Han, Y., Li, M., Qiu, F., Zhang, M., and Zhang, Y. H. (2017). Cell-permeable Organic Fluorescent Probes for Live-Cell Long-Term Super-resolution Imaging Reveal Lysosome-Mitochondrion Interactions. *Nat. Commun.* 8, 1307. doi:10.1038/s41467-017-01503-6

Harbauer, A. B., Zahedi, R. P., Sickmann, A., Pfanner, N., and Meisinger, C. (2014). The Protein Import Machinery of Mitochondria-A Regulatory Hub in Metabolism, Stress, and Disease. *Cell. Metab.* 19 (3), 357–372. doi:10.1016/j.cmet.2014.01.010

Hauser, D. N., and Hastings, T. G. (2013). Mitochondrial Dysfunction and Oxidative Stress in Parkinson's Disease and Monogenic Parkinsonism. *Neurobiol. Dis.* 51, 35–42. doi:10.1016/j.nbd.2012.10.011

Hell, S. W. (2007). Far-field Optical Nanoscopy. *SCIENCE* 316 (5828), 1153–1158. doi:10.1126/science.1137395

Hess, S. T., Girirajan, T. P., and Mason, M. D. (2006). Ultra-high Resolution Imaging by Fluorescence Photoactivation Localization Microscopy. *Biophys. J.* 91 (11), 4258–4272. doi:10.1529/biophysj.106.091116

Huang, B., Jones, S. A., Brandenburg, B., and Zhuang, X. (2008). Whole-cell 3D STORM Reveals Interactions between Cellular Structures with Nanometer-Scale Resolution. *Nat. Methods* 5 (12), 1047–1052. doi:10.1038/nmeth.1274

Huang, C. Y., Chiang, S. F., Lin, T. Y., Chiou, S. H., and Chow, K. C. (2012). HIV-1 Vpr Triggers Mitochondrial Destruction by Impairing Mfn2-Mediated ER-Mitochondria Interaction. *PLOS ONE* 7 (3), e33657. doi:10.1371/journal.pone.0033657

Huang, H., Yang, L., Zhang, P., Qiu, K., Huang, J., Chen, Y., et al. (2016). Real-time Tracking Mitochondrial Dynamic Remodeling with Two-Photon Phosphorescent Iridium (III) Complexes. *BIOMATERIALS* 83, 321–331. doi:10.1016/j.biomaterials.2016.01.014

Hurley, J. H., and Young, L. N. (2017). "Mechanisms of Autophagy Initiation," 86, 225–244. doi:10.1146/annurev-biochem-061516-044820*Annu. Rev. Biochem.*

Iinuma, R., Ke, Y., Jungmann, R., Schlichthaerle, T., Woehrstein, J. B., and Yin, P. (2014). Polyhedra Self-Assembled from DNA Tripods and Characterized with 3D DNA-PAINT. *SCIENCE* 344 (6179), 65–69. doi:10.1126/science.1250944

Jiang, W., and Napoli, J. L. (2013). The Retinol Dehydrogenase Rdh10 Localizes to Lipid Droplets during Acyl Ester Biosynthesis. *J. Biol. Chem.* 288 (1), 589–597. doi:10.1074/jbc.M112.402883

Jin, H., Kanthasamy, A., Ghosh, A., Anantharam, V., Kalyanaraman, B., and Kanthasamy, A. G. (2014). Mitochondria-targeted Antioxidants for Treatment of Parkinson's Disease: Preclinical and Clinical Outcomes. *Biochim. Biophys. Acta* 1842 (8), 1282–1294. doi:10.1016/j.bbadis.2013.09.007

Kaksonen, M., and Roux, A. (2018). Mechanisms of Clathrin-Mediated Endocytosis. *Nat. Rev. Mol. Cell. Biol.* 19 (5), 313–326. doi:10.1038/nrm.2017.132

Kim, H. M., and Cho, B. R. (2015). Small-Molecule Two-Photon Probes for Bioimaging Applications. *Chem. Rev.* 115 (11), 5014–5055. doi:10.1021/cr5004425

Klar, T. A., Jakobs, S., Dyba, M., Egner, A., and Hell, S. W. (2000). Fluorescence Microscopy with Diffraction Resolution Barrier Broken by Stimulated Emission. *Proc. Natl. Acad. Sci. U. S. A.* 97 (15), 8206–8210. doi:10.1073/pnas.97.15.8206

Kornmann, B., Currie, E., Collins, S. R., Schuldiner, M., Nunnari, J., Weissman, J. S., et al. (2009). An ER-Mitochondria Tethering Complex Revealed by a Synthetic Biology Screen. *SCIENCE* 325 (5939), 477–481. doi:10.1126/science.1175088

Kucukelbir, A., Sigworth, F. J., and Tagare, H. D. (2014). Quantifying the Local Resolution of Cryo-EM Density Maps. *Nat. Methods* 11 (1), 63–65. doi:10.1038/NMETH.2727

Kuwana, T. (2019). Cryo-Electron Microscopy to Study Bax Pores and MOMP. *Methods Mol. Biol.* 1877, 247–256. doi:10.1007/978-1-4939-8861-7_17

Kuwana, T., Olson, N. H., Kiosses, W. B., Peters, B., and Newmeyer, D. D. (2016). Pro-apoptotic Bax Molecules Densely Populate the Edges of Membrane Pores. *Sci. Rep.* 6, 27299. doi:10.1038/srep27299

Li, D., Shao, L., Chen, B. C., Zhang, X., Zhang, M., Moses, B., et al. (2015). ADVANCED IMAGING. Extended-Resolution Structured Illumination Imaging of Endocytic and Cytoskeletal Dynamics. *SCIENCE* 349 (6251), aab3500. doi:10.1126/science.aab3500

Li, L.-D., Wang, D.-F., Liu, F.-J., Zhang, H., Li, H.-L., and Wu, G.-Y. (2017). Localization in Organelles and Function Analysis of Aquaporin 1 (AQP1) Protein in Ectropis Obliqua (Lepidoptera: Geometridae). *Acta Entomol. Sin.* 60 (7), 750–759. doi:10.16380/j.kcxb.2017.07.003

Li, Y. H., Yu, C. Y., Li, X. X., Zhang, P., Tang, J., Yang, Q., et al. (2018). Therapeutic Target Database Update 2018: Enriched Resource for Facilitating Bench-To-Clinic Research of Targeted Therapeutics. *Nucleic Acids Res.* 46 (D1), D1121–D1127. doi:10.1093/nar/gkx1076

Luo, J., Xie, Z., Lam, J. W., Cheng, L., Chen, H., Qiu, C., et al. (2001). Aggregation-induced Emission of 1-Methyl-1,2,3,4,5-Pentaphenylsilole. *Chem. Commun. (Camb)* 381 (18), 1740–1741. doi:10.1039/b105159h

Marrink, S. J., Corradi, V., Souza, P. C. T., Ingólfsson, H. I., Tieleman, D. P., and Sansom, M. S. P. (2019). Computational Modeling of Realistic Cell Membranes. *Chem. Rev.* 119 (9), 6184–6226. doi:10.1021/acs.chemrev.8b00460

Mc Donald, J. M., and Krainc, D. (2017). Lysosomal Proteins as a Therapeutic Target in Neurodegeneration. *Annu. Rev. Med.* 68, 445–458. doi:10.1146/annurev-med-050715-104432

Murata, K., and Wolf, M. (2018). Cryo-electron Microscopy for Structural Analysis of Dynamic Biological Macromolecules. *Biochim. Biophys. Acta Gen. Subj.* 1862 (2), 324–334. doi:10.1016/j.bbagen.2017.07.020

Nakane, T., Kotecha, A., Sente, A., McMullan, G., Masiulis, S., Brown, P. M. G. E., et al. (2020). Single-particle Cryo-EM at Atomic Resolution. *NATURE* 587(7832), 152, 156-+. doi: doi:10.1038/s41586-020-2829-0

Ng, C. T., and Gan, L. (2020). Investigating Eukaryotic Cells with Cryo-ET. *Mol. Biol. Cell.* 31 (2), 87–100. doi:10.1091/mbc.E18-05-0329

Ni, X., Zhang, X., Duan, X., Zheng, H. L., Xue, X. S., and Ding, D. (2019). Near-Infrared Afterglow Luminescent Aggregation-Induced Emission Dots with Ultrahigh Tumor-To-Liver Signal Ratio for Promoted Image-Guided Cancer Surgery. *Nano Lett.* 19 (1), 318–330. doi:10.1021/acs.nanolett.8b03936

Ning, P., Wang, W., Chen, M., Feng, Y., and Meng, X. (2017). Recent Advances in Mitochondria- and Lysosomes-Targeted Small-Molecule Two-Photon Fluorescent Probes. *Chin. Chem. Lett.* 28 (10), 1943–1951. doi:10.1016/j.cclet.2017.09.026

Nixon, R. A. (2013). The Role of Autophagy in Neurodegenerative Disease. *Nat. Med.* 19 (8), 983–997. doi:10.1038/nm.3232

Ohta, K., Hirashima, S., Miyazono, Y., Togo, A., and Nakamura, K. I. (2021). Correlation of Organelle Dynamics between Light Microscopic Live Imaging and Electron Microscopic 3D Architecture Using FIB-SEM. *Microsc. (Oxf)* 70 (2), 161–170. doi:10.1093/jmicro/dfaa071

Park, H., Hoang, D. T., Paeng, K., and Kaufman, L. J. (2015). Localizing Exciton Recombination Sites in Conformationally Distinct Single Conjugated Polymers by Super-resolution Fluorescence Imaging. *ACS Nano* 9 (3), 3151–3158. doi:10.1021/acsnano.5b00086

Parnis, J., Montana, V., Delgado-Martinez, I., Matyash, V., Parpura, V., Kettenmann, H., et al. (2013). Mitochondrial Exchanger NCLX Plays a Major Role in the Intracellular Ca2+ Signaling, Gliotransmission, and Proliferation of Astrocytes. *J. Neurosci.* 33 (17), 7206–7219. doi:10.1523/JNEUROSCI.5721-12.2013

Passmore, J. B., Nijenhuis, W., and Kapitein, L. C. (2021). From Observing to Controlling: Inducible Control of Organelle Dynamics and Interactions. *Curr. Opin. Cell. Biol.* 71, 69–76. doi:10.1016/j.ceb.2021.02.002

Patterson, G., Davidson, M., Manley, S., and Lippincott-Schwartz, J. (2010). Superresolution Imaging Using Single-Molecule Localization. *Annu. Rev. Phys. Chem.* 61, 345–367. doi:10.1146/annurev.physchem.012809.103444

Pendergrass, W., Wolf, N., and Poot, M. (2004). Efficacy of MitoTracker Green and CMXrosamine to Measure Changes in Mitochondrial Membrane Potentials in Living Cells and Tissues. *Cytom. A* 61 (2), 162–169. doi:10.1002/cyto.a.20033

Peng, H. C., and Long, F. H. (2011). "Seeing More Is Knowing More: V3D Enables Real-Time 3D Visualization and Quantitative Analysis of Large-Scale Biological Image Data Sets," in RESEARCH IN COMPUTATIONAL MOLECULAR BIOLOGY, Vancouver, BC, Canada, March 28-31, 2011. doi:10.1007/978-3-642-20036-6_30

Phaniraj, S., Gao, Z., Rane, D., and Peterson, B. R. (2016). Hydrophobic Resorufamine Derivatives: Potent and Selective Red Fluorescent Probes of the Endoplasmic Reticulum of Mammalian Cells. *Dyes Pigm* 135, 127–133. doi:10.1016/j.dyepig.2016.05.007

Pickrell, A. M., and Youle, R. J. (2015). The Roles of PINK1, Parkin, and Mitochondrial Fidelity in Parkinson's Disease. *NEURON* 85 (2), 257–273. doi:10.1016/j.neuron.2014.12.007

Plotegher, N., and Duchen, M. R. (2017). Mitochondrial Dysfunction and Neurodegeneration in Lysosomal Storage Disorders. *Trends Mol. Med.* 23 (2), 116–134. doi:10.1016/j.molmed.2016.12.003

Pluhackova, K., and Böckmann, R. A. (2015). Biomembranes in Atomistic and Coarse-Grained Simulations. *J. Phys. Condens Matter* 27 (32), 323103. doi:10.1088/0953-8984/27/32/323103

Raffaello, A., Mammucari, C., Gherardi, G., and Rizzuto, R. (2016). Calcium at the Center of Cell Signaling: Interplay between Endoplasmic Reticulum, Mitochondria, and Lysosomes. *Trends Biochem. Sci.* 41 (12), 1035–1049. doi:10.1016/j.tibs.2016.09.001

Reiter, L., Rinner, O., Picotti, P., Hüttenhain, R., Beck, M., Brusniak, M. Y., et al. (2011). mProphet: Automated Data Processing and Statistical Validation for Large-Scale SRM Experiments. *Nat. Methods* 8 (5), 430–435. doi:10.1038/NMETH.1584

Renken, C., Hsieh, C. E., Marko, M., Rath, B., Leith, A., Wagenknecht, T., et al. (2009). Structure of Frozen-Hydrated Triad Junctions: A Case Study in Motif Searching inside Tomograms. *J. Struct. Biol.* 165 (2), 53–63. doi:10.1016/j.jsb.2008.09.011

Rust, M. J., Bates, M., and Zhuang, X. (2006). Sub-diffraction-limit Imaging by Stochastic Optical Reconstruction Microscopy (STORM). *Nat. Methods* 3 (10), 793–795. doi:10.1038/nmeth929

Sakhrani, N. M., and Padh, H. (2013). Organelle Targeting: Third Level of Drug Targeting. *Drug Des. Devel Ther.* 7, 585–599. doi:10.2147/DDDT.S45614

Salka, K., Bhuvanendran, S., Wilson, K., Bozidis, P., Mehta, M., Rainey, K., et al. (2017). Superresolution Imaging Identifies that Conventional Trafficking Pathways Are Not Essential for Endoplasmic Reticulum to Outer Mitochondrial Membrane Protein Transport. *Sci. Rep.* 7, 16. doi:10.1038/s41598-017-00039-5

Samanta, S., He, Y., Sharma, A., Kim, J., Pan, W., Yang, Z., et al. (2019). Fluorescent Probes for Nanoscopic Imaging of Mitochondria. *CHEM* 5 (7), 1697–1726. doi:10.1016/j.chempr.2019.03.011

Santos, R. X., Correia, S. C., Wang, X., Perry, G., Smith, M. A., Moreira, P. I., et al. (2010). A Synergistic Dysfunction of Mitochondrial Fission/Fusion Dynamics and Mitophagy in Alzheimer's Disease. *J. Alzheimers Dis.* 20 Suppl 2, S401–S412. doi:10.3233/JAD-2010-100666

Saunders, M. G., and Voth, G. A. (2013). Coarse-Graining Methods for Computational Biology. *Annu. Rev. Biophys.* 42, 73–93. doi:10.1146/annurev-biophys-083012-130348

Schafer, B., Quispe, J., Choudhary, V., Chipuk, J. E., Ajero, T. G., Du, H., et al. (2009). Mitochondrial Outer Membrane Proteins Assist Bid in Bax-Mediated Lipidic Pore Formation. *Mol. Biol. Cell.* 20 (8), 2276–2285. doi:10.1091/mbc.E08-10-1056

Schindelin, J., Arganda-Carreras, I., Frise, E., Kaynig, V., Longair, M., Pietzsch, T., et al. (2012). Fiji: an Open-Source Platform for Biological-Image Analysis. *Nat. Methods* 9 (7), 676–682. doi:10.1038/NMETH.2019

Schulze, M., Violonchi, C., Swoboda, S., Welz, T., Kerkhoff, E., Hoja, S., et al. (2018). RELN Signaling Modulates Glioblastoma Growth and Substrate-dependent Migration. *Brain Pathol.* 28 (5), 695–709. doi:10.1111/bpa.12584

Schwarz, D. S., and Blower, M. D. (2016). The Endoplasmic Reticulum: Structure, Function and Response to Cellular Signaling. *Cell. Mol. Life Sci.* 73 (1), 79–94. doi:10.1007/s00018-015-2052-6

Sharonov, A., and Hochstrasser, R. M. (2006). Wide-field Subdiffraction Imaging by Accumulated Binding of Diffusing Probes. *Proc. Natl. Acad. Sci. U. S. A.* 103 (50), 18911–18916. doi:10.1073/pnas.0609643104

Shen, Q., Xu, R., Wang, Z., Zhao, T., Zhou, Y., Xu, Y., et al. (2021). Donor-Acceptor Typed AIE Luminogens with Near-Infrared Emission for Super-resolution Imaging. *Chem. Res. Chin. Univ.* 37 (1), 143–149. doi:10.1007/s40242-021-0390-5

Shen, Y., Shao, T., Fang, B., Du, W., Zhang, M., Liu, J., et al. (2018). Visualization of Mitochondrial DNA in Living Cells with Super-resolution Microscopy Using Thiophene-Based Terpyridine Zn(II) Complexes. *Chem. Commun. (Camb)* 54 (80), 11288–11291. doi:10.1039/c8cc06276e

Shewring, J. R., Cankut, A. J., McKenzie, L. K., Crowston, B. J., Botchway, S. W., Weinstein, J. A., et al. (2017). Multimodal Probes: Superresolution and Transmission Electron Microscopy Imaging of Mitochondria, and Oxygen Mapping of Cells, Using Small-Molecule Ir(III) Luminescent Complexes. *Inorg. Chem.* 56 (24), 15259–15270. doi:10.1021/acs.inorgchem.7b02633

Sighel, D., Notarangelo, M., Aibara, S., Re, A., Ricci, G., Guida, M., et al. (2021). Inhibition of Mitochondrial Translation Suppresses Glioblastoma Stem Cell Growth. *Cell. Rep.* 35 (4), 109024. doi:10.1016/j.celrep.2021.109024

Sintes, E., and del Giorgio, P. A. (2010). Community Heterogeneity and Single-Cell Digestive Activity of Estuarine Heterotrophic Nanoflagellates Assessed Using Lysotracker and Flow Cytometry. *Environ. Microbiol.* 12 (7), 1913–1925. doi:10.1111/j.1462-2920.2010.02196.x

Song, C., and Murata, K. (2018). Cryo-electron Microscopy for Structural Analysis ofDynamic Biological Macromolecules. *J. Comput. Chem. Jpn.* 17 (1), 38–45. doi:10.2477/jccj.2018-0007

Specht, E. A., Braselmann, E., and Palmer, A. E. (2017). A Critical and Comparative Review of Fluorescent Tools for Live-Cell Imaging. *Annu. Rev. Physiol.* 79, 93–117. doi:10.1146/annurev-physiol-022516-034055

Stone, S. J., Levin, M. C., Zhou, P., Han, J., Walther, T. C., and Farese, R. V. (2009). The Endoplasmic Reticulum Enzyme DGAT2 Is Found in Mitochondria-Associated Membranes and Has a Mitochondrial Targeting Signal that Promotes its Association with Mitochondria. *J. Biol. Chem.* 284 (8), 5352–5361. doi:10.1074/jbc.M805768200

Takamori, S., Holt, M., Stenius, K., Lemke, E. A., Grønborg, M., Riedel, D., et al. (2006). Molecular Anatomy of a Trafficking Organelle. *Cell* 127 (4), 831–846. doi:10.1016/j.cell.2006.10.030

Tang, J., Zhang, M., Yin, H. Y., Jing, J., Xie, D., Xu, P., et al. (2016). A Photoactivatable Znsalen Complex for Super-resolution Imaging of Mitochondria in Living Cells. *Chem. Commun. (Camb)* 52 (77), 11583–11586. doi:10.1039/c6cc06531g

Todkar, K., Ilamathi, H. S., and Germain, M. (2017). Mitochondria and Lysosomes: Discovering Bonds. *Front. Cell. Dev. Biol.* 5, 106. doi:10.3389/fcell.2017.00106

Uno, S. N., Kamiya, M., Yoshihara, T., Sugawara, K., Okabe, K., Tarhan, M. C., et al. (2014). A Spontaneously Blinking Fluorophore Based on Intramolecular Spirocyclization for Live-Cell Super-resolution Imaging. *Nat. Chem.* 6 (8), 681–689. doi:10.1038/NCHEM.2002

Valm, A. M., Cohen, S., Legant, W. R., Melunis, J., Hershberg, U., Wait, E., et al. (2017). Applying Systems-Level Spectral Imaging and Analysis to Reveal the Organelle Interactome. *NATURE* 546(7656), 162, 167.doi:10.1038/nature22369

Vermaas, J. V., Mayne, C. G., Shinn, E., and Tajkhorshid, E. (2022). Assembly and Analysis of Cell-Scale Membrane Envelopes. *J. Chem. Inf. Model.* 62 (3), 602–617. doi:10.1021/acs.jcim.1c01050

Wagner, J., Schaffer, M., and Fernández-Busnadiego, R. (2017). Cryo-electron Tomography-The Cell Biology that Came in from the Cold. *FEBS Lett.* 591 (17), 2520–2533. doi:10.1002/1873-3468.12757

Wei, M. T., Elbaum-Garfinkle, S., Holehouse, A. S., Chen, C. C., Feric, M., Arnold, C. B., et al. (2017). Phase Behaviour of Disordered Proteins Underlying Low Density and High Permeability of Liquid Organelles. *Nat. Chem.* 9 (11), 1118–1125. doi:10.1038/NCHEM.2803

Winters, C. M., Hong-Brown, L. Q., and Chiang, H. L. (2020). Intracellular Vesicle Clusters Are Organelles that Synthesize Extracellular Vesicle-Associated Cargo Proteins in Yeast. *J. Biol. Chem.* 295 (9), 2650–2663. doi:10.1074/jbc.RA119.008612

Wishart, D. S. (2016). Emerging Applications of Metabolomics in Drug Discovery and Precision Medicine. *Nat. Rev. Drug Discov.* 15 (7), 473–484. doi:10.1038/nrd.2016.32

Wöll, D., and Flors, C. (2017). Super-resolution Fluorescence Imaging for Materials Science. *SMALL METHODS* 1 (10), 1700191. doi:10.1002/smtd.201700191

Wong, Y. C., Ysselstein, D., and Krainc, D. (2018). Mitochondria-lysosome Contacts Regulate Mitochondrial Fission via RAB7 GTP Hydrolysis. *NATURE* 554 (7692), 382–386. doi:10.1038/nature25486

Wu, D., Sedgwick, A. C., Gunnlaugsson, T., Akkaya, E. U., Yoon, J., and James, T. D. (2017). Fluorescent Chemosensors: the Past, Present and Future. *Chem. Soc. Rev.* 46 (23), 7105–7123. doi:10.1039/c7cs00240h

Wu, L., Wang, Y., Weber, M., Liu, L., Sedgwick, A. C., Bull, S. D., et al. (2018). ESIPT-based Ratiometric Fluorescence Probe for the Intracellular Imaging of Peroxynitrite. *Chem. Commun. (Camb)* 54 (71), 9953–9956. doi:10.1039/c8cc04919j

Xiao, P., Yan, W., Gou, L., Zhong, Y. N., Kong, L., Wu, C., et al. (2021). Ligand Recognition and Allosteric Regulation of DRD1-Gs Signaling Complexes. *Cell* 184 (4), 943–e18. doi:10.1016/j.cell.2021.01.028

Xiao, P., Guo, S., Wen, X., He, Q.-T., Lin, H., Huang, S.-M., et al. (2022). Tethered Peptide Activation Mechanism of the Adhesion GPCRs ADGRG2 and ADGRG4. *Nature* 604, 771–778. doi:10.1038/s41586-022-04590-8

Xing, X., Jia, Y., Zhang, J., Wu, Z., Qin, M., Li, P., et al. (2021). A Novel Aggregation Induced Emission (AIE) Fluorescence Probe by Combining Tetraphenylethylene and 2′,3′-O-Isopropylideneadenosine for Localizing Golgi Apparatus. *Sensors Actuators B Chem.* 329, 129245. doi:10.1016/j.snb.2020.129245

Xu, D., Jin, T., Zhu, H., Chen, H., Ofengeim, D., Zou, C., et al. (2018). TBK1 Suppresses RIPK1-Driven Apoptosis and Inflammation during Development and in Aging. *Cell* 174 (6), 1477–e19. doi:10.1016/j.cell.2018.07.041

Xu, R., Dang, D., Wang, Z., Zhou, Y., Xu, Y., Zhao, Y., et al. (2022). Facilely Prepared Aggregation-Induced Emission (AIE) Nanocrystals with Deep-Red Emission for Super-resolution Imaging. *Chem. Sci.* 13 (5), 1270–1280. doi:10.1039/d1sc04254h

Xu, W., Zeng, Z., Jiang, J. H., Chang, Y. T., and Yuan, L. (2016). Discerning the Chemistry in Individual Organelles with Small-Molecule Fluorescent Probes. *Angew. Chem. Int. Ed. Engl.* 55 (44), 13658–13699. doi:10.1002/anie.201510721

Yang, S. H., Chien, C. M., Lu, M. C., Lin, Y. H., Hu, X. W., and Lin, S. R. (2006). Up-regulation of Bax and Endonuclease G, and Down-Modulation of Bcl-XL Involved in Cardiotoxin III-Induced Apoptosis in K562 Cells. *Exp. Mol. Med.* 38 (4), 435–444. doi:10.1038/emm.2006.51

Yang, Z., Sharma, A., Qi, J., Peng, X., Lee, D. Y., Hu, R., et al. (2016). Super-resolution Fluorescent Materials: an Insight into Design and Bioimaging Applications. *Chem. Soc. Rev.* 45 (17), 4651–4667. doi:10.1039/c5cs00875a

Zachäus, C., Abdi, F. F., Peter, L. M., and van de Krol, R. (2017). Photocurrent of BiVO4 Is Limited by Surface Recombination, Not Surface Catalysis. *Chem. Sci.* 8 (5), 3712–3719. doi:10.1039/c7sc00363c

Zhan, Q., Liu, H., Wang, B., Wu, Q., Pu, R., Zhou, C., et al. (2017). Achieving High-Efficiency Emission Depletion Nanoscopy by Employing Cross Relaxation in Upconversion Nanoparticles. *Nat. Commun.* 8, 1058. doi:10.1038/s41467-017-01141-y

Zhang, J., Wang, Q., Guo, Z., Zhang, S., Yan, C., Tian, H., et al. (2019a). High-Fidelity Trapping of Spatial-Temporal Mitochondria with Rational Design of Aggregation-Induced Emission Probes. *Adv. Funct. Mat.* 29 (16), 1808153. doi:10.1002/adfm.201808153

Zhang, Q., Mao, S., Khan, M., Feng, S., Zhang, W., Li, W., et al. (2019b). *In Situ* Partial Treatment of Single Cells by Laminar Flow in the "Open Space". *Anal. Chem.* 91 (2), 1644–1650. doi:10.1021/acs.analchem.8b05313

Zhang, T., Peng, Y., Tong, H., Rames, M. J., Zhang, L., and Ren, G. (2013). IPET : An Experimental Method to Determine the 3-Dimensional Structure of an Individual Macromolecule. *Prog. Chem.* 25 (5), 669–676.

Zhang, W., Yu, C. Y. Y., Kwok, R. T. K., Lam, J. W. Y., and Tang, B. Z. (2018). A Photostable AIE Luminogen with Near Infrared Emission for Monitoring Morphological Change of Plasma Membrane. *J. Mater Chem. B* 6 (10), 1501–1507. doi:10.1039/c7tb02947k

Zhang, X., Chen, J., Davis, B., and Kiechle, F. (1999). Hoechst 33342 Induces Apoptosis in HL-60 Cells and Inhibits Topoisomerase I *In Vivo*. *Arch. Pathol. Lab. Med.* 123 (10), 921–927. doi:10.1043/0003-9985(1999)123<0921:HIAIHC>2.0.CO;2

Zhitomirsky, B., Farber, H., and Assaraf, Y. G. (2018). LysoTracker and MitoTracker Red Are Transport Substrates of P-Glycoprotein: Implications for Anticancer Drug Design Evading Multidrug Resistance. *J. Cell. Mol. Med.* 22 (4), 2131–2141. doi:10.1111/jcmm.13485

Zhu, F., Shi, Z., Qin, C., Tao, L., Liu, X., Xu, F., et al. (2012). Therapeutic Target Database Update 2012: a Resource for Facilitating Target-Oriented Drug Discovery. *Nucleic Acids Res.* 40 (D1), D1128–D1136. doi:10.1093/nar/gkr797

Zielonka, J., Joseph, J., Sikora, A., Hardy, M., Ouari, O., Vasquez-Vivar, J., et al. (2017). Mitochondria-Targeted Triphenylphosphonium-Based Compounds: Syntheses, Mechanisms of Action, and Therapeutic and Diagnostic Applications. *Chem. Rev.* 117 (15), 10043–10120. doi:10.1021/acs.chemrev.7b00042

Zivanov, J., Nakane, T., and Scheres, S. H. W. (2020). Estimation of High-Order Aberrations and Anisotropic Magnification from Cryo-EM Data Sets in RELION-3.1. *IUCRJ* 7, 253–267. doi:10.1107/S2052252520000081

Conflict of Interest: The authors declare that the research was conducted in the absence of any commercial or financial relationships that could be construed as a potential conflict of interest.

Publisher's Note: All claims expressed in this article are solely those of the authors and do not necessarily represent those of their affiliated organizations, or those of the publisher, the editors and the reviewers. Any product that may be evaluated in this article, or claim that may be made by its manufacturer, is not guaranteed or endorsed by the publisher.

Copyright © 2022 Yang, Zhang, Zhao, Ye, Li, Meng, Long, Zhang and Zhang. This is an open-access article distributed under the terms of the Creative Commons Attribution License (CC BY). The use, distribution or reproduction in other forums is permitted, provided the original author(s) and the copyright owner(s) are credited and that the original publication in this journal is cited, in accordance with accepted academic practice. No use, distribution or reproduction is permitted which does not comply with these terms.

frontiers | Frontiers in Pharmacology

BRIEF RESEARCH REPORT
published: 06 July 2022
doi: 10.3389/fphar.2022.932116

Super-Resolution Quantification of T2DM-Induced Mitochondrial Morphology Changes and Their Implications in Pharmacodynamics of Metformin and Sorafenib

Yang Du[1†], *Ya-Juan Zhu*[1†], *Bo Zeng*[2†], *Xiao-Li Mu*[1] *and Ji-Yan Liu*[1*]

[1]Cancer Center, State Key Laboratory of Biotherapy, Department of Biotherapy, West China Hospital, West China Medical School, Sichuan University, Chengdu, China, [2]Dean's Office, West China Hospital, Sichuan University, Chengdu, China

OPEN ACCESS

Edited by:
Qixin Chen,
Shandong First Medical University, China

Reviewed by:
Yang Chen,
Dalian Institute of Chemical Physics (CAS), China
Xin Wei,
University of Texas Health Science Center at Houston, United States

***Correspondence:**
Ji-Yan Liu
liujiyan1972@163.com

[†]These authors have contributed equally to this work and share first authorship

Specialty section:
This article was submitted to Pharmacology of Anti-Cancer Drugs, a section of the journal Frontiers in Pharmacology

Received: 29 April 2022
Accepted: 07 June 2022
Published: 06 July 2022

Citation:
Du Y, Zhu Y-J, Zeng B, Mu X-L and Liu J-Y (2022) Super-Resolution Quantification of T2DM-Induced Mitochondrial Morphology Changes and Their Implications in Pharmacodynamics of Metformin and Sorafenib. Front. Pharmacol. 13:932116. doi: 10.3389/fphar.2022.932116

Mitochondria, as the powerhouse of cells, are involved in various processes of cellular homeostasis, especially energy metabolism. The morphology of mitochondria is a critical indicator for their functions, referring to mitochondrial fusion and fission. Here, we performed structured illumination microscopy (SIM) to measure the mitochondrial morphology in living cells. Benefitting from its nano-scale resolution, this SIM-based strategy can quantify the fusion and fission of mitochondria with high sensitivity. Furthermore, as type 2 diabetes mellitus (T2DM) is caused by a disorder of energy substrate utilization, this strategy has the potential to study T2DM by analyzing the mitochondrial morphology of insulin-resistant (IR) cells. With SIM, we found that mitochondrial fission was increased in IR MRC-5, LO2, FHs 74 Int, and HepG2 cells but not in IR Huh7 cells with high-invasiveness ability. Furthermore, we found that metformin could inhibit mitochondrial fission in IR cells, and sorafenib could promote mitochondrial fusion in HepG2 cancer cells, especially in those IR cells. To conclude, mitochondrial fission is involved in T2DM, and cancer cells with high-invasiveness ability may be equipped with stronger resistance to energy metabolism disorder. In addition, the pharmacodynamics of metformin and sorafenib in cancer may be related to the inhibition of mitochondrial fission, especially for patients with T2DM.

Keywords: mitochondria, structured illumination microscopy, T2DM, metformin, sorafenib

INTRODUCTION

Type 2 diabetes mellitus (T2DM), a serious health problem worldwide, is caused by insulin resistance and is related to abnormal energy substrate use in cells (Petersen and Shulman, 2018; Cole and Florez, 2020). Mitochondria play pivotal roles in cellular energy metabolism, and increasing pieces of evidence have pointed out that mitochondrial dysfunction and T2DM are reciprocally influenced (Szendroedi et al., 2012; Prasun, 2020). Thus, studying the role of mitochondria in the pathogenesis of T2DM has attracted more attention from researchers.

Mitochondria are a dynamical organelle, and their morphology can range from tubular networks to sphere structure through fusion and fission events (Scorrano, 2005). Accordingly, as the balance between fusion and fission has direct or indirect effects on mitochondrial function by controlling its

quality, content exchange, and ATP production (Mao et al., 2013; Kandul et al., 2016; Chan, 2020), it is increasingly recognized that the function of mitochondria varies with their morphology.

Therefore, expanding our understanding of the changes in mitochondrial morphology is of great significance for T2DM pathogenesis and pharmacodynamics evaluation. To date, the measurement of mitochondrial morphology mainly depended on confocal fluorescence microscopy and transmission electron microscopy (TEM). However, because of the resolution limitation of confocal fluorescence microscopy, it is difficult to sensitively identify and quantify morphological changes in mitochondria in insulin-resistant (IR) cells (Chen et al., 2019). In addition, due to the complicated process, images captured by TEM could rarely reflect the true situation of mitochondrial morphology and cannot be applied in evaluating mitochondria in living cells. Hence, it is essential to develop a more accurate strategy for mitochondrial morphology quantification in living cells. As SIM illuminates the sample with a defined illumination pattern (usually a sine wave grating formed by the interference of two lights) to obtain an image that is beyond the general optical resolution (Gustafsson, 2005), it can capture the morphology of the sample with 100 nm spatial resolution, and has been applied in studying mitochondria and their connections with other organelles in several studies (Chen et al., 2018; Chen et al., 2020; Chen et al., 2021; Wang et al., 2022). But it remains a vacant premise for the SIM-based strategy for mitochondrial morphology in T2DM.

Here, we established IR cells, and performed SIM to capture their mitochondrial morphology at the nano-scale and analysis software to automatically quantify the morphological changes of mitochondria. In addition, to confirm the achieved results and further detect the relationship between T2DM and cancer metastasis, we investigated mitochondrial morphology in IR hepatoma carcinoma cells with different invasive abilities under SIM. Moreover, we measured the changes in mitochondrial morphology in IR cells after being treated with metformin, a classical diabetes drug, or sorafenib, a most-used cancer targeted-therapy drug for hepatocellular carcinoma (HCC), under SIM. Taken together, based on the super-resolution of SIM, we proposed a new strategy for studying T2DM and evaluating the pharmacodynamics of related drugs by quantifying mitochondrial morphology. Also, this method may be a potential tool to guide the therapeutic regimen for T2DM patients with cancers.

METHODS

Cell Culture

MRC-5, LO2, FHs 74 Int, HepG2, and Huh7 cells were obtained from ATCC and cultured in Dulbecco's modified Eagle's medium (DMEM) with 1% penicillin–streptomycin and 10% fetal bovine serum (FBS). All cell lines are cultured under optimal conditions in a humidified atmosphere (95%), 5% CO2 at 37°C. Metformin (Sigma-Aldrich, United States) was dissolved in phosphate-buffered saline (Gibco, United States) as a stock solution of 1M. Sorafenib was purchased from Selleck and dissolved in DMSO (Sigma-Aldrich, United States) as a 50 mM stock solution. For each experiment, fresh appropriate working concentrations were prepared with the DMEM medium. Diluted drugs were filtered through a 0.22-μm PTFE filter (Macherey-Nagel, Germany) before use. MitoTracker® Mitochondrion-Selective Probes were purchased from Invitrogen.

Cellular Insulin-Resistant Models

To induce insulin resistance, cells were cultured in serum-free, low-glucose (1 g/L) DMEM containing 0.5% BSA and 5 nM of TNF-a (R&D Systems) for 24 h.

Structured Illumination Microscopy (SIM)-Based Mitochondrial Imaging

Cells were split and cultured in a glass-bottomed micro-well dish and incubated with 2 ml of DMEM supplemented with 10% FBS for 24 h. After being washed with PBS, the cells were treated with metformin (1 mM) or sorafenib (2ug/ml) for 24 h. Afterward, the cells were incubated with 100 nM of MitoTracker Green (MTG) at 37°C for 30 min. Then, the cells were washed with PBS five times and incubated in a phenol-free medium for SIM imaging (Nikon, Tokyo, Japan).

Statistical Analysis

SIM images were analyzed with Nikon Elements and ImageJ software. Statistical analysis was performed with GraphPad Prism 7.0. The statistical comparison was performed through Student's t-test at significance levels of $^{*}p < 0.05$, $^{**}p < 0.01$, $^{***}p < 0.001$, and $^{****}p < 0.0001$. Data appeared as mean ± SD.

RESULTS

Structured Illumination Microscopy (SIM)-Based Imaging of Mitochondrial Morphology for Quantitative Analysis in Insulin-Resistant Cells

As the super-resolution of structured illumination microscopy (SIM), which can reach the 100 nm-scale, we combined it with ImageJ software to quantify the mitochondrial morphology in living cells. First, 100 nM MitoTracker Green (MTG) was used to stain 786-O renal cancer cells for 30 min to allow the mitochondria to be captured with SIM. The image showed various morphologies of mitochondria, such as punctate, rod-like, and fibrous. Then, the image was transformed to an 8-bit format by ImageJ software for the next automatical analysis. Next, referring to a previous study (Shao et al., 2020), we used the length-to-width (L/W) method to quantify the mitochondrial morphology and assigned it into four classes: round or round-like ($1.0 \leq L/W < 1.5$), intermediate ($1.5 \leq L/W < 2.0$), tubular ($2.0 \leq L/W < 5.0$), and hyper-fused ($L/W \geq 5.0$) (**Figure 1A**). Thus, we could intuitively observe the distribution of mitochondrial morphology in one cell, and then quantify the morphological changes among cells.

To validate the application of this mitochondrial morphology quantitative strategy based on SIM, and explore the role of

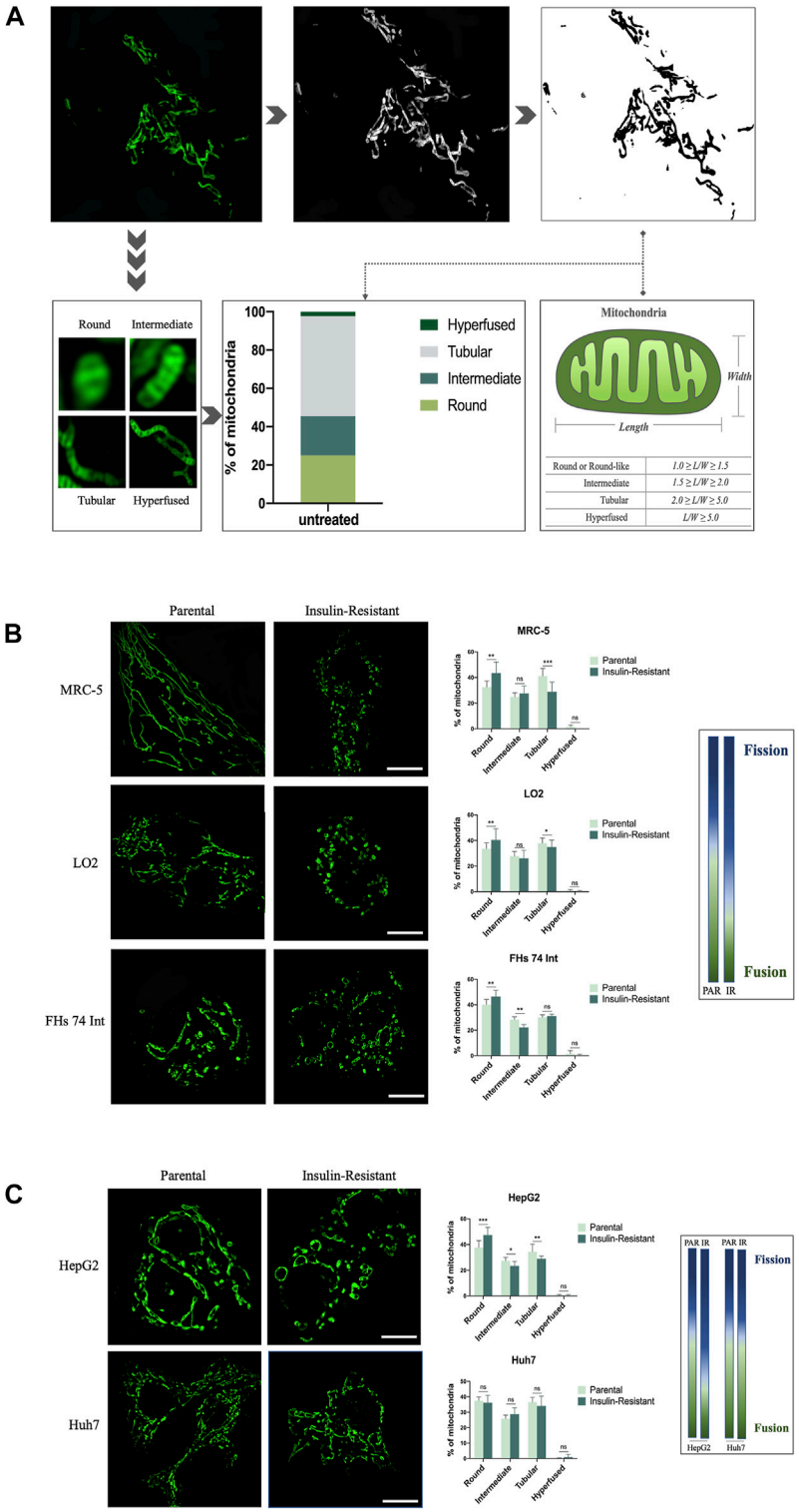

FIGURE 1 | SIM-based imaging of mitochondrial morphology for quantitative analysis in IR cells. **(A)** After being captured by SIM, the image of mitochondria in a 786-O cancer cell was transformed to an 8-bit format, and the length/width of the mitochondria was further analyzed by ImageJ software. **(B)** Representative images of mitochondrial morphology and corresponding quantitative analysis for the four morphological groups (round, intermediate, tubular, and hyper-fused) in parental and IR MRC-5, LO2, and FHs 74 Int cells, respectively. **(C)** Representative images of mitochondrial morphology and corresponding quantitative analysis for the four morphological groups (round, intermediate, tubular, and hyperfused) in parental and IR HepG2 and Huh7 cancer cells, respectively. Scale bar: 10 μm. Data showed as mean ± SD. $^{*}p < 0.05$, $^{**}p < 0.01$, and $^{***}p < 0.001$, ns: no significance. The gradient column chart indicates the trend of morphological changes, referring to the fission and fusion of the mitochondria.

morphological changes in mitochondria in T2DM, we first established IR cells with fibroblasts, intestine epithelial cells, and hepatocytes by culturing these three cell lines in a low-glucose medium with TNF-α and 0.5% BSA. This method has been widely used to establish IR cells *in vitro* (Lo et al., 2013). Under SIM, we observed that the round-like mitochondria significantly increased in MRC-5, LO2, and FHs 74 Int cells after they were induced to be resistant to insulin. On the contrary, the tubular mitochondria were decreased, especially in MRC-5 cells. These morphological changes conformed to the mitochondrial fission process. Quantitative analysis results indicated that compared with 32.48 ± 4.77%, 33.51 ± 4.66%, and 40.08 ± 4.06% in parental MRC-5, LO2, and FHs 74 Int cells, respectively, the ratio of round or round-like mitochondria increased to 43.43 ± 8.64%, 40.41 ± 8.73%, and 46.43 ± 4.95% in their corresponding IR cells. Conversely, the ratio of tubular mitochondria decreased to 28.94 ± 7.54% and 34.95 ± 5.36% in IR MRC-5 and LO2 cells, respectively, while they were 41.16 ± 5.85% and 37.87 ± 4.09% in parental MRC-5 and LO2 cells, respectively. The ratio of intermediate mitochondria in FHs 74 Int cells also decreased from 28.24 ± 2.17% to 22.20 ± 2.24% after changing to being insulin-resistant (**Figure 1B**). Altogether, these data implied that mitochondrial fission is positively correlated with insulin resistance in cells, especially in fibroblasts.

Next, to expand the application of this new strategy in the T2DM area, we continued to measure the mitochondrial morphology in IR cancer cells. We first used HepG2, a hepatoma carcinoma cell line with low-invasive ability, to develop an IR model. We observed that the mitochondria presented as more punctate-like but less fibrosis-like after being induced to be resistant to insulin. Our data also showed the ratio of round or round-like mitochondria increased to 47.34 ± 5.99% in IR HepG2 cells, which was only 37.68 ± 5.39% in its parental cells. Meanwhile, the ratio of intermediate and tubular mitochondria both emerged as opposite changes in IR HepG2 cells compared to their parental cells, decreasing from 27.37 ± 2.56% to 23.43 ± 3.41%, and 34.37 ± 5.93% to 28.99 ± 2.07%, respectively. The balance between fission and fusion tilted to fission. Next, to figure out whether this balance–imbalance is connected with the invasive ability of cancer cells, we induced Huh7 cells, another hepatoma carcinoma cell line but with high-invasive ability, to be resistant to insulin. However, the SIM images showed that there were no obvious changes in mitochondrial morphology after Huh7 cells became insulin-resistant. The data also showed that the distributions of these four morphological classifications in parental Huh7 cells and IR Huh7 cells were similar (**Figure 1C**). These results implied that the effect of T2DM on cancer may vary from cancer metastatic abilities.

Decreased Mitochondrial Fission in IR Cells Treated With Metformin or Sorafenib

As metformin is one of the most used drugs for T2DM therapy, we further evaluated the influence of metformin on the morphological changes of mitochondria in IR cells. With SIM, we observed that the mitochondria exhibited refusion states in the IR MRC-5, LO2, FHs 74 Int, and HepG2 cells after being treated with metformin (**Figure 2A**). The quantitative data further confirmed this phenomenon. In IR MRC-5 cells, ratios of round or round-like and intermediate mitochondria both slipped from 43.43 ± 8.63% to 32.00 ± 2.72% and from 27.62 ± 5.77% to 20.72 ± 2.24%, respectively, but the ratio of tubular mitochondria increased from 28.94 ± 7.54% to 46.42 ± 2.71%. In IR LO2 cells, ratios of round or round-like and intermediate mitochondria both dropped from 40.41 ± 8.73% to 37.03 ± 2.51% and from 26.09 ± 6.30% to 19.33 ± 1.19%, respectively, but the ratio of tubular mitochondria went up from 34.95% ± 5.36 to 43.31 ± 1.52%. In IR FHs 74 Int cells, the ratios of round or round-like and intermediate mitochondria both dropped from 46.43 ± 4.95% to 35.23 ± 2.52% and from 22.20 ± 2.24% to 19.87 ± 2.91%, respectively, while the ratio of tubular mitochondria increased from 31.08 ± 1.53% to 44.18 ± 3.73%. In HepG2 cancer cells, the ratio of round or round-like mitochondria was also down from 47.34 ± 5.99% to 40.44 ± 10.00%, and the ratio of intermediate mitochondria was up from 23.43 ± 3.41% to 31.38 ± 6.21%; however, the ratio of tubular mitochondria barely changed (**Figure 2B**). The results gave a hint that metformin might improve insulin resistance in cells by inhibiting their mitochondrial fission, and this refusion effect might also play a role in the anti-cancer effect of metformin.

In addition, as sorafenib is the most commonly used targeted-drug for hepatocellular carcinoma (HCC) therapy, to explore the T2DM influence on sorafenib efficiency for hepatoma carcinoma patients, we proceeded to measure the effect of sorafenib on mitochondrial morphology in parental HepG2 cells and IR HepG2 cells. The images captured by SIM indicated that sorafenib could lead to mitochondria fusion both in these two cells (**Figure 2C**). With quantitative analysis, the data showed that after treatment with sorafenib, the ratio of round or round-like mitochondria was reduced from 37.68 ± 5.39% to 34.50 ± 2.88% and from 47.34 ± 5.99% to 35.72 ± 4.84%, while the ratio of tubular mitochondria was increased from 34.37 ± 5.93% to 37.32 ± 4.17% and from 28.99 ± 2.07% to 33.97 ± 2.50% in parental and IR HepG2 cells, respectively. Moreover, the ratio of intermediate mitochondria also increased from 23.43 ± 3.41% to 30.12 ± 2.44% in IR HepG2 cells but nearly did not change in parental HepG2 cells (**Figure 2D**). Overtly, a more distinct fusion trend was detected in IR HepG2 cells, which indicated that sorafenib might be more effective for HCC patients with T2DM.

DISCUSSION

Increasing amount of evidence has shown that T2DM caused by insulin resistance is characterized by impaired mitochondrial function, and it is also widely accepted that there is an exact link between morphology and function of mitochondria. Thus, studying T2DM from the perspective of mitochondrial morphology will be more intuitional, and it has the potential to provide a quantifiable biomarker for studying and monitoring T2DM. In this study, we used a super-sensitive method, SIM, to examine the morphological changes in mitochondria. The results indicated that the fission of mitochondria was enhanced after

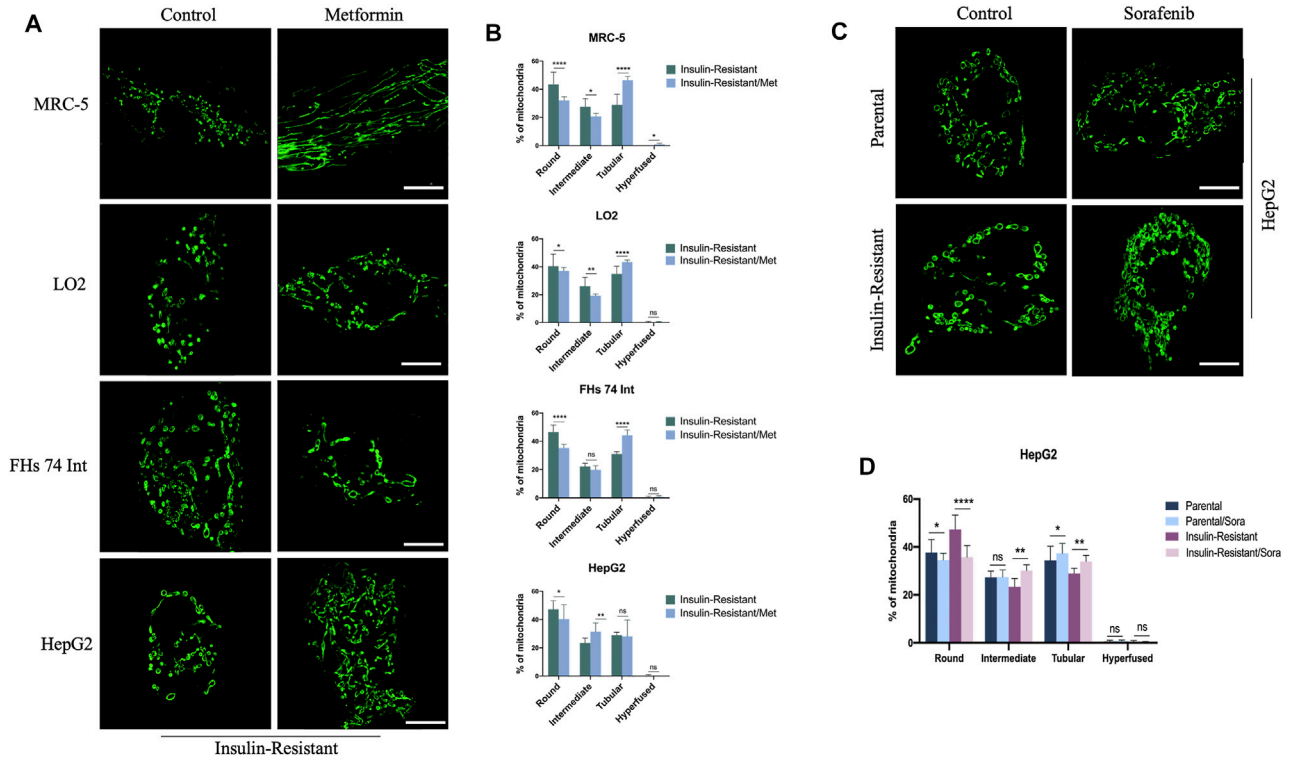

FIGURE 2 | Effect of metformin or sorafenib on mitochondrial morphology in IR cells. **(A)** Representative images of mitochondrial morphology in IR MRC-5, LO2, FHs 74 Int, and HepG2 cells treated or untreated with metformin. **(B)** Quantitative analysis for the four morphological groups (round, intermediate, tubular, and hyper-fused) in IR MRC-5, LO2, FHs 74 Int, and HepG2 cells treated or untreated with metformin. **(C)** Representative images of mitochondrial morphology in IR HepG2 cancer cells with or without sorafenib treatment. **(D)** Quantitative analysis for the four morphological groups (round, intermediate, tubular, and hyper-fused) in IR HepG2 cancer cells with or without sorafenib treatment, respectively. Scale bar: 10 μm. Data showed as mean ± SD. $^{*}p < 0.05$, $^{**}p < 0.01$, $^{***}p < 0.001$, and $^{****}p < 0.0001$, ns: no significance.

normal fibroblasts, hepatocytes, and intestine epithelial cells were induced to be resistant to insulin, especially in fibroblasts. A similar phenomenon has also been reported that the fission of mitochondria can lead to insulin resistance in skeletal muscle cells and dorsal vagal complex (Filippi et al., 2017; Axelrod et al., 2021; Kugler et al., 2021). It should be noted that it is first reported that this phenomenon can be detected in fibroblasts and intestinal epithelial cells in our study. Furthermore, benefitting from the super-sensitivity of SIM, we could accurately quantify the morphological changes of mitochondria with ImageJ software, and the data showed insulin resistance had the greatest influence on fibroblasts among these three cell types. We speculated that the reason for this result is that insulin has a greater effect on mesenchymal cells, such as adipocytes which can be differentiated from fibroblasts *in vitro* (Benito et al., 1991).

In addition, in the past decades, there has been an explosion in knowledge about the role of T2DM in promoting cancer metastasis (Brown et al., 2020; Fan et al., 2020), but the underlying mechanism is still under study. Hence, we further quantified the mitochondrial morphology in IR HepG2 cancer cells and found that mitochondrial fission was also increased. Considering previous research studies which showed that mitochondrial fission was significantly unregulated in distant metastasis of hepatocellular carcinoma and mitochondrial fission can promote breast cancer and hepatocellular carcinoma metastasis (Zhang et al., 2017; Sun et al., 2018; Yu et al., 2021), it is tempting to speculate that T2DM can facilitate cancer metastasis by boosting mitochondrial fission according to our results. Furthermore, we also noted that compared with HepG2 cells of weakly potential invasion and low frequent metastasis, Huh7 cells of strongly potential invasion and high frequent metastasis are less sensitive to insulin resistance; the results suggested that insulin resistance may have a greater effect on the early stage of cancer rather than metastatic cancer. Together, our work added a novel explanation for the metastasis-promoting effect of T2DM in different cancer stages.

As one of the most used first-line drugs for T2DM, metformin also has anticancer effects (Vancura et al., 2018; Cheng et al., 2021; Xiao et al., 2022). Here, our data indicated that metformin could alleviate the mitochondrial fission exerted by insulin resistance in cells. Previous research studies have reported that mitochondrial refusion by the overexpression of Mfn-2, a mitochondrial fusion protein, or inhibition of Drp-1, a mitochondrial fission protein, could lead to a decrease in cell proliferation and an increase in apoptosis in lung cancer (Rehman et al., 2012). It also has been observed that induction of mitochondrial fission is required for the maintenance of liver cancer-initiating cells, and the inhibition of fission could result in

the apoptosis of brain tumor-initiating cells; thus, tumor growth was halted (Xie et al., 2015; Tang et al., 2021). Furthermore, mitochondrial fission is important for damaged mitochondrion elimination by mitophagy, so it is possible that the refusion of mitochondria can accumulate damaged mitochondria which go against cancer cells' survival and proliferation (Grandemange et al., 2009). Given this, we reasoned that the inhibition of mitochondrial fission might be the underlying mechanism of the anticancer effect of metformin. Moreover, we also found that sorafenib could enhance mitochondrial fusion in HepG2 cells, and this effect is stronger in IR HepG2 cells, which is consistent with a previous study which showed that sorafenib might have a better anticancer effect in hepatocellular carcinoma patients with T2DM than those without T2DM (Di Costanzo et al., 2017). Consequently, our data provided a possible explanation for this phenomenon and a new direction to investigate the mechanism for the anti-cancer effect of sorafenib.

By using the super-resolution characteristic of SIM to precisely quantify the morphological changes of mitochondria, we found that insulin resistance could lead to mitochondrial fission in living cells, and metformin and sorafenib can both weaken this mitochondrial fission-promoting effect of insulin resistance. Our work confirmed the viability of the SIM-based strategy in studying T2DM at the nano-scale level. Moreover, the results might provide a new perspective to clarify the mechanism for the effect of T2DM on promoting cancer metastasis and guidelines for medication regimens for cancer patients with T2DM.

DATA AVAILABILITY STATEMENT

The original contributions presented in the study are included in the article/Supplementary Material; further inquiries can be directed to the corresponding author.

AUTHOR CONTRIBUTIONS

YD and J-YL contributed to the conception and design of the study. YD and Y-JZ finished the experimental works. YD and BZ wrote the first draft of the manuscript. J-YL critically revised the manuscript. All authors contributed to the manuscript revision and approved the submitted version.

REFERENCES

Axelrod, C. L., Fealy, C. E., Erickson, M. L., Davuluri, G., Fujioka, H., Dantas, W. S., et al. (2021). Lipids Activate Skeletal Muscle Mitochondrial Fission and Quality Control Networks to Induce Insulin Resistance in Humans. *Metabolism* 121, 154803. doi:10.1016/j.metabol.2021.154803

Benito, M., Porras, A., Nebreda, A. R., and Santos, E. (1991). Differentiation of 3T3-L1 Fibroblasts to Adipocytes Induced by Transfection of Ras Oncogenes. *Science* 253 (5019), 565–568. doi:10.1126/science.1857988

Brown, J. C., Zhang, S., Ou, F. S., Venook, A. P., Niedzwiecki, D., Lenz, H. J., et al. (2020). Diabetes and Clinical Outcome in Patients with Metastatic Colorectal Cancer: CALGB 80405 (Alliance). *JNCI Cancer Spectr.* 4 (1), pkz078. doi:10.1093/jncics/pkz078

Chan, D. C. (2020). Mitochondrial Dynamics and its Involvement in Disease. *Annu. Rev. Pathol. Mech. Dis.* 15, 235–259. doi:10.1146/annurev-pathmechdis-012419-032711

Chen, Q., Fang, H., Shao, X., Tian, Z., Geng, S., Zhang, Y., et al. (2020). A Dual-Labeling Probe to Track Functional Mitochondria-Lysosome Interactions in Live Cells. *Nat. Commun.* 11 (1), 6290–6310. doi:10.1038/s41467-020-20067-6

Chen, Q., Jin, C., Shao, X., Guan, R., Tian, Z., Wang, C., et al. (2018). Super-Resolution Tracking of Mitochondrial Dynamics with an Iridium(III) Luminophore. *Small* 14 (41), e1802166. doi:10.1002/smll.201802166

Chen, Q., Hao, M., Wang, L., Li, L., Chen, Y., Shao, X., et al. (2021). Prefused Lysosomes Cluster on Autophagosomes Regulated by VAMP8. *Cell. death Dis.* 12 (10), 1–10. doi:10.1038/s41419-021-04243-0

Chen, Q., Shao, X., Tian, Z., Chen, Y., Mondal, P., Liu, F., et al. (2019). Nanoscale Monitoring of Mitochondria and Lysosome Interactions for Drug Screening and Discovery. *Nano Res.* 12 (5), 1009–1015. doi:10.1007/s12274-019-2331-x

Cheng, L., Zhang, X., Huang, Y. Z., Zhu, Y. L., Xu, L. Y., Li, Z., et al. (2021). Metformin Exhibits Antiproliferation Activity in Breast Cancer *via* miR-483-3p/METTL3/m6A/p21 Pathway. *Oncogenesis* 10 (1), 7. doi:10.1038/s41389-020-00290-y

Cole, J. B., and Florez, J. C. (2020). Genetics of Diabetes Mellitus and Diabetes Complications. *Nat. Rev. Nephrol.* 16 (7), 377–390. doi:10.1038/s41581-020-0278-5

Di Costanzo, G. G., Tortora, R., Morisco, F., Addario, L., Guarino, M., Cordone, G., et al. (2017). Impact of Diabetes on Outcomes of Sorafenib Therapy for Hepatocellular Carcinoma. *Target Oncol.* 12 (1), 61–67. doi:10.1007/s11523-016-0454-5

Fan, Z., Gong, Y., Huang, Q., Yang, C., Cheng, H., Jin, K., et al. (2020). Diabetes Is Associated with the Metastasis of Pancreatic Neuroendocrine Tumors. *Pancreas* 49 (6), 751–756. doi:10.1097/MPA.0000000000001564

Filippi, B. M., Abraham, M. A., Silva, P. N., Rasti, M., LaPierre, M. P., Bauer, P. V., et al. (2017). Dynamin-related Protein 1-dependent Mitochondrial Fission Changes in the Dorsal Vagal Complex Regulate Insulin Action. *Cell. Rep.* 18 (10), 2301–2309. doi:10.1016/j.celrep.2017.02.035

Grandemange, S., Herzig, S., and Martinou, J.-C. (2009). "Mitochondrial Dynamics and Cancer," in *Seminars in Cancer Biology* (Elsevier), 50–56.

Gustafsson, M. G. (2005). Nonlinear Structured-Illumination Microscopy: Wide-Field Fluorescence Imaging with Theoretically Unlimited Resolution. *Proc. Natl. Acad. Sci. U. S. A.* 102 (37), 13081–13086. doi:10.1073/pnas.0406877102

Kandul, N., Zhang, T., Hay, B., and Guo, M. (2016). *Selective Removal of Deletion-Bearing Mitochondrial DNA in Heteroplasmic*. Drosophila.

Kugler, B. A., Deng, W., Duguay, A. L., Garcia, J. P., Anderson, M. C., Nguyen, P. D., et al. (2021). Pharmacological Inhibition of Dynamin-Related Protein 1 Attenuates Skeletal Muscle Insulin Resistance in Obesity. *Physiol. Rep.* 9 (7), e14808. doi:10.14814/phy2.14808

Lo, K. A., Labadorf, A., Kennedy, N. J., Han, M. S., Yap, Y. S., Matthews, B., et al. (2013). Analysis of *In Vitro* Insulin-Resistance Models and Their Physiological Relevance to *In Vivo* Diet-Induced Adipose Insulin Resistance. *Cell. Rep.* 5 (1), 259–270. doi:10.1016/j.celrep.2013.08.039

Mao, K., Wang, K., Liu, X., and Klionsky, D. J. (2013). The Scaffold Protein Atg11 Recruits Fission Machinery to Drive Selective Mitochondria Degradation by Autophagy. *Dev. Cell.* 26 (1), 9–18. doi:10.1016/j.devcel.2013.05.024

Petersen, M. C., and Shulman, G. I. (2018). Mechanisms of Insulin Action and Insulin Resistance. *Physiol. Rev.* 98 (4), 2133–2223. doi:10.1152/physrev.00063.2017

Prasun, P. (2020). Role of Mitochondria in Pathogenesis of Type 2 Diabetes Mellitus. *J. Diabetes Metab. Disord.* 19 (2), 2017–2022. doi:10.1007/s40200-020-00679-x

Rehman, J., Zhang, H. J., Toth, P. T., Zhang, Y., Marsboom, G., Hong, Z., et al. (2012). Inhibition of Mitochondrial Fission Prevents Cell Cycle Progression in Lung Cancer. *FASEB J.* 26 (5), 2175–2186. doi:10.1096/fj.11-196543

Scorrano, L. (2005). Proteins that Fuse and Fragment Mitochondria in Apoptosis: Con-Fissing a Deadly Con-Fusion? *J. Bioenerg. Biomembr.* 37 (3), 165–170. doi:10.1007/s10863-005-6572-x

Shao, X., Chen, Q., Hu, L., Tian, Z., Liu, L., Liu, F., et al. (2020). Super-resolution Quantification of Nanoscale Damage to Mitochondria in Live Cells. *Nano Res.* 13 (8), 2149–2155. doi:10.1007/s12274-020-2822-9

Sun, X., Cao, H., Zhan, L., Yin, C., Wang, G., Liang, P., et al. (2018). Mitochondrial Fission Promotes Cell Migration by Ca2+/CaMKII/ERK/FAK Pathway in Hepatocellular Carcinoma. *Liver Int.* 38 (7), 1263–1272. doi:10.1111/liv.13660

Szendroedi, J., Phielix, E., and Roden, M. (2012). The Role of Mitochondria in Insulin Resistance and Type 2 Diabetes Mellitus. *Nat. Rev. Endocrinol.* 8 (2), 92–103. doi:10.1038/nrendo.2011.138

Tang, M., Yang, M., Wu, G., Mo, S., Wu, X., Zhang, S., et al. (2021). Epigenetic Induction of Mitochondrial Fission Is Required for Maintenance of Liver Cancer-Initiating Cells. *Cancer Res.* 81 (14), 3835–3848. doi:10.1158/0008-5472.CAN-21-0436

Vancura, A., Bu, P., Bhagwat, M., Zeng, J., and Vancurova, I. (2018). Metformin as an Anticancer Agent. *Trends Pharmacol. Sci.* 39 (10), 867–878. doi:10.1016/j.tips.2018.07.006

Wang, H., Fang, G., Chen, H., Hu, M., Cui, Y., Wang, B., et al. (2022). Lysosome-Targeted Biosensor for the Super-resolution Imaging of Lysosome-Mitochondrion Interaction. *Front. Pharmacol.* 13, 865173. doi:10.3389/fphar.2022.865173

Xiao, Q., Xiao, J., Liu, J., Liu, J., Shu, G., and Yin, G. (2022). Metformin Suppresses the Growth of Colorectal Cancer by Targeting INHBA to Inhibit TGF-B/pi3k/AKT Signaling Transduction. *Cell. Death Dis.* 13 (3), 202. doi:10.1038/s41419-022-04649-4

Xie, Q., Wu, Q., Horbinski, C. M., Flavahan, W. A., Yang, K., Zhou, W., et al. (2015). Mitochondrial Control by DRP1 in Brain Tumor Initiating Cells. *Nat. Neurosci.* 18 (4), 501–510. doi:10.1038/nn.3960

Yu, Y., Peng, X. D., Qian, X. J., Zhang, K. M., Huang, X., Chen, Y. H., et al. (2021). Fis1 Phosphorylation by Met Promotes Mitochondrial Fission and Hepatocellular Carcinoma Metastasis. *Signal Transduct. Target Ther.* 6 (1), 401–415. doi:10.1038/s41392-021-00790-2

Zhang, J., Zhang, Y., Wu, W., Wang, F., Liu, X., Shui, G., et al. (2017). Guanylate-binding Protein 2 Regulates Drp1-Mediated Mitochondrial Fission to Suppress Breast Cancer Cell Invasion. *Cell. death Dis.* 8 (10), e3151.

Conflict of Interest: The authors declare that the research was conducted in the absence of any commercial or financial relationships that could be construed as a potential conflict of interest.

Publisher's Note: All claims expressed in this article are solely those of the authors and do not necessarily represent those of their affiliated organizations, or those of the publisher, the editors, and the reviewers. Any product that may be evaluated in this article, or claim that may be made by its manufacturer, is not guaranteed or endorsed by the publisher.

Copyright © 2022 Du, Zhu, Zeng, Mu and Liu. This is an open-access article distributed under the terms of the Creative Commons Attribution License (CC BY). The use, distribution or reproduction in other forums is permitted, provided the original author(s) and the copyright owner(s) are credited and that the original publication in this journal is cited, in accordance with accepted academic practice. No use, distribution or reproduction is permitted which does not comply with these terms.

frontiers | Frontiers in Pharmacology

ORIGINAL RESEARCH
published: 13 July 2022
doi: 10.3389/fphar.2022.932807

Optical Visualization of Red-GQDs' Organelles Distribution and Localization in Living Cells

Haifeng Hu[1], Peng Li[1], Jie Qiu[1], Meiji Zhao[1], Mingjie Kuang[1], Zhaoyan Zhang[2]* and Dachuan Wang[1]**

[1]Shandong Provincial Hospital, Shandong University, Jinan, China, [2]The 1st Department of Geriatrics of the 960th Hospital of the PLA Joint Logistics Support Force, Jinan, China

Recently, there has been a rapidly expanding interest in a new nanomaterial, graphene quantum dots (GQDs), owing to its profound potential in various advanced applications. At present, the study of GQDs mainly focuses on the new synthesis methods and surface modification. However, revealing the intracellular distribution of GQDs is currently not available, limiting in-depth understanding of its biological regulatory mechanism. To fill up this gap, the visualization study of red fluorescent graphene quantum dots (Red-GQDs) is helpful to clarify their subcellular distribution and metabolism in living cells system. Here, in this study, two-photon laser confocal microscopy was used to deeply analyze the uptake and subcellular distribution of Red-GQDs by HeLa cells at different concentrations and times through visual observation and discussed the effect of Red-GQDs on the metabolic of HeLa cells. The results indicated that Red-GQDs could be well-absorbed by HeLa cells and further revealed the differential distribution of Red-GQDs in different organelles (lysosomes and mitochondria) in a time-dependent manner. In addition, we confirmed that Red-GQDs significantly affect cell biological functions. Low concentrations of Red-GQDs are related to the autophagy pathway of cells, and high concentrations of Red-GQDs can induce ferroptosis in cells and promote the secretion of cellular exosomes. In the present study, the distribution and metabolic pathways of Red-GQDs in the subcellular structure of cells were characterized in detail through visual analysis, which can bring positive reference for the application of Red-GQDs in the future.

Keywords: GQDs, subcellular distribution, lysosome, autolysosome, mitochondrion

OPEN ACCESS

Edited by:
Qixin Chen,
Shandong First Medical University, China

Reviewed by:
Lei Wang,
University of Cincinnati, United States
Congcong Chen,
Georgia State University, United States

****Correspondence:***
Mingjie Kuang
doctorkmj@tmu.edu.cn
Zhaoyan Zhang
237991738@qq.com
Dachuan Wang
wangdachuan@medmail.com.cn

Specialty section:
This article was submitted to Pharmacology of Anti-Cancer Drugs, a section of the journal Frontiers in Pharmacology

Received: *30 April 2022*
Accepted: *13 June 2022*
Published: *13 July 2022*

Citation:
Hu H, Li P, Qiu J, Zhao M, Kuang M, Zhang Z and Wang D (2022) Optical Visualization of Red-GQDs' Organelles Distribution and Localization in Living Cells. Front. Pharmacol. 13:932807. doi: 10.3389/fphar.2022.932807

INTRODUCTION

With the rapid development of nanoscopic imaging technology, more and more nanomaterials are used in the field of life sciences. Carbon dots (CDs) are a new type of fluorescent nanomaterials with carbon atoms as the basic structural unit. According to the different chemical structures, they are divided into spherical carbon nanodots (carbon nanodots, CNDs), graphene quantum dots (GQDs) with single-layer or multi-layer sheet structure, or aggregated granular polymer dots (polymer dots, PDs) (Tian et al., 2018). GQDs are a kind of carbon quantum dots (carbon dots, CDs). GQDs can be regarded as graphene fragments of less than 100 nm in lateral size (Chen et al., 2017; Tian et al., 2018). In contrast, GQD has "molecular" features rather than colloids and is a nanocarbon material with a honeycomb-like hexagonal lattice structure with sp^2–sp^2 carbon bonds. In recent years, many studies have converted two-dimensional graphene into zero-dimensional graphene quantum dots

(GQDs), which have broad and continuous absorption bands in the ultraviolet region, and the absorption is strong, but the ultraviolet absorption of GQDs prepared by different methods peaks are different. The transition from the π orbital of the C=C bond to the π* orbital in the GQDs structure (Abdullah Al et al., 2013), or the transition from the n orbital of the C=O bond to the π* orbital can cause characteristic peaks (Mihalache et al., 2014), and some GQDs can cause characteristic peaks. There may also be no obvious absorption peaks (Shen et al., 2011). GQDs are very small, and the movement of the internal electrons in all directions is limited, and they have significant quantum confinement effects (QCEs), quantum tunneling effects, and boundary effects (Zhu et al., 2014), which will induce the stability of GQDs fluorescence with high quantum yield (Hai et al., 2015). GQDs have attracted much attention due to their unique structures, boundary effects, and quantum confinement effects (Chen et al., 2017; Tian et al., 2018).

It was found that the surface of GQDs has a large number of hydrophilic groups (such as hydroxyl and carboxyl groups) (Gan et al., 2016; Hai et al., 2018). It has excellent water solubility, photobleaching resistance, biocompatibility, and low toxicity; meanwhile, GQDs also have a high specific surface area, multiphoton excitation ability, and abundant surface photoenergy groups, which are helpful for their surface modification (Schroeder et al., 2016; Xu et al., 2018; Zhu et al., 2015). With the abovementioned advantages, GQDs have received extensive attention and research in scientific research, such as bioimaging, biosensing, and biopharmaceuticals (Tan et al., 2012; Xu et al., 2016; Yoo et al., 2015). In the field of biomedicine, some researchers (Wang et al., 2013) used GQDs for stem cell labeling and found that GQDs were easier to enter cells, showed lower cytotoxicity, and could produce clear and stable images. Markovic et al. (2012) reported that GQDs could induce the production of reactive oxygen species ROS in human glioma U251 cells, causing oxidative stress and further leading to autophagy and apoptosis. In addition, researchers also synthesized GQDs that can emit multiple colors (blue, green, and yellow) with unique optical properties, low cytotoxicity, and good biocompatibility, which can be used as potential bioimaging agents *in vitro*. GQDs can interact with organic or inorganic substances through energy resonance transfer and other forms to quench the fluorescence of GQDs. According to this principle, biosensors can be fabricated, which can be used for the detection of specific gene sequences. Using the properties of GQDs that can be combined with a variety of molecules, some studies have proved that GQDs can be used as excellent carriers for drugs and can enhance the therapeutic effect of drug-loading systems by virtue of their own photothermal properties (Wang et al., 2013).

In recent years, researchers in the field of biomedical research have applied GQDs to a variety of living cell markers (Kim et al., 2017), including HeLa cells, dental pulp stem cells, neural stem cells, human lung cancer, and breast cancer cells (Shang et al., 2014; Ku et al., 2021). The research is mostly focused on the cytotoxicity, surface modification and modification, drug delivery, and tumor cell imaging of GQDs, and there are few studies on their visualization and biological functions in cells. The recently developed two-photon laser confocal microscope, LSM980, provides a powerful tool for visualizing the distribution of GQDs in organelles. In this study, we selected a kind of Red-GQDs for further study. In order to study the distribution of Red-GQDs more accurately, we tracked their distribution in organelles with LSM980 and found that low concentrations of Red-GQDs were distributed in mitochondria and lysosomes, and they participated in the autophagy of cells. High concentrations of Red-GQDs can participate in ferroptosis and promote the secretion of exosomes. In conclusion, this work provides a powerful method for the biological function research and application of GQDs.

RESULTS AND DISCUSSIONS

The Characterization of Red-GQDs

Red-GQDs were obtained and characterized from Nanjing XFNANO Materials Tech. Co., Ltd and the zeta potential of Red-GQDs was measured using Dylisizer NS-90Z (**Supplementary Figures S1–5**). Then, we detected the UV-vis absorption band and the fluorescence band of Red-GQDs. The absorption peak and the strongest fluorescence absorption peak of Red-GQDs were at 514.5 and 599 nm separately (**Figures 1A and B**). Red-GQDs with strong fluorescence properties provide important conditions for their visualization in cells. It is consistent with the fluorescence features of Red-GQDs, which we subsequently observe with LSM980. As shown in **Figure 1C**, the cells were divided into three groups: normal group (37°C), low-temperature treatment group (4°C), and endocytosis inhibitor (chlorpromazine, CPZ)–treated group in order to examine how Red-GQDs enter into HeLa cells. The results showed that the fluorescence intensity of Red-GQDs in the low-temperature treatment group (at 4°C) and the endocytosis inhibitor treatment group was significantly lower than that in the normal group (at 37°C). This result indicated that Red-GQDs entered cells in an energy-dependent endocytic manner (**Figures 1C and D**; **Supplementary Figure S6**). Based on this, we carried out cellular uptake experiments of Red-GQDs and incubated HeLa cells with 25 μg/ml of Red-GQDs for 1, 6, 8, and 10 h, respectively. The results showed that the fluorescence intensity of Red-GQDs gradually increased with the extension of incubation time, indicating that Red-GQDs had better cell permeability (**Figures 1E and F**). We detected the viability of HeLa cells incubated with different concentrations of Red-GQDs for 24 h by CCK8S assay. The decreased cell viability became different from the control when the concentration was above 50 μg/ml (**Figure 1G**).

Studies have shown that the imaging effect of GQDs is related to the uptake rate of cells, and the uptake of nanoparticles by cells is inseparable from factors such as particle size, shape, specific surface area, surface charge, and surface modification (Agarwal et al., 2013). The smaller the particle size of the nanoparticle, the higher the fluorescence intensity (Eda et al., 2010) and the easier it is to be taken up by cells (Xu et al., 2018). The particle size of the Red-GQDs selected in this study was less than 10 nm, and the results of the study are consistent with those of previous studies and also show better cell permeability. We used Red-GQDs, with a particle size less than 10 nm, that showed better cell

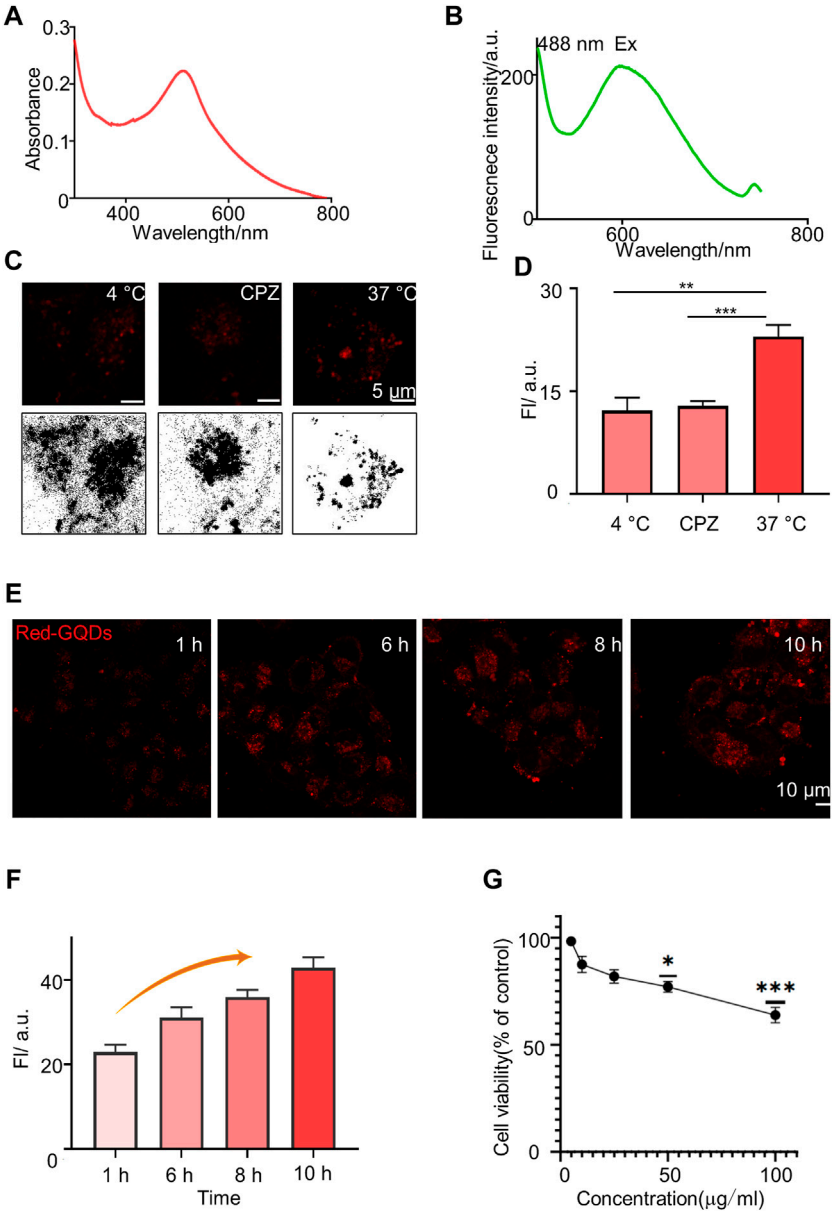

FIGURE 1 | Characterization of Red-GQDs. **(A)** Absorption spectrum of Red-GQDs (10 μg/ml). **(B)** Fluorescence spectra changes of Red-GQDs (10 μg/ml). λex = 488 nm and λem = 599.6 nm. **(C)** Fluorescence and grayscale images of HeLa cells pretreated with lower temperature (4°C), chlorpromazine (CPZ, 20 μM) and then co-stained with Red-GQDs (10 μg/ml, 1 h). **(D)** Fluorescence intensity of Red-GQDs with 4°C, CPZ and 37 °C. Data are presented as mean ± SEM. $p < 0.05$ is considered significant ($n = 3$, $^{**}p < 0.01$, $^{***}p < 0.001$, and $^{****}p < 0.0001$). All compared with 37°C. **(E)** Permeability of the Red-GQDs (10 μg/ml) at times of 1, 6, 8, and 10 h in HeLa cells. **(F)**Fluorescence intensity changes of HeLa cells treated with Red-GQDs (10 μg/ml) for 1, 6, 8, and 10 h. **(G)** Effects of Red-GQDs on cell viability in HeLa cells treated with concentrations ranging from 5 to 100 μg/ml for 24 h measured by CCK8 assay.

permeability, which is consistent with the previous research conclusions. In addition, the surface charge of nanoparticles is another important factor affecting their uptake by cells. Studies have found that due to the negative charge on the surface of the cell membrane, nanoparticles with a positive potential are easier than those with a negative potential. It is adsorbed to the cell surface and even enters the cell (Zhuo et al., 2012). GQDs with a particle size of 15 nm have a higher positive surface charge than those of 50 nm and are more easily taken up by cells. The Red-GQDs selected in this study have amino groups and are more easily adsorbed to the cell surface.

According to the report, long-term exposure to GQDs can lead to decreased motor frequency and abnormal head and pharyngeal movements in *C. elegans*, reflecting the chronic toxicity of GQDs to dopamine and glutamate neurons (Li et al., 2017). A study on graphene toxicity showed that GQDs smaller than 50 nm did not cause significant damage to cells (Tabish et al., 2018). The results of the CCK8 assay showed that 15 nm GQDs had no obvious

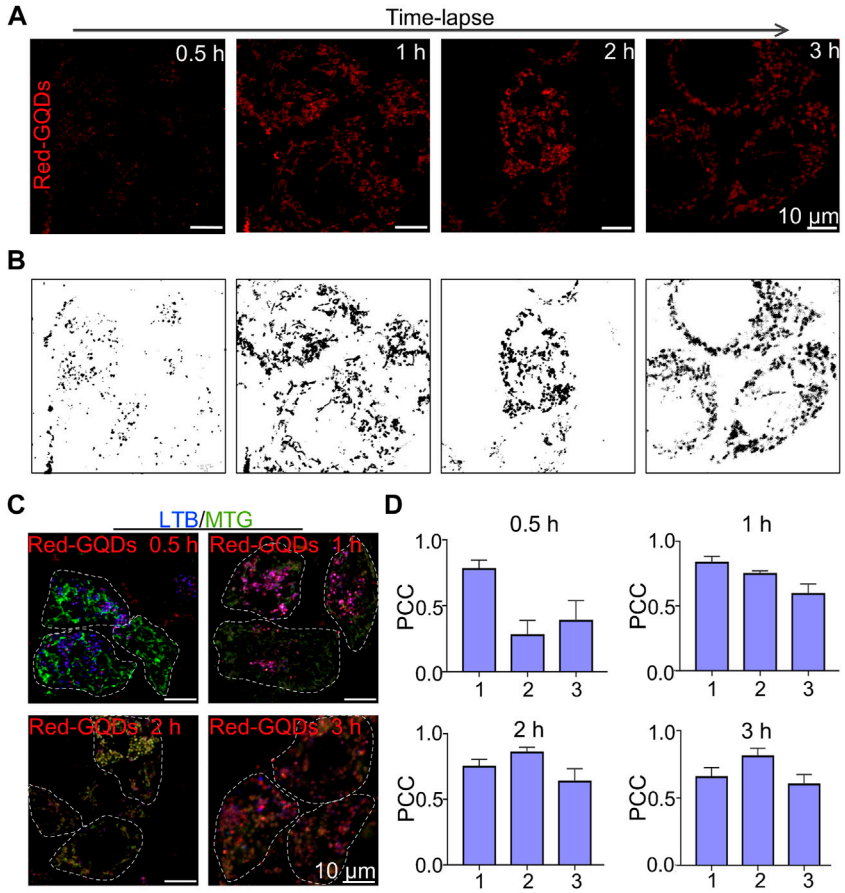

FIGURE 2 | Visualization of Red-GQDs description in living cells. **(A,B)** Fluorescence images and grayscale images of HeLa cells incubated with Red-GQDs (25 μg/ml) for 0.5, 1, 2, and 3 h **(C)** HeLa cells were co-stained with Red-GQDs (10 μg/ml, 1 h) and LTB and MTG commercial probes. LTB: λex = 405 nm and MTG:λex = 488 nm. **(D)** PCC value in various groups. 1: Red-GQDs and LTB; 2: Red-GQDs and MTG; 3: LTB and MTG. Data are presented as mean ± SEM (*n* = 4).

toxicity to PC12 cells, and 50 nm GQDs had lower cytotoxicity. However, with the increase of the intervention concentration and the prolongation of the intervention time, it still showed a certain toxic effect. In this study, Red-GQDs, less than 10 nm, were selected for the experiment, and the self-cytotoxicity of Red-GQDs could be ignored. We incubated cells with different concentrations of Red-GQDs, and the results of the CCK8 assay were consistent with the results in the previous research (Wu et al., 2013; Yuan et al., 2014). In conclusion, low concentrations of Red-GQDs are nanomaterials with good biosafety.

Distribution of Red-GQDs With Low-Concentration in Subcellular Structures

Red-GQDs with the usage of 25 μg/ml were co-incubated with HeLa cells for 0.5, 1, 2, and 3 h, respectively, to observe the distribution of Red-GQDs in subcellular structures. The results illustrated that Red-GQDs exhibited red globular structures when HeLa cells were incubated for 0.5 h (**Figures 2A and B**), which was consistent with the reported lysosome morphology (Chen et al., 2022; Chen et al., 2020b). In addition to the red globules, we also observed red fibrous structures (**Figures 2A and B**) when Red GQDs were co-incubated with HeLa cells for 1 h. This result is consistent with the morphology of mitochondrion (Chen et al., 2022; Chen et al., 2020a). The red fibrous structure decreased, and then the phenomenon of rupture and expansion gradually appeared while the co-incubation time was extended for 2 or 3 h. The spherical structure increased significantly (**Figures 2A and B**).

HeLa cells were incubated with Red-GQDs (25 μg/ml) for 0.5, 1, 2, and 3 h, respectively, to confirm the distribution of Red-GQDs in organelles at different times. Then the incubated HeLa cells were co-stained with a commercial lysosome probe (LysoTracker Blue, LTB) and a commercial mitochondrial probe (MitoTracker Green, MTG) (**Figure 2C**). As shown in **Figure 2D**, a large number of red spheres were overlapped with LTB-labeled lysosomes, and a small amount of them overlapped with MTG mitochondrion, as Red-GQDs were incubated for 0.5 h. The Red-GQDs were still mainly located in lysosomes labeled by LTB, but the co-localization coefficient of Red-GQDs with MTG-labeled mitochondrion increased significantly. In addition, the co-localization coefficient of MTG-labeled mitochondrion with LTB-labeled lysosomes also

increased while Red-GQDs were incubated with HeLa cells for 1 h (**Figure 2D**). The overlap between Red-GQDs and MTG-labeled green mitochondrion was significantly increased, and the co-localization coefficient of Red-GQDs with LTB-labeled blue lysosomes decreased as long as Red-GQDs were incubated for 2 h (**Figure 2D**). Red-GQDs still exhibited high overlap with MTG-labeled green mitochondrion. At this time, the co-localization coefficients of Red-GQDs with LTB and MTG with LTB also increased slightly with the extension of the incubated time for 3 h (**Figure 2D**). These results suggested that Red-GQDs were distributed in lysosomes and mitochondria in a time-dependent manner after entering the cell

Lysosomes are considered to be intracellular "scavengers" (Mijaljica et al., 2011) and are rich in more than 60 acid hydrolytic enzymes. The enzymes contained in each lysosome are different, but acid phosphatase is ubiquitous in lysosomes, and so it can be used as a marker enzyme of lysosomes. It has been reported that the pH value in the lysosome ranges from 3.5 to 5.5, and the optimum pH value for the enzymatic reaction is 5.0. The acidic environment in the lysosome is closely related to the proton pump V-ATPases on the lysosomal membrane, which hydrolyzes ATP to generate energy, and, at the same time, transports H^+ into the lysosome, causing the pH value to drop, thereby maintaining the acidic environment in the lysosome. This acidic microenvironment of lysosomes is beneficial for maintaining the activity of acid hydrolases and the hydrolysis process and for regulating the transport of biological macromolecules across the lysosomal membrane. If the H^+ in the lysosome leaks, the transmembrane concentration gradient of H^+ decreases, which can destroy the permeability balance of other ions, resulting in the stability of decreased lysosomal membrane (Serrano-Puebla and Boya, 2016). In addition, since most enzymes in the lysosome have M6P with negative charges, the inner surface of the lysosomal membrane also has negative charges, which maintain a free state for the enzymes in the lysosome, a feature that helps prevent the lysosome itself was digested (Settembre et al., 2013). The particle size of the Red-GQDs we selected was less than 10 nm and contained amino and hydroxyl groups. So, it was quickly captured by lysosomes after entering cells. After Red-GQDs entered the lysosome, the charge balance in the lysosome was destroyed. In addition, the hydroxyl group could form hydrogen bonds with the phospholipids or proteins on the lysosomal membrane, which could increase the permeability of the lysosomal membrane or even rupture. Under these factors, the lysosomal membrane becomes unstable, the integrity is lost, the permeability is enhanced, and lysosome membrane permeabilization (LMP) occurs (Yoo et al., 2015), resulting in the release of cathepsins and hydrolases from the lysosomal lumen into the cytoplasm (Tan et al., 2012). Red-GQDs captured by lysosomes during this study also re-entered the cytoplasm for this reason, and Red-GQDs contacted mitochondrion with increasing incubation time. One of the reasons is that the mitochondrial surface carries negative charges, while the Red-GQDs have positive charges. Apart from this reason, it is unknown whether the change of lysosomal membrane permeabilization and the release of cathepsins and hydrolases within the lysosomal lumen trigger the mitochondrial stress response. After entering cells, Red-GQDs are distributed in lysosomes and mitochondrion in a time-dependent manner. The molecular mechanism of this visual phenomenon needs to be further studied and perfected.

Red-GQDs With Low Concentration Participating in Autophagy

These results showed that mitochondrion gradually became spherical and merged with lysosomes with increasing the incubation time. We further examined the relationship between Red-GQDs and mitochondria or lysosomes in order to confirm whether Red-GQDs with low concentration are involved in the process of autophagy. It is shown that mitochondrion and lysosomes were dispersed, while Red-GQDs were incubated for 0.5 h. Under this condition, by increasing the incubation time, mitochondrion and lysosomes were gradually contacted with each other and even merged together (**Figure 3A**). This result suggested that Red-GQDs might be involved in the process of autophagy with the increase in incubation time.

HeLa cells were incubated with Red-GQDs for 1 h and a commercial autophagy–lysosome probe (DAPGreen) for 0.5 h, and then the co-localization analysis was in agreement with the conjecture. The results in **Figure 3B** exhibit that the fluorescence of Red-GQDs overlapped with that of DAPGreen. Through the quantitative analysis of the underlined part, Red-GQDs overlapped with fluorescence ranges of DAPGreen (**Figures 3C and D**). These results indicated that Red-GQDs participated in autophagy after entering cells and formed autolysosomes (**Figure 3E**). Substances in autolysosomes were degraded by digestive enzymes in the lysosomes. In addition, we selected specific proteins (p62、LC3B) related to autophagy for Western blot assay. The results showed that the protein levels of p62 were reduced in control compared with a low concentration of Red-GQDs, and the protein levels of LC3B-II were increased **(Figures 5A–D)**.

Autophagy is a highly conserved catabolic process (Menzies et al., 2017; Liao et al., 2021) that is critical for cellular homeostasis. At the same time, it participates in and regulates life processes such as differentiation, development, and tissue remodeling of organisms (Li et al., 2015). In the process of autophagy, abnormal components in the cytoplasm are packaged by autophagosomes and transported to lysosomes, forming autophagolysosomes and degrading them (Tan et al., 2012). Autophagy under normal conditions can maintain the normal function of cells and is usually beneficial to cell survival. However, excessive autophagy often causes cell death (Zhang et al., 2012). As one of the important organelles involved in autophagy, lysosomes can sensitively sense intracellular dynamic changes, including nutrients, energy levels, and harmful factors (Luzio et al., 2007; Lim and Zoncu, 2016). In this study, a commercial autophagy–lysosome probe (DAPGreen) was used to visually observe the metabolic pathway of low-concentration Red-GQDs after entering cells under the visualization study.

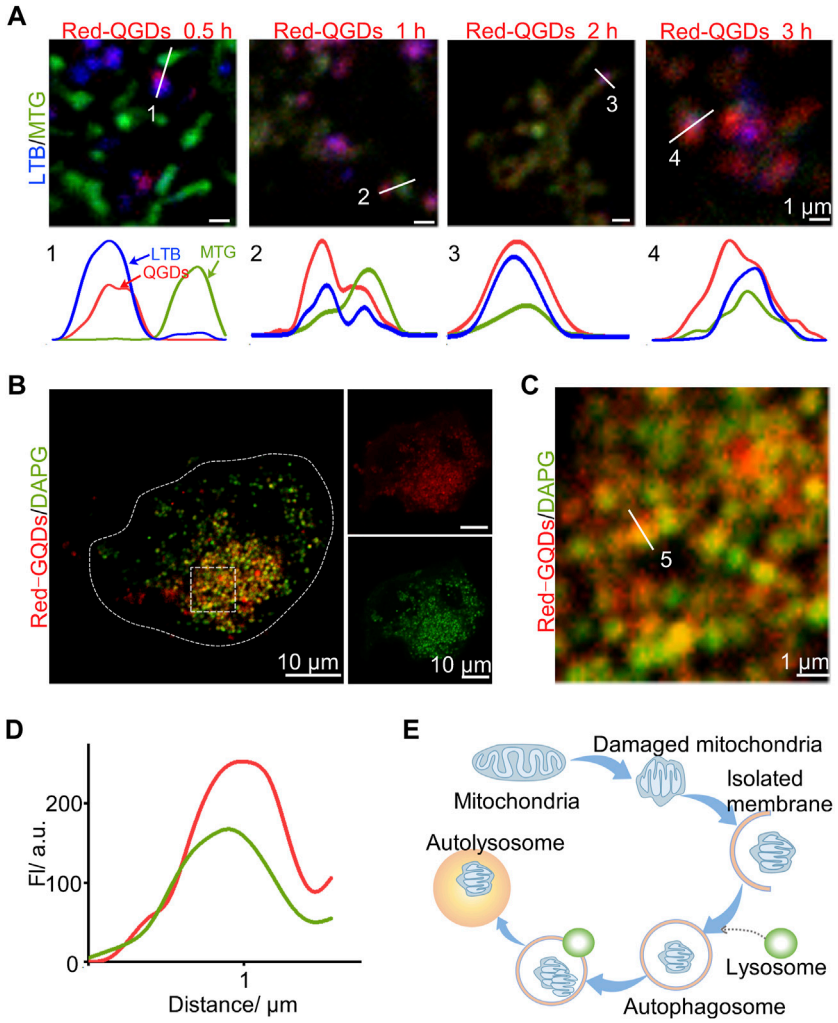

FIGURE 3 | Red-GQDs of lower concentration associated with autophagosomes. **(A)** Co-localization of LTB, MTG, and Red-GQDs (25 μg/ml) for 0.5, 1, 2, and 3 h in HeLa cells was observed by LSM980. **(B)** HeLa cells were co-stained with Red-GQDs (25 μg/ml, 1 h) and DAPGreen. DAPGreen: λex = 488 nm. **(C)** Fluorescence image of the enlarged region indicated by the white rectangle in **(B)**. **(D)** White solid lines labeled 5 in **(C)** indicate fluorescence intensity. **(E)** Schematic diagram of the influence of Red-GQDs on mitophagy.

After Red-GQDs enter cells, they damage lysosomes and participate in autophagy to form autolysosomes. During this process, a separation membrane composed of a double-layered membrane is formed, which continuously wraps accumulated proteins or damaged lysosomes, forming autophagosomes. Autophagosome Rab GTPases, anchoring factors, and SNAREs undergo multiple fusion processes at different stages of the endolysosomal system, finally forming autophagosomes with degradative functions to degrade and recycle phagocytosed substances (Menzies et al., 2017; Lawrence and Zoncu, 2019; Zhao and Zhang, 2019). It has been reported that galectin-3 within the cytoplasm is a key protein involved in lysosomal autophagy, which can recognize glycoproteins exposed to the lysosomal membrane in the cytoplasm after lysosome rupture. It further binds to tripartite domain-containing protein 16 (TRIM16), the regulatory factor E3 ubiquitin ligase (Hung et al., 2013; Maejima et al., 2013). After that, TRIM16 recruits autophagy regulator Unc-51-like kinase 1 (ULK1), Beclin 1, and autophagy-related protein 16L1 (Thurston et al., 2012), and is modified by the K63 ubiquitin chain, and finally interacts with the key protein LC3 on the autophagy bubble membrane through the autophagy receptor p62. After binding, the damaged lysosomes are packaged to form autophagosomes, which are transported to normal lysosomes for degradation. This process is a key step in the formation of autolysosomes. Therefore, further exploration and screening of key autophagy molecules to target activation or inhibition of autophagy is expected to make breakthroughs in the prevention and treatment of autophagy-related diseases. Given that lysosomes are key organelles in cellular metabolism, understanding the function of lysosomes in the autophagy pathway is of great physiopathological value for in-depth exploration of the mechanism of autophagy. Since lysosomes are key organelles in cellular metabolism, understanding the function of lysosomes in the autophagy pathway is of great

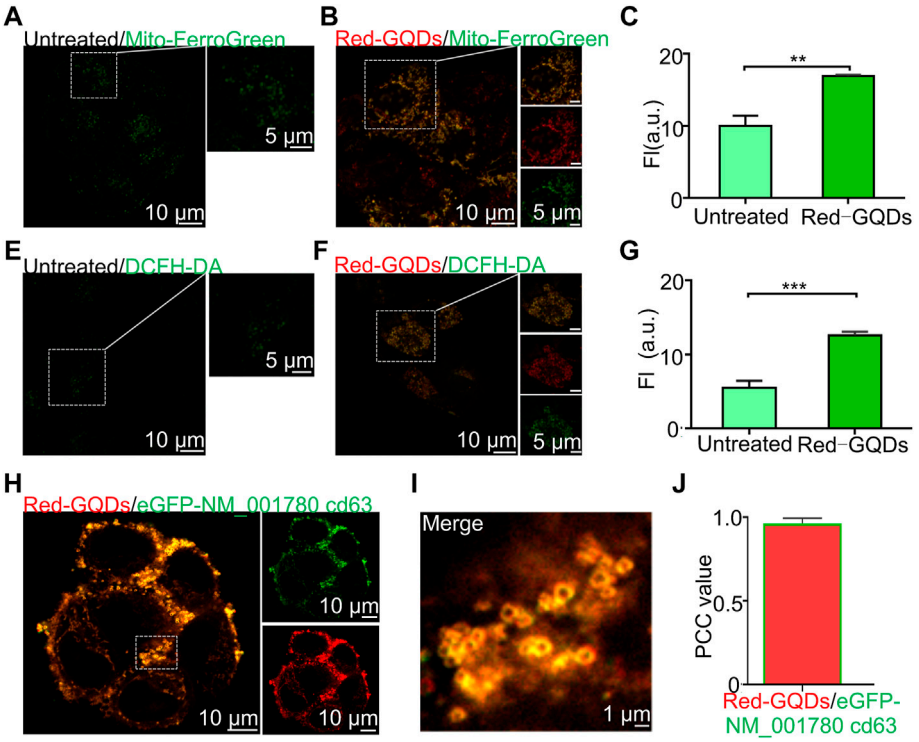

FIGURE 4 | Red-GQDs of higher concentration induce ferroptosis and exosome secretion. **(A,B)** Fluorescence image of mitochondrion Fe^{2+} with and without treated with Red-GQDs (50 μg/ml, 1 h), Mito-FerroGreen: λex = 488 nm. **(C)** Mitochondrion Fe^{2+} level with and without Red-GQD**s** (50 μg/ml, 1 h)-treated. **(E** and **F)** Fluorescence image of mitochondrion ROS with and without Red-GQDs (50 μg/ml, 1 h), DCFH-DA: λex = 488 nm. **(G)** Mitochondrion ROS level with and without Red-GQDs (50 μg/ml, 1 h)-treated. **(H)** Co-localization of Red-GQDs (50 μg/ml, 1 h) and commercial exosomes probes eGFP-NM_001780 cd63 (λex = 488 nm). **(I)** Fluorescence image of the enlarged region indicated by the white rectangle in **(H)**. **(J)** Co-localization value of Red-GQDs and eGFP-NM_001780 cd63. Data are presented as mean ± SEM (*n* = 3).

physiopathological value for in-depth exploration of the mechanism of autophagy.

Red-GQDs With High Concentration Induce Ferroptosis and Exosome Secretion

Mitochondria are the main organelles that regulate iron metabolism and fatty acid metabolism (Nunnari and Suomalainen, 2012). Mitochondria play an important role in the induction of ferroptosis (Gao et al., 2019). Excessive reactive oxygen species (ROS) production is a direct revulsant of cellular ferroptosis, while mitochondria are the main source of ROS (Wang et al., 2020; Xie et al., 2016). It has been reported that the morphology of mitochondrion is changed, such as mitochondrial shrinkage and loss of cristae during the process of ferroptosis (Wang et al., 2020) (Doll et al., 2017). It has been reported that the morphology change of mitochondrion also occurred while microglia BV2 was treated with high concentrations of GQDs (>50 μg/ml) (Wu et al., 2020). Intracellular iron overload, glutathione (GSH) depletion, and excessive ROS and lipid peroxidation (LPO) occurred in the cells after microglia BV2 was treated with GQDs with high concentration. These results indicated that GQDs could damage the iron metabolism and redox balance in microglial cells (Wu et al., 2020; Xie et al., 2016). Red-GQDs in a high concentration could cause significant ferroptosis and reduced membrane motility in cells.

In our study, mitochondria were damaged (**Supplementary Figure S7**; labeled 1) after incubating cells with a high concentration of Red-GQDs (50 μg/ml) for 1 h. HeLa cells were incubated with a commercial mitochondrial Fe^{2+} green probe (Mito-FerroGreen) and a commercial ROS green probe (DCFH-DA) for 0.5 h separately, and then the incubated HeLa cells were incubated again with 50 μg/ml Red-GQDs for 1 h to verify the relation of mitochondrial damage and ferroptosis.

The results showed that the fluorescence signals of Mito-FerroGreen and DCFH-DA in HeLa cells without incubation with Red-GQDs were weaker, while the fluorescence signals of Mito-FerroGreen and DCFH-DA in HeLa cells treated with Red-GQDs significantly enhanced (**Figures 4A–F**). The contents of Fe^{2+} and ROS were increased in HeLa cells while the cells were treated with Red-GQDs *via* quantitative analysis (**Figures 4C and G**). From this, it was concluded that mitochondrial damage occurred, and the contents of Fe^{2+} and ROS were increased in HeLa cells in the presence of 50 μg/ml Red-GQDs. It demonstrated that Red-GQDs with high concentration could interfere with iron metabolism and redox balance in HeLa

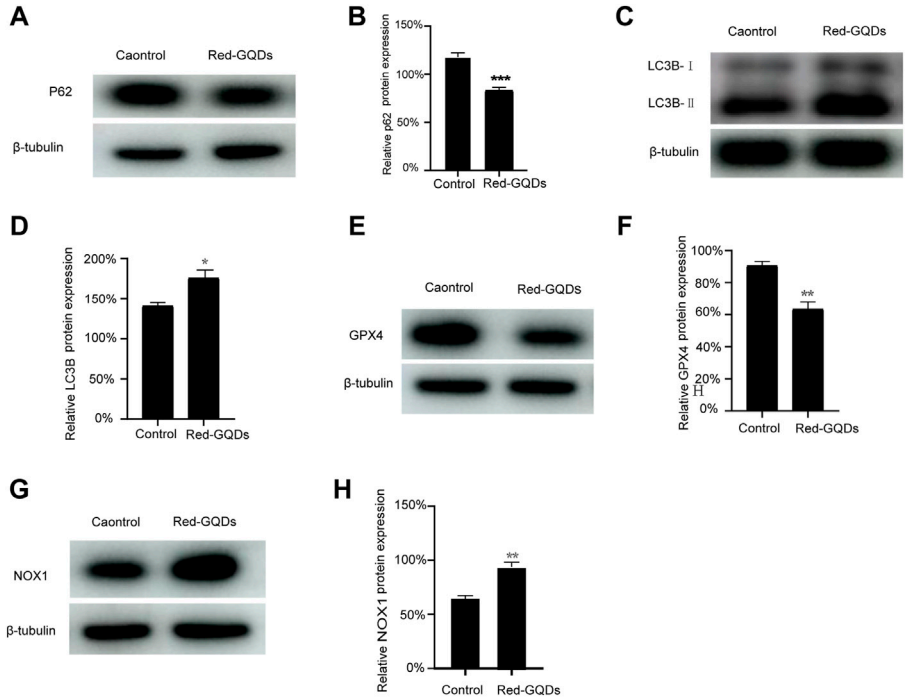

FIGURE 5 | Red-GQDs with low concentration were involved in autophagy, **(A–D)** WB analysis of p62 and LC3B-II protein expression in HeLa cells. Red-GQDs with high concentration increased the content of ROS and induced ferroptosis, **(E–H)** WB analysis of GPX4 and NOX1 protein expression in HeLa cells. Statistical significance was determined by one-way ANOVA and Dunnett's *t*-test (*$p < 0.05$, **$p < 0.01$, and ***$p < 0.001$ vs. the control group).

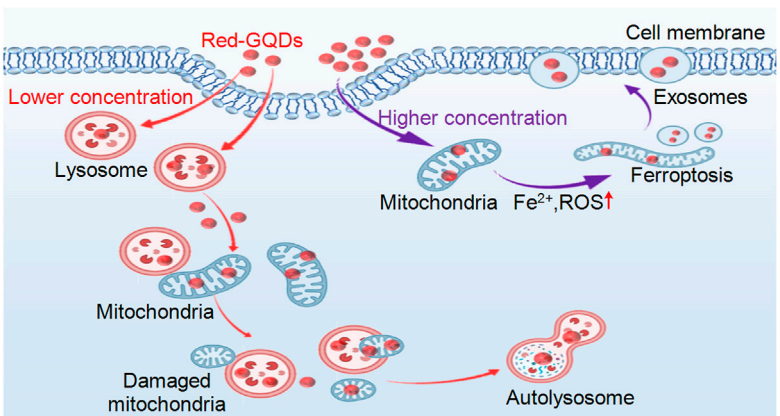

FIGURE 6 | Schematic illustration of Red-GQDs distribution and biological function in living HeLa cells.

cells, leading to lipid peroxidation and ferroptosis in cells. These results are consistent with previous reports (Wu et al., 2020). In addition, we selected ferroptosis-related proteins (GPX4 and NOX1) for Western blot assay. The results showed that high concentrations of Red-GQDs led to decreased GPX4 expression, increased ROS production, and ferroptosis in HeLa cells. The protein expression level of NOX1 reflects the degree of lipid peroxidation **(Figures 5E–H)**.

As can be observed in fluorescence images (**Supplementary Figure S7**; labeled 2), red circles appeared on the cell membrane while 50 μg/ml Red-GQDs were co-incubated with HeLa cells for 1 h. It is consistent with the morphology of exosomes previously reported (Dixon et al., 2012; Gurunathan et al., 2019). Based on the above-stated phenomenon, 50 μg/ml Red-GQDs were first co-incubated with HeLa cells for 1 h and then co-stained with the exosome green fluorescent dye eGFP-NM_001780 cd63. As shown in **Figure 4I**, a large number of Red-GQDs were accumulated on the cell membrane, and the fluorescence of Red-GQDs was highly coincident with that of eGFP-NM_001780 cd63 (**Figures 4H–J**).

These results exhibit that Red-GQDs with high concentration can promote Fe^{2+} overload, ROS, and lipid peroxidation (LPO) in mitochondrion in HeLa cells. These factors lead to the damage of mitochondrial morphology, decreasing cellular activity and impairing normal metabolic pathways in cells. At the same time, the increase of lipid peroxides and the significant decrease of cell membrane fluidity also lead to the accumulation of Red-GQDs in the cell membrane.

CONCLUSION

Two-photon confocal microscopy was used to track the location of Red-GQDs in live cells at different incubation times to visualize them. Compared with traditional techniques, two-photon confocal microscopy can better achieve nanoscale imaging of fluorescence in living cells. Our work highlighted the biological mechanism of action of Red-GQDs, showing how Red-GQDs are captured by cells and localized to different organelles over time. On this basis, we systematically analyzed the uptake and metabolism of Red-GQDs in HeLa cells and confirmed that Red-GQDs mainly entered cells through energy-dependent endocytosis and showed significant concentration and time dependence in subcellular distribution. In this work, Red-GQDs at a low concentration (25 μg/ml) were absorbed by cells and distributed in different organelles (lysosomes and mitochondria) in a time-dependent manner. During the incubation time of 0.5–1 h, Red-GQDs were mainly distributed in lysosomes and were gradually enriched in mitochondria over time. Red-GQDs also participate in autophagy and form autolysosomes. A high concentration (50 μg/ml) of Red-GQDs can promote mitochondrial Fe^{2+} overload, ROS and lipid peroxidation (LPO) increase, and induce ferroptosis in cells. In addition, a high concentration (50 μg/ml) of Red-GQDs can also promote the secretion of cellular exosomes (**Figure 6**). This study improves the mechanism of action of graphene quantum dots (GQDs) in the biomedical field and provides a basis for further research and applications of Red-GQDs.

EXPERIMENTAL SECTIONS

Materials and Instruments

General methods were used unless otherwise stated. Materials and solvents were purchased from commercial suppliers and used without further purification. The super-resolution imaging of organelles was taken using a two-photon laser confocal microscope (LSM980NLO, ZEISS, Germany). Red-GQDs (Particle size<10 nm) were custom synthesized by Nanjing XFNANO Materials Tech. Co., and the data characterizing Red-GQDs were also measured by Nanjing XFNANO Materials Tech. Co.

Cell Culture and Staining

HeLa cells were seeded on Dulbecco's modified Eagle's medium, DMEM (VivaCell, Shanghai, China) with 10% fetal bovine serum, FBS (VivaCell, Shanghai, China), 1% penicillin and streptomycin. The stock solution of Red-GQDs was prepared in DMSO and then diluted with a cultural medium of HeLa cells at a required concentration of 37°C in an environment containing 5% CO_2. The cells were washed five times with prewarmed PBS and three times with the complete medium before imaging.

Western Blot

TP from HeLa cells was isolated *via* RIPA assay in keeping with the manufacturer's specifications. The isolated proteins were quantitated *via* BCA Protein Assay Kit (Solarbio, Beijing, China, PC0020). The proteins were segregated by 12% SDS-PAGE and then transferred onto polyvinylidene fluoride film. The films were sealed with 5% fat-free milk and probed with the primary antibodies against GPX4 (#ab125066, Abcam, Cambridge, United Kingdom), P62 (#18420-1-AP, Proteintech Group, Chicago, IL, United States), LC3B (#18725-1-AP, Proteintech Group, Chicago, IL, United States), NOX1 (#17772-1-AP, Proteintech Group, Chicago, IL, United States), and β-tubulin (#10094-1-AP, Proteintech Group, Chicago, IL, United States) at 4°C for one night, followed by 1-h immunoblot with the secondary antibodies at indoor temperature. After washing with TBS/Tween, the PVDF membranes were incubated with secondary antibodies at indoor temperature for 1 h. Blots were developed with an ECL kit (Millipore Corporation, Billerica, United States) and analyzed *via* Image J.

Two-Photon Laser Confocal Microscope-LSM980NLO

HeLa cells were seeded in 35-mm glass-bottom microwell dishes to image. The fluorescence images were obtained using a two-photon laser confocal microscope (LSM980NLO) and analyzed using ImageJ software. Red-GQDs and commercial dyes were prepared with complete DMEM, and then cells were stained in a cell incubator. Fluorescence images were obtained using LSM980NLO.

In Vitro Endocytic Pathways

HeLa cells were divided into three groups: pre-treated with chlorpromazine (CPZ, 20.0 μM, 1 h, inhibitor endocytosis), lower temperature (4°C, 1 h, energy inhibitor), and control group (37°C, 1 h). The cells were washed with PBS two times and then stained with Red-GQDs (10 μg/ml) for 1 h at 37°C. Finally, the cells were washed with PBS five times and with complete DMEM three times. Then, they were visualized under an LSM980NLO microscope with 488 nm excitation.

Cell Transfection

In brief, 2,500 ng of DNA was combined with 8 μl of TurboFect transfection solution in 250 μl free DMEM to form the transfection mixtures. As the mixtures were incubating at room temperature for 20 min, cells in 35-mm dishes were replaced with 750 μl complete DMEM and then the mixtures were added to the cells. After transfecting the cells for 3 h, the transfection medium was replaced with 1 ml of complete DMEM with a penicillin–streptomycin solution. The cells were incubated at 37°C and then stained with Red-GQDs (50 μg/ml) for a colocalization assay.

Quantitative Detection of Mitochondrial Fe^{2+} and ROS Level in SIM Image

The normal group of HeLa cells were stained with commercial Mito-FerroGreen and DCFH-DA probes, and the other groups were stained with Red-GQDs and commercial Mito-FerroGreen and DCFH-DA probes, which were imaged using a two-photon laser confocal microscope–LSM980NLO. Quantitative analysis of fluorescence intensities was performed using ImageJ.

Data Analysis

Statistical analysis was performed using GraphPad Prism 7, and Origin 2018. Normality and log-normality tests were performed to check the normal distribution. In the case of normal distribution, the statistical comparison of results was tested with a Student's *t*-test. Data are presented as mean ± SEM. SEM was used to compare experimental results with controls. In the case of non-normal distribution, the statistical comparison of results was tested with a Mann–Whitney test, with levels of significance set at n.s. (no significant difference), $^{*}p < 0.05$, $^{**}p < 0.01$, $^{***}p < 0.001$, and $^{****}p < 0.0001$. Statistical significance and sample sizes in all graphs are indicated in the corresponding figure legends.

DATA AVAILABILITY STATEMENT

The original contributions presented in the study are included in the article/**Supplementary Material**; further inquiries can be directed to the corresponding authors.

AUTHOR CONTRIBUTIONS

HH, PL, JQ, and MZ contributed to the conception and design of the study. HH wrote the first draft of the manuscript. MK, ZZ, and DW critically revised the manuscript. All authors contributed to manuscript revision, read, and approved the submitted version.

FUNDING

This work was supported by the Rongxiang Regenerative Medicine Foundation of Shandong University (No.26020112001919), Shandong National Science Foundation of China (No. ZR2020QH074).

ACKNOWLEDGMENTS

The authors thank the Institute of Shandong Provincial Hospital for instrument support.

SUPPLEMENTARY MATERIAL

The Supplementary Material for this article can be found online at: https://www.frontiersin.org/articles/10.3389/fphar.2022.932807/full#supplementary-material

REFERENCES

Abdullah-Al-Nahain, N., Lee, J.-E., In, I., Lee, H., Lee, K. D., Jeong, J. H., et al. (2013). Target Delivery and Cell Imaging Using Hyaluronic Acid-Functionalized Graphene Quantum Dots. *Mol. Pharm.* 10 (10), 3736–3744. doi:10.1021/mp400219u

Agarwal, R., Singh, V., Jurney, P., Shi, L., Sreenivasan, S. V., and Roy, K. (2013). Mammalian Cells Preferentially Internalize Hydrogel Nanodiscs over Nanorods and Use Shape-specific Uptake Mechanisms. *Proc. Natl. Acad. Sci. U. S. A.* 110 (43), 17247–17252. doi:10.1073/pnas.1305000110

Chen, F., Gao, W., Qiu, X., Zhang, H., Liu, L., Liao, P., et al. (2017). Graphene Quantum Dots in Biomedical Applications: Recent Advances and Future Challenges. *Front. Laboratory Med.* 1 (4), 192–199. doi:10.1016/j.flm.2017.12.006

Chen, H., Wang, H., Wei, Y., Hu, M., Dong, B., Fang, H., et al. (2022). Super-resolution Imaging Reveals the Subcellular Distribution of Dextran at the Nanoscale in Living Cells. *Chin. Chem. Lett.* 33 (4), 1865–1869. doi:10.1016/j.cclet.2021.10.025

Chen, Q., Fang, H., Shao, X., Tian, Z., Geng, S., Zhang, Y., et al. (2020a). A Dual-Labeling Probe to Track Functional Mitochondria-Lysosome Interactions in Live Cells. *Nat. Commun.* 11 (1), 6290. doi:10.1038/s41467-020-20067-6

Chen, Q., Shao, X., Hao, M., Fang, H., Guan, R., Tian, Z., et al. (2020b). Quantitative Analysis of Interactive Behavior of Mitochondria and Lysosomes Using Structured Illumination Microscopy. *Biomaterials* 250, 120059. doi:10.1016/j.biomaterials.2020.120059

Dixon, S. J., Lemberg, K. M., Lamprecht, M. R., Skouta, R., Zaitsev, E. M., Gleason, C. E., et al. (2012). Ferroptosis: an Iron-dependent Form of Nonapoptotic Cell Death. *Cell* 149 (5), 1060–1072. doi:10.1016/j.cell.2012.03.042

Doll, S., Proneth, B., Tyurina, Y. Y., Panzilius, E., Kobayashi, S., Ingold, I., et al. (2017). ACSL4 Dictates Ferroptosis Sensitivity by Shaping Cellular Lipid Composition. *Nat. Chem. Biol.* 13 (1), 91–98. doi:10.1038/nchembio.2239

Eda, G., Lin, Y. Y., Mattevi, C., Yamaguchi, H., Chen, H. A., Chen, I. S., et al. (2010). Blue Photoluminescence from Chemically Derived Graphene Oxide. *Adv. Mater* 22 (4), 505–509. doi:10.1002/adma.200901996

Gan, Z., Xu, H., and Hao, Y. (2016). Mechanism for Excitation-dependent Photoluminescence from Graphene Quantum Dots and Other Graphene Oxide Derivates: Consensus, Debates and Challenges. *Nanoscale* 8 (15), 7794–7807. doi:10.1039/c6nr00605a

Gao, M., Yi, J., Zhu, J., Minikes, A. M., Monian, P., Thompson, C. B., et al. (2019). Role of Mitochondria in Ferroptosis. *Mol. Cell* 73 (2), 354–363. doi:10.1016/j.molcel.2018.10.042

Gurunathan, S., Kang, M. H., Jeyaraj, M., Qasim, M., and Kim, J. H. (2019). Review of the Isolation, Characterization, Biological Function, and Multifarious Therapeutic Approaches of Exosomes. *Cells* 8 (4), 307. doi:10.3390/cells8040307

Hai, X., Feng, J., Chen, X., and Wang, J. (2018). Tuning the Optical Properties of Graphene Quantum Dots for Biosensing and Bioimaging. *J. Mater Chem. B* 6 (20), 3219–3234. doi:10.1039/c8tb00428e

Hai, X., Mao, Q. X., Wang, W. J., Wang, X. F., Chen, X. W., and Wang, J. H. (2015). An Acid-free Microwave Approach to Prepare Highly Luminescent Boron-Doped Graphene Quantum Dots for Cell Imaging. *J. Mater Chem. B* 3 (47), 9109–9114. doi:10.1039/c5tb01954k

Hung, Y. H., Chen, L. M., Yang, J. Y., and Yang, W. Y. (2013). Spatiotemporally Controlled Induction of Autophagy-Mediated Lysosome Turnover. *Nat. Commun.* 4, 2111. doi:10.1038/ncomms3111

Kim, T. H., Lee, D., and Choi, J. W. (2017). Live Cell Biosensing Platforms Using Graphene-Based Hybrid Nanomaterials. *Biosens. Bioelectron.* 94, 485–499. doi:10.1016/j.bios.2017.03.032

Ku, T., Hao, F., Yang, X., Rao, Z., Liu, Q. S., Sang, N., et al. (2021). Graphene Quantum Dots Disrupt Embryonic Stem Cell Differentiation by Interfering with the Methylation Level of Sox2. *Environ. Sci. Technol.* 55 (5), 3144–3155. doi:10.1021/acs.est.0c07359

Lawrence, R. E., and Zoncu, R. (2019). The Lysosome as a Cellular Centre for Signalling, Metabolism and Quality Control. *Nat. Cell Biol.* 21 (2), 133–142. doi:10.1038/s41556-018-0244-7

Li, P., Xu, T., Wu, S., Lei, L., and He, D. (2017). Chronic Exposure to Graphene-Based Nanomaterials Induces Behavioral Deficits and Neural Damage in *Caenorhabditis elegans*. *J. Appl. Toxicol.* 37 (10), 1140–1150. doi:10.1002/jat.3468

Li, R., Ma, H., Zhang, X., Li, C., Xiong, J., Lu, T., et al. (2015). Impaired Autophagosome Clearance Contributes to Local Anesthetic Bupivacaine-Induced Myotoxicity in Mouse Myoblasts. *Anesthesiology* 122 (3), 595–605. doi:10.1097/aln.0000000000000568

Liao, Z., Wang, B., Liu, W., Xu, Q., Hou, L., Song, J., et al. (2021). Dysfunction of Chaperone-Mediated Autophagy in Human Diseases. *Mol. Cell Biochem.* 476 (3), 1439–1454. doi:10.1007/s11010-020-04006-z

Lim, C. Y., and Zoncu, R. (2016). The Lysosome as a Command-And-Control Center for Cellular Metabolism. *J. Cell Biol.* 214 (6), 653–664. doi:10.1083/jcb.201607005

Luzio, J. P., Pryor, P. R., and Bright, N. A. (2007). Lysosomes: Fusion and Function. *Nat. Rev. Mol. Cell Biol.* 8 (8), 622–632. doi:10.1038/nrm2217

Maejima, I., Takahashi, A., Omori, H., Kimura, T., Takabatake, Y., Saitoh, T., et al. (2013). Autophagy Sequesters Damaged Lysosomes to Control Lysosomal Biogenesis and Kidney Injury. *Embo J.* 32 (17), 2336–2347. doi:10.1038/emboj.2013.171

Markovic, Z. M., Ristic, B. Z., Arsikin, K. M., Klisic, D. G., Harhaji-Trajkovic, L. M., Todorovic-Markovic, B. M., et al. (2012). Graphene Quantum Dots as Autophagy-Inducing Photodynamic Agents. *Biomaterials* 33 (29), 7084–7092. doi:10.1016/j.biomaterials.2012.06.060

Menzies, F. M., Fleming, A., Caricasole, A., Bento, C. F., Andrews, S. P., Ashkenazi, A., et al. (2017). Autophagy and Neurodegeneration: Pathogenic Mechanisms and Therapeutic Opportunities. *Neuron* 93 (5), 1015–1034. doi:10.1016/j.neuron.2017.01.022

Mihalache, I., Radoi, A., Munteanu, C., Kusko, M., and Kusko, C. (2014). Charge Storage and Memory Effect in Graphene Quantum Dots - PEG600 Hybrid Nanocomposite. *Org. Electron.* 15 (1), 216–225. doi:10.1016/j.orgel.2013.10.031

Mijaljica, D., Prescott, M., and Devenish, R. J. (2011). V-ATPase Engagement in Autophagic Processes. *Autophagy* 7 (6), 666–668. doi:10.4161/auto.7.6.15812

Nunnari, J., and Suomalainen, A. (2012). Mitochondria: in Sickness and in Health. *Cell* 148 (6), 1145–1159. doi:10.1016/j.cell.2012.02.035

Schroeder, K. L., Goreham, R. V., and Nann, T. (2016). Graphene Quantum Dots for Theranostics and Bioimaging. *Pharm. Res.* 33 (10), 2337–2357. doi:10.1007/s11095-016-1937-x

Serrano-Puebla, A., and Boya, P. (2016). Lysosomal Membrane Permeabilization in Cell Death: New Evidence and Implications for Health and Disease. *Ann. N. Y. Acad. Sci.* 1371 (1), 30–44. doi:10.1111/nyas.12966

Settembre, C., Fraldi, A., Medina, D. L., and Ballabio, A. (2013). Signals from the Lysosome: a Control Centre for Cellular Clearance and Energy Metabolism. *Nat. Rev. Mol. Cell Biol.* 14 (5), 283–296. doi:10.1038/nrm3565

Shang, W., Zhang, X., Zhang, M., Fan, Z., Sun, Y., Han, M., et al. (2014). The Uptake Mechanism and Biocompatibility of Graphene Quantum Dots with Human Neural Stem Cells. *Nanoscale* 6 (11), 5799–5806. doi:10.1039/c3nr06433f

Shen, J., Zhu, Y., Chen, C., Yang, X., and Li, C. (2011). Facile Preparation and Upconversion Luminescence of Graphene Quantum Dots. *Chem. Commun. (Camb)* 47 (9), 2580–2582. doi:10.1039/c0cc04812g

Tabish, T. A., Scotton, C. J., Ferguson, D. C. J., Lin, L., der Veen, A. V., Lowry, S., et al. (2018). Biocompatibility and Toxicity of Graphene Quantum Dots for Potential Application in Photodynamic Therapy. *Nanomedicine (Lond)* 13 (15), 1923–1937. doi:10.2217/nnm-2018-0018

Tan, D., Zhou, S., and Qiu, J. (2012). Comment on "Upconversion and Downconversion Fluorescent Graphene Quantum Dots: Ultrasonic Preparation and Photocatalysis". *ACS Nano* 6(8), 6530–6532. doi:10.1021/nn3016822

Thurston, T. L., Wandel, M. P., von Muhlinen, N., Foeglein, A., and Randow, F. (2012). Galectin 8 Targets Damaged Vesicles for Autophagy to Defend Cells against Bacterial Invasion. *Nature* 482 (7385), 414–418. doi:10.1038/nature10744

Tian, P., Tang, L., Teng, K. S., and Lau, S. P. (2018). Graphene Quantum Dots from Chemistry to Applications. *Mater. Today Chem.* 10, 221–258. doi:10.1016/j.mtchem.2018.09.007

Wang, H., Liu, C., Zhao, Y., and Gao, G. (2020). Mitochondria Regulation in Ferroptosis. *Eur. J. Cell Biol.* 99 (1), 151058. doi:10.1016/j.ejcb.2019.151058

Wang, Z., Xia, J., Zhou, C., Via, B., Xia, Y., Zhang, F., et al. (2013). Synthesis of Strongly Green-Photoluminescent Graphene Quantum Dots for Drug Carrier. *Colloids Surf. B Biointerfaces* 112, 192–196. doi:10.1016/j.colsurfb.2013.07.025

Wu, C., Wang, C., Han, T., Zhou, X., Guo, S., and Zhang, J. (2013). Insight into the Cellular Internalization and Cytotoxicity of Graphene Quantum Dots. *Adv. Healthc. Mater* 2 (12), 1613–1619. doi:10.1002/adhm.201300066

Wu, T., Liang, X., Liu, X., Li, Y., Wang, Y., Kong, L., et al. (2020). Induction of Ferroptosis in Response to Graphene Quantum Dots through Mitochondrial Oxidative Stress in Microglia. *Part Fibre Toxicol.* 17 (1), 30. doi:10.1186/s12989-020-00363-1

Xie, Y., Hou, W., Song, X., Yu, Y., Huang, J., Sun, X., et al. (2016). Ferroptosis: Process and Function. *Cell Death Differ.* 23 (3), 369–379. doi:10.1038/cdd.2015.158

Xu, G., Zeng, S., Zhang, B., Swihart, M. T., Yong, K. T., and Prasad, P. N. (2016). New Generation Cadmium-Free Quantum Dots for Biophotonics and Nanomedicine. *Chem. Rev.* 116 (19), 12234–12327. doi:10.1021/acs.chemrev.6b00290

Xu, Y., Wang, X., Zhang, W. L., Lv, F., and Guo, S. (2018). Recent Progress in Two-Dimensional Inorganic Quantum Dots. *Chem. Soc. Rev.* 47 (2), 586–625. doi:10.1039/c7cs00500h

Yoo, J. M., Kang, J. H., and Hong, B. H. (2015). Graphene-based Nanomaterials for Versatile Imaging Studies. *Chem. Soc. Rev.* 44 (14), 4835–4852. doi:10.1039/c5cs00072f

Yuan, X., Liu, Z., Guo, Z., Ji, Y., Jin, M., and Wang, X. (2014). Cellular Distribution and Cytotoxicity of Graphene Quantum Dots with Different Functional Groups. *Nanoscale Res. Lett.* 9 (1), 108. doi:10.1186/1556-276x-9-108

Zhang, Y., Zheng, F., Yang, T., Zhou, W., Liu, Y., Man, N., et al. (2012). Tuning the Autophagy-Inducing Activity of Lanthanide-Based Nanocrystals through Specific Surface-Coating Peptides. *Nat. Mater* 11 (9), 817–826. doi:10.1038/nmat3363

Zhao, Y. G., and Zhang, H. (2019). Autophagosome Maturation: An Epic Journey from the ER to Lysosomes. *J. Cell Biol.* 218 (3), 757–770. doi:10.1083/jcb.201810099

Zhu, S., Song, Y., Zhao, X., Shao, J., Zhang, J., and Yang, B. (2015). The Photoluminescence Mechanism in Carbon Dots (Graphene Quantum Dots, Carbon Nanodots, and Polymer Dots): Current State and Future Perspective. *Nano Res.* 8 (2), 355–381. doi:10.1007/s12274-014-0644-3

Zhu, X., Zuo, X., Hu, R., Xiao, X., Liang, Y., and Nan, J. (2014). Hydrothermal Synthesis of Two Photoluminescent Nitrogen-Doped Graphene Quantum Dots Emitted Green and Khaki Luminescence. *Mater. Chem. Phys.* 147 (3), 963–967. doi:10.1016/j.matchemphys.2014.06.043

Zhuo, S., Shao, M., and Lee, S. T. (2012). Upconversion and Downconversion Fluorescent Graphene Quantum Dots: Ultrasonic Preparation and Photocatalysis. *ACS Nano* 6 (2), 1059–1064. doi:10.1021/nn2040395

Conflict of Interest: The authors declare that the research was conducted in the absence of any commercial or financial relationships that could be construed as a potential conflict of interest.

Publisher's Note: All claims expressed in this article are solely those of the authors and do not necessarily represent those of their affiliated organizations, or those of the publisher, the editors, and the reviewers. Any product that may be evaluated in this article, or claim that may be made by its manufacturer, is not guaranteed or endorsed by the publisher.

Copyright © 2022 Hu, Li, Qiu, Zhao, Kuang, Zhang and Wang. This is an open-access article distributed under the terms of the Creative Commons Attribution License (CC BY). The use, distribution or reproduction in other forums is permitted, provided the original author(s) and the copyright owner(s) are credited and that the original publication in this journal is cited, in accordance with accepted academic practice. No use, distribution or reproduction is permitted which does not comply with these terms.

frontiers | Frontiers in Pharmacology

REVIEW
published: 19 July 2022
doi: 10.3389/fphar.2022.915609

Fluorescent Probes Design Strategies for Imaging Mitochondria and Lysosomes

Huimin Chen[1,2], *Zhenjie Yu*[1], *Shiwei Ren*[1] *and Yuyu Qiu*[2]*

[1]Institute of Materia Medica, Science and Technology Innovation Center, Shandong First Medical University and Shandong Academy of Medical Sciences, Jinan, China, [2]Department of Biochemistry, Shandong First Medical University and Shandong Academy of Medical Sciences, Tai'an, China

Modern cellular biology faces several major obstacles, such as the determination of the concentration of active sites corresponding to chemical substances. In recent years, the popular small-molecule fluorescent probes have completely changed the understanding of cellular biology through their high sensitivity toward specific substances in various organisms. Mitochondria and lysosomes are significant organelles in various organisms, and their interaction is closely related to the development of various diseases. The investigation of their structure and function has gathered tremendous attention from biologists. The advanced nanoscopic technologies have replaced the diffraction-limited conventional imaging techniques and have been developed to explore the unknown aspects of mitochondria and lysosomes with a sub-diffraction resolution. Recent progress in this field has yielded several excellent mitochondria- and lysosome-targeted fluorescent probes, some of which have demonstrated significant biological applications. Herein, we review studies that have been carried out to date and suggest future research directions that will harness the considerable potential of mitochondria- and lysosome-targeted fluorescent probes.

Keywords: lysosomes, mitochondria, small-molecule fluorescent probe, interaction, imaging

OPEN ACCESS

Edited by:
Peixue Ling,
Shandong University, China

Reviewed by:
Kai Wang,
Chinese Academy of Medical Sciences and Peking Union Medical College, China
Lei Wang,
University of Cincinnati, United States

***Correspondence:**
Yuyu Qiu
qyyu1979@163.com

Specialty section:
This article was submitted to Pharmacology of Anti-Cancer Drugs, a section of the journal Frontiers in Pharmacology

Received: *08 April 2022*
Accepted: *30 May 2022*
Published: *19 July 2022*

Citation:
Chen H, Yu Z, Ren S and Qiu Y (2022) Fluorescent Probes Design Strategies for Imaging Mitochondria and Lysosomes. Front. Pharmacol. 13:915609. doi: 10.3389/fphar.2022.915609

1 INTRODUCTION

Mitochondria, popularly termed the cellular "powerhouses," are one of the most significant constituents of eukaryotic cells. The mitochondria not only plays an important role in adenosine triphosphate (ATP) production but also performs numerous essential functions within the cells, such as transmission of information, induction of cell differentiation, growth, and apoptosis (Vakifahmetoglu-Norberg et al., 2017). Mitochondria have a distinctive double-membrane structure, playing important roles in their unique and complicated functions. Lysosomes are "digestion workshops" in cells, participating in the apoptotic process and other types of cell death (Luzio et al., 2007). They can function alone to participate in normal biological processes and can also interact with each other to accelerate the transmission of materials and communication with the external environment, which allows cells to improve their biological functions.

Apart from playing their own distinctive function, mitochondria could interact with lysosomes. At present, the interactions between mitochondria and lysosomes have been extensively explored, such as the fusion of the lysosomes with mitochondria during the process of autophagy (Chen et al., 2019a) and the mitochondrial and lysosomal contact (MLC) (Wong et al., 2019). Their contact promotes transmission of materials and information. When their contacting function is disrupted,

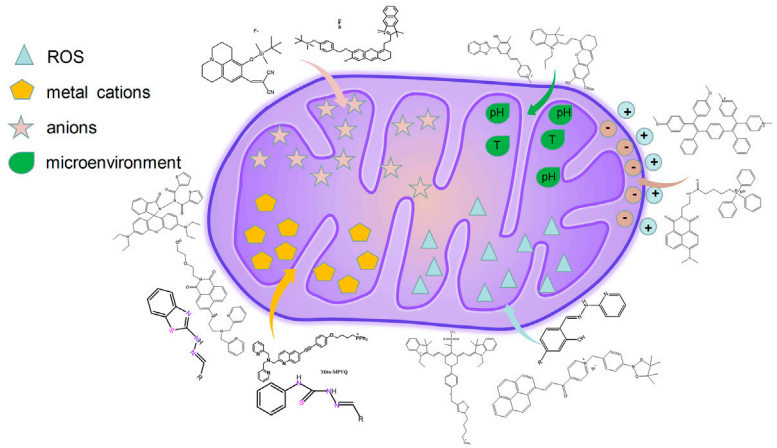

FIGURE 1 | The design strategies of fluorescence probes targeting mitochondria.

the occurrence of human-related diseases, such as Parkinson's and lysosomal storage–related diseases, is noted (Wong et al., 2019). Therefore, the timely monitoring of their dynamic changes and the estimation of the reactive small-molecule (RSM) levels are very important for identifying their physiological function and the pathogenesis of the related diseases. Several RSMs have been found in the mitochondria and various enzymes exist in the lysosome, whose dysfunction can participate in the progression of human-related diseases, such as metabolic diseases, heart failure, neurodegenerative diseases (Marc et al., 2009), Alzheimer's disease (Nixon et al., 2000), and Parkinson disease (Daniel et al., 2008).

Fluorescence microscopy (FM) is a powerful tool for studying cellular dynamics, which has been used widely to study the interaction mechanism between mitochondria and lysosomes (Chen et al., 2019b; Chen et al., 2020). However, among imaging organelle interaction, the systematic introduction of mitochondrial and lysosomal imaging strategy is rare. Therefore, the present review focuses on some new imaging strategies of fluorescence probes targeting mitochondria and lysosomes.

2 FLUORESCENCE PROBES DESIGN STRATEGIES FOR MITOCHONDRIA IMAGING

Small-molecule fluorescent probes targeting mitochondria can enable the imaging of these organelles to detect the dynamic location and morphological changes of the mitochondria and observe their physiological process (Wei et al., 2022). The fluorescent probes used for imaging mitochondria are mainly divided into the following two types: bearing unique positive charge and targeting the contents of mitochondria and lysosomes. Hence, membrane permeable cationic compounds could be enriched into mitochondria because of their electrophoresis effect. The commercial probe targeting mitochondria, MitoTracker Green (MTG) with positive charge, has been widely used to target mitochondria selectively. In addition, triphenylphosphonium (TPP) with large hydrophobic radius has also been used as a targeting group for mitochondria owing to its high membrane permeability (**Figure 1**) (Tian et al., 2022).

2.1 Single Functional Fluorescent Probes Targeting Mitochondria *via* Positive Charge

Mitochondrial membrane potential is the main component of proton motion dynamics, which is formed by protons pumped from the mitochondrial matrix to membrane. The mitochondria keep the negative transmembrane potential up to −180 mV if the potential in the cytoplasm is 0 mV (Tian et al., 2022). Based on these characterizations, positive charge has been widely applied to target mitochondria.

Recently, Gu et al. have designed a novel photoactivatable bio-probe, ***o*-TPE-ON+** (Gu et al., 2016), which can indicate the characterization of spontaneous scintillation without any imaging buffer or additives. Interestingly, this probe can target the mitochondria specifically, which is probably owing to the accumulation of negative charge of mitochondrial outer membrane. In addition, ***o*-TPE-ON+** has been thought as a better choice for fluorescence imaging on the basis of its better cell permeability and outstanding biocompatibility. And the probe ***o*-TPE-ON+** has tracked the high-resolution nanoscopic imaging and dynamic changes of the mitochondria (Gu et al., 2016). Huimin et al. (2022) utilized Cy5 to link with dextran to target and visualize the mitochondrial changes under dextran, which realizes the drug-visualized study at the organelle scale. Saipeng et al. (2015) also designed a mitochondrial fluorescence probe, **NPA-TPP**, with a fluorescent group of 1,8-naphthalimide group and the targeting group of TPP (**Figure 2**).

2.2 Fluorescent Probes Detecting Mitochondrial Contents

It has been demonstrated that there are several RSMs in the mitochondria. The RSMs mainly include reactive oxygen species

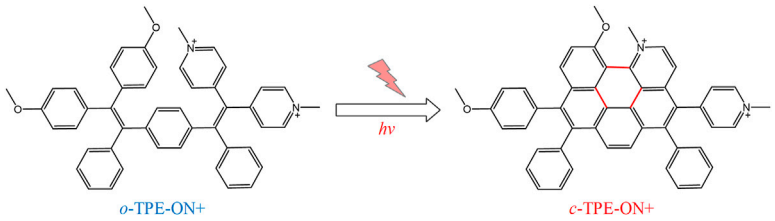

FIGURE 2 | The photocyclodehydrogenation process of ***o*-TPE-ON+** (Gu et al., 2016)

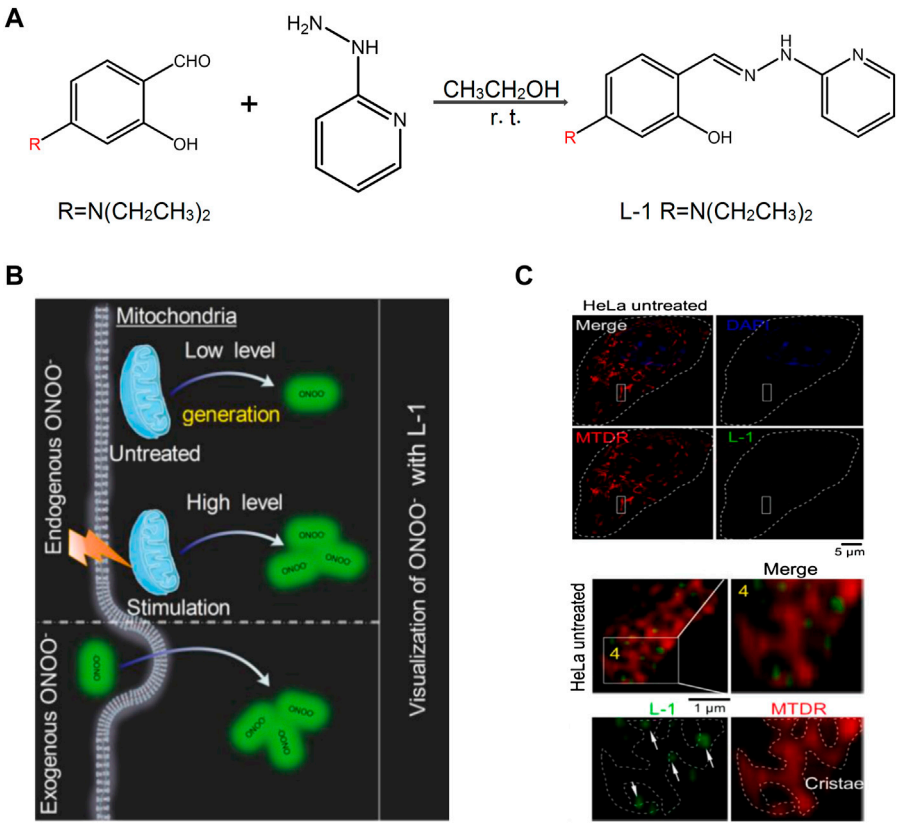

FIGURE 3 | The design of **L-1** and its response with $ONOO^-$ (Liu et al., 2021). **(A)** Synthetic route of probe **L-1**. **(B)** Proposed $ONOO^-$ visualization mechanisms for probe **L-1** in living cells. **(C)** Super-resolution visualization of $ONOO^-$ using **L-1** in living cells.

(ROS), active nitrogen, metal cations, protons, and anions. Therefore, to visualize the distribution and action mechanism of RSMs in the mitochondria, various researchers have designed and synthesized several small-molecule fluorescent probes that target specific mitochondrial contents to further study the action targets and mechanism of drugs, which provides a powerful tool for the integration of diagnosis and treatment of diseases (Liu et al., 2021; Huimin et al., 2022).

2.2.1 Application of the Fluorescent Probes in the Detection of Reactive Oxygen Species in Mitochondria

The survival of cells depends largely on mitochondrial function, which was recognized as an important target for potential drug development (Bras et al., 2005). In recent years, the mitochondria has been recognized as an important target of many drugs. It has been reported that one of the main ways of causing mitochondrial damage is the abnormal level of intracellular ROS. The ROS includes peroxides, super oxides, hydroxyl radicals, singlet oxygen, etc.

Among them, peroxynitrite ($ONOO^-$) is a major one because of its function of signal transduction and antibacterial activities in the biosystems (Radi, 2013). To detect $ONOO^-$ selectively, Liu et al. (2021) designed a probe **L-1**, a "landmine," to monitor the $ONOO^-$ levels in living cells with higher selectivity. In addition, they proposed a novel strategy "landmine warfare strategy." "Landmine" **L-1** without fluorescence was distributed evenly in the cell matrix and could release fluorophore when "engineer"

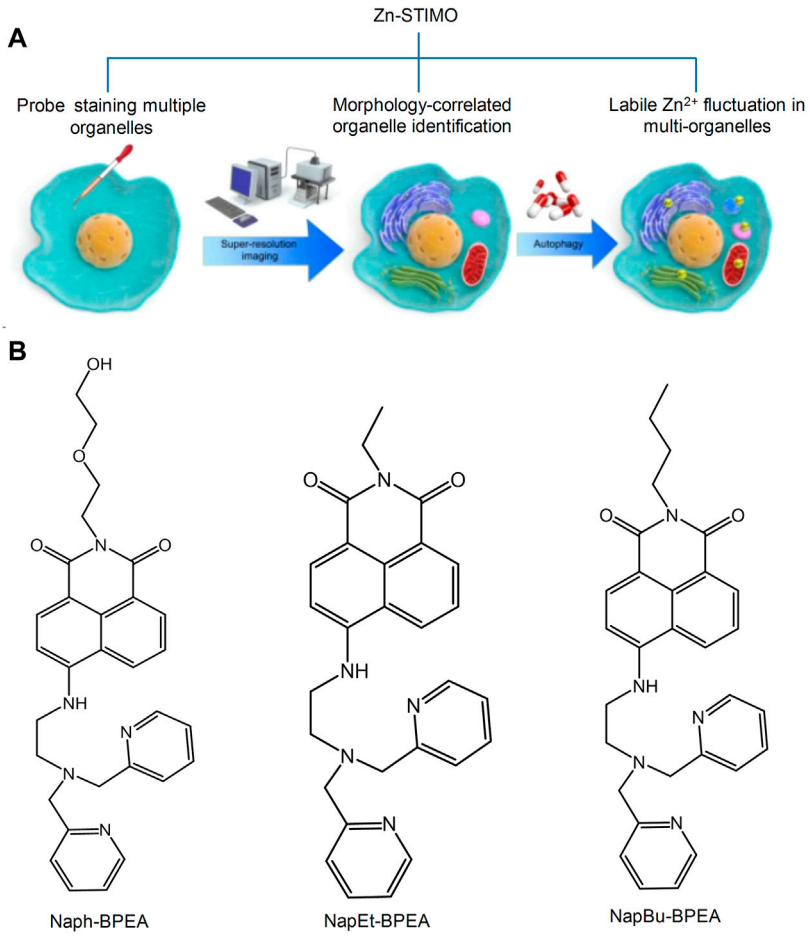

FIGURE 4 | Schematic illustration of Zn-STIMO, and the design of probe candidate for Zn-STIMO (Fang et al., 2021). **(A)** The scheme of Zn-STIMO; **(B)** the structure of fluorescent probes targeting Zn^{2+}, **Naph-BPEA**, **NapEt-BPEA**, and **NapBu-BPEA**.

$ONOO^-$ was generated in the mitochondria (**Figure 3**). Under SIM, it could be found that the "engineer" $ONOO^-$ acted alone at the mitochondrial cristae and emitted fluorescence. The "landmine warfare strategy" provided a novel designed method for innovative drugs development of diseases which resulted owing to the abnormal $ONOO^-$ concentration and provided a novel research direction for other ROS materials in the mitochondria. H_2O_2 is one of the major forms of ROS, which participates in the process of a cell's growth metabolism and energy production (Chen et al., 2014; Kangnan et al., 2020a). Kangnan et al. (2020b) designed a TP probe, **Pyp-B**, to detect the concentration of H_2O_2 in the mitochondria. Xiaoyue et al. (2018) developed the near-infrared fluorescent probe **Mito-Cy-Tfs** to detect the level of superoxide anion ($O_2^{\bullet-}$) and the relationship between $O_2^{\bullet-}$ concentration and apoptosis during ischemia/reperfusion.

2.2.2 Fluorescent Probe Detection of Metal Cations in Mitochondria

Metal ions are required for mitochondrial physiology in many aspects. Copper, iron, manganese, and zinc play an important role in organ metalloenzymes and metalloproteins (Pierrel et al., 2007). In biological systems, the zinc ion (Zn^{2+}) mainly participates in certain life processes, such as DNA synthesis, enzyme catalysis, and gene transcription. In recent years, a large number of evidence have proved that Zn^{2+} is essential to the autophagy process, and autophagy can promote large changes of Zn^{2+}. Therefore, the detection of the levels of Zn^{2+} has become one of the research hotspots of mitochondrial fluorescent probes. In recent years, researchers have designed and synthesized various fluorescent probes for the intracellular detection of Zn^{2+} in the cells; however, certain probes cannot target the mitochondria (Hung et al., 2013; Liuzzi and Yoo, 2013; Ding and Zhong, 2017). To determine the importance of Zn^{2+} in autophagy and signal transformation, Fang's group developed a series of probe targeting Zn^{2+} in many organelles simultaneously and proposed a novel concept, Zn-STIMO, of tracking Zn^{2+} in multiple organelles (**Figure 4**) (Fang et al., 2021). They found that mitochondrial autophagy inducer CCCP-induced mitophagy in HeLa cells is associated with unstable Zn^{2+} enhancement. The results showed that SIM technology would become a reliable tool detecting unstable Zn^{2+}, which also demonstrated that the organelle identification related with

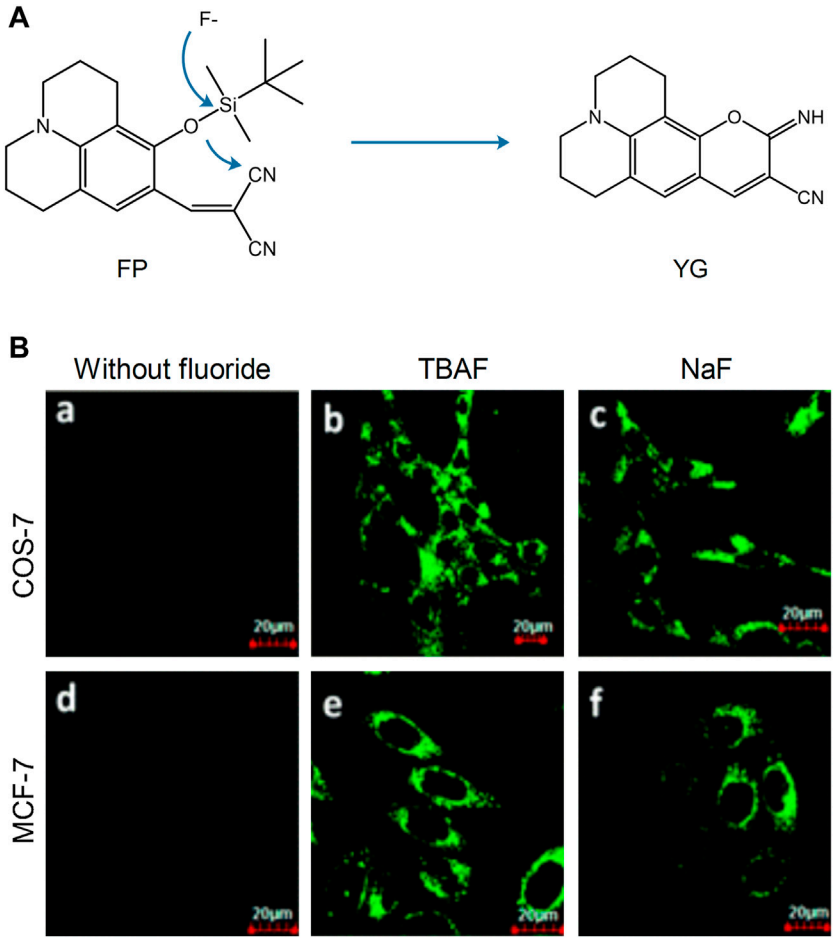

FIGURE 5 | The reaction mechanism and fluorescence imaging of probe **FP** (Shiling et al., 2014). **(A)** Proposed reaction mechanism of **FP**. **(B)** Fluorescence imaging of COS-7 and MCF-7 cells incubated with probe **FP** (2.5 μM) before (a and d) and after (b, c, e, and f) being treated with TBAF, NaF (100 μM).

super resolution morphological study would have an amazing potential in tracking the biological species and events of specific organelles in organoids. Ning et al. (2016) developed a two-photon ratio probe (**Mito-MPVQ**) targeting the mitochondria to detect Zn^{2+} levels. Triphenylphosphine was used as the targeting group of the probe. Following the attachment of a fluorescent group, this probe was localized in the mitochondria and improved the two-photon signal detection for Zn^{2+}.

In addition, during these years, previous researchers have designed and synthesized several fluorescent probes to detect other metal cations in the mitochondria. For example, Wang et al. (2018) designed the mitochondria-targeting fluorescent probe (**PyCM-2**) and (**PyCM-3**) to detect Au^{3+} levels.

2.2.3 Fluorescent Probe Detection of Anions in Mitochondria

Although the detection of cations in the mitochondria has been extensively examined, the role of anions is also very important. Fluorine ions can cause metabolic diseases following their accumulation in the mitochondria. In 2014, Shiling et al. designed and synthesized the mitochondrial fluorescent probe **FP**, which was used to detect fluorine (Shiling et al., 2014). This probe was localized in the mitochondria. The fluoride ions could knock out the silyl protecting group, and subsequently the phenoxide reacted with the −CN group, which induced nonfluorescent **FP** to highly fluorescent **YG** and emitted strong green fluorescence (**Figure 5**). Therefore, **FP** was used to detect and image fluorine in the mitochondria and has been thoroughly examined in the fields of cell biology and medical science. Xu' group developed a mitochondrial-targeting fluorescent probe for the detection of fluorine in viable cells, which was denoted as **Mito-FP** (Xu et al., 2019). The probe could be successfully localized in the mitochondria and has been used for the imaging of fluorine in HeLa cells.

2.2.4 Fluorescent Probes Detecting Mitochondrial Microenvironment

In addition to the mitochondrial morphology, several microenvironmental factors are regarded as the significant factors of the mitochondrial status, such as the mitochondrial pH value, polarity, and temperature. Normal polarization is necessary for cellular energy metabolism (Nemoto et al., 2000),

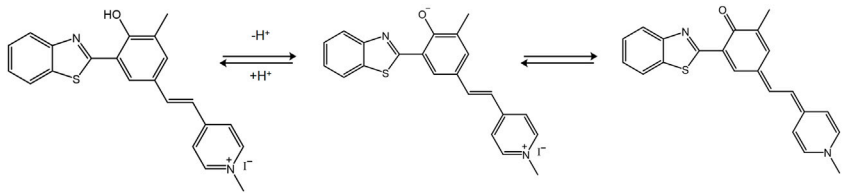

FIGURE 6 | The pH sensing mechanism for the probe **HBTMP** (Gaoqing et al., 2020).

and the appropriate pH value could also keep the normal membrane potential, which forces ATP generation and Ca^{2+} homeostasis regulation (Crompton and Heid, 1978).

Gaoqing et al. (2020) designed the fluorescent probe **HBTMP** to detect the mitochondrial pH value. This probe emitted red fluorescence in acidic and neutral environments and blue fluorescence in alkaline environments (**Figure 6**). Furthermore, **HBTMP** exhibited improved photostability and lower cytotoxicity. The fluorescent image of the viable cells demonstrated that **HBTMP** could easily spread in the mitochondria and detect changes in the pH with high sensitivity. We concluded that **HBTMP** could be used to study the pH changes of the mitochondria in viable cells in a more efficient way. Li et al. (2019) reported a near-infrared fluorescence probe of hydroxy-L-lysine in 2019, denoted as **HXPI-P**. This probe was used to detect mitochondrial polarity changes through drug induction and starvation, which contributed to distinguish the differences in polarity between normal and cancer cells *via* ratio fluorescence imaging.

3 FLUORESCENT PROBES DESIGN STRATEGIES FOR TARGETING THE LYSOSOMES

Lysosomes are important acidic organelles in eukaryotic cells. They involve more than 60 hydrolases and proteases and are considered to be the "digestive organs" of the cells. In addition, they can also participate in the regulation of the secretory function of cells. Lysosomes also contain various RSMs that participate in the corresponding biological reactions, such as ROS and metal cations. The visualization of RSMs in the lysosome plays an important role in understanding their mechanism of action and their therapeutic application in the treatment of various related diseases (Chen et al., 2021; Wang and Diao, 2022).

A single functional fluorescent probe targeting lysosomes can enable imaging the lysosomes to detect their dynamic location and morphological changes and track their physiological processes (Qiu et al., 2020). However, the majority of the available commercial probes targeting lysosomes are amine-based compounds and exhibit certain limitations, such as lower specificity of their localization and reducing suitability for long time detection. To address these problems, researchers have carried out research on lysosomal probes (**Figure 7**).

3.1 Fluorescence Probes Detecting Reactive Oxygen Species in the Lysosome

In cancer cells, the lysosomal content is high, and oncogene-driven transformation will alter the lysosomal membrane in cancer cells, which makes them more sensitive to lysosomal membrane permeability (LMP) and promotes tumor progression (Boya and Kroemer, 2008; Kallunki et al., 2013). Among the various intracellular stimuli (e.g., LMP), the ROS are the most closely related to lysosomal death (Vila et al., 2011; Melina-Theoni and Athanasios, 2014). In order to assess the ROS-related lysosomal cell death in cancer cells, Zhang et al. (2017) designed and synthesized a near-infrared fluorescent probe (**PSiR**) targeting the lysosomes, which could timely detect the generation of lysosomal ROS in cancer cells (**Figure 8**). The experimental results indicated that the probe exhibited strong resistance to photooxidation, fast reaction, and high selectivity and sensitivity. The anticancer drug β-lapachone (β-lap) could stimulate the generation of ROS in lysosomes, which was accompanied by a dose-dependent fluorescence enhancement. Due to its sensitivity in detecting ROS in cancer cells, the probe could distinguish normal cells from cancer cells according to specific images; it could also distinguish the presence of cancer cells in healthy tissues (**Figure 8C**).

The hydroxyl radical (•OH) is one of the most active free radicals noted in ROS, which can destroy various biomacromolecules. In order to detect the generation and function of lysosomal •OH in viable cells, Benitez-Martin et al. (2018) developed an active probe targeting lysosomes, denoted as **1-Red** ("off" state). HOCl is a type of ROS and lysosome is one of the main sources of HOCl. Therefore, the detection of lysosomal HOCl plays an important role in studying its biological process. In 2017, Yawei et al. (2017) designed and synthesized a pH-mediated lysosomal targeted fluorescent probe (**Lyso-HOCl**). The probe contained pH-sensitive phenol, which was used as its targeting group. A similar structure of rhodamine demonstrated a unique chlorination effect in an acidic environment, which could be used to specifically detect HOCl. Meng et al. (2019) developed the fluorescent probe **CR-Ly** using coumarin as a donor, rhodamine as the receptor, and morpholine as the lysosomal targeting group.

3.2 Fluorescent Probe Detection of Reactive Nitrogen Species in the Lysosome

Nitric oxide (NO) plays an important role in the process of cell catabolism, whose quantity can influence lysosomal function.

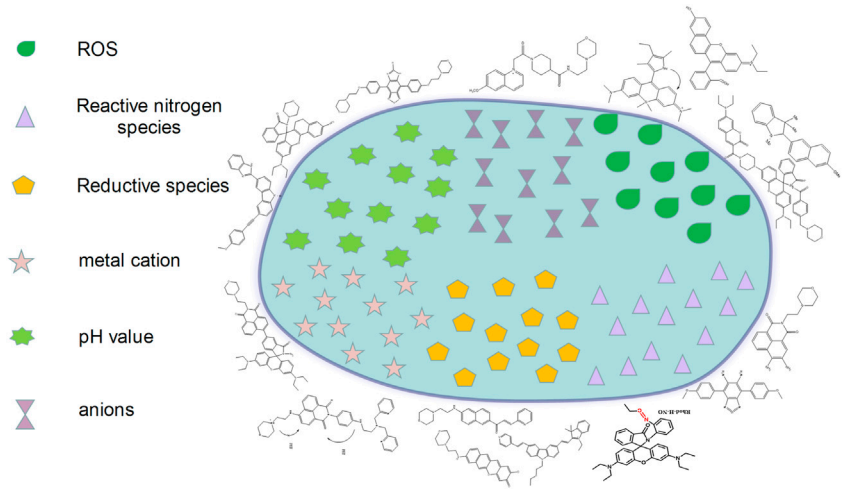

FIGURE 7 | The design strategies of fluorescence probes targeting lysosomes.

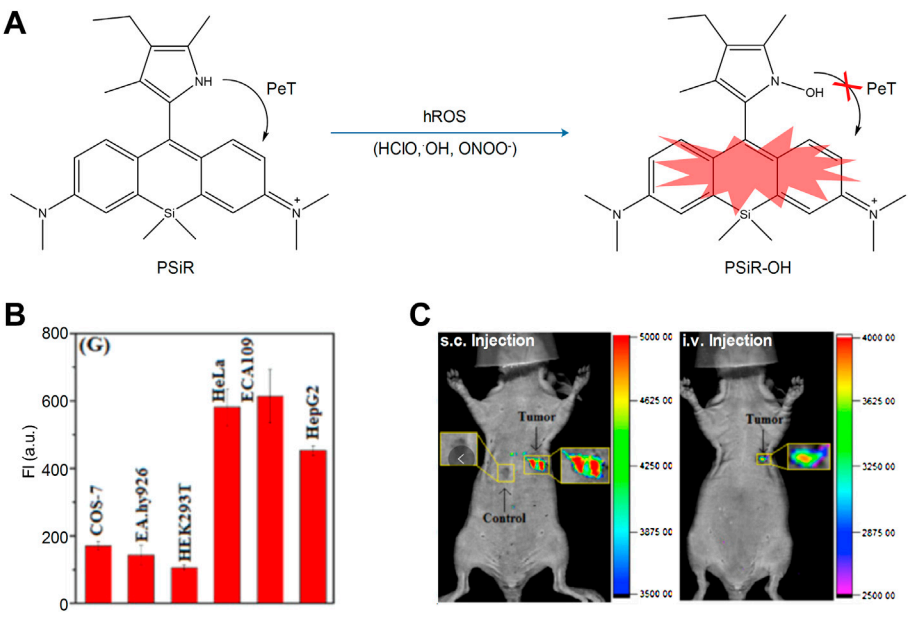

FIGURE 8 | The sensing mechanisms of **PSiR** for hROS and imaging characterization (Zhang et al., 2017). **(A)** The sensing mechanisms of **PSiR** for hROS. **(B)** Average fluorescence intensity from images in various cells. **(C)** Imaging tumor using **PSiR** in tumor-bearing mouse with HeLa cells.

Abnormal NO can induce the development of cardiovascular and nervous system diseases. Therefore, the function of NO in lysosomes remains to be studied, which requires the design and development of ideal lysosomal targeting fluorescent probes detecting the change in the concentration of NO. Feng et al. (2016) synthesized the fluorescent probe **LysoNO-Naph** to detect NO in lysosomes on the basis of 1,8-naphthalimide (**Figure 9**). The probe was synthesized by using 4-(2-aminoethyl)-morpholine as a targeting group and o-phenylene-diamine as the reacting site of NO. And it could be used for lysosomal imaging. In addition, hemolysin-Naph exhibited higher selectivity and sensitivity for NO, indicating that this probe could be used to detect lysosomal NO successfully. In the same year, Yinhui et al. (2016) designed the pH-activated fluorescent probe **Rhod-H-NO** for detecting lysosomal NO levels. When the diameter of the nanoparticles was less than 200 nm, MSNs could enter into the lysosome, resulting in its successful tracking and imaging. Therefore, embedding **Rhode-H-NO** into the nanopore with MSNs can prevent it from being degraded, which leads to the accumulation of the probe in the lysosomes and the detection of NO. Fengyang et al. (2018) designed and synthesized the novel fluorescent probe **MBTD** in 2018. **MBTD**

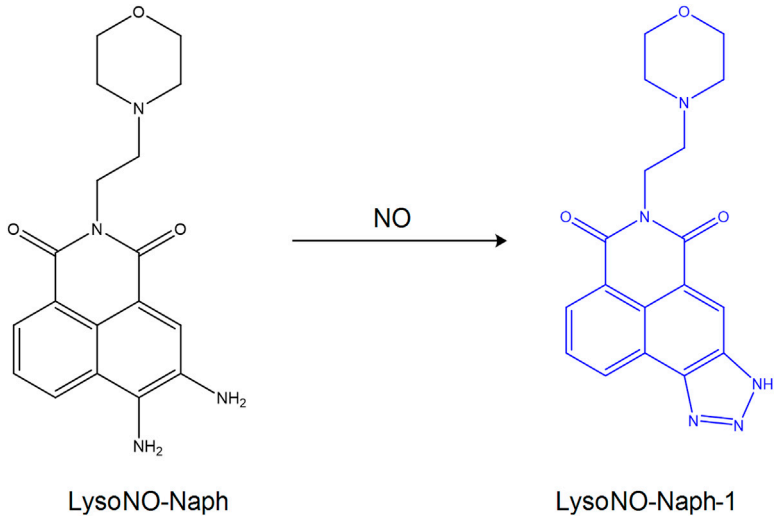

FIGURE 9 | The reaction process of probe **LysoNO-Naph** with NO (Feng et al., 2016).

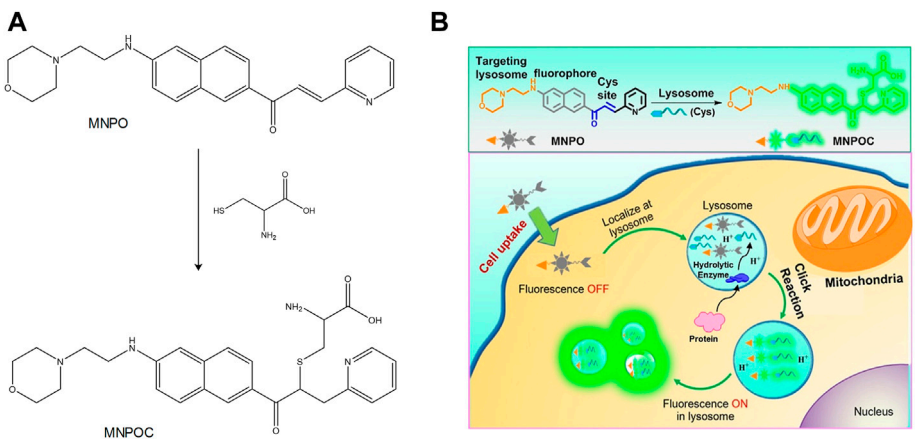

FIGURE 10 | The action mechanism of **MNPO** with Cys in lysosomes (Long et al., 2019). **(A)** Proposed response mechanism of **MNPO** to Cys. **(B)** Schematic showing the general design of lysosome-targeting fluorogenic probe **MNPO** for Cys.

could specifically be used to image NO in lysosomes due to its large stroke shift and stable fluorescence; its D-A-D-structure probe exhibited improved photostability and higher NO selectivity.

3.3 Fluorescent Probe Detection of Reductive Species in Lysosomes

Hydrogen sulfide (H_2S) is very important in various physiological processes. It can regulate cardiovascular and neuronal functions. H_2S can also cause instability of the lysosomal membrane, which leads to autophagy and cell death. Low molecular weight mercaptans, such as cysteine (Cys) and glutathione (GSH), play an important role in the pathogenesis of related human diseases (Baocun et al., 2010). Therefore, the detection of the levels of H_2S and mercaptans in the cells is very important for the identification of biological processes and the diagnosis and treatment of related diseases.

The hydrolysis of various proteins in the lysosome is closely related to mercaptan (T et al., 2000). In the lysosomes of the liver cells, Cys is a main stimulant for the degradation of albumin (Arunachalam et al., 2000). To investigate the function of Cys in lysosomes, Long et al. synthesized the TP probe **MNPO** (**Figure 10**) (Long et al., 2019). The probe was designed and synthesized with a naphthalene derivative as the fluorescent group, morpholine as the lysosomal targeting group, and α,β-unsaturated ketone as the action site of Cys. The introduction of the pyridine group into the molecule could improve water solubility and selectivity of Cys. It was found using specific experiments that the increase of Cys concentration increased

the fluorescence intensity of the probe at 524 nm. Moreover, when the concentration range of Cys was 0–10 μM, the fluorescence intensity indicated a linear relationship with Cys. Therefore, the probe could be a useful tool to detect the dynamic changes of Cys in lysosomes. In addition, Tamima et al. (2020) developed a novel lysosome-targeted fluorescent probe **ABXO1** for the detection of the levels of Cys. Interestingly, the probe and cysteine adduct exhibited optimal two-photon absorption properties, which could achieve the two-photon imaging of lysosomal cysteine under excitation at near-infrared wavelengths.

H_2S is an antioxidant that participates in various physiological reactions in the liver, spleen, and kidneys. Traditional lysosomal-targeting H_2S fluorescent probes cannot provide adequate imaging of the lysosome with an open fluorescent signal; therefore, the design of fluorescent probes targeting lysosomal and mitochondrial H_2S has high application value. Yong et al. (2016) designed and synthesized the TP probe **TP-PMVC**, which could be used to image lysosomal and mitochondrial H_2S by using a dual channel. The probe used carbazole MVC as a TP platform. Since the pKa of pyridine was 5.0, it was used as the site of H^+ and as the targeting unit of the lysosome. In addition, indole exhibited potent electrophilicity required for the generation of H_2S. In an acidic environment, pyridine was protonated to produce red fluorescence for lysosomal imaging. By using specific experiments, it was shown that the fluorescent intensity was significantly improved under acidic conditions, while lysosomes and lysosomal H_2S could be detected at 960 nm and 810 nm. In addition, Cai et al. (2018) synthesized the ratio fluorescent probe **SN-N3** for the detection of lysosomal H_2S.

3.4 Fluorescent Probes Used for the Detection of the Metal Cation in Lysosomes

In recent years, a novel function of the lysosomes has been discovered which is the regulation of the steady state of the transition metals, such as copper and zinc (Blaby-Haas and Merchant, 2014). Various enzymes in the body can catalyze biochemical reactions by using specific transition metals. Therefore, lysosomes can maintain the metal steady state in cells by regulating the metal content and controlling its downstream signaling (Kurz et al., 2011; E. and S., 2014).

Copper is related to the activity of various essential enzymes in the body. When copper is absent, the activity of the enzymes dependent to copper will decrease leading to the occurrence of related diseases, such as Menkes syndrome (Bie et al., 2007; Tümer and Møller, 2010). In addition, excessive copper can also lead to cellular toxicity, affect lipid metabolism, and other biological processes, and subsequently lead to certain related diseases, such as Wilson's disease (Seth et al., 2004). Therefore, in recent years, fluorescent probes detecting copper ions (Cu^{2+}) in lysosomes have become a major focus of research investigation. In 2015, Mingguang et al. developed a lysosomal targeted Cu^{2+} fluorescent probe (**Lys-Cu**) with dual channel emission, which used rhodamine as a dye (Mingguang et al., 2015). The carbonyl oxygen atoms in 1,8-naphthalimide can combine with metal ions and can be used as a binding unit and a fluorescent group. During the process of photoinduced electron transfer, PET is inhibited following the combination of Cu^{2+} with 1,8-naphthalimide, leading to a significant enhancement of the fluorescent intensity at 440 nm and 580 nm. In addition, the probe exhibited lower cytotoxicity and higher affinity and could be used to image Cu^{2+} in lysosomes more efficiently. The hydrazone-containing pyrrole exhibited high affinity for Cu^{2+} and, in 2018, synthesized a hydrazone probe from sunitinib (Wu et al., 2018). The results indicated that when Cu^{2+} was combined with the probe, rhodamine was used to induce a ring opening reaction; pyrrole could then react with rhodamine resulting in the imaging of Cu^{2+} in lysosomes.

Zinc ions (Zn^{2+}) are important metal ions involved in several biological reactions. They are closely related to lysosomal dysfunction and autophagy. The abnormal Zn^{2+} concentration levels can result in the development of human diseases, such as coronary heart disease (Heyu et al., 2021) and allergic inflammation (Masanobu et al., 2020). Currently, various fluorescent probes have been developed to detect Zn^{2+}; however, only a few can be used to detect Zn^{2+} in lysosomes. In 2015, Hyo-Jun et al. introduced an N,N-di-(2-pyridyl)ethylenediamine (DPEN) group into the naphthalimide dye (Hyo-Jun et al., 2016). The oxygen atom in the carbonyl group of the imide was combined with Zn^{2+} and with the nitrogen atom in DPEN, subsequently a two-photon fluorescence probe was synthesized for the detection of Zn^{2+} in the lysosomes (**Figure 11**). It was found that the probe exhibited an optimal linear response to Zn^{2+}; the fluorescent intensity of the probe was low following combination with Zn^{2+} when pH = 7.4. When pH = 4.5–5.5, the fluorescent intensity was significantly enhanced. The high sensitivity and affinity of the probe for Zn^{2+} was optimal for the detection of the dynamic changes of lysosomal Zn^{2+}. In addition, Duan et al. designed the fluorescent probe **DR**, which was synthesized using N,N-bis(2-pyridylmethyl) ethylenediamine (BPEN) and morpholine as a ligand (Duan et al., 2019). When BPEN was connected with the fluorescent group by benzene on the imide, the probe could achieve high sensitivity to Zn^{2+}. When the probe was combined with Zn^{2+}, the fluorescent intensity increased at a pH range of 7.0–10.0 and was significantly increased when the pH range was 4.0–7.5, which indicated that the probe could be used to detect Zn^{2+} in lysosomes.

3.5 Fluorescent Probe Detecting Anions in Lysosomes

The maintenance of lysosomal pH is achieved by the synergy of the proton pump and the chloride channel. Moreover, the chloride (Cl^-) ion plays an important role in the development of brain diseases, such as Alzheimer's disease (Hui et al., 2017). Therefore, the development of fluorescent probes that can specifically detect Cl^- in lysosomes has become one of the major research hotspots in recent years. Sang-Hyun et al. (2019) developed the fluorescent probe **MQAE-MP** in 2019 to specifically detect lysosomal Cl^-. It was found by using specific experiments that the concentration of Cl^- in lysosomes was decreased following treatment with the substances that could destroy their normal function. The concentration of Cl^- depended on whether **MQAE-MP** was used or not. Therefore, due to the targeting effect of the morpholine group, **MQAE-MP** was mainly accumulated in lysosomes and could be used to fully detect the levels of Cl^- in these organelles (**Figure 12**).

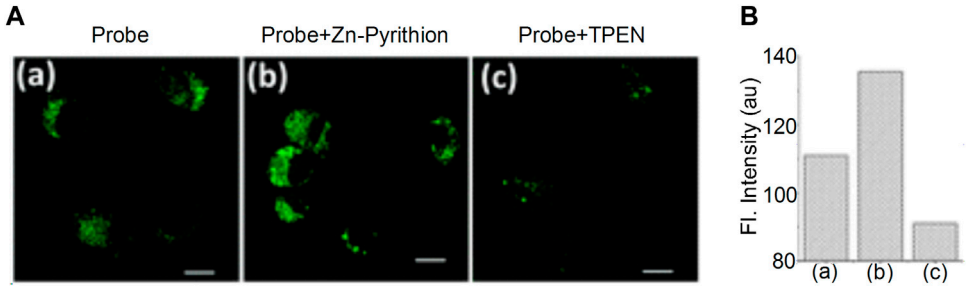

FIGURE 11 | The fluorescence characteristics of probe (Hyo-Jun et al., 2016). **(A)** TPM imaging of Zn(ii) ions in live NIH 3T3 cells. **(B)** The substantial increase in fluorescence intensity after being uncubated with Zn-Pyrithion in the cells.

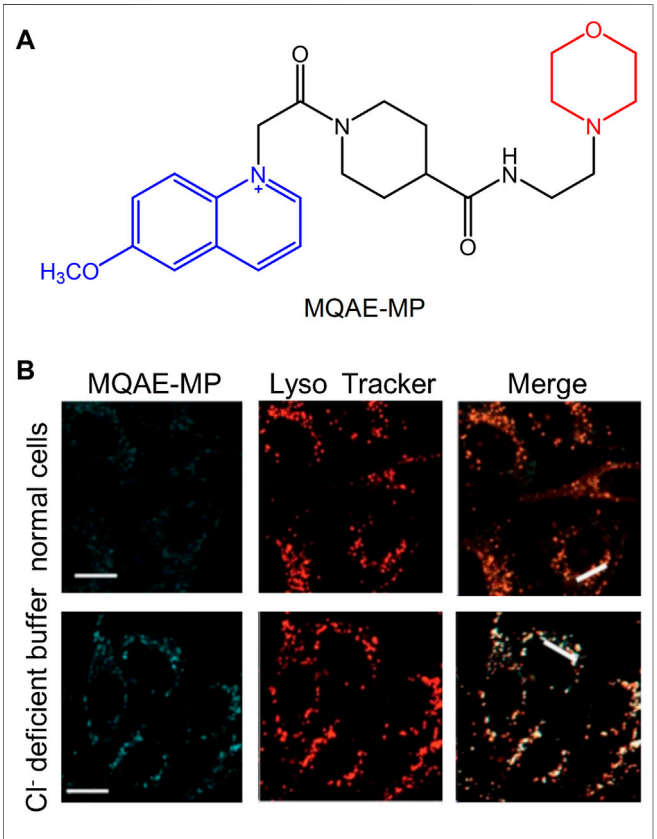

FIGURE 12 | The structure and fluorescence characteristic of **MQAE-MP** (Sang-Hyun et al., 2019). **(A)** The chemical structure of **MQAE-MP**. **(B)** The detection of Cl^- ions in cells with **MQAE-MP**.

3.6 Fluorescent Probes Targeting pH Value in the Lysosome

The normal pH of the lysosome is 4.5–5.5, which demonstrates weak acidity. An abnormal pH value can lead to corresponding changes in the cell function, and subsequently cause human-related diseases, such as cardiovascular and neurodegenerative diseases (Onyenwoke and Brenman, 2015). Therefore, the detection of the changes in lysosomal pH is important for understanding their biological functions in the related diseases. In the recent 10 years, various small-molecule fluorescent probes have been developed to detect the changes in the lysosomal pH (Wen et al., 2014; Jun et al., 2015; Yongkang et al., 2016; Ji-Ting et al., 2017). Despite these efforts, considerable work is required to improve their detection sensitivity. Peng et al. (2019) developed a two-photon fluorescence probe, which was sensitive to pH changes, and was denoted as **Lyso-MPCB** (**Figure 13**). The probe was equipped with the lysosome-located group morpholine, and it could monitor the pH value of the lysosome in real time. Moreover, it could specifically detect autophagy. **Lyso-MPCB** exhibited blue fluorescent emission at basic conditions and could emit green fluorescence at acidic conditions. The results indicated that the pKa value of the probe was 4.86, which was suitable for detecting the normal pH changes of the lysosomes (4.5–5.5). In addition, the ratio signal of the lysosome was linear with the pH when the range was 4.2–5.6. Therefore, the probe was a powerful tool for monitoring pH changes in lysosomes.

In addition, Lee et al. (2018) designed and synthesized a rhodamine pH fluorescent probe, which exhibited improved water solubility, higher quantum yield, and sensitivity and selectivity. The probe's pKa value was 4.10, and therefore it was used to detect the acidic environment. Gong et al. (2019) designed a fluorescent probe detecting the pH changes in lysosomes, denoted as **Ly-HN2AM**, which used N-aminomorpholine as a closed loop switch and could react strongly under the range: pH = 4.79–6.07. The probe exhibited lower cytotoxicity and improved photostability and could be used to visualize the pH changes in lysosomes under physiological and pathological conditions. Lingling et al. (2020) synthesized a series of fluorescent probes in 2020 based on imidazole-benzothiadiazole compounds to detect the changes in pH of the lysosomes. The probe **MIBTAA** could react strongly in an acidic environment and exhibited higher sensitivity and selectivity for detecting pH changes.

4 DUAL-LABELING PROBES TARGETING LYSOSOMES AND MITOCHONDRIA

The lysosome is an acidic organelle that can decompose proteins, and mitochondria is considered the energy source of the cells. The dynamic changes and biological functions of lysosomes and mitochondria in viable cells can be detected simultaneously with fluorescence microscopy.

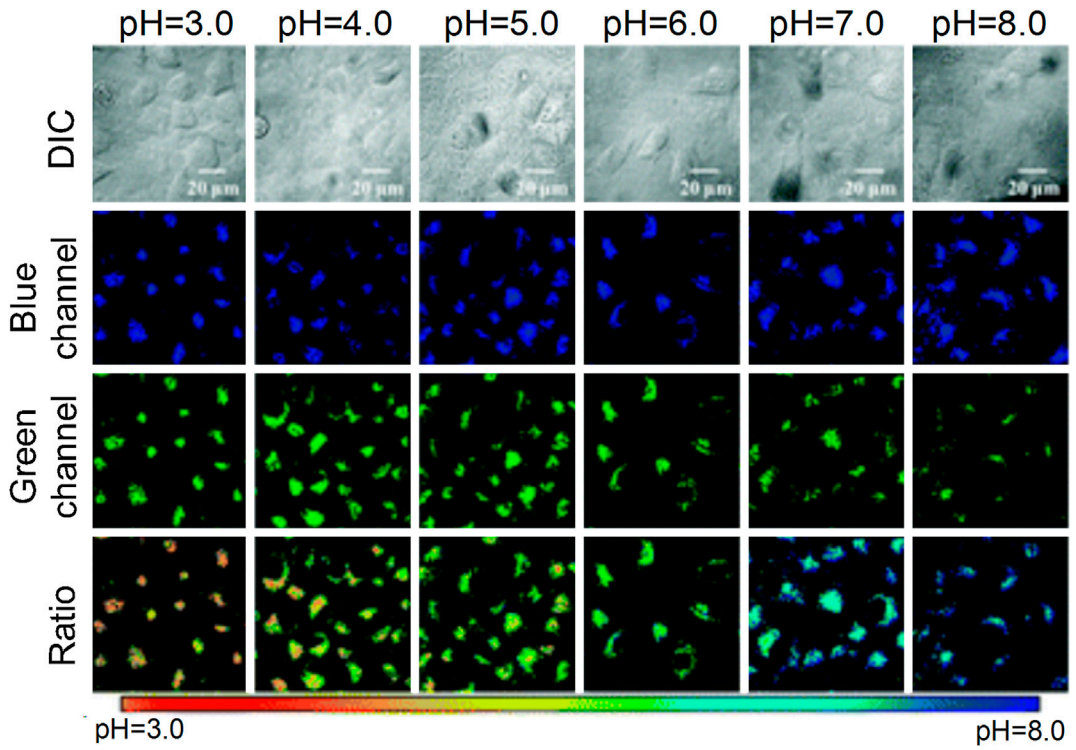

FIGURE 13 | The action mechanism of **Lyso-MPCB** to lysosome pH value (Peng et al., 2019)

The interaction between the mitochondria and lysosomes is an important biological process in eukaryotic cells. When their interaction is dysfunctional, certain neurodegenerative diseases develop (Nixon, 2013), such as cancer (Beth, 2007) and Parkinson's disease (Burbulla et al., 2017). Therefore, an increased number of studies have visually assessed the interaction between mitochondria and lysosomes. Qixin et al. (2020) developed the hemicyanine fluorescent probe **Coupa** in 2020, which included a specific organelle-targeting ability (**Figure 14**). By using the technology of super-resolution illustrated microscopy (SIM), the **Coupa** dye could label mitochondria and lysosomes simultaneously and reveal the interaction between them by functional fluorescence conversion and co-localization. Staining with **Coupa** indicated that the local viscosity was increased, which was consistent with the biological characteristics of MLC. This may be the result of protein aggregation in the process of MLC. Therefore, the probe could be used efficiently to locate and track the interaction of the lysosomes with mitochondria in viable cells.

The abnormal viscosity of the mitochondria and lysosomes can lead to their dysfunction and eventually to the development of related diseases (Lu et al., 2013; Bochao et al., 2019). Wei et al. (2021) had developed a cyanine compound in 2020 for the detection of medium viscosity. The probe had near-infrared emission (650 nm) and improved sensitivity and selectivity. It could simultaneously target the lysosomes and mitochondria. In addition, this compound could distinguish normal cells and cancer cells by identifying the changes in viscosity; it could also detect and image the changes in the mitochondrial and lysosomal viscosity in HeLa cells.

SO_2 is an important gaseous messenger, which plays a significant role in the induction of apoptosis in lysosomes and mitochondria. When SO_2 exhibits abnormal levels, the N-acetylneuraminic acid present in lysosomes and mitochondria will redistribute, which exhibits adverse effects on the induction of apoptosis (Merkur'eva et al., 1981). Therefore, it is necessary to develop a fluorescent probe that can detect SO_2 and simultaneously target the lysosomes and mitochondria. Kong et al. (2019) synthesized the novel fluorescent probe **DML-P** in 2019 by using a FRET-based method, which could simultaneously detect SO_2 levels in lysosomes and mitochondria. The probe was the first double-targeted fluorescent probe that could simultaneously track SO_2 in mitochondria and lysosomes. **DML-P** exhibited higher selectivity and stability. In addition, **DML-P** could detect cellular endogenous SO_2 both in the single-photon and two-photon modes, indicating that it could become a powerful tool to study the action mechanism and relationship of the lysosomes and mitochondria.

Nitroreductase (NTR) plays an important role in human health, and the mitochondria and lysosomes are its main sources (Yang et al., 2018; Klockow et al., 2020). Therefore, the development of fluorescent probes for the detection of NTR in mitochondria and lysosomes has become one of the main research hotspots. Sha et al. (2020) developed a dye with aromatic azonia and benzo(e)indol anion skeleton in 2020. On the basis of this dye, the authors of the study synthesized a probe

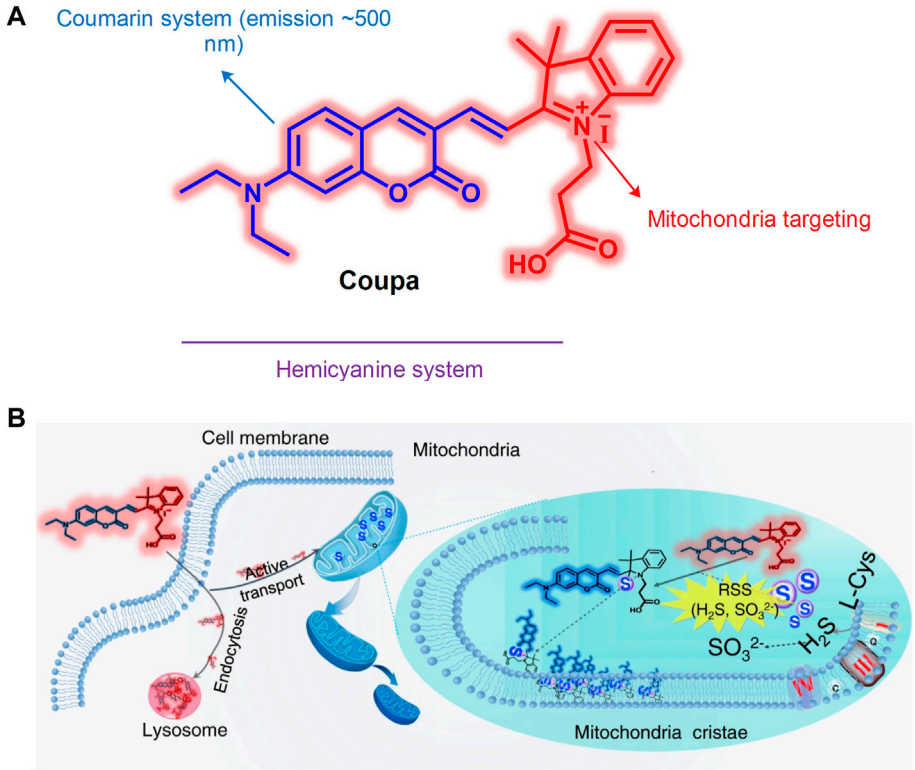

FIGURE 14 | The structure and action mechanism of probe Coupa (Qixin et al., 2020). **(A)** The chemical structure of Coupa; **(B)** The mitochondria- and lysosome-staining mechanisms of Coupa.

containing 2-ethyl-5-nitrofuran or 4-nitrobenzoyl moiety to detect NTR. The probe emitted in the near infrared. It could target lysosomes and mitochondria simultaneously and exhibited higher sensitivity to NTR. This probe could detect and image lysosomal and mitochondrial NTR in HeLa cells. Therefore, it became the first fluorescent compound which could simultaneously detect lysosomal and mitochondrial NTR.

5 CONCLUSION AND OUTLOOK

Small-molecule fluorescent probes located in the mitochondria and lysosomes have been used to detect and image RSMs in recent years. This area has become a research hotspot and involves the identification of fluorescent probes targeting the mitochondria and lysosomes. These probes exhibit specific targeting capabilities and have become a popular research tool in the field of biology, pharmacy, and clinical medicine. Among them, two-photo fluorescent probes have been widely included in the study of lysosomal and mitochondrial targeted fluorescent probes due to the advantages of high resolution and long-time observation. At present, various fluorescent probes have been designed and synthesized to simultaneously target the mitochondria and lysosomes, which provides important tools for the study of RSMs and their mechanisms of action.

According to the present review, the probes detecting lysosomal and mitochondrial RSMs fit the following characteristics: 1) higher selectivity toward certain RSMs compared with other RSMs noted in the organelles; 2) higher quantum yield and longer emission wavelength; 3) higher photostability of product with probe and RSMs; 4) improved biocompatibility. Currently, the emission wavelength of the fluorescent group in certain probes remains short and subject to interference; therefore, the research and development of fluorescent probes require further studies to be completed.

At present, various mitochondrial and lysosomal targeted fluorescent probes have enabled the dynamic monitoring and imaging of RSMs, and certain probes have been used in the diagnosis and treatment of human-related diseases, which will become one of the important research directions in the future.

AUTHOR CONTRIBUTIONS

HC and ZY investigated the literature. HC wrote the manuscript. ZY and SR revised the figures. YQ guided and revised the overall structure and content of the review.

REFERENCES

Arunachalam, B., Phan, U. T., Geuze, H. J., and Cresswell, P. (2000). Enzymatic Reduction of Disulfide Bonds in Lysosomes: Characterization of a Gamma-Interferon-Inducible Lysosomal Thiol Reductase (GILT). *Proc. Natl. Acad. Sci. U. S. A.* 97, 745–750. doi:10.1073/pnas.97.2.745

Baocun, Z., Xiaoling, Z., Yamin, L., Pengfei, W., Hongyan, Z., and Xiaoqing, Z. (2010). A colorimetric and ratiometric fluorescent probe for thiols and its bioimaging applications. *Chemical communications (Camb)* 46, 5710-2.doi:10.1039/c0cc00477d

Benitez-Martin, C., Guadix, J. A., Pearson, J. R., Najera, F., Perez-Pomares, J. M., and Perez-Inestrosa, E. (2018). A Turn-On Two-Photon Fluorescent Probe for Detecting Lysosomal Hydroxyl Radicals in Living Cells. *Sensors Actuators B. Chem.* 284, 744–750. doi:10.1016/j.snb.2018.12.163

Beth, L. (2007). Cell Biology: Autophagy and Cancer. *Nature* 446.

de Bie, P., Muller, P., Wijmenga, C., and Klomp, L. W. (2007). Molecular Pathogenesis of Wilson and Menkes Disease: Correlation of Mutations with Molecular Defects and Disease Phenotypes. *J. Med. Genet.* 44, 673–688. doi:10.1136/jmg.2007.052746

Blaby-Haas, C. E., and Merchant, S. S. (2014). Lysosome-related Organelles as Mediators of Metal Homeostasis. *J. Biol. Chem.* 289, 28129–28136. doi:10.1074/jbc.R114.592618

Bochao, C., Chengde, L., Jie, Z., Jianfei, K., Tiantian, J., Jin, Z., et al. (2019). Sensing and Imaging of Mitochondrial Viscosity in Living Cells Using a Red Fluorescent Probe with a Long Lifetime. *Chem. Commun. (Camb)* 55, 7410–7413. doi:10.1039/c9cc03977e

Boya, P., and Kroemer, G. (2008). Lysosomal Membrane Permeabilization in Cell Death. *Oncogene* 27, 6434–6451. doi:10.1038/onc.2008.310

Bras, M., Queenan, B., and Susin, S. A. (2005). Programmed Cell Death via Mitochondria: Different Modes of Dying. *Biochem. (Mosc)* 70, 231–239. doi:10.1007/s10541-005-0105-4

Burbulla, L. F., Song, P., Mazzulli, J. R., Zampese, E., Wong, Y. C., Jeon, S., et al. (2017). Dopamine Oxidation Mediates Mitochondrial and Lysosomal Dysfunction in Parkinson's Disease. *Science* 357, 1255–1261. doi:10.1126/science.aam9080

Cai, G., Xianjun, L., Wen, C., Fenglin, W., and Jian-Hui, J. (2018). A Naphthalene-Based Fluorescent Probe for Ratiometric Imaging of Lysosomal Hydrogen Sulfide in Living Cells. *Methods Appl. Fluoresc.* 7, 014002. doi:10.1088/2050-6120/aae9c4

Chen, J., Sun, S., Zha, D., Wu, J., Mao, L., Deng, H., et al. (2014). Soyasaponins Prevent H2O2-Induced Inhibition of Gap Junctional Intercellular Communication by Scavenging Reactive Oxygen Species in Rat Liver Cells. *Nutr. Cancer* 66, 1342–1351. doi:10.1080/01635581.2014.956245

Chen, Q., Shao, X., Tian, Z., Chen, Y., Mondal, P., Liu, F., et al. (2019a). Nanoscale Monitoring of Mitochondria and Lysosome Interactions for Drug Screening and Discovery. *Nano Res.* 12, 1–222. doi:10.1007/s12274-019-2331-x

Chen, Q., Shao, X., Tian, Z., Chen, Y., Mondal, P., Liu, F., et al. (2019b). Nanoscale Monitoring of Mitochondria and Lysosome Interactions for Drug Screening and Discovery. *Nano Res.* 12, 1009–1015. doi:10.1007/s12274-019-2331-x

Chen, Q., Fang, H., Shao, X., Tian, Z., Geng, S., Zhang, Y., et al. (2020). A Dual-Labeling Probe to Track Functional Mitochondria-Lysosome Interactions in Live Cells. *Nat. Commun.* 11, 6290. doi:10.1038/s41467-020-20067-6

Chen, Q., Hao, M., Wang, L., Li, L., Chen, Y., Shao, X., et al. (2021). Prefused Lysosomes Cluster on Autophagosomes Regulated by VAMP8. *Cell. Death Dis.* 12, 939. doi:10.1038/s41419-021-04243-0

Crompton, M., and Heid, I. (1978). The Cycling of Calcium, Sodium, and Protons across the Inner Membrane of Cardiac Mitochondria. *Eur. J. Biochem.* 91, 599–608. doi:10.1111/j.1432-1033.1978.tb12713.x

Daniel, S., Peizhou, J., and C, Y.S.-H. (2008). Cathepsin D is the main lysosomal enzyme involved in the degradation of alpha-synuclein and generation of its carboxy-terminally truncated species. *Biochemistry* 47, 9678-87.doi:10.1021/bi800699v

Ding, B., and Zhong, Q. (2017). Zinc Deficiency: An Unexpected Trigger for Autophagy. *J. Biol. Chem.* 292, 8531–8532. doi:10.1074/jbc.H116.762948

Duan, H., Ding, Y., Huang, C., Zhu, W., Wang, R., and Xu, Y. (2019). A Lysosomal Targeting Fluorescent Probe and its Zinc Imaging in SH-Sy5y Human Neuroblastoma Cells. *Chin. Chem. Lett.* 30, 55–57. doi:10.1016/j.cclet.2018.03.016

Fang, H., Geng, S., Hao, M., Chen, Q., Liu, M., Liu, C., et al. (2021). Simultaneous Zn2+ Tracking in Multiple Organelles Using Super-resolution Morphology-Correlated Organelle Identification in Living Cells. *Nat. Commun.* 12, 109. doi:10.1038/s41467-020-20309-7

Feng, W., Qiao, Q.-L., Leng, S., Miao, L., Yin, W.-T., Wang, L.-Q., et al. (2016). A 1,8-Naphthalimide-Derived Turn-On Fluorescent Probe for Imaging Lysosomal Nitric Oxide in Living Cells. *Chin. Chem. Lett.* 27, 1554–1558. doi:10.1016/j.cclet.2016.06.016

Fengyang, W., Shujuan, Y., Zhiai, X., Lingling, L., Yijing, D., Xiaowei, X., et al. (2018). Acid-Promoted D-A-D Type Far-Red Fluorescent Probe with High Photostability for Lysosomal Nitric Oxide Imaging. *Anal. Chem.* 90, 7953–7962. doi:10.1021/acs.analchem.8b00612

Gaoqing, F., Guoxing, Y., Tingting, N., Wei, W., Hui, H., Haimin, C., et al. (2020). A Novel Ratiometric Fluorescent Probe for the Detection of Mitochondrial pH Dynamics during Cell Damage. *Analyst* 146, 620–627. doi:10.1039/d0an01240h

Gong, Y. J., Kong, Z. Z., Zhang, M.-L., Lv, M. K., and Zhang, G. (2019). A Structure Optimized Fluorescent Probe for Highly Sensitive Monitoring Drug Induced Lysosomal pH Value Changes. *Talanta* 203, 1–8. doi:10.1016/j.talanta.2019.05.037

Gu, X., Zhao, E., Zhao, T., Kang, M., Gui, C., Lam, J. W., et al. (2016). A Mitochondrion-Specific Photoactivatable Fluorescence Turn-On AIE-Based Bioprobe for Localization Super-Resolution Microscope. *Adv. Mater* 28, 5064–5071. doi:10.1002/adma.201505906

Heyu, M., Yueying, W., Fengfeng, Z., Jianjun, R., Meiyu, D., Xue, W., et al. (2021). Reduced Serum Zinc Ion Concentration Is Associated with Coronary Heart Disease. *Biol. trace Elem. Res.* 199, 4109–4118. doi:10.1007/s12011-020-02551-8

Hui, D., Limin, Z., Wei, L., and Yang, T. (2017). Label-Free Electrochemical Biosensor for Monitoring of Chloride Ion in an Animal Model of Alzhemier's Disease. *ACS Chem. Neurosci.* 8, 339–346. doi:10.1021/acschemneuro.6b00296

Huimin, C., Han, W., Yongchun, W., Maomao, H., Bo, D., Hongbao, F., et al. (2022). Super-resolution Imaging Reveals the Subcellular Distribution of Dextran at the Nanoscale in Living Cells. *J. Chin. Chem. Lett.* 33, 1865–1869. doi:10.1016/j.cclet.2021.10.025

Hung, H. H., Huang, W. P., and Pan, C. Y. (2013). Dopamine- and Zinc-Induced Autophagosome Formation Facilitates PC12 Cell Survival. *Cell. Biol. Toxicol.* 29, 415–429. doi:10.1007/s10565-013-9261-2

Hyo-Jun, L., Chang-Woo, C., Hyewon, S., Subhankar, S., Woong, J. Y., Kyung-Ha, L., et al. (2016). A Two-Photon Fluorescent Probe for Lysosomal Zinc Ions. *Chem. Commun. (Camb)* 52, 124–127. doi:10.1039/C5CC06976A

Ji-Ting, H., Xiu, R. W., Kun, L., Jinho, S., Amit, S., Xiao-Qi, Y., et al. (2017). Fluorescent Bioimaging of pH: from Design to Applications. *Chem. Soc. Rev.* 46, 2076–2090. doi:10.1039/c6cs00719h

Yin, J., Hu, Y., and Yoon, J. (2015). Fluorescent Probes and Bioimaging: Alkali Metals, Alkaline Earth Metals and pH. *Chem. Soc. Rev.* 44, 4619–4644. doi:10.1039/c4cs00275j

Kallunki, T., Olsen, O. D., and Jäättelä, M. (2013). Cancer-associated Lysosomal Changes: Friends or Foes? *Oncogene* 32, 1995–2004. doi:10.1038/onc.2012.292

Kangnan, W., Shuyue, M., Yanyan, M., Yuping, Z., Miaomiao, X., Liyu, Z., et al. (2020a). Aurone Derivative Revealing the Metabolism of Lipid Droplets and Monitoring Oxidative Stress in Living Cells. *Anal. Chem.* 92, 6631–6636. doi:10.1021/acs.analchem.0c00456

Kangnan, W., Wen, M., Yuchun, X., Xin, L., Gui, C., Meng, Y., et al. (2020b). Design of a Novel Mitochondria Targetable Turn-On Fluorescence Probe for Hydrogen Peroxide and its Two-Photon Bioimaging Applications. *Chin. Chem. Lett.* 31, 3149–3152. doi:10.1016/j.cclet.2020.08.039

Klockow, J. L., Hettie, K. S., Lagory, E. L., Moon, E. J., Giaccia, A. J., Graves, E. E., et al. (2020). An Activatable NIR Fluorescent Rosol for Selectively Imaging Nitroreductase Activity. *Sens. Actuators B Chem.* 306, 127446. doi:10.1016/j.snb.2019.127446

Kong, X., Yin, J., Li, M., Zhu, L., Dong, B., Ma, Y., and Lin, W. (2019). Simultaneously imaging of SO 2 in lysosomes and mitochondria based on a dual organelle-targeted fluorescent probe. *Sensors & Actuators: B. Chemical* 292, 80-87.doi:10.1016/j.snb2019.04.094

Kurz, T., Eaton, J. W., and Brunk, U. T. (2011). The Role of Lysosomes in Iron Metabolism and Recycling. *Int. J. Biochem. Cell. Biol.* 43, 1686–1697. doi:10.1016/j.biocel.2011.08.016

Lee, D., Swamy, K.M.K., Hong, J., Lee, S., and Yoon, J. (2018). A rhodamine-based fluorescent probe for the detection of lysosomal pH changes in living cells. *Sensors and Actuators: B. Chemical* 266, 416-421.doi:10.1016/j.snb2018.03.133

Li, X., Li, X., and Ma, H. (2019). A Near-Infrared Fluorescent Probe Reveals Decreased Mitochondrial Polarity during Mitophagy. *Chem. Sci.* 11, 1617–1622. doi:10.1039/c9sc05505c

Li, L., Li, Y., Dang, Y., Chen, T., Zhang, A., Ding, C., et al. (2020). Imidazole-fused Benzothiadiazole-Based Red-Emissive Fluorescence Probe for Lysosomal pH Imaging in Living Cells. *Talanta* 217, 121066. doi:10.1016/j.talanta.2020.121066

Liu, Y., Zhang, C., Wei, Y., Chen, H., Kong, L., Chen, Q., et al. (2021). De Novo-Designed Landmine Warfare Strategy Luminophore for Super-resolution Imaging Reveal ONOO- Evolution in Living Cells. *Chem. Eng. J.* 422, 130151. doi:10.1016/j.cej.2021.130151

Liuzzi, J. P., and Yoo, C. (2013). Role of Zinc in the Regulation of Autophagy during Ethanol Exposure in Human Hepatoma Cells. *Biol. Trace Elem. Res.* 156, 350–356. doi:10.1007/s12011-013-9816-3

Long, Z., Chen, L., Dang, Y., Chen, D., Lou, X., and Xia, F. (2019). An Ultralow Concentration of Two-Photon Fluorescent Probe for Rapid and Selective Detection of Lysosomal Cysteine in Living Cells. *Talanta* 204, 762–768. doi:10.1016/j.talanta.2019.06.064

Lu, W., Yi, X., Wenming, T., and Liezheng, D. (2013). Activatable Rotor for Quantifying Lysosomal Viscosity in Living Cells. *J. Am. Chem. Soc.* 135, 2903–2906. doi:10.1021/ja311688g

Luzio, J. P., Pryor, P. R., and Bright, N. A. (2007). Lysosomes: Fusion and Function. *Nat. Rev. Mol. Cell. Biol.* 8, 622–632. doi:10.1038/nrm2217

Marc, L., Manuel, P., and Antonio, Z. (2009). Mitochondrial Dynamics in Mammalian Health and Disease. *Physiol. Rev.* 89, 799–845. doi:10.1152/physrev.00030.2008

Masanobu, S., Takayoshi, S., Masashi, W., Shigetsugu, H., Shogo, K., Akira, N., et al. (2020). Role of Intracellular Zinc in Molecular and Cellular Function in Allergic Inflammatory Diseases. *Allergol. Int.*, 70, 190–200. doi:10.1016/j.alit.2020.09.007

Melina-Theoni, G., and Athanasios, G. P. (2014). Lysosome: the Cell's 'suicidal Bag' as a Promising Cancer Target. *Trends Mol. Med.* 20.

Meng, H., Huang, X. Q., Lin, Y., Yang, D. Y., Lv, Y. J., Cao, X. Q., et al. (2019). A New Ratiometric Fluorescent Probe for Sensing Lysosomal HOCl Based on Fluorescence Resonance Energy Transfer Strategy. *Spectrochim. Acta A Mol. Biomol. Spectrosc.* 223, 117355. doi:10.1016/j.saa.2019.117355

Merkur'eva, R. V., Bushinskaia, L. I., Skvortsova, N. I., Dolinskaia, S. I., and Shaternikova, I. S. (1981). Membrane-bound Sialoglycoproteins of the Rat Liver as Affected by the Combined Action of Benz(a)pyrene and Sulfur Dioxide. *Vopr. meditsinskoi khimii* 27, 791–794.

Mingguang, R., Beibei, D., Jian-Yong, W., Zhan-Rong, L., and Weiying, L. (2015). A Dual-Emission Fluorescence-Enhanced Probe for Imaging Copper(ii) Ions in Lysosomes. *J. Mater. Chem. B* 3, 6746–6752. doi:10.1039/c5tb01184a

Nemoto, S., Takeda, K., Yu, Z. X., Ferrans, V. J., and Finkel, T. (2000). Role for Mitochondrial Oxidants as Regulators of Cellular Metabolism. *Mol. Cell. Biol.* 20, 7311–7318. doi:10.1128/mcb.20.19.7311-7318.2000

Ning, P., Jiang, J., Li, L., Wang, S., Yu, H., Feng, Y., et al. (2016). A Mitochondria-Targeted Ratiometric Two-Photon Fluorescent Probe for Biological Zinc Ions Detection. *Biosens. Bioelectron.* 77, 921–927. doi:10.1016/j.bios.2015.10.061

Nixon, R. A., Cataldo, A. M., and Mathews, P. M. (2000). The Endosomal-Lysosomal System of Neurons in Alzheimer's Disease Pathogenesis: A Review. *Neurochem. Res.* 25, 1161–1172. doi:10.1023/a:1007675508413

Nixon, R. A. (2013). The Role of Autophagy in Neurodegenerative Disease. *Nat. Med.* 19, 983–997. doi:10.1038/nm.3232

Onyenwoke, R. U., and Brenman, J. E. (2015). Lysosomal Storage Diseases-Regulating Neurodegeneration. *J. Exp. Neurosci.* 9, 81–91. doi:10.4137/JEN.S25475

Peng, N., Liling, H., Yan, F., Guoyong, X., Yuyuan, B., Haizhu, Y., et al. (2019). Real-time Visualization of Autophagy by Monitoring the Fluctuation of Lysosomal pH with a Ratiometric Two-Photon Fluorescent Probe. *Chem. Commun. (Camb)* 55, 1782–1785. doi:10.1039/c8cc09517e

Phan, U. T., Arunachalam, B., and Cresswell, P. (2000). Gamma-interferon-inducible Lysosomal Thiol Reductase (GILT). Maturation, Activity, and Mechanism of Action. *J. Biol. Chem.* 275, 25907–25914. doi:10.1074/jbc.M003459200

Pierrel, F., Cobine, P. A., and Winge, D. R. (2007). Metal Ion Availability in Mitochondria. *BioMetals* 20, 675–682. doi:10.1007/s10534-006-9052-9

Qiu, K., Du, Y., Liu, J., Guan, J. L., Chao, H., and Diao, J. (2020). Super-resolution Observation of Lysosomal Dynamics with Fluorescent Gold Nanoparticles. *Theranostics* 10, 6072–6081. doi:10.7150/thno.42134

Qixin, C., Hongbao, F., Xintian, S., Zhiqi, T., Shanshan, G., Yuming, Z., et al. (2020). A Dual-Labeling Probe to Track Functional Mitochondria-Lysosome Interactions in Live Cells. *Nat. Commun.* 11, 6290. doi:10.1038/s41467-020-20067-6

Radi, R. (2013). Peroxynitrite, a Stealthy Biological Oxidant. *J. Biol. Chem.* 288, 26464–26472. doi:10.1074/jbc.R113.472936

Saipeng, H., Rongcheng, H., Qianfen, Z., Libo, D., Hongying, J., Yangping, L., et al. (2015). New Photostable Naphthalimide-Based Fluorescent Probe for Mitochondrial Imaging and Tracking. *Biosens. Bioelectron.* 71, 313–321. doi:10.1016/j.bios.2015.04.056

Sang-Hyun, P., Young, H. J., and Injae, S. (2019). A Lysosomal Chloride Ion-Selective Fluorescent Probe for Biological Applications. *Chem. Sci.* 10, 56–66. doi:10.1039/c8sc04084b

Seth, R., Yang, S., Choi, S., Sabean, M., and Roberts, E. A. (2004). *In Vitro* assessment of Copper-Induced Toxicity in the Human Hepatoma Line, Hep G2. *Toxicol. Vitro* 18, 501–509. doi:10.1016/j.tiv.2004.01.006

Sha, X.-L., Yang, X.-Z., Wei, X.-R., Sun, R., Xu, Y.-J., and Ge, J.-F. (2020). A Mitochondria/lysosome-Targeting Fluorescence Probe Based on Azonia-Cyanine Dye and its Application in Nitroreductase Detection. *Sensors Actuators B. Chem.* 307, 127653. doi:10.1016/j.snb.2019.127653

Shiling, Z., Jiangli, F., Shuangzhe, Z., Jingyun, W., Xianwu, W., Jianjun, D., et al. (2014). Lighting up Fluoride Ions in Cellular Mitochondria Using a Highly Selective and Sensitive Fluorescent Probe. *Chem. Commun. (Camb)* 50, 14021–14024. doi:10.1039/c4cc05094k

Tamima, U., Song, C. W., Santra, M., Reo, Y. J., Banna, H., Islam, M. R., et al. (2020). A Benzo[B]xanthene-Derived Fluorescent Probe Capable of Two-Photon Ratiometric Imaging of Lysosomal Cysteine with High Specificity. *Sensors Actuators B. Chem.* 322, 128588. doi:10.1016/j.snb.2020.128588

Tian, M., Zhan, J., and Lin, W. (2022). Single Fluorescent Probes Enabling Simultaneous Visualization of Duple Organelles: Design Principles, Mechanisms, and Applications. *Coord. Chem. Rev.* 451, 214266. doi:10.1016/j.ccr.2021.214266

Tümer, Z., and Møller, L. B. (2010). Menkes Disease. *Eur. J. Hum. Genet.* 18, 511–518. doi:10.1038/ejhg.2009.187

Vakifahmetoglu-Norberg, H., Ouchida, A. T., and Norberg, E. (2017). The Role of Mitochondria in Metabolism and Cell Death. *Biochem. Biophys. Res. Commun.* 482, 426–431. doi:10.1016/j.bbrc.2016.11.088

Vila, M., Bové, J., Dehay, B., Rodríguez-Muela, N., and Boya, P. (2011). Lysosomal Membrane Permeabilization in Parkinson Disease. *Autophagy* 7, 98–100. doi:10.4161/auto.7.1.13933

Wang, L., and Diao, J. (2022). VAMP8 Phosphorylation Regulates Lysosome Dynamics during Autophagy. *Autophagy Rep.* 1, 79–82. doi:10.1080/27694127.2022.2031378

Wang, W., Zhang, W., Feng, Y., Wang, S., Lei, H., Huang, J., et al. (2018). Strategically Modified Highly Selective Mitochondria-Targeted Two-Photon Fluorescent Probe for Au 3+ Employing Schiff-Base: Inhibited C=N Isomerization vs. Hydrolysis Mechanism. *Dyes Pigments* 150, 241–251. doi:10.1016/j.dyepig.2017.12.019

Wei, Y.-F., Weng, X.-F., Sha, X.-L., Sun, R., Xu, Y.-J., and Ge, J.-F. (2021). Simultaneous Imaging of Lysosomal and Mitochondrial Viscosity under Different Conditions Using a NIR Probe. *Sensors Actuators B. Chem.* 326, 128954. doi:10.1016/j.snb.2020.128954

Wei, Y., Kong, L., Chen, H., Liu, Y., Xu, Y., Wang, H., et al. (2022). Super-resolution Image-Based Tracking of Drug Distribution in Mitochondria of a Label-free Naturally Derived Drug Molecules. *Chem. Eng. J.* 429, 132134. doi:10.1016/j.cej.2021.132134

Wen, S., Xiaohua, L., and Huimin, M. (2014). Fluorescent Probes and Nanoparticles for Intracellular Sensing of pH Values. *Methods Appl. Fluoresc.* 2, 042001. doi:10.1088/2050-6120/2/4/042001

Wong, Y. C., Kim, S., Peng, W., and Krainc, D. (2019). Regulation and Function of Mitochondria-Lysosome Membrane Contact Sites in Cellular Homeostasis. *Trends Cell. Biol.* 29, 500–513. doi:10.1016/j.tcb.2019.02.004

Wu, W.-N., Wu, H., Zhong, R.-B., Wang, Y., Xu, Z.-H., Zhao, X.-L., et al. (2018). Ratiometric Fluorescent Probe Based on Pyrrole-Modified Rhodamine 6G Hydrazone for the Imaging of Cu 2+ in Lysosomes. *Spectrochimica Acta Part A Mol. Biomol. Spectrosc.* 212, 121–127. doi:10.1016/j.saa.2018.12.041

Xiaoyue, H., Rui, W., Xinyu, S., Fabiao, Y., Changjun, L., and Lingxin, C. (2018). A Mitochondrial-Targeting Near-Infrared Fluorescent Probe for Bioimaging and Evaluating Endogenous Superoxide Anion Changes during Ischemia/reperfusion Injury. *Biomaterials*, 156, 134–146. doi:10.1016/j.biomaterials.2017.11.039

Xu, X., Chen, W., Yang, M., Liu, X. J., Wang, F., Yu, R. Q., et al. (2019). Mitochondrial-targeted Near-Infrared Fluorescence Probe for Selective Detection of Fluoride Ions in Living Cells. *Talanta* 204, 655–662. doi:10.1016/j.talanta.2019.06.028

Yang, L., Niu, J.-Y., Sun, R., Xu, Y.-J., and Ge, J.-F. (2018). The Application of Mitochondrial Targetable Pyronine-Pyridinium Skeleton in the Detection of Nitroreductase. *Sensors Actuators B. Chem.* 259, 299–306. doi:10.1016/j.snb.2017.12.011

Yawei, W., Liu, W., Caiyun, L., Bingpeng, G., Baocun, Z., Zuokai, W., et al. (2017). A Highly Specific and Ultrasensitive Fluorescent Probe for Basal Lysosomal HOCl Detection Based on Chlorination Induced by Chlorinium Ions (Cl^+). *J. Mater. Chem. B* 5, 3377–3382. doi:10.1039/c6tb03345h

Li, Y., Wu, W., Yang, J., Yuan, L., Liu, C., Zheng, J., et al. (2016). Engineering a Nanolab for the Determination of Lysosomal Nitric Oxide by the Rational Design of a pH-Activatable Fluorescent Probe. *Chem. Sci.* 7, 1920–1925. doi:10.1039/c5sc04415d

Yong, L., Fangfang, M., Longwei, H., Keyin, L., and Weiying, L. (2016). A Dual-Site Two-Photon Fluorescent Probe for Visualizing Lysosomes and Tracking Lysosomal Hydrogen Sulfide with Two Different Sets of Fluorescence Signals in the Living Cells and Mouse Liver Tissues. *Chem. Commun. (Camb)* 52, 7016–7019. doi:10.1039/c6cc02368a

Yongkang, Y., Fangjun, H., Songyi, L., Caixia, Y., and Juyoung, Y. (2016). A Review: the Trend of Progress about pH Probes in Cell Application in Recent Years. *Analyst* 142, 30–41. doi:10.1039/c6an01942k

Zhang, H., Liu, J., Liu, C., Yu, P., Sun, M., Yan, X., et al. (2017). Imaging Lysosomal Highly Reactive Oxygen Species and Lighting up Cancer Cells and Tumors Enabled by a Si-Rhodamine-Based Near-Infrared Fluorescent Probe. *Biomaterials* 133, 60–69. doi:10.1016/j.biomaterials.2017.04.023

Conflict of Interest: The authors declare that the research was conducted in the absence of any commercial or financial relationships that could be construed as a potential conflict of interest.

Publisher's Note: All claims expressed in this article are solely those of the authors and do not necessarily represent those of their affiliated organizations, or those of the publisher, the editors, and the reviewers. Any product that may be evaluated in this article, or claim that may be made by its manufacturer, is not guaranteed or endorsed by the publisher.

Copyright © 2022 Chen, Yu, Ren and Qiu. This is an open-access article distributed under the terms of the Creative Commons Attribution License (CC BY). The use, distribution or reproduction in other forums is permitted, provided the original author(s) and the copyright owner(s) are credited and that the original publication in this journal is cited, in accordance with accepted academic practice. No use, distribution or reproduction is permitted which does not comply with these terms.

frontiers | Frontiers in Pharmacology

ORIGINAL RESEARCH
published: 22 July 2022
doi: 10.3389/fphar.2022.943272

Nodosin Exerts an Anti-Colorectal Cancer Effect by Inhibiting Proliferation and Triggering Complex Cell Death *in Vitro* and *in Vivo*

Huixia Fan[1,2,3†], *Xiaopeng Hao*[2†], *Yuan Gao*[2], *Jian Yang*[4], *Aojun Liu*[2], *Yarui Su*[1*] and *Yong Xia*[2*]

[1]School of Life Sciences, Henan University, Kaifeng, China, [2]Key Laboratory of Precision Oncology of Shandong Higher Education, Institute of Precision Medicine, Jining Medical University, Jining, China, [3]School of Pharmacy, Henan University, Kaifeng, China, [4]State Key Laboratory Breeding Base of Dao-di Herbs, National Resource Center for Chinese Materia Medica, China Academy of Chinese Medical Sciences, Beijng, China

OPEN ACCESS

Edited by:
Qixin Chen,
Shandong First Medical University, China

Reviewed by:
Yang Chen,
Dalian Institute of Chemical Physics (CAS), China
Uthayashanker Ezekiel,
Saint Louis University, United States

***Correspondence:**
Yarui Su
10140037@vip.henu.edu.cn
Yong Xia
xiayong@mail.jnmc.edu.cn

[†]These authors have contributed equally to this work

Specialty section:
This article was submitted to Pharmacology of Anti-Cancer Drugs, a section of the journal Frontiers in Pharmacology

Received: 13 May 2022
Accepted: 20 June 2022
Published: 22 July 2022

Citation:
Fan H, Hao X, Gao Y, Yang J, Liu A, Su Y and Xia Y (2022) Nodosin Exerts an Anti-Colorectal Cancer Effect by Inhibiting Proliferation and Triggering Complex Cell Death in Vitro and in Vivo. Front. Pharmacol. 13:943272. doi: 10.3389/fphar.2022.943272

Colorectal cancer (CRC) is one of the most common digestive system cancer in the world. Its incidence and mortality are increasing annually. Presently, CRC lacks long-term effective treatment methods and drugs. Therefore, finding new treatment methods and drugs is of great significance for CRC treatment. Compounds derived from natural plants have been widely used in tumor research and treatment because of their good antitumor activity these years. This study found that nodosin, a diterpenoid extracted from the medicinal plant *Rabdosia serra (Maxim.) Hara,* inhibited the growth of CRC cells SW480, HT-29 and LoVo in a dose- and time-dependent manner, with inhibitory concentrations (IC_{50}) of 7.4, 7.7, and 6.6 μM respectively. We selected highly metastatic and poorly differentiated SW480 cells for further studies. We found that nodosin could inhibit cell proliferation by inhibiting DNA synthesis and induce cell death by inducing oxidative stress, apoptosis and autophagy in cells. Through *in vitro* assays combined with transcriptomic analysis, it was found that nodosin could downregulate tribbles pseudokinase 3 and upregulate oxidative stress-induced growth inhibitor 1 to induce oxidative stress in cells; nodosin-induced reactive oxygen species were able to upregulate the expression of heme oxygenase 1 to induce apoptosis and the expression of cathepsin L. and light chain-3 to induce autophagy. *In vivo*, we found that nodosin inhibited tumor growth and induced cells to undergo apoptosis and autophagy without significant toxic effects. In conclusion, our findings suggest that nodosin exerts anti-CRC effects mainly through its ability to induce apoptosis and autophagy *in vitro* and *in vivo*. Therefore, our study contributes to the development of nodosin-based potential CRC therapeutic drugs.

Keywords: nodosin, colorectal cancer, oxidative stress, apoptosis, autophagy

INTRODUCTION

Colorectal cancer (CRC) is a common cancer of the digestive system. Among the common malignant tumors, CRC ranks second in the mortality rate (Keum and Giovannucci, 2019). In recent years, studies have found that an increase in unhealthy eating habits has led to a gradual onset of CRC at younger ages, and CRC incidence has gradually increased among people under the age of 50

(Akimoto et al., 2021). Most patients have progressed to metastatic CRC during diagnosis, and their survival is 1–5 years (Van der Jeught et al., 2018). Current treatments for CRC are limited, and conventional anticancer methods, such as surgery, radiotherapy, and chemotherapy, are highly toxic and nonspecific (Johdi and Sukor, 2020). Cetuximab and panitumumab are often used in clinical practice to treat and extend the survival period of patients (Biller and Schrag, 2021). However, there is no complete cure, and drug resistance emergence is gradually increasing (Talib et al., 2020). Therefore, studying more effective treatment methods and drugs for treating CRC is crucial.

In recent years, natural medicines have been considered essential sources of medicines for treating different diseases. Studies have found that natural compounds can exert anti-proliferative, pro-apoptotic, anti-angiogenic, and anti-mutagenic effects by regulating various biological processes, including the cell epigenome (Samec et al., 2019). In addition, plant-derived compounds can suppress cancer invasion, transfer, and proliferation by regulating various signaling pathways (Sarwar et al., 2018). Therefore, natural compounds have become a relatively widespread antitumor drug for clinical applications. The search for novel antitumor active substances from naturally derived compounds has become a research hotspot for anticancer drugs.

Rabdosia serra (Maxim.) Hara, called Xihuangcao in Chinese, is widely used to treat various diseases because of its diverse biological activities, including anti-inflammatory, anti-oxidation, antibacterial, and antitumor activities (Chen et al., 2014). Diterpenoids and phenolics extracted from *Rabdosia serra (Maxim.) Hara* have good medical and health value (Lin et al., 2013). This study found that the diterpenoid nodosin extracted from *Rabdosia serra (Maxim.) Hara* inhibits the activity of CRC cells. Nowadays, most researches on nodosin mainly focus on three aspects: anti-inflammatory, antibacterial, and anticancer activities. In terms of anti-inflammatory activity, nodosin can inhibit mouse ear swelling and serum interleukin-2 (IL-2) levels by regulating the cell cycle of mouse T lymphocytes (Li et al., 2010); In terms of antibacterial activity, the minimal inhibitory concentration 90 (MIC_{90}) of nodosin against gram-positive bacteria *Staphylococcus aureus* and *Streptococcus mutans* was 25 μg/ml, and the antibacterial activity was high, while the antibacterial activity against gram-negative bacteria was weak (Isobe and Nagata, 2010); In terms of antitumor activity, nodosin can inhibit the proliferation of CRC HCT116 cells by regulating the Wnt/β-catenin signaling pathway (Bae et al., 2020). However, we found that nodosin had a lower inhibitory concentration (IC_{50}) and better anticancer activity against SW480 cells than against HCT116 cells. Moreover, previous studies have been limited to the Wnt/β-catenin signaling pathway, and their effects on animals have not been studied. Therefore, this study aimed to determine the pharmacological mechanism of nodosin in CRC SW480 cells and to verify its effect *in vivo*.

This study conducted an in-depth investigation of the potential anticancer mechanism of nodosin in CRC *in vivo* and *in vitro*. Nodosin was found to inhibit the proliferation, migration, and clonogenicity of SW480 cells by cell counting kit-8 (CCK-8), clone formation, cell migration, 5-ethynyl-2′-deoxyuridine (EdU), and cell immunofluorescence (IF) assays. In addition, combined the transcriptomic analysis results indicated that nodosin could downregulate *tribbles pseudokinase 3* (*TRIB3*) and upregulate *oxidative stress-induced growth inhibitor 1* (*OSGIN1*) to induce oxidative stress in cells. Nodosin-induced reactive oxygen species (ROS) were able to upregulate the expression of *heme oxygenase 1* (*HMOX1*) to induce apoptosis and upregulate the expression of *cathepsin L* (*CTSL*) and *light chain-3* (*LC3*) to induce autophagy. *In vivo*, nodosin inhibited the growth of CRC transplant tumors and induced apoptosis and autophagy through hematoxylin and eosin (H&E) staining and immunohistochemistry assays (IHC). In conclusion, the results of this study will better reveal the anticancer mechanism of nodosin in CRC, provide some ideas and strategies for treating CRC, and help develop nodosin-based anti-CRC drugs.

MATERIALS AND METHODS

Cell Culture

Human CRC SW480, HT-29, Lovo, and NCM460 cells were purchased from American Type Culture Collection (ATCC), and cells were cultured in DMEM medium (06-1055-57-1ACS, BI, Israel), which added 10% Fetal Bovine Serum (FBS, A3160801, Hyclone, United States) and 1% Pecinillin-Streptomycin (P/S, UB89609, GBICO, United States), cultured in 37°C incubation containing 5% CO_2.

Chemicals

Nodosin was purchased from Huzhou Zhanshu Biotechnology Co., Ltd. (10391-09-0, molecular formula: $C_{20}H_{26}O_6$, molecular weight: 362.42, purity: 99.98%). DMSO (dimethyl sulfoxide, D8371) was obtained from Solarbio Technology Ltd.

Cell Viability Assay

Cells with a density of 25% were seeded in 96-well plates, and treated with 0–16 μM nodosin when the total cell density was about 40%. The relative cell activities of SW480, HT-29, LoVo, and NCM460 after nodosin treatment were then detected following the manufacturer's instruction of CCK-8 kit (CK04, DOJINDO, Japan).

Cell Morphological Assay

SW480 cells were seeded in the 12-well plates at the confluence of 1×10^5 cells/well. After the cells adhered and returned to normal, the cell morphology at T0 moment was recorded, then treated with 0–12 μM of nodosin for 48 h, and recorded the morphological changes after different times of treatment with an inverted microscope (Nikon, Japan).

Cell Migration Assay

Before the cells were seeded into 12-well plates, the inserts (80469, IBIDI, Germany) were stuck onto plate bottom following the manufacturer's instruction. When the cell confluence reached 80%, the insert was removed with forceps to produce a scratch of

500 μm width. The T0 moment was recorded with an inverted microscope (Nikon, Japan). Then added 0–12 μM nodosin and incubated with cells for 24 h, observed and recorded the width of cell scratches with a microscope (Nikon, Japan).

Cell Membrane Staining Assay

An appropriate amount of cells were seeded in 12-well plates, treated with nodosin for 24 h. Nodosin-treated cells were washed using PBS and fixed with 4% paraformaldehyde for 15 min. After washed 2 to 3 times with PBS, the fixed cells were stained with double dyes (Hoechst 33342 1:1000, C1022, Beyotime; Dio 1:100, C1038, Beyotime) for 20 min, washed twice with PBS, and then photographed with a fluorescence inverted microscope (Nikon, Japan).

Clone Formation Assay

The cells were seeded in a 12-well plate at a confluence of 500 cells/well. 48 h later, different concentration of nodosin was added. The medium with nodosin was changed every 3 days. After incubation with/without nodosin, the cells were fixed with 4% paraformaldehyde for 20 min at ambient temperature and then stained with crystal violet staining solution (KGA229, KeyGEN BioTECH, China) for 5–10 min. The stained colonies were recorded under an inverted microscope (Nikon, Japan).

Live/Dead Cell Detection

SW480 cells were seeded in 12-well plates at a number of 1×10^5 cells/well. After the cell density was about 50%, nodosin was added for treatment. The cell viability was detected using a Calcein AM Cell Viability Assay Kit (C2013FT, Beyotime, China), and the stained cells were recorded microscopically (Nikon, Japan).

Measurement of DNA Synthesis Rate by EdU Method

DNA synthesis in nodosin-treated SW480 cells was detected using EdU-594 Cell Proliferation Assay Reagent (C0078S, Beyotime, China) in the light of the manufacturer's instruction. The staining results were recorded microscopically (Nikon, Japan), followed by quantitative analysis using ImageJ software.

Cell Cycle Assay

The nodosin-treated SW480 cells were centrifuged and collected. The cells were resuspended with 70% cold ethanol, fixed on ice for 60 min. After centrifugated at 2,000 rpm, the supernatant was discarded and the pellet cells were resuspended with a mixed solution containing PI (KGA214, KeGEN BioTECH, China), RNase (ST579, Beyotime, China) and Triton X-100 (P0096, Beyotime, China). The stained cells were detected with a flow cytometer (Beckman, cytolfex, United States).

IF Staining

The cultured cells were fixed with 4% paraformaldehyde at room temperature for 20 min, then permeabilized with 0.3% Triton X-100 for 15 min, blocked with 3% BSA for 30 min. After discarding the block solution, the samples were incubated with Ki67 (1:300, ab15580, abcam, United Kingdom) overnight, and then incubated with CoraLite 488-conjugated Affinipure Goat Anti-Rabbit IgG (H + L) (SA00013-2, proteintech, China) for 1.5 h. The nucleus was stained with DAPI (C1002, Beyotime, China) and the cytoskeleton was stained with Actin-Tracker Red 594 (F-Actin, C2205S, Beyotime, China). The number of the cell proliferation marker Ki67 was observed and recorded with a fluorescence inverted microscope (Nikon, Japan) at a wavelength of 550 nm.

Detection of ROS by H_2DCFDA

The changes of ROS in nodosin-induced SW480 cells were detected with the cell-permeable ROS probe H_2DCFDA (HY-D0940, MCE, United States). SW480 cells in the nodosin-treated and control group were incubated with H_2DCFDA in a CO_2 incubator at 37°C for 30 min in the dark. The changes of ROS in the cells were detected by flow cytometry (Beckman, cytolfex, United States). To detect whether ROS was involved nodosin-inhibited cell activity, SW480 cells were pretreated with the antioxidant NAC (ST1546, Beyotime, China) for 1 h, and co-incubated with 12 μM nodosin for 48 h. Finally, the cell activity was detected using the CCK-8 kit.

Apoptosis Detection

Nodosin-treated SW480 cells were digested with EDTA-free trypsin (T1350, Solarbio, China). The cells were incubated with Annexin V-FITC (C1062M, Beyotime, China) and PI (KGA214, KeyGEN BioTECH, China) for 20 min in the dark. The rate of apoptosis was determined and recorded by flow cytometry (Beckman, cytolfex, United States).

Plasmid Transfection

Lipofectamine 3000 Transfection Kit (L3000015, Invitrogen, United States) was used to transfer lamp1 OFP, ER, and mito plasmids (gifts from Camilla Raiborg, University of Oslo, Norway) into SW480 cells. After the target plasmids expressed, different concentrations of nodosin were added. Then the confocal laser microscopy (Leica TCS SP8, Leica, Germany) was used to examine the changes of intracellular lysosomes, endoplasmic reticulum, and mitochondria.

Autophagy Detection

SW480 cells were cultured in a 96-well plate at 37°C with 5% CO_2 for 12 h. Next, they were treated with 12 μM of nodosin for 48 h. SW480 cells were then incubated with 6.25–250 nM of the autophagy blocker chloroquine (CQ, HY-17589A, MCE, United States) for 2 h, and cell viability was detected using the CCK-8 kit.

Transcriptome Assay

In transcriptome sequencing, three nodosin-treated samples and three control samples were lysed with Trizol reagent (15596026, ambition, Japan) respectively (5×10^6 cells in each sample). Library construction, mRNA sequencing, and bioinformatics analysis were performed at BIOMARKER (Beijing, China).

TABLE 1 | The primer sequences for PCR.

Primer	PCR primer
HMOX1	Forword: CAGGCAGAGAATGCTGAGT
	Reverse: TTGAACTTGGTGGCACTG
CTSL	Forword: TCCTACACTCATCCTTGCTG
	Reverse: AACCACACTGACCCTGATTC
β-actin	Forword: CACTCTTCCAGCCTTCCTT
	Reverse: ACAGGTCTTTGCGGATGT

Reverse Transcriptional PCR and Real-Time PCR

Total RNA in cells was extracted with Trizol reagent (15596026, ambition, Japan), then RNA was reversed into cDNA with FastKing RT Kit (With gDNase) (KR116, TIANGEN, China), validated with agarose gel, and then qPCR was conducted using SuperReal PreMix Color (SYBR Green, FP215, TIANGEN, China), relative mRNA levels were normalized to β-actin levels, and relative gene expression changes were calculated. The primers of PCR and q-PCR are shown in **Tables 1**, **2**.

Western Blotting

The nodosin-treated SW480 cells were lysed and proteins were extracted from them using lysis buffer (P0013, Beyotime, China). The protein extracts were processed by SDS polyacrylamide gel electrophoresis and blotted on PVDF membranes. Western blotting (WB) was performed using the following primary antibodies: HMOX1 (Rabbit, 1:3,000, 10701-1-AP, proteintech, China), LC3 (Rabbit, 1:2,000, 14600-1-AP, proteintech, China), β-Actin (Rabbit, 1:2,000, GB11001, Servicebio, China). After the primary antibody was incubated and washed, the immunohy bridization signal was captured using HRP-conjugated secondary antibody. The secondary antibodies were listed as follows: HRP Goat Anti-Rabbit IgG (H + L) (1:4,000, AS014, ABclonal, China). The development was then performed using ECL solution (P0018S, Beyotime, China).

Xenograft in Nude Mice

BALB/c-nude nude mice were provided by Jinan Pengyue Laboratory Animal Breeding Co.,Ltd., eight females, 6 weeks old, about 20 g, SPF grade, the laboratory animal certificate number was No. 370726211100958867. This assay was performed with the approval of the Ethics Committee of Jining Medical University. BALB/c-nude female mice were subcutaneously injected with CRC SW480 cells. The mice were randomly divided into two groups (4 nude mice/group) when the tumor grew to 100 mm^3. In the nodosin-treated group, the mice were treated by nodosin with a dose of 3 mg/kg, once every 3 days. The control group was treated with DMSO at the same injection volume and frequency. After 10 injections, the CRC xenograft tumors of mice were removed, weighed and photographed. Paraffin blocks were made after the tumors were fixed with 10% neutral formalin and dehydrated for subsequent studies.

H&E Staining

The CRC xenograft tumors paraffin blocks were cut into slices (the thickness was 4 μm). The tumor sections were stained in the light of the instructions of the HE staining kit (G1120, Solarbio, China). The changes of the pathological sections were observed under a Pannoramic Desk (3DHISTECH, Hungary).

IHC Staining

The biomarkers in nude mice transplanted tumors were detected by IHC methods. Cut the wax block into 4-μm wax slices, and use an oven at 60°C for 1–2 h. The sections were removed for dewaxing, hydration, and then antigen repair with improved sodium citrate antigen repair solution (P0083, Beyotime, China). Incubated for 30 min with inactivated endogenous peroxidase 3% H_2O_2 (SV0004, BOSTER, China) to avoid light. Afterwards, they were blocked with ready-to-use normal goat serum (AR0009, BOSTER, China) for 30 min. After shaking off the blocking solution, Ki67 (1:300, ab15580, abcam, United Kingdom), HMOX1 (Rabbit, 1:200, 10701-1-AP, proteintech, China), LC3 (Rabbit, 1:500, 14600-1-AP, proteintech, China), CTSL (Rabbit, 1:500, proteintech, China) were added and placed in a refrigerator at 4°C overnight for incubation. Polymeric HRP-labeled anti-rabbit/mouse IgG (SV0004, BOSTER, China) was added after washing with PBS and incubated for 30 min at room temperature in the dark. The color was developed with DAB chromogen solution (C02-12, ORIGENE, America). After color development, counterstain with hematoxylin (AR0005, BOSTER, China). Afterwards, it was blue with alkaline PBS. Finally, dehydration was performed and the slides were mounted. Scanning observations were performed using a Pannoramic Desk (3DHISTECH, Hungary).

Statistics

The difference between the two groups was assessed by two-tailed *t*-test. The three groups and above were evaluated with one-way ANOVA analysis followed by LSD Post Hoc multiple comparison to assess its significance, and p-value < 0.05 was considered significant.

RESULTS

Nodosin Repressed CRC Cells in a Dose- and Time-Dependent Way *in vitro*

The chemical structure of nodosin is shown in **Figure 1A**. According to the CCK-8 assay results (**Figures 1B–D**), nodosin significantly repressed CRC cells proliferation in a dose-dependent manner. The IC_{50} of nodosin in SW480, HT-29, and LoVo cells were 7.4, 7.7, and 6.6 μM, respectively.

TABLE 2 | The primer sequences for realtime-PCR.

Primer	Quantitative RT-PCR primer
HMOX1	Forword: ATTGCCAGTGCCACCAAGT
	Reverse: TGAGCAGGAACGCAGTCTT
CTSL	Forword: TCCTACACTCATCCTTGCTG
	Reverse: TCCACTGTGCCTCTAAACTG
β-actin	Forword: CACTCTTCCAGCCTTCCTT
	Reverse: ACAGGTCTTTGCGGATGT

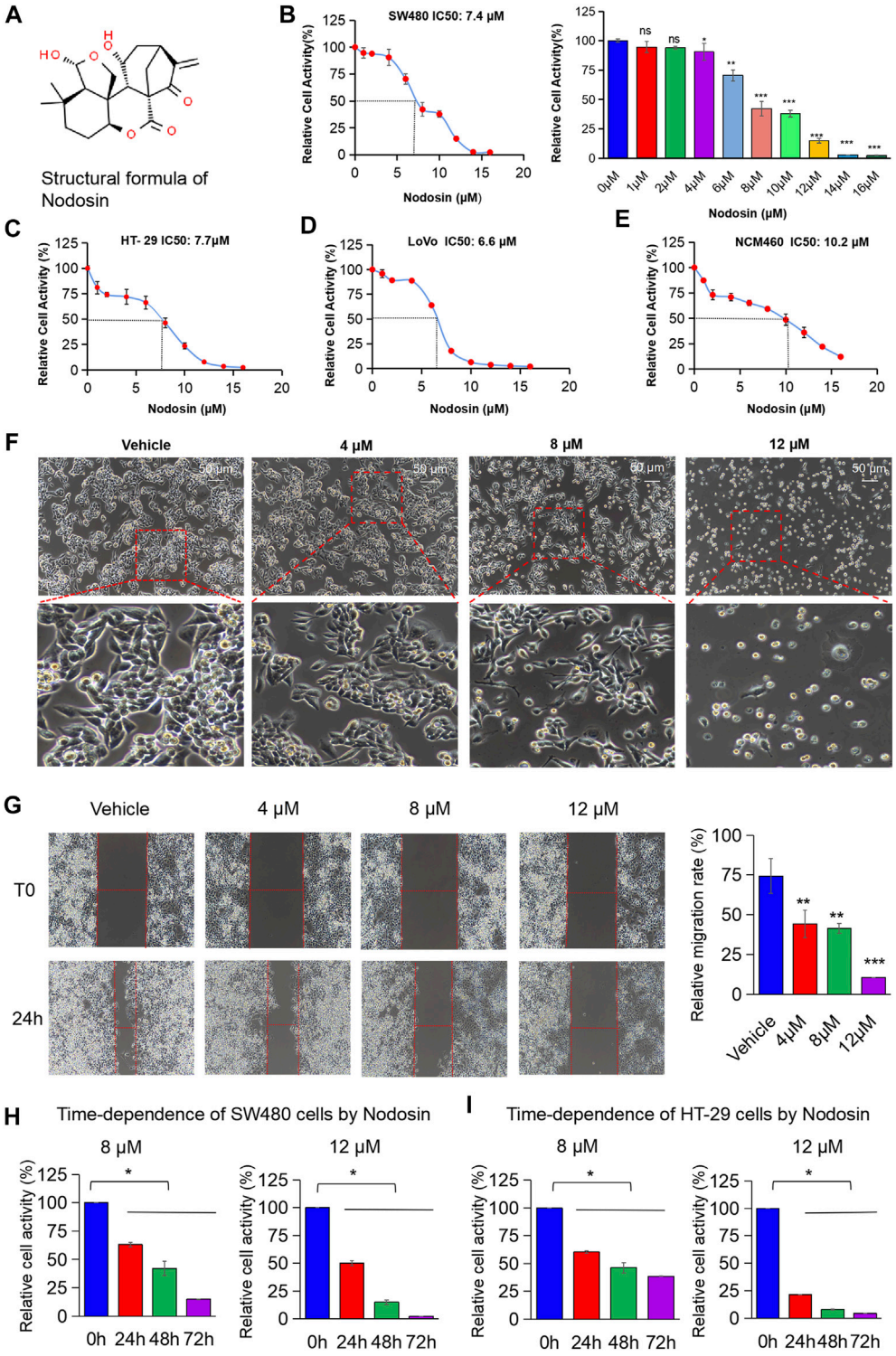

FIGURE 1 | Nodosin suppressed CRC cells in dose- and time-dependent way *in vitro*. **(A)** The chemical structural formula of nodosin (http://www.chemspider.com). **(B)** CRC SW480 cells were treated with 0–16 μM nodosin for 48 h. The relative viability of cells was detected by CCK-8 kit. Each group was repeated three times. The significant difference between the nodosin treated and control group (without nodosin) was evaluated by the two-tailed *t*-test, $^{*}p < 0.05$, $^{**}0.01 < p < 0.05$, $^{***}p < 0.01$. **(C)** HT-29 cells were treated with 0–16 μM nodosin for 48 h. The cell viability was tested by CCK-8 kit. **(D)** LoVo cells were treated with 0–16 μM nodosin for 48 h. The cell viability was tested by CCK-8 kit. **(E)** NCM460 cells were treated with 0–16 μM nodosin for 48 h. The cell activity was tested by CCK-8 kit. **(F)** SW480 cells were treated with nodosin for 48 h, and the morphological changes of SW480 cells were recorded by fluorescence inverted microscope. **(G)** The repressive effect of

(*Continued*)

FIGURE 1 | nodosin on the migration of SW480 cells was tested by cell scratch method. SW480 cells were treated with different concentrations of nodosin for 24 h to measure the scratch width and calculate the cell scratch closure rate. The relative migration rate significant difference between the nodosin treated group and the control group (without nodosin) was evaluated by the two-tailed *t*-test, $^{*}p < 0.05$, $^{**}p < 0.01$, $^{***}p < 0.001$. **(H)** Nodosin reduced the relative activity of SW480 cells in a dose- and time-dependent manner. The significant difference was evaluated with one-way ANOVA analysis followed by LSD Post Hocnultiple comparison, and *p*-value < 0.05 was considered significant. **(I)** Nodosin reduced the relative activity of HT-29 cells in a dose-dependent and time-dependent way. The significance difference was evaluated with one-way ANOVA analysis followed by LSD Post Hocnultiple comparison, and *p*-value < 0.05 was considered significant.

However, the toxicity to human normal colonic mucosal epithelial cells NCM460 was lower, with an IC_{50} of 10.2 μM (**Figure 1E**). In addition, the morphological characteristics of CRC SW480 cells were significantly changed after nodosin treatment (**Figure 1F**). At low concentrations, the cells underwent significant shrinkage and elongation; at high concentrations, the cells were unable to adhere and became rounded. **Figure 1G** shows that nodosin dose-dependently restrained the migration ability of SW480 cells. Cell mobility decreased gradually with increased nodosin concentration, and almost no cell migration occurred at 12 μM. Therefore, the relative activity of cells gradually decreased with increased nodosin concentration and prolonged treatment (**Figures 1H,I**), indicating that nodosin could inhibit the proliferation of CRC cells in a dose- and time-dependent manner.

Nodosin Suppressed CRC Cells Proliferation and Triggered Cells Death

Proliferation and death are important processes in the development of tumor cells. As nodosin concentration increased, the number of cells gradually decreased, and the cell membrane became larger and damaged (**Figure 2A**). Additionally, nodosin inhibited the clonogenic ability of SW480 cells. When nodosin concentration was greater than 4 μM, the cells could not form clonal colonies (**Figure 2B**). Interestingly, nodosin only inhibited 10% of cell activity at a concentration of 4 μM, whereas nodosin at the same concentration inhibited majority of the clonogenic ability of SW480 cells. Moreover, the number of live cells decreased, and the number of dead cells gradually became elevated with increased nodosin concentrations in the live/dead cell staining assay (**Figure 2C**).

Nodosin Inhibited DNA Synthesis Rate in CRC Cells

DNA replication speed is an important indicator for evaluating the cell proliferation rate, activity, and physiological status. This study found that nodosin inhibited DNA replication ability of SW480 cells by EdU assay (**Figure 3A**). After nodosin treatment, the total number of cells decreased to a certain extent. The relative ratio of EdU/H33342 gradually decreased as the nodosin concentration increased, which indicated that nodosin effectively inhibited the DNA replication ability of SW480 cells. Moreover, the cell cycle of SW480 cells was detected after nodosin treatment, and nodosin affected the synthesis (S) phase of the cell cycle; the S phase gradually decreased with increased nodosin concentration (**Figure 3B**). Ki67 is an antigen related to cell proliferation and exerts an important role in mitosis. In Ki67 immunofluorescence staining (**Figure 3C**), the Ki67-labeled antigen gradually decreased with an increase in nodosin treatment concentrations, which is consistent with the experimental results shown in **Figures 3A,B**. These results demonstrate that nodosin can inhibit DNA synthesis from multiple perspectives.

Nodosin Induced Oxidative Stress, Apoptosis, and Autophagy in SW480 Cells

To further study the antitumor mechanism of nodosin, H_2DCFDA fluorescent probe was used to test intracellular ROS levels after nodosin treatment. **Figure 4A** shows that after the cells were stimulated by nodosin, oxidative stress occurred, and the ROS level in the cells increased continuously with an increase in nodosin treatment concentration. In this regard, after pretreatment with the antioxidant N-acetylcysteine (NAC), the relative cell activity reached saturation when the NAC concentration was 0.5 mM, and the relative cell activity could be increased to 80%, indicating that nodosin induced oxidative stress-mediated cell death. The evidence that pretreatment with NAC reversed oxidative stress-induced changes in SW480 cell death validated the dependence on oxidative stress (**Figure 4B**). Oxidative stress may lead to cell apoptosis and autophagy; therefore, an apoptosis assay using flow cytometry was performed. These results revealed that nodosin induced cell apoptosis. The apoptosis rate gradually elevated with increased nodosin concentration. When the concentration of nodosin was 12 μM, the apoptosis rate of the cells was 16.11% (**Figures 4C,D**). Therefore, we speculated that there are other modes of cell death in addition to apoptosis. Elevated levels of ROS usually lead to stress in mitochondria, endoplasmic reticulum, and lysosomes; therefore, the changes in these cell organelles after nodosin treatment were observed by plasmid transfection assay. This study's findings showed that mitochondria and endoplasmic reticulum gradually disappeared with increased nodosin concentration, while lysosomes gradually increased. The endoplasmic reticulum and mitochondria almost completely disappeared at a nodosin concentration of 6 μM (**Figure 4E**). Based on this phenomenon, we hypothesized that these cells may have undergone autophagy. To verify whether nodosin can induce autophagy in cells, the autophagy blocker chloroquine was used to rescue nodosin-treated SW480 cells. Chloroquine rescued nodosin-induced SW480 cells cell death to a certain extent. At a chloroquine concentration of 6.25 nM, the relative cell activity increased by approximately 10%. These results illustrate that nodosin induced autophagy in SW480 cells (**Figure 4F**).

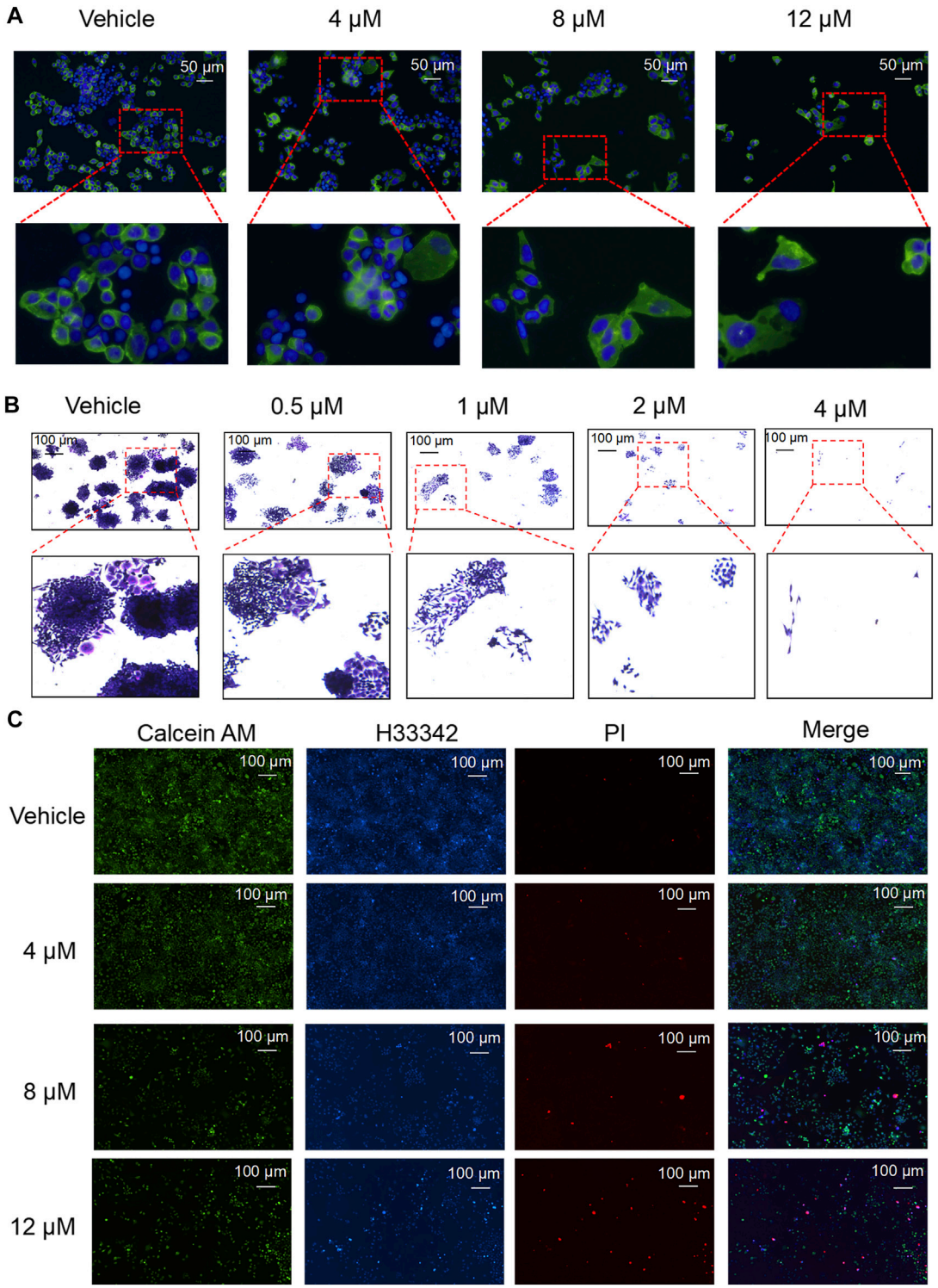

FIGURE 2 | Nodosin supressed cell proliferation and triggered cell death. **(A)** Nodosin-treated SW480 cells were stained with Dio and Hoechst 33342 (Dio stained membranes in green and Hoechst 33342 stained nucleus in blue). **(B)** Different concentrations of nodosin treated SW480 cells for 12 days. Crystal violet stained cell communities were observed with an inverted microscope. **(C)** Nodosin-treated SW480 cells were stained with Hoechest 33342, Calcein AM and PI. The stained results were recorded by fluorescence inverted microscope (Hoechest 33342 stained cells in blue, Calcein AM stained cells in green and PI stained cells in red).

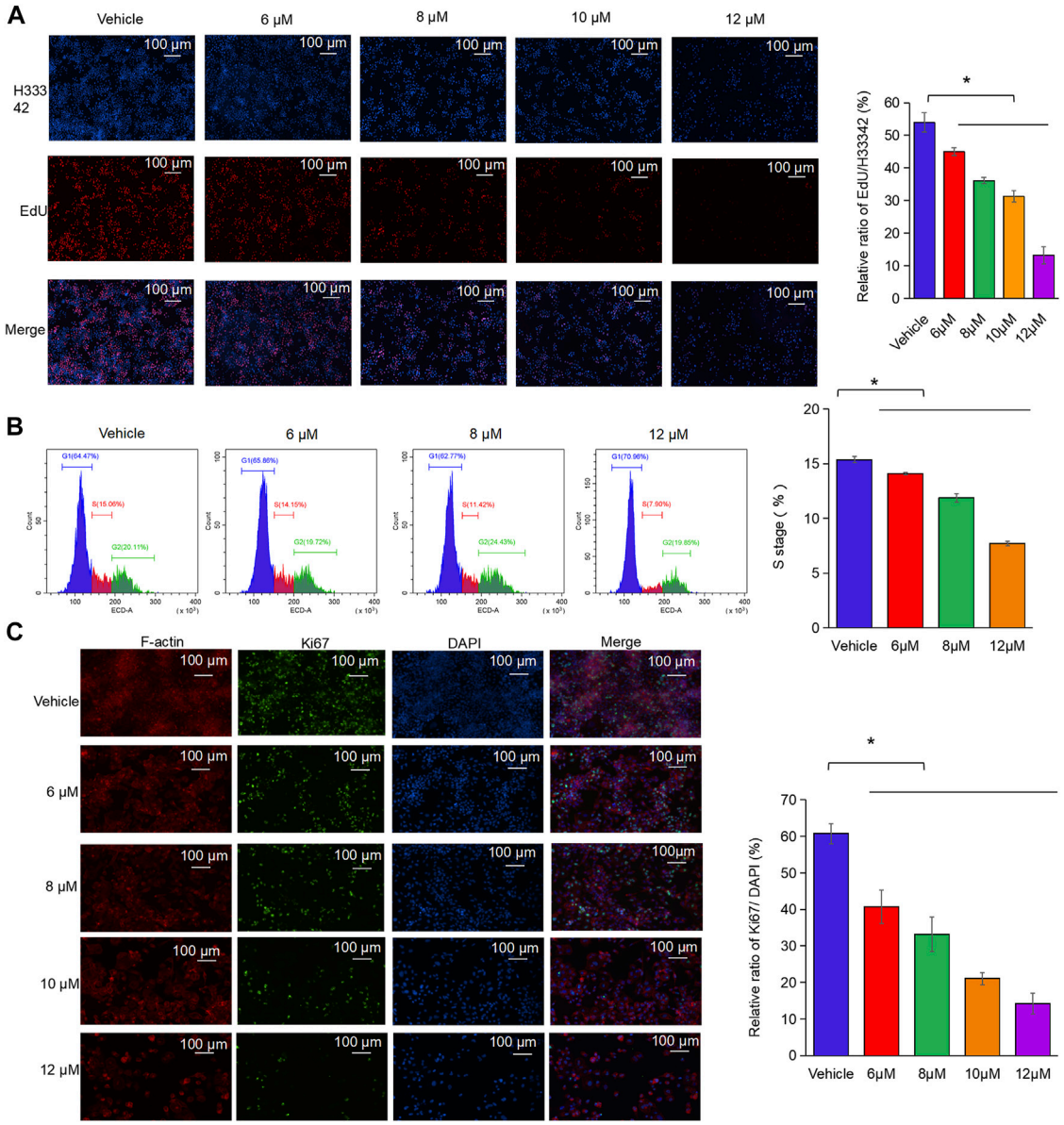

FIGURE 3 | Nodosin repressed the proliferation of CRC cells by inhibiting DNA synthesis. **(A)** Nodosin-treated SW480 cells were stained with EdU and Hoechst 33342, and then cell proliferation was observed with fluorescence inverted microscope (EdU stained cells in red, Hoechst 33342 stained cells in blue). **(B)** Nodosin-treated SW480 cells were stained with PI. The cell cycle of staining cells was detected by flow cytometry. The blue area was G1 phase cells, the red area was S phase cells, and the green area was G2 phase cells. The significant difference was evaluated with one-way ANOVA analysis followed by LSD Post Hocmultiple comparison, and p-value < 0.05 was considered significant. **(C)** SW480 cells were treated with different concentrations of nodosin for 24 h. The Ki67 was detected by IF. F-actin was red fluoreacence, Ki67 was green fluorescence, and DAPI was blue fluorescence. The significance difference was evaluated with one-way ANOVA analysis followed by LSD Post Hocmultiple comparison, and p-value < 0.05 was considered significant.

Transcriptomic Analysis of Nodosin Inhibition of CRC Tumors

To investigate the anticancer mechanism of nodosin, transcriptomic sequencing was performed. **Figure 5A** shows a volcano plot of differentially expressed genes (DEGs) between the nodosin treatment and control groups. With nodosin treatment, 205 genes were upregulated, and 376 genes were downregulated. Among them, *aldo-keto reductase family 1 member C1* (*AKR1C1*), *aldo-keto reductase family 1 member B10* (*AKRIB10*), *OSGIN1*, *HMOX1*, and *CTSL* were significantly upregulated, whereas *transcription factor 4* (*TCF4*), *TRIB3*, *syntrophin beta 1* (*SNTB1*), *kinase family member 21B* (*KIF21B*), *mitogen-activated protein kinase 6* (*MAP2K6*), *cadherin 11* (*CDH11*), *amphiregulin* (*AREG*), and *epiregulin* (*EREG*) were significantly downregulated. Most of these genes were involved in signaling pathways related to cell proliferation inhibition and

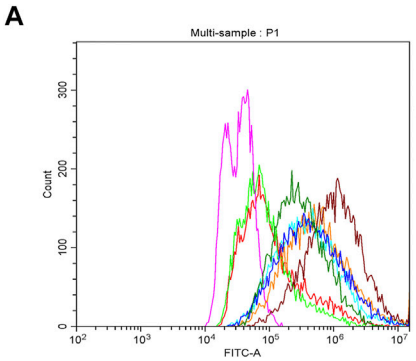

B

Group	Relative cell activity (%)
Vehicle	100%
Nodosin 12 μM	37.41%
NAC 2 mM	80.92%
Nodosin 12 μM+NAC 0.05 mM	65.83%
Nodosin 12 μM+NAC 0.1 mM	69.67%
Nodosin 12 μM+NAC 0.2 mM	71.25%
Nodosin 12 μM+NAC 0.5 mM	80.35%
Nodosin 12 μM+NAC 1 mM	78.64%
Nodosin 12 μM+NAC 1.5 mM	72.76%
Nodosin 12 μM+NAC 2 mM	64.42%

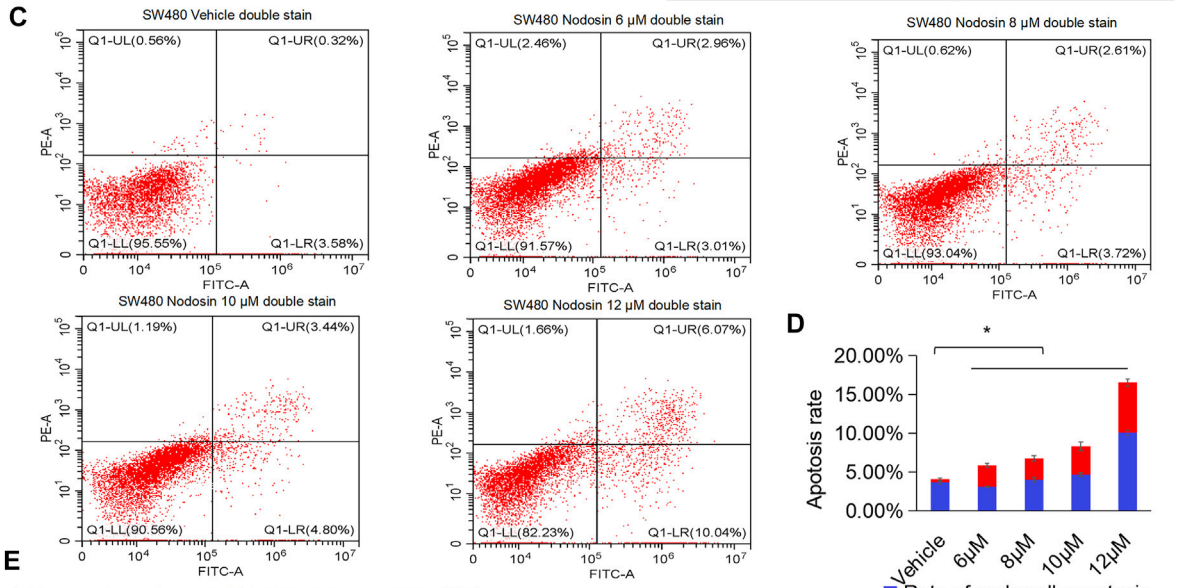

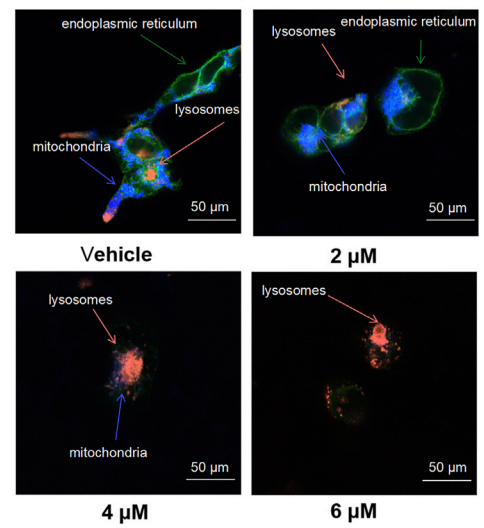

F

Group	Relative cell activity (%)
Vehicle	100%
Nodosin 12 μM	40.90%
CQ 250 nM	96.33%
Nodosin 12 μM+CQ 6.25 nM	50.41%
Nodosin 12 μM+CQ 12.5 nM	48.71%
Nodosin 12 μM+CQ 25 nM	48.61%
Nodosin 12 μM+CQ 50 nM	48.42%
Nodosin 12 μM+CQ 100 nM	46.76%
Nodosin 12 μM+CQ 125 nM	36.85%
Nodosin 12 μM+CQ 250 nM	32.52%

FIGURE 4 | Nodosin triggered cell death in CRC in a manner of oxidative stress, apoptosis and autophagy. **(A)** Intracellular ROS changes in SW480 caused by nodosin were determined by H_2DCFDA, red indicated the blank control (no ROS probe), light green indicated the solvent control (DMSO treatment, including the ROS probe), purple indicated the negative control (8 μM nodosin treatment, but with no ROS probe available), orange indicated the 5 μM nodosin treated and containing the ROS probe, light blue indicated the 8 μM nodosin treated and containing the ROS probe, dark blue indicated the 12 μM nodosin treated and containing the ROS probe, brown indicated the 16 μM nodosin treated and containing the ROS probe, dark green indicated a positive control (treated with 1 mM H_2O_2). **(B)** SW480 cells were pretreated with ROS inhibitor NAC for 1 h and treated with nodosin for 48 h. The relative viability of cells was detected by CCK-8 kit. **(C)** Flow cytometry was

(*Continued*)

FIGURE 4 | employed to determine the apoptosis rate. X axis represented FITC intensity of Annexin-V on the extracellular membrane, Y axis represented PI staining intensity of cells, early apoptotic cell populations were in Q1-LR, late apoptotic cell populations were in Q1-UR. **(D)** The rate of SW480 cells apoptosis. The significant difference was evaluated with one-way ANOVA analysis followed by LSD Post Hocmultiple comparison, and p-value < 0.05 was considered significant. **(E)** SW480 cells (transfected with lamp1 OFP, ER, and mito) were treated with different concentrations of nodosin. The intracellular changes in lysosomes, endoplasmic reticulum, and mitochondria were recorded by laser confocal microscopy. Orange represented lysosomes, blue represented mitochondria, and green representsed endoplasmic reticulum. **(F)** After SW480 cells were treated with nodosin for an appropriate period, different concentrations of chloroquine were added to rescue the nodosin-inactivated cells with the CCK-8 kit.

cell death induction. **Figure 5B** shows that gene ontology (GO) analysis was enriched in biological processes with more significant DEGs changes. We drew a heatmap of the DEGs involved in apoptosis and death. *HMOX1* was also upregulated (**Figure 5C**). These changes induced oxidative stress in the cells, which in turn induced apoptosis. To verify the high-throughput sequencing results, specific primers were designed for verification at the messenger RNA (mRNA) level. The results of PCR and qPCR showed that the *HMOX1* and *CTSL* levels, which are related to apoptosis and autophagy, were significantly increased (**Figures 5D,E**). Furthermore, WB was performed to verify whether nodosin affected the above pathways at the protein level. The results showed that the apoptosis-and autophagy-positive relative molecules HMOX1 and LC3 were significantly elevated (**Figure 5F**). Since the transcriptomic results indicated that nodosin affected the expression of genes related to oxidative stress, apoptosis, and autophagy in CRC cells, we validated it using the commonly used gene expression profiling interactive analysis (GEPIA) database in clinical practice. The results revealed that the gene TRIB3 negatively associated with oxidative stress was significantly downregulated, the genes *PHLDA3*, *LC3*, and *CTSL* related to apoptosis and autophagy were significantly upregulated in normal colorectal tissues compared to colorectal tumors (**Figure 5G**), while nodosin also reversed the expression of these genes, indicating that nodosin is beneficial for the treatment of CRC.

Nodosin Suppressed the Growth of CRC Xenografted Tumors *in Vivo*

To investigate the antitumor effect of nodosin on CRC *in vivo*, nude mouse subcutaneous tumorigenesis models were used for administration. **Figure 6A** shows the growth process of xenografted tumors in nude mice. Tumors in the nodosin-treated group grew slower than those in the control group. After the mice were terminated, tumors were isolated and photographed (**Figure 6B**). When the tumors were weighed, there was a significant difference in tumors weight between the treatment and control group (**Figure 6C**). There was no significant change in the bodyweight of nude mice in the two groups (**Figure 6D**), indicating that nodosin had no obvious side effects. H&E and IHC stainings of the pathological tumor sections were performed. H&E staining showed that compared with the control group, the cell structure of the tumor was destroyed, and the number of nuclei was also reduced (**Figure 6E**). The results of IHC staining revealed that the level of proliferation marker Ki67 was significantly lower in the nodosin-treated group than in the control group, indicating that treatment with nodosin could supress the proliferation of colorectal xenografted tumors. In addition, the expression of the apoptosis marker HMOX1 and the autophagy markers LC3 and CTSL were significantly increased in the nodosin-treated group, which indicated that nodosin could induce apoptosis and autophagy in colorectal tumor cells (**Figure 6F**).

DISCUSSION

It is difficult to completely cure CRC due to its high recurrence, easy metastasis, short survival time, limited treatment, and easy drug resistance emergence, which has become a challenging problem in the medical community (Vaghari-Tabari et al., 2020). The increasing incidence of CRC and the trend toward a younger onset have forced researchers to develop new drugs to replace existing drugs (Stoffel and Murphy, 2020). In recent years, natural plant-derived compounds have been found to target various signaling pathways with good tolerance and few toxic side effects (Rejhova et al., 2018). The combination of natural compounds and traditional chemotherapeutic drugs can be considered to provide new directions for the research and treatment of cancer.

Using cell and animal models, this study discovered that nodosin, a diterpenoid extracted from *Rabdosia serra (Maxim.) Hara* has antitumor activity against CRC. Furthermore, combined transcriptomic analysis revealed that nodosin could promote SW480 cell death through multiple pathways, including oxidative stress, apoptosis, and autophagy.

Oxidative stress and the resulting oxidative damage are important factors in tumorigenesis and progression (Klaunig 2018). Basak et al. (2020) found that oxidative stress is closely associated with the occurrence and development of CRC and that oxidative stress caused by excessive production of ROS can selectively eradicate tumor cells. This study found that nodosin increased ROS levels in CRC SW480 cells (**Figure 4A**). After the rescue of the antioxidant NAC, the activity of the cells significantly increased, indicating that the cells underwent oxidative stress (**Figure 4B**). *TRIB3*, a modulator of cellular responses to various stresses, is upregulated in various cancers (Tang et al., 2020). *TRIB3* expression in colorectal tumors was also higher compared to normal colorectal tissues in the GEPIA database (**Figure 5G**). This study found that nodosin could downregulate *TRIB3* expression, implying that nodosin may induce oxidative stress in cells. In addition, excessive ROS production can lead to oxidative stress and programmed cell

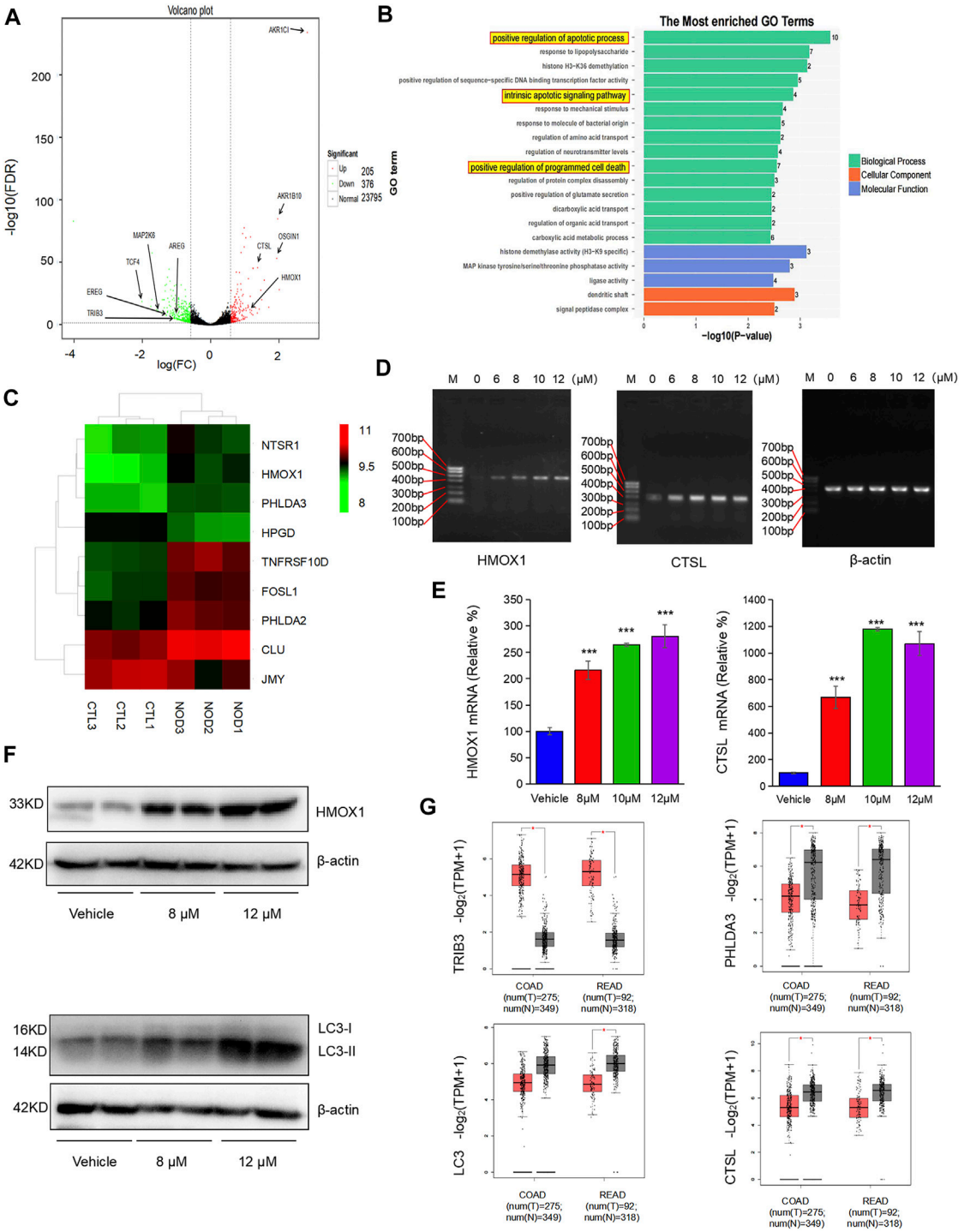

FIGURE 5 | Transcripptomic results demonstrated that nodosin induced oxidative stress, apoptosis, and autophagy. **(A)** Voclano plot of the differential genes between the nodosin treated and control groups. **(B)** GO analysis enriched for biological processes with more obvious differential gene changes, with more differential genes in biological processes related to apoptosis. **(C)** Heatmap of the differential genes associated with apoptosis between the nodosin treated and control groups. **(D)** The cDNA levels of *HMOX1*, *CTSL*, and *β-actin* were measured by PCR. **(E)** The mRNA levels of *HMOX1*, *CTSL*, and *β-actin* were detected by q-PCR. Each test was repeated three times, and the difference was tested by a two-tailed *t*-test. $^{*}p < 0.05$, $^{**}p < 0.01$, $^{***}p < 0.001$. **(F)** The protein levels of HMOX1, β-actin, and LC3 were tested by western blotting. **(G)** Expression of the oxidative stress, apoptotic and autophagy-related genes *TRIB3*, *PHLDA3*, *LC3*, and *CTSL* in clinical CRC and normal tissues (http://gepia.cancer-pku.cn/index.html, COAD: Colon adenocarcinoma; READ: Rectal adenocarcinoma, $^{*}p < 0.05$).

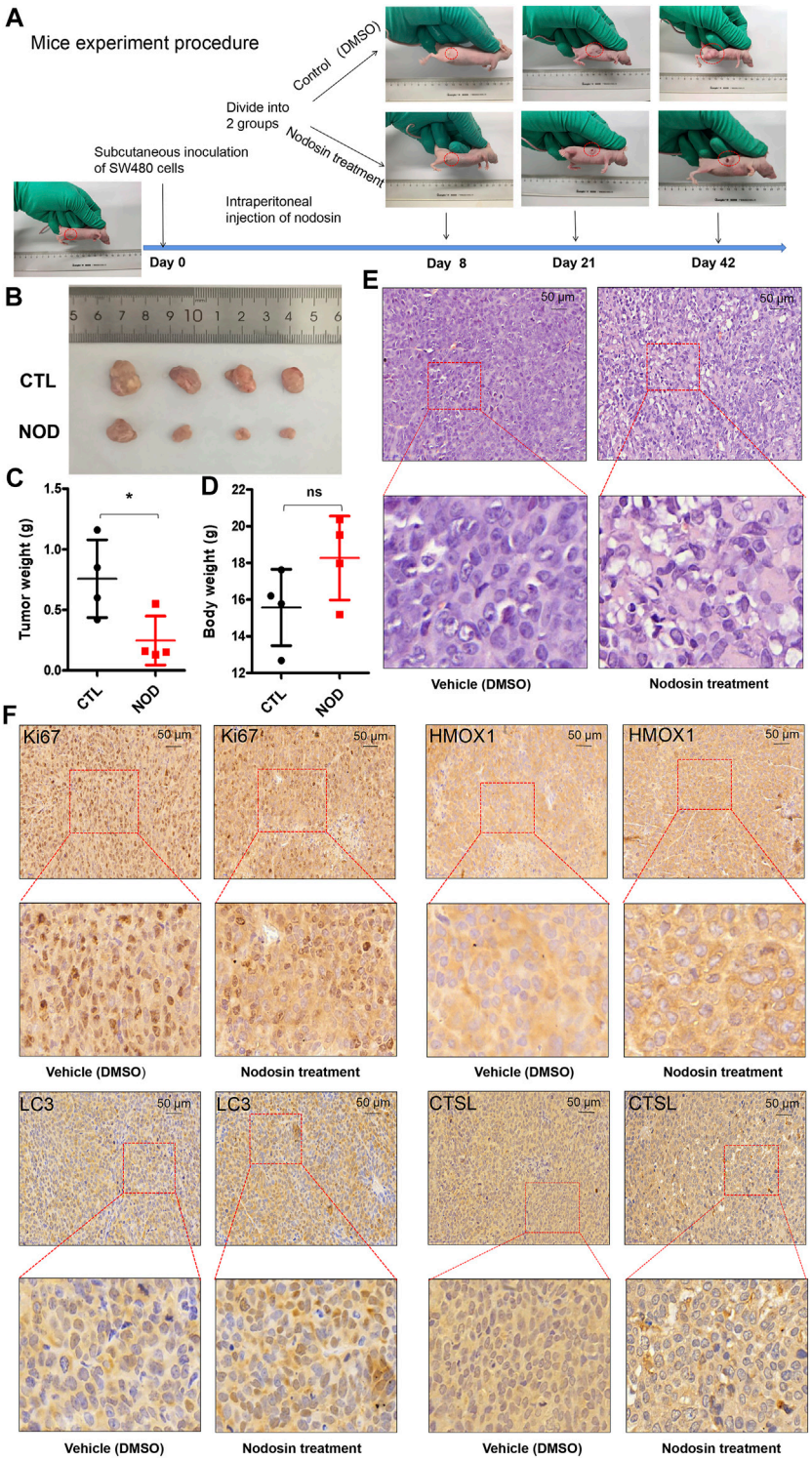

FIGURE 6 | Nodosin supressed the growth of CRC xenograft tumors in nude mice. **(A)** The whole procedure of the nude mice experiment. **(B)** The xenograft tumors isolated from nude mice. **(C)** Tumor weights were compared in nude mice from nodosin treated and control groups. **(D)** Body weight was compared from nodosin treated versus control groups. **(E)** The nodosin-treated and control xenograft tumors were stained with H&E. **(F)** IHC was used to detect the expression of Ki67, HMOX1, LC3, and CTSL in nodosin-treated and control group, and photographed under microscope.

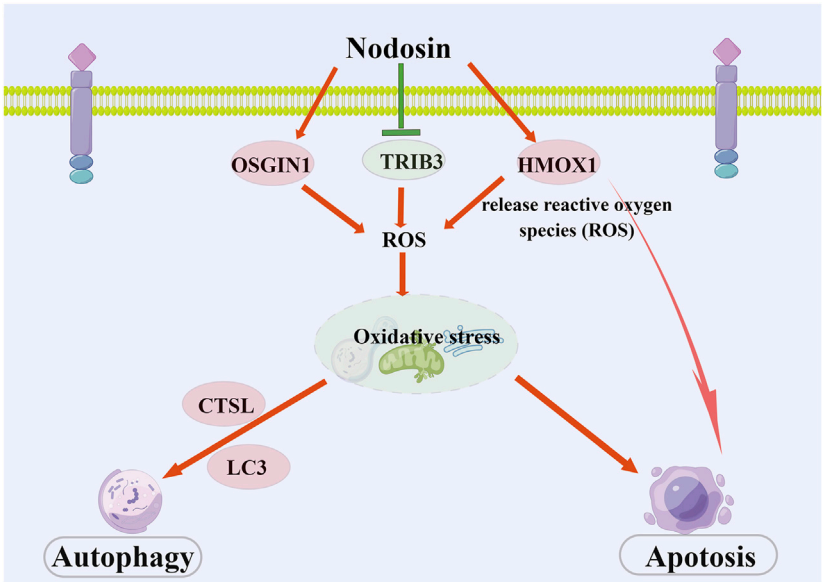

FIGURE 7 | The schematic diagram of pharmacological mechanism of nodosin against CRC. Nodosin inhibited CRC mainly by triggering oxidative stress, apoptosis, and autophagy. The observed pharmacological mechanism of action of nodosin on CRC is as follows: 1) Nodosin could downregulate TRIB3 and upregulate OSGIN1 to elevate ROS levels and induce oxidative stress in cells. Moreover, nodosin could upregulate HMOX1, induce heme breakdown, release ROS, promote oxidative stress in cells, and induce apoptosis. 2) Excessive ROS production could lead to oxidative stress in cells. Oxidative stress was able to induce apoptosis. Finally, mitochondria and endoplasmic reticulum were destroyed in response to oxidative stress. Lysosomes removed damaged organelles and induced cells to undergo autophagy, inducing upregulation of autophagy markers LC3 and CTSL expression. Nodosin promoted cell death by inducing CRC cells to undergo apoptosis and autophagy. This figure is drawn by Figdraw (www.figdraw.com).

death, such as apoptosis and autophagy (Gao et al., 2020). Tsai et al. (2017) found that the upregulation of *OSGIN1* could elevate ROS levels, activate PI3K/Akt/Nrf2 signaling, and trigger apoptosis in cells. Wang et al. (2017) found that OSGIN1 could induce autophagy-positive related molecules, such as LC3, at the protein and mRNA levels. Interestingly, our study found nodosin upregulated the expression of *OSGIN1* and *LC3*. Therefore, we speculated that nodosin was able to trigger oxidative stress, apoptosis, and autophagy in SW480 cells by increasing cellular ROS levels.

The transcriptomic analysis revealed that nodosin was able to activate intrinsic and extrinsic apoptotic signaling pathways in SW480 cells (**Figure 5B**). *HMOX1* was upregulated in the apoptotic signaling pathway. *HMOX1* triggered heme breakdown, releasing reactive oxide species and enhancing intercellular oxidative stress-induced apoptosis (Chiang et al., 2019). PCR, RT-PCR, WB, and IHC results showed that nodosin upregulated the HMOX1 expression, indicating that nodosin induced cell death in an *HMOX1* modulation-related manner. These results suggested that the cell death-promoting mechanism of nodosin was to induce apoptosis by upregulating *HMOX1*. Moreover, Gandini et al. (2019) found that upregulation of *HMOX1* could inhibit the growth of breast cancer tumors and prolong patient survival. Therefore, we considered the development of nodosin-based apoptosis inducers to induce CRC cells death.

ROS induces apoptosis and autophagy in cells. Autophagy is another programmed cell death pathway in addition to apoptosis. It has been reported that autophagy can kill anti-apoptotic cells (Li et al., 2017). In addition, autophagy responds to stressful conditions, including oxidative stress (Zhou et al., 2021). In different types of autophagy, lysosomes can degrade and remove oxidized/damaged proteins and large organelles that produce ROS (such as mitochondria and peroxisomes) (Mahapatra et al., 2021). Through co-transfection with three markers labeled endoplasmic reticulum, mitochondria, and lysosomes, we found that nodosin could cause the endoplasmic reticulum and mitochondria to vanish but increase lysosomes in a dose-dependent manner (**Figure 4E**). More importantly, nodosin-induced cell inactivation was significantly rescued by the autophagy blocker chloroquine, suggesting that autophagy may be an essential pathway in nodosin-triggered cell death (**Figure 4F**). Presently, markers related to autophagy mainly include CTSL and LC3. *CTSL*, which encodes lysosomal cysteine protease, promotes autophagic flux (Thirusangu et al., 2021). Han et al. (2016) found that upregulation of CTSL enhances the efficacy of anticancer drugs against lung cancer and other types of malignant tumor cells. Furthermore, the expression of another key autophagy-related protein, LC3, was significantly increased following nodosin treatment. LC3 plays a crucial role in autophagosome formation and autophagy development (Song et al., 2019). This study demonstrated that nodosin could upregulate the expression of CTSL (**Figures 5D–F**), suggesting that the cell death-promoting mechanism of nodosin-modulated CTSL, which in turn, caused autophagy in CRC cells. See et al. (2018) found that upregulation of the autophagy marker LC3 promotes autophagy and induces CRC cell death. Therefore, targeting autophagy-related proteins may be an effective treatment strategy for CRC.

In conclusion, nodosin repressed CRC mainly through the induction of oxidative stress, triggering apoptosis, and autophagy. This study revealed the molecular mechanisms of nodosin against CRC: 1) Downregulation of *TRIB3* and upregulation of *OSGIN1* to induce oxidative stress in cells; 2) Elevation of *HMOX1* expression to induce apoptosis; 3) Upregulation of *CTSL* and *LC3* expression to trigger autophagy (As shown in **Figure 7**). However, we could not exclude other possible molecular mechanisms. This research provides solid experimental evidence for the suppression of CRC and greatly contributes to developing novel drugs for CRC therapy.

DATA AVAILABILITY STATEMENT

Publicly available datasets were analyzed in this study. This data can be found here: The transcriptome data are uploaded on NCBI Sequence Read Archive and available *via* http://www.ncbi.nlm.nih.gov/bioproject/831009 (Bioproject ID: PRJNA831009).

ETHICS STATEMENT

The animal study was reviewed and approved by Ethics Committee of Jining Medical University.

AUTHOR CONTRIBUTIONS

Conceptualization: YS and YX; Methodology: HF, XH, and AL; Investigation: HF, XH, and YG; Formal analysis: HF and YX; Resources: YS and YX; Writing-original draft: HF; Writing-review and writing: all authors; Funding acquisition: JY and YX.

FUNDING

This work was supported by the Taishan Scholars Program of Shandong Province (tsqn201909147), the National Natural Science Foundation of China (82172978), the Key Project at Central Government Level: the ability establishment of sustainable use for valuable Chinese medicine resources (2060302), and the Scientific and technological innovation project of China Academy of Chinese Medical Sciences (CI 2021A01809).

ACKNOWLEDGMENTS

We would like to thank Editage (www.editage.cn) for English language checking.

REFERENCES

Akimoto, N., Ugai, T., Zhong, R., Hamada, T., Fujiyoshi, K., Giannakis, M., et al. (2021). Rising Incidence of Early-Onset Colorectal Cancer - a Call to Action. *Nat. Rev. Clin. Oncol.* 18 (4), 230–243. doi:10.1038/s41571-020-00445-1

Bae, E. S., Kim, Y. M., Kim, D. H., Byun, W. S., Park, H. J., Chin, Y. W., et al. (2020). Anti-Proliferative Activity of Nodosin, a Diterpenoid from Isodon Serra, via Regulation of Wnt/β-Catenin Signaling Pathways in Human Colon Cancer Cells. *Biomol. Ther. Seoul.* 28 (5), 465–472. doi:10.4062/biomolther.2020.003

Basak, D., Uddin, M. N., and Hancock, J. (2020). The Role of Oxidative Stress and its Counteractive Utility in Colorectal Cancer (CRC). *Cancers (Basel)* 12 (11). doi:10.3390/cancers12113336

Biller, L. H., and Schrag, D. (2021). Diagnosis and Treatment of Metastatic Colorectal Cancer. *Jama* 325 (7), 669–685. doi:10.1001/jama.2021.0106

Chen, C., Chen, Y., Zhu, H., Xiao, Y., Zhang, X., Zhao, J., et al. (2014). Effective Compounds Screening from Rabdosia Serra (Maxim) Hara against HBV and Tumor *In Vitro*. *Int. J. Clin. Exp. Med.* 7 (2), 384–392.

Chiang, S. K., Chen, S. E., and Chang, L. C. (2019). A Dual Role of Heme Oxygenase-1 in Cancer Cells. *Int. J. Mol. Sci.* 20 (1). doi:10.3390/ijms20010039

Gandini, N. A., Alonso, E. N., Fermento, M. E., Mascaró, M., Abba, M. C., Coló, G. P., et al. (2019). Heme Oxygenase-1 Has an Antitumor Role in Breast Cancer. *Antioxid. Redox Signal* 30 (18), 2030–2049. doi:10.1089/ars.2018.7554

Gao, L., Loveless, J., Shay, C., and Teng, Y. (2020). Targeting ROS-Mediated Crosstalk between Autophagy and Apoptosis in Cancer. *Adv. Exp. Med. Biol.* 1260, 1–12. doi:10.1007/978-3-030-42667-5_1

Han, M. L., Zhao, Y. F., Tan, C. H., Xiong, Y. J., Wang, W. J., Wu, F., et al. (2016). Cathepsin L Upregulation-Induced EMT Phenotype Is Associated with the Acquisition of Cisplatin or Paclitaxel Resistance in A549 Cells. *Acta Pharmacol. Sin.* 37 (12), 1606–1622. doi:10.1038/aps.2016.93

Isobe, T., and Nagata, K. (2010). Study on the Antibacterial Activity of Compounds from the Isodon Species. *Yakugaku Zasshi* 130 (3), 447–450. doi:10.1248/yakushi.130.447

Johdi, N. A., and Sukor, N. F. (2020). Colorectal Cancer Immunotherapy: Options and Strategies. *Front. Immunol.* 11, 1624. doi:10.3389/fimmu.2020.01624

Keum, N., and Giovannucci, E. (2019). Global Burden of Colorectal Cancer: Emerging Trends, Risk Factors and Prevention Strategies. *Nat. Rev. Gastroenterol. Hepatol.* 16 (12), 713–732. doi:10.1038/s41575-019-0189-8

Klaunig, J. E. (2018). Oxidative Stress and Cancer. *Curr. Pharm. Des.* 24 (40), 4771–4778. doi:10.2174/1381612825666190215121712

Li, J., Du, J., Sun, L., Liu, J., and Quan, Z. (2010). Anti-Inflammatory Function of Nodosin via Inhibition of IL-2. *Am. J. Chin. Med.* 38 (1), 127–142. doi:10.1142/S0192415X10007713

Li, Y. J., Lei, Y. H., Yao, N., Wang, C. R., Hu, N., Ye, W. C., et al. (2017). Autophagy and Multidrug Resistance in Cancer. *Chin. J. Cancer* 36, 52. doi:10.1186/s40880-017-0219-2

Lin, L., Zhuang, M., Lei, F., Yang, B., and Zhao, M. (2013). GC/MS Analysis of Volatiles Obtained by Headspace Solid-phase Microextraction and Simultaneous-Distillation Extraction from Rabdosia Serra (MAXIM.) HARA Leaf and Stem. *Food Chem.* 136 (2), 555–562. doi:10.1016/j.foodchem.2012.08.048

Mahapatra, K. K., Mishra, S. R., Behera, B. P., Patil, S., Gewirtz, D. A., and Bhutia, S. K. (2021). The Lysosome as an Imperative Regulator of Autophagy and Cell Death. *Cell Mol. Life Sci.* 78 (23), 7435–7449. doi:10.1007/s00018-021-03988-3

Rejhová, A., Opattová, A., Čumová, A., Vodička, D. P., and Vodicka, P. (2018). Natural Compounds and Combination Therapy in Colorectal Cancer Treatment. *Eur. J. Med. Chem.* 144, 582–594. doi:10.1016/j.ejmech.2017.12.039

Samec, M., Liskova, A., Koklesova, L., Mestanova, V., Franekova, M., Kassayova, M., et al. (2019). Fluctuations of Histone Chemical Modifications in Breast, Prostate, and Colorectal Cancer: An Implication of Phytochemicals as Defenders of Chromatin Equilibrium. *Biomolecules* 9 (12). doi:10.3390/biom9120829

Sarwar, M. S., Zhang, H. J., and Tsang, S. W. (2018). Perspectives of Plant Natural Products in Inhibition of Cancer Invasion and Metastasis by Regulating Multiple Signaling Pathways. *Curr. Med. Chem.* 25 (38), 5057–5087. doi:10.2174/0929867324666170918123413

See, C. S., See, M., Liao, P. J., Lee, K. H., Wong, J., Lee, S. H., et al. (2018). Discovery of the Cancer Cell Selective Dual Acting Anti-cancer Agent (Z)-2-(1H-indol-3-yl)-3-(isoquinolin-5-yl)acrylonitrile (A131). *Eur. J. Med. Chem.* 156, 344–367. doi:10.1016/j.ejmech.2018.07.011

Song, T., Su, H., Yin, W., Wang, L., and Huang, R. (2019). Acetylation Modulates LC3 Stability and Cargo Recognition. *FEBS Lett.* 593 (4), 414–422. doi:10.1002/1873-3468.13327

Stoffel, E. M., and Murphy, C. C. (2020). Epidemiology and Mechanisms of the Increasing Incidence of Colon and Rectal Cancers in Young Adults. *Gastroenterology* 158 (2), 341–353. doi:10.1053/j.gastro.2019.07.055

Talib, W. H., Alsalahat, I., Daoud, S., Abutayeh, R. F., and Mahmod, A. I. (2020). Plant-Derived Natural Products in Cancer Research: Extraction, Mechanism of Action, and Drug Formulation. *Molecules* 25 (22). doi:10.3390/molecules25225319

Tang, Z., Chen, H., Zhong, D., Wei, W., Liu, L., Duan, Q., et al. (2020). TRIB3 Facilitates Glioblastoma Progression via Restraining Autophagy. *Aging (Albany NY)* 12 (24), 25020–25034. doi:10.18632/aging.103969

Thirusangu, P., Pathoulas, C. L., Ray, U., Xiao, Y. N., Staub, J., Jin, L., et al. (2021). Quinacrine-Induced Autophagy in Ovarian Cancer Triggers Cathepsin-L Mediated Lysosomal/Mitochondrial Membrane Permeabilization and Cell Death. *Cancers* 13 (9). doi:10.3390/cancers13092004

Tsai, C. H., Shen, Y. C., Chen, H. W., Liu, K. L., Chang, J. W., Chen, P. Y., et al. (2017). Docosahexaenoic Acid Increases the Expression of Oxidative Stress-Induced Growth Inhibitor 1 through the PI3K/Akt/Nrf2 Signaling Pathway in Breast Cancer Cells. *Food Chem. Toxicol.* 108, 276–288. doi:10.1016/j.fct.2017.08.010

Vaghari-Tabari, M., Majidinia, M., Moein, S., Qujeq, D., Asemi, Z., Alemi, F., et al. (2020). MicroRNAs and Colorectal Cancer Chemoresistance: New Solution for Old Problem. *Life Sci.* 259, 118255. doi:10.1016/j.lfs.2020.118255

Van der Jeught, K., Xu, H. C., Li, Y. J., Lu, X. B., and Ji, G. (2018). Drug Resistance and New Therapies in Colorectal Cancer. *World J. Gastroenterol.* 24 (34), 3834–3848. doi:10.3748/wjg.v24.i34.3834

Wang, G., Zhou, H., Strulovici-Barel, Y., Al-Hijji, M., Ou, X., Salit, J., et al. (2017). Role of OSGIN1 in Mediating Smoking-Induced Autophagy in the Human Airway Epithelium. *Autophagy* 13 (7), 1205–1220. doi:10.1080/15548627.2017.1301327

Zhou, J., Li, X. Y., Liu, Y. J., Feng, J., Wu, Y., Shen, H. M., et al. (2021). Full-coverage Regulations of Autophagy by ROS: from Induction to Maturation. *Autophagy* 18 (6), 1240–1255. doi:10.1080/15548627.2021.1984656

Conflict of Interest: The authors declare that the research was conducted in the absence of any commercial or financial relationships that could be construed as a potential conflict of interest.

Publisher's Note: All claims expressed in this article are solely those of the authors and do not necessarily represent those of their affiliated organizations, or those of the publisher, the editors and the reviewers. Any product that may be evaluated in this article, or claim that may be made by its manufacturer, is not guaranteed or endorsed by the publisher.

Copyright © 2022 Fan, Hao, Gao, Yang, Liu, Su and Xia. This is an open-access article distributed under the terms of the Creative Commons Attribution License (CC BY). The use, distribution or reproduction in other forums is permitted, provided the original author(s) and the copyright owner(s) are credited and that the original publication in this journal is cited, in accordance with accepted academic practice. No use, distribution or reproduction is permitted which does not comply with these terms.

frontiers | Frontiers in Pharmacology

TYPE Review
PUBLISHED 08 August 2022
DOI 10.3389/fphar.2022.957771

Check for updates

OPEN ACCESS

EDITED BY
Peixue Ling,
Shandong University (Qingdao), China

REVIEWED BY
Lei Wang,
University of Cincinnati, United States
Xin Wei,
University of Texas Health Science Center at Houston, United States

*CORRESPONDENCE
Wei Xu,
weixu@sdu.edu.cn

SPECIALTY SECTION
This article was submitted to Pharmacology of Anti-Cancer Drugs, a section of the journal Frontiers in Pharmacology

RECEIVED 31 May 2022
ACCEPTED 27 June 2022
PUBLISHED 08 August 2022

CITATION
Lv H, Liu H, Sun T, Wang H, Zhang X and Xu W (2022), Exosome derived from stem cell: A promising therapeutics for wound healing.
Front. Pharmacol. 13:957771.
doi: 10.3389/fphar.2022.957771

COPYRIGHT
© 2022 Lv, Liu, Sun, Wang, Zhang and Xu. This is an open-access article distributed under the terms of the Creative Commons Attribution License (CC BY). The use, distribution or reproduction in other forums is permitted, provided the original author(s) and the copyright owner(s) are credited and that the original publication in this journal is cited, in accordance with accepted academic practice. No use, distribution or reproduction is permitted which does not comply with these terms.

Exosome derived from stem cell: A promising therapeutics for wound healing

Hui Lv, Hanxiao Liu, Ting Sun, Han Wang, Xiao Zhang and Wei Xu*

Department of Clinical Pharmacy, The First Affiliated Hospital of Shandong First Medical University & Shandong Provincial Qianfoshan Hospital, Jinan, China

A wound occurs when the epidermis and dermis of the skin are damaged internally and externally. The traditional wound healing method is unsatisfactory, which will prolong the treatment time and increase the treatment cost, which brings economic and psychological burdens to patients. Therefore, there is an urgent need for a new method to accelerate wound healing. As a cell-free therapy, exosome derived from stem cell (EdSC) offers new possibilities for wound healing. EdSC is the smallest extracellular vesicle secreted by stem cells with diameters of 30–150 nm and a lipid bilayer structure. Previous studies have found that EdSC can participate in and promote almost all stages of wound healing, including regulating inflammatory cells; improving activation of fibroblasts, keratinocytes, and endothelial cells; and adjusting the ratio of collagen I and III. We reviewed the relevant knowledge of wounds; summarized the biogenesis, isolation, and identification of exosomes; and clarified the pharmacological role of exosomes in promoting wound healing. This review provides knowledge support for the pharmacological study of exosomes.

KEYWORDS

exosome, stem cell, wound healing, therapeutics, wound

Introduction

The skin is the largest multifunctional organ in the body. It can prevent bacterial invasion and resist chemical and physical assaults by forming a strong barrier between the organism and the environment (Proksch et al., 2008; Wang et al., 2019). A wound is a disruption of normal anatomic structure and function because of internal and external breakage of the epidermis and dermis and occurs when the skin is torn and burned and has pressure ulcer and diabetes ulcer (Reinke and Sorg, 2012; Kanji and Das, 2017; Ayavoo et al., 2021). A prompt and suitable wound healing is necessary for the repair of functional tissues as well as disordered structures after an injury (Gurtner et al., 2008; Ayavoo et al., 2021). Normal wound healing is a sophisticated and dynamic activity that involves many physiological activities, such as inflammation, cell proliferation, and extracellular matrix remodeling (Wang et al., 2018). Chronic wounds fail to heal orderly and timely through

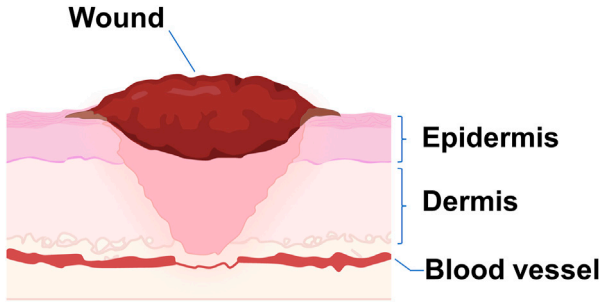

FIGURE 1
Schematical illustration of a wound. A wound occurs when the dermis and epidermis of the skin, as well as blood vessels, are damaged.

normal healing mechanisms (Velnar et al., 2009), which are characterized by long healing time and scar hyperplasia.

According to the statistics, chronic wounds affect more than 6 million people. It is anticipated that the number of people with chronic wounds will increase among our growing elderly and diabetes population (Powers et al., 2016). Chronic nonhealing wounds will make patients experience serious pain and become physically anxious (Järbrink et al., 2017), which would bring strong pressure on society (Järbrink et al., 2017). Therefore, the development of novel technologies and practices in the best practice clinical management of chronic wounds is imperative to diminish the possible burdens on the health and economy of the society and optimize the healthcare management for this prospective silent pandemic.

Conventional wound care methods include wound dressings (Han and Ceilley, 2017), skin substitutes (Dai et al., 2020), and growth factors (Shpichka et al., 2019). However, the drawbacks of these methods such as long healing time, immune rejection, high cost, and easy infection (Goodarzi et al., 2018; Vu et al., 2021) limit their application. In recent years, stem cells for wound healing have become one of their most important tools because of their strong self-renewal and differentiation ability (Nourian Dehkordi et al., 2019). Studies have confirmed that the effect of stem cell therapy has to do with the paracrine effect mediated by stem cell secretory factor exosomes (Yang J. et al., 2020). The exosome is the smallest extracellular vesicle, which is released into the extracellular environment after the fusion of late endosomes with the plasma membrane (Hessvik and Llorente, 2018). Exosome derived from stem cell (EdSC) is secreted by stem cells, which can transfer functional cargos such as proteins, DNA, and RNA from donor cells to the recipient cells (Nikfarjam et al., 2020; Gurung et al., 2021) and mediate intercellular communication to promote the activities of wound healing–related cells, such as fibroblasts and keratinocytes (Arishe et al., 2021). In this review, we reported the biogenesis, isolation, and identification of exosomes; elaborated on the mechanism of exosomes promoting wound healing; and discussed the clinical trials of exosomes in the treatment of wound healing.

Representative therapeutics for wound healing

Wounds are disruption of normal anatomic structure and function because of internal and external breakage of the epidermis and dermis (Reinke and Sorg, 2012; Kanji and Das, 2017; Ayavoo et al., 2021) (Figure 1). Current strategies for wound healing include wound dressings (Han and Ceilley, 2017), skin substitutes (Dai et al., 2020), and growth factors (Shpichka et al., 2019).

Wound dressings

Wound dressing is a sterile pad that is used in direct contact with the injury (Tang et al., 2021), which can keep a local moist environment around the wound, protect the wound from micro-organisms, and sustain good gas transmission (Kamoun et al., 2017). Common wound dressings include cotton gauze, human amniotic membrane, and polysaccharide-based factors (Zeng et al., 2018). However, traditional wound dressings are limited in providing a proper sterile environment for wounds (Farahani and Shafiee, 2021).

Skin substitutes

Skin substitutes are heterogenous biomaterials that can provide a substitute for the extracellular matrix to accelerate the healing process of wounds (Auger et al., 2009; Dai et al., 2020). According to different sources, it can be divided into allografts of human origin and xenografts of animal origin (FerreiraCastropaggiaro et al., 2011). This way provides a physical barrier from bacteria (Wei et al., 2022) and trauma and can keep a moist microenvironment in the wound bed (Dai et al., 2020), but allogenic skin grafts have the risk of immune rejection (Iy and Al-Rubaiy, 2009).

Growth factors

Growth factors can affect the microenvironment in the wound bed when released. (Dolati et al., 2020), such as promoting intercellular communication, including endothelial cells and fibroblasts (Werner and Grose, 2003). Although the direct application of growth factors is beneficial to wound healing, it also has certain limitations. For example, under the action of protein hydrolases, growth factors will degrade quickly (Golchin et al., 2018).

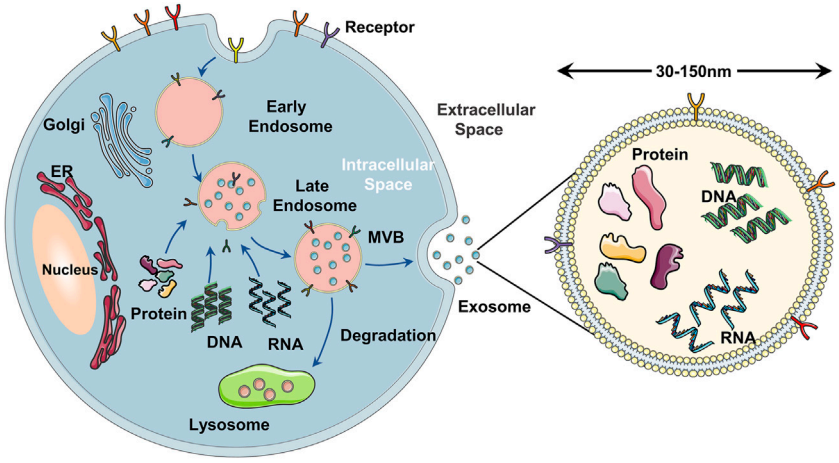

FIGURE 2
Schematical illustration of the exosome biogenesis. **(A)** the cell membrane forms early endosomes in the form of endocytosis. **(B)** the early endosomes mature into MVB containing exosomes after further acidification. **(C)** the MVB fuses with the cell membrane and releases exosomes into the extracellular space in the form of exocytosis.

Recent emerging novel tool: exosome derived from stem cell

Stem cells play an important role in wound healing and skin regeneration because of their strong self-renewal and differentiation ability (Mazini et al., 2020; Guillamat-Prats, 2021; Jo et al., 2021). The main tissue sources of stem cells for wound healing and skin regeneration include fat, bone marrow, and umbilical cord. In the process of wound treatment, using stem cells can close the wound early and reduce scar formation (Isakson et al., 2015; Guillamat-Prats, 2021). Of note, many studies have reported the effect of mesenchymal stem cells (MSCs) in wounds and regenerative medicine through their paracrine factors such as exosomes.

The emergence of EdSC offers new possibilities for wound healing. As a cell-free therapy, EdSC overcomes the limitations of stem cells. EdSC therapy is easy to use and time-saving and has low immune rejection (Ha et al., 2020). Studies have found that EdSC can induce benefits in nearly all phases of wound healing. For instance, it can inhibit inflammation, control immune responses, and promote cell proliferation and angiogenesis (He et al., 2019; Chen Md et al., 2021).

Biogenesis of exosome derived from stem cell

Exosomes are a subset of extracellular vesicles that are secreted by the majority of the types of cell-like dendritic cells, T cells, stem cells, and a variety of cancer cells (Isaac et al., 2021). According to the biogenesis and size, extracellular vesicles can be divided into exosomes, microvesicles, and apoptotic bodies (Crescitelli et al., 2013; Thakur et al., 2021). The diameter of exosomes is 30–150 nm, which is the smallest extracellular vesicle (Raposo and Stoorvogel, 2013). The release of exosomes occurs via three major steps (Figure 2): 1) Cell membrane invaginates to form primary endosomes, and the early endosomes are acidified into late endosomes. 2) The late endosomes bud inward to form a multivesicular body (MVB) (Tiwari A. et al., 2021). 3) Exosomes are released into the extracellular environment after the fusion of MVB and plasma membrane by exocytosis (Huotari and Helenius, 2011; Van Niel et al., 2018; Gurunathan et al., 2021). The exosomes secreted by stem cells such as adipose-derived stem cells and umbilical cord MSCs are EdSCs (Yu et al., 2014). EdSC contains many biomolecules of donor stem cells, such as DNA, RNA, nucleic acid, lipids, metabolites, and cytosolic (Kalluri and Lebleu, 2020; Gurung et al., 2021). Surrounded by lipid bilayers, EdSC can regulate cell–cell communication by transferring a lot of functional biomolecules to recipient cells (Tran et al., 2020; An et al., 2021; Arishe et al., 2021). As the main paracrine factors of stem cells, many studies established that EdSCs are also involved in the immune response (Hodge et al., 2021; Dai et al., 2022), cancer prevention and treatment (Jiang et al., 2022; Nik Nabil et al., 2022), antigen presentation (You et al., 2021; Zheng et al., 2022), angiogenesis (Yang et al., 2021), drug delivery (Riau et al., 2019; Ding et al., 2022; Rao et al., 2022), and inflammation (Shen et al., 2021). Multiple pharmacological effects make EdSC attract much attention in enhancing skin wound healing (Las Heras et al., 2020; Al Gailani et al., 2022; Dong et al., 2022; Opoku-Damoah et al., 2022).

Technologies for isolating exosome derived from stem cell

The isolation of pure EdSC is critical to understanding its mechanism and application to wound healing. Conventional methods include ultracentrifugation-based techniques, size-based techniques, and immunoaffinity capture-based techniques (Wu et al., 2019).

(1) For ultracentrifugation-based techniques: Ultracentrifugation-based techniques are known as the "gold standard" for EdSC isolation technology (Yang D. et al., 2020), which is according to the difference in size and density of each constituent in mixture solution (Livshits et al., 2015; Saad et al., 2021). Ultracentrifugation can be divided into density gradient ultracentrifugation and differential ultracentrifugation (Konoshenko et al., 2018; Gurunathan et al., 2019). Differential ultracentrifugation is easy to operate and low in cost (Zhao R. et al., 2021). However, compared with differential centrifugation, the purity of EdSC isolated by density gradient centrifugation is higher (Shirejini and Inci, 2021; Tarasov et al., 2021).
(2) For size-based techniques: Size exclusion chromatography is a typical technology for separation based on the size of exosomes. The sample containing exosomes flows through a stationary phase column filled with a porous matrix. The sample molecules smaller than the pore size can diffuse into the matrix and need a longer time to pass through the column, whereas large molecules get eluted faster (Tiwari S. et al., 2021). This method cannot distinguish EdSC and microvesicles of the same size, and the yield of exosomes is low. However, it is quick, easy, and cheap, and the isolated EdSCs are uniform in size and intact biophysically and functionally (Heydari et al., 2021; Purghe et al., 2021; Saad et al., 2021).
(3) For immunoaffinity capture-based techniques: Immunoaffinity-based isolation strategies use antibodies that were embedded with different materials such as magnetic beads (Kandimalla et al., 2021) to target the specific surface antigens of exosomes (Li S. et al., 2021). Then, antibody-recognized exosomes are captured (Alzhrani et al., 2021). This method can evidently increase the purity of EdSC and save time and samples of isolation (Li S. et al., 2021). However, the defect of this method is that it is not suitable for the isolation of large sample volumes (Alzhrani et al., 2021). Moreover, it only works with cell-free samples and isolates EdSC with low yield (Fu et al., 2019).

Tools for identifying exosome derived from stem cell

Once EdSCs are isolated, they need to be further quantified and analyzed (Li S. et al., 2021). According to the International Society of Extracellular Vesicles, the identification techniques of EdSCs can be based on morphology, size, and specific proteins on the surface of exosomes (Thery et al., 2018), such as electron microscope, nanoparticle tracking analysis (NTA), and western blot.

(1) For electron microscope: Electron microscopy techniques have been widely used to detect the morphology and size of EdSC (Alzhrani et al., 2021). It mainly includes a cryo-electron microscope and a transmission electron microscope (TME). In TME, two electron beams pass through the samples and are subsequently collected and magnified (Liu Q. et al., 2021). However, EdSCs show a saucer-like structure under TME (Zhao R. et al., 2021). Many researchers attribute this phenomenon to the collapse of samples caused by drying during sample processing (Cizmar and Yuana, 2017). Unlike TME, EdSCs detected using a cryo-electron microscope are round (Jin et al., 2021). This technique is now widely used since the destruction of the sample is avoided.
(2) For NTA: NTA can identify the dimension as well as the concentration of EdSC (Zara et al., 2020). The Brownian motion of suspended particles and light scattering are the basic principles of NTA (Pelissier Vatter et al., 2020; Zhao R. et al., 2021). By viewing in the mind each very small bit through image observations using either distributed widely light or gave out fluorescence, NTA measures the Brownian motion of person EdSC and connects it to a very small bit size (Carnino et al., 2019; Alzhrani et al., 2021). The advantages of this method include high detection sensitivity, easy sample preparation, fast analysis speed, and suitability for a large number of samples (Zara et al., 2020; Singh et al., 2021). However, this technique is accompanied by the problems of poor sensitivity, low efficiency of sorting targeted EdSC, and poor reproducibility (Jin et al., 2021).
(3) For western blot: Western blot identifies EdSC based on the specific proteins on the surface. Specific proteins (such as CD9, CD81, and CD63) are separated by electrophoresis and then combined with the corresponding antibodies (Zhao et al., 2019; Jalaludin et al., 2021). This identification method has high sensitivity and specificity (Singh et al., 2021). However, workflow is prolonged (Singh et al., 2021).

A promising therapeutics, exosome derived from stem cell, for wound healing

EdSC can be administered to the wound through intravenous injection and subcutaneous injection (Hu et al., 2016). After administration of EdSC to the wound site, it can induce benefits in almost all stages of wound healing, such as inhibiting

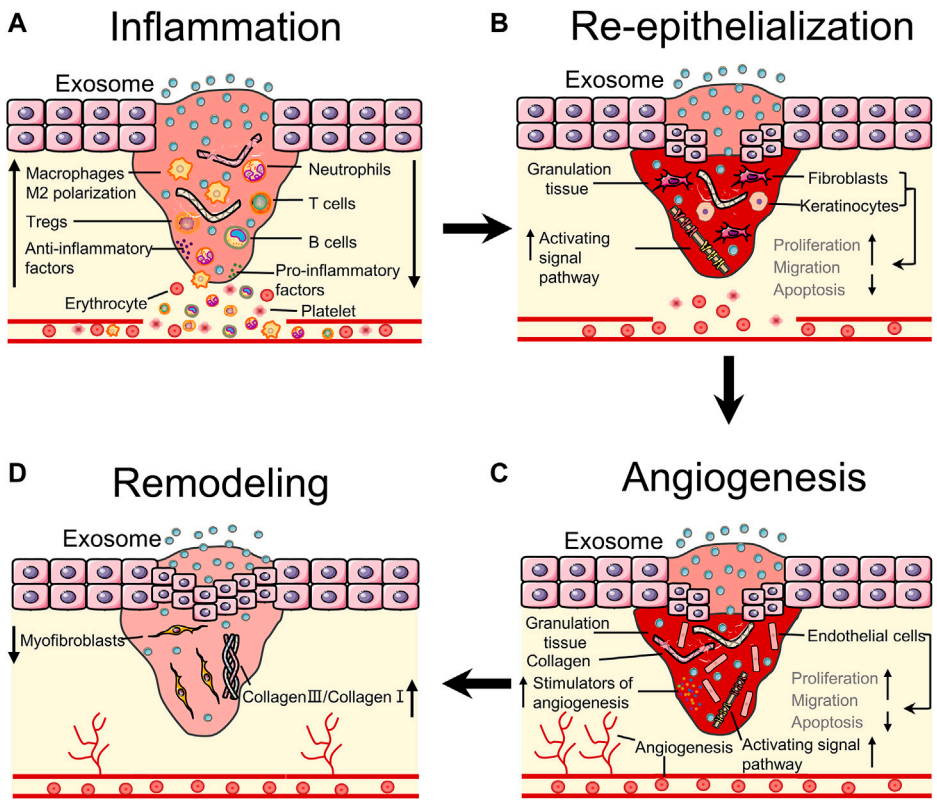

FIGURE 3
Bioeffects of stem cells derived exosomes on wound healing. **(A)** EdSC can inhibit inflammation by regulating the number of inflammatory cells and the polarization of macrophages. **(B)** EdSC can promote re-epithelialization by increasing the activity of fibroblasts as well as keratinocytes and activating pathways. **(C)** EdSC can improve angiogenesis by stimulating the release of angiogenic factors and regulating the activity of endothelial cells. **(D)** EdSC can improve tissue remodeling by regulating the ratio of collagen and myofibroblast differentiation.

inflammation by controlling immune cells, accelerating wound closure and angiogenesis by promoting proliferation and migration of cells, and reducing scar formation by regulating the proportion of collagen (Li D. et al., 2018; Wei et al., 2021). This part mainly discusses the delivery systems and mechanisms of EdSC that promote wound healing (Figure 3).

Exosome derived from stem cell delivery systems for wound healing

The most common way of administration of EdSC is intravenous injection. For instance, delivering EdSC to the wound site of mice through intravenous injection can stimulate the activities of fibroblasts, to accelerate wound healing (Hu et al., 2016). Subcutaneous injection is another delivery method of EdSC for wound healing. Liu et al. injected melatonin-stimulated EdSCs subcutaneously into the wound and found that EdSCs enhance diabetic wound healing by regulating the polarization of macrophage M1 phenotype to M2 phenotype through targeting PTEN/AKT pathway (Liu et al., 2020). Although the method of direct injection seems more efficient, it is highly invasive (Kosaka et al., 2012; Akbari et al., 2020). Although injection is simple and effective, it can limit EdSC therapeutic function because the clearance rate of this route is relatively rapid (Takahashi et al., 2013). In recent years, many researchers have combined EdSC with hydrogel to prolong the efficacy time and improve the stability of EdSC, to accelerate wound healing. As a new dressing, a hydrogel is a three-dimensional structure formed by physical or chemical crosslinking between hydrophilic polymer chains (Zhao Y. et al., 2021; Ma and Wu, 2022; Safari et al., 2022). Hydrogels can load EdSC by absorbing a large amount of solution containing EdSC because of the hydrophilic functional groups in polymers (Xu et al., 2018; Golchin et al., 2022). Applying the EdSC-loaded hydrogel dressing to the wound bed, the hydrogel network can control the release concentration and time of EdSC and increase the moisture content of the wound (Kim et al., 2017; Shafei et al., 2020). It maintains a good microenvironment in the wound bed that supports the activities of loaded cells to accelerate wound healing (Kim et al., 2017; Riha et al., 2021). Hence, hydrogels are utilized as desirable therapeutic agents for EdSC on wound healing.

Inflammation

Inflammation is characterized by removing debris and preventing infection through activation and recruitment of resident immune cells, such as neutrophils, mast cells, and eosinophils (Wang et al., 2018). Accumulating evidence suggests that EdSCs inhibit the process of inflammation in various pathways. Studies have confirmed that MSC-exosomes can block the infiltration of neutrophils and reduce the number of neutrophils in wounds to prevent excessive inflammation (Li et al., 2016; Shojaati et al., 2019). In addition, MSC-exosomes from different sources reduce pro-inflammatory factors such as IL-1, IL-6, TNF-α, IFN-γ, IL-17, TNF-α, and IL-1β along with increase anti-inflammatory factors such as IL-10, TSG-6, IL-4, and TGF-β in wounds to accelerate the inflammatory process (Liu et al., 2014; Chen et al., 2016; Nojehdehi et al., 2018; Li K. L. et al., 2021; Shen et al., 2021). In the later stage of inflammatory, pro-inflammatory M1 macrophages are transformed into anti-inflammatory M2 macrophages, which can activate fibroblasts, keratinocytes, and endothelial cells to promote re-epithelialization as well as angiogenic processes (Rani and Ritter, 2016; Sorg et al., 2017). For one thing, Xu et al. found that under LPS stimulation, exosomes from BMSCs resulted in an increase in M2 macrophage polarization and a decrease in M1 macrophage polarization (Xu et al., 2019). For another thing, some researchers have found that stem cell–derived exosomes from different sources can also induce the polarization of macrophage M1 phenotype to M2 phenotype through various biological pathways. For example, exosomes derived from MSCs stimulated by melatonin have been shown to enhance diabetic wound healing by targeting the PTEN/AKT pathway (Liu et al., 2020). Meanwhile, Khare et al. demonstrated that BMSC-derived exosomes promote the inflammation process by decreasing the proliferation and activation of B cells (Khare et al., 2018). In addition, EdSC also can suppress inflammatory T cell proliferation (Blazquez et al., 2014; Di Trapani et al., 2016; Monguio-Tortajada et al., 2017), activate T cells into T regulatory cells (Chen et al., 2016), and increase the number and proliferation of Tregs (Del Fattore et al., 2015; Chen et al., 2016; Du et al., 2018; Nojehdehi et al., 2018; Zhang et al., 2018; Riazifar et al., 2019; Li K. L. et al., 2021). In the immune system, dendritic cells are the cells that present antigens that can enhance T cell proliferation (Xie et al., 2020). Reis et al. found that dendritic cells can be inhibited by exosome treatment, which indirectly inhibits T cell activity (Reis et al., 2018). Therefore, all evidence suggests that SCdEs have anti-inflammatory potential and the ability to prevent excessive inflammation.

Re-epithelialization

In the phase of re-epithelialization, fibroblasts proliferate and migrate in large numbers and produce and deposit ECM to form granulation tissues that replace initial fibrin clots and repair tissue losses (Wilkinson and Hardman, 2020). EdSCs were readily taken up by fibroblasts that stimulate cell activity to promote wound healing (Hu et al., 2016; Chen Md et al., 2021; Tutuianu et al., 2021). As a scaffold, granulation tissue supports migration as well as the proliferation of wound cells and promotes new angiogenesis. Meanwhile, fibroblasts can stimulate keratinocytes by secreting keratinocyte-derived growth factors, which can undergo a partial epithelial–mesenchymal transition (Sorg et al., 2017). Then, keratinocytes proliferate and migrate toward the wound center until contact with reverse cells stops (Han and Ceilley, 2017). EdSC can promote wound healing by regulating keratinocyte and fibroblast characteristics and enhancing re-epithelialization. In addition, ADSC-derived exosomes enhance keratinocyte activities by activating Wnt/β-catenin signaling, AKT/HIF-1alpha signaling, or AKT pathway to promote wound healing (Ma et al., 2019; Zhang et al., 2020). According to Chen et al., highly expressed microRNA-21 in ADSC-exosomes can increase the MMP-9 expression via the PI3K/AKT to promote the activity of the keratinocytes (Yang C. et al., 2020). Moreover, ADSC-exosomes inhibited miR-19b expression via lncRNA H19 (H19) and activated the Wnt/β-catenin pathway using upregulated SPY-related high-mobility group box 9 (SOX9), resulting in enhanced human skin fibroblast function (Miao et al., 2021; Qian et al., 2021). Human ADSC-exosomes contain lncRNA MALAT1, which is capable of increasing fibroblast migration in the dermis (Cooper et al., 2018). Jeffrey et al. suggested that $CD63^{+}$ exosomes from BMSCs contribute to the transport exterior Wnt3a signal to recipient cells significantly, thereby promoting fibroblast and endothelial functions (Mcbride et al., 2017). In addition, the study also found that umbilical cord–derived MSC (uMSC)-exosomes contain microRNAs such as miR-21, miR-23a, and miR-125b, which can suppress the differentiation of fibroblasts into myofibroblasts formation via inhibiting collagen deposition (Mcbride et al., 2017) to accelerated re-epithelialization (Fang et al., 2016; Li D. et al., 2021). Taken together, the role of exosomes in promoting re-epithelialization is mainly achieved by enhancing the function of keratinocytes and fibroblasts.

Angiogenesis

Angiogenesis is another important process in the proliferative phase. Promoting angiogenesis is the main factor for stem cell–derived exosomes to promote wound healing. Angiogenesis provides oxygen, blood supply, and metabolic pathways for wound healing. Hypoxic environment after injury has induced the release of fibroblast growth factor 2 and vascular endothelial growth factor A. This stimulates vascular endothelial cell proliferation to build new blood vessels. TutuiaNu et al. demonstrated that exosomes

stimulated endothelial cell migration via scratch test assay (Tutuianu et al., 2021). In addition, stimulators of angiogenesis such as angiopoietin-2 (Ang-2) and endothelin (ET-1) were found in EdSC (Tutuianu et al., 2021). Meanwhile, exosomes derived from human uMSCs can improve angiogenesis by delivering angiopoietin-2 to promote wound healing (Liu J. et al., 2021). Wounds in the feet of diabetic rats treated with exosomes from ADSCs overexpressing Nrf2 exhibited reduced ulcer area, granulation tissue formation, enhanced growth factor expression, and increased angiogenesis (Li X. et al., 2018). In recent years, it is reported that embryonic stem cell–derived exosomes can activate Nrf2 to improve endothelial senescence (Chen B. et al., 2019). Some studies have found that stem cell–derived exosomes can transfer RNA or protein, such as miR-125a (Liang et al., 2016), miR-31 (Kang et al., 2016), miR-21 (An et al., 2019), and DMBT1 protein (Chen et al., 2018), to promote angiogenesis for wound healing. Ding et al. demonstrated that exosomes from human BMSCs can stimulate angiogenesis by activating the PI3K/AKT signaling pathway *in vitro* (Ding et al., 2019). Signaling pathways with similar efficacy include AKT/eNOS pathway (Yu et al., 2020) and Wnt4/β-Catenin pathway (Zhang et al., 2015). As mentioned above, stem cell–derived exosomes accelerate wound healing via promoting angiogenesis.

Remodeling

In the remodeling stage, the primary task is to reduce scar formation. Uncontrolled accumulation of myofibroblasts that contract the wound and excessive proportion of collagen III in the wound lead to scar formation (Zeng and Liu, 2021). In granulation tissue, collagen I replaced collagen III gradually to promote scar-free repair. In recent years, some studies observed the effects of exosomes on matrix remodeling. Liu et al. injected exosomes secreted by human ADSCs intravenously into murine incisional wounds and found that ADSC-exosomes can reconstruct ECM in wound bed by regulating the proportion of collagen-like type III to type I and reduce scar formation by regulating differentiation of fibroblast (Wang et al., 2017; Wang et al., 2021). MiR-192-5p expressing exosomes derived from human ADSCs can mitigate hypertrophic scar fibrosis by modulating the smad pathway. Its performance in wound healing is attenuated collagen deposition, transdifferentiation of fibroblasts to myofibroblasts, and formation of hypertrophic scars (Li Y. et al., 2021). In addition, microRNAs enriched in epidermal stem cell–derived exosomes (EPSC-exos) include miR-16, let-7a, miR-425-5p, and miR-142-3p (Duan et al., 2020). EPSC-exos-specific microRNAs, such as miR-425-5p and miR-142-3p, can reduce the TGF-β1 expression in dermal fibroblasts to inhibit myofibroblast differentiation (Duan et al., 2020). Furthermore, EdSC suppressed scar formation by reducing collagen deposition and regulating inflammation (Jiang et al., 2020). The findings of li et al. indicated that ADSCs-exosomes facilitate scar-free healing by enhancing the characteristics of fibroblasts (Hu et al., 2016; 2020). EdSC increased collagen I and III production through systemic administration at the initial stage of wound healing, whereas EdSC may inhibit collagen expression to reduce scar formation in the late stage (Hu et al., 2016). Taken together, EdSC can reduce scar formation by regulating the proportion of collagen.

Clinical applications of exosomes in wound healing therapy

The therapeutic potential of stem cells and EdSC for wound treatment have been conducted in various kinds of animal studies. It demonstrated that stem cell injection not only effectively suppresses inflammation but also enhances re-epithelialization and angiogenesis and reduces scar formation, which can promote the repair of skin wounds through secretion of stem cell-like EdSC. However, the structure and physiology of animal skin are different from those of human skin. Therefore, it is important to understand the mechanism of EdSC in human skin wounds.

From clinicaltrials.gov, we retrieved several clinical trials about wound healing treated with MSCs, but only two have exosomes. Using stem cells to treat burns as early as 2005, this study demonstrates that BM-MSC therapy is safe, which promoted angiogenesis and accelerated granulation tissue formation (Rasulov et al., 2005). Another completed clinical trial, which began in 2019, used stem cell–conditioned medium containing exosomes or microbubbles to treat chronic ulcerative wounds and found that conditioned medium stem cells can improve skin ulcer healing as an additional growth factor for the first time (NCT04134676). In addition, we retrieved a clinical trial initiated by Kumamoto University—the effect of plasma-derived exosomes on skin wound healing. Participants' wounds were treated with plasma rich in exosomes for 28 days to evaluate the effect of exosomes on skin wound healing (NCT0256526). This study found that compared with normal subjects, patients with chronic wounds such as skin ulcers had significantly lower levels of serum exosomes. In conclusion, the results of existing clinical trials show that exosomes can accelerate skin wound healing.

Similar to wound treatment, we can retrieve 258 clinical trials when the key word is exosome, such as for periodontitis (NCT04270006), melanoma (NCT02310451), chronic low back pain (NCT04849429), knee osteoarthritis (NCT05060107), and COVID-19 (NCT05216562). With the increasing number of clinical trials on the therapeutic effect of exosomes, it is believed that exosomes will come out as a therapeutic drug as soon as possible.

Conclusion

EdSCs are small in size and efficient, have low immune rejection, and have special physiological and biological functions, which have significant advantages for the treatment of wounds. With scientific and technological progress, a deeper understanding of EdSC, and the treatment of related diseases in the medical field, interdisciplinary integration will complement and enhance the application of EdSC in various fields. For example, combining the advantages of exosomes as carriers with advanced design methods of nano-medicine can establish a nano-treatment platform based on EdSC. In addition, understanding the interaction between exosomes and other organelles is helpful to better understand the process of disease (Chen Q. et al., 2019; Chen et al., 2020). The most difficult component of the research of exosomes is the inadequate number of exosomes meeting the application standards. In the near future, advances in the scaling-up technology for GMP-compliant exosome manufacturing will enhance the applications of exosomes for wound healing.

Author contributions

HL investigated the literature. TS wrote the manuscript, and HW and XZ revised the figures. WX guided and revised the overall structure and content of the review.

Funding

Mild photothermal targeted therapy remolds the microenvironment to improve the therapeutic sensitivity of PD-1 breast cancer and its mechanism (ZR2021MH118). Application of multifunctional liposome nanoreactor in tumor therapy (202102065). Study on the synergistic effect of PD-1 on triple-negative breast cancer based on tumor microenvironment remodeling (202019176).

Conflict of interest

The authors declare that the research was conducted in the absence of any commercial or financial relationships that could be construed as a potential conflict of interest.

Publisher's note

All claims expressed in this article are solely those of the authors and do not necessarily represent those of their affiliated organizations, or those of the publisher, the editors, and the reviewers. Any product that may be evaluated in this article, or claim that may be made by its manufacturer, is not guaranteed or endorsed by the publisher.

References

Akbari, A., Jabbari, N., Sharifi, R., Ahmadi, M., Vahhabi, A., Seyedzadeh, S. J., et al. (2020). Free and hydrogel encapsulated exosome-based therapies in regenerative medicine. *Life Sci.* 249, 117447. doi:10.1016/j.lfs.2020.117447

Al Gailani, M., Liu, M., and Wen, J. (2022). Ligands for oral delivery of peptides across the blood-brain-barrier. *Acta Mater. Medica* 1, 1. doi:10.15212/amm-2021-0007

Alzhrani, G. N., Alanazi, S. T., Alsharif, S. Y., Albalawi, A. M., Alsharif, A. A., Abdel-Maksoud, M. S., et al. (2021). Exosomes: Isolation, characterization, and biomedical applications. *Cell Biol. Int.* 45, 1807–1831. doi:10.1002/cbin.11620

An, T., Chen, Y., Tu, Y., and Lin, P. (2021). Mesenchymal stromal cell-derived extracellular vesicles in the treatment of diabetic foot ulcers: Application and challenges. *Stem Cell Rev. Rep.* 17, 369–378. doi:10.1007/s12015-020-10014-9

An, Y., Zhao, J., Nie, F., Qin, Z., Xue, H., Wang, G., et al. (2019). Exosomes from adipose-derived stem cells (ADSCs) overexpressing miR-21 promote vascularization of endothelial cells. *Sci. Rep.* 9, 12861. doi:10.1038/s41598-019-49339-y

Arishe, O. O., Priviero, F., Wilczynski, S. A., and Webb, R. C. (2021). Exosomes as intercellular messengers in hypertension. *Int. J. Mol. Sci.* 22, 11685. doi:10.3390/ijms222111685

Auger, F. A., Lacroix, D., and Germain, L. (2009). Skin substitutes and wound healing. *Skin. Pharmacol. Physiol.* 22, 94–102. doi:10.1159/000178868

Ayavoo, T., Murugesan, K., and Gnanasekaran, A. (2021). Roles and mechanisms of stem cell in wound healing. *Stem Cell Investig.* 8, 4. doi:10.21037/sci-2020-027

Blazquez, R., Sanchez-Margallo, F. M., De La Rosa, O., Dalemans, W., Alvarez, V., Tarazona, R., et al. (2014). Immunomodulatory potential of human adipose mesenchymal stem cells derived exosomes on *in vitro* stimulated T cells. *Front. Immunol.* 5, 556. doi:10.3389/fimmu.2014.00556

Carnino, J. M., Lee, H., and Jin, Y. (2019). Isolation and characterization of extracellular vesicles from broncho-alveolar lavage fluid: A review and comparison of different methods. *Respir. Res.* 20, 240. doi:10.1186/s12931-019-1210-z

Chen, B., Sun, Y., Zhang, J., Zhu, Q., Yang, Y., Niu, X., et al. (2019a). Human embryonic stem cell-derived exosomes promote pressure ulcer healing in aged mice by rejuvenating senescent endothelial cells. *Stem Cell Res. Ther.* 10, 142. doi:10.1186/s13287-019-1253-6

Chen, C. Y., Rao, S. S., Ren, L., Hu, X. K., Tan, Y. J., Hu, Y., et al. (2018). Exosomal DMBT1 from human urine-derived stem cells facilitates diabetic wound repair by promoting angiogenesis. *Theranostics* 8, 1607–1623. doi:10.7150/thno.22958

Chen Md, G., Wu Md, Y., Zou Md, L., and Zeng Md, Y. (2021). Effect of MicroRNA-146a modified adipose-derived stem cell exosomes on rat back wound healing. *Int. J. Low. Extrem. wounds* 1. doi:10.1177/15347346211038092

Chen, Q., Shao, X., Hao, M., Fang, H., Guan, R., Tian, Z., et al. (2020). Quantitative analysis of interactive behavior of mitochondria and lysosomes using structured illumination microscopy. *Biomaterials* 250, 120059. doi:10.1016/j.biomaterials.2020.120059

Chen, Q., Shao, X., Tian, Z., Chen, Y., Mondal, P., Liu, F., et al. (2019b). Nanoscale monitoring of mitochondria and lysosome interactions for drug screening and discovery. *Nano Res.* 12, 1009–1015. doi:10.1007/s12274-019-2331-x

Chen, W., Huang, Y., Han, J., Yu, L., Li, Y., Lu, Z., et al. (2016). Immunomodulatory effects of mesenchymal stromal cells-derived exosome. *Immunol. Res.* 64, 831–840. doi:10.1007/s12026-016-8798-6

Cizmar, P., and Yuana, Y. (2017). Detection and characterization of extracellular vesicles by transmission and cryo-transmission electron microscopy. *Methods Mol. Biol.* 1660, 221–232. doi:10.1007/978-1-4939-7253-1_18

Cooper, D. R., Wang, C., Patel, R., Trujillo, A., Patel, N. A., Prather, J., et al. (2018). Human adipose-derived stem cell conditioned media and exosomes containing MALAT1 promote human dermal fibroblast migration and ischemic wound healing. *Adv. Wound Care* 7, 299–308. doi:10.1089/wound.2017.0775

Crescitelli, R., Lässer, C., Szabó, T. G., Kittel, A., Eldh, M., Dianzani, I., et al. (2013). Distinct RNA profiles in subpopulations of extracellular vesicles: Apoptotic bodies, microvesicles and exosomes. *J. Extracell. Vesicles* 2, 20677. doi:10.3402/jev.v2i0.20677

Dai, C., Shih, S., and Khachemoune, A. (2020). Skin substitutes for acute and chronic wound healing: An updated review. *J. Dermatol. Treat.* 31, 639–648. doi:10.1080/09546634.2018.1530443

Dai, H., Fan, Q., and Wang, C. (2022). *Recent applications of immunomodulatory biomaterials for disease immunotherapy*. Hoboken, NJ: Exploration, 20210157. n/a.

Del Fattore, A., Luciano, R., Pascucci, L., Goffredo, B. M., Giorda, E., Scapaticci, M., et al. (2015). Immunoregulatory effects of mesenchymal stem cell-derived extracellular vesicles on T lymphocytes. *Cell Transpl.* 24, 2615–2627. doi:10.3727/096368915X687543

Di Trapani, M., Bassi, G., Midolo, M., Gatti, A., Kamga, P. T., Cassaro, A., et al. (2016). Differential and transferable modulatory effects of mesenchymal stromal cell-derived extracellular vesicles on T, B and NK cell functions. *Sci. Rep.* 6, 24120. doi:10.1038/srep24120

Ding, J., Wang, X., Chen, B., Zhang, J., and Xu, J. (2019). Exosomes derived from human bone marrow mesenchymal stem cells stimulated by deferoxamine accelerate cutaneous wound healing by promoting angiogenesis. *Biomed. Res. Int.* 2019, 9742765. doi:10.1155/2019/9742765

Ding, Y., Wang, Y., and Hu, Q. (2022). Recent advances in overcoming barriers to cell-based delivery systems for cancer immunotherapy. *Exploration* 2, 20210106. doi:10.1002/exp.20210106

Dolati, S., Yousefi, M., Pishgahi, A., Nourbakhsh, S., Pourabbas, B., Shakouri, S. K., et al. (2020). Prospects for the application of growth factors in wound healing. *Growth Factors (Chur, Switz.* 38, 25–34. doi:10.1080/08977194.2020.1820499

Dong, N., Lv, H., Liu, C., and Zhang, P. (2022). Research progress in 3D-printed medicinal tablets. *Acta Mater. Medica* 1, 1. doi:10.15212/amm-2021-0010

Du, Y. M., Zhuansun, Y. X., Chen, R., Lin, L., Lin, Y., Li, J. G., et al. (2018). Mesenchymal stem cell exosomes promote immunosuppression of regulatory T cells in asthma. *Exp. Cell Res.* 363, 114–120. doi:10.1016/j.yexcr.2017.12.021

Duan, M., Zhang, Y., Zhang, H., Meng, Y., Qian, M., Zhang, G., et al. (2020). Epidermal stem cell-derived exosomes promote skin regeneration by downregulating transforming growth factor-β1 in wound healing. *Stem Cell Res. Ther.* 11, 452. doi:10.1186/s13287-020-01971-6

Fang, S., Xu, C., Zhang, Y., Xue, C., Yang, C., Bi, H., et al. (2016). Umbilical cord-derived mesenchymal stem cell-derived exosomal MicroRNAs suppress myofibroblast differentiation by inhibiting the transforming growth factor-β/SMAD2 pathway during wound healing. *Stem Cells Transl. Med.* 5, 1425–1439. doi:10.5966/sctm.2015-0367

Farahani, M., and Shafiee, A. (2021). Wound healing: From passive to smart dressings. *Adv. Healthc. Mat.* 10, e2100477. doi:10.1002/adhm.202100477

FerreiraCastropaggiaro, M., Oliveiraisaac, A., Neto, C. T., and Dos, G. B. (2011). Substitutos cutâneos: Conceitos atuais e proposta de classificação??o. *Rev. Bras. Cir. Plast.* 26, 696–702. doi:10.1590/s1983-51752011000400028

Fu, M., Gu, J., Jiang, P., Qian, H., Xu, W., Zhang, X., et al. (2019). Exosomes in gastric cancer: Roles, mechanisms, and applications. *Mol. Cancer* 18, 41. doi:10.1186/s12943-019-1001-7

Golchin, A., Hosseinzadeh, S., and Roshangar, L. (2018). The role of nanomaterials in cell delivery systems. *Med. Mol. Morphol.* 51, 1–12. doi:10.1007/s00795-017-0173-8

Golchin, A., Shams, F., Basiri, A., Ranjbarvan, P., Kiani, S., Sarkhosh-Inanlou, R., et al. (2022). Combination therapy of stem cell-derived exosomes and biomaterials in the wound healing. *Stem Cell Rev. Rep.* 1, 1. doi:10.1007/s12015-021-10309-5

Goodarzi, P., Larijani, B., Alavi-Moghadam, S., Tayanloo-Beik, A., Mohamadi-Jahani, F., Ranjbaran, N., et al. (2018). Mesenchymal stem cells-derived exosomes for wound regeneration. *Adv. Exp. Med. Biol.* 1119, 119–131. doi:10.1007/5584_2018_251

Guillamat-Prats, R. (2021). The role of MSC in wound healing, scarring and regeneration. *Cells* 10, 1729. doi:10.3390/cells10071729

Gurtner, G. C., Werner, S., Barrandon, Y., and Longaker, M. T. (2008). Wound repair and regeneration. *Nature* 453, 314–321. doi:10.1038/nature07039

Gurunathan, S., Kang, M.-H., Jeyaraj, M., Qasim, M., and Kim, J.-H. (2019). Review of the isolation, characterization, biological function, and multifarious therapeutic approaches of exosomes. *Cells* 8, 307. doi:10.3390/cells8040307

Gurunathan, S., Kang, M. H., and Kim, J. H. (2021). A comprehensive review on factors influences biogenesis, functions, therapeutic and clinical implications of exosomes. *Int. J. Nanomedicine* 16, 1281–1312. doi:10.2147/IJN.S291956

Gurung, S., Perocheau, D., Touramanidou, L., and Baruteau, J. (2021). The exosome journey: From biogenesis to uptake and intracellular signalling. *Cell Commun. Signal.* 19, 47. doi:10.1186/s12964-021-00730-1

Ha, D. H., Kim, H.-K., Lee, J., Kwon, H. H., Park, G.-H., Yang, S. H., et al. (2020). Mesenchymal stem/stromal cell-derived exosomes for immunomodulatory therapeutics and skin regeneration. *Cells* 9, 1157. doi:10.3390/cells9051157

Han, G., and Ceilley, R. (2017). Chronic wound healing: A review of current management and treatments. *Adv. Ther.* 34, 599–610. doi:10.1007/s12325-017-0478-y

He, X., Dong, Z., Cao, Y., Wang, H., Liu, S., Liao, L., et al. (2019). MSC-derived exosome promotes M2 polarization and enhances cutaneous wound healing. *Stem Cells Int.* 2019, 7132708. doi:10.1155/2019/7132708

Hessvik, N. P., and Llorente, A. (2018). Current knowledge on exosome biogenesis and release. *Cell. Mol. Life Sci.* 75, 193–208. doi:10.1007/s00018-017-2595-9

Heydari, R., Abdollahpour-Alitappeh, M., Shekari, F., and Meyfour, A. (2021). Emerging role of extracellular vesicles in biomarking the gastrointestinal diseases. *Expert Rev. Mol. diagn.* 21, 939–962. doi:10.1080/14737159.2021.1954909

Hodge, A. L., Baxter, A. A., and Poon, I. K. H. (2021). Gift bags from the sentinel cells of the immune system: The diverse role of dendritic cell-derived extracellular vesicles. *J. Leukoc. Biol.* 111, 903–920. doi:10.1002/JLB.3RU1220-801R

Hu, L., Wang, J., Zhou, X., Xiong, Z., Zhao, J., Yu, R., et al. (2020). Author Correction: Exosomes derived from human adipose mensenchymal stem cells accelerates cutaneous wound healing via optimizing the characteristics of fibroblasts. *Sci. Rep.* 10, 6693. doi:10.1038/s41598-020-63068-7

Hu, L., Wang, J., Zhou, X., Xiong, Z., Zhao, J., Yu, R., et al. (2016). Exosomes derived from human adipose mensenchymal stem cells accelerates cutaneous wound healing via optimizing the characteristics of fibroblasts. *Sci. Rep.* 6, 32993. doi:10.1038/srep32993

Huotari, J., and Helenius, A. (2011). Endosome maturation. *EMBO J.* 30, 3481–3500. doi:10.1038/emboj.2011.286

Isaac, R., Reis, F. C. G., Ying, W., and Olefsky, J. M. (2021). Exosomes as mediators of intercellular crosstalk in metabolism. *Cell Metab.* 33, 1744–1762. doi:10.1016/j.cmet.2021.08.006

Isakson, M., De Blacam, C., Whelan, D., Mcardle, A., and Clover, A. J. P. (2015). Mesenchymal stem cells and cutaneous wound healing: Current evidence and future potential. *Stem Cells Int.* 2015, 831095. doi:10.1155/2015/831095

Iy, A. B., and Al-Rubaiy, K. K. (2009). Skin substitutes: A brief review of types and clinical applications. *Oman Med. J.* 24, 4–6. doi:10.5001/omj.2009.2

Jalaludin, I., Lubman, D. M., and Kim, J. (2021). A guide to mass spectrometric analysis of extracellular vesicle proteins for biomarker discovery. *Mass Spectrom. Rev.* 8, e21749. doi:10.1002/mas.21749

Järbrink, K., Ni, G., Sönnergren, H., Schmidtchen, A., Pang, C., Bajpai, R., et al. (2017). The humanistic and economic burden of chronic wounds: A protocol for a systematic review. *Syst. Rev.* 6, 15. doi:10.1186/s13643-016-0400-8

Jiang, J., Mei, J., Ma, Y., Jiang, S., Zhang, J., Yi, S., et al. (2022). Tumor hijacks macrophages and microbiota through extracellular vesicles. *Exploration* 2, 20210144. doi:10.1002/exp.20210144

Jiang, L., Zhang, Y., Liu, T., Wang, X., Wang, H., Song, H., et al. (2020). Exosomes derived from TSG-6 modified mesenchymal stromal cells attenuate scar formation during wound healing. *Biochimie* 177, 40–49. doi:10.1016/j.biochi.2020.08.003

Jin, C., Wu, P., Li, L., Xu, W., and Qian, H. (2021). Exosomes: Emerging therapy delivery tools and biomarkers for kidney diseases. *Stem Cells Int.* 2021, 7844455. doi:10.1155/2021/7844455

Jo, H., Brito, S., Kwak, B. M., Park, S., Lee, M.-G., Bin, B.-H., et al. (2021). Applications of mesenchymal stem cells in skin regeneration and rejuvenation. *Int. J. Mol. Sci.* 22, 2410. doi:10.3390/ijms22052410

Kalluri, R., and Lebleu, V. S. (2020). The biology, function, and biomedical applications of exosomes. *Science* 367, eaau6977. doi:10.1126/science.aau6977

Kamoun, E. A., Kenawy, E.-R. S., and Chen, X. (2017). A review on polymeric hydrogel membranes for wound dressing applications: PVA-based hydrogel dressings. *J. Adv. Res.* 8, 217–233. doi:10.1016/j.jare.2017.01.005

Kandimalla, R., Aqil, F., Tyagi, N., and Gupta, R. (2021). Milk exosomes: A biogenic nanocarrier for small molecules and macromolecules to combat cancer. *Am. J. Reprod. Immunol.* 85, e13349. doi:10.1111/aji.13349

Kang, T., Jones, T. M., Naddell, C., Bacanamwo, M., Calvert, J. W., Thompson, W. E., et al. (2016). Adipose-derived stem cells induce angiogenesis via microvesicle transport of miRNA-31. *Stem Cells Transl. Med.* 5, 440–450. doi:10.5966/sctm.2015-0177

Kanji, S., and Das, H. (2017). Advances of stem cell therapeutics in cutaneous wound healing and regeneration. *Mediat. Inflamm.* 2017, 5217967. doi:10.1155/2017/5217967

Khare, D., Or, R., Resnick, I., Barkatz, C., Almogi-Hazan, O., Avni, B., et al. (2018). Mesenchymal stromal cell-derived exosomes affect mRNA expression and function of B-lymphocytes. *Front. Immunol.* 9, 3053. doi:10.3389/fimmu.2018.03053

Kim, Y.-J., Yoo, S. M., Park, H. H., Lim, H. J., Kim, Y.-L., Lee, S., et al. (2017). Exosomes derived from human umbilical cord blood mesenchymal stem cells stimulates rejuvenation of human skin. *Biochem. Biophys. Res. Commun.* 493, 1102–1108. doi:10.1016/j.bbrc.2017.09.056

Konoshenko, M. Y., Lekchnov, E. A., Vlassov, A. V., and Laktionov, P. P. (2018). Isolation of extracellular vesicles: General methodologies and latest trends. *Biomed. Res. Int.* 2018, 8545347. doi:10.1155/2018/8545347

Kosaka, N., Iguchi, H., Yoshioka, Y., Hagiwara, K., Takeshita, F., Ochiya, T., et al. (2012). Competitive interactions of cancer cells and normal cells via secretory microRNAs. *J. Biol. Chem.* 287, 1397–1405. doi:10.1074/jbc.M111.288662

Las Heras, K., Igartua, M., Santos-Vizcaino, E., and Hernandez, R. M. (2020). Chronic wounds: Current status, available strategies and emerging therapeutic solutions. *J. Control. Release* 328, 532–550. doi:10.1016/j.jconrel.2020.09.039

Li, D., Zhang, P., Yao, X., Li, H., Shen, H., Li, X., et al. (2018a). Exosomes derived from miR-133b-modified mesenchymal stem cells promote recovery after spinal cord injury. *Front. Neurosci.* 12, 845. doi:10.3389/fnins.2018.00845

Li, D., Zhao, Y., Zhang, C., Wang, F., Zhou, Y., Jin, S., et al. (2021a). Plasma exosomes at the late phase of remote ischemic pre-conditioning attenuate myocardial ischemia-reperfusion injury through transferring miR-126a-3p. *Front. Cardiovasc. Med.* 8, 736226. doi:10.3389/fcvm.2021.736226

Li, K. L., Li, J. Y., Xie, G. L., and Ma, X. Y. (2021b). Exosomes released from human bone marrow-derived mesenchymal stem cell attenuate acute graft-versus-host disease after allogeneic hematopoietic stem cell transplantation in mice. *Front. Cell Dev. Biol.* 9, 617589. doi:10.3389/fcell.2021.617589

Li, S., Yi, M., Dong, B., Tan, X., Luo, S., Wu, K., et al. (2021c). The role of exosomes in liquid biopsy for cancer diagnosis and prognosis prediction. *Int. J. Cancer* 148, 2640–2651. doi:10.1002/ijc.33386

Li, X., Liu, L., Yang, J., Yu, Y., Chai, J., Wang, L., et al. (2016). Exosome derived from human umbilical cord mesenchymal stem cell mediates MiR-181c attenuating burn-induced excessive inflammation. *EBioMedicine* 8, 72–82. doi:10.1016/j.ebiom.2016.04.030

Li, X., Xie, X., Lian, W., Shi, R., Han, S., Zhang, H., et al. (2018b). Exosomes from adipose-derived stem cells overexpressing Nrf2 accelerate cutaneous wound healing by promoting vascularization in a diabetic foot ulcer rat model. *Exp. Mol. Med.* 50, 29. doi:10.1038/s12276-018-0058-5

Li, Y., Zhang, J., Shi, J., Liu, K., Wang, X., Jia, Y., et al. (2021d). Exosomes derived from human adipose mesenchymal stem cells attenuate hypertrophic scar fibrosis by miR-192-5p/IL-17RA/Smad axis. *Stem Cell Res. Ther.* 12, 221. doi:10.1186/s13287-021-02290-0

Liang, X., Zhang, L., Wang, S., Han, Q., and Zhao, R. C. (2016). Exosomes secreted by mesenchymal stem cells promote endothelial cell angiogenesis by transferring miR-125a. *J. Cell Sci.* 129, 2182–2189. doi:10.1242/jcs.170373

Liu, J., Yan, Z., Yang, F., Huang, Y., Yu, Y., Zhou, L., et al. (2021a). Exosomes derived from human umbilical cord mesenchymal stem cells accelerate cutaneous wound healing by enhancing angiogenesis through delivering angiopoietin-2. *Stem Cell Rev. Rep.* 17, 305–317. doi:10.1007/s12015-020-09992-7

Liu, L., Yu, Y., Hou, Y., Chai, J., Duan, H., Chu, W., et al. (2014). Human umbilical cord mesenchymal stem cells transplantation promotes cutaneous wound healing of severe burned rats. *PLoS One* 9, e88348. doi:10.1371/journal.pone.0088348

Liu, Q., Piao, H., Wang, Y., Zheng, D., and Wang, W. (2021b). Circulating exosomes in cardiovascular disease: Novel carriers of biological information. *Biomed. Pharmacother.* 135, 111148. doi:10.1016/j.biopha.2020.111148

Liu, W., Yu, M., Xie, D., Wang, L., Ye, C., Zhu, Q., et al. (2020). Melatonin-stimulated MSC-derived exosomes improve diabetic wound healing through regulating macrophage M1 and M2 polarization by targeting the PTEN/AKT pathway. *Stem Cell Res. Ther.* 11, 259. doi:10.1186/s13287-020-01756-x

Livshits, M. A., Livshts, M. A., Khomyakova, E., Evtushenko, E. G., Lazarev, V. N., Kulemin, N. A., et al. (2015). Isolation of exosomes by differential centrifugation: Theoretical analysis of a commonly used protocol. *Sci. Rep.* 5, 17319. doi:10.1038/srep17319

Ma, J., and Wu, C. (2022). *Bioactive inorganic particles-based biomaterials for skin tissue engineering*. Hoboken, NJ: Exploration, 20210083. n/a.

Ma, T., Fu, B., Yang, X., Xiao, Y., and Pan, M. (2019). Adipose mesenchymal stem cell-derived exosomes promote cell proliferation, migration, and inhibit cell apoptosis via Wnt/β-catenin signaling in cutaneous wound healing. *J. Cell. Biochem.* 120, 10847–10854. doi:10.1002/jcb.28376

Mazini, L., Rochette, L., Admou, B., Amal, S., and Malka, G. (2020). Hopes and limits of adipose-derived stem cells (ADSCs) and mesenchymal stem cells (MSCs) in wound healing. *Int. J. Mol. Sci.* 21, E1306. doi:10.3390/ijms21041306

Mcbride, J. D., Rodriguez-Menocal, L., Guzman, W., Candanedo, A., Garcia-Contreras, M., Badiavas, E. V., et al. (2017). Bone marrow mesenchymal stem cell-derived CD63(+) exosomes transport Wnt3a exteriorly and enhance dermal fibroblast proliferation, migration, and angiogenesis *in vitro*. *Stem Cells Dev.* 26, 1384–1398. doi:10.1089/scd.2017.0087

Miao, C., Zhou, W., Wang, X., and Fang, J. (2021). The research progress of exosomes in osteoarthritis, with particular emphasis on the mediating roles of miRNAs and lncRNAs. *Front. Pharmacol.* 12, 685623. doi:10.3389/fphar.2021.685623

Monguio-Tortajada, M., Roura, S., Galvez-Monton, C., Pujal, J. M., Aran, G., Sanjurjo, L., et al. (2017). Nanosized UCMSC-derived extracellular vesicles but not conditioned medium exclusively inhibit the inflammatory response of stimulated T cells: Implications for nanomedicine. *Theranostics* 7, 270–284. doi:10.7150/thno.16154

Nik Nabil, W. N., Xi, Z., Liu, M., Li, Y., Yao, M., Liu, T., et al. (2022). Advances in therapeutic agents targeting quiescent cancer cells. *Acta Mater. Medica* 1, 1. doi:10.15212/amm-2021-0005

Nikfarjam, S., Rezaie, J., Zolbanin, N. M., and Jafari, R. (2020). Mesenchymal stem cell derived-exosomes: A modern approach in translational medicine. *J. Transl. Med.* 18, 449. doi:10.1186/s12967-020-02622-3

Nojehdehi, S., Soudi, S., Hesampour, A., Rasouli, S., Soleimani, M., Hashemi, S. M., et al. (2018). Immunomodulatory effects of mesenchymal stem cell-derived exosomes on experimental type-1 autoimmune diabetes. *J. Cell. Biochem.* 119, 9433–9443. doi:10.1002/jcb.27260

Nourian Dehkordi, A., Mirahmadi Babaheydari, F., Chehelgerdi, M., and Raeisi Dehkordi, S. (2019). Skin tissue engineering: Wound healing based on stem-cell-based therapeutic strategies. *Stem Cell Res. Ther.* 10, 111. doi:10.1186/s13287-019-1212-2

Opoku-Damoah, Y., Zhang, R., Ta, H. T., and Xu, Z. P. (2022). *Therapeutic gas-releasing nanomedicines with controlled release: Advances and perspectives*. Hoboken, NJ: Exploration, 20210181. n/a.

Pelissier Vatter, F. A., Lucotti, S., and Zhang, H. (2020). Recent advances in experimental models of breast cancer exosome secretion, characterization and function. *J. Mammary Gland. Biol. Neoplasia* 25, 305–317. doi:10.1007/s10911-020-09473-0

Powers, J. G., Higham, C., Broussard, K., and Phillips, T. J. (2016). Wound healing and treating wounds: Chronic wound care and management. *J. Am. Acad. Dermatol.* 74, 607–625. doi:10.1016/j.jaad.2015.08.070

Proksch, E., Brandner, J. M., and Jensen, J.-M. (2008). The skin: An indispensable barrier. *Exp. Dermatol.* 17, 1063–1072. doi:10.1111/j.1600-0625.2008.00786.x

Purghe, B., Manfredi, M., Ragnoli, B., Baldanzi, G., and Malerba, M. (2021). Exosomes in chronic respiratory diseases. *Biomed. Pharmacother.* 144, 112270. doi:10.1016/j.biopha.2021.112270

Qian, L., Pi, L., Fang, B. R., and Meng, X. X. (2021). Adipose mesenchymal stem cell-derived exosomes accelerate skin wound healing via the lncRNA H19/miR-19b/SOX9 axis. *Lab. Invest.* 101, 1254–1266. doi:10.1038/s41374-021-00611-8

Rani, S., and Ritter, T. (2016). The exosome - a naturally secreted nanoparticle and its application to wound healing. *Adv. Mat.* 28, 5542–5552. doi:10.1002/adma.201504009

Rao, D., Huang, D., Sang, C., Zhong, T., Zhang, Z., Tang, Z., et al. (2022). Advances in mesenchymal stem cell-derived exosomes as drug delivery vehicles. *Front. Bioeng. Biotechnol.* 9, 797359. doi:10.3389/fbioe.2021.797359

Raposo, G., and Stoorvogel, W. (2013). Extracellular vesicles: Exosomes, microvesicles, and friends. *J. Cell Biol.* 200, 373–383. doi:10.1083/jcb.201211138

Rasulov, M. F., Vasilchenkov, A. V., Onishchenko, N. A., Krasheninnikov, M. E., Kravchenko, V. I., Gorshenin, T. L., et al. (2005). First experience of the use bone marrow mesenchymal stem cells for the treatment of a patient with deep skin burns. *Bull. Exp. Biol. Med.* 139, 141–144. doi:10.1007/s10517-005-0232-3

Reinke, J. M., and Sorg, H. (2012). Wound repair and regeneration. *Eur. Surg. Res.* 49, 35–43. doi:10.1159/000339613

Reis, M., Mavin, E., Nicholson, L., Green, K., Dickinson, A. M., Wang, X. N., et al. (2018). Mesenchymal stromal cell-derived extracellular vesicles attenuate dendritic cell maturation and function. *Front. Immunol.* 9, 2538. doi:10.3389/fimmu.2018.02538

Riau, A. K., Ong, H. S., Yam, G. H. F., and Mehta, J. S. (2019). Sustained delivery system for stem cell-derived exosomes. *Front. Pharmacol.* 10, 1368. doi:10.3389/fphar.2019.01368

Riazifar, M., Mohammadi, M. R., Pone, E. J., Yeri, A., Lasser, C., Segaliny, A. I., et al. (2019). Stem cell-derived exosomes as nanotherapeutics for autoimmune and neurodegenerative disorders. *ACS Nano* 13, 6670–6688. doi:10.1021/acsnano.9b01004

Riha, S. M., Maarof, M., and Fauzi, M. B. (2021). Synergistic effect of biomaterial and stem cell for skin tissue engineering in cutaneous wound healing: A concise review. *Polymers* 13, 1546. doi:10.3390/polym13101546

Saad, M. H., Badierah, R., Redwan, E. M., and El-Fakharany, E. M. (2021). A comprehensive insight into the role of exosomes in viral infection: Dual faces bearing different functions. *Pharmaceutics* 13, 1405. doi:10.3390/pharmaceutics13091405

Safari, B., Aghazadeh, M., Davaran, S., and Roshangar, L. (2022). Exosome-loaded hydrogels: A new cell-free therapeutic approach for skin regeneration. *Eur. J. Pharm. Biopharm.* 171, 50–59. doi:10.1016/j.ejpb.2021.11.002

Shafei, S., Khanmohammadi, M., Heidari, R., Ghanbari, H., Taghdiri Nooshabadi, V., Farzamfar, S., et al. (2020). Exosome loaded alginate hydrogel promotes tissue regeneration in full-thickness skin wounds: An *in vivo* study. *J. Biomed. Mat. Res. A* 108, 545–556. doi:10.1002/jbm.a.36835

Shen, K., Jia, Y., Wang, X., Zhang, J., Liu, K., Wang, J., et al. (2021). Exosomes from adipose-derived stem cells alleviate the inflammation and oxidative stress via regulating Nrf2/HO-1 axis in macrophages. *Free Radic. Biol. Med.* 165, 54–66. doi:10.1016/j.freeradbiomed.2021.01.023

Shirejini, S. Z., and Inci, F. (2021). The yin and yang of exosome isolation methods: Conventional practice, microfluidics, and commercial kits. *Biotechnol. Adv.* 54, 107814. doi:10.1016/j.biotechadv.2021.107814

Shojaati, G., Khandaker, I., Funderburgh, M. L., Mann, M. M., Basu, R., Stolz, D. B., et al. (2019). Mesenchymal stem cells reduce corneal fibrosis and inflammation via extracellular vesicle-mediated delivery of miRNA. *Stem Cells Transl. Med.* 8, 1192–1201. doi:10.1002/sctm.18-0297

Shpichka, A., Butnaru, D., Bezrukov, E. A., Sukhanov, R. B., Atala, A., Burdukovskii, V., et al. (2019). Skin tissue regeneration for burn injury. *Stem Cell Res. Ther.* 10, 94. doi:10.1186/s13287-019-1203-3

Singh, K., Nalabotala, R., Koo, K. M., Bose, S., Nayak, R., Shiddiky, M. J. A., et al. (2021). Separation of distinct exosome subpopulations: Isolation and characterization approaches and their associated challenges. *Analyst* 146, 3731–3749. doi:10.1039/d1an00024a

Sorg, H., Tilkorn, D. J., Hager, S., Hauser, J., and Mirastschijski, U. (2017). Skin wound healing: An update on the current knowledge and concepts. *Eur. Surg. Res.* 58, 81–94. doi:10.1159/000454919

Takahashi, Y., Nishikawa, M., Shinotsuka, H., Matsui, Y., Ohara, S., Imai, T., et al. (2013). Visualization and *in vivo* tracking of the exosomes of murine melanoma B16-BL6 cells in mice after intravenous injection. *J. Biotechnol.* 165, 77–84. doi:10.1016/j.jbiotec.2013.03.013

Tang, N., Zheng, Y., Cui, D., and Haick, H. (2021). Multifunctional dressing for wound diagnosis and rehabilitation. *Adv. Healthc. Mat.* 10, e2101292. doi:10.1002/adhm.202101292

Tarasov, V. V., Svistunov, A. A., Chubarev, V. N., Dostdar, S. A., Sokolov, A. V., Brzecka, A., et al. (2021). Extracellular vesicles in cancer nanomedicine. *Semin. Cancer Biol.* 69, 212–225. doi:10.1016/j.semcancer.2019.08.017

Thakur, A., Ke, X., Chen, Y. W., Motallebnejad, P., Zhang, K., Lian, Q., et al. (2021). The mini player with diverse functions: Extracellular vesicles in cell biology, disease, and therapeutics. *Protein Cell* 13, 631–654. doi:10.1007/s13238-021-00863-6

Thery, C., Witwer, K. W., Aikawa, E., Alcaraz, M. J., Anderson, J. D., Andriantsitohaina, R., et al. (2018). Minimal information for studies of extracellular vesicles 2018 (MISEV2018): A position statement of the international society for extracellular vesicles and update of the MISEV2014 guidelines. *J. Extracell. Vesicles* 7, 1535750. doi:10.1080/20013078.2018.1535750

Tiwari, A., Singh, A., Verma, S., Stephenson, S., Bhowmick, T., Sangwan, V. S., et al. (2021a). Mini review: Current trends and understanding of exosome therapeutic potential in corneal diseases. *Front. Pharmacol.* 12, 684712. doi:10.3389/fphar.2021.684712

Tiwari, S., Kumar, V., Randhawa, S., and Verma, S. K. (2021b). Preparation and characterization of extracellular vesicles. *Am. J. Reprod. Immunol.* 85, e13367. doi:10.1111/aji.13367

Tran, P. H. L., Xiang, D., Tran, T. T. D., Yin, W., Zhang, Y., Kong, L., et al. (2020). Exosomes and nanoengineering: A match made for precision therapeutics. *Adv. Mat.* 32, e1904040. doi:10.1002/adma.201904040

Tutuianu, R., Rosca, A. M., Iacomi, D. M., Simionescu, M., and Titorencu, I. (2021). Human mesenchymal stromal cell-derived exosomes promote *in vitro* wound healing by modulating the biological properties of skin keratinocytes and fibroblasts and stimulating angiogenesis. *Int. J. Mol. Sci.* 22, 6239. doi:10.3390/ijms22126239

Van Niel, G., D'angelo, G., and Raposo, G. (2018). Shedding light on the cell biology of extracellular vesicles. *Nat. Rev. Mol. Cell Biol.* 19, 213–228. doi:10.1038/nrm.2017.125

Velnar, T., Bailey, T., and Smrkolj, V. (2009). The wound healing process: An overview of the cellular and molecular mechanisms. *J. Int. Med. Res.* 37, 1528–1542. doi:10.1177/147323000903700531

Vu, N. B., Nguyen, H. T., Palumbo, R., Pellicano, R., Fagoonee, S., Pham, P. V., et al. (2021). Stem cell-derived exosomes for wound healing: Current status and promising directions. *Minerva Med.* 112, 384–400. doi:10.23736/S0026-4806.20.07205-5

Wang, L., Hu, L., Zhou, X., Xiong, Z., Zhang, C., Shehada, H. M. A., et al. (2021). Author Correction: Exosomes secreted by human adipose mesenchymal stem cells promote scarless cutaneous repair by regulating extracellular matrix remodelling. *Sci. Rep.* 11, 7066. doi:10.1038/s41598-018-24991-y

Wang, L., Hu, L., Zhou, X., Xiong, Z., Zhang, C., Shehada, H. M. A., et al. (2017). Exosomes secreted by human adipose mesenchymal stem cells promote scarless cutaneous repair by regulating extracellular matrix remodelling. *Sci. Rep.* 7, 13321. doi:10.1038/s41598-017-12919-x

Wang, P. H., Huang, B. S., Horng, H. C., Yeh, C. C., and Chen, Y. J. (2018). Wound healing. *J. Chin. Med. Assoc.* 81, 94–101. doi:10.1016/j.jcma.2017.11.002

Wang, W. M., Wu, C., and Jin, H. Z. (2019). Exosomes in chronic inflammatory skin diseases and skin tumors. *Exp. Dermatol.* 28, 213–218. doi:10.1111/exd.13857

Wei, T., Thakur, S. S., Liu, M., and Wen, J. (2022). Oral delivery of glutathione: Antioxidant function, barriers and strategies. *Acta Mater. Med.* 1, 1. doi:10.15212/amm-2022-0005

Wei, W., Ao, Q., Wang, X., Cao, Y., Liu, Y., Zheng, S. G., et al. (2021). Mesenchymal stem cell–derived exosomes: A promising biological tool in nanomedicine. *Front. Pharmacol.* 11, 1. doi:10.3389/fphar.2020.590470

Werner, S., and Grose, R. (2003). Regulation of wound healing by growth factors and cytokines. *Physiol. Rev.* 83, 835–870. doi:10.1152/physrev.2003.83.3.835

Wilkinson, H. N., and Hardman, M. J. (2020). Wound healing: Cellular mechanisms and pathological outcomes. *Open Biol.* 10, 200223. doi:10.1098/rsob.200223

Wu, X., Showiheen, S. a. A., Sun, A. R., Crawford, R., Xiao, Y., Mao, X., et al. (2019). Exosomes extraction and identification. *Methods Mol. Biol.* 2054, 81–91. doi:10.1007/978-1-4939-9769-5_4

Xie, M., Xiong, W., She, Z., Wen, Z., Abdirahman, A. S., Wan, W., et al. (2020). Immunoregulatory effects of stem cell-derived extracellular vesicles on immune cells. *Front. Immunol.* 11, 13. doi:10.3389/fimmu.2020.00013

Xu, N., Wang, L., Guan, J., Tang, C., He, N., Zhang, W., et al. (2018). Wound healing effects of a Curcuma zedoaria polysaccharide with platelet-rich plasma exosomes assembled on chitosan/silk hydrogel sponge in a diabetic rat model. *Int. J. Biol. Macromol.* 117, 102–107. doi:10.1016/j.ijbiomac.2018.05.066

Xu, R., Zhang, F., Chai, R., Zhou, W., Hu, M., Liu, B., et al. (2019). Exosomes derived from pro-inflammatory bone marrow-derived mesenchymal stem cells reduce inflammation and myocardial injury via mediating macrophage polarization. *J. Cell. Mol. Med.* 23, 7617–7631. doi:10.1111/jcmm.14635

Yang, C., Luo, L., Bai, X., Shen, K., Liu, K., Wang, J., et al. (2020a). Highly-expressed micoRNA-21 in adipose derived stem cell exosomes can enhance the migration and proliferation of the HaCaT cells by increasing the MMP-9 expression through the PI3K/AKT pathway. *Arch. Biochem. Biophys.* 681, 108259. doi:10.1016/j.abb.2020.108259

Yang, D., Zhang, W., Zhang, H., Zhang, F., Chen, L., Ma, L., et al. (2020b). Progress, opportunity, and perspective on exosome isolation - Efforts for efficient exosome-based theranostics. *Theranostics* 10, 3684–3707. doi:10.7150/thno.41580

Yang, J., Chen, Z., Pan, D., Li, H., and Shen, J. (2020c). Umbilical cord-derived mesenchymal stem cell-derived exosomes combined pluronic F127 hydrogel promote chronic diabetic wound healing and complete skin regeneration. *Int. J. Nanomedicine* 15, 5911–5926. doi:10.2147/IJN.S249129

Yang, Y., Guo, Z., Chen, W., Wang, X., Cao, M., Han, X., et al. (2021). M2 macrophage-derived exosomes promote angiogenesis and growth of pancreatic ductal adenocarcinoma by targeting E2F2. *Mol. Ther.* 29, 1226–1238. doi:10.1016/j.ymthe.2020.11.024

You, L., Wu, W., Wang, X., Fang, L., Adam, V., Nepovimova, E., et al. (2021). The role of hypoxia-inducible factor 1 in tumor immune evasion. *Med. Res. Rev.* 41, 1622–1643. doi:10.1002/med.21771

Yu, B., Zhang, X., and Li, X. (2014). Exosomes derived from mesenchymal stem cells. *Int. J. Mol. Sci.* 15, 4142–4157. doi:10.3390/ijms15034142

Yu, M., Liu, W., Li, J., Lu, J., Lu, H., Jia, W., et al. (2020). Exosomes derived from atorvastatin-pretreated MSC accelerate diabetic wound repair by enhancing angiogenesis via AKT/eNOS pathway. *Stem Cell Res. Ther.* 11, 350. doi:10.1186/s13287-020-01824-2

Zara, M., Amadio, P., Campodonico, J., Sandrini, L., and Barbieri, S. S. (2020). Exosomes in cardiovascular diseases. *Diagn. (Basel)* 10, E943. doi:10.3390/diagnostics10110943

Zeng, Q. L., and Liu, D. W. (2021). Mesenchymal stem cell-derived exosomes: An emerging therapeutic strategy for normal and chronic wound healing. *World J. Clin. Cases* 9, 6218–6233. doi:10.12998/wjcc.v9.i22.6218

Zeng, R., Lin, C., Lin, Z., Chen, H., Lu, W., Lin, C., et al. (2018). Approaches to cutaneous wound healing: Basics and future directions. *Cell Tissue Res.* 374, 217–232. doi:10.1007/s00441-018-2830-1

Zhang, B., Wu, X., Zhang, X., Sun, Y., Yan, Y., Shi, H., et al. (2015). Human umbilical cord mesenchymal stem cell exosomes enhance angiogenesis through the Wnt4/β-catenin pathway. *Stem Cells Transl. Med.* 4, 513–522. doi:10.5966/sctm.2014-0267

Zhang, B., Yeo, R. W. Y., Lai, R. C., Sim, E. W. K., Chin, K. C., Lim, S. K., et al. (2018). Mesenchymal stromal cell exosome-enhanced regulatory T-cell production through an antigen-presenting cell-mediated pathway. *Cytotherapy* 20, 687–696. doi:10.1016/j.jcyt.2018.02.372

Zhang, Y., Han, F., Gu, L., Ji, P., Yang, X., Liu, M., et al. (2020). Adipose mesenchymal stem cell exosomes promote wound healing through accelerated keratinocyte migration and proliferation by activating the AKT/HIF-1α axis. *J. Mol. Histol.* 51, 375–383. doi:10.1007/s10735-020-09887-4

Zhao, L., Jiang, X., Shi, J., Gao, S., Zhu, Y., Gu, T., et al. (2019). Exosomes derived from bone marrow mesenchymal stem cells overexpressing microRNA-25 protect spinal cords against transient ischemia. *J. Thorac. Cardiovasc. Surg.* 157, 508–517. doi:10.1016/j.jtcvs.2018.07.095

Zhao, R., Zhao, T., He, Z., Cai, R., and Pang, W. (2021a). Composition, isolation, identification and function of adipose tissue-derived exosomes. *Adipocyte* 10, 587–604. doi:10.1080/21623945.2021.1983242

Zhao, Y., Zhang, Z., Pan, Z., and Liu, Y. (2021b). Advanced bioactive nanomaterials for biomedical applications. *Exploration* 1, 20210089. doi:10.1002/exp.20210089

Zheng, Y., Han, Y., Sun, Q., and Li, Z. (2022). Harnessing anti-tumor and tumor-tropism functions of macrophages via nanotechnology for tumor immunotherapy. *Exploration* 2, 20210166. doi:10.1002/exp.20210166

frontiers | Frontiers in Pharmacology

TYPE Original Research
PUBLISHED 09 August 2022
DOI 10.3389/fphar.2022.962763

Check for updates

OPEN ACCESS

EDITED BY
Qixin Chen,
Shandong First Medical University, China

REVIEWED BY
Lei Wang,
University of Cincinnati, United States
Yang Chen,
Dalian Institute of Chemical Physics (CAS), China
Xin Wei,
University of Texas Health Science Center at Houston, United States

*CORRESPONDENCE
E. Tolstik,
elen.tolstik@isas
L. A. Osminkina,
osminkina@physics.msu.ru
K. Lorenz,
lorenz@toxi.uni-wuerzburg.de

†These authors have contributed equally to this work

SPECIALTY SECTION
This article was submitted to Pharmacology of Anti-Cancer Drugs, a section of the journal Frontiers in Pharmacology

RECEIVED 06 June 2022
ACCEPTED 05 July 2022
PUBLISHED 09 August 2022

CITATION
Tolstik E, Gongalsky MB, Dierks J, Brand T, Pernecker M, Pervushin NV, Maksutova DE, Gonchar KA, Samsonova J, Kopeina G, Sivakov V, Osminkina LA and Lorenz K (2022), Raman and fluorescence micro-spectroscopy applied for the monitoring of sunitinib-loaded porous silicon nanocontainers in cardiac cells. *Front. Pharmacol.* 13:962763. doi: 10.3389/fphar.2022.962763

COPYRIGHT
© 2022 Tolstik, Gongalsky, Dierks, Brand, Pernecker, Pervushin, Maksutova, Gonchar, Samsonova, Kopeina, Sivakov, Osminkina and Lorenz. This is an open-access article distributed under the terms of the Creative Commons Attribution License (CC BY). The use, distribution or reproduction in other forums is permitted, provided the original author(s) and the copyright owner(s) are credited and that the original publication in this journal is cited, in accordance with accepted academic

Raman and fluorescence micro-spectroscopy applied for the monitoring of sunitinib-loaded porous silicon nanocontainers in cardiac cells

E. Tolstik[1]*, M. B. Gongalsky[2], J. Dierks[1], T. Brand[3], M. Pernecker[1], N. V. Pervushin[4], D. E. Maksutova[2], K. A. Gonchar[2], J. V. Samsonova[5], G. Kopeina[4], V. Sivakov[6], L. A. Osminkina[2,7]*† and K. Lorenz[1,3,8]*†

[1]Leibniz-Institut für Analytische Wissenschaften—ISAS—e.V., Dortmund, Germany, [2]Lomonosov Moscow State University, Faculty of Physics, Moscow, Russia, [3]Institute of Pharmacology and Toxicology, University of Würzburg, Würzburg, Germany, [4]Lomonosov Moscow State University, Faculty of Medicine, Moscow, Russia, [5]Lomonosov Moscow State University, Faculty of Chemistry, Moscow, Russia, [6]Leibniz Institute of Photonic Technology, Department Functional Interfaces, Jena, Germany, [7]Institute for Biological Instrumentation of Russian Academy of Sciences, Moscow, Russia, [8]Comprehensive Heart Failure Center, University Hospital of Würzburg, Würzburg, Germany

Nanomaterials are a central pillar in modern medicine. They are thought to optimize drug delivery, enhance therapeutic efficacy, and reduce side-effects. To foster this technology, analytical methods are needed to validate not only the localization and distribution of these nanomaterials, but also their compatibility with cells, drugs, and drug release. In the present work, we assessed nanoparticles based on porous silicon (pSiNPs) loaded with the clinically used tyrosine kinase inhibitor sunitinib for their effectiveness of drug delivery, release, and toxicity in colon cancer cells (HCT 116 cells) and cardiac myoblast cells (H9c2) using Raman micro-spectroscopy, high-resolution fluorescence microscopy, along with biological methods for toxicological effects. We produced pSiNPs with a size of about 100 nm by grinding mesoporous silicon layers. pSiNPs allowed an effective loading of sunitinib due to their high porosity. Photoluminescence properties of the nanoparticles within the visible spectrum allowed the visualization of their uptake in cardiac cells. Raman micro-spectroscopy allowed not only the detection of the uptake and distribution of pSiNPs within the cells via a characteristic silicon Raman band at about 518–520 cm^{-1}, but also the localization of the drug based on its characteristic molecular fingerprints. Cytotoxicity studies by Western blot analyses of apoptotic marker proteins such as caspase-3, and the detection of apoptosis by subG1-positive cell fractions in HCT 116 and MTT analyses in H9c2 cells, suggest a sustained release of sunitinib from pSiNPs and delayed cytotoxicity of sunitinib in HCT 116 cells. The analyses in cardiac cells revealed that pSiNPs are well tolerated and that they may even protect from toxic effects in these cells to some extent. Analyses of the integrity of mitochondrial networks as an early indicator for apoptotic cellular effects seem to validate these observations. Our study

suggests pSiNPs-based nanocontainers for efficient and safe drug delivery and Raman micro-spectroscopy as a reliable method for their detection and monitoring. Thus, the herein presented nanocontainers and analytical methods have the potential to allow an efficient advancement of nanoparticles for targeted and sustained intracellular drug release that is of need, e.g., in chronic diseases and for the prevention of cardiac toxicity.

KEYWORDS

porous silicon nanoparticles, sunitinib, Raman imaging, micro-spectroscopy imaging, high-resolution fluorescence microscopy, cardiomyoblast, colon cancer cells

1 Introduction

The application of novel bioimaging techniques and high-resolution optical modalities supports the understanding of cellular distribution and the drug's effects on organelles and cellular dynamics. This is particularly relevant for cardiomyocytes as these are non-dividing cells that are especially vulnerable. Depending on the respective drug, cardiotoxicity impacts, e.g., on mitochondrial function, cardiomyocyte survival, oxidative stress levels, DNA damage, endothelial cell permeability, or disturbance of the conduction system, leading to reversible or irreversible damages. Overall, cardiotoxicity is one of the most significant adverse effects of drugs in general and of chemotherapeutics in particular and strongly impacts on morbidity and mortality of the cancer patients (Pai and Nahata, 2000; Palmer et al., 2020). Hence, there is an urgent need to understand the cell-type-specific localization of antitumor drugs on heart cells and to use the knowledge for the reduction or circumvention of cardiotoxic side-effects of anticancer therapies.

The search for new and innovative ways to reduce cardiac side-effects via optimized drug uptake and release is one of the major challenges in the field of cardio-oncology (Chu et al., 2007). To prevent chemotherapy from affecting the whole body, novel drug delivery systems based on nanocontainers for the transport for the sustained and/or the targeted release of the drug have been developed (Yao et al., 2020). Especially, sustained drug release, i.e. delayed release, allows a particular drug to be delivered at a programmed rate, leading therewith to a longer and controlled drug impact on the body avoiding toxic peak concentrations of a drug (Moghimi et al., 2001). Drug delivery based on nanoparticles has several advantages over the delivery of free chemotherapeutic agents (Fornaguera and García-Celma, 2017): the small size of the containers (less than 200 nm) enables efficient intracellular drug delivery and controlled release, a large surface-to-volume ratio increases drug payload in case of porous nanocontainers, and a specific surface activation allows targeted drug delivery. In addition to therapy, the same nanoparticles can also be used for diagnostics to monitor the distribution of nanoparticles as contrast agents (Park et al., 2009). Among the available nanomaterials, porous silicon nanoparticles (pSiNPs) belong to promising delivery vehicles due to their high drug-loading capacity, biocompatibility, and biodegradability (Fornaguera and García-Celma, 2017; Wan et al., 2018). The pSiNPs are degraded to non-toxic and well-tolerated silicic acid species (Anderson et al., 2003; Park et al., 2009; Gu et al., 2013; Gongalsky et al., 2020). Moreover, the morphology and porosity of pSiNPs can easily be adapted by modification of certain fabrication parameters (Herino et al., 1987; Lehmann et al., 2000). The intrinsic photoluminescence (PL) properties of pSiNPs, which consist of silicon quantum dots and pores, provide sufficient contrast for fluorescent bio-visualization both *in vitro* and *in vivo* (Osminkina et al., 2012; Peng et al., 2013).

Recently, vibrational spectroscopy like Raman micro-spectroscopy (Pliss et al., 2010; Bocklitz et al., 2016; Petersen et al., 2017; Yosef et al., 2017; Guo et al., 2018; Kirchberger-Tolstik et al., 2020; Gongalsky et al., 2021a; Tolstik et al., 2022) has emerged as a powerful and well-suited tool in bioanalytics. Raman spectroscopy detects molecular vibrations, which are activated by laser radiation. Based on Raman spectra, chemical fingerprints of the molecules can be determined (Krafft et al., 2009), which allow the localization of substances within a cell. Raman micro-spectroscopy allows spectroscopic monitoring of the uptake, intracellular localization, and dissolution of pSiNPs in living tumor cells through the detection of a specific Raman band at 520 cm^{-1} based on crystalline silicon band (Tolstik et al., 2016b; Tolstik et al., 2016a). Biodegradation of pSiNPs is accompanied by a decrease in the size of silicon nanocrystals and their oxidation and, according to the quantum confinement effect, is detected as a low-frequency shift with a significant decrease in the intensity and broadening of the Raman signal (Tolstik et al., 2016b; Gongalsky et al., 2021a). Raman spectroscopy also enables time-resolved 3D mapping of the distribution of drugs and nanoparticle drug reservoirs (Chernenko et al., 2009; Gordon and McGoverin, 2011; Matthäus et al., 2011; Choi et al., 2013). Differences in the chemical composition of certain cellular compartments allow to localize drugs at subcellular resolution and thus achieve a sophisticated evaluation of drug uptake and its subsequent release (Matthaus et al., 2008; Krafft et al., 2009; Peng et al., 2014; Eberhardt et al., 2015; Tolstik et al., 2016b).

In the present study, we focused on an orally active compound sunitinib malate (SU), a multi-targeted tyrosine

kinase inhibitor, approved by the FDA as therapy for renal cell carcinoma and gastrointestinal stromal tumors (Chu et al., 2007). It has also been used for other malignancies, including colon cancer, breast cancer, neuroendocrine cancer, and lung cancer in preclinical and clinical trials (Demetri et al., 2006; Motzer et al., 2007). Along with the fact that cancer patients undergoing successful chemotherapy with SU often have an improved overall survival, a wide range of severe cardiac side-effects have been reported that lead to severe symptomatic heart failure in about 2% of the patients (Gorini et al., 2018; Silva et al., 2018; Palmer et al., 2020). SU has a poor solubility in water, which leads to the instability of its therapeutic effects (Alshehri and Shakeel, 2020). To increase the solubility and bioavailability of SU, it was proposed to deliver it in nanoform (Chakravarty et al., 2015). Thereby, it is crucial to study the interaction of SU with the respective nanocontainers to investigate the benefits of SU delivery using a nanoform compared to pure drug delivery, along with its impact on cells *in vitro*.

In the current work, we assessed the use of pSiNPs loaded with SU to evaluate the effectiveness of drug delivery, release, and its toxicity on cancer and cardiac cells using several imaging modalities including confocal fluorescence microscopy with high spatial resolution and Raman micro-spectroscopy, along with the biological methods for toxicological and morphological studies. The choice of pSiNPs as nanocontainers is driven by their proven unique physico-chemical properties: biocompatibility, biodegradability, and high loading efficiency for drug delivery. Moreover, PL properties of pSiNPs enable fast intracellular imaging and mapping of the SU loaded in nanocontainers applying standard fluorescence staining techniques. The presence of characteristic Raman modes of SU (Litti et al., 2016) and pSiNPs (Tolstik et al., 2016b) can facilitate its label-free tracking by applying Raman spectroscopy. For *in vitro* studies, to evaluate the cardiotoxicity of SU-loaded pSiNPs, the following two cell lines were chosen: the human colon carcinoma HCT 116 cell line (Rajput et al., 2008) that is applied widely as a model to study the cellular effects of SU (Sun et al., 2012; Ban et al., 2017; Elgendy et al., 2017) and the rat cardiomyoblast cell line H9c2 (Korashy et al., 2015; Tomasovic et al., 2020; Merches et al., 2022). Thereby, the intracellular delivery, localization, and toxicity of pure SU substance and SU-loaded pSiNPs were analyzed *in vitro* using cell viability assays and linear optical imaging techniques.

2 Materials and methods

2.1 Porous silicon nanoparticles preparation

Porous silicon (pSi) layers were prepared by anodizing p-type heavily boron-doped (100)-oriented silicon (SiMat, Germany) wafers with resistivity of 0.001–0.002 Ω cm in a hydrogen fluoride (HF, CAS 7664-39-3, 48%, Merck)/ethanol (CAS 64-17-5, ≥99.8%, VWR Chemicals) mixture 1:1 v/v and current density of 50 mA/cm^2 for 1 h. The obtained porous layers were separated from the wafer by applying 3 pulses of current density of 600 mA/cm^2 for 3 s. After drying at room temperature (RT) overnight, the layers were ground in agar mortar into millimeter-sized particles. The obtained particles were then ball milled in deionized water in the planetary mill (Fritsch Pulverisette 7 premium line, FRITSCH GmbH) for 30 min with zirconium oxide balls of diameter 2.5 μm and then for 30 min with balls of diameter 0.1 μm. Nanoparticles (NPs) were collected from the sample by centrifugation at 12,500 rpm for 20 min, leaving the supernatant for further work. The obtained pSiNPs were stored in deionized water.

2.2 Nanoparticle characterization

Structural analysis of the pSiNPs was carried out by transmission electron microscopy (TEM, LEO912 AB OMEGA). The samples of pSiNPs for TEM studies were prepared by deposition of a drop of the aqueous suspension of NPs on standard carbon-coated copper TEM-grids followed by air drying for 10 min. The dynamic light scattering (DLS) measurements were performed with a Malvern Zetasizer Nano ZS instrument to determine the size distribution and zeta potential (ZP) of NPs in aqueous suspensions. Nanoparticles with a zeta potential between −10 and +10 mV were considered approximately neutral, while nanoparticles with zeta potential of greater than +30 mV or less than −30 mV were considered strongly cationic and strongly anionic, respectively. In addition, zeta potential of the surface reflects the solubility and stability of colloidal NPs. The infrared transmission spectra of pSiNPs were measured on a Bruker IFS 66 v/S (FTIR) infrared spectrometer with Fourier transformation, for which a drop of suspension was dried on a silicon high-resistance substrate with two-sided polishing. Raman micro-spectroscopy data were acquired using a confocal Raman microscope Confotec™ MR350 system, with a laser excitation at 633 nm wavelength and 0.5 mW power.

2.3 Cell culture and experimental procedures

Cell culture experiments were performed using human colorectal carcinoma HCT 116 cell line, which was provided by the Department of Toxicology of the Karolinska Institute (Stockholm, Sweden), and rat cardiac myoblast H9c2 cells (ATTC, Manassas, VA, United States). The HCT 116 cells were grown in 5% CO_2 at 37°C, in Dulbecco's Modified Eagle Medium (DMEM) with high glucose (Gibco, Waltham, MA, United States), supplemented by 10% fetal bovine serum (Gibco),

1 mM sodium pyruvate (PanEco, Moscow, Russia), and a mixture of antibiotics and antimycotics (penicillin, streptomycin, and amphotericin B; CAS 15240-062, Gibco). The rat cardiomyoblast cell line H9c2 (CRL-1446™, ATCC, United States) was cultured at 37°C under a humidified atmosphere of 5% CO_2 in DMEM (P04-03596, Pan Biotech, Germany) supplemented with 10% fetal calf serum (FCS; S0115, Sigma Aldrich, United Kingdom), 100 U ml^{-1} penicillin G and 100 μg ml^{-1} streptomycin sulfate (P06-07100, Pan Biotech, Germany), and 2 mM L-glutamine (P04-80100, Pan Biotech, Germany). All cells were reseeded every 3 days and maintained in the logarithmic growth phase for experiments. Before treatment with nanoparticles and/or SU malate (Sigma-Aldrich, St. Louis, MO, United States, >98% (HPLC)), the culture medium was replaced with fresh medium. Cells were treated with nanoparticles at a concentration of 200 μg/mL, SU malate at 5–50 μM, and nanoparticles loaded with SU malate at the same concentrations. Then, the cells were incubated for 24–120 h with various concentrations of SU.

2.4 Drug loading and release

An aqueous solution of 0.2 mM sunitinib malate (SU, ≥98% (HPLC), Sigma-Aldrich, Germany) was mixed with 1 mg/ml pSiNPs overnight. Unbound SU was removed by two centrifugation steps: removal of the supernatant and resuspension in water. The SU loading percentage was calculated according to the formula $100\%\cdot(I_{ini}-I_{s1}-I_{s2})/I_{ini}$, where I_{ini} is the absorption intensity of the initial solution and I_{s1} and I_{s2} are the absorption intensities of the supernatants after the first and second centrifugations, respectively. SU release from pSiNPs was analyzed in PBS at 37°C. At pre-defined time intervals, the samples were centrifuged and the supernatant with the released SU was taken in Varioscan flash (Thermo Fisher Scientific, United States) at 429 nm. The spectrophotometer Genesys 20 (4001/4, Thermo Fisher Scientific Inc., Oberhausen, Germany) was used to determine the concentration of SU in a sample by measuring the absorption of visible light in the sample.

2.5 Gel electrophoresis and Western blot analysis

HCT 116 and H9c2 cells were lysed using lysis buffer containing 1% (v/v) Triton-X-100, 5 mM EDTA, 300 mM NaCl, 50 mM Tris (pH 7.4), 20 μg/ml soybean trypsin inhibitor, 0.4 mM benzamidine, 1 mM PMSF, 50 mM NaF, 5 mM $Na_4P_3O_7$, 1 mM Na_3VO_4, and 1.5 mM NaN_3 on ice for 20 min. Next, cells were centrifuged (1000 rcf, 4 min, +4°C) and washed twice with ice-cold phosphate-buffered saline (PBS) solution (PanEco). Then, the pellet was lysed in radioimmunoprecipitation assay (RIPA) buffer, which contains 50 mM Tris-HCl (pH 7.4), 150 mM NaCl, 2 mM EDTA, 0.5% SDS, 0.5% sodium deoxycholate, 1% NP-40, 1 mM phenylmethylsulfonyl fluoride (PMSF), and cOmplete™ Protease Inhibitor Cocktail (Roche, Basel, Switzerland), for 20 min on ice. After centrifugation (15,000 rcf, 15 min, +4°C), a part of the supernatant was taken for protein concentration assay, and another part was used for Western blot (WB) analysis, as previously described (Gongalsky et al., 2021b).

The following primary antibodies were used for WB: anti-rabbit full and cleaved caspase-3 (#9662) antibodies (Cell Signaling Technology, Danvers, MA, United States); Gβ (1: 5,000; sc-378; Santa Cruz Biotechnology); and anti-poly(ADP ribose) polymerase (PARP) (#137653 or ab137653) and anti-mouse tubulin-a (#7291) (both from Abcam, Cambridge, United Kingdom). Horseradish peroxidase (HRP)-linked goat anti-mouse and anti-rabbit antibodies (#97046 and #97200, respectively; Abcam) were used as secondary antibodies. For detection, Pierce ECL Plus Kit was used (32132, Thermo Fisher Scientific Inc., United States).

2.6 SubG1 test of HCT 116 cells

After the indicated time of treatment, cells were collected and fixed in 70% ethanol during 1 h at −20°C. Next, ethanol was washed off and the cells were re-suspended in PBS, supplemented with 1% RNase A, and stained with 20 μg/ml propidium iodide (PI) for 15 min at 37°C. After staining, the cells were examined using the FACSCanto II cell analyzer (BD Biosciences).

2.7 MTT assay of H9c2 cells

The MTT (3-(4,5-dimethylthiazol-2-yl)-2,5-diphenyl-tetrazolium bromide) assay assesses the cell metabolic activity as an indicator for cell viability. For the assay, the cell culture medium was removed and replaced with 0.5 mg ml^{-1} MTT (M5655, Sigma-Aldrich, United States) dissolved in the respective cell culture medium. After 2 h at 37°C and 5% CO_2, the staining solution was discarded and the cells were lysed using 0.1 M HCl diluted in isopropanol (CP41.2, Carl Roth, Germany). For quantification, the cell lysate was transferred to a 96-well plate and the absorbance measured at 570 nm with reference at 650 nm using a microplate reader (Spark 20M, Tecan, Switzerland). The measured values were normalized to untreated control cells.

2.8 Cell staining for fluorescence microscopy

For fluorescence imaging, the H9c2 and HCT 116 cells were grown on the coverslips in standard 10 cm Petri dishes filled with

DMEM culture medium. When cells reached the desired confluency, the medium was replaced with fresh medium. The cells were treated with nanoparticles at a concentration of 200 μg/ml, SU malate at 5–50 μM, and nanoparticles loaded with SU malate at the same concentrations. The cells were treated for indicated time intervals. The medium was removed from the dishes, and pre-warmed (37°C) staining solutions containing MitoTracker® Orange (100 nM) (Thermo Fischer Scientific Inc., United States) were added for 1 h under growth conditions (at 37°C and 5% CO_2); all cells were washed two times for 3 min with PBS and fixed in 4% paraformaldehyde (PFA) solution for 10 min. If required, an additional staining of the cytoskeleton was performed: the cells were incubated in 0.2 vol.% Triton X-100 for 10 min to permeabilize the cell membrane and thereafter stained with Alexa Fluor 488 Phalloidin (Thermo Fischer Scientific Inc., United States) for 45 min. At the end, the stained cells were fixed on the microscope slides (Epredia™ SuperFrost Plus™ Adhesion slides 75 × 25 mm, Lauda Königshofen, Germany) by Fluoromount-G® and dried overnight.

2.9 Confocal fluorescence imaging and mitochondrial analyses

Fluorescence microscopy images were acquired using a fluorescence microscope (TCS SP8 DLS, Leica Microsystems, Germany). Lasers with several excitation wavelengths were applied simultaneously for various staining of the samples: a 488-nm laser was used to activate Alexa Fluor 488 Phalloidin, a 552-nm laser for MitoTracker® Orange CMTMRos, and a 638-nm laser for the pSiNPs. As was mentioned earlier, PL properties of pSiNPs in the range of 600–800 nm allow a label-free activation and determination of the nanocontainers (Tolstik et al., 2016a). The LAS X software (Leica Application Suite X, version: 3.5.7.23225) was utilized for the data acquisition. All cells were measured using a 63×/1.3 NA oil objective (Zeiss, Germany). The images format was 1024 × 1024 pixels and the speed of image acquisition was 100 Hz. For the quantitative analysis of the mitochondrial structures, Fiji program was used to preprocess the measurements, to create a segmentation map of the mitochondria, and to perform a binary skeleton analysis, following the protocol presented by Haupt et al. (2022) (Schindelin et al., 2012). Based on this, the percentage of branched mitochondrial networks was calculated and compared through the different concentrations.

2.10 Raman micro-spectroscopy imaging, data preprocessing, and data analyses

Raman micro-spectroscopy imaging of H9c2 cells was performed using a confocal Raman microscope (alpha300R, WITec, Germany). The software WITec Control FIVE (version: 5.3.12.104), a laser source at 785-nm excitation wavelength, 200 mW power, 7–8 s integration time, 300 g/mm based spectrometer grating, and 63×/1.0 NA water immersion objective (Zeiss, Germany) were utilized for data acquisition. Spatial resolution was 0.5 μm/pixel for all three dimensions. Additionally, crystallized SU (Cayman Chemical, Michigan, United States) was measured as a reference spectrum with 100 mW power, 30 s integration time, 20 accumulations, and a 50×/0.75 NA dry objective (Zeiss, Germany). Additionally, Raman spectra of the solutions of pure pSiNPs and pSiNPs loaded with SU (dissolved in deionized H_2O) were measured on CaF_2 slides. The WITec software (Control FIVE 5.3.12.104) was used for data acquisition.

Data preprocessing and reconstruction of all spectral measurements were implemented and performed in Python 3 (version 3.9.5) programming language, using mainly "numpy," "scipy," and "scikit-learn" for computation and "matplotlib" for visualization tools. The data were preprocessed by homemade algorithms, including a cosmic spike correction (Ryabchykov et al., 2016), baseline correction using sensitive nonlinear iterative peak (SNIP) clipping (Morháč and Matoušek, 2008), Savitzky–Golay filtering, background segmentation in case of cell images, spectral truncation to Raman fingerprint region, and vector normalization. After data preprocessing, a combination of principal component analysis (PCA) and hierarchical cluster analysis (HCA) was applied, aiming to identify the drug intracellularly, combining cell spectra in representable groups (Pearson, 1901; Hierarchical Cluster Analysis - Cecil C. Bridges, 1966; Wold et al., 1987). The clustering was performed on all selected data at once, where a mix of untreated cells was compared to cells treated with pure SU or cells treated with SU loaded in pSiNPs. The resulting mean spectra were evaluated manually and compared to the measured reference spectra. Also, the number of clusters for HCA was set manually as low as possible to still detect a meaningful difference between the groups. In addition, the spectra were divided with respect to different spectral meaning and not by different measurement properties and conditions. Based on this, a reasonable amount of clusters (e.g., nucleus, cytoplasm, and, in rare cases, clusters with mitochondrial contribution) was expected to be found in both groups.

3 Result and discussion

3.1 pSiNPs characterization

For the assessment of the compatibility of pSiNPs in cancer and cardiac cells, pSiNPs are required to fulfill certain quality measures, such as nanoparticle diameter of less than 200 nm for effective internalization into the cells, a porous structure for an effective drug loading and drug delivery, and the presence of PL

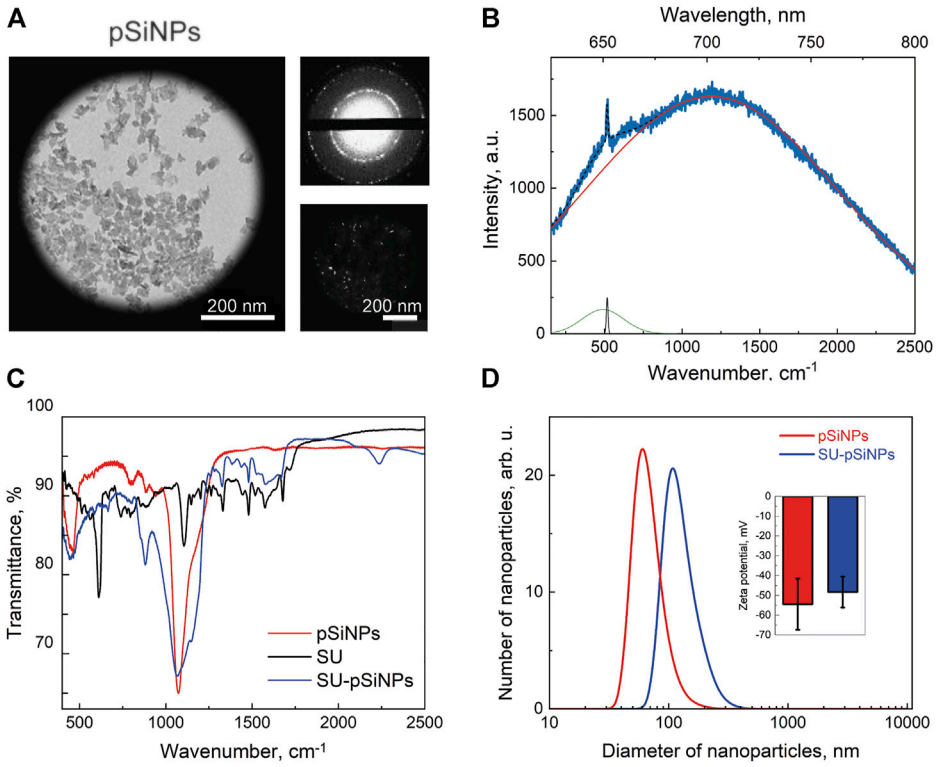

FIGURE 1
Characterization of pSiNPs. **(A)** TEM image of pSiNPs (left) with an electron diffraction pattern (top small picture) and a dark-field image (bottom small picture). **(B)** PL and Raman spectra of pSiNPs. Experimental spectrum (blue line) and its deconvolution, i.e., resulted spectrum (dashed black line) and components: PL (red line), Raman amorphous Si (480 cm^{-1}—green line), and nc-Si (518 cm^{-1}—black line) peaks. Laser excitation wavelength is 633 nm. **(C)** FTIR spectrum of pSiNPs, SU, and SU-pSiNPs. **(D)** Diameter distribution of pSiNPs before (red) and after (blue) loading of SU in aqueous suspension measured by means of dynamic light scattering. The inset shows zeta potentials of pSiNPs.

properties and nanocrystallinity to be well identified by luminescence and Raman microscopy methods (Osminkina and Gongalsky, 2018). To achieve these characteristics, pSiNPs were prepared by electrochemical etching of crystalline silicon substrate in HF and ethanol solution, lifting off the obtained porous silicon layer, ball-milling, and centrifugation. The preparation conditions were optimized to provide pore size and surface area of the nanoparticles suitable for efficient loading of chemotherapeutics while maintaining an acceptable pSiNPs biodegradation rate (Maximchik et al., 2019). According to TEM micrographs presented in Figure 1A, nanoparticles of about 100 nm in diameter were achieved, with an irregular shape due to the top-down fabrication process and consisting of smaller silicon nanocrystals (nc-Si) and pores. The crystallinity of pSiNPs was confirmed by the pattern of nc-Si electron diffraction, which contains both diffraction rings and bright spots, along with dark-field TEM images, where bright spots from nc-Si were also observed (Figure 1A, *top and bottom images*) (Osminkina and Gongalsky, 2018).

The PL spectrum of the pSiNPs is shown together with their Raman spectrum in Figure 1B. The experimentally obtained spectrum (blue line) was approximated by superposition of the wide Gaussian PL band (red line) and Raman spectrum (black line). Deconvolution of the Raman spectrum showed two maxima corresponding to amorphous Si at 480 cm^{-1} and nc-Si at 518 cm^{-1} (Tolstik et al., 2016b). The RT PL band has a maximum at 690 nm that is well explained by the radiative recombination of excitons confined in nc-Si with an average size of about 3.5 nm. The exact position of the Raman band was determined by the average diameter of the Si nanocrystals, which represent the size of about 3.6 nm (Gongalsky et al., 2020; 2021b).

Figure 1C shows FTIR spectra for pSiNPs, SU, and SU-loaded pSiNPs (SU-pSiNPs). The surface of pSiNPs is oxidized in either the air atmosphere or the aqueous suspension. That is, nc-Si core is surrounded by SiO_x shell with possible amorphous Si interface between them. The oxidation of pSiNPs is visible in Figure 1C by IR absorption bands, which correspond to the δSi–O–Si deformation vibration mode at 484 cm^{-1}, to Si_xO_y vibration mode at 800 cm^{-1}, and to νSi–O–Si vibration mode of the transversal optic modes at 1060 cm^{-1} and longitudinal optic phonons at 1200 cm^{-1}. This oxygen coating of nanoparticles provides a negative charge on their surface and

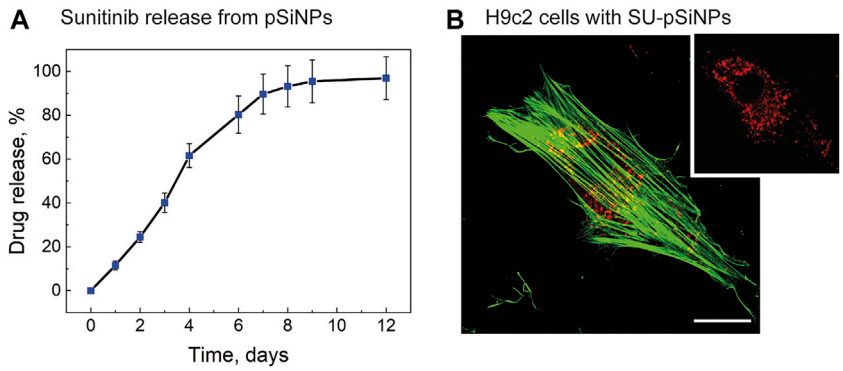

FIGURE 2
(A) Drug release profile of SU loaded into pSiNPs over time (days). Typical release time (50% of payload) is demonstrated after 4 days. **(B)** A representative fluorescence image of H9c2 cell treated with SU-loaded nanoparticles for 24 h; the content of SU in the particles was 20 μM. The cytoskeleton was labeled with Alexa Fluor 488 Phalloidin and is depicted in green. For the visualization of pSiNPs, the laser at 638-nm excitation wavelength was used; the pSiNPs are depicted in red. SU could not be detected with the fluorescence microscopy without labeling. The scale bar represents 20 μm.

their hydrophilic properties (Sailor, 2022). The FTIR spectrum of SU contains a large number of components responsible for the absorption of IR radiation by various vibrations of bonds within the molecule (Tarasi et al., 2022). It should be noted that the spectrum of SU-pSiNPs contains both the absorption bands of silicon–oxygen bonds described earlier and the absorption bands of SU. This testifies to the effective adsorption of SU in the pores of pSiNPs.

Next, we monitored the drug release from SU-loaded pSiNPs (Figure 2A). The typical release duration (50% of payload) was 4 days, which can be considered as sustained release. SU retention in pSiNPs is most likely due to the "electrostatic adsorption" or coulombic forces between negative SiO_2 surface of pSiNPs and the positively charged SU molecules (Anglin et al., 2008), and the moderate solubility of SU malate in aqueous medium (Alshehri and Shakeel, 2020).

For the loading of the pSiNPs with SU, SU was stirred together with the pSiNPs in water for 24 h at RT. After loading, the unbound drug was removed by a washing process using two centrifugation steps. The SU loading efficiency into the pSiNPs was determined by comparing the optical transmission intensities of the initial drug solution and the supernatant after loading and was about 45% of the initial concentration of the drug solution. The mean hydrodynamic size of pSiNPs, measured by DLS, was consistent with the TEM measurements (Figure 1D). SU loading leads to an increase in the size of pSiNPs (about 185 nm). This may be explained by the positive charge of SU, which can partially neutralize the negative charge of the pSiNPs and thereby increase their van der Waals interactions. It is clearly visible in Figure 1D; the presented statistically non-significant change in the value of zeta potential shows that the particles partially lose their negative charge when they are loaded with SU.

To test the uptake and distribution of SU-pSiNPs intracellularly, the cardiac myoblast cell line H9c2 was investigated as the heart has been reported to be a target of the drug's side-effect by SU therapy. The cells were incubated with SU-pSiNPs for 24 h. To monitor the SU-pSiNPs localization, the actin filaments of the cytoskeleton were stained with Alexa Fluor 488 Phalloidin. Due to their strong PL features, pSiNPs possess well-visible fluorescence properties, with absorption in the range of 600–800 nm (see Figure 1B). A representative confocal fluorescence image in Figure 2B demonstrates that pSiNPs (depicted in red) effectively penetrated into the cells within 1 day of incubation and localized mostly inside the cytoplasm. Thus, the uptake of the nanocontainers seems efficient and can easily be detected by fluorescence microscopy. However, no detection of the drug and its release could be studied by standard confocal fluorescence imaging. Commonly used methods, e.g., immunofluorescence or mass spectrometry, do not also allow a longitudinal monitoring of the drug release. Thus, confocal Raman micro-spectroscopy can have decisive advantages here, as the drug distribution in the cells can be traced without labeling (Aljakouch et al., 2018; El-Mashtoly, 2020). For example, the release of doxorubicin from pSiNPs in cancer cells was precisely visualized in our previous studies by applying Raman spectroscopy (Maximchik et al., 2019).

3.2 Raman micro-spectroscopy studies of sunitinib, pSiNPs, and SU-pSiNPs *in vitro*

To localize pSiNPs, SU, and SU-pSiNPs intracellularly, Raman imaging was utilized. Raman micro-spectroscopy allows the detection of compounds based on their biochemical

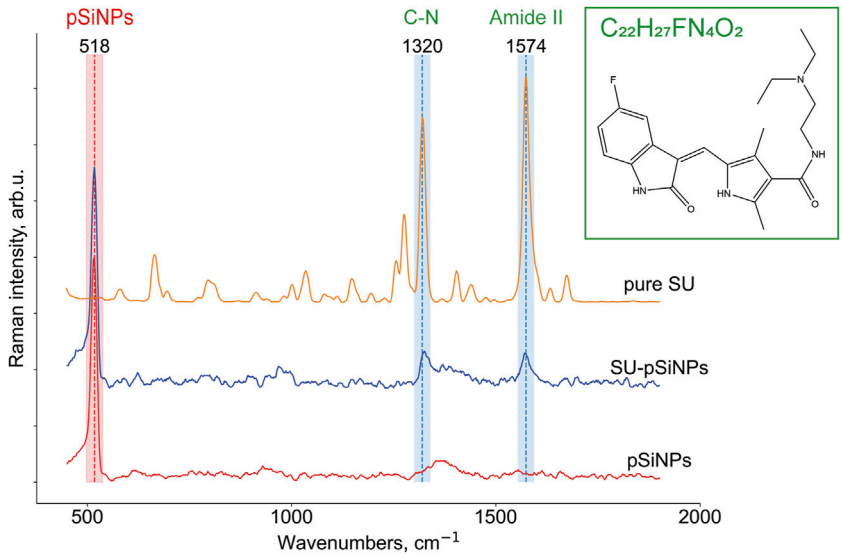

FIGURE 3
Raman reference spectra of crystallized SU ($C_{22}H_{27}FN_4O_2$; *N*-[2-(diethylamino)ethyl]-5-[(*Z*)-(5-fluor-1,2-dihydro-2-oxo-3H-indol-3-ylidene)-methyl]-2,4-dimethyl-1H-pyrrole-3-carboxamide), depicted in orange, of solutions of SU loaded in pSiNPs (SU-pSiNPs, depicted in blue) and of pure Si nanocontainers (pSiNPs, depicted in red) dissolved in deionized water for 24 h. The Raman spectra were preprocessed (see Section 2 for the details) and the characteristic Raman bands at 518 cm^{-1} for pSiNPs, and 1320 cm^{-1} and 1574 cm^{-1} for SU, respectively, were specified.

differences within biological samples. The advantage of this label-free method is in the possibility to identify molecules and compounds based on their molecular fingerprints, i.e., molecular vibrations. To our knowledge, there are no studies performed on the interaction of pSiNPs and cardiac cells. Using Raman spectroscopy can prove the uptake of pSiNPs by cardiomyocytes and the safety of these nanocontainers as "transporters" of cargo into cardiomyoblasts. Thus, porous silicon nanoparticles promise to be a safe and effective delivery system for drugs like SU in cardiomyoblasts. Thereby, aiming to detect the localization of the drug and nano-containers intracellularly, we first recorded Raman reference spectra of crystalline SU, pSiNPs, and SU-pSiNPs (Figure 3). SU (depicted in orange) contains dominant intensity peaks at 1320 cm^{-1} and 1574 cm^{-1} that are associated with C–N and amide stretching vibrations, respectively (Litti et al., 2016). It is known that the amide II band consists of 60% N–H and 40% C–N stretches and is presented near 1550 cm^{-1} and the amide III band consists of 40% C–N and 30% N–H stretches and is presented near 1300 cm^{-1} (Horiba, 2021). The predominant Raman band of pSiNPs (depicted in red) was slightly shifted from the characteristic wavenumber at 520 cm^{-1} to 518 cm^{-1}. This shift is explained by the dissolution processes of pSiNPs, as this is associated with a decrease in the Si crystal size and therewith a Raman band shift to the lower wavenumbers (Tolstik et al., 2016b). The reference Raman spectrum of SU-pSiNPs in aqueous solution (depicted in blue) possesses Raman bands of both molecules: SU-associated stretching vibrations at 1324 cm^{-1} and 1572 cm^{-1} and the silicon signal at 518 cm^{-1}.

To prove the intracellular uptake of SU with and without nanocontainers, we incubated the H9c2 cells with pure SU and with unloaded pSiNPs for 24–72 h using concentrations of SU in the first case between 5 and 50 μM. First, Raman spectroscopy images of H9c2 cells incubated with pure pSiNPs were recorded by performing a 3D scan over several XY-layers within the cell with 1 μm step in all spatial dimensions aiming to detect intracellular accumulations of nanoparticles. The representative 3D image for the pSiNPs in a concentration of 200 μg/ml is demonstrated in Figure 4A. The dominant Raman band of nc-Si at 518 cm^{-1} enables the separation of clusters containing pSiNPs (depicted in red) from clusters containing signals of the cytoplasm (for simplicity, here all spectra of cytosolic cellular components are depicted in green shades). This 3D scan of a cytoplasmic part of the cell covering 3 μm shows that pSiNPs have indeed passed the cell membrane and have entered the cytoplasm. It suggests an efficient uptake of the nanoparticles into the cytoplasm, which confirmed the results obtained by fluorescence microscopy (Figure 2B). Moreover, as the interior part of the cell was measured in z-direction, the localization of pSiNPs was primarily referred to the cytoplasm with no Si accumulations at the cell membrane. Comparable incubation steps followed by Raman imaging were also performed using HCT 116 cells with similar results.

To localize the anticancer drug SU within the cell interior, Raman imaging of cells incubated with SU (20 μM) was

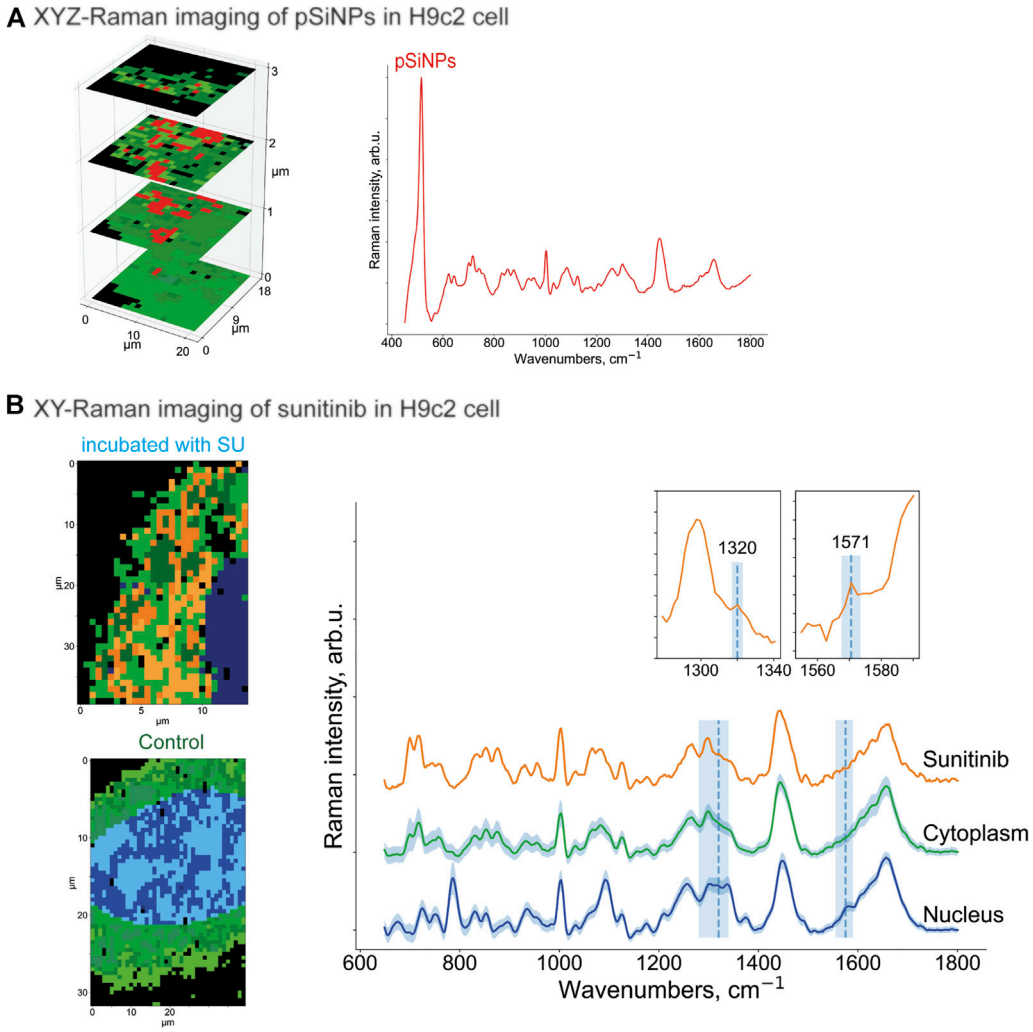

FIGURE 4
(A) XYZ-Raman micro-spectroscopy image within a H9c2 cell incubated with pSiNPs in a concentration of 200 μg/ml. The spectrum of the cluster that corresponds to the pSiNPs has a Si-specific peak at 518 cm^{-1} and is depicted in red; the cluster that corresponds to cytoplasm is depicted in green shades. **(B)** XY-Raman micro-spectroscopy images of H9c2 cell incubated with 20 μM of SU for 24 h (upper image, left), control H9c2 cell (lower image, left) and the corresponding Raman spectra of three dominant clusters with sunitinib, cytoplasmic, and nuleus inputs. Thus, after data preprocessing, HCA clustering was applied to distinguish the following main components: cytoplasm (multiple green colors), nucleus (multiple blue colors), and orange containing SU with characteristic Raman bands at 1320 cm^{-1} and 1574 cm^{-1}. While the peak at 1320 cm^{-1} is only minor ones, the Raman band at 1574 cm^{-1} is more pronounced. Both SU-specific peaks have low intensity compared to the reference spectra, and the orange SU cluster also has a partial overlap with the cell interior signals (characteristic Raman bands at 1450 cm^{-1} and 1650 cm^{-1}).

performed, followed by data preprocessing and hyperspectral analyses (Figure 4B). Using the clustering algorithms described in the Methods section, the clusters corresponding to SU, cytoplasm, and nuclei were identified. Thus, SU enrichments were detected throughout the cell interior based on the SU-associated Raman bands as depicted in Figure 4B as orange cluster, which are in good agreement with the ones in the reference Raman spectra of SU (see Figure 3). Both Raman bands at 1320 cm^{-1} and 1571 cm^{-1} are clearly visible; however, the intensities are low compared to the cell interior signal (characteristic stretching vibrations at 1450 cm^{-1} represent CH_2/CH_3 groups bending for proteins and CH scissoring for lipids; and 1650 cm^{-1} stretching vibrations represent random coil of amide 1 for proteins and C=C stretching for lipids) (Risi et al., 2012; Tolstik et al., 2016b). The reason is the low abundance of SU compared to the cell components. It is hardly possible to unambiguously visualize pure SU molecules intracellularly with the provided resolution of the microscope and herein used concentrations. However, we succeeded in visualizing SU-associated enrichments intracellularly. The spectra of the nucleus and the cytoplasm are depicted in blue and green, respectively. The majority of the SU-assigned pixels were

10.3389/fphar.2022.962763

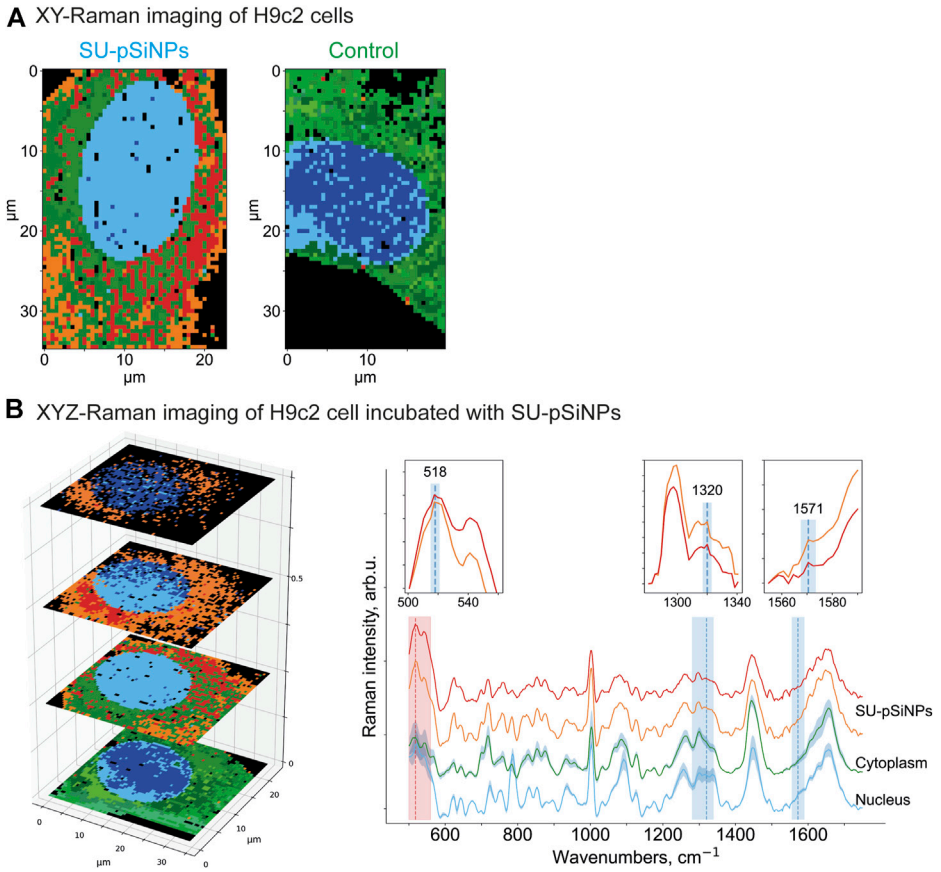

FIGURE 5
(A) XY- and **(B)** XYZ-Raman micro-spectroscopy images of a H9c2 cell incubated with 20 µM of SU loaded in pSiNPs for 24 h [**(A)**, left] and of a control H9c2 cell [**(A)**, right]. After data preprocessing, HCA clustering was applied to distinguish the following main components: pure cytoplasmic components (multiple green colors), nucleus (multiple blue colors), and red and orange clusters containing—next to cytoplasmic signal—SU and nanocontainer-specific peaks at 518 cm^{-1} for pSiNPs, and 1320 cm^{-1} and 1571 cm^{-1} for SU, respectively. The clusters were plotted with standard deviations shown as shadows.

located within the cytoplasm and did not penetrate into the nucleus. The comparison of these measurements with those in control H9c2 cells (Figure 4B, below) validated the detection of SU-associated Raman bands only in the SU-treated cells. Taken together, we showed that Raman imaging allowed the detection of compounds, nanocontainers, or cellular components without applying additional staining procedures or chemical modifications, which may allow the longitudinal and non-invasive monitoring of the kinetics of the drugs within the cells.

Further, the H9c2 cells were incubated with SU-loaded nanocontainers. The cells treated with SU-pSiNPs and untreated cells were then compared by applying multivariate data analyses (HCA clustering; see Methods section) to separate the spectra in several clusters of interest. Thereby, SU-pSiNPs-treated cells were clustered with a ground-truth set (a set of control cells for comparison) of up to eight randomly selected untreated cells at once to find component-specific clusters in both groups. The assumption was that components that only appear in treated cells will result in unique clusters of treated cells. Also, we aimed to hold the total number of data points equal for both groups and balanced the number of control cells based on the number of data points in the treated cells. Here, the nucleus (identified by the DNA/RNA-specific band at 785 cm^{-1}) was depicted in different shades of blue, while different shades of green referred to cytoplasmic clusters and are presented in 2D scans of both SU-pSiNP-treated and untreated groups (Figure 5A). For the identification of clusters as potential candidates for cellular spectra of pSiNPs or SU, the proportion of all clusters per group was determined and the clusters that are represented only in the treated group were taken for further investigation. Due to low drug concentrations and the drug's strong spectral overlap with the Raman bands of Si and cell organelles, the differentiation of pure SU spectra with the presented optical resolution was challenging. However, two different clusters encoding SU or SU-pSiNPs were clearly separated in the treated group (Figure 5A, left panel) and are

depicted in orange and red, combining cytoplasmic background and SU-pSiNPs-characteristic Raman bands. For comparison, an untreated cell was also analyzed and clustered and is shown in Figure 5B, right panel. The dominant clusters, depicted in shades of green, correspond to the cytoplasmic background; however, no characteristic Raman shifts for SU, SU-pSiNPs, or pSiNPs were detected. Also, it is visible that both orange and red clusters cannot be identified in the control group, supporting our assumption that the cluster is only present in the treated group, which thus validates our data analysis.

In addition, to confirm the localization of the SU-loaded nanoparticles within the H9c2 cell, we also performed 3D measurements of H9c2 cells along the z-axis. In the representative 3D (XYZ) scan, the same color scheme was applied as for the 2D (XY) scan above, and the 2D scan represents the second layer of the 3D scan (Figure 5). Thus, the mean spectra of two clusters containing SU-pSiNPs (red and orange spectra), the mean spectrum of the nucleus (blue), and the mean spectrum of the cytoplasm (green) were calculated, analyzed, compared, and plotted with their respective standard deviations (Figure 5B). Both red and orange spectra show a band at 518 cm^{-1}, which is characteristic for pSiNPs, although the intensities are significantly weaker with respect to the remaining signals of the cytoplasmic components, especially compared to the reference spectra of nc-Si. Besides, the Si-characteristic Raman band has undergone a slight Raman shift from 520 to 518 cm^{-1} (compared to the reference spectra of Si in Figure 3). Two low-intensity Raman bands at 1320 cm^{-1} and 1569 cm^{-1} refer to SU-loaded pSiNPs. The changes in drug-specific vibrational fingerprints and the decrease in Raman intensities can be explained by the interaction of the nanocontainers and the drug with cellular components, pSiNP dissolution, and subsequent drug release (Tolstik et al., 2016b; Maximchik et al., 2019). The SU-specific peaks within the cytoplasm are of low intensity, making a pixel-wise identification challenging. Slight changes in laser intensity, the applied drug concentration, the focus plane, and other parameters can impact on the visibility/identification of their peaks. Nevertheless, our analyses validated the uptake of SU-pSiNPs, i.e., SU and pSiNPs, into the cells. Besides, the nuclear spectrum (in blue) does not contain any Raman band of Si, in contrast to the cytoplasm, even though the cellular Raman spectrum of Si has a slightly decreased Raman peak intensity around 518 cm^{-1} that is obviously due to a low pSiNP contribution. Of note, the Raman signal was integrated with 500 nm per pixel in spatial dimensions, which significantly extends the size of pSiNPs. Consequently, the silicon signal in the cytoplasmic spectrum can be a result of a small amount of randomly distributed pSiNPs or an agglomeration of pSiNPs. The high contribution of the orange cluster in the top layers, close to the cell membrane, validates the uptake of SU-pSiNPs into the cytoplasm and was found with higher concentrations close to the cell membrane after 24 h of incubation. Thus, this 3D scan with spectral information of both pSiNPs and SU further proves that the SU-loaded NPs were taken up by the cells and can be well localized by the application of Raman spectroscopy, and in principle the cells can be re-used for further analyses, e.g., immunofluorescence or MALDI mass spectrometry imaging (Ryabchykov et al., 2018). The application of Raman imaging *in vivo* would be of great benefit for clinical applications (Caspers et al., 2003; Cordero et al., 2018). Thus, first fiber-optic-based prototypes for tissue characterization are under development. However, there are several technical hurdles that need further sophisticated technical developments to translate Raman spectroscopy into clinical use.

3.3 Toxicity studies of pSiNPs, SU, and SU-loaded pSiNPs in cancer and cardiac muscle cells

For the evaluation of pSiNPs and their impact on the toxicity of SU, we examined H9c2 cells along with human colon carcinoma cell line HCT 116 as SU "target" cells, which are commonly used in the gastrointestinal oncology research (Sun et al., 2012). To assess whether the SU-loaded nanoparticles are similarly efficient to reduce cell survival as pure SU, we analyzed different markers of cell death and studied the toxicity of unloaded nanoparticles (NP) on H9c2 cells. The cleavage of the effector caspase-3 and its substrate PARP [poly (ADPribose) polymerase] was evaluated by WB analyses. These proteins are well-known apoptotic markers: active caspase-3 is a key effector enzyme in apoptotic signaling, which cleaves several substrates including PARP. PARP is engaged in the repair of DNA damage, and its cleavage by caspase-3 reflects the intensity of apoptosis (Lazebnik et al., 1994; Crowley et al., 2016). Cells were incubated with SU-loaded nanoparticles (concentration range from 5 to 50 μM) or SU (in concentrations of 5 and 10 μM) for 24, 48, and 72 h. As was shown previously, the pSiNPs themselves did not show cell toxic properties up to a concentration of 700 μg/mL in HCT 116 cells (Maximchik et al., 2019), thus allowing us to variate the concentration of SU loaded into the nanoparticles for further cytotoxicity studies to higher content of nanoparticles.

According to the WB analyses, the treatment of HCT 116 with 5 or 10 μM of SU for 24 or 48 h caused an increase of cleaved caspase-3 (p19/p17 caspase-3). Also, slight decreases of procaspase-3 and full PARP were detected after 24 h and more pronounced decreases after 48 h of treatment. These data suggest the induction of apoptosis in HCT 116 cells by SU. In contrast, at least 25 μM of SU loaded in pSiNPs was needed to trigger a comparable increase of cleaved caspase-3 (p19/p17 caspase-3) (Figure 6A). After a 72 h treatment of HCT 116 cells with SU loaded in pSiNPs, 10 μM of SU appears to induce apoptotic effects as well, i.e., the signal for cleaved caspase-3 was increased and the signal for full PARP was decreased, which may suggest a delayed toxic effect of SU if loaded in pSiNPs.

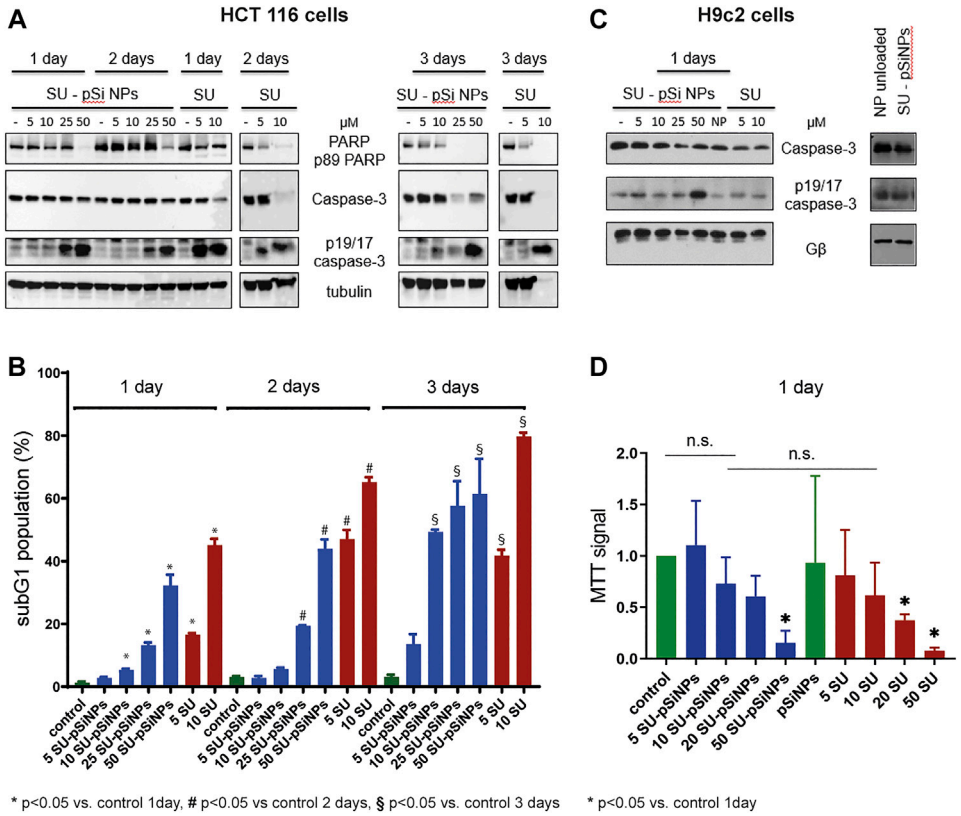

FIGURE 6
(A–D) HCT 116 cells and H9c2 cells were treated with sunitinib-loaded nanoparticles (SU-pSiNP) or pure sunitinib (SU) or unloaded nanoparticles (NP unloaded, **(C)**, right panel) in the indicated concentrations (μM) and for the indicated time intervals. In **(A)** and **(C),** the representative WB of expression levels of apoptotic marker proteins PARP, caspase-3, and cleaved caspase (p19/17 fragments of caspase-3, p19/17 caspase-3) are shown. Gβ and tubulin were used as loading controls. Blots were reproduced at least three times with similar results. **(B)** The histogram of flow cytometric analysis data for HCT 116 cells using subG1 assay; %: percent of SubG1 population. Results are shown as mean values ± standard deviation (SD), $n = 3$, $^*p < 0.05$ vs. control 1 day, $\#p < 0.05$ vs. control 2 days, §$p < 0.05$ vs. control 3 days, n.s. not significant. **(D)** MTT cell viability assay of H9c2 cells upon treatment with SU-pSiNPs and pure SU in indicated concentrations (μM) for 1 day. Results are presented as mean values ± standard deviation (SD), $n = 3$, $^*p < 0.05$ vs. untreated control and pSiNPs-treated group. Ordinary one-way ANOVA was applied with Dunnett test to correct for multiple comparison.

To further validate these results, we performed flow cytometric analyses assessing the subG1 cell population, which monitors cells with accumulations of small DNA fragments in late stages of apoptosis due to increased endonuclease activity. The relative proportion of the subG1 population reflects the percentage of apoptotic cells (Plesca et al., 2008). Cell death analyses using subG1 test have revealed that the incubation of HCT 116 cells with SU (5 and 10 μM) for 24, 48, and 72 h significantly increased the subG1 population compared to the untreated controls (Figure 6B). Similarly as seen for the apoptotic markers in the WB analyses of HCT 116 cells, a delayed apoptotic response was induced by SU loaded in pSiNPs compared to SU treatment without the use of nanocontainers (see Figure 6B). While the cells treated with SU alone reached the maximum of apoptotic cells after 48 h, SU loaded in nanocontainers showed a further increase of apoptotic cells after 72 h (compare, e.g., the 10 μM condition after 48 and 72 h for SU alone and SU-pSiNPs).

Further, the toxicity of the chemotherapeutic agent SU was studied *in vitro* using the cardiomyoblast cell line H9c2 as a model system for cardiomyocyte toxicity (Merches et al., 2022). WB of cleaved caspase-3 (p19/p17 caspase-3) and caspase-3 revealed slight changes after a 24 h treatment of SU loaded in pSiNPs or SU alone (Figure 6C); the effects were more pronounced when the cells were treated with higher concentration of SU-pSiNPs (50 μM), similar to that seen in HCT 116 cells. In line with these results, the MTT test revealed a significant decrease in the viability of H9c2 cells, only after a 24 h treatment with 50 μM of SU-pSiNPs or 20 or 50 μM of SU alone (Figure 6D).

Taken together, our results show a time shift in the induction of a comparable level of apoptosis in HCT 116 cells by pure SU

versus SU loaded in nanoparticles, which is most likely due to the sustained release of the drug from the nanoparticles that slows down cellular distribution of the drug. H9c2 cells seemed to be relatively resistant to SU treatment since at least 20 μM of pure SU was needed to induce cell death in H9c2 cells after 24 h treatment. Furthermore, the application of SU via pSiNPs or purely SU hardly affected the outcome on the cell survival. Even though, the cardiotoxicity of SU was hardly reduced by pSiNPs, WB analyses showed that pure pSiNPs are very well tolerated by these cardiomyoblast cells at least up to a concentration of 200 μg/ml as shown in Figure 6C, right panel. No accumulation of cleaved caspase-3 (p19/p17 caspase-3) or cleavage of caspase-3 was detectable after 24 h of incubation with nanoparticles. Thus, pSiNPs loaded with SU might be considered as a promising approach as drug depot with sustained drug release.

As cardiotoxicity of SU is linked to changes at mitochondrial level (Bouitbir et al., 2019), we aimed to study the impact of SU in comparison to SU-pSiNPs on these sensitive organelles. We thus analyzed the mitochondrial distribution as an early indicator for apoptotic changes (Karbowski and Youle, 2003). Therefore, confocal fluorescence microscopy was applied for H9c2 cells to study SU's impact on the mitochondrial network. The cells were stained with MitoTracker® Orange (λ_{ex} = 552 nm) and incubated with SU or SU-loaded nanoparticles in concentrations between 5 and 50 μM for 24 h (Supplementary Figure S1). The images were analyzed as described in Haupt et al. (2022). These analyses suggest that the mitochondrial network might be affected by SU. Cells treated with SU or SU-pSiNPs at concentrations shown to be toxic (20 and 50 μM; Figures 6C,D) were analyzed and they indeed revealed a reduction of the proportion of mitochondria within "networks" if pure SU was applied (depicted in red) compared to the incubation with SU loaded in nanocontainers (depicted in blue). These data indeed suggest that there may be a slight prevention of cell death if nanocontainers are used for SU administration; however, these data cannot exclude that the SU-induced cardiotoxicity is just delayed by nanoparticles since H9c2 cells were not yet investigated for longer than 24 h. Representative images are shown in Supplementary Figure S1B, where the mitochondrial network seems to have a rather comparable structure for control and SU-treated cells in concentrations up to 10 μM applied alone or in nanocontainers. The treatment with pure SU at higher concentrations (20 and 50 μM) caused a negative impact on the mitochondrial structures that were approved by quantitative analysis in Supplementary Figure S1A. A similar effect is visible for SU-pSiNPs treatment for 50 μM (but not 20 μM) of SU, validating therewith the quantitative analysis in the Supplementary Figure S1A.

Summing up the results, flow cytofluorometry and WB analysis showed that SU induces death of cancer and cardiac cells. Our experiments hint to apoptosis as a mode of programmed cell death and are in line with results that show SU-induced apoptosis in different cell types (Lin et al., 2011; Guo et al., 2021). However, further studies would be needed to rigorously assess the mode and time course of cytotoxicity. This cytotoxic effect in cancer cells was significantly delayed at comparable concentrations of the drug delivered in nanocontainers. Thus far, the experiments suggest that SU delivery via nanocontainers did not prevent cardiomyocyte death. The pSiNPs do not seem to be suitable for the prevention of cardiotoxicity per se; however, future studies will show whether functionalization of the nanocontainers for targeted drug delivery to cancer cells may reduce cardiotoxicity or whether intracellular drug depots may improve the effects of drugs, e.g., applied for heart failure. Thus, along with the assessed *in vitro* cardiosafety of pSiNPs in this study, new perspectives for their application, e.g., for controlled drug delivery with slow and sustained release, will open new prospects for patients with chronic heart diseases.

4 Conclusion

In this article, we monitored the uptake and distribution of the anticancer drug sunitinib (SU), delivered in nanocontainers based on pSiNPs or as a dissolved pure compound, with a set of biophotonics and analytical techniques. The first results suggest that pSiNPs are effectively taken up into the cytoplasm of several cell types and can build an intracellular drug depot that facilitates continuous drug release. Porous silicon nanoparticles have great advantages for the delivery of the drug. Since they exhibit luminescent properties and a characteristic Raman band that does not overlap with the Raman bands of cellular organelles, these nanoparticles can easily be detected in cells and within the cellular compartment by Raman micro-spectroscopy. 2D and 3D Raman micro-spectroscopy imaging has the advantage of enabling the label-free visualization of drug depots and potentially the drug release as well.

Flow cytofluorometry and WB analysis further showed that sunitinib triggers apoptotic death of cancer and cardiac cells. This cytotoxic effect in cancer cells was significantly delayed if SU was delivered in nanocontainers. The observed slight differences of cell survival and the integrity of mitochondrial networks whether SU was applied to H9c2 cells within nanoparticles or not may also be due to a delayed toxicity. Even if pSiNPs may not be suitable for the prevention of cardiotoxicity *per se*, future studies will show whether functionalization of the nanocontainers for targeted drug delivery to cancer cells may reduce cardiotoxicity or whether intracellular drug depots may improve the effects of drugs, e.g., applied for heart failure. Thus, along with the here assessed *in vitro* cardiosafety of pSiNPs, new perspectives for their application, e.g., for controlled drug delivery with slow and sustained release, will open new prospects for pharmacological treatment options.

Data availability statement

The raw data supporting the conclusions of this article will be made available by the authors, without undue reservation.

Author contributions

The manuscript was written through contributions of all authors. All authors have given approval to the final version of the manuscript.

Funding

This study was supported by the German Ministry of Research and Education BMBF: ChinValue (03INT703AB) and ERK-Casting (16GW0262K), the Deutsche Forschungsgemeinschaft SFB1525 (453989101) and SFB/TR 296 (424957847), the Drug Discovery Hub Dortmund (DDHD), and the Russian Science Foundation (grant 19-72-10131).

Acknowledgments

This work was conducted as a collaboration of ISAS in Dortmund and Leibniz-IPHT in Jena within the Leibniz Research Network Health Technologies. We greatly appreciate the participation and scientific input of S. Dörr, I. Schuler, J. Fender, and S. Rebs and the excellent help of N. Yurdagül-Hemmrich, A. Weiss, and E. Hoffmann-Posorske. This research was performed according to the Development Program of the Interdisciplinary Scientific and Educational School of Lomonosov Moscow State University "Photonics and quantum technologies. Digital medicine." LAO and MBG greatly acknowledge the financial support by the program DAAD "Research Stays for University Academics and Scientists."

Conflict of interest

The authors declare that the research was conducted in the absence of any commercial or financial relationships that could be construed as a potential conflict of interest.

Publisher's note

All claims expressed in this article are solely those of the authors and do not necessarily represent those of their affiliated organizations, or those of the publisher, the editors and the reviewers. Any product that may be evaluated in this article, or claim that may be made by its manufacturer, is not guaranteed or endorsed by the publisher.

Supplementary material

The Supplementary Material for this article can be found online at: https://www.frontiersin.org/articles/10.3389/fphar.2022.962763/full#supplementary-material

SUPPLEMENTARY FIGURE S1
Analysis and representative images of H9c2 cells treated for 24 h with pure sunitinib (SU) or with sunitinib loaded in nanoparticles (SU-pSiNPs) with the indicated concentrations. The H9c2 cells were stained with MitoTracker™ Orange to visualize mitochondrial network complexity. **(A)** Percentage of mitochondrial networks at different concentrations and the ways of treatment: SU with pSiNPs depicted in blue and without pSiNPs depicted in red. Results are presented as mean ± standard deviation (SD) and shown as blocks for each case. For the quantitative analysis of the mitochondrial structures, Fiji program was used to preprocess the measurements, to create a segmentation map of the mitochondria and to perform a binary skeleton analysis, following the protocol presented by Haupt et al., 2022. Based on this, the percentage of branched mitochondrial networks was calculated and compared through the different concentrations. (B) Representative fluorescence images of H9c2 stained with MitoTracker™ Orange to visualize mitochondrial network; the scale bar was 20 μm. The H9c2 cells were treated for 24 h with pure sunitinib (SU, *upper row*) or with sunitinib loaded in nanoparticles (SU-pSiNPs, *lower row*). At least 5 to 10 cells of each SU concentration and each pSiNPs were analyzed and the representative images are shown.

References

Aljakouch, K., Lechtonen, T., Yosef, H. K., Hammoud, M. K., Alsaidi, W., Kötting, C., et al. (2018). Raman-mikrospektroskopischer Nachweis für den Metabolismus eines Tyrosinkinase-Inhibitors, Neratinib, in Krebszellen. *Angew. Chem.* 130, 7370–7374. doi:10.1002/ange.201803394

Alshehri, S., and Shakeel, F. (2020). Solubility determination, various solubility parameters and solution thermodynamics of sunitinib malate in some cosolvents, water and various (Transcutol + water) mixtures. *J. Mol. Liq.* 307, 112970. doi:10.1016/j.molliq.2020.112970

Anderson, S. H. C., Elliott, H., Wallis, D. J., Canham, L. T., and Powell, J. J. (2003). Dissolution of different forms of partially porous silicon wafers under simulated physiological conditions. *Phys. Stat. Sol.* 197, 331–335. doi:10.1002/pssa.200306519

Anglin, E. J., Cheng, L., Freeman, W. R., and Sailor, M. J. (2008). Porous silicon in drug delivery devices and materials. *Adv. Drug Deliv. Rev.* 60, 1266–1277. doi:10.1016/j.addr.2008.03.017

Ban, H. S., Kim, B.-K., Lee, H., Kim, H. M., Harmalkar, D., Nam, M., et al. (2017). The novel hypoxia-inducible factor-1α inhibitor IDF-11774 regulates cancer metabolism, thereby suppressing tumor growth. *Cell. Death Dis.* 8, e2843. doi:10.1038/cddis.2017.235

Bocklitz, T. W., Salah, F. S., Vogler, N., Heuke, S., Chernavskaia, O., Schmidt, C., et al. (2016). Pseudo-HE images derived from CARS/TPEF/SHG multimodal imaging in combination with Raman-spectroscopy as a pathological screening tool. *BMC Cancer* 16, 534. doi:10.1186/s12885-016-2520-x

Bouitbir, J., Alshaikhali, A., Panajatovic, M. V., Abegg, V. F., Paech, F., Krähenbühl, S., et al. (2019). Mitochondrial oxidative stress plays a critical role in the cardiotoxicity of sunitinib: Running title: Sunitinib and oxidative stress in hearts. *Toxicology* 426, 152281. doi:10.1016/j.tox.2019.152281

Caspers, P. J., Lucassen, G. W., and Puppels, G. J. (2003). Combined *in vivo* confocal Raman spectroscopy and confocal microscopy of human skin. *Biophys. J.* 85, 572–580. doi:10.1016/S0006-3495(03)74501-9

Chakravarty, R., Goel, S., Hong, H., Chen, F., Valdovinos, H. F., Hernandez, R., et al. (2015). Hollow mesoporous silica nanoparticles for tumor vasculature targeting and PET image-guided drug delivery. *Nanomedicine* 10, 1233–1246. doi:10.2217/nnm.14.226

Chernenko, T., Matthäus, C., Milane, L., Quintero, L., Amiji, M., Diem, M., et al. (2009). Label-free Raman spectral imaging of intracellular delivery and degradation of polymeric nanoparticle systems. *ACS Nano* 3, 3552–3559. doi:10.1021/nn9010973

Choi, D. H., Kim, K. H., Park, J. S., Jeong, S. H., and Park, K. (2013). Evaluation of drug delivery profiles in geometric three-layered tablets with various mechanical properties, *in vitro-in vivo* drug release, and Raman imaging. *J. Control. Release* 172, 763–772. doi:10.1016/j.jconrel.2013.08.301

Chu, T. F., Rupnick, M. A., Kerkela, R., Dallabrida, S. M., Zurakowski, D., Nguyen, L., et al. (2007). Cardiotoxicity associated with tyrosine kinase inhibitor sunitinib. *Lancet* 370, 2011–2019. doi:10.1016/S0140-6736(07)61865-0

Cordero, E., Latka, I., Matthäus, C., Schie, I. W., and Popp, J. (2018). *In-vivo* Raman spectroscopy: From basics to applications. *J. Biomed. Opt.* 23, 1. doi:10.1117/1.JBO.23.7.071210

Crowley, L. C., Marfell, B. J., Scott, A. P., Boughaba, J. A., Chojnowski, G., Christensen, M. E., et al. (20162016). Dead cert: Measuring cell death. *Cold Spring Harb. Protoc.*, top070318. doi:10.1101/pdb.top070318

Demetri, G. D., van Oosterom, A. T., Garrett, C. R., Blackstein, M. E., Shah, M. H., Verweij, J., et al. (2006). Efficacy and safety of sunitinib in patients with advanced gastrointestinal stromal tumour after failure of imatinib: A randomised controlled trial. *Lancet* 368, 1329–1338. doi:10.1016/S0140-6736(06)69446-4

Eberhardt, K., Stiebing, C., Matthäus, C., Schmitt, M., and Popp, J. (2015). Advantages and limitations of Raman spectroscopy for molecular diagnostics: An update. *Expert Rev. Mol. diagn.* 15, 773–787. doi:10.1586/14737159.2015.1036744

El-Mashtoly, S. F. (2020). Drug distribution in living cells via label-free molecular fingerprint. *J. Med. Chem.* 63, 3472–3474. doi:10.1021/acs.jmedchem.0c00392

Elgendy, M., Abdel-Aziz, A. K., Renne, S. L., Bornaghi, V., Procopio, G., Colecchia, M., et al. (2017). Dual modulation of MCL-1 and mTOR determines the response to sunitinib. *J. Clin. Investig.* 127, 153–168. doi:10.1172/JCI84386

Fornaguera, C., and García-Celma, M. J. (2017). Personalized nanomedicine: A revolution at the nanoscale. *J. Pers. Med.* 7, E12. doi:10.3390/jpm7040012

Gongalsky, M. B., Muftieva, D. A., Saarinen, J. K. S., Isomaki, A., Pervushin, N. V., Kopeina, G. S., et al. (2021a). Nonresonant CARS imaging of porous and solid silicon nanoparticles in human cells. *ACS Biomater. Sci. Eng.*, acsbiomaterials.1c00771. doi:10.1021/acsbiomaterials.1c00771

Gongalsky, M. B., Pervushin, N. V., Maksutova, D. E., Tsurikova, U. A., Putintsev, P. P., Gyuppenen, O. D., et al. (2021b). Optical monitoring of the biodegradation of porous and solid silicon nanoparticles. *Nanomaterials* 11, 2167. doi:10.3390/nano11092167

Gongalsky, M. B., Sviridov, A. P., Bezsudnova, Yu. I., and Osminkina, L. A. (2020). Biodegradation model of porous silicon nanoparticles. *Colloids Surf. B Biointerfaces* 190, 110946. doi:10.1016/j.colsurfb.2020.110946

Gordon, K. C., and McGoverin, C. M. (2011). Raman mapping of pharmaceuticals. *Int. J. Pharm.* 417, 151–162. doi:10.1016/j.ijpharm.2010.12.030

Gorini, S., De Angelis, A., Berrino, L., Malara, N., Rosano, G., Ferraro, E., et al. (2018). Chemotherapeutic drugs and mitochondrial dysfunction: Focus on doxorubicin, trastuzumab, and sunitinib. *Oxid. Med. Cell. Longev.* 2018, 7582730. doi:10.1155/2018/7582730

Gu, L., Hall, D. J., Qin, Z., Anglin, E., Joo, J., Mooney, D. J., et al. (2013). *In vivo* time-gated fluorescence imaging with biodegradable luminescent porous silicon nanoparticles. *Nat. Commun.* 4, 2326. doi:10.1038/ncomms3326

Guo, L., Gong, H., Tang, T.-L., Zhang, B.-K., Zhang, L.-Y., Yan, M., et al. (2021). Crizotinib and sunitinib induce hepatotoxicity and mitochondrial apoptosis in L02 cells via ROS and Nrf2 signaling pathway. *Front. Pharmacol.* 12, 620934. Available at: https://www.frontiersin.org/article/10.3389/fphar.2021.620934 (Accessed June 28, 2022).

Guo, S., Kohler, A., Zimmermann, B., Heinke, R., Stöckel, S., Rösch, P., et al. (2018). Extended multiplicative signal correction based model transfer for Raman spectroscopy in biological applications. *Anal. Chem.* 90, 9787–9795. doi:10.1021/acs.analchem.8b01536

Haupt, L. P., Rebs, S., Maurer, W., Hübscher, D., Tiburcy, M., Pabel, S., et al. (2022). Doxorubicin induces cardiotoxicity in a pluripotent stem cell model of aggressive B cell lymphoma cancer patients. *Basic Res. Cardiol.* 117, 13. doi:10.1007/s00395-022-00918-7

Herino, R., Bomchil, G., Barla, K., Bertrand, C., and Ginoux, J. L. (1987). Porosity and pore size distributions of porous silicon layers. *J. Electrochem. Soc.* 134, 1994–2000. doi:10.1149/1.2100805

Hierarchical Cluster Analysis - Cecil C. Bridges (1966). *Hierarchical cluster Analysis - Cecil C. Bridges*. Available at: https://journals.sagepub.com/doi/10.2466/pr0.1966.18.3.851 (Accessed May 24, 2022).

HORIBA (2021). *Raman Spectroscopy for proteins*. Available at: https://www.horiba.com/fileadmin/uploads/Scientific/Documents/Raman/HORIBA_webinar_proteins.pdf.

Karbowski, M., and Youle, R. J. (2003). Dynamics of mitochondrial morphology in healthy cells and during apoptosis. *Cell. Death Differ.* 10, 870–880. doi:10.1038/sj.cdd.4401260

Kirchberger-Tolstik, T., Pradhan, P., Vieth, M., Grunert, P., Popp, J., Bocklitz, T. W., et al. (2020). Towards an interpretable classifier for characterization of endoscopic mayo scores in ulcerative colitis using Raman spectroscopy. *Anal. Chem.* 92, 13776–13784. doi:10.1021/acs.analchem.0c02163

Korashy, H. M., Al-Suwayeh, H. A., Maayah, Z. H., Ansari, M. A., Ahmad, S. F., Bakheet, S. A., et al. (2015). Mitogen-activated protein kinases pathways mediate the sunitinib-induced hypertrophy in rat cardiomyocyte H9c2 cells. *Cardiovasc. Toxicol.* 15, 41–51. doi:10.1007/s12012-014-9266-y

Krafft, C., Dietzek, B., and Popp, J. (2009). Raman and CARSmicrospectroscopy of cells and tissues. *Analyst* 134, 1046–1057. doi:10.1039/B822354H

Lasagna-Reeves, C., Gonzalez-Romero, D., Barria, M. A., Olmedo, I., Clos, A., Sadagopa Ramanujam, V. M., et al. (2010). Bioaccumulation and toxicity of gold nanoparticles after repeated administration in mice. *Biochem. Biophys. Res. Commun.* 393, 649–655. doi:10.1016/j.bbrc.2010.02.046

Lazebnik, Y. A., Kaufmann, S. H., Desnoyers, S., Poirier, G. G., and Earnshaw, W. C. (1994). Cleavage of poly(ADP-ribose) polymerase by a proteinase with properties like ICE. *Nature* 371, 346–347. doi:10.1038/371346a0

Lehmann, V., Stengl, R., and Luigart, A. (2000). On the morphology and the electrochemical formation mechanism of mesoporous silicon. *Mater. Sci. Eng. B* 70, 11–22. doi:10.1016/S0921-5107(99)00286-X

Lin, Q., Cong, X., and Yun, Z. (2011). Differential hypoxic regulation of hypoxia-inducible factors 1alpha and 2alpha. *Mol. Cancer Res.* 9, 757–765. doi:10.1158/1541-7786.MCR-11-0053

Litti, L., Amendola, V., Toffoli, G., and Meneghetti, M. (2016). Detection of low-quantity anticancer drugs by surface-enhanced Raman scattering. *Anal. Bioanal. Chem.* 408, 2123–2131. doi:10.1007/s00216-016-9315-4

Matthäus, C., Chernenko, T., Quintero, L., Miljković, M., Milane, L., Kale, A., et al. (2011). "Raman micro-spectral imaging of cells and intracellular drug delivery using nanocarrier systems," in Confocal Raman microscopy *springer series in optical Sciences*. Editors T. Dieing, O. Hollricher, and J. Toporski (Berlin, Heidelberg: Springer), 137–163. doi:10.1007/978-3-642-12522-5_7

Matthaus, C., Kale, A., Chernenko, T., Torchilin, V., and Diem, M. (2008). New ways of imaging uptake and intracellular fate of liposomal drug carrier systems inside individual cells, based on Raman microscopy. *Mol. Pharm.* 5, 287–293. doi:10.1021/mp7001158

Maximchik, P. V., Tamarov, K., Sheval, E. V., Tolstik, E., Kirchberger-Tolstik, T., Yang, Z., et al. (2019). Biodegradable porous silicon nanocontainers as an effective drug carrier for regulation of the tumor cell death pathways. *ACS Biomater. Sci. Eng.* 5, 6063–6071. doi:10.1021/acsbiomaterials.9b01292

Merches, K., Breunig, L., Fender, J., Brand, T., Bätz, V., Idel, S., et al. (2022). The potential of remdesivir to affect function, metabolism and proliferation of cardiac and kidney cells *in vitro*. *Arch. Toxicol.* 96, 2341–2360. doi:10.1007/s00204-022-03306-1

Moghimi, S. M., Hunter, A. C., and Murray, J. C. (2001). Long-circulating and target-specific nanoparticles: Theory to practice. *Pharmacol. Rev.* 53, 283–318.

Morháč, M., and Matoušek, V. (2008). Peak clipping algorithms for background estimation in spectroscopic data. *Appl. Spectrosc.* 62, 91–106. doi:10.1366/000370208783412762

Motzer, R. J., Hutson, T. E., Tomczak, P., Michaelson, M. D., Bukowski, R. M., Rixe, O., et al. (2007). Sunitinib versus interferon alfa in metastatic renal-cell carcinoma. *N. Engl. J. Med.* 356, 115–124. doi:10.1056/NEJMoa065044

Osminkina, L. A., and Gongalsky, M. B. (2016). "Porous silicon suspensions and colloids,". *Handbook of porous silicon*. Editor L. Canham (Cham: Springer International Publishing), 1–19. doi:10.1007/978-3-319-04508-5_125-1

Osminkina, L. A., and Gongalsky, M. B. (2018). "Porous silicon suspensions and colloids," in *Handbook of porous silicon*. Editor L. Canham (Cham: Springer International Publishing), 227–245. doi:10.1007/978-3-319-71381-6_125

Osminkina, L. A., Tamarov, K. P., Sviridov, A. P., Galkin, R. A., Gongalsky, M. B., Solovyev, V. V., et al. (2012). Photoluminescent biocompatible silicon nanoparticles for cancer theranostic applications. *J. Biophot.* 5, 529–535. doi:10.1002/jbio.201100112

Pai, V. B., and Nahata, M. C. (2000). Cardiotoxicity of chemotherapeutic agents: Incidence, treatment and prevention. *Drug Saf.* 22, 263–302. doi:10.2165/00002018-200022040-00002

Palmer, J. A., Smith, A. M., Gryshkova, V., Donley, E. L. R., Valentin, J.-P., Burrier, R. E., et al. (2020). A targeted metabolomics-based assay using human induced pluripotent stem cell-derived cardiomyocytes identifies structural and functional cardiotoxicity potential. *Toxicol. Sci.* 174, 218–240. doi:10.1093/toxsci/kfaa015

Park, J.-H., Gu, L., von Maltzahn, G., Ruoslahti, E., Bhatia, S. N., Sailor, M. J., et al. (2009). Biodegradable luminescent porous silicon nanoparticles for *in vivo* applications. *Nat. Mat.* 8, 331–336. doi:10.1038/nmat2398

Pearson, K. (1901). LIII. On lines and planes of closest fit to systems of points in space. *Lond. Edinb. Dublin Philosophical Mag. J. Sci.* 2, 559–572. doi:10.1080/14786440109462720

Peng, F., Su, Y., Wei, X., Lu, Y., Zhou, Y., Zhong, Y., et al. (2013). Silicon-nanowire-based nanocarriers with ultrahigh drug-loading capacity for *in vitro* and *in vivo* cancer therapy. *Angew. Chem. Int. Ed. Engl.* 52, 1457–1461. doi:10.1002/anie.201206737

Peng, F., Su, Y., Zhong, Y., Fan, C., Lee, S.-T., He, Y., et al. (2014). Silicon nanomaterials platform for bioimaging, biosensing, and cancer therapy. *Acc. Chem. Res.* 47, 612–623. doi:10.1021/ar400221g

Petersen, D., Mavarani, L., Niedieker, D., Freier, E., Tannapfel, A., Kötting, C., et al. (2017). Virtual staining of colon cancer tissue by label-free Raman micro-spectroscopy. *Analyst* 142, 1207–1215. doi:10.1039/c6an02072k

Plesca, D., Mazumder, S., and Almasan, A. (2008). DNA damage response and apoptosis. *Methods Enzymol.* 446, 107–122. doi:10.1016/S0076-6879(08)01606-6

Pliss, A., Kuzmin, A. N., Kachynski, A. V., and Prasad, P. N. (2010). Nonlinear optical imaging and Raman microspectrometry of the cell nucleus throughout the cell cycle. *Biophys. J.* 99, 3483–3491. doi:10.1016/j.bpj.2010.06.069

Rajput, A., Martin, I. D. S., Rose, R., Beko, A., LeVea, C., Sharratt, E., et al. (2008). Characterization of HCT116 human colon cancer cells in an orthotopic model. *J. Surg. Res.* 147, 276–281. doi:10.1016/j.jss.2007.04.021

Risi, R., Manti, L., Perna, G., Lasalvia, M., Capozzi, V., Delfino, I., et al. (2012). "X-ray radiation-induced effects in human mammary epithelial cells investigated by Raman microspectroscopy," in *Biophotonics: Photonic solutions for better Health care III* (SPIE), 437–446. doi:10.1117/12.921389

Ryabchykov, O., Bocklitz, T., Ramoji, A., Neugebauer, U., Foerster, M., Kroegel, C., et al. (2016). Automatization of spike correction in Raman spectra of biological samples. *Chemom. Intell. Lab. Syst.* 155, 1–6. doi:10.1016/j.chemolab.2016.03.024

Ryabchykov, O., Popp, J., and Bocklitz, T. (2018). Fusion of MALDI spectrometric imaging and Raman spectroscopic data for the analysis of biological samples. *Front. Chem.* 6, 257. doi:10.3389/fchem.2018.00257

Sailor, M. J. (2022). *Porous silicon in practice: Preparation, characterization and applications.* Available at: https://www.wiley.com/en-us/Porous+Silicon+in+Practice%3A+Preparation%2C+Characterization+and+Applications-p-9783527313785 (Accessed May 31, 2022).

Schindelin, J., Arganda-Carreras, I., Frise, E., Kaynig, V., Longair, M., Pietzsch, T., et al. (2012). Fiji: An open-source platform for biological-image analysis. *Nat. Methods* 9, 676–682. doi:10.1038/nmeth.2019

Silva, J. M. da, Lima, B. da S., Araújo, T. L. de, Lima, F. E. T., and Cunha, G. H. da (2018). Cardiovascular adverse events associated with oral antineoplastic therapy. *Rev. Bras. Enferm.* 71, 2561–2569. doi:10.1590/0034-7167-2017-0450

Sun, J., Sun, Q., Brown, M. F., Dudgeon, C., Chandler, J., Xu, X., et al. (2012). The multi-targeted kinase inhibitor sunitinib induces apoptosis in colon cancer cells via PUMA. *PLOS ONE* 7, e43158. doi:10.1371/journal.pone.0043158

Tarasi, F., Lanza, P. A., Ferretti, V., Echeverría, G. A., Piro, O. E., Cacicedo, M., et al. (2022). Synthesis and characterization of novel copper(II)-Sunitinib complex: Molecular docking, DFT studies, Hirshfeld analysis and cytotoxicity studies. *Inorganics* 10, 3. doi:10.3390/inorganics10010003

Tolstik, E., Ali, N., Guo, S., Ebersbach, P., Möllmann, D., Arias-Loza, P., et al. (2022). CARS imaging advances early diagnosis of cardiac manifestation of Fabry disease. *Int. J. Mol. Sci.* 23, 5345. doi:10.3390/ijms23105345

Tolstik, E., Osminkina, L. A., Akimov, D., Gongalsky, M. B., Kudryavtsev, A. A., Timoshenko, V. Y., et al. (2016a). Linear and non-linear optical imaging of cancer cells with silicon nanoparticles. *Int. J. Mol. Sci.* 17, E1536. doi:10.3390/ijms17091536

Tolstik, E., Osminkina, L. A., Matthäus, C., Burkhardt, M., Tsurikov, K. E., Natashina, U. A., et al. (2016b). Studies of silicon nanoparticles uptake and biodegradation in cancer cells by Raman spectroscopy. *Nanomedicine* 12, 1931–1940. doi:10.1016/j.nano.2016.04.004

Tomasovic, A., Brand, T., Schanbacher, C., Kramer, S., Hümmert, M. W., Godoy, P., et al. (2020). Interference with ERK-dimerization at the nucleocytosolic interface targets pathological ERK1/2 signaling without cardiotoxic side-effects. *Nat. Commun.* 11, 1733. doi:10.1038/s41467-020-15505-4

Wan, X., Min, Y., Bludau, H., Keith, A., Sheiko, S. S., Jordan, R., et al. (2018). Drug combination synergy in worm-like polymeric micelles improves treatment outcome for small cell and non-small cell lung cancer. *ACS Nano* 12, 2426–2439. doi:10.1021/acsnano.7b07878

Wold, S., Esbensen, K., and Geladi, P. (1987). Principal component analysis. *Chemom. Intell. Lab. Syst.* 2, 37–52. doi:10.1016/0169-7439(87)80084-9

Yao, Y., Zhou, Y., Liu, L., Xu, Y., Chen, Q., Wang, Y., et al. (2020). Nanoparticle-based drug delivery in cancer therapy and its role in overcoming drug resistance. *Front. Mol. Biosci.* 7, 193. doi:10.3389/fmolb.2020.00193

Yosef, H. K., Krauß, S. D., Lechtonen, T., Jütte, H., Tannapfel, A., Käfferlein, H. U., et al. (2017). Noninvasive diagnosis of high-grade urothelial carcinoma in urine by Raman spectral imaging. *Anal. Chem.* 89, 6893–6899. doi:10.1021/acs.analchem.7b01403

Advantages of publishing in Frontiers

OPEN ACCESS
Articles are free to read for greatest visibility and readership

FAST PUBLICATION
Around 90 days from submission to decision

HIGH QUALITY PEER-REVIEW
Rigorous, collaborative, and constructive peer-review

TRANSPARENT PEER-REVIEW
Editors and reviewers acknowledged by name on published articles

Frontiers
Avenue du Tribunal-Fédéral 34
1005 Lausanne | Switzerland

Visit us: www.frontiersin.org
Contact us: frontiersin.org/about/contact

REPRODUCIBILITY OF RESEARCH
Support open data and methods to enhance research reproducibility

DIGITAL PUBLISHING
Articles designed for optimal readership across devices

FOLLOW US
@frontiersin

IMPACT METRICS
Advanced article metrics track visibility across digital media

EXTENSIVE PROMOTION
Marketing and promotion of impactful research

LOOP RESEARCH NETWORK
Our network increases your article's readership